

**Development and characterisation of different inorganic  
biocomposite materials suitable for craniofacial  
reconstruction: An in vitro and in vivo approach**

**Thesis**

Submitted by

**Arnab Mahato**

(Index No.: 99/15/Chem./24)

(Examination Roll no.: PHDCHEM15249)

**Doctor of Philosophy (Science)**

**Department of Chemistry**

**Faculty of Science**

**Jadavpur University**

**Kolkata, India**

**May 2022**

**Dedicated to:**

my parents in love and gratitude...

## ACKNOWLEDGEMENTS

First and foremost, I would like to express my deepest gratitude to my Dad, without whom I couldn't even dreamt of doing research. I offer my sincere gratitude to my moms, as they were my backbone throughout my research tenure, in absence of my Dad. My moms have been a constant support system for me. Not only they supported and loved me throughout my life, but also taught how to keep patient during the stressful times of life. I want to acknowledge them for always inspiring me to be a strong and hardworking person like them.

I take this opportunity to express my deep respect and sincere gratitude to my esteemed supervisor, Dr. Biswanath Kundu, Principal Scientist, Bioceramics & Coating Division, CSIR- Central Glass & Ceramic Research Institute, Kolkata. He has been an excellent friend, mentor, and an encouraging scientist. During the whole tenure he continuously pushed me, taught me, guided me to be a better researcher, as well as a better human being. His continuous effort to do research with a motive to help humankind directly always gain my respect. He is so hard-working that he inspired us to work more than our abilities.

I would also like to express my gratitude to my supervisor, Dr. Vamsi Krishna Balla, Chief Scientist & Head, Bioceramics & Coating Division, CSIR- Central Glass & Ceramic Research Institute, Kolkata. He has been an excellent support in every step of my research. Without his valuable instruction or suggestion, it couldn't be possible.

I am also grateful to Dr. Samit K. Nandi, Department of Veterinary Surgery and Radiology, West Bengal University of Animal and Fishery Sciences (WBUAFS), Kolkata. Without his help *in vivo* assessments could not be possible. Not only assessments, but he was also always by my side throughout the journey. Without his support it could not be possible.

I would also like to express my respect to Dr. Sandip Bysakh, Senior Scientist & Head, Materials Characterization & Instrumentation Division, CSIR- Central Glass & Ceramic Research Institute, Kolkata. He had devoted so much effort in giving me insight of SEM/TEM whenever I asked. His continuous help made the characterizations way better than what I might have done.

Financial assistance for this research was provided by Central Scientific & Industrial Research (CSIR). I acknowledge the infrastructural assistance given by the Institute authorities. I am thankful to my thesis committee for their contribution to the completion of this manuscript.

I would like to mention each and every technician from our department and other departments. Specially, Ujjwal da, Swapan da, Anath da, Mouli da, Pradeep and Ajay da. Without your help I couldn't be able to complete my research.

I would like to express my sincere gratitude to Dr Somnath Dutta (retired) and, for sharing their immense knowledge during my initial days in the research field.

I also acknowledge indebtedness for the invaluable help of the books, journals, and reports, mentioned in the references.

Finally, I would love to thank my lab mates Akrity Anand and Himank, for their guidance and support throughout this research. Thank you for sharing your opinions and positive inputs.

Thank you all for your cooperation, love, and affection. You have upheld me through many challenging times. I am a more contented person because of you, and I can complete this thesis for all of you.

(Arnab Mahato)

## ABSTRACT

**Title of the thesis:** Development and characterisation of different inorganic biocomposite materials suitable for craniofacial reconstruction: An *in vitro* and *in vivo* approach

Craniofacial bone reconstruction is preferred to correct large skull bone defects arising from the treatment of tumours, infections, trauma intracranial haemorrhage or necrosis. These defects cause both functional and aesthetic discomfort to patients. In worse case, this may cause swelling of brain tissue for which suitable solution is required. There is a long history of reconstructing large skull bone defects with autogenous bone, and it remains the gold standard of treatments. But disadvantages of this type of reconstruction are related to possible infection of the bone graft, donor site morbidity, and cumbersome handling of the bone graft.

To overcome these concerns, several alloplastic materials including metals, plastic, ceramics, and composites are used with limited success and most importantly these never achieved patient compliance. For reconstruction, patient specific implants can be manufactured directly or indirectly. Each method has a set of advantages and disadvantages and till now no perfect solution for craniofacial reconstruction is available.

Thus, in the present investigation biocompatible and osteoconductive composites were fabricated using HAp and bioinert E-glass as base or matrix. Nano-hydroxyapatite (n-HAp) was developed by sol-gel method (with Ca/P molar ratio close to 1.67) and suitably applied/ coated on E-glass substrates. Thorough physical, chemical, mechanical, and biological characterisation was carried out. XRD, FTIR, Raman spectroscopy were undertaken for phase analysis and evaluation, while FESEM-EDAX, TEM for detailed layer-wise microstructural characterisation; MTT assay, SEM and cell viability using MG63 and NIH3T3 cell line. Also *in vitro* studies, cell proliferation by Alamar blue assay, alkaline phosphatase assay, gene expression by real-time RT-PCR, and mineralization assay by ARS staining were done to predict the nature of the sample *in vivo*.

In our second study we tried to assess the beneficial effects of  $\text{Sr}^{2+}$  and  $\text{Li}^{+}$  doping on *in vivo* bone formation of an interconnected bioactive glass porous scaffold developed in the laboratory through rabbit bone defect model. Detailed phase, composition and microstructure analysis were performed prior using tools like X-ray diffraction (XRD), Fourier transformed infrared spectroscopy (FTIR), differential thermal analysis-thermo-gravimetric analysis (DTA-TGA), quantitative EDAX analysis and scanning electron microscopy (SEM) respectively. The scaffolds were also assessed for its bioactivity in contact with simulated body fluid (SBF) and *in vitro* cyto-toxicity by MTT assay using NIH3T3. The *in vivo* bone regeneration was analysed using chronological radiography, fluorochrome labelling, SEM, histology, and micro-computed tomography ( $\mu$ -CT).

On the other hand, plasma spray grade HAp and bioactive glass (S53P4) granules were used for coating on commercially available Mg-alloy implant varying the coating parameters including current, voltage, stand-off distance, powder flowability and primary/secondary gas. Mg-alloy is known for their bioresorbable properties with higher degree of corrosion *in vitro*. HAp/S53P4 coating on the substrate, thus, not only act as a source for bone bonding interface, but also protects from corrosion when used in physiological fluid. As before the coated substrates were studied for different physical, chemical, mechanical, and biological characterisation including XRD, FTIR, Raman spectroscopy for phase analysis and evaluation; FESEM-EDAX at the interface for detailed layer-wise microstructural characterisation; electrochemical corrosion test using SBF solution. *In vitro* biocompatibility assessments like cell viability and proliferation assay using MG63 cell line, alkaline phosphatase assay,

mineralization assay by ARS staining, gene expression by real time RT-PCR, cell morphology within the scaffold constructs by Laser confocal, were done prior to *in vivo* study.

### Publications from the work:

#### In Journals:

- 1) **A. Mahato**, M. De, P. Bhattacharjee, V. Kumar, P. Mukherjee, G. Singh, B. Kundu, V.K. Balla, S.K. Nandi, J. Mater. Sci.: Mater. Med., 32 (2021) 55. **(Impact factor: 3.896)**
- 2) **A. Mahato**, P.K. Khan, B. Kundu, S.K. Nandi, P. Mukherjee, S. Datta, S. Sarkar, J. Mukherjee, S. Nath, V.K. Balla, Nature Scientific Reports 6 (2016) 32964. **(Impact factor: 4.380)**
- 3) **A. Mahato**, Z. Sandy, S. Bysakh, L. Hupa, I. Das, P. Bhattacharjee, B. Kundu, G. De, S.K. Nandi, P. Vallittu, Mater. Sci. Eng.: C 111 (2020) 110764. **(Impact factor: 7.328)**
- 4) **A. Mahato**, B. Kundu, P. Mukherjee, S.K. Nandi, Trans. Ind. Ceram. Soc. 76(3) (2017) 149-158. **(Impact factor: 1.729)**

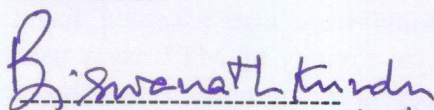
#### In Book Chapters:

- 1) **A. Mahato**, B. Kundu, Bioactive glass based composites for cranioplasty implants, in: G. Kaur (Ed.) Clinical Applications of Biomaterials: State-of-the-Art Progress, Trends, and Novel Approaches, **Springer**, Gewerbestrasse, Switzerland, 2017, pp. 337-356.
- 2) S.K. Nandi, **A. Mahato**, B. Kundu, P. Mukherjee, Doped bioactive glass materials in bone regeneration, in: A.R. Zorzi, J.B. de Miranda (Eds.) Advanced Techniques in Bone Regeneration, **InTech Open**, Rijeka, Croatia, 2016, pp. 275.
- 3) S.K. Nandi, **A. Mahato**, B. Kundu, P. Mukherjee, Organic-inorganic micro/nanofiber composites for biomedical applications, in: V. Grumezescu, A.M. Grumezescu (Eds.) Materials for Biomedical Engineering: Biopolymer Fibers, **Elsevier**, Bucharest, Romania, 2019, pp. 21-55.
- 4) P. Barua, **A. Mahato**, P. Datta, S.K. Nandi, R. Sen, B. Kundu, Fiber-nano bio-compositions for cranioplasty and other orthopaedic applications, in: B. Han, S. Sharma, T.A. Nguyen, K. Subrahmanya Bhat, L. Longbiao (Eds.) Fiber-Reinforced Nanocomposites: Fundamentals and Applications, **Elsevier**, Amsterdam, Netherlands, 2020, pp. 525-558.

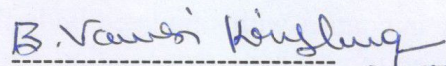
Arnab Mahato  
12/05/2022

(Arnab Mahato)

Forwarded.



Dr. Biswanath Kundu 12/05/2022  
Principal Scientist & Supervisor  
Bioceramics and Coating Division  
CSIR-Central Glass and Ceramic  
Research Institute,  
196, Raja S.C. Mullick Road,  
P.O. Jadavpur University  
Kolkata 700032, India



Dr. Vamsi K. Balla 12/05/2022  
Chief Scientist, HoD & Co-Supervisor  
Bioceramics and Coating Division  
CSIR-Central Glass and Ceramic  
Research Institute  
196, Raja S.C. Mullick Road,  
P.O. Jadavpur University  
Kolkata 700032, India

डॉ० विश्वनाथ कुंडू / Dr. Biswanath Kundu  
प्रमुख वैज्ञानिक / Principal Scientist  
सीएसआईआर - केंद्रीय काँव एवं सिरामिक अनुसंधान संस्थान  
(विज्ञान और प्रौद्योगिकी मंत्रालय के अधीन, भारत सरकार)  
CSIR - Central Glass & Ceramic Research Institute  
(Under Ministry of Science & Technology, Govt. of India)  
196, राजा एस. सी. मुल्लिक रोड / Raja S C Mullick Road  
कोलकाता / Kolkata 700032, भारत / India

डॉ० वंशु क. बल्ल / DR. VAMSI K. BALLA  
वरिष्ठ प्रमुख वैज्ञानिक एवं प्रमुख / Sr. Principal Scientist & Head  
बायोसिरामिक एवं काँव विभाग / Bio-Ceramics & Coating Division  
सिरेमिक-केंद्रीय काँव एवं सिरामिक अनुसंधान संस्थान  
CSIR-Central Glass & Ceramic Research Institute  
कोलकाता / Kolkata - 700 032, भारत / India

## 1. List of publications:

### a. In Book Chapters:

- (i) **A. Mahato**, B. Kundu, Bioactive glass based composites for cranioplasty implants, in: G. Kaur (Ed.) Clinical Applications of Biomaterials: State-of-the-Art Progress, Trends, and Novel Approaches, **Springer**, Gewerbestrasse, Switzerland, 2017, pp. 337-356.
- (ii) S.K. Nandi, **A. Mahato**, B. Kundu, P. Mukherjee, Doped bioactive glass materials in bone regeneration, in: A.R. Zorzi, J.B. de Miranda (Eds.) Advanced Techniques in Bone Regeneration, **InTech Open**, Rijeka, Croatia, 2016, pp. 275.
- (iii) S.K. Nandi, **A. Mahato**, B. Kundu, P. Mukherjee, Organic-inorganic micro/nanofiber composites for biomedical applications, in: V. Grumezescu, A.M. Grumezescu (Eds.) Materials for Biomedical Engineering: Biopolymer Fibers, **Elsevier**, Bucharest, Romania, 2019, pp. 21-55.
- (iv) P. Barua, **A. Mahato**, P. Datta, S.K. Nandi, R. Sen, B. Kundu, Fiber-nano bio-compositions for cranioplasty and other orthopaedic applications, in: B. Han, S. Sharma, T.A. Nguyen, K. Subrahmanya Bhat, L. Longbiao (Eds.) Fiber-Reinforced Nanocomposites: Fundamentals and Applications, **Elsevier**, Amsterdam, Netherlands, 2020, pp. 525-558.

### b. In SCI Journals:

- (i) **A. Mahato**, M. De, P. Bhattacharjee, V. Kumar, P. Mukherjee, G. Singh, B. Kundu, V.K. Balla, S.K. Nandi, Role of calcium phosphate and bioactive glass coating on in vivo bone healing of new Mg-Zn-Ca implant, **Journal of Materials Science: Materials in Medicine** 32 (2021) 55. **(Impact factor: 3.896)**
- (ii) **A. Mahato**, P.K. Khan, B. Kundu, S.K. Nandi, P. Mukherjee, S. Datta, S. Sarkar, J. Mukherjee, S. Nath, V.K. Balla, Influence of single and binary doping of strontium and lithium on in vivo biological properties of bioactive glass scaffolds, **Nature Scientific Reports** 6 (2016) 32964. **(Impact factor: 4.380)**
- (iii) **A. Mahato**, Z. Sandy, S. Bysakh, L. Hupa, I. Das, P. Bhattacharjee, B. Kundu, G. De, S.K. Nandi, P. Vallittu, Development of nano-porous hydroxyapatite coated e-glass for potential bone-tissue engineering application: An in vitro approach, **Materials Science and Engineering: C** 111 (2020) 110764. **(Impact factor: 7.328)**
- (iv) **A. Mahato**, B. Kundu, P. Mukherjee, S.K. Nandi, Applications of different bioactive glass and glass-ceramic materials for osteoconductivity and

- osteointegrability, Transactions of the Indian Ceramic Society 76(3) (2017) 149-158. **(Impact factor: 1.729)**
- (v) C. Soundrapandian, **A. Mahato**, B. Kundu, S. Datta, B. Sa, D. Basu, Development and effect of different bioactive silicate glass scaffolds: In vitro evaluation for use as a bone drug delivery system, Journal of the Mechanical Behavior of Biomedical Materials 40 (2014) 1-12. **(Impact factor: 3.902)**
- (vi) I. Das, S. Chattopadhyay, **A. Mahato**, B. Kundu, G. De, Fabrication of a cubic zirconia nanocoating on a titanium dental implant with excellent adhesion, hardness and biocompatibility, *RSC Advances* 6(64) (2016) 59030-59038.
- (vii) S.K. Nandi, B. Kundu, **A. Mahato**, N.L. Thakur, S.N. Joardar, B.B. Mandal, In vitro and in vivo evaluation of the marine sponge skeleton as a bone mimicking biomaterial, *Integrative Biology* 7(2) (2015) 250-262.
- (viii) S.K. Nandi, B. Kundu, **A. Mahato**, P. Das, P. Mukherjee, In vivo performance analysis of snail extract incorporated coralline hydroxyapatite in bone healing, *The Global Journal of Environmental Sciences and Research* 2 (2015) 45-52.
- (ix) S. Dutta, K.B. Devi, S. Mandal, **A. Mahato**, S. Gupta, B. Kundu, V.K. Balla, M. Roy, In vitro corrosion and cytocompatibility studies of hot press sintered magnesium-bioactive glass composite, *Materialia* 5 (2019) 100245.
- (x) S.K. Nandi, B. Kundu, J. Mukherjee, **A. Mahato**, S. Datta, V.K. Balla, Converted marine coral hydroxyapatite implants with growth factors: In vivo bone regeneration, *Materials Science and Engineering: C* 49 (2015) 816-823.

## 2. List of Presentations in National/ International:

- (i) **A. Mahato**, B. Kundu, D. Zhang, I. Das, L. Hupa, G. De, P. Vallittu, Development of nano-porous hydroxyapatite coated e-glass for potential bone-tissue engineering application: An in vitro approach, Workshop on Nanoengineering in Medicine (NANOENG.MED 2014), All India Institute of Medical Sciences (AIIMS), New Delhi, 2014. **(Invited Talk)**; *Later published in Journal of Biotechnology and Biomaterials* 5 (2015) 159.
- (ii) **A. Mahato**, B. Kundu, D. Zhang, I. Das, L. Hupa, G. De, P. Vallittu, A new nano-material option for bone-tissue engineering application: A primary in vitro approach, Second International Conference on Nanostructured Materials and Nanocomposites (ICNM 2014), Mahatma Gandhi University, Kottayam, Kerala, 2014, pp. 34. **(Invited Talk)**
- (iii) **A. Mahato**, B. Kundu, D. Zhang, I. Das, L. Hupa, G. De, P. Vallittu, Development of nano-porous hydroxyapatite coated e-glass for potential bone-tissue



engineering application: An in vitro approach, 26th AGM of MRSI, University of Rajasthan, Jaipur, 2015, pp. 193. **(Poster)**

- (iv) **A. Mahato**, Development and effect of different bioactive silicate glass scaffolds: In vitro evaluation for use as a bone drug delivery system, Research Scholar Day 2015 CSIR-CGCRI Kolkata, 2015, pp. 125. **(Poster)**
- (v) **A. Mahato**, Development of nano-porous hydroxyapatite coated e-glass for potential bone-tissue engineering application: An in vitro approach, Research Scholar Day 2014 CSIR-CGCRI Kolkata, 2014, pp. 57. **(Poster)**

# CERTIFICATE FROM THE SUPERVISOR/S

*This is to certify that the thesis entitled "Development and characterization of different inorganic biocomposite materials for possible craniofacial reconstruction application: An in vitro and in vivo approach" submitted by Shri Arnab Mahato, who got his name registered on 13/04/2015 (Index no. 99/15/Chem./24) for the award of Ph. D. (Sc.) degree of Jadavpur University is absolutely based upon his own work under the supervision of Dr. Biswanath Kundu and Dr. Vamsi K. Balla and that neither his thesis nor any part of the thesis has been submitted for any degree / diploma or any other academic award anywhere before.*

1. Biswanath Kundu

Signature of the Supervisor 12/05/2022  
And date with Office Seal

**डॉ० विश्वनाथ कुंडू / Dr. Biswanath Kundu**  
प्रमुख वैज्ञानिक / Principal Scientist  
सीएसआईआर - केंद्रीय काँच एवं शिवांगिक अनुसंधान संस्थान  
(विज्ञान और प्रौद्योगिकी मंत्रालय के अधीन, भारत सरकार)  
**CSIR - Central Glass & Ceramic Research Institute**  
(Under Ministry of Science & Technology, Govt. of India)  
196, राजा एस. सी. मल्लिक रोड / Raja S C Mullick Road  
कोलकाता / Kolkata 700032, भारत / India

2. B. Vamsi Krishna Balla

Signature of the Supervisor 12/05/2022  
And date with Office Seal

**डॉ० वंशो कृष्ण बल्ल / DR. VAMSI KRISHNA BALLA**  
वरिष्ठ प्रमुख वैज्ञानिक एवं प्रमुख / Sr. Principal Scientist & Head  
बायोसिरेमिक्स एवं कोटिंग विभाग / Bio-Ceramics & Coating Division  
सिएसआईआर-केंद्रीय काँच एवं शिवांगिक अनुसंधान संस्थान  
**CSIR-Central Glass & Ceramic Research Institute**  
कोलकाता / Kolkata - 700 032, भारत / India

# *Table of Contents*

<b>LIST OF TABLES</b>	14
<b>LIST OF FIGURES</b>	15
<b>ABBREVIATIONS AND TERMINOLOGY</b>	19
<b>1. INTRODUCTION</b>	21
<b>2. LITERATURE REVIEW</b>	24
2.1 Cranioplasty	24
2.1.1 History and evolution of cranioplasty	24
2.1.2 Requirements of craniofacial surgery	27
2.1.3 Mechanical properties of cranial bone	28
2.1.4 Requirements for ideal craniofacial implant material	29
2.2 Bone grafting and bone graft substitutes	29
2.2.1 Definition of Bone graft	29
2.2.2 Types of bone graft	30
2.2.2.1 Biological bone graft	30
2.2.2.1.1 Autogenous bone graft	30
2.2.2.1.2 Allogenic bone graft	31
2.2.2.1.3 Xenograft	31
2.2.2.2 Non-biological bone graft	31
2.2.3 Bioactive glass as a craniofacial implant	32
2.2.3.1 Strontium-bioactive glass	34
2.2.3.2 Lithium-bioactive glass	36
2.2.4 E-glass substrate	37
2.2.5 Magnesium and its alloys	37
<b>3. AIMS AND OBJECTIVES</b>	40
<b>4. MATERIALS AND METHODS</b>	43
4.1 HAp coated E-Glass preparation	43
4.1.1 Materials	43
4.1.2 Formation of gel	43
4.1.3 Fabrication of coated e-glass substrates	44
4.1.4 Characterisation of coated e-glass substrates	44
4.1.5. Immersion tests in simulated body fluid (SBF)	46
4.1.6. <i>In vitro</i> biocompatibility study	47
4.1.6.1 Cell culture procedure	47
4.1.6.2 Cell viability assay	47
4.1.6.3 Cell proliferation by Alamar blue assay	48
4.1.6.4 Alkaline Phosphatase assay (ALP)	48
4.1.6.5 Cellular morphology	49
4.1.6.6 Gene expression by real-time RT-PCR	49
4.1.6.7 Mineralization assay by ARS staining	51

4.1.7 Statistics	51
4.2 Li-Sr substituted bioactive glass scaffold preparation	52
4.2.1 Bioactive glass scaffold preparation	52
4.2.2 Bioactive glass powders and scaffold characterization	54
4.2.3 SBF bioactivity study	54
4.2.4 <i>In vitro</i> cell cytotoxicity	55
4.2.5 Cell morphology by SEM	56
4.2.6 <i>In vivo</i> study of rabbit femoral bone defect model	56
4.2.7 Characterization of <i>in vivo</i> samples	58
4.2.8 Statistical analysis	59
4.3 Calcium phosphate and bioactive glass coating on Magnesium alloy	60
4.3.1 Fabrication of samples	60
4.3.1.1 Sample preparation	60
4.3.1.2 Feedstock powder and coating characterization	62
4.3.1.3 Electrochemical corrosion test	63
4.3.1.4 SBF immersion test	64
4.3.2 <i>In vitro</i> biocompatibility assessments	64
4.3.2.1 Cell culture procedure	64
4.3.2.2 Cell viability assay	65
4.3.2.3 Cell proliferation by alamar blue (AB) assay	65
4.3.2.4 Alkaline phosphatase assay (ALP)	66
4.3.2.5 Cellular morphology	66
4.3.2.6 Gene expression by real-time RT-PCR	67
4.3.2.7 Mineralization assay by ARS staining	68
4.3.3 <i>In vivo</i> biocompatibility studies	69
4.3.3.1 Surgical procedure	69
4.3.3.2 Postoperative clinical examinations	70
4.3.3.3 Radiological examinations	70
4.3.4 Histological study	70
4.3.5. Scanning electron microscopy study	71
4.3.6. Fluorochrome labelling study	71
4.3.7. Toxicological study	72
4.3.8. Immunocompatibility study	72
<b>5. RESULTS AND DISCUSSION</b>	73
5.1 HAp coated e-glass characterization	73
5.1.1 Characterisation of the coating	73
5.1.2 SBF immersion study (static and quasi-dynamic)	77
5.1.3. <i>In vitro</i> biocompatibility studies	87
5.1.3.1 Cell viability, proliferation assay and Alkaline Phosphatase assay (ALP)	87
5.1.3.2 Cell morphology within the samples by Laser confocal microscopy	89
5.1.3.3 Gene Expression by real time RT-PCR	90
5.2 Li-Sr substituted bioactive glass scaffold	93
5.2.1 Bioactive glass powder characterization	93

5.2.2 Bioactive glass scaffolds characterization	97
5.2.3 Simulated body fluid (SBF) study	99
5.2.4 <i>In vitro</i> cell cyto-toxicity study	101
5.2.5 Bone in-growth evaluation by micro-CT	104
5.2.6 Radiological examination	108
5.2.7 Histological evaluation	110
5.2.8 Fluorochrome labelling study	113
5.2.9 Scanning electron microscopic (SEM) study	114
5.3. Calcium phosphate and bioactive glass coating on Magnesium alloy	120
5.3.1. Material characterization	120
5.3.1.1. Substrate characterization	120
5.3.1.2. Powder characterization	121
5.3.1.3. Coating characterization	122
5.3.1.4. Electrochemical properties	123
5.3.1.5. SBF immersion test	124
5.3.1.6. <i>In vitro</i> biocompatibility assessments	129
5.3.1.7. Cell morphology	129
5.3.1.8. <i>In vivo</i> studies	132
5.3.1.8.1. Bone histology	132
5.3.1.8.2. Radiology	133
5.3.1.8.3. Fluorochrome labelling study	135
5.3.1.8.4. SEM of bone-implant interface	135
5.3.1.8.5. Toxicity study of vital organs	136
5.3.1.8.6. <i>In vivo</i> immune response	137
<b>6. CONCLUSIONS</b>	148
<b>7. FUTURE SCOPE</b>	150
<b>8. REFERENCES</b>	151
<b>9. PUBLICATIONS</b>	169

## **LIST OF TABLES**

Table 1: Chemical composition of the as-prepared powders by ICP-AES

Table 2: Radiological scoring system (adopted as per Zhukauskas et al.[153])

Table 3: Spray condition used for plasma spray coating of HAp and bioactive glass on Mg-alloy

Table 4: RT-PCR primer sequences (forward and reverse) used in the current gene expression study

Table 5: Nano indentation values of H and E of different samples

Table 6: Band assignments for the peaks obtained for all samples (cf. Fig. 17)

Table 7: A.P. and B.D. data of the porous scaffolds

Table 8: Radiological scoring values of different samples at different time intervals

Table 9: Histological scoring values of different samples at 2 and 4 months

Table 10: Percentage of bone formation through fluorochrome labeling images at two time point of 2 and 4 months

Table 11: FTIR peak analysis after SBF immersion study

## **LIST OF FIGURES**

Fig. 1: Surgical placement of the porous scaffolds (with or without doped BAG).

Fig. 2: (a) XRD patterns [along with bare e-glass substrate (i)], (b) FTIR and (c) Raman spectra acquired from the top coated surface.

Fig. 3: FESEM microstructure of (a) top coated surface and (b) cross-sectional image showing the interface.

Fig. 4: Cross-sectional TEM images of coated e-glass taken at different regions showing the micro/nano-structural features of the coating's depth and the interface (a-c), EDX line scan (d and e) and SAED pattern (f).

Fig. 5: XRD patterns acquired from the top surface after 7 and 14 days of (a) static and (b) quasi-dynamic SBF study [after (i) 7 and (ii) 14 days] [H = hydroxyapatite, H1= calcium phosphate hydroxide and C = calcium carbonate].

Fig. 6: FTIR spectra of the top surface after 7 and 14 days of (a) static and (b) quasi-dynamic SBF study [after (i) 7 and (ii) 14 days].

Fig. 7: Microstructure of top surface after static (a – 7 days and b – 14 days) and quasi-dynamic (c – 7 days and d – 14 days) SBF studies.

Fig. 8: TEM images of different regions after 7 days of static SBF studies; microstructure (a and the inset, b), EDX (c and d) and HRTEM showing crystalline fringes along with SAED pattern in the inset (e).

Fig. 9: TEM images of different regions after 14 days of static SBF studies; microstructure (a and b), EDX (c and d) and SAED pattern (e).

Fig. 10: TEM images of different regions after 7 and 14 days of quasi-dynamic SBF studies; (a, b and c) microstructure and SAED pattern after 7 days and (d, e and f) microstructure and SAED pattern after 14 days.

Fig. 11: Concentration of different ions of supernatant in (a) static and (b) quasi-dynamic SBF study at day 7 and 14.

Fig. 12: Response of osteoblast like cells (MG-63) seeded on e-glass substrate and coated surfaces, cultured for 21 days at 37°C and 5% CO<sub>2</sub> humidified atmosphere; (a) viability (b) proliferation of cells and (c) alkaline phosphatase (ALP) activity, (d) quantification of mineral deposition using ARS staining. \*\*\*  $p < 0.001$ , \*\*  $p < 0.01$  and \*  $p < 0.05$ ,  $n=3$  at each time point.

Fig. 13: Cytoskeletal actin organization and distribution of MG-63 cells grown on (a) e-glass substrate and (b) coated surface at day 7.

Fig. 14: Levels of mRNA for osteogenic specific genes [(a) Runx2, (b) OPN, (c) OCN and (d) COL1) of MG-63 cultured on e-glass substrate and coated surface for 3 weeks. \*\*\*  $p < 0.001$ , \*\*  $p < 0.01$  and \*  $p < 0.05$ , data are presented as mean $\pm$ SD,  $n=3$ .

Fig. 15: DTA profile of as-prepared samples for (a) BAG, (b) L-BAG, (c) S-BAG and (d) LS-BAG.

Fig. 16: XRD patterns of (a) BAG, (b) L-BAG, (c) S-BAG and (d) LS-BAG samples heat treated at their respective temperatures.

Fig. 17: FTIR spectra of (a) BAG, (b) L-BAG, (c) S-BAG and (d) LS-BAG samples heat treated at their respective temperatures.

Fig. 18: SEM microstructure of the porous scaffolds for all compositions (inset: higher magnified site).

Fig. 19: Variations of (a) concentration of supernatant (Ca<sup>2+</sup>, HCO<sub>3</sub><sup>-</sup> and HPO<sub>4</sub><sup>2-</sup>), (b) pH of SBF after days 7 and 14 in contact with the porous scaffolds (BAG, L-BAG, S-BAG and LS-BAG); (c) is the magnified part of HPO<sub>4</sub><sup>2-</sup> (a).

Fig. 20: SEM microstructure of the porous scaffold surface after day 14 of SBF study; for (a) BAG, (b) L-BAG, (c) S-BAG and (d) LS-BAG.



Fig. 21: MTT assay results; calculated OD values for NIH3T3 expressed on the samples of BAG, L-BAG, S-BAG and LS-BAG after days 3 and 7.

Fig. 22: SEM cell morphology on the samples of (a) BAG, (b) L-BAG, (c) S-BAG and (d) LS-BAG after 7 days.

Fig. 23: Serial slices along the Z-axis in micro-CT. Images are obtained for implanted BAG scaffolds. (a) After 2 months; (b) After 4 months.

Fig. 24: Serial slices along the Z-axis in micro-CT. Images are obtained for implanted L-BAG scaffolds. (a) After 2 months; (b) After 4 months.

Fig. 25: Serial slices along the Z-axis in micro-CT. Images are obtained for implanted S-BAG scaffolds. (a) After 2 months; (b) After 4 months.

Fig. 26: Serial slices along the Z-axis in micro-CT. Images are obtained for implanted LS-BAG scaffolds. (a) After 2 months; (b) After 4 months.

Fig. 27: Radiographs taken at '0' day, 1, 2, 3 and 4 months post-operatively implanted with (a) BAG, (b) L-BAG, (c) S-BAG and (d) LS-BAG.

Fig. 28: Histological sections taken after 2 and 4 months post-operatively implanted with (a) BAG, (b) S-BAG, (c) L-BAG and (d) LS-BAG.

Fig. 29: Fluorochrome labeling study (after oxytetracycline markings) taken after 2 and 4 months post-operatively implanted with (a) BAG, (b) S-BAG, (c) L-BAG and (d) LS-BAG.

Fig. 30: SEM images of bone-material (BAG, L-BAG, S-BAG and LS-BAG) interface taken after 2 months (a-d) and 4 months (e-h) post-operatively respectively.

Fig. 31: (A)XRD pattern and (B) FTIR spectra of (a) BM, (b) HAp granules fired at 1250°C, (c) bioactive glass, (d) BMH (• HAp phase) and (e) BMG.

Fig. 32: (A) Top surface FESEM [(a), (b) and (d) for BM, BMH and BMG respectively] and interface FESEM-EDAX [(c) and (e) for BMH and BMG]; (B) Scratch profile of (a) BMH and

(b) BMG [Inset: optical microscope image of surface]; and (C) Tafel plot recorded during corrosion testing in contact with SBF for (a) BM, (b) BMH and (c) BMG samples.

Fig. 33: XRD pattern and FTIR spectra of the samples after 7 and 14 days of SBF test; (A) for BM, (B) for BMH and (C) BMG; (a) & (b) are XRDs and (c) & (d) are FTIRs after 7 and 14 days respectively; [• HAp phase and ■ Mg phase].

Fig. 34: (A) FESEM microstructures after 14 days of SBF study; change of (B) pH, (C) weight and (D) magnesium, calcium & phosphate ion concentration of supernatant of different samples at day 0, 7 and 14; (a) is for BM, (b) is for BMH and (c) is for BMG; '1', '2', '3' stands for three samples of same type.

Fig. 35: MG-63 (A) Cell viability, (B) proliferation, (C) ALP expression and (D) mineralization assay of different samples; (E) cell morphology (by confocal laser microscopy) of (a) BM, (b) BMH and (c) BMG samples.

Fig. 36: Relative gene expressions (normalized by reference gene GAPDH) w.r.t. (A)OPN, (B) OCN, (C) Runx2 and (D) COLI expression of different samples.

Fig. 37: (A) Histology [(i) Haversian canal, (ii) Osteoblasts, (iii) Osteoclasts] (B) Fluorochrome labelling [Blue arrow - new bone formation; Red arrow- old bone] and (C) SEM images of implanted bone samples after 2 months [(a) for BM, (b) for BMH and (c) for BMG].

Fig. 38: (A) Radiographs of BM (a-c), BMH (d-f) and BMG (g-i) implanted bone immediately after implantation (day '0'), 1 month and 2 months post-surgery; (B) Histological images of heart (j-l), kidney (m-o) and liver (p-r) of BM, BMH and BMG implanted at 2 months post-surgery.

Fig. 39: Expressions of (A) TNF- $\alpha$ , (B) IL-2 and (C) IL-6 at 1, 2, 4 and 8 weeks for different samples with the reference of control (normal healthy animals).

Fig. 40: Proposed mechanism of corrosion and apatite formation when immersed in SBF.

## **ABBREVIATIONS AND TERMINOLOGY**

HAp: Hydroxyapatite  
XRD: X-ray powder diffraction  
FTIR: Fourier-transform infrared spectroscopy  
FESEM: Field Emission Scanning Electron Microscope  
EDAX: Energy dispersive X-ray analysis  
TEM: Transmission electron microscopes  
MTT: 3-(4,5-dimethylthiazol-2-yl)-2,5-diphenyltetrazolium bromide  
SEM: Scanning electron microscope  
RT-PCR: Reverse transcription-polymerase chain reaction  
DTA-TGA: Differential Thermal Analysis- Thermogravimetric Analysis  
SBF: Simulated body fluid  
 $\mu$ -CT: Micro-Computed Tomography  
BC: Before Christ  
GPa: Gigapascal  
BV/TV: Bone volume fraction  
PMMA: Polymethyl methacrylate  
PE: Polyethylene  
PEEK: Polyether ether ketone  
cm: Centimetre  
 $\mu$ m: Micrometre  
HCA: Hydroxy-carbonated apatite  
Pa: Pascal  
mL: milli Litre  
ICSD: Inorganic Crystal Structure Database  
PDF: Powder Diffraction File  
EDX: Energy-dispersive X-ray spectroscopy  
mm: milli metre  
keV: kilo electron volt  
QD: Quasi-Dynamic  
pH: Potential of hydrogen  
 $\mu$ N: micro-Newton  
mN: millinewton  
DMEM: Dulbecco's Modified Eagle Medium  
PBS: Phosphate-buffered saline  
h: hour  
ALP: Alkaline Phosphatase  
M: Mol  
 $^{\circ}$ C: degree centigrade  
 $\mu$ L: microlitre  
BSA: Bovine serum albumin  
g: Gram  
cDNA: Complementary Deoxyribonucleic acid  
RNA: Ribonucleic acid  
pmol: Picomoles  
OPN: Osteopontin  
OCN: Osteocalcin

GAPDH: Glyceraldehyde 3-phosphate dehydrogenase  
SD: Standard deviation  
BAG: Bioactive glass scaffold  
L-BAG: Li doped Bioactive glass scaffold  
S-BAG: Sr doped Bioactive glass scaffold  
LS-BAG: Li-Sr doped Bioactive glass scaffold  
ICP-AES: Inductively coupled plasma atomic emission spectroscopy  
NPa: Newton pascal  
T<sub>g</sub>: Glass transition temperature  
AP: Apparent Porosity  
BD: Bulk density  
IMDM: Iscove's Modified Dulbecco's Medium  
DMSO: Dimethylsulfoxide  
FBS: Fetal Bovine Serum  
EDTA: Ethylenediaminetetraacetic acid  
IAEC: Institute Animal Ethics Committee  
BG: Bioactive glass  
BM: Base Mg alloy sample  
BMG: Bioactive glass coated Mg-alloy sample  
BMH: Hydroxyapatite coated Mg-alloy sample  
ID: Internal diameter  
SCE: Saturated calomel electrode  
AB: Alamar blue  
RT: Room temperature  
TNF: Tumour Necrosis Factor  
SAED: Selected area (electron) diffraction  
HRTEM: High-Resolution Transmission Electron Microscopy  
CEG: Coated e-glass sample  
COLI: Collagen type I  
OD: Optical density  
SE: Standard electrode  
XRF: X-ray fluorescence

## 1. INTRODUCTION

Skull serves as home and protecting unit of the brain and other crucial components of central nervous system. And to repair any skull vault defect cranioplasty is important. Cranioplasty is the surgical procedure to repair any cranial defects, congenital or acquired, by insertion of an object (bone or nonbiological materials). Head injuries, cerebral tumors, ischemia, and infections on the calvaria bones like frontal, parietal, temporal and occipital require reconstruction [1-3]. In general, cranioplasty is performed following craniectomy or craniotomy. Complication post-craniectomy includes herniation of the cortex through the bone defect, seizures, subdural effusion, and syndrome of the trephined (i.e., headaches, dizziness, intolerance of vibration and noise, loss of concentration, depression, and anxiety) [4, 5]. The time interval between craniectomy and cranioplasty depends upon various factors like the cause and condition of the defect, age and health of the patient, availability of suitable substitute etc. Major aims of cranioplasty are minimizing the post-craniectomy complications, brain protection and restoring its cosmetic integrity [6]. Cranioplasty ensures biochemical protection of the brain, as well as stabilize normal intracranial pressure, which helps reestablishing the dynamics of cerebrospinal fluid and cerebral blood flow [3, 7-14]. Moreover, cranioplasty also shown to be decrease the incidence of epilepsy and increase social performance.

With its long history, Cranioplasty has always been a subject of conflict for both plastic surgeons and neurosurgeons, because the optimal result depends on a thorough multidisciplinary approach. The stages of the treatment and the surgical steps must be conducted in a well-strategic collaboration by the two specialists to get the best possible outcome [15].

History of reconstruction of large skull bone defects dates back to antiquity. Till then autogenous bone grafts remains the gold standard, which is generally harvested from calvarium, iliac crest, tibia, or fibula [16]. Though use of metal plates in 2000 BC was found where the material used was contingent upon the socioeconomic rank of the patient [17]. With time and extended research, the disadvantages of different grafts pointed out and respectively the use of grafts become more interesting topic of research. Problems like, infection of the bone graft, donor-site morbidity, handling of bone graft, wastage of time reduced the usage of autogenous grafts. According to the source of the graft material, craniofacial implants are being called xenografts, allografts, autogenous bone graft and synthetic materials.

Along with the advantages and disadvantages of the said implants, an ideal craniofacial implant is yet to come. Depending on the research of craniofacial implants and subsequent case studies the ideal material used for cranioplasty would be *radiolucent, resistant to infections, not conductive of heat or cold, resistant to biochemical processes, malleable to fit defects, complete closure of the defect site* [8]. The requirements and expectations from a synthetic graft material are quite high. An ideal graft material should be strong, lightweight, easily shaped, osteoinductive or osteoconductive, and enable osteointegration. The best substitute should have the mechanical properties close to the surrounding bone. It was found that depending upon the species and age a wide range of anisotropic elastic moduli of craniofacial bone can be obtained. The average elastic modulus of cranial bone, both fetal and matured, tested in a three-point bend set-up were  $7.467 \pm 5.39$  GPa (0.5 m/s),  $10.777 \pm 9.38$  GPa (1.0 m/s) and  $15.547 \pm 10.29$  GPa (2.5 m/s), whereas the average porosity of cranial bones was  $13.087 \pm 4.23\%$  and the average percent bone volume (BV/TV) was  $70.847 \pm 10.13\%$ [18].

Several synthetic biomaterials are available for craniofacial bone substitute, such as titanium, polymethylmethacrylate (PMMA), polyethylene (PE), polyetheretherketone (PEEK), hydroxyapatite (HAp), or combinations/ composites of these materials. The principal aim of the current clinical biomaterial research is to address the limitations of now-available materials. Bioactive glasses are a group of non-metallic ceramic biomaterials with osteoconductive, osteoinductive, and bacteriostatic properties which was first introduced in the field by prof. L Hench and his team. Apart from the unique advantageous features of bioactive glass ceramics, their heterogeneous macrostructure restricts their versatility and mechanical strength [19]. Evolution of research in this field evolved the area tremendously and the limitations are now taken care of by going interdisciplinary and making composites with other materials for particular purposes. The components of the composite are chosen very wisely and calculatedly to overcome certain limitations. Composites have an interesting aspect of high adaptiveness and tuneable properties by varying the component ratio which is helpful to fabricate patient specific implants [20-22].

## 2. LITERATURE REVIEW

### 2.1 Cranioplasty

#### 2.1.1 History and evolution of cranioplasty

The first ever report regarding craniofacial reconstruction was written in 1505, though evidence of cranioplasty dates back to 7000 BC [23]. Ancient civilizations like the Incans, the Britons, the Asiatics, the North Africans, and the Polynesians practiced cranioplasty quite experimentally using mostly metals. Socioeconomic rank of the patient decided the type of material to be used. The first documented description of cranioplasty explains the technique used in the 16<sup>th</sup> century written by Fallopius. He proposed that bone could be replaced in cranial fractures if the dura stays intact. Another textbook from 1505 guides the physicians to treat the wounds with the help of xenograft obtained from a goat or a dog. Another well-known and successful cranioplasty published by Van Meekeren in 1668, illustrates a treatment of a Russian man after a word injury using canine xenograft and the outcome was good[24-26]. Bone grafts from dog, ape, goose, rabbit, calf, and eagle have been implanted into humans after boiling. Xenografts were diminished by the high rate of infections and the better outcome of the autografts. In 1821, Walther first successfully transplanted autologous bone graft where the removed bone flap has been attached again on the site. This procedure avoids host-tissue rejection, but the main disadvantage is related to donor site morbidity [26-28]. In 1889, Seydel used pieces of tibia to cover a parietal defect as a plastic reconstruction. Many other bone harvest sites were experimented such as ilium, ribs, sternum, scapula, fascia, etc. however the need of two operative fields creates hesitation. Use of the cranium became more popular comparing other donor sites by the Miil-ler-Konig procedure [29]. These types of grafts can be preserved by cryopreservation or by placing in an abdominal pocket. The common disadvantage related to autologous bone grafts is bone flap resorption causing structural



breakdown. In addition to it, Matsuno et al. showed that autologous bone grafts has very high rates of infection compared to other synthetic materials [30].

As we know that cranioplasty was started by using synthetic materials like metals which resurged in the early 1900s. Metals were experimented excessively till then as they are strong but malleable. Aluminium was the first metal used in cranioplasty but was prone to infect and irritate surrounding tissues. Although gold was used by people with high status, it is unfavourable for general use because of its high cost and softness. In the 20<sup>th</sup> century silver was tested along with gold before and during World War I, but later made obsolete by other advanced materials. After World War I different alloys were investigated and proved as a potential candidate for reconstruction of cranial defects. These included a wide range of metals like platinum, lead, aluminium, tantalum, cobalt, chromium, steel, and their different alloys. During World War II tantalum was largely used due to its bioinert, malleable, and noncorrosive nature [31]. Based on the advances in research and case studies more disadvantages came to notice, and alloying was readily accepted at that time due to their tuneable properties. Alloys are known to bend their properties according to the requirement by changing the metal proportions. This feature made them irresistible for a range of different types of cranial defects. Titanium was introduced in the late 1965 and found that it is better than other metals in biocompatibility and mechanical strength [32-34].

Celluloid, a synthetic plastic was first used as an implant in late 19<sup>th</sup> century; however, it was not completely biocompatible. In the mid-20<sup>th</sup> century, more suitable alternatives of thermoplastic resins were introduced. Methyl methacrylate was discovered in 1939 and introduced in cranioplasty in 1940. It is a polymerised ester of acrylic acid with a compatible mechanical strength. However, the difficulty in the preparation of the implant was a major limitation along with its brittle nature [35]. Despite these drawbacks, PMMA was used widely

in that span of time as a cranial bone graft. Polyethylene was developed in 1936 but used in this field in 1948 in case of smaller cranial defects. The low mechanical strength barred its use for reconstruction of large-size defects [26, 36]. Development of porous polyethylene made it more suitable to use as a bone graft by allowing soft-tissue ingrowth [37, 38]. In the beginning of 21<sup>st</sup> century the modern era of cranioplasty has been initiated in search of patient specific implant. In this era with the specific requirement of the patient like, size, shape, bioactivity, biocompatibility, implantation period etc. the properties of the grafts have been chosen. In order to get grafts with such tuneable properties the horizon of this field increased tremendously, and different new types of implants has been introduced. Also different modifications of old implant materials like calcium phosphates, especially hydroxyapatites; bioactive glasses came to the picture [39]. New polymer materials like PEEK were introduced to cranial reconstruction [3, 40]. Plates and screws of variety of new synthetic resorbable polymers with innovative design were introduced to clinical practice. Research related to bone-forming cell activity at the defect site has been prioritised using a combination of bone particles and growth factors. Also composites of different materials like calcium phosphates, bioactive glasses with a range of different elements, polymers, metals have been experimented extensively to reconstruct cranial defects.

The use of bioactive glass composites in craniofacial application is still limited, but the possibility is enormous as bioactive glass has all the required eligibility as a craniofacial implant and by making composites the possibility will increase further as the properties can be tailored. The aim of this chapter is to draw the attention of the scientists and researchers by summarise the recent advancement of craniofacial implants based on composites of bioactive glass and their studies in craniofacial surgical challenges along with their aftermath. Our discussion tactfully covers the current innovations in implant-material development and fine

tuning together with structural and functional modifications. With the vast versatility of bioactive glass composite materials this area is waiting to be explored more and more.

### 2.1.2 Requirements of craniofacial surgery:

Depending upon the factors like, size, shape and position of the defect, implantation time, mechanical properties of the surrounding bone, age of the patient; the requirements of cranioplastic implants differ. With the aim of making patient specific implant the factors are taken in consideration for the better future of craniofacial reconstruction. The desired properties of the implant can be achieved by making different composites, to use in unique surroundings of the respective patient.

According to the origin, cranial bone defects may be of congenital or acquired. Congenital defects mostly come from craniosynostosis, whereas the acquired cranial bone defects mainly occur as a result from head injury or surgical action upon an intracranial lesion, cranial bone tumour, bone resorption, or osteomyelitis. Tendency of traumatic etiology is higher in children and young people, mostly male. There are two types of bone tumour, primary and secondary which can cause skull defect. Primary bone tumours are namely fibrosarcomas, osteosarcomas, chondrosarcomas, osteomas, etc and secondary bone tumours like dermoids, epidermoids, Ewing sarcomas may affect cranial bones by means of pressure or they may force the bone out of its normal position, even sometimes destroying the bone.

Though the cranial bone defect size is not very significant for surgical purposes, but it is an important parameter for engineering the implant. The materials required and their properties are vastly dependent on the shape and size of the defect. Recently Uygur et al proposed a classification from small-sized (smaller than 25 cm<sup>2</sup>), medium-sized (between 25 to 200 cm<sup>2</sup>) and large sized (larger than 200 cm<sup>2</sup>) defect [41]. However, a standard classification of cranial bone defect size is not available yet.

### 2.1.3 Mechanical properties of cranial bone:

The mechanical properties of skull bones have been extensively characterised and it was found that cranial bone is comprised of a three sandwich type layered structure: external layers are made of compact, high density cortical bone whereas the central layer consists of a low-density, irregularly porous bone structure [18, 42-45]. Studies showed that fetal and adult cranial bones are vastly different in properties. Fetal cranial bone is thin and non-homogeneous which displays a highly directional fibre orientation [46]. With the maturity of the cranium the bones structurally differentiate into a three-layered composite structure. With the structural development, the mechanical properties of the skull bones change diversely. The large variation of the mechanical properties can be attributed to the morphological differences between the subjects.

It was found that depending upon the species and age a wide range of anisotropic elastic moduli of craniofacial bone can be obtained. The average elastic modulus of cranial bone, both fetal and matured, tested in a three-point bend set-up were  $7.467 \pm 5.39$  GPa (0.5 m/s),  $10.777 \pm 9.38$  GPa (1.0 m/s) and  $15.547 \pm 10.29$  GPa (2.5 m/s), whereas the average porosity of cranial bones was  $13.087 \pm 4.23\%$  and the average percent bone volume (BV/TV) was  $70.847 \pm 10.13\%$ . A correlation between percent bone volume (BV) and the elastic modulus ( $r^2=0.1963$ ;  $p=0.0004$ ) and maximum bending stress ( $r^2=0.2708$ ;  $p< 0.0001$ ) was found [18]. These results reported plays very important role in the processing of patient specific implant. The maximum force to failure, the elastic modulus and the maximum bending stress are very significant to make a suitable implant. Porosity and bone thickness are two other important variants which also control the role of the bone graft.

#### 2.1.4 Requirements for ideal craniofacial implant material:

The requirements and expectations of an optimal graft material vary from patient to patient. The complexity of the required properties is increasing day by day. An optimal biomaterial should have certain qualities like mechanical strength, lightweight, easily shaped, osteoinductive or osteoconductive, and have a structure, which enables osseointegration. Density, surface area and porosity are some other properties which also play significant part to make an implant appropriate for application. Depending upon the requirement it can be biodegradable or biostable, and it may be bioinert or bioactive. The suitable structural design would support ingrowth of bone so that the implant could be integrated with the surrounding bone. Hence an implant with porous structure with more size in the range of 50-400  $\mu\text{m}$  is beneficial for osseointegration [47]. Porous structure works as a scaffold for osteoblast cells, which later forms bony ingrowth.

### 2.2 Bone grafting and bone graft substitutes

#### 2.2.1 Definition of Bone graft:

The definition of bone graft as Muschler & Lane is “a bone graft is any implanted material that, alone or in combination with other materials, promotes a bone healing response by providing osteogenic, osteoconductive, or osteoinductive activity to a local site” [48, 49]. The definition of these healing responses is as follow:

**Osteogenesis:** Formation of new bone from osteocompetent cells that survived in the graft.

**Osteoinduction:** Formation of new bone from the differentiation of mesenchymal cells from the host stimulated by osteoinductive proteins such as bone morphogenic proteins (BMP) and insulin-like growth factors 1 and 2 (IGF-1 and -2).

Osteoconduction: Formation of new bone by ingrowth of vascular tissue and mesenchymal cells from the host along a scaffold presented by the graft [50].

## 2.2.2 Types of bone graft

### 2.2.2.1 Biological bone graft

Substances of biological origin include autograft, xenograft, demineralized bone matrix, collagens, stem cells and various osteoinductive growth factors.

#### 2.2.2.1.1 Autogenous bone graft:

When a bone graft is being harvested from the body of the recipient itself, it becomes easily available as well as inexpensive. The advantages like, high efficacy, better patient acceptability, no immunogenicity made it considered as the gold standard for bone reconstruction [51]. It can be harvested in the form of cancellous, cortical or cortico-cancellous grafts. Though cortical bone graft has higher mechanical strength than cancellous bone grafts, lack of osteoblast or mesenchymal cells make osteogenesis impossible. Cancellous bone grafts show greater capacity for osteogenesis with its abundant osteoblasts and osteocompetent progenitor cells. The cortico-cancellous graft poses properties of both and is the mostly used autogenous bone graft [48, 52]. Autograft generally harvested “fresh” or extracted during craniectomy and preserved. The reliable way to preserve autografts is to either pocketed to the abdomen or cryopreserved [53]. Autograft generally harvested fresh from calvarium, tibia, iliac crest, or fibula and this method is considered the most reliable method. The disadvantages however include increased surgical complexity and a requirement for a second surgical site which comes with additional surgical time and morbidity.

#### 2.2.2.1.2 Allogenic bone graft:

Allograft harvested from a member of same species as the recipient, but not from the host. The graft must undergo various process to minimize the chances of host rejection. These processing steps decide the classification of the allograft, fresh-frozen, free-dried, demineralized freeze-dried bone allograft (DFDBA), and demineralized bone matrix (DBM) [51]. However, lack of mechanical strength and transmission of prion diseases make it difficult to use it as a bone graft.

#### 2.2.2.1.3 Xenograft:

When grafts are derived from different species than they are called xenografts. Bio-OSS (Osteohealth, Shirley,NY) is the most common xenograft, which is derived from bovine bone. Prior use it is deproteinated, particulated, and contained in a porous scaffold to make it oteoconductive.

#### 2.2.2.2 Non-biological bone graft:

In case of better cosmetic outcome in lower cost autogenous bone graft is used widely, but non-biological/synthetic materials are considered as an alternative to avoid various complications like, infection, donor side morbidity and reduced strength and malleability for aesthetic contour [54]. Availability of Osteoconduction and/or osteoinduction properties categories synthetic bone grafts. Researches were directed to develop synthetic materials having bio-features like, biocompatibility, osteo-integration, osteo-conduction etc. One such biomaterial is acrylic composition based on PMMA (polymethylmethacrylate) [8, 55-58]. PMMA was found to be nontoxic due to absence of monomers, strong and impact resistant. It can be formed to near net shape of application area of skull during operation itself. Another polymeric compound recently developed is PEEK (polyether ether ketone) [11, 59, 60]. It is radiolucent, chemically

inert, strong, and elastic. Not only that it is comfortable and neither creates artifacts on imaging nor generates heat while in use. Ceramic compositions based on  $\text{Al}_2\text{O}_3$ , hydroxyapatite and calcium sulphate have been developed as biomaterials [61]. Ceramic materials are highly biocompatible, bioactive and have good mechanical strength. However, they are known to possess poor impact strength and therefore brittle in nature. Bioglasses are another category of bioactive ceramic material and their inclusion as nano- and micro-sized particles in synthetic cranial flaps has been found to induce osteo-induction, osteo-conduction and osteo-integration property. Titanium metal still has a good share as material for cranioplasty due to its good biocompatibility, mechanical strength and radiolucency. The bio-features have been enhanced by application of bioactive ceramic (hydroxyapatite) coatings on the surface. Another area of current work is inclusion of controlled drug delivery feature in these synthetic materials.

### 2.2.3 Bioactive glass as a craniofacial implant:

The maxillofacial area is a unique challenge for many decades to the surgeons because of its versatile properties (mechanical strength, thickness, bone structure) and infection-sensitivity. Especially paranasal sinuses, upper respiratory tract and oral cavity are among the most sensitive areas which needs special attention. Since the first use of bioactive glass, it has been attracted the attention of the respective surgeons due to their osteoconductive as well as antimicrobial properties [62-67]. During the initial times it was found to be very successful in dental applications with promising results. Bioactive glass has been used frequently in the treatment of intra-bony defects and in dental extraction sites as filler before dental implant placement [68, 69]. Also the anti-gingivitis and anti-plaque effects of bioactive glass (NovaMin®) have been studied with evident proof of gingival bleeding reduction and oral plaque formation [70]. The success in the dental field leads to the use of bioactive glass implant in the other areas related to cranioplasty. Bioactive glass S53P4 was used in frontal sinus



elimination and frontal bone reconstruction, nasal septum defect repair, orbital wall and nasal septum reconstruction and canal wall down mastoidectomy [71-73]. Middle ear implant made by bioactive glass for ossicular chain reconstruction also showed very good success rate even after eight years [74].

However, bioactive glasses are a very rigid material with high compressive strength but are also very brittle and thus have limitations in shaping and flexibility for specific clinical requirements. These properties also prevent the use of bioactive glass in load bearing applications. Limitations led to the development of composite materials using bioactive glass to make use of its benefits up to full extent. Composite material is by definition a material composed of at least two different biomaterials. Over the last two decades composites of bioactive glass has been used in different aspects and fields according to the properties of the composite materials. The arsenal of the application of bioactive glass has been increased enormously as the mechanical, biological, and physiological properties of the composite materials can be tailored by changing the concentrations of the components.

The field of bioactive glass composite for craniofacial reconstruction has been nurtured a lot in the last two decades, but there are still a lot of vacant spaces to fill up the arsenal. A vast number of composites were tried with success, sometimes without success, but all the data made us more accurate in planning for the upcoming fabrication of composite materials. With the introduction of 3D scaffold designing in tissue engineering a new door has opened, patient specific implant got a new definition because of this technology. In the coming years more emphasis will be given to make 3D implants based on bioactive glass or bioactive glass composites as bioactive glass can be used as to fabricate 3D scaffold. New ideas of adding stem cells and/ or growth factors will get attention of the researchers. The bioactive glass-based composites have been used *in vitro* using a wide range of cell types and its high time to use

those data to apply the composites in clinical trials *in vivo*. The long-term understanding of *in vivo* in this field is still limited, specially related to the kinetics of degradation and ion release. The use of nano scale composites will need to be investigated too. The results of these investigations will give a better insight of the synergic effect of bioactive glass composites leading to more control over the strategies.

In order to improve the bioactivity, stimulating effects on osteogenesis, angiogenesis and antibacterial effects of bioactive glasses in a specific physiological environment, many methods have been studied incorporating various metal ions in the silicate network. Different substituted silicate glasses exhibit a certain level of acellular bioactivity when tested *in vitro* through standard SBF test, according to Kokubo et al. [75]. Mechanical and osteoinductive properties of bioactive glass scaffold materials can be improved via metallic ion substitution [76]. Among various ion substitutions, strontium ( $\text{Sr}^{2+}$ ), zinc ( $\text{Zn}^{2+}$ ), magnesium ( $\text{Mg}^{2+}$ ) and silicon ( $\text{Si}^{4+}$ ) have been widely studied[77-83].

#### 2.2.3.1 Strontium-bioactive glass

Strontium (Sr) is a naturally occurring mineral found in water and food. It is also an essential trace element of human body. The total amount of Sr in human body of a 70 kg “standard” man is around 0.32 g. Recently, researchers found that Sr positively effects bone metabolism to promote bone formation and osteoblast replication while inhibiting bone resorption by osteoclasts [84]. Evidence also showed that strontium not only enhances osteogenic differentiation, it also helps to stabilize bone structure [85]. However too much Sr may increase the number of osteoclast cells which can inhibit bone regeneration and remodelling, leading to osteonecrosis. Thus, Strontium has very good effects up to an optimum level. Among the trace elements human body have, only Sr was correlated with bone compression strength [86]. *In vitro* and *in vivo* studies showed that strontium ions up-regulate osteoblasts and down regulate

osteoclasts [87, 88]. Presence of Sr on the surface of a biomaterial, decrease the rate of ion-release at the defect site, which is therapeutically beneficial [89]. Sr-substituted boron glasses show a good adhesion with osteoblast-like cells, Saos-2, thus enhances the cyto-compatibility of borate glass.

Jonathan Lao et al. confirmed that Sr-doped bioactive glasses are more bioactive *in vitro* than their original counterparts. Sr-doped glasses are also able to increase the rate of bonelike apatite layer formation on their surface. Moreover, it also decreases the Ca/P ratio very rapidly, which leads to faster stability of apatite layer, hence greater bioactivity [90]. Substitution of 5 wt% strontium in place of calcium shows advantageous effect on fetal mouse calvarial bone cells [91].

Strontium based bioactive glasses tends to increase metabolic activity in osteoblasts and to decrease osteoclast activity. The decrease of osteoclasts is may be caused by decreasing tartrate resistant acid phosphate activity and inhibiting resorption of calcium phosphate films [92]. In some cases it was found that substitution of Sr in place of Ca is more effective strategy for building materials suitable for bone regeneration therapies [92]. Substitution of Ca by Sr by mol% sometimes increase silica content as Sr is heavier than Ca, which results in reduced solubility and hence bioactivity. Though replace by weight% sometimes increase the rate of HCA formation [90, 93].

In comparison, Sr is slightly larger than Ca, which expands the silica network and increases ion dissolution rates, leading to significantly increased *in vitro* and *in vivo* reactivity. The *in vivo* bioactivity is greater in case of Sr-doped bioactive glasses due to the biological effects of Sr on bone-forming cells [94].

Very recently D. Sriranganathan et al. reported that with increase of the Sr-substitution for Ca in high phosphate bioactive glasses decrease the formation of apatite layer directly. They

proposed that the apatite formation proceeds via the formation of an octacalcium phosphate ( $\text{Ca}_8(\text{PO}_4)_6\text{H}_2.5\text{H}_2\text{O}$ ) phase, which then transform into hydroxycarbonate apatite. Above a certain concentration of strontium the octacalcium phosphate phase is unable to form, which ultimately delay the HCA formation [95].

#### 2.2.3.2 Lithium-bioactive glass:

Lithium has a prolonged medical history as it has been used for over 100 years to treat manic depression [96]. Lithium also marked its importance in treatment of both bipolar and unipolar depressive disorders. Along with that lithium also has several other effects on blood and brain [97]. Clinicians also observed that lithium often increase the white blood cell count (granulocytosis) and reduce blood lymphocyte count (lymphopenia). Lithium also tends to enhance immunological activities of monocytes and lymphocytes. Researchers also found evidence of lithium in bone mineral metabolism [98-100].

*In vitro* bioactivity test indicates a decrease in bioactivity with increase in lithium-ion concentration. The theory behind it is that lithium forms lithium oxide groups by reacting with the hydroxyl groups present in the pure sol-gel, which limits crystal formation. Recently M. Khorami et al observed the *in vitro* bioactivity of lithium substituted 45S5 glasses and found no certain advantage of lithium in the reactivity of the bioactive glass composition. A theory based on observations state that *in vitro* reactivity increases with increasing glass solubility. In this study, lithium was replaced for sodium in wt% and hence a little decrease in the molar concentration of glass network formers ( $\text{SiO}_2$  and  $\text{P}_2\text{O}_5$ ) takes place, which may result in an increase in glass solubility. However, the ionic radius of  $\text{Li}^+$  is lower than  $\text{Na}^+$ . Thus, lithium has a strong affinity for bonding to oxygen and tends to contract the free spaces in the silicate network. This phenomenon reduces the rate of glass dissolution and improves chemical durability [101].

The release of lithium ions in SBF is higher for sample with higher lithium content, with an initial burst in the first 24 h followed by more sustained release. Lithium also shows ALP activity and mineralisation in a dose dependent manner from 0.2 to 0.85 ppm when exposed to murine osteoblast cells [102].

#### 2.2.4 E-glass substrate

Chemically durable alumino borosilicate glasses are generally known as e-glass. E-glass fibers are generally used as a reinforcement for polymer matrix or composites to increase their flexural strength. These glasses are considered inert in body environment; hence it does not dissolve and doesn't show any indication of cytotoxicity. E-glass comprised of low alkali oxide content than other melt-derived bioactive glasses (<2 wt%) and high Al<sub>2</sub>O<sub>3</sub> (14 wt%) and B<sub>2</sub>O<sub>3</sub> contents (10 wt%). Currently e-glass is used as unidirectional rovings and bidirectional woven fabrics and used in the treatments of segmental defects, in oral implants, and in cranial implants replacing lamellar bone [103].

Aitasalo et al. used E-glass to couple with bisphenol-a-glycidyl methacrylate and triethylene glycol di-methacrylate matrix to achieve an implant for craniofacial bone reconstruction. The e-glass weave was used as a supporting framework for the inner layers of glass veil, between particles of bioactive glass [104].

#### 2.2.5 Magnesium and its alloys

Biomedical use of magnesium and its alloys initiated nearly a century ago, was not very successful since *in vivo* corrosion of magnesium could not be addressed [105]. Being biodegradable and having a Young's modulus close to that of bone, use of Mg-alloys for biomedical implants is receiving renewed interest. The Young's modulus (E=41-45 GPa, for Mg-alloys vs. E=3-20 GPa for bones) implies that usage of these alloys in orthopaedics reduces

occurrence of stress shielding [106]. Biodegradability of these alloy implants implies that they need not be removed using a second round of surgery, thus minimizing trauma and medical expenses [107-109]. Recent works have used magnesium alloy based wound closing for gastrointestinal procedure [110] and Mg-based material coated with a conducting polymer as a biocompatible platform for controlled drug release [111]. Biocompatibility and biodegradation studies, *in vitro* and *in vivo*, have been carried out for several commercially available Mg-alloys [112-117]. This is an important step in adoption of Mg-alloys for biomedical purposes since most of the commercially available alloys were developed for other sectors like automobiles and aviation.

Magnesium corrodes in water to dislodge hydrogen from water, forming a basic solution. This gets further complicated *in vivo* since if the pH is high enough, Ca (or Mg) phosphates will tend to precipitate and form a layer on the surface [118]. Additionally, the alkaline surface and evolving hydrogen bubbles are liable to influence cell adhesion and tissue growth. *In vivo* early stage degradation rates for most Mg-alloys have been found to be high [119], implying the corrosion process in a physiological environment will rapidly change the surface interaction of a Mg-based biomaterial. This is of prime concern as implant surface composition, morphology, and microstructure are important determinants of its propriety for cell adhesion and protein absorption [120].

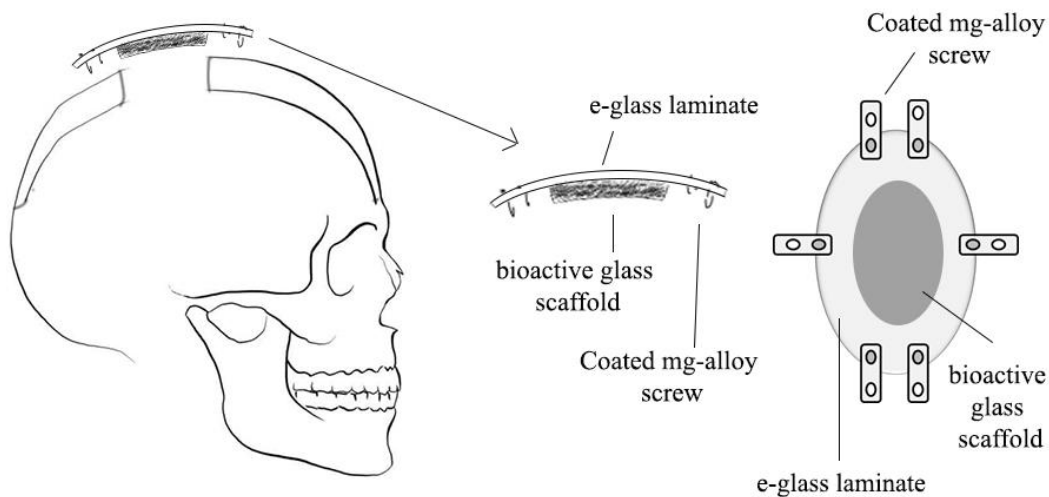
One approach towards improving suitability of these alloys has been including biologically important elements, formulating binary Mg-based alloys, for example, with zinc [121, 122], strontium [123], or calcium [124]. Other combinations tried including Mg-Zn-Ca [125] and Mg-Nd-Zn-Zr [126, 127]. The challenge is thus fabrication of Mg-alloy implants that do not succumb to fast, early-stage degradation due to corrosion and avoiding the problem of hydrogen formation and alkalization. The obvious choice towards such fabricates is surface

modification [128]. These could include techniques like electrochemical deposition [129, 130], electroless plating [131-133], plasma electrolytic oxidation [134-137], physical vapour deposition[138-142], ion implantation[143-147] and laser treatment[148, 149]. Surface treatments should not permanently affect structure and properties of Mg-alloys or effect biodegradability. The interface must be dynamic in nature.

### 3. AIMS AND OBJECTIVES

The ideal material used for cranioplasty would be biocompatible, mechanically strong, radiolucent, resistant to infections, not conductive of heat or cold, resistant to biomechanical processes, light weight, malleable to fit defects with complete closure, inexpensive, non-magnetic with low thermal conductivity and long-term stability.

The prime objective of this study is to find suitable material for a composite three-element bone graft, consisting of a laminate to hold the scaffold as well as supply necessary mechanical



strength, a scaffold to bond with the host bone, and screws to hold the graft in position.

The laminate must be

- Non-metallic non-toxic glass matrix with high mechanical stability.
- Leaching of glass former/ modifier is less, Ease of preparation, availability.
- Necessitates bone bonding/ soft tissue bonding at the surface and potentially impregnate biological moieties.

Bioactive glass scaffold should have



- Suitable mechanical and osteoinductive properties.
- Fast early-stage bone forming ability.
- Better anchorage of newly formed tissues.
- Stability of the scaffold till the formation of mature bone at the site.

Screw-material should have the properties as follows

- Mechanically compatible to hold the implant at the same time biologically active and non-toxic.
- Suitable combination of mechanical properties and fracture toughness.
- Better resistance against corrosion than the available mg-alloys.
- Degradability in such way that it will hold the implant till needed but relieves the patient from the pain of second surgery to remove the implant.

Hence the specific aims of the study is

**I.** To examine the effect of bioactive glass coating on the surface of inert e-glass and evaluate the bioactivity of the sample. Phase, composition, and microstructural analysis will be done thoroughly before going into bioactivity studies. Static and dynamic bioactivity studies will be done to get a better understanding about the substrate.

**II.** To assess the beneficial effects of  $\text{Sr}^{2+}$  and  $\text{Li}^{+}$  doping on *in vivo* bone formation of an interconnected bioactive glass porous scaffold developed in the laboratory through rabbit bone defect model. Detailed phase, composition and microstructure analysis were performed prior using tools like X-ray diffraction (XRD), Fourier transformed infrared spectroscopy (FTIR), differential thermal analysis-thermo-gravimetric analysis (DTA-TGA), quantitative EDAX analysis and scanning electron microscopy (SEM) respectively.

**III.** To investigate the effect of HAp and bioactive glass (S53P4) coating on electrochemical and biological properties of commercially available Mg-alloy implant. Mg-alloy is known for their bioresorbable properties with higher degree of corrosion *in vitro*. As before the coated substrates will be studied for different physical, chemical, mechanical and biological characterisation including XRD, FTIR, Raman spectroscopy for phase analysis and evaluation; FESEM-EDAX at the interface for detailed layer-wise microstructural characterisation; electrochemical corrosion test using SBF solution. *In vitro* biocompatibility assessments like cell viability and proliferation assay using MG63 cell line, alkaline phosphatase assay, mineralization assay by ARS staining, gene expression by real time RT-PCR, cell morphology within the scaffold constructs by Laser confocal will be done thoroughly.

The fabricated materials will be checked for their efficacy by extensive *in vivo* animal trial. *In vivo* studies like radiology, histology, fluorochrome labelling study, SEM of bone-implant interface, toxicity, *in vivo* immune response was observed to ensure the applicability of the implant as a better craniofacial bone reconstruction material.

## 4. MATERIALS AND METHODS

### 4.1 HAp coated E-Glass preparation

#### 4.1.1 Materials

Chemically pure and having more than 99.5% assay calcium nitrate tetrahydrate  $[\text{Ca}(\text{NO}_3)_2 \cdot 4\text{H}_2\text{O}]$ , sodium chloride  $[\text{NaCl}]$ , sodium hydrogen carbonate  $[\text{NaHCO}_3]$ , magnesium chloride hexahydrate  $[\text{MgCl}_2 \cdot 6\text{H}_2\text{O}]$ , Tris(hydroxymethyl)aminomethane [Tris buffer,  $\text{C}_4\text{H}_{11}\text{NO}_3$ ], calcium chloride dihydrate  $[\text{CaCl}_2 \cdot 2\text{H}_2\text{O}]$  and sodium sulfatedecahydrate  $[\text{NaSO}_4 \cdot 8\text{H}_2\text{O}]$  were procured from Merck (Mumbai, India), while phosphorous pentoxide  $[\text{P}_2\text{O}_5]$ , potassium chloride  $[\text{KCl}]$  and 35.4% hydrochloric acid  $[\text{HCl}]$  were purchased from S.D. Fine-Chem Ltd. (Mumbai, India). Di-potassium hydrogen phosphate trihydrate  $[\text{K}_2\text{HPO}_4 \cdot 3\text{H}_2\text{O}]$  was from Sigma-Aldrich (Steinheim, Germany) and ethanol (absolute) was from Merck KGaA (Darmstadt, Germany). Doubly distilled water was used throughout the conducted experiment. Commercially available e-glass (having a composition of 54.3% $\text{SiO}_2$ -15.2% $\text{Al}_2\text{O}_3$ -17.2% $\text{CaO}$ -4.7% $\text{MgO}$ -8.0% $\text{B}_2\text{O}_3$ -0.6% $\text{Na}_2\text{O}$ ) fibers were used to obtain plates after remelting and casting them in a polished steel mould. Plates were used instead of fibers for allowing more precise chemical and biological analysis of the material surface.

#### 4.1.2 Formation of gel

Two clear solutions of  $\text{Ca}(\text{NO}_3)_2 \cdot 4\text{H}_2\text{O}$  (0.1 mol) and  $\text{P}_2\text{O}_5$  (0.003 mol) were made at room temperature separately by stirring them for 30 min., using ethanol (99%, 10 mL) as mutual solvent. Subsequently, they were mixed slowly and stirring was continued for 2 h at room

temperature, followed by aging for another 2 h. Increasing viscosity of the gel after first hour was also measured by creep test (Bohlin GEMINI, UK) using cup-and-bob method (shear stress: 0.002 Pa, time: 7200s).

#### 4.1.3 Fabrication of coated e-glass substrates

Viscous solution, thus obtained (as mentioned in 4.1.2), was tipped on e-glass plate substrates (50  $\mu$ L on 1 cm x 1 cm plates with average roughness ( $R_a$ ) of 0.7 $\mu$ m) dropwise followed by drying at room temperature for 18 h. Further, the coated sample was pre-freezed at -20°C overnight followed by freeze drying (Eyela FDU.2200, Japan) at 70-80 MPa pressure and -83°C for 20 h. The samples were then thermally treated at 850°C (heating rate 2°C/min. with 15 min dwelling time). A low-speed diamond saw (Buehler, Isomet, USA) was used further for sectioning and characterization.

#### 4.1.4 Characterisation of coated e-glass substrates

Surface roughness of the coated and uncoated samples were measured by contact profilometer (Form Talysurf, i120, Taylor Hobson, UK). Phase analysis of the coating was done by X-ray diffraction (XRD) technique in a powder diffractometer using  $CuK_{\alpha}$  ( $\lambda = 1.54178 \text{ \AA}$ ) radiation [PANalytical, The Netherlands]. 'High Score Plus' software was used to analyse the XRD data with the help of Inorganic Crystal Structure Database (ICSD, PDF4). To identify the functional groups, Fourier-transformed infrared spectroscopy (FTIR) was performed using PerkinElmer Spectrum 100, USA spectrophotometer with HeNe laser (Class II/2) following the KBr pellet method (2 mg sample: 200 mg KBr). Scratched-off material from surface was used for preparing KBr pellets. To compliment, Raman spectra was performed as well by using STR500

Raman Spectrometer (Technos Instrument, Seki technotron, Japan. The top-surface microstructure and interface of coating cross-section was assessed by field-emission scanning electron microscope (FESEM) (Supra 35VP, Zeiss, Germany). Ca/P molar ratio was measured by taking average from energy dispersive X-ray analysis (EDX) taken at different points of the sample with an accelerating voltage of 15 kV.

Transmission electron microscopy (TEM) (Tecnai G2 30ST, FEI, Natherlands) was performed to obtain the finer details of the microstructure of coating cross-section. Local crystallographic structure was gathered from the selected-area electron-diffraction (SAED) patterns in the TEM. As for the cross-sectional sample preparation for TEM characterization, the coated glass substrates were first cut into pieces of about 2.5 mm x 10 mm area. Two such cut pieces were glued with coated surfaces face-to-face with 'Gatan G-1 Epoxy' (Gatan Inc., USA) and grinded suitably to give a rod like shape of 2.5 mm diameter and 10 mm length. This rod of sandwiched coatings was further glued inside a hollow stainless-steel tube of 3 mm outer diameter using the 'Gatan G-1 Epoxy' resin. Cross-sectional slices of about 0.25 mm thickness were cut from the tube filled with the sandwiched coating sample using Buehler low speed diamond saw. Using Gatan Disk Grinder (Gatan Inc., USA) the slices were thinned down to 80 microns and further dimpled at the centre using Gatan dimple grinder (Model 656, Gatan Inc., USA) down to 30 microns at the centre. The dimpled cross-section specimens were finally ion-polished by using Gatan model 691 precision ion polishing system (PIPS, Gatan Inc., USA) with 4 keV Argon ion-beams at 4° incidence angle on both sides of the cross-sectioned surfaces till perforations to generate electron-transparent thin area of the coating suitable for TEM observation.

#### 4.1.5. Immersion tests in simulated body fluid (SBF)

Static *in vitro* bioactivity (in terms of capability of forming carbonated hydroxyapatite) of coated samples was evaluated in contact with simulated body fluid (SBF) prepared as per Kokubo[150]. Concentrations of the different constituting elements of SBF solution (in mM) taken are as follows: Na<sup>+</sup> 142.0; K<sup>+</sup> 5.0; Ca<sup>2+</sup> 2.5; Mg<sup>2+</sup> 1.5; Cl<sup>-</sup> 147.8; HCO<sup>3-</sup> 4.2; HPO<sub>4</sub><sup>2-</sup> 1.0; SO<sub>4</sub><sup>2-</sup> 0.5. pH was maintained ~ 7.4 by using Tris buffer during preparation. Surface area (SA) / volume (V) ratio of the samples to SBF added was maintained as 1 cm<sup>2</sup>/15 mL with constant temperature (37.4 °C) during the study (in an incubator in closed test tubes for 7 and 14 days without refreshing SBF solution in between) [75]. Quasi-dynamic (QD) SBF study was performed by following the same method but by replenishing with fresh SBF solution after every 24 hours and up to 14 days. Weight changes of samples and pH change of the dissolution medium (SBF) were recorded up to 14 days.

Samples after static and QD SBF studies after 7 and 14 days were analysed for structure by XRD, FTIR and Raman while surface microstructure evolved were analysed by FESEM and TEM. Samples for microstructural analyses were prepared as described earlier. Top surface of the samples was again assessed for hardness and elastic modulus by nano-indentation method.

Nanoindentation experiments were conducted utilizing a 5×5 array on both uncoated and coated e-glass substrates after static and QD SBF studies for 7 and 14 days by load controlled nanoindentation technique with a Berkovich nanoindenter of tip radius 150 nm. A commercial machine (Fischerscope H100-XYp; Fischer, Switzerland) with depth and load sensing resolutions of 1 nm and 0.2 μN respectively was used. In the present experiments, the peak load was kept constant at 10mN, while both the loading and the unloading times were kept

fixed at 30 seconds. For all experimental data reported in this work the error bars represent  $\pm 1$  standard deviation of the data.

#### 4.1.6. In vitro biocompatibility study

##### 4.1.6.1 Cell culture procedure

The cell culture medium, for the human osteoblasts like cells (MG-63 cell line) was made of DMEM, 10% foetal calf serum, and 1% penicillin/streptomycin. The cultures were kept till they reached 90% confluence in a humidified environment of 5% CO<sub>2</sub>, at 37°C. Following confluence, the cells were trypsinized, centrifuged, and suspended back in media for counting. The samples (both bare e-glass and HAp coated e-glass) were sterilized for 30 min. with 70% ethanol and UV light, washed repeatedly with sterile PBS (pH 7.4) followed by treatment with DMEM medium for 4 h to create a better environment for the cells. Just prior to cell seeding, to ensure better penetration of cells, the scaffolds were partially dried for 2 h. Twenty micro-litres of the cell suspension in medium, containing 10<sup>5</sup> cells, were added drop-by-drop on to each sample. Following seeding, to boost cell adhesion in the initial hour, the matrices were maintained in a humidified environment, at 37°C, 5% CO<sub>2</sub>. The matrices were kept in medium for 14 days, while the medium was replaced every alternate day.

##### 4.1.6.2 Cell viability assay

MTT assay was performed at different points of time over full cell culture duration to investigate the cell viability. The samples were incubated in 5 mg/mL MTT stock solution which was diluted at a ratio of 1:10 using PBS (pH 7.4). Formazan crystal formed post

incubation was dissolved in dimethyl sulfoxide and the absorbance of the resulting solutions was measured using the Manufacturer's protocol with spectrophotometer (Bio-Rad, iMark).

#### 4.1.6.3 Cell proliferation by Alamar blue assay

Cell proliferation on samples over 14 days was assessed by Alamar blue dye-reduction. Alamar blue dye was diluted in the culture medium with a 1:10 dye-to-media ratio. Samples were incubated in the dye solution for 4 h in the dark. Dye reduction was determined spectrophotometrically in a microplate reader (Thermo Scientific Multiskan Spectrum, Japan) at 570 and 600 nm. The percentage of dye reduction was calculated from the below-mentioned equation:

$$\% \text{ AB reduction} = [(\epsilon_{\text{ox}}\lambda_2)(A\lambda_1) - (\epsilon_{\text{ox}}\lambda_1)(A\lambda_2)] / [(\epsilon_{\text{red}}\lambda_1)(A'\lambda_2) - (\epsilon_{\text{red}}\lambda_2)(A'\lambda_1)] \times 100$$

where  $\epsilon\lambda_1$  and  $\epsilon\lambda_2$  were molar extinction coefficient of Alamar blue at 570 and 600 nm respectively,  $\epsilon_{\text{ox}}$  in oxidized and  $\epsilon_{\text{red}}$  in reduced form;  $A\lambda_1$  and  $A\lambda_2$  were absorbance of the test wells; and  $A'\lambda_1$  and  $A'\lambda_2$  were the absorbance of the negative control wells. All given pairs were values at 570 and 600 nm.

#### 4.1.6.4 Alkaline Phosphatase assay (ALP)

Spectrophotometric measurements of the alkaline phosphatase produced by MG-63 cultured on the different samples were carried out [151]. At specific day points, the cell laden constructs were washed with PBS (pH 7.4), homogenized with 1 mL Tris buffer (1 M, pH 8.0), and



sonicated for 4 min. on ice. A volume of 20  $\mu$ L of this suspension, was incubated with 1 mL of 16 mM p-nitrophenyl phosphate (Sigma) solution for 5 min., at 30 °C. To measure p-nitrophenol produced in presence of ALP, the absorbance at 405 nm was evaluated and ALP activity was reported as p-nitrophenol produced, normalized by incubation duration and cell count:  $\mu$ mole/min/ $10^5$  cells.

#### 4.1.6.5 Cellular morphology

Laser confocal microscopy was used to examine the cell morphology and the dispersion of the cells on the samples. For confocal laser microscopy, samples after 7 days culture were fixed using 4% paraformaldehyde for 1 h and the cells were then permeabilized over 5 min. by use of 0.1% Triton X-100, prepared in BSA. Samples were then blocked with 1% bovine serum albumin (BSA) for 1 h. The actin filaments were stained using Alexa Fluor<sup>®</sup> 488 and the nuclei with Hoechst 33342. The confocal laser microscopy was performed on Olympus FV 1000 (Olympus, Japan) and post-processing was carried out with Olympus FV 1000 Advanced software version 4.1 (Olympus, Japan).

#### 4.1.6.6 Gene expression by real-time RT-PCR

For total RNA extraction, different samples cultured in MG-63 for 21days were transferred into 2-mL plastic tubes containing 1.5 mL of Trizol solution (Invitrogen, USA). After brief incubation for 15 min., the treated samples were centrifuged at 12000 g for 10 min./4°C. The supernatant liquid was transferred to a new tube and 200 mL of chloroform was added to it. After further incubation for 5 min. at room temperature, the solution was gently mixed for 15 s, followed by incubation for 5 min. at room temperature. The tubes were further centrifuged

for 15 min. at 12000 g/4 °C. The upper aqueous layer was transferred to a RNeasy Plus mini-spin column (Qiagen, Germany). The RNA was washed and eluted according to the manufacturer's protocol. RNA samples were reverse transcribed into cDNA using High capacity cDNA reverse transcription kit (Applied Biosystems, USA) according to the manufacturer's protocol.

Real-time PCR conditions were optimized and were performed with SYBR Green (Applied Biosystems, USA) in an ABI Prism® 7000 Sequence Detection System (Applied Biosystems, USA). For real-time analysis, SYBR Green supermix, 5 pmol/mL of each forward and reverse primers and 5 µL cDNA templates were used in a final reaction volume of 50 µL and plates were loaded using a RT loading platform. Cycling conditions included an initial denaturation step of 8 min. and 45 s at 95 °C followed by 45 cycles of 30 s at 95 °C, 30 s at 58 °C, and 30 s at 72 °C. Data collection was enabled at 72 °C in each cycle. CT (threshold cycle) values were calculated using the Relative Quantification software (Applied Biosystems).

Highly purified gene-specific primers for osteopontin (OPN), collagen I, osteocalcin (OCN), Runx2, and housekeeping gene GAPDH were designed based on previous reports [30] and synthesized commercially (MWG-Biotech AG Ltd, India). Relative expression levels for each target gene were normalized by the Ct value of the housekeeping GAPDH gene using an identical procedure ( $2^{-\Delta\Delta Ct}$  formula, Perkin Elmer User Bulletin s $\neq$  2). Each sample was analysed in triplicate.

#### 4.1.6.7 Mineralization assay by ARS staining

Alizarin Red-S (ARS) staining was used to detect and quantify mineralization. ARS is a dye which binds calcium salts selectively and is widely used for calcium mineral histochemistry. Growth factors loaded samples with MG-63 cells (constructs) were washed three times in PBS and fixed in ice cold 70% ethanol for 1 h. These constructs were washed three times with distilled water and stained with ARS (40 mM) for 20 min. at room temperature. After several washes with distilled water, these constructs were observed under optical microscope and the stain was desorbed with the use of 10%-cetylpyridinium chloride for 1 h. The dye was collected, and absorbance read at 540 nm in microplate reader.

#### 4.1.7 Statistics

Mean  $\pm$  standard deviation (SD) data of samples in triplicate ( $n = 3$ ) have been presented. Statistical comparison for different samples were shown using one way analysis of variance (ANOVA). Significant differences were presented as \*\*\*  $p < 0.001$ ; \*\*  $p < 0.01$ ; \*  $p < 0.05$ . Cases where ANOVA gave significant difference, subsequent Tukey's Honest Significant Difference (HSD) method has been adopted.

## 4.2 Li-Sr substituted bioactive glass scaffold preparation

### 4.2.1 Bioactive glass scaffold preparation

Bioactive glass (with or without doping of Li or Sr) was prepared through conventional glass melting procedure using appropriate amounts of reagents like silica ( $\text{SiO}_2$ ), calcium carbonate ( $\text{CaCO}_3$ ), dry soda ash ( $\text{Na}_2\text{CO}_3$ ), decahydrated borax ( $\text{Na}_2\text{B}_4\text{O}_7 \cdot 10\text{H}_2\text{O}$ ),  $\text{TiO}_2$ , di-ammonium hydrogen ortho-phosphate, lithium and strontium carbonate (all inorganic chemicals including the ones referred later in the manuscript were analytical grade from M/s S.D. Fine-Chem Limited, India until specified separately). Briefly, reagents were first mixed homogeneously, melted at  $1450\text{ }^\circ\text{C}$  in a Pt-crucible, homogeneity was maintained while melting and finally quenched in water to obtain the cullet. Dried cullets were further milled in a high energy ball mill for 3 h in aqueous medium. The final composition of the as-prepared glass powders (obtained by ICP-AES chemical analysis) is given in Table 1. 0.25%  $\text{Li}_2\text{O}$  and 1%  $\text{SrO}$  (by weight) doping was used strategically for the base glass composition and nomenclatures like BAG, L-BAG, S-BAG and LS-BAG were given for bioactive glass without doping, Li-, Sr- and binary Li+Sr substitution respectively and used throughout the manuscript.

Table 1: Chemical composition of the as-prepared powders by ICP-AES

Constituent	Mean wt. %			
	BAG	L-BAG	S-BAG	LS-BAG
SiO <sub>2</sub>	55.50	55.77	53.92	55.02
B <sub>2</sub> O <sub>3</sub>	1.38	1.76	2.33	1.00
CaO	23.60	23.95	23.00	23.36
Na <sub>2</sub> O	10.80	10.01	11.00	9.94
P <sub>2</sub> O <sub>5</sub>	5.74	5.85	5.59	5.59
TiO <sub>2</sub>	1.64	1.71	2.00	1.88
Li <sub>2</sub> O	-	0.22	-	0.30
SrO <sub>2</sub>	-	-	1.12	1.00

To fabricate porous scaffolds, milled as-prepared respective glass powders were first mixed with an equal quantity of porogen (scintillation grade naphthalene). The resultant mix was compacted at 150 MPa in a cold-isostatic press (EPSI, Belgium); cut into 8 mm diameter specimens using a low-speed diamond saw (Isomet, Buehler, USA). Subsequently, naphthalene was driven off very slowly (from r.t. to 80 °C) with pre-determined rate of schedule, followed by heat treatment at 675 °C except for LS-BAG (650 °C) on a Pt-plate for 6 min. These temperatures were selected after careful assessment of glass-transition temperatures ( $T_g$ ) mentioned later. The samples were finally stored in a vacuum desiccator until further use.

#### 4.2.2 Bioactive glass powders and scaffold characterization

Both as-prepared and heat-treated powders were analyzed for phase by XRD at a diffraction angle of 10-80 °2 $\theta$  [X'Pert Pro, Phillips Analytical, Netherlands; Cu K $\alpha$ 1 radiation; scan speed 2° min<sup>-1</sup>. FTIR transmittance spectra was recorded at mid-IR range (4000-400 cm<sup>-1</sup>) [Spectrum 100, PerkinElmer, USA; resolution: 2 cm<sup>-1</sup>; by KBr pellet method] to confirm the functional groups present. On the other hand, DTA-TGA was conducted to determine the thermal profiles of the glass powders [STA 449C, Netzsch, Germany; rate of heating upto 1000°C: 10° C/min. with initial sample mass of 5 ± 0.5 mg]. Heat treatment temperatures of BAG, L-BAG, S-BAG and LS-BAG were selected by assessing the Tg by the same DTA-TGA analysis.

Further, porous scaffolds were first physically characterized for open or apparent porosity (A.P.) and bulk density (B.D.) by water displacement method (Archimedes' principle), then by a table-top SEM (Phenom pro-X, Netherlands) for detailed microstructural characterization and assessment of pore size, shape and morphology with Au/Pd sputter coating on the samples prior. B.D. was calculated by  $[D/(W-S)]$  and A.P. by  $[(W-D)/(W-S)] \times 100\%$ , where D, W and S are dry, soaked and suspended weight of the samples respectively while calculating by the methods mentioned. Variations of pore sizes were calculated by processing several SEM images thus obtained and using free software available (Perfect Screen Ruler v. 2.0) subsequently.

#### 4.2.3 SBF bioactivity study

Primary bioactivity study of the bare scaffolds was carried out in contact with SBF, before *in vitro* cell cytotoxicity and *in vivo* pre-clinical study just to check calcium and phosphate ion

deposition ability of the samples. Supernatants were analyzed for  $\text{Ca}^{2+}$ ,  $\text{HCO}_3^-$ , and  $\text{HPO}_4^-$  ions. SBF was prepared as per Kokubo *et al.* (1990) [152]. All the samples were selected with surface area of sample and volume of SBF taken with ratio of  $2 \text{ mm}^2/\text{mL}$  (e.g.,  $40 \text{ mm}^2/20 \text{ mL}$ ) and soaked for 7 and 14 days. Samples were kept statically at a temperature  $37.4^\circ \text{C}$  with pH 7.4 inside an incubator. After 7 and 14 days, ion concentrations were plotted and analyzed. One of respective samples (from BAG, L-BAG, S-BAG and LS-BAG) was seen for microstructure by FESEM (using Sigma, Carl Zeiss, Germany) after day 14. The samples were dried, and carbon sputter coated prior observation.

#### 4.2.4 *In vitro* cell cytotoxicity

Chemicals used: Iscove's modified Dulbecco's medium (IMDM), phosphate-buffered saline (PBS), formaldehyde, 3-(4,5 dimethyl thiazol-2yl)-2,5 diphenyltetrazolium bromide (MTT), osmium tetroxide, paraformaldehyde, dimethyl sulfoxide (DMSO) were from Sigma Aldrich, St. Louis USA; fetal bovine serum (FBS) and penicillin/streptomycin, trypsin-ethylene diamine tetra acetic acid (EDTA), L-glutamine were from Invitrogen, CA,USA.

Fibroblast (NIH3T3) cell line (NCCS, Pune, India) was cultured in IMDM supplemented with 10% FBS and 1% penicillin-streptomycin (Complete Medium) in a humidified atmosphere of 5%  $\text{CO}_2$  at  $37^\circ\text{C}$ . BAG, S-BAG, L-BAG, LS-BAG scaffolds were autoclaved and then rinsed with 70% alcohol for sterilization. NIH3T3 ( $2 \times 10^3$ ) cells were seeded on scaffolds which were previously placed in a 24 well plate. Cells were allowed to attach on the surface of scaffolds for 2 h. Subsequently another 1.0 mL of complete medium was added in each well and cultured on for 3 and 7 days. Culture medium was changed in every 2 days.

To test cytotoxicity of BAG, S-BAG, L-BAG, LS-BAG scaffolds on cells, MTT assay was carried out after 3 and 7 days of culture. Cell without scaffold was used as control. MTT solution was prepared by dissolving MTT (5.0 mg) in DMSO (1.0 mL). MTT (100  $\mu$ L) solution was diluted with IMDM (900  $\mu$ L). After removing the previous medium diluted MTT solution was added in each well and incubated for 3 h. Purple coloured formazan crystal which are formed by the oxidation of tetrazolium salt by mitochondrial succinate dehydrogenase enzyme was dissolved in DMSO (500  $\mu$ L). The resulting solution (200  $\mu$ L) was placed into a 96 well plate and the optical density at 550 nm was measured using plate reader (Thermo Scientific). Each experiment was carried out in triplicate and the results were presented as means  $\pm$  SD.

#### 4.2.5 Cell morphology by SEM

NIH3T3 ( $2 \times 10^3$ ) cells were seeded on scaffolds and cultured for 7 days. Scaffolds containing cells were washed with PBS (0.1 M) and fixed with paraformaldehyde (2%) overnight at 4°C. Subsequently, it was fixed with 2% osmium tetroxide ( $\text{OsO}_4$ ) for 2 h at 25°C. The fixed samples were then dehydrated in an ethanol series 30%, 50%, 70%, 90% and 100% each for three times, followed by gold sputter coating for SEM observation of cell morphology.

#### 4.2.6 *In vivo* study of rabbit femoral bone defect model

The animal experiments were performed following an ethical committee approved protocol in accordance with Institutional Animal Ethical Committee (IAEC), West Bengal University of Animal and Fishery Sciences (WBUAFS), West Bengal, India (Permit No. Pharma/IAEC/34 dated 30 June 2014). Sixteen adult New Zealand White rabbits (1.5-2 kg) were randomized into four groups ( $n = 4$ ): control group I (pure BAG) and the test animals, group II (S-BAG), group III (L-BAG) and group IV (LS-BAG) with bilateral implantation. All surgeries were



performed under general intramuscular anesthesia using xylazine hydrochloride (6 mg/kg) (Xylaxin, Indian Immunologicals, India) and ketamine hydrochloride (33 mg/kg) (Ketalar, Parke-Davis, India). Scaffolds were press fitted within the created defects in the distal metaphyseal region of femur and wounds were sutured in three layers (Fig. 1). Subsequently, animals were administered with cefotaxime sodium (Mapra India, India) at 20 mg/kg body weight intramuscularly for 5 days twice daily at 12 h interval and meloxicam at 0.2 mL (Intas Pharmaceuticals, India) once daily. Animals were finally sacrificed after 2 and 4 months of implantation.



Fig. 1: Surgical placement of the porous scaffolds (with or without doped BAG).

#### 4.2.7 Characterization of in vivo samples

Bone healing in the defect was monitored using chronological radiographs taken immediately after implantation and once in a month up to 4 months. Radiographs were scored independently by double blinded investigators per methods described by Zhukauskas *et al.* [153] (Table 2). For histological analysis, the bone specimens from the healed bone defect were collected, washed thoroughly with normal saline and was immediately fixed in 10% formalin for 7 days. Subsequently, the bone tissues were decalcified using Goodling and Stewart's fluid containing 15 mL formic acid, 5 mL formalin and 80 mL distilled water, followed by fixation with 4% paraformaldehyde. Finally, the samples were embedded in paraffin wax and 4 µm sections were cut from the mount and stained with haematoxyline and eosin finally. Additional scoring system was developed from the histological slide using several *in vivo* biological activities (cellular response) and the response score was marked with '0' for absence, '1' for mild, '2' for moderate, '3' for marked and '4' for severe activity.

Table 2. Radiological scoring system (adopted as per Zhukauskas *et al.* [153])

<b>Animal response</b>	<b>Score description</b>
1	Bone just extending into the defect
2	Bone substantially bridging the cortical defect
3	Bone fully bridging the cortex without significant callus
4	Bone fully bridging the cortex with distinct overlying callus

For another set of samples, fluorochrome, i.e., oxytetracycline dehydrate (Pfizer India, India) was intramuscularly injected 3 weeks before sacrifice at two time points, i.e., 2 and 4 months

(administered at 25 mg/kg body weight). Undecalcified ground sections (20  $\mu\text{m}$ ) were prepared from implanted segments of bone using different grades of sandpaper and observed under UV light with Leica DM 2000 bright light phase contrast and fluorescence microscope including Leica Qwain software. Golden yellow fluorescing area was observed to identify newly formed bone and was also measured in  $\mu\text{m}^2$  and converted to percentage of bone formation. The extracted samples were also observed using SEM for bone-implant interfacial characteristics. Samples were first fixed in 5% glutaraldehyde in PBS buffer for 48 hours followed by gradual ethanol series drying. Dried samples were gold coated before imaging using the same desktop SEM, described earlier.

Micro-computed tomography ( $\mu\text{-CT}$ ) images of extracted bone samples with inserted scaffolds (BAG, L-BAG, S-BAG and LS-BAG) were taken using XT-H 225 (Nikon Metrology, Belgium) with maximum 110 kV rotating target X-ray source (75  $\mu\text{A}$  test current), spot size 3  $\mu\text{m}$ , resolution:  $\sim 12 \mu\text{m}$  and 5-axis manipulator. Images thus obtained were qualitatively assessed for bone in-growth into the scaffolds.

#### 4.2.8 Statistical analysis

Radiological and histological images for all groups of animals were analyzed as means  $\pm$  standard deviations and data has been analyzed by SPSS software package (Version 16, SPSS Inc., Chicago, USA) employing two-way ANOVA considering group and month as factors.

## 4.3 Calcium phosphate and bioactive glass coating on Magnesium alloy

### 4.3.1 Fabrication of samples

#### 4.3.1.1 Sample preparation

The Mg-alloy with alloying elements of approximately (22.5 w/o Zn and 0.5 w/o Ca) was used for the present study. (Henceforth, the samples will be referred as BM). The alloying elements were quantified by X-ray fluorescence spectroscopy (XRF). Further, the phases of the alloys were analysed by XRD (PANalytical, Netherlands) and FTIR (Spectrum 100, PerkinElmer, USA) and SEM-EDX (Scanning Electron Microscopy-Energy Dispersive Analysis of X-Ray) (PhenomproX, Phenom-World B.V., Netherlands) was used for microstructural and approximate qualitative elemental determination. Samples were cut into rectangular strip/plate with size 10 mm x 100 mm x 3 mm using abrasive cutting machine. The surface of the specimens was roughened by 99.9% high pure alumina grit (16 mesh) using a pressure blast (MEC Shot Blasting Equipments Pvt. Ltd., India). The roughness of the surface was around 6-10  $\mu\text{m}$  (average). Subsequently, acetone was used to clean all the samples ultrasonically and dried at room temperature for further use.

Bioactive glass S53P4 was synthesized by conventional melt-quench method using  $\text{SiO}_2$  (LobaChemie, Mumbai, India, Min. assay 99.7%),  $\text{CaCO}_3$  (Min. assay 98.5%),  $\text{Na}_2\text{CO}_3$  (Min. assay 99.9%) and  $(\text{NH}_4)_2\text{HPO}_4$  (Min. assay 99%) (Merck, Mumbai, India) as raw materials. Calculated batches were mixed thoroughly and melted at  $1360^\circ\text{C}$  followed by quenching in double distilled water (DDW). Frits were collected and extensively milled at 250 rpm using a planetary ball mill (PM100, Retsch, Germany) followed by further grinding and sieving to obtain granules ranging between 70-150  $\mu\text{m}$ . The powder chemical composition was checked

by wavelength dispersive X-ray fluorescence spectrometry. The final powder was also tested to ensure particle size distribution (Microtrac S3500, USA).

Hydroxyapatite was prepared by conventional wet chemical method using A.R. grade calcium hydroxide [ $\text{Ca}(\text{OH})_2$ , Central Drug House, India] and ortho-phosphoric acid ( $\text{H}_3\text{PO}_4$ , Merck, India) as raw materials. Stoichiometry of reagent materials was maintained in a way (1.67) that pure phase can be obtained. After completion of drop-wise mixing of  $\text{H}_3\text{PO}_4$ , solution was kept for 24 h for precipitation. Precipitate was then washed and filtered followed by drying at  $80^\circ\text{C}$  for 24 h. After drying, this was ground and sieved to get homogeneously sized powders. Powder was fired at  $800^\circ\text{C}$  to obtain phase pure hydroxyapatite. Finally, the same was graded sieved to obtain granules ranging between 70-150  $\mu\text{m}$ . Sintered (at  $1250^\circ\text{C}$ ) free flowing granules were used for subsequent plasma spray coating purpose. Further details have been reported elsewhere [154].

Strips/ plates of BM were used for hydroxyapatite (HAp) and bioactive glass (BG) coating by using air plasma spray system (SulzerMetco, USA) (henceforth, BG and HAp coated BM samples shall be referred as BMG and BMH respectively). Six (6)-axis manipulator (ABB Engineering, China) was used to obtain uniformity of the coating on substrate. Plasma cathode, a conical tip was made of thoriated tungsten, while copper was used to make anode/ nozzle of the torch with a conical shape that finished in a cylindrical duct 6 mm in internal diameter (ID). Torch generation was carried out using argon (primary plasma gas) and hydrogen (secondary plasma gas). Spray conditions used are detailed in Table 3.

Table 3: Spray condition used for plasma spray coating of HAp and bioactive glass on Mg-alloy

<b>Coating parameters</b>	<b>HAp coating (BMH)</b>	<b>S53P4 coating (BMG)</b>
Arc current	500 A	350 A
Current	458 A	357 A
Voltage	62.2 V	58.2 V
Argon	55 NLPM	55 NLPM
Hydrogen	3 NLPM	2 NLPM
Flow rate	21 g/min	28 g/min.
Water conductivity	39.9 $\mu$ s	39.9 $\mu$ s
Gun distance	6 inch	6 inch
Average time	40 sec	35 sec

#### 4.3.1.2 Feedstock powder and coating characterization

Phase analyses of the powders were carried out by powder X-ray diffraction (XRD) using a diffractometer (PANalytical, Netherlands) with Cu K $\alpha$  ( $\lambda = 1.54178 \text{ \AA}$ ) radiation [40 kV/ 30 mA with  $2\theta$  between  $20\text{--}60^\circ$ , step size of  $0.05^\circ$ ] and further verified by Fourier transformed infrared spectroscopy (FTIR) [KBr pallet method; mid-IR range of  $4000\text{--}400 \text{ cm}^{-1}$ , resolution

4 cm<sup>-1</sup>] using Spectrum 100 spectrometer (PerkinElmer, USA) having He-Ne laser as IR source.

Similarly, phase analyses of the coatings before and after immersion in stimulated body fluid (SBF) were carried out by XRD and confirmed by FTIR for molecular structural information. Field-emission scanning electron microscope (FESEM) (Zeiss Supra, 35VP, Germany) equipped with energy-disperse spectrometer attachment were utilized to evaluate both top surface and cross-section morphologies and quantitative elemental allocations of the samples before and after immersion. Prior the study, carbon sputter coating was given (~ 30 nm) to make the surface conductive. Coating delamination strength was assessed in a scratch tester (Scratch Adhesion Tester, Ducom, USA) using a diamond indenter Rockwell C, with tip radius 200 µm with increasing load from 1-35 N.

#### 4.3.1.3 Electrochemical corrosion test

Electrochemical corrosion of coated and uncoated samples was carried out in SBF solution with an electrochemical workstation (Bio-Logic Science Instruments SAS, France). Atypical three-electrode cell at 36.5±0.5°C was used to carry out all the measurements. A reference electrode called Saturated calomel electrode (SCE), a counter electrode called platinum mesh was used and sample with 0.64 cm<sup>2</sup> surface area exposed to the solution was used as working electrode. Prior the experiment, samples were ground using 1200 grit emery paper, followed by polishing with 1 µm alumina powder and washing with ethanol (99%). The potentiodynamic polarisation data were collected from -0.25 V (with reference to SCE) to 1.6 V with a scanning rate 10 mV sec<sup>-1</sup>.

#### 4.3.1.4 SBF immersion test

*In vitro* bioactivity was studied in simulated body fluid (SBF) maintained at a temperature of  $37.4 \pm 0.2^\circ\text{C}$ . Method as reported by Kokubo et al. [155] was used to prepare SBF, pH was maintained  $\sim 7.4$  by using tris (tris(hydroxymethyl)aminomethane) buffer during preparation. Surface area (SA) of samples is to volume (V) of SBF added was maintained at  $1 \text{ cm}^2/15 \text{ mL}$  with constant temperature ( $37.4 \pm 0.2^\circ\text{C}$ ) during the study (inside incubator in closed test tubes for 7 and 14 days without replenishing SBF solution in between). Change of weight, pH and supernatant ion concentrations ( $\text{Mg}^{2+}$ ,  $\text{Ca}^{2+}$ ,  $\text{PO}_4^{3-}$ ) were noted with time. After 7 and 14 days, low angle XRD and FTIR were used for assessment of coating composition while FESEM photograph was taken on top surface to verify the microstructure. Quantitative phase analysis of the XRD data was done by using RIR method in X'pert pro HighScore Plus software.

#### 4.3.2 In vitro biocompatibility assessments

##### 4.3.2.1 Cell culture procedure

Cell culture medium containing DMEM, 10% fetal calf serum and 1% penicillin/streptomycin with human osteoblasts like cells (MG-63) was used and kept in a humidified atmosphere of 5%  $\text{CO}_2$  at  $37^\circ\text{C}$ . The 90% confluence cells were counted following the procedure of trypsinization, centrifugation and finally suspended back in media. Sterilization of the samples was carried out using 70% ethanol and UV light for 30 minutes followed by washing with sterile PBS (pH 7.4) and treated with DMEM medium for 4 h to generate a conducive atmosphere for better sustaining of cells. Implants were partially dried for 2 h to make certain for superior cell penetration. The next step includes drop-by-drop addition of twenty  $\mu\text{L}$  of the



cell suspension in medium, containing  $10^5$  cells in each sample. The cell loaded samples were kept in a humidified environment, at  $37^\circ\text{C}$ , 5%  $\text{CO}_2$  to facilitate better cell adhesion in the early hour. The cell seeded matrices were kept in medium for 21 days with alternate day replacement of medium.

#### 4.3.2.2 Cell viability assay

The MTT assay was carried out to examine the viability of cells at several time points. The procedure involved the incubation of samples in 5 mg/mL MTT stock solution (1:10 dilution) using PBS (pH 7.4). After 4 h of incubation, formazan crystals were dissolved in DMSO, and the optical density was measured in spectrophotometer (Bio-Rad, iMark) as per the Manufacturer's guidelines.

#### 4.3.2.3 Cell proliferation by alamar blue (AB) assay

Cell proliferation on matrices was measured using Alamar blue dye-reduction assay over 21 days using dye-to-media ratio of 1:10. Amicroplate reader (Thermo Scientific Multiskan Spectrum, Japan) was used to estimate the dye reduction of the incubated samples at 570 and 600 nm (For 4h in dark condition) using equation (1).

$$\% \text{ AB reduction} = [(\epsilon_{\text{ox}\lambda_2})(A\lambda_1) - (\epsilon_{\text{ox}\lambda_1})(A\lambda_2)] / [(\epsilon_{\text{red}\lambda_1})(A'\lambda_2) - (\epsilon_{\text{red}\lambda_2})(A'\lambda_1)] \times 100 \dots (1)$$

where  $\epsilon\lambda_1$  (570 nm) and  $\epsilon\lambda_2$  (600 nm) represents the molar extinction coefficient of alamar blue;  $\epsilon_{\text{ox}}$  and  $\epsilon_{\text{red}}$  in oxidised and reduced form respectively; absorbance of test wells was  $A\lambda_1$

and  $A_{\lambda 2}$ ; and  $A_{\lambda 1}$  and  $A_{\lambda 2}$  correspond to the absorbance of negative control wells. All given pairs were evaluated are values at 570 and 600 nm.

#### 4.3.2.4 Alkaline phosphatase assay (ALP)

The MG-63 cells (NCCS, Pune, India), seeded with scaffolds were cultured for a definite time point to quantify the produced alkaline phosphatase spectrophotometrically. Briefly, the cell laden constructs were rinsed with PBS (pH 7.4), homogenised with 1 mL Tris buffer (1 M, pH 8.0), and finally sonicated for 4 min in chilled condition. Next, 1 mL of 16 mM p-nitrophenyl phosphate (Sigma) solution was added to 20  $\mu$ L of the supernatant and incubated for 5 min., at 30 °C. The p-nitrophenol produced in presence of ALP was measured by observing the absorbance at 405 nm depicting absorbance was calculated at 405 nm, as p-nitrophenol formed, normalized by incubation duration and cell count:  $\mu$ mole/min/ $10^5$  cells.

#### 4.3.2.5 Cellular morphology

The orientation, distribution and morphology of cells were monitored by Laser confocal microscopy. In brief, the samples were fixed with 4 % paraformaldehyde for 1 h followed by 5 min cellular permeabilization using 0.1 % Triton X-100 in bovine serum albumin (BSA). Post blocking of samples with 1% BSA for 1 h, actin filaments were stained using Alexa Fluor<sup>®</sup> 488 and the nuclei with Hoechst 33342. Later, these were imaged by confocal laser microscopy (Olympus FV 1000, Olympus, Japan) and analysed with Olympus FV 1000 Advanced software version 4.1 (Olympus, Japan).

#### 4.3.2.6 Gene expression by real-time RT-PCR

RNA extraction was performed on 21 days cultured MG-63 cells on different samples by using Trizol solution (Invitrogen, USA). In brief, cell seed samples were transferred to small vials containing 1.5 mL of Trizol solution and incubated for 15 min. After that centrifugation was done at 12000 rpm for 10 min/ 4 °C and the clear supernatant was collected in a fresh tube followed by addition of chloroform, incubated for 5 min at RT. The sample was then mixed for 15 s and again incubated for 5 min at RT. Again, the samples were centrifuged at 12000 rpm for 15 min at 4 °C and the topmost aqueous layer was transferred to a RNeasy Plus mini-spin column (Qiagen, Germany). According to the manufacturer's protocol the RNA was washed and eluted repeatedly. Then the RNA samples were reverse transcribed into cDNA using High-capacity cDNA reverse transcription kit (Applied Biosystems, USA) in line with the manufacturer's guidelines.

Using SYBR Green (Applied Biosystems, USA), gene-expression was performed by Real-time PCR conditions in an ABI Prism® 7000 Sequence Detection System (Applied Biosystems, USA). SYBR Green supermix, 5 µL cDNA templates and 5 pmol/mL of each primer (forward and reverse) were used for real time analysis in a final solution of 50 µL volume and plates were loaded using a RT loading platform. Cycling conditions involved an initial denaturation step of 8 min. and 45 s at 95 °C followed by 45 cycles of 30 s at 95 °C, 30 s at 58 °C and 30 s at 72 °C. Data was collected at 72 °C in each cycle. CT (threshold cycle) values were calculated using the Relative Quantification software (Applied Biosystems).

Highly purified gene-specific primers for osteopontin (OPN), collagen I, osteocalcin (OCN), Runx2, and housekeeping gene GAPDH (Table 4) were selected bearing in mind the literature

and synthesized commercially (MWG-Biotech AG Ltd, India). The Ct value of the housekeeping GAPDH gene was used to normalise relative expression levels for each target gene using an identical procedure ( $2^{-\Delta\Delta Ct}$  formula, Perkin Elmer User Bulletin  $\neq$  2). Each sample was experimented in triplicate.

Table 4: RT-PCR primer sequences (forward and reverse) used in the current gene expression study

<b>Genes</b>	<b>Forward primer</b>	<b>Reverse primer</b>
<b>Runx2</b>	5'-GCTTCTCCAACCCACGAATG-3'	5'-GAACTGATAGGACGCTGACGA-3'
<b>OCN</b>	5'-AAAGCCCAGCGACTCT-3'	5'-CTAAACGGTGGTGCCATAGAT-3'
<b>Osteonectin</b>	5'-ACAAGCTCCACCTGGACTACA-3'	5'-TCTTCTTCACACGCAGTTT-3'
<b>OPN</b>	5'-GACGGCCGAGGTGATAGCTT-3'	5'-CATGGCTGGTCTTCCCGTTGC-3'
<b>ALP</b>	5'-TCAGAAGCTCAACACCAACG-3'	5'-TTGTACGTCTTGGAGAGGGC-3'
<b>BSP</b>	5'-CAGGGAGGCAGTGACTCTTC-3'	5'-AGTGTGGAAAGTGTGGCGTT-3'
<b>COL I</b>	5'-TCCTGCCGATGTGCTATC-3'	5'-CAAGTTCCGGTGTGACTCGTG-3'
<b>GAPDH</b>	5'-AGGTCCGGTGTGAACGGATTTG-3'	5'-TGTAGACCATGTAGTTGAGGTCA-3'

#### 4.3.2.7 Mineralization assay by ARS staining

The mineralization study was assessed by using the Alizarin Red-S (ARS) staining dye. In brief, prior to washing thrice with PBS, the MG-63 cells loaded constructs were fixed in ice cold 70 % ethanol for 1 hr. Next, constructs were again washed with distilled water and stained with ARS (40 mM) for 20 min at RT. At the end, the stained constructs were viewed under

optical microscope after rigorous washing with distilled water. The principle of the study is to observe the mineralization which occurs due to binding of the ARS with calcium salts. This can be qualified by imaging (mentioned above) and quantified by reading the absorbance at 540 nm in microplate reader prior to desorbing the stain by using 10% cetylpyridinium chloride for 1 h respectively.

#### 4.3.3 *In vivo* biocompatibility studies

Nine (9) mature New Zealand white rabbit (1.5-1.8 kg body weight) were utilized in the present *in vivo* experiment. The rabbits were maintained in separate cages of temperature and humidity-controlled room including provision of standard diet and water. The animals were assigned into three random groups consisting of three animals each. In group I (3 animals) bare Mg alloy scaffolds (BM) were implanted bilaterally in distal part of femur bone; whereas hydroxyapatite coated Mg alloy implants (BMH) and bioactive glass coated Mg alloy implants (BMG) were placed in other two groups (group II and III respectively). The protocol of Institutional Animal Ethical Committee (IAEC), West Bengal University of Animal and Fishery Sciences (WBUAFS), India (Approval No. Pharma/188 (viii) dated 31.07.2015) was strictly followed.

##### 4.3.3.1 Surgical procedure

Before surgery, distal femur of both hind legs was shaved, cleaned, and aseptically prepared. Anaesthesia was achieved with a combination of xylazine hydrochloride (Injection Xylaxin, Indian Immunologicals, Ahmedabad, India) at 6 mg/kg body weight and ketamine hydrochloride (Ketalar, Parke-Davis, Hyderabad, India) @33 mg/kg body weight intramuscularly (IM). Skin incision was made in the distal lateral part of the femoral bone in

all groups. The femur bone was approached by surgically exposing the skin, subcutaneous tissue, the muscle and finally periosteum. A circular bone defect was created by micromotor dental drilling to press fit the implants. During this procedure, constant sterile cold water was irrigated at the defect site to prevent thermal necrosis of bone. The respective implants were then press fitted and the incised muscles, fascia and skin were apposed with standard suturing techniques.

#### 4.3.3.2 Postoperative clinical examinations

During the post-operative period, animals were checked for any lameness, swelling of the operated site, edema and the cardinal signs of local inflammatory reaction up to 2 months.

#### 4.3.3.3 Radiological examinations

Chronological radiographs of the operated limb were performed at day 0 and afterwards on 1 and 2 months postoperatively (300 mA, M.E. X-Ray Machine, India) to ascertain the proper position of implant within the bony defect.

#### 4.3.4 Histological study

Implanted bone area was collected for histology to assess the status of cell-material interaction. Accordingly, implanted bone tissue samples were collected for all the groups on 2 months postoperatively. Bone sections were initially fixed in 10 % formalin for 7 days and afterwards decalcified using Goodling and Stewart's fluid (15 ml formic acid, 5 ml formalin and 80 ml distilled water). The resultant decalcified bone samples were fixed in paraformaldehyde and

4µm tissue sections was prepared from the paraffin embedded block and stained with haematoxylin and eosin. The stained tissue sections were finally examined under the Leica microscope (Leica Microsystems, Weztlar, Germany) for histological examination.

#### 4.3.5. Scanning electron microscopy study

Two-month post-implanted bone samples were also checked for interfacial study of new osseous tissue formation using SEM. After carefully removing the soft tissue from the bone, the samples were fixed in 2 % E. M. grade glutaraldehyde phosphate solution for 48 h, washed thrice for 30 min. with PBS (pH 7.4) and distilled water and finally drying the samples in a series of graded alcohol solutions. Gold sputter coated bone samples were imaged using an FESEM (LEO, U.K.) for microstructural analysis of newly formed osseous tissue at the interface of bone and material.

#### 4.3.6. Fluorochromelabelling study

Oxytetracycline as fluorochrome marker (Terramycin; Pfizer India, India) @ 25mg /kg body weight was injected 25 days prior to euthanasia of the animals at 2 month i.e., on the days 35, 36 and 3, 4 (2-6-2 manner) postoperatively . The retrieved implanted bone samples were grounded to 20 µm thickness and finally placed under ultraviolet incidental light with a Leica DM 2000 fluorescence microscope. The golden yellow fluorescence (new bone formation) pixels were measured and consequently transformed to percentage of new osseous tissue formation.

#### 4.3.7. Toxicological study

Toxicological study of BM, BMH and BMG implanted bone was carried out by histology of three major organs, like heart, liver and kidney. To carry out the same, the H & E stained histological sections of heart, liver and kidney from the sacrificed animals were prepared to observe any presence of significant cellular changes or not.

#### 4.3.8. Immunocompatibility study

The amount of host-implant immune-compatibility was determined by measuring the concentration of IL2, IL6 and TNF- $\alpha$  cytokine response of the animals post *in vivo* implantation with biomaterials (i.e., BM, BMH and BMG implants). Blood serum was collected at 1, 2, 4 and 8 weeks post-surgery and concentrations of IL2, IL6 and TNF- $\alpha$  were estimated using ELISA kits for rabbit (Invitrogen, USA).



## 5. RESULTS AND DISCUSSION

### 5.1 HAp coated e-glass characterization

In this part, the main objective was to coat bio-inert E-glass fibers with materials having better corrosion properties than commonly used ceramics. Thus, HAp was selected as a coating material and as a first step, a coating was successfully developed for the first time on e-glass coupons aiming better implant-bone interaction on the substrate with high mechanical strength.

#### 5.1.1 Characterisation of the coating

Reaction of  $\text{Ca}(\text{NO}_3)_2 \cdot 4\text{H}_2\text{O}$  with  $\text{P}_2\text{O}_5$  in ethanol results in the formation of a translucent gel, which is a mixture of amorphous HAp, calcium nitrate and  $x\text{CaO} \cdot y[\text{PO}_{m+1}(\text{OH})_n(\text{OEt})_o]$  ( $x$  and  $y$ : arbitrary,  $2m+n+o = 3$ )[156]. The gel was used for coating only after 2h from termination of mixing, as its viscosity remains low initially. To get the desired phase, crystallinity and pore size, the coated substrates were sintered at 850 °C. Optical microscope images after sintering showed micro-cracks on top of the coatings due to thermal-expansion co-efficient mismatch between e-glass ( $5.4 \times 10^{-6}/^\circ\text{C}$  at 25°C) and HAp ( $14.75 \times 10^{-6}/^\circ\text{C}$  at 25°C for HAp)[157].

XRD studies (Fig. 2a) of coated substrate confirmed the presence of only hydroxyapatite phase. The major diffraction peaks found at  $31.67^\circ$ ,  $32.83^\circ$ , and  $25.79^\circ$   $2\theta$  matched well with the standard peaks of pure hydroxyapatite crystals as in JCPDS PDF #09-0432 data card. Hence the peaks can be indexed as those of the HAp having hexagonal crystal structure with space group  $\text{P6}_3/\text{m}$ [158]. The average crystallite size calculated from Debye-Scherrer equation was found to be  $26 \pm 3$  nm. The slight expansion of lattice parameters with respect to the standard

values has also been observed. The “a/b” axis of the hexagonal crystal expanded from 9.432 Å to 9.4484 Å and “c” axis expanded from 6.881 Å to 6.907 Å. Accordingly, the unit cell volume of the crystal structure was also increased from 530 Å<sup>3</sup> (standard hydroxyapatite) to 534.02 Å<sup>3</sup> hinting at some effects of thermal stress. The Percentage of crystallinity calculated by using Landi’s et al method [159] was found to be moderately high (~ 89%) on top surface which is desirable for *in vitro* or *in vivo* dissolution with time. A small hump at 30.46° 2θ was due to the presence of β-TCP phase as impurity. As expected, there was no crystalline peak in the bare substrate (Fig. 2a(i)), and typical amorphous nature of e-glass was noticed.

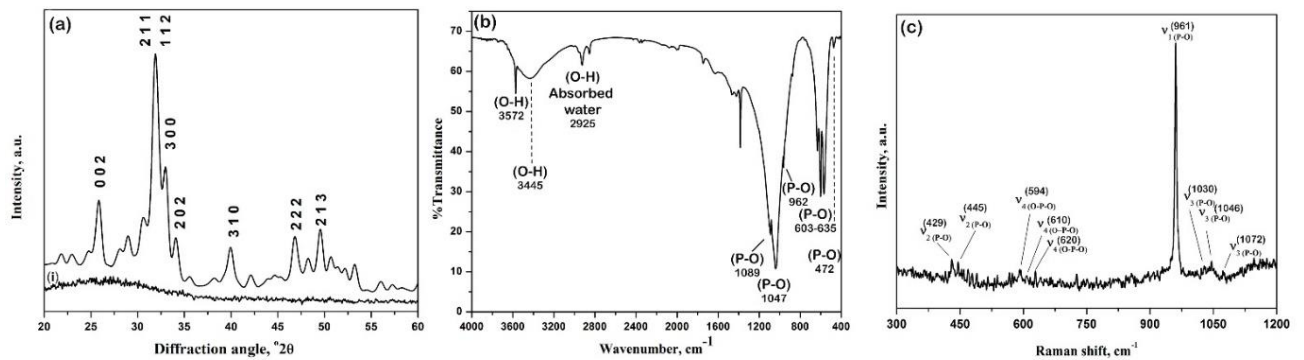


Fig. 2: (a) XRD patterns [along with bare e-glass substrate (i)], (b) FTIR and (c) Raman spectra acquired from the top coated surface.

The FTIR (Fig. 2b) spectrum of the coating showed four typical vibrational modes of PO<sub>4</sub><sup>3-</sup> (ν<sub>1</sub>, ν<sub>2</sub>, ν<sub>3</sub> and ν<sub>4</sub>) which are found to be present at 962 cm<sup>-1</sup>, 472 cm<sup>-1</sup>, 1047/1089 cm<sup>-1</sup> and 603 cm<sup>-1</sup>, respectively. The peak at 962 cm<sup>-1</sup> (ν<sub>1</sub>) corresponds to non-degenerate symmetry stretching of P-O bond in the PO<sub>4</sub><sup>3-</sup> group and the peak at 472 cm<sup>-1</sup> (ν<sub>2</sub>) is the doubly degenerate phosphate bending mode[160]. The stretching vibration modes of PO<sub>4</sub><sup>3-</sup> (ν<sub>3</sub>) group were reflected at 1047 cm<sup>-1</sup> and 1089 cm<sup>-1</sup>. Another peak at 603 cm<sup>-1</sup> states the presence of triply degenerate O-P-O bending (ν<sub>4</sub>). The peaks at 635 cm<sup>-1</sup> and 3572 cm<sup>-1</sup> reflect the vibrational

and intramolecular-stretching-vibrational mode of hydroxyapatite phase. Especially OH<sup>-</sup> peak at 3572 cm<sup>-1</sup> and PO<sub>4</sub><sup>3-</sup> peak at 962 cm<sup>-1</sup> indicate highly crystalline nature of the coating corroborating the findings of XRD [161]. Raman spectrum (Fig. 2c) acquired from the top coated surface showed characteristic peak of PO<sub>4</sub><sup>3-</sup> ( $\nu_1$ ) at 961 cm<sup>-1</sup> which confirms the HAp phase. There were also two doubly degenerate bending mode ( $\nu_2$ ) at 429 and 445 cm<sup>-1</sup> (P-O bond), four triply degenerate asymmetric stretching mode ( $\nu_3$ ) at 1030, 1046, 1054 and 1076 cm<sup>-1</sup> (P-O bond), and four triply degenerate bending mode ( $\nu_4$ ) at 582, 594, 610 and 620 cm<sup>-1</sup> (O-P-O bond) of phosphate groups present[162]. All bands are characteristically assigned to internal vibrational modes of the phosphate groups.

The FESEM images of the coated top surface after sintering (Fig. 3a) showed mainly rod-like morphology of HAp crystallites with diameters 200-300 nm and lengths between 1-1.5  $\mu\text{m}$ . Some plate-like morphologies with irregular surface were also observed. HAp crystallites were also found on the crack regions acting as bridge which indicates the coating coverage of the substrate surface. FESEM imaging carried out at interface (Fig. 3b) showed no interfacial gap between substrate and coating and the coating thickness was approximately 10  $\mu\text{m}$ . There was no microstructural feature at the cross-section indicating dense structure.

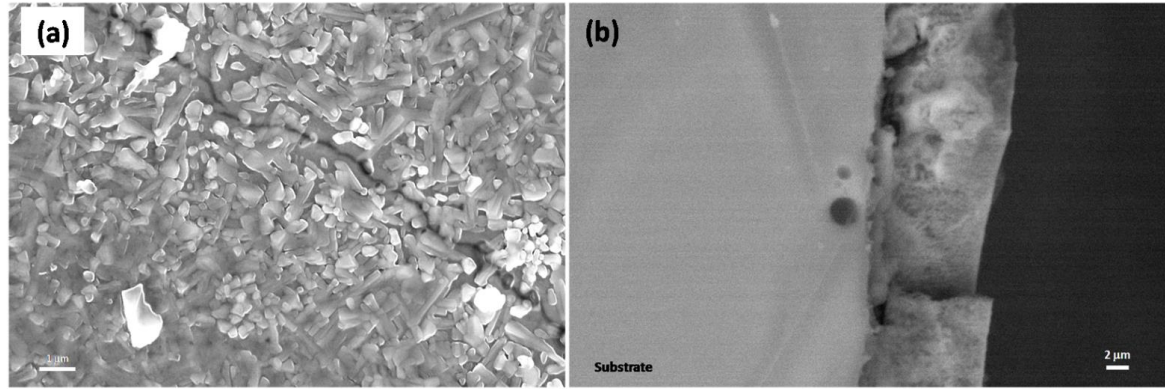


Fig. 3: FESEM microstructure of (a) top coated surface and (b) cross-sectional image showing the interface.

Further detailed study on the cross-section of microstructure using TEM (Figs. 4a-c) showed interconnectivity of pores with diameters of about 300-500 nm, along with certain agglomeration of crystals. The population density of HAp crystals was found to decrease with a slight increase in crystal size towards periphery of coating layer which is also a reason behind the occurrence of cracks at the surface of coating. With decreasing HAp crystal density, interconnectivity of pores increased along the outer region which were considered to be important, as they acted as path channels for supply of micronutrients and removal of cell excretions required for tissue in-growth in the scaffold [163]. Interface study confirmed firm apposition and close contact of coating with the substrate. Line scan EDX showed (Figs. 4d-e) clear demarcation of phases from substrate to coating, also showing absence of interfacial gap. Ca/P ratio was calculated and found to be  $\sim 1.67$ , which also confirms the purity of the hydroxyapatite phase and thus conforms with the XRD and FTIR analyses. The SAED patterns (Fig. 4f) of HAp layer showed clear electron diffraction rings of pure crystalline hydroxyapatite phase, for which  $d = 2.81 \text{ \AA}$  and  $d = 3.44 \text{ \AA}$  correspond to the (211) and the (002)

crystallographic planes respectively, of hexagonal hydroxyapatite, which was also found to be in good agreement with the XRD findings.

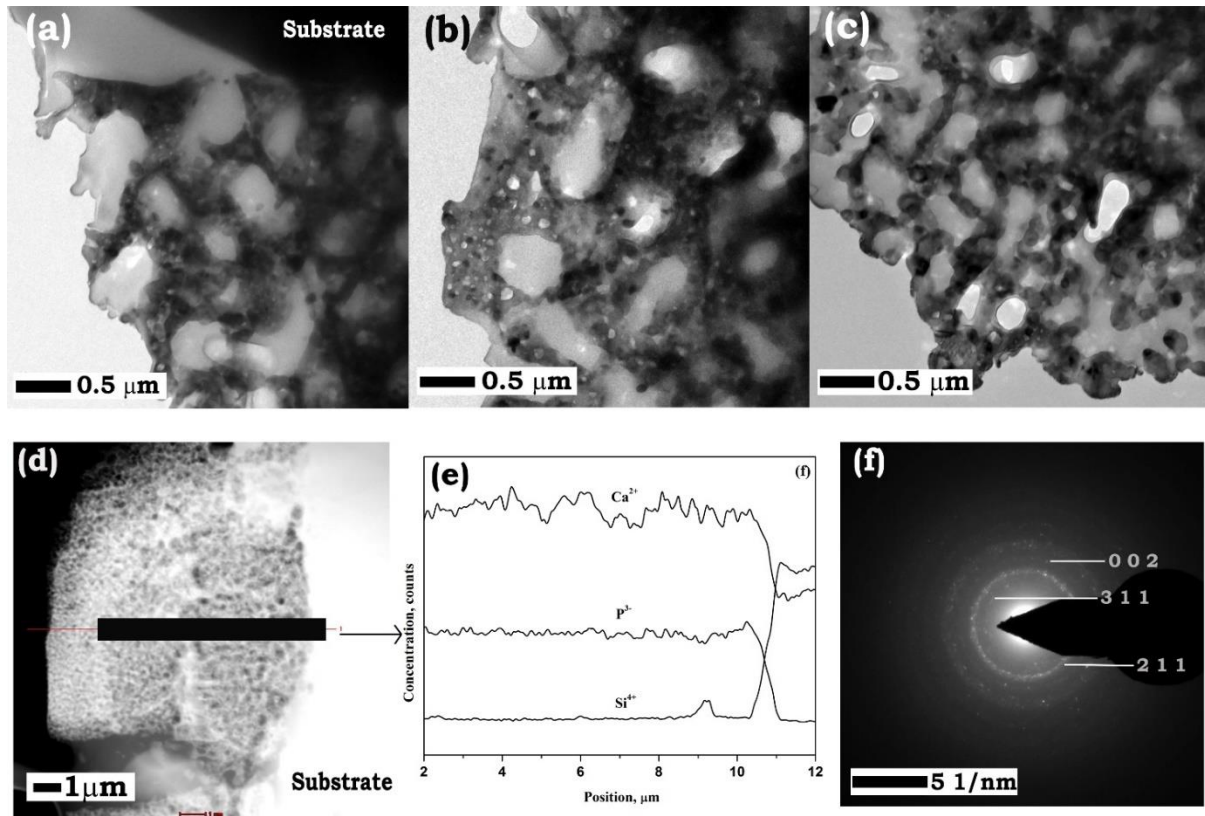


Fig. 4: Cross-sectional TEM images of coated e-glass taken at different regions showing the micro/nano-structural features of the coating's depth and the interface (a-c), EDX line scan (d and e) and SAED pattern (f).

#### 5.1.2 SBF immersion study (static and quasi-dynamic):

Kinetic SBF study depends on two main factors, dissolution, and deposition of ions. These mechanisms in turn depend on the differences of ionic concentration between the sample and the solution in which the former is immersed [164]. Both dissolution and deposition processes

take place simultaneously at different rates. XRD patterns of coated samples after 7 days of static bioactivity study (Fig. 5a-(i)) indicated the formation of calcium phosphate hydroxide  $[\text{Ca}_{10}(\text{PO}_4)_6(\text{OH})_2]$  (matched with JCPDS PDF #00-054-0022) and calcium carbonate (matched with JCPDS PDF #00-029-0305) with relative percentage of phases being 32.7% and 67.3%, respectively. High percentage of calcium carbonate is due to a higher rate of calcium deposition than its dissolution. The higher deposition of calcium carbonate can be explained by solubility products of calcium carbonate and calcium phosphate hydroxide. This phenomenon is possible only if the solubility product of calcium carbonate is higher than the solubility product of calcium phosphate hydroxide. After 14 days of immersion (Fig. 5a-(ii)), due to high rate of phosphate deposition, more hydroxyapatite formed (approx. 69.1%) (matched with JCPDS PDF #04-014-8416) with about 30.1% calcium carbonate. Calcium carbonate may accelerate interaction between implant and body fluid as blood plasma also contains  $\text{Ca}^{2+}$  and  $\text{CO}_3^{2-}$  ions, hence creating a resemblance between the host and foreign body.

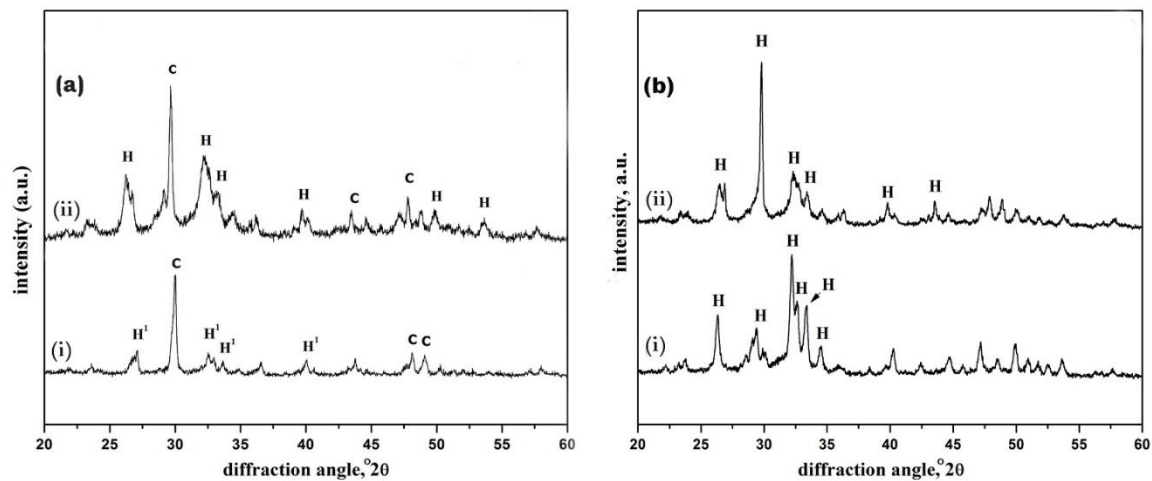


Fig. 5: XRD patterns acquired from the top surface after 7 and 14 days of (a) static and (b) quasi-dynamic SBF study [after (i) 7 and (ii) 14 days] [H = hydroxyapatite, H<sup>1</sup>= calcium phosphate hydroxide and C = calcium carbonate].

In quasi-dynamic study, deposition or dissolution process cannot be completed when the reacting SBF was replaced with fresh volume of SBF, which increased the difference in the ionic concentrations of the solution and the sample. Therefore, the characteristic peaks of hydroxyapatite (matched with JCPDS PDF #01-086-0740) was seen after 7 days (Fig. 5b-(i)), however, with time due to the increased difference in the ionic concentrations, the deposition rate increased. After 14 days of quasi-dynamic study (Fig. 5b-(ii)), the x-ray diffraction peaks of carbonated hydroxyapatite phase (matched with JCPDS PDF #00-019-0272) was seen. This phase might form due to A-type substitution (i.e., carbonate replacing a hydroxyl group) or B-type substitution (i.e., carbonate replacing phosphate group) or both [165].

FTIR spectrum supports the above findings, where the coated e-glass substrates after 7 and 14 days of static SBF study (Fig. 6a-(i) and (ii)) showed a decrease in  $\text{PO}_4^{3-}$  peaks at  $958\text{ cm}^{-1}$  and  $\text{CO}_3^{2-}$  peaks at  $873\text{ cm}^{-1}$  (related to hydroxyapatite). The presence of carbonate group could be confirmed by the peak at  $2347\text{ cm}^{-1}$  [161]. In addition, the decrease in peak intensity hints at a reduction in the amount of calcium carbonate phase from day 7 to 14, which corroborates with the XRD findings. The sharp peak of structural  $-\text{OH}$  group at  $3572\text{ cm}^{-1}$  could not be found after SBF study, which implies that the A-type substitution by carbonate group (replacing hydroxyl group) was more prevalent [165]. The peaks representing P–O vibrations at  $\nu_2$  bending ( $\sim 472\text{ cm}^{-1}$ ),  $\nu_4$  bending ( $\sim 603\text{ cm}^{-1}$ ),  $\nu_3$  (asymmetric stretching around  $\sim 1033\text{--}1067\text{ cm}^{-1}$ ) indicated the presence of calcium phosphate hydroxide formation on day 7. A similar trend was noticed on day 14 as well. When subjected to quasi-dynamic SBF study (shown in Fig. 6b-(i) and (ii)), a similar reaction behaviour as that of static SBF study (with similar peaks as just mentioned) was observed. The characteristic apatite  $\text{PO}_4^{3-}$  peaks were noticed at  $560$ ,  $603$  and  $635\text{ cm}^{-1}$ , while the peak at  $575\text{ cm}^{-1}$  appeared for crystallites of small size [166]. The increasing intensity of  $\text{CO}_3^{2-}$  peak around  $1428\text{ cm}^{-1}$  after 14 days of the quasi-dynamic SBF

study, indicates A-type substitution of carbonate group (i.e., carbonate replacing a hydroxyl group)[165].

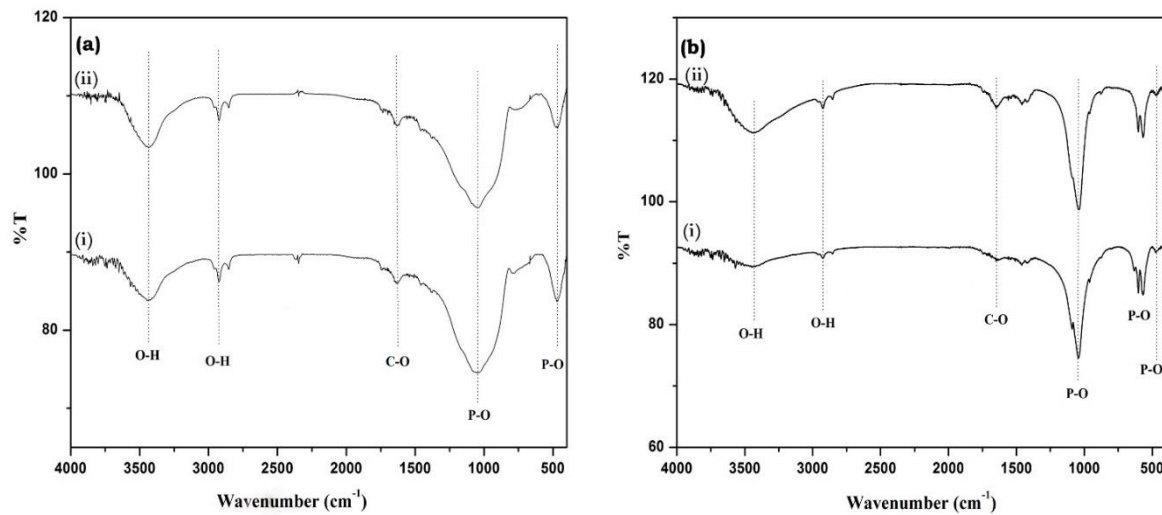


Fig. 6: FTIR spectra of the top surface after 7 and 14 days of (a) static and (b) quasi-dynamic SBF study [after (i) 7 and (ii) 14 days].

Microstructures of top surface of the samples after static SBF study are shown in Figs. 7a and b after 7 and 14 days, respectively. After 7 days (Fig. 7a), dissolution phenomena were dominant so that the needle-like structure of coated sample was missing, with concomitant deposition of calcium carbonate crystals at microcrack regions. As the solubility product of calcium carbonate is higher, it will capture nucleation sites faster than others and the cracks/edges are most favourable sites for crystal growth. Such transformed crystal structures on the top surface signifies prominence of calcium carbonate phase over calcium phosphate hydroxide phase and was also confirmed from XRD (Fig. 5a-(i)) and FTIR (Fig. 6a-(i)). The calculated molar ratio of Ca/P from EDX data of corresponding sample was 1.4, which is the indication of non-stoichiometry [163, 167]. After 14 days (Fig. 7b), fresh deposition of HAp crystals could be seen on top surface. The deposits appeared as densely populated with pores



of variable dimensions, spread throughout the surface, and contained cracks as well. The Ca/P molar ratio after 14 days was found to be 1.67 as calculated from EDX data. In case of quasi-dynamic SBF study, FESEM microstructure depicted a layer of apatite on the top surface of the samples after 7 days (Fig. 7c) and 14 days (Fig. 7d). For day 14, the thickness of the layer increased. Ca/P molar ratio after 7 days was 1.667 which signified the formation of hydroxyapatite phase whereas, after day 14, the ratio became  $\sim 1.87$ , which was the indication of carbonated-hydroxyapatite phase formation, as was also observed in XRD (Fig. 5b-(ii)).

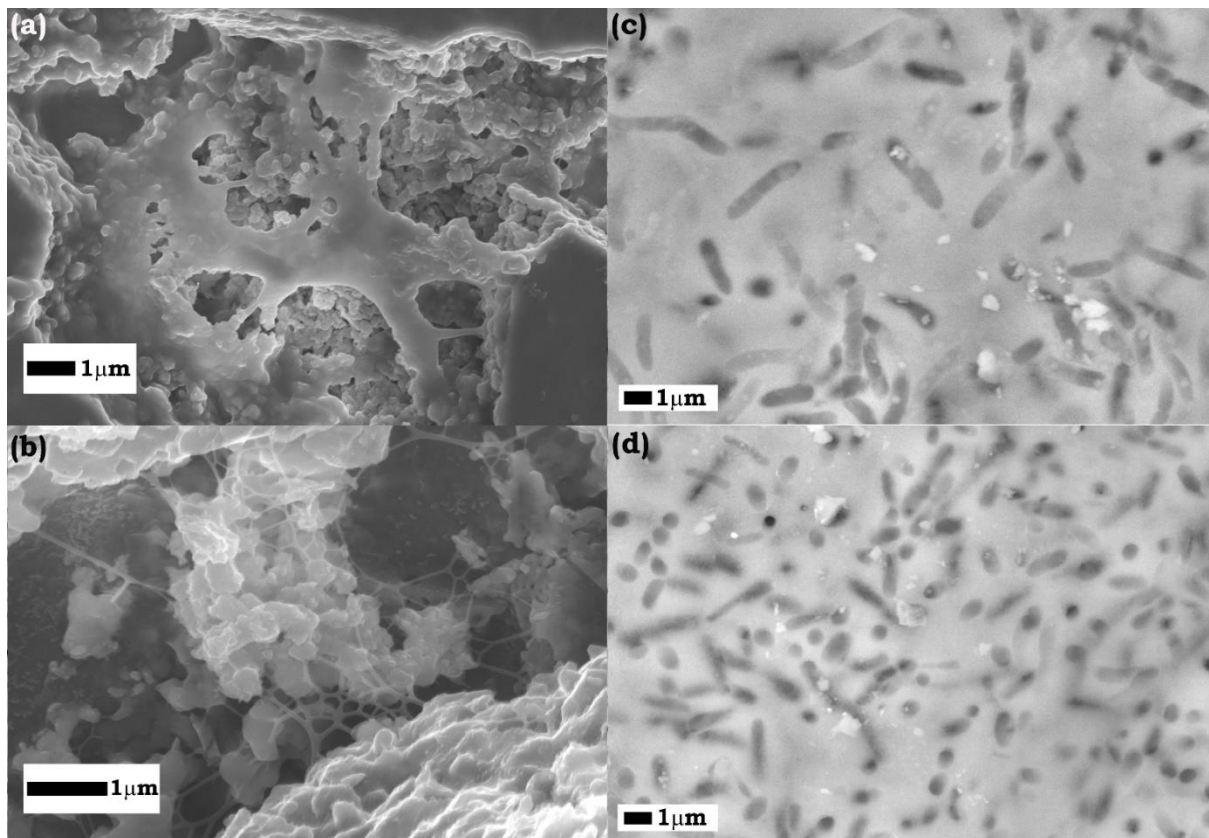


Fig. 7: Microstructure of top surface after static (a – 7 days and b – 14 days) and quasi-dynamic (c – 7 days and d – 14 days) SBF studies.

TEM (Figs. 8a-e) studies revealed the formation of dense calcium phosphate hydroxide nanocrystals after 7 days of static SBF study (Fig. 8a-inset). Apatite formation on top of the

coating was found not to be in a colonised manner; rather it covered the coating surface. The absence of any interfacial gap indicates high biocompatibility and good availability of nucleation sites of the sample. Crystals could also be seen inside surface pores which act as anchor point, and can contribute in favour of increasing the adherence of the apatite layer. In lower magnification (Fig.8b) imaging, bigger calcium carbonate nanocrystals can be seen, but with less density. EDX (Figs. 8c-d) data supported the existence of the calcium carbonate nanocrystals, by showing different calcium and oxygen ion concentrations at different regions of the coating section. These calcium carbonate nanocrystals are indicated by arrow-heads in the dark-field TEM image (Fig.8b). The regions with higher concentration of carbon and oxygen represent the calcium carbonate crystal filled region and the rest is covered with calcium phosphate hydroxide. SAED pattern (Fig. 8e-inset) showed clear diffraction rings of crystalline calcium phosphate hydroxide of  $d = 2.72 \text{ \AA}$  corresponding to the (300) crystallographic plane.

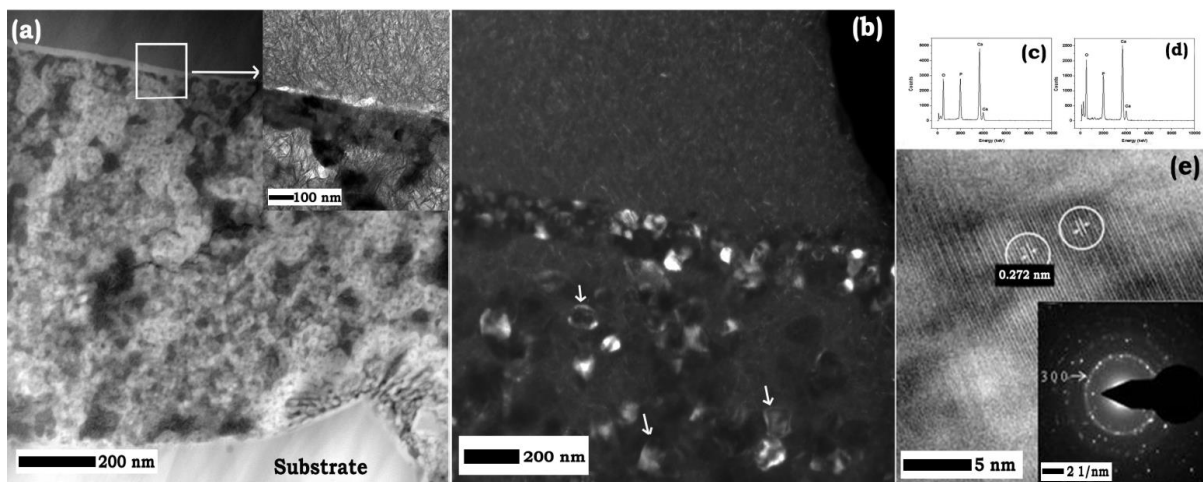


Fig. 8: TEM images of different regions after 7 days of static SBF studies; microstructure (a and the inset, b), EDX (c and d) and HRTEM showing crystalline fringes along with SAED pattern in the inset (e).

After 14 days of static bioactivity study (Figs. 9a-b), extensive apatite deposition almost completely covering the pores of the coating was found on the outer surface. Nucleation of elongated HAP nanocrystals were seen along the periphery of the pores, and this is also the primary stage of crystal growth. Crystal growth is a thermodynamically controlled process, in which the guest crystals use host crystal surface as nucleation sites, or template, for deposition of their own phase [168]. In this case, crystals were found to be more orderly arranged than the 7-day sample which indicates settling and maturation of the crystals with time. EDX (Figs. 9c-d) showed homogeneity in concentrations of Ca and P ions in different regions proving the formation of HAp in higher percentage to be the major phase, which is also in agreement with the XRD analysis. The SAED pattern (Fig. 9e) depicted highly crystalline nature of the coating as strong diffraction rings could be observed clearly. The most prominent diffraction ring corresponds to a “d-spacing” of 2.794 Å representing the (211) crystallographic plane of pure HAp.

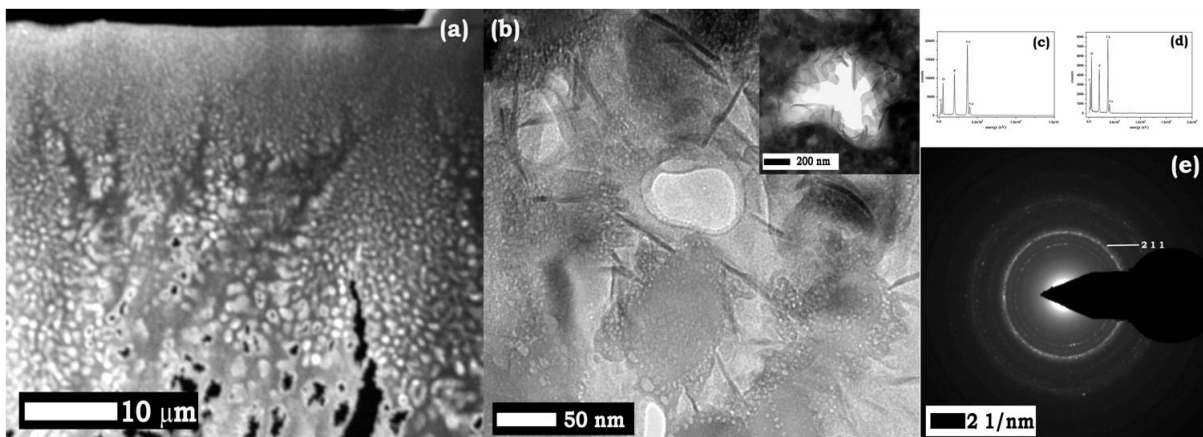


Fig. 9: TEM images of different regions after 14 days of static SBF studies; microstructure (a and b), EDX (c and d) and SAED pattern (e).

In quasi-dynamic SBF study, the TEM images (Figs. 10 a,b and c,d) showed moderate crystallinity near the surface of coating after 7 and 14 days which could be corroborated by the SAED patterns of the respective samples. After 7 days, a crystalline layer composed of hydroxyapatite crystals covered the surface of HAp coated sample. However, initially after day 7, the arrangement of crystals was found to be randomly oriented, indicating the effect of daily replacement of fresh SBF. After 14 days, the population of the crystals were increased which is due to the daily layer by layer deposition of apatite. Also, the crystals were found to be smaller than those of static SBF study as they get less time to complete their crystallization process.

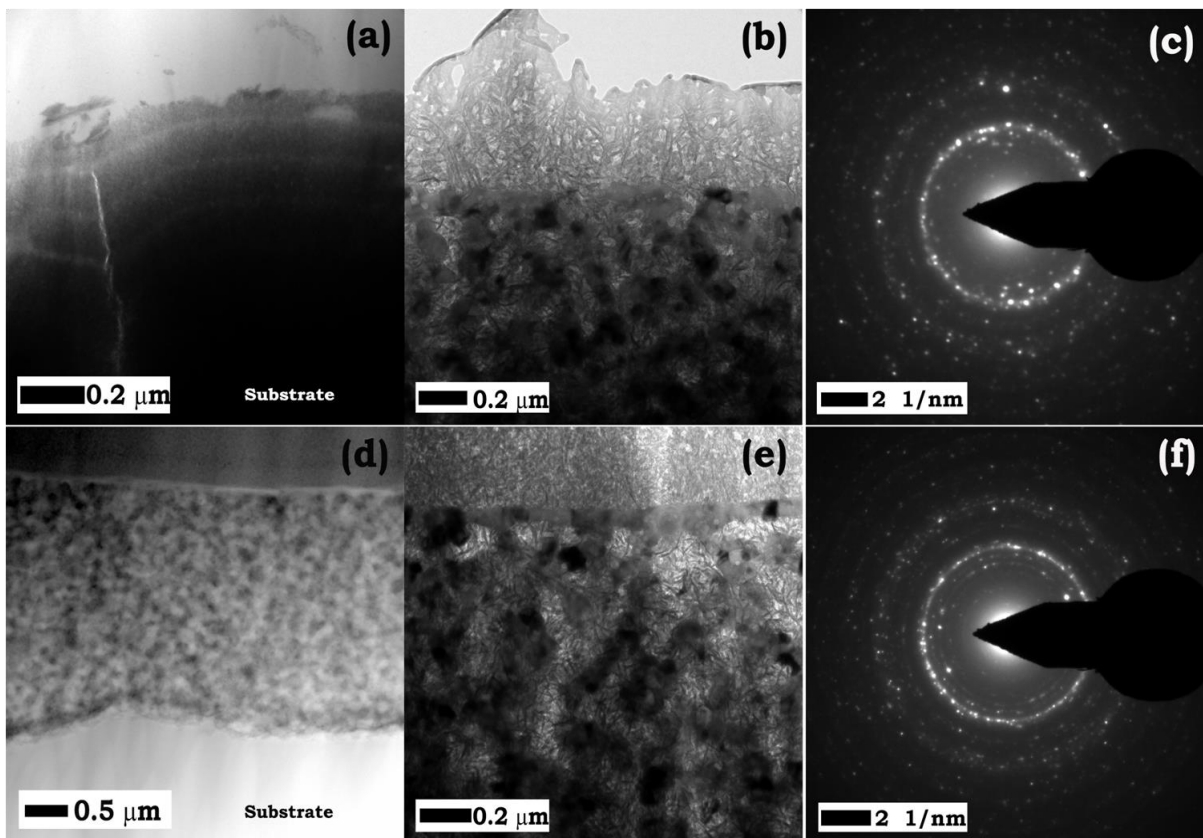


Fig. 10: TEM images of different regions after 7 and 14 days of quasi-dynamic SBF studies; (a, b and c) microstructure and SAED pattern after 7 days and (d, e and f) microstructure and SAED pattern after 14 days.

Ca and P ions of the supernatant liquid were analysed by ICP-AES after static and quasi-dynamic SBF study collected at day 7 and 14 and are given in Figs. 10a and b respectively. Static SBF study (Fig. 11a) showed a decrease in concentration of both calcium and phosphate ions after 7 days. This was due to the deposition of ions on the surface of coated samples, leading to the formation of calcium carbonate crystals as well. After 14 days, a slight increase in calcium and phosphate ions helped in decreasing calcium carbonate concentration and changing of phase from calcium phosphate hydroxide to HAp. The supernatant fluid after quasi-dynamic SBF study (Fig. 11b) showed a series of small changes in calcium and phosphate ion concentrations leading to variation in Ca/P molar ratio and ultimately resulting in different CaP phase/s in XRD.

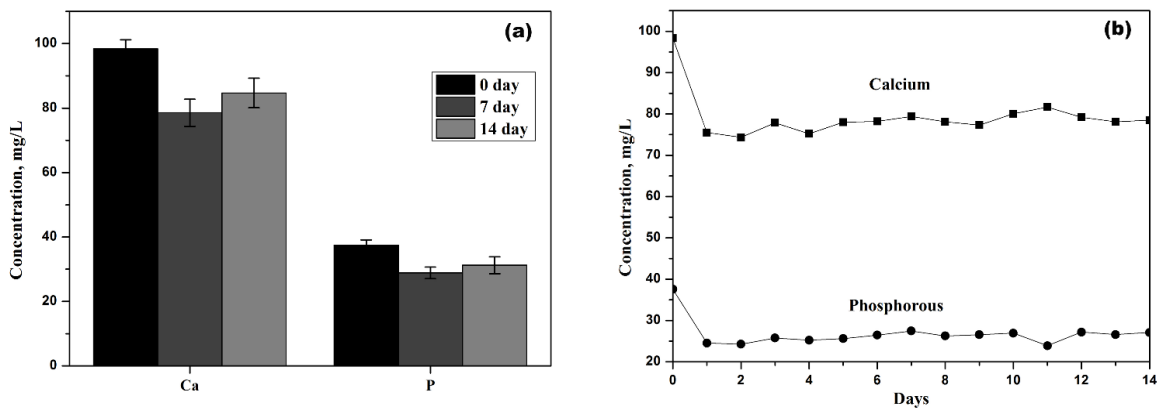


Fig. 11: Concentration of different ions of supernatant in (a) static and (b) quasi-dynamic SBF study at day 7 and 14.

From load-displacement curves, Young's modulus (E) and hardness (H) were calculated based on Oliver and Pharr method [169]. When indenter is pressed against sample, elastic and plastic deformation occurs simultaneously, resulting impression conforming indenter shape. During

unloading, displacement recovered for elastic, eventually providing elastic solution for modeling contact process. H is defined as indentation load divided by projected contact area (measured from contact depth from load-displacement curve). Thus, it's the mean pressure which a material can support under load. E, on the other hand, can be calculated from initial unloading contact stiffness or the initial slope of unloading curve. We have calculated the parameters for both coated e-glass substrates (CEG) and after 7 and 14 days immersion under static (7d-s and 14d-s) and quasi-dynamic (7d-Q and 14d-Q) condition and are shown in Table 5. It has been found that both H and E of HAp coating on e-glass substrates were increased after static and QD studies. The effect is more pronounced for static SBF immersion as there is no fresh replenishment each day like QD process. Significant kinetic enhancement of H and E for static samples were due to more ordered crystalline deposition of apatites after 14 days, thus corroborating the findings of TEM. Significant increase of H and E after 7 days of QD study was due to uniform apatite crystal formation on top which became disordered after day 14 owing to daily change of fresh buffer and hence decrement of E and close values of H.

Table 5: Nano indentation values of H and E of different samples

<b>Sample</b>	<b>H (GPa)</b>	<b>E (GPa)</b>
CEG	0.05 ± 0.01	2.46 ± 0.7
7d-s	0.16 ± 0.07	11.9 ± 2.2
14d-s	1.57 ± 0.14	32.9 ± 2.4
7d-Q	0.37 ± 0.07	33.1 ± 5.7
14d-Q	0.37 ± 0.07	24.3 ± 5.3

### 5.1.3. *In vitro* biocompatibility studies

#### 5.1.3.1 Cell viability, proliferation assay and Alkaline Phosphatase assay (ALP):

Cell viability (by MTT), proliferation (by Alamar blue assay) and ALP expression of MG-63 on bare and coated e-glass samples were measured on days 5, 7, 14 and 21. Maximum cell viability was recorded for coated e-glass after 21 days of cell culture (statistically significant  $**p<0.01$ ,  $***p<0.001$ ) (Fig. 12a). Leachates obtained after 7 and 14 days showed noticeable difference of cell viability between the control and the sample (Fig 11a). Maximum cell proliferation in Alamar Blue<sup>TM</sup> test was recorded for coated e-glass after day 21 (statistically significant,  $*p<0.05$   $***p<0.001$ ) (Fig. 12b). Starting from initial days, the HAp coated e-glass sample was found to be way more prone towards cell proliferation than being under control. This can be justified by the fact that the HAp coated surface exhibits a greater availability of potentially colonisable space by the grown osteoblasts, which once attached, can spread at a higher rate than the control. Another crucial factor for the cell to adhere and increase cellular activity is the adsorption of protein on the surfaces, which are abundant in case of HAp coated samples due to its interconnected porous structure [170] MTT and Alamar blue result supported each other's interpretation that both samples do not have any associated cytotoxicity. ALP expression indicates surface activity of the sample towards bone mineralization. ALP occurs at very early stages of osteogenesis and hydrolyses of the organic phosphates releasing phosphorus ions, which are important for the process of extracellular matrix mineralization. High ALP expression of the coated sample shows higher activity, which is beneficial to the collagen fiber synthesis, formation of calcium nodules, and the maturation of bone mineralization. It also increases with the maturation of osteoblasts [171, 172]. Maximum ALP expression was recorded for coated samples after 21 days of cell culture (statistically

significant, \*\* $p < 0.01$ , \*\*\* $p < 0.001$ ) (Fig. 12c) that clearly indicates the non-cytotoxicity as well as the bioactivity of the coated samples.

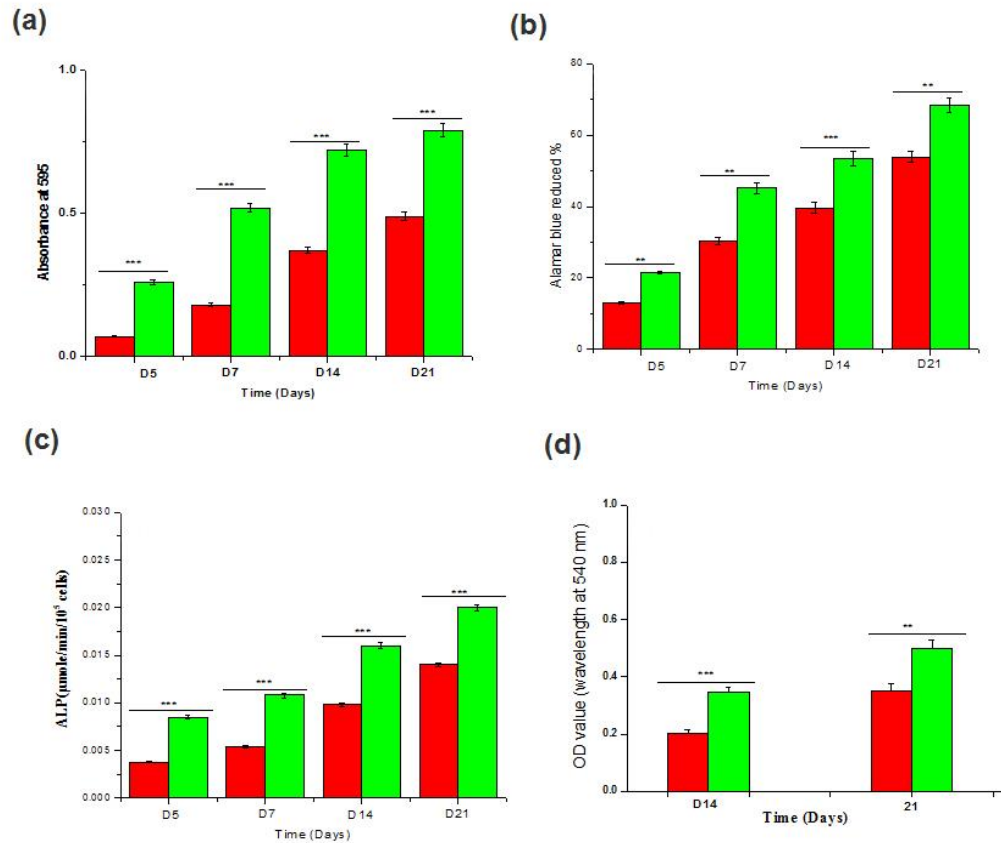


Fig. 12: Response of osteoblast like cells (MG-63) seeded on e-glass substrate and coated surfaces, cultured for 21 days at 37°C and 5% CO<sub>2</sub> humidified atmosphere; (a) viability (b) proliferation of cells and (c) alkaline phosphatase (ALP) activity, (d) quantification of mineral deposition using ARS staining. \*\*\*  $p < 0.001$ , \*\*  $p < 0.01$  and \*  $p < 0.05$ ,  $n=3$  at each time point.

ARS staining helps to measure the mineral content of the sample which is important for apatite formation on the surface. Calcium (Ca<sup>2+</sup>) deposition was measured on day 14 and 21 (Fig. 12d). Maximum Ca<sup>2+</sup> deposition was recorded for coated e-glass substrates after 21 days of cell culture (statistically significant, \*\* $p < 0.01$ , \*\*\* $p < 0.001$ ).



### 5.1.3.2 Cell morphology within the samples by Laser confocal microscopy:

Cell morphology on bare and coated e-glass samples are given in Figs. 13a and b respectively. Maximum number of cells was present in coated e-glass compared to the bare substrate. For coated samples, actin covers the entire surface, forming neo matrix and penetrated into the sample, due to the porous nature of the coating. Since cell cytoskeleton organization is important for cell attachment and morphology, the actin filaments were stained using Alexa Fluor® 488 (green), nuclei were stained with Hoechst 33342 (blue) and examined under confocal at 20X [173]. 3D constructs were Z-scanned during confocal microscopy to examine cell growth upon different layers. Scans across multiple layers were then merged into the final image. The images showed extensive and uniform distribution of the actin filaments on coated e-glass. However, for bare e-glass, actin distribution was sparse and isolated to be present just around the cell nuclei.

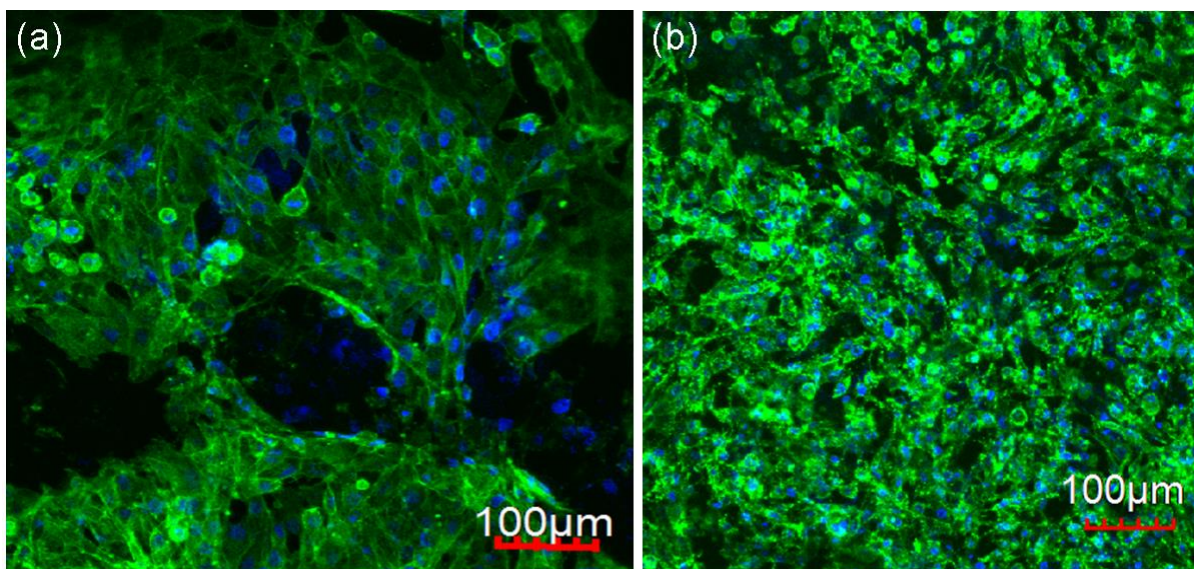


Fig. 13: Cytoskeletal actin organization and distribution of MG-63 cells grown on (a) e-glass substrate and (b) coated surface at day 7.

#### 5.1.3.3 Gene Expression by real time RT-PCR:

Gene expression involved in bone mineralization and maturation in the osteoblastic cells was analysed when in contact with the materials. Osteogenesis process evolves proteins such as osteopontin (OPN), osteocalcin (OCN), collagen type I (COL-I) and RUNX-2. In the early stages of osteoblastic development and mineralization, OPN is secreted, and acts by binding with the organic and inorganic phase to promote tissue adhesion. OPN gene expression is also associated with increased cell adhesion [174]. Variations in mRNA expression levels of bone specific (OCN, OPN, RUNX2 and COLI) markers were detected (Figs. 14a-d) in each sample, when the samples (n=3) were averaged and normalized against the housekeeping gene (GAPDH). Coated e-glass showed significantly higher level of gene expression of markers such as OPN and OCN than control (bare e-glass), indicating an advanced differentiation process, osteoblastic maturation and bone mineralization.

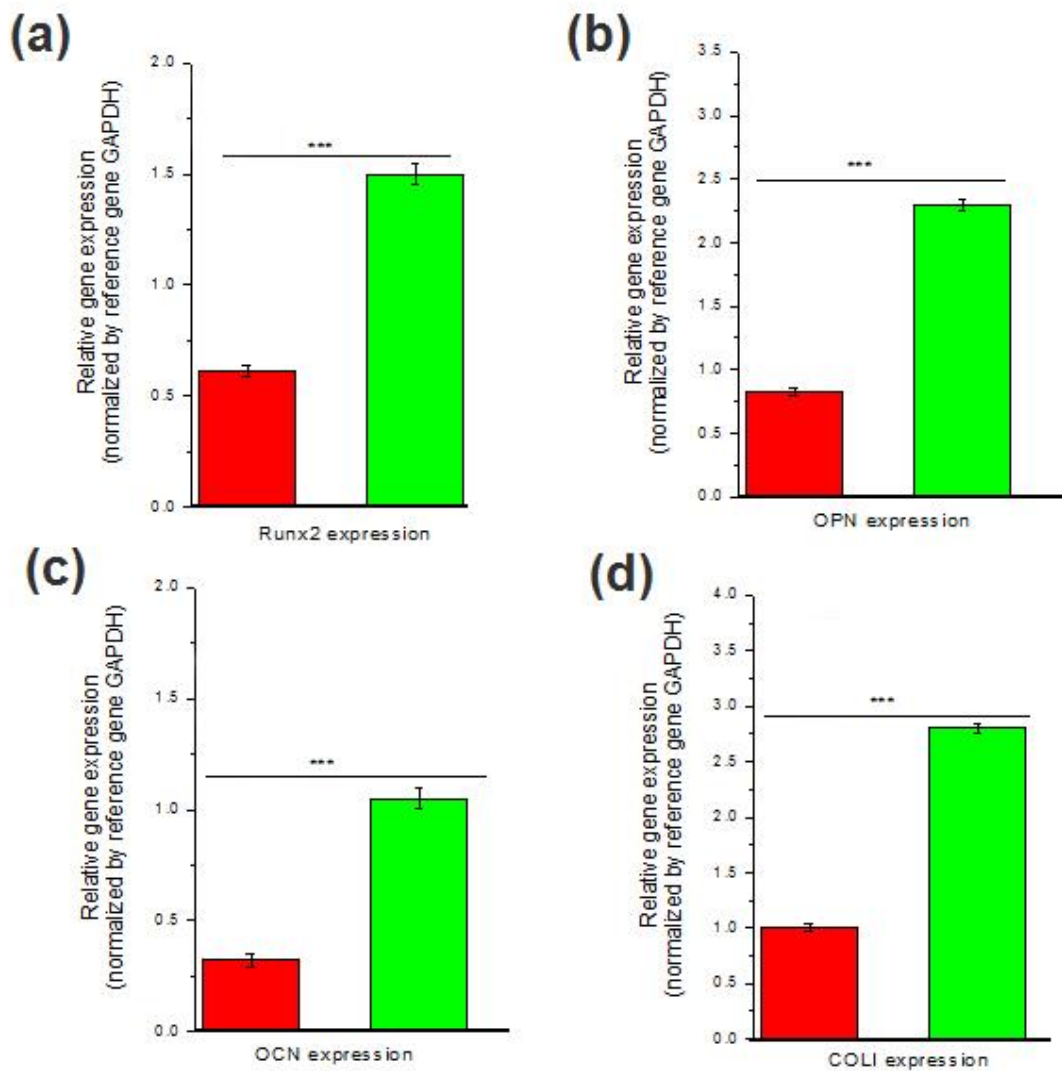


Fig. 14: Levels of mRNA for osteogenic specific genes [(a) Runx2, (b) OPN, (c) OCN and (d) COL1] of MG-63 cultured on e-glass substrate and coated surface for 3 weeks. \*\*\*  $p < 0.001$ , \*\*  $p < 0.01$  and \*  $p < 0.05$ , data are presented as mean $\pm$ SD, n=3.

*In vitro* biocompatibility evaluation, a basic biological test for biomaterials plays a significant role to assess cell/biomaterial interactions. A prerequisite step in the process of cell-material surface interactions is the attachment of dependent cells, which in turn can influence ensuing cellular and tissue responses [175]. The E-glass is known to be bio-inert, chemically durable,

strong with high mechanical strength, and can be used as an implant when composed with other bioactive materials. HAp is classified as osteoconductive, because it supports new bone growth on the implant along bone-implant interface. Hence, e-glass can hold the mechanical integrity of the sample, while HAp provides the necessary ingredients for bone regeneration.

Since a categorical attribute of osteoblasts is mineralization as osteogenesis matures, ALP activity and ARS mineralization assay are used to quantify such mineralization upon implants [176]. Substantial levels of mineralization lead to cells having an orderly, sheet-like structure. Increasing ALP activity over the culture duration, intensity of Alizarin Red staining, and confocal images that show stressed actin arrangement of cells upon the implants. Encouraging results were found for samples particularly with HAp coated e-glass compared to bare e-glass. Similarly, the images from confocal laser microscopy show random actin-stress fibers along with dense cell colony deposits across the coated implant and to a slightly less extent on the bare implant. Effective adherence of cells onto implants leads to formation of ordered ECM [176] and the presence of ECM is a requirement for successful tissue reconstruction. Nano-scaled structure of HAp conceivably contributes to the favourable cyto-compatibility of the implants. Progression of cell proliferation from Day 7 to Day 14 is a little slow for all the implants [Fig. 12(b)]. This slightly restricted progress may be ascribed to the cells requiring some time to adjust and adapt to the 3D matrix upon being transferred from the 2D cultures [176].

Overall, the *in vitro* analyses show that the HAp coated e-glass leads to significant improvement of implant properties in terms of biocompatibility, cell viability and proliferation, osteoinductivity and osteoconductivity. HAp coating of e-glass can potentially be utilized in fabrication of durable bioactive non-metallic implants and tissue engineering scaffolds.

## 5.2 Li-Sr substituted bioactive glass scaffold

### 5.2.1 Bioactive glass powder characterization

Figs. 15a-d shows the DTA thermogram of as-prepared powder samples (melted at 1450°C) without and with Li/ Sr doping. Glass transition temperatures ( $T_g$ ) was found to be around 750°C for BAG and 790, 780 and 770°C respectively for L-BAG, S-BAG and LS-BAG with crystallization temperature 862 and 865°C for BAG and L-BAG respectively. With the addition of dopants,  $T_g$  increases from the base composition (BAG) with associated enthalpy increase as well. No adsorbed or structural water loss noticed throughout the temperature regime. Heat treatment temperature of the porous green specimens fabricated later with these powders were selected based on the repeated trials on the porous green specimens with suitable strength, unaffected porous network inside and no incipience of glassy or crystalline phase.

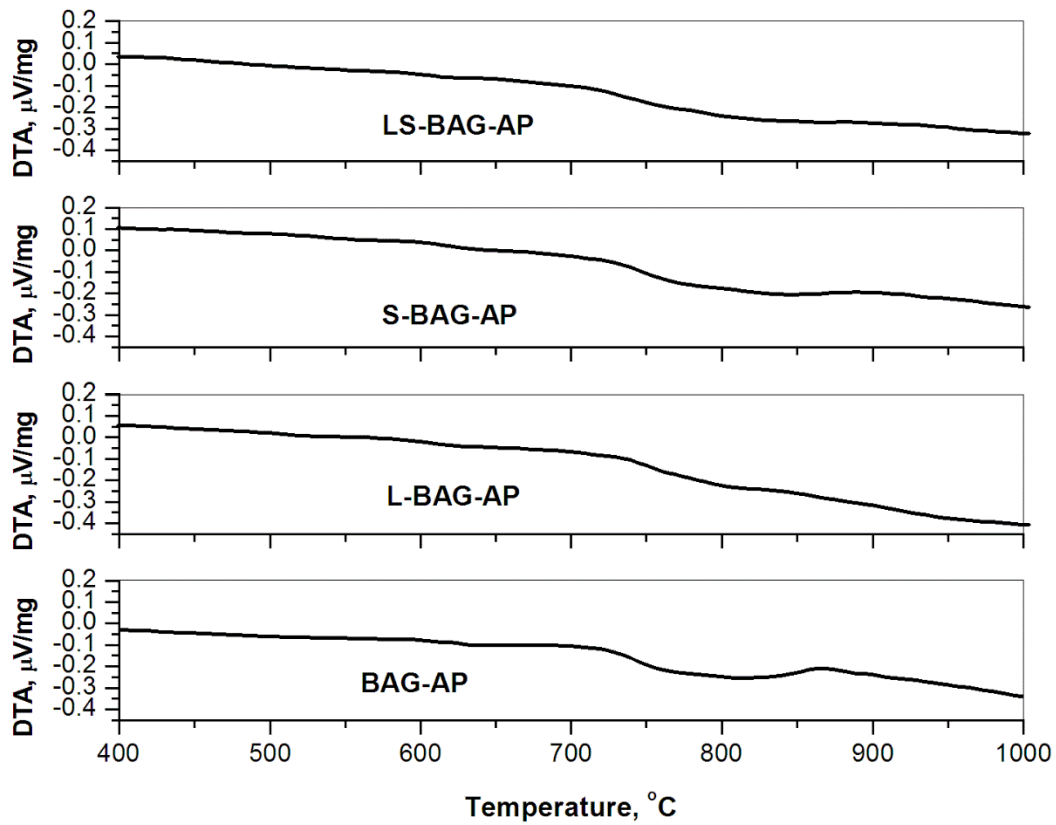


Fig. 15: DTA profile of as-prepared samples for (a) BAG, (b) L-BAG, (c) S-BAG and (d) LS-BAG.

XRD pattern (Fig. 16) of respective heat-treated specimens for each composition confirms amorphous nature with broad diffraction at  $2\theta$  ranging between  $20\text{-}35^{\circ}$  indicative of disorder in the structure and glassy nature of powders. Addition of dopants had no appreciable influence on the glassy structure of base material except slight changes in amorphicity and no appearance of any crystalline peak.

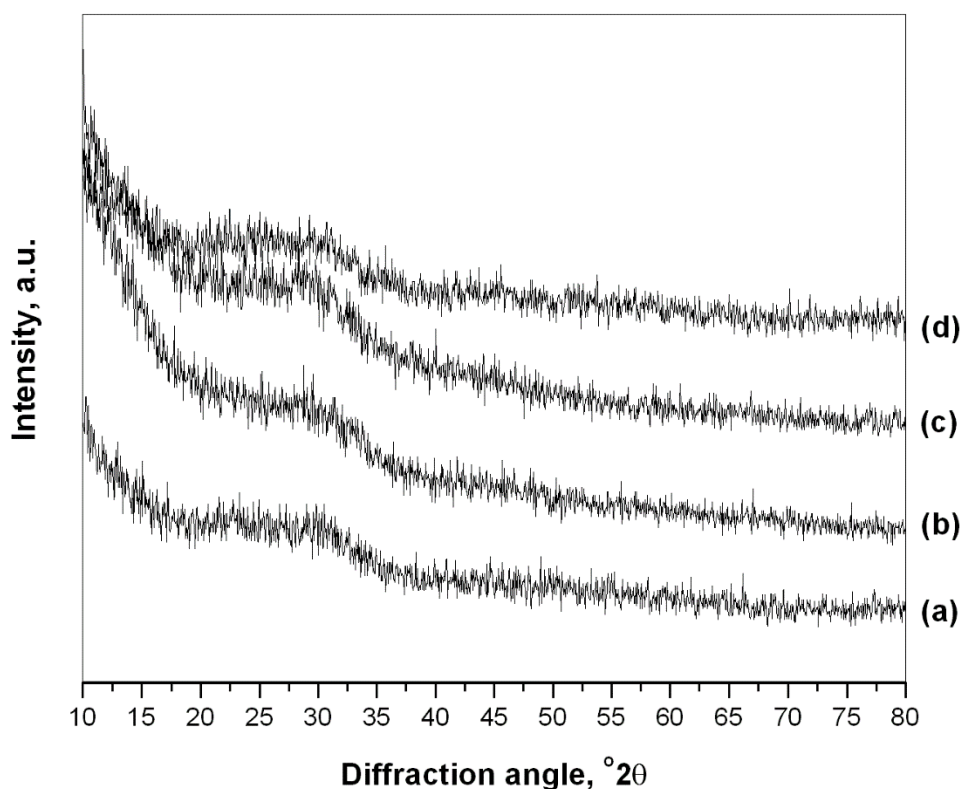


Fig. 16: XRD patterns of (a) BAG, (b) L-BAG, (c) S-BAG and (d) LS-BAG samples heat treated at their respective temperatures.

FTIR spectra (Fig. 17) of same powders show presence of hydroxyl (-OH) group around  $3445\text{ cm}^{-1}$ , along with Si-O-Si stretching frequency around  $465\text{ cm}^{-1}$  and Si-O-Si bending frequency around  $1020\text{ cm}^{-1}$  for all samples [177]. Other band assignments included Si-OH symmetric stretch at  $780\text{-}980\text{ cm}^{-1}$  and vibrational mode of asymmetric stretch of Si-O-Si between  $1100\text{-}1000\text{ cm}^{-1}$ . The band assignments are summarized and are given in Table 6.

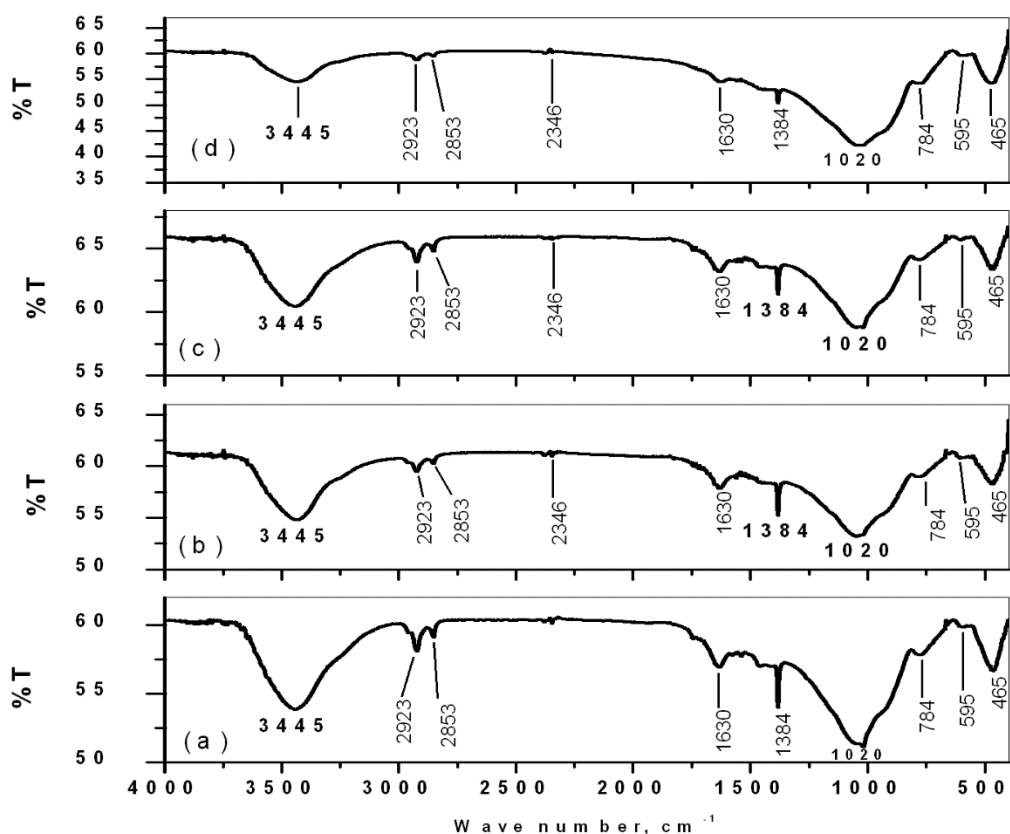


Fig. 17: FTIR spectra of (a) BAG, (b) L-BAG, (c) S-BAG and (d) LS-BAG samples heat treated at their respective temperatures.

Table 6: Band assignments for the peaks obtained for all samples (cf. Fig. 17)

Wave number ( $\text{cm}^{-1}$ )	Band assignment	Wave number ( $\text{cm}^{-1}$ )	Band assignment
465	$\delta$ (Si-O-Si) bending	1630	$\delta$ (OH)
595	P-O of $\text{PO}_3^{2-}$ group	2853	-OH (water)
784	$\nu$ (Si-O-Si) tetrahedral	2923	$\nu$ (CH)
1020	$\nu$ (Si-O-Si) asymmetric	3445	$\nu$ (OH)



### 5.2.2 Bioactive glass scaffolds characterization

Figs. 18a-d shows the SEM microstructure of the porous scaffolds for all compositions. Highly amorphous microstructures were obtained with presence of granular appearance throughout of the samples taken at different magnifications. A range of micro- to macro-pores were observed without any grains or crystals.

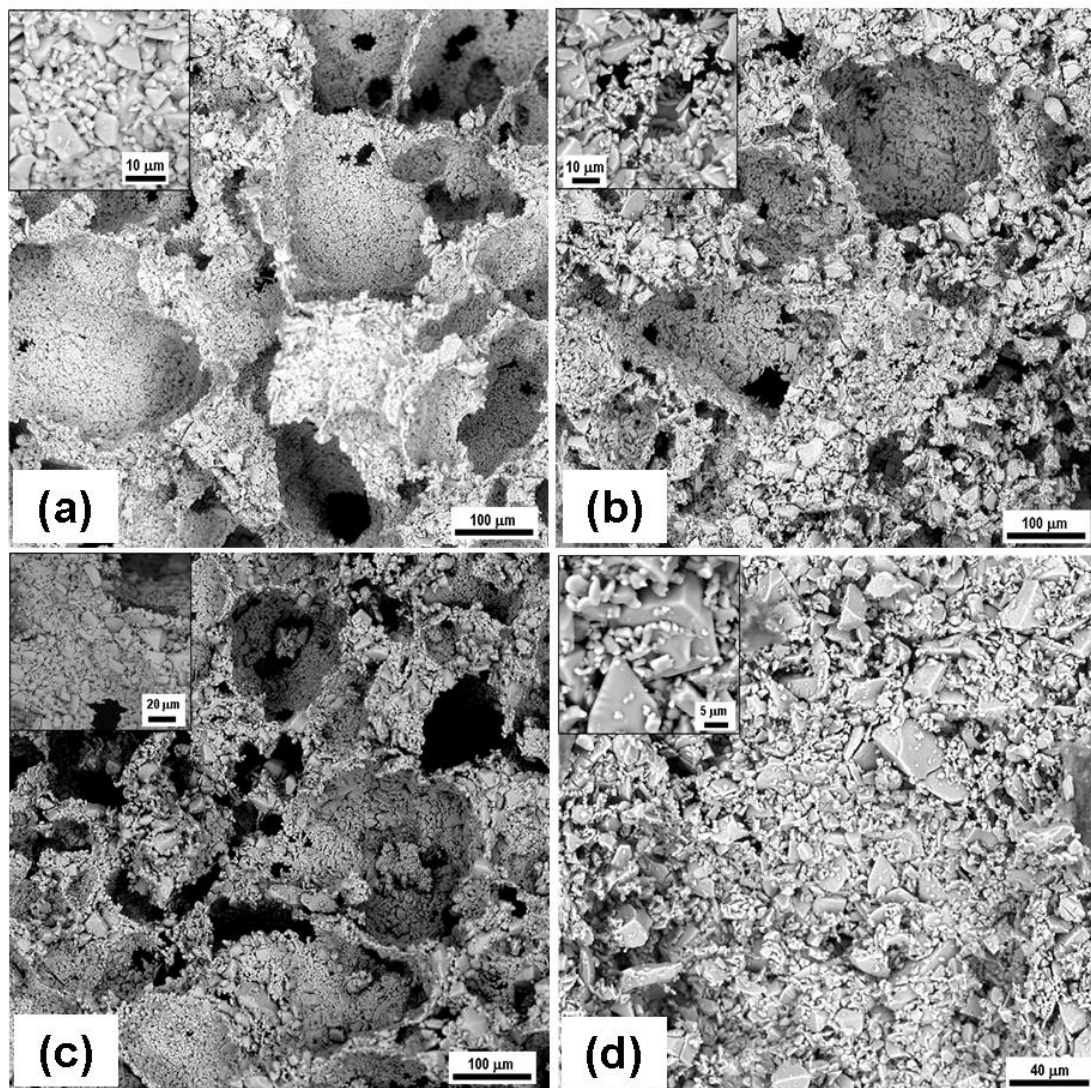


Fig. 18: SEM microstructure of the porous scaffolds for all compositions (inset: higher magnified site).

Due to the amorphous nature, green powders were fused at the boundary with presence of micro-pores between the fused powders. Mean pore sizes of BAG and L-BAG samples calculated by image processing was about 20  $\mu\text{m}$ , while this was 47  $\mu\text{m}$  and 8  $\mu\text{m}$  for S-BAG and LS-BAG respectively. All the samples except LS-BAG showed presence of both micro- (10-50  $\mu\text{m}$ ) and macro-pores (> 50  $\mu\text{m}$ ). For LS-BAG, it was more of coarsening than sintering of particles. For L-BAG, pore size was found to be in the range of 20-230  $\mu\text{m}$  with 1-2  $\mu\text{m}$  small pores throughout the microstructure. S-BAG on the other hand had pore size in the range of 30-260  $\mu\text{m}$  with bi-modal distribution of pores in the range from 1-2  $\mu\text{m}$  and 10-20  $\mu\text{m}$ . Pore size range for LS-BAG was mainly in the range of 10-50  $\mu\text{m}$  with presence of 1-2  $\mu\text{m}$  of micro-pores. Amorphous content was found to be more in case of L-BAG and LS-BAG compared to S-BAG and BAG. Most probably Li had played a solute-drag effect for coarsening of the base glass particles. That means Li actually facilitated the coarsening so that green powder particles move against each other due to appearance of sharp melt at the interface. The effect was more evident in case of LS-BAG. Strontium on the other hand, did not have such effect as mentioned. As a consequence, porous scaffolds made of BAG and S-BAG showed similar percentage of apparent porosity when heat treated as that of % naphthalene added while preparing the green compacts. But L-BAG and LS-BAG had much higher percentage of open porosity. As a result, bulk densities of the samples were found to be higher in case of BAG and S-BAG than L-BAG and LS-BAG. The data (average values) are presented in Table 7.

Table 7: A.P. and B.D. data of the porous scaffolds

<b>Sample</b>	<b>A.P., %</b>	<b>B.D., g/c.c.</b>
<b>BAG</b>	54.4±1.63	1.16±0.02
<b>L-BAG</b>	61.3±1.84	0.97±0.02
<b>S-BAG</b>	56.5±1.7	1.09±0.02
<b>LS-BAG</b>	64.5±1.94	0.84±0.02

### 5.2.3 Simulated body fluid (SBF) study

Fig. 19 shows a composite image showing variations of pH, concentrations of calcium, bi-carbonate and bi-phosphate in the supernatant with time, in contact with SBF. pH of the supernatant of all samples showed slight decreasing tendency with time and upto day 14, which corroborates our earlier findings on similar base glass [178]. For all the samples, Ca ion concentration of the supernatant was increased from 7 to 14 days except S-BAG, which showed increment of Ca ions at day 7 and continuous maintenance upto day 14. For BAG, L-BAG and LS-BAG this increase of Ca was due to dissolution from sample surface.  $\text{HPO}_4^{2-}$  ion conc. on the other hand was decreased from pure SBF, most probably due to phosphate deposition on the surface. Carbonate in the supernatant, showed a decrement at day 7 and subsequent increment at day 14 which was possibly due to more carbonate deposition on the surface at day 7, more dissolution upto day 14 and eventually becoming saturated with the sample. The concentration of the supernatant analysis upto day 14 revealed bioactivity of the samples in terms of more and more  $-\text{OH}$  and  $\text{PO}_4^{3-}$  ion deposition on the sample surface, which is a potential nucleation site for Ca after day 14 to form hydroxyapatite or carbonated apatite on its surface; but, S-BAG showed better bioactivity as the same deposition was prominent within day 14. The results obtained were compared with the MTT assay study shown later.

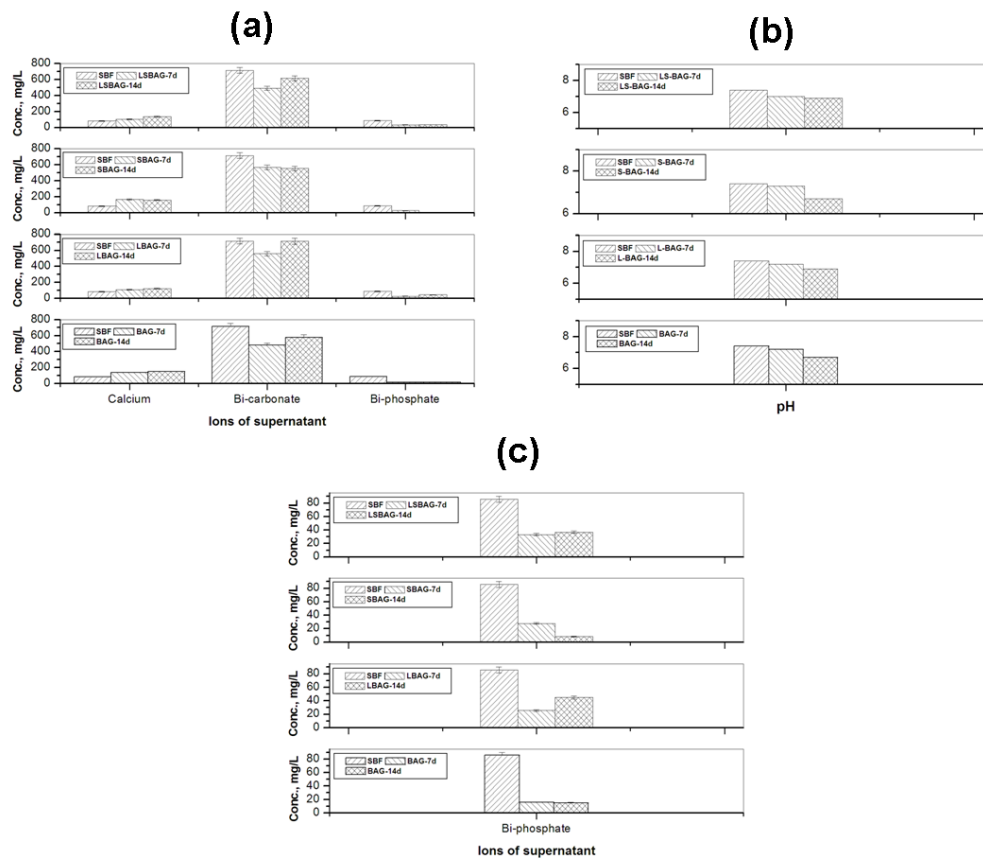


Fig. 19: Variations of (a) concentration of supernatant ( $\text{Ca}^{2+}$ ,  $\text{HCO}_3^-$  and  $\text{HPO}_4^{2-}$ ), (b) pH of SBF after days 7 and 14 in contact with the porous scaffolds (BAG, L-BAG, S-BAG and LS-BAG); (c) is the magnified part of  $\text{HPO}_4^{2-}$  (a).

Fig. 20 show the SEM microstructure of the porous scaffold surface after day 14 of SBF study. This shows formation of apatite like crystals on the surface of S-BAG (Fig. 20c) which was not very clear in case of other samples surfaces. L-BAG and LS-BAG showed amorphous nature of their respective surfaces (Figs. 20b and d), as kinetics of dynamic dissolution and deposition process of  $\text{Ca}^{2+}$ ,  $\text{HCO}_3^-$  and  $\text{HPO}_4^{2-}$  ions were still in continuation while for BAG (Fig. 20a), deposition of apatite like crystals have started.

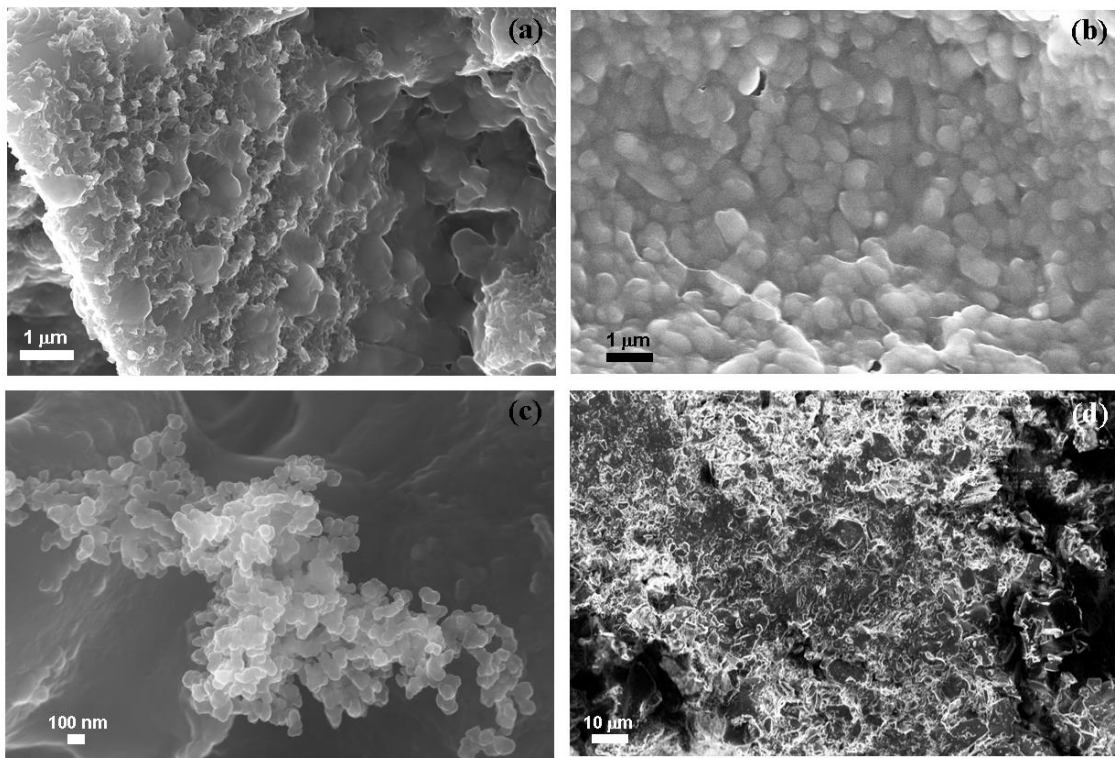


Fig. 20: SEM microstructure of the porous scaffold surface after day 14 of SBF study; for (a) BAG, (b) L-BAG, (c) S-BAG and (d) LS-BAG.

#### 5.2.4 *In vitro* cell cyto-toxicity study

From the calculated OD values (550 nm), percent cell (NIH3T3) proliferation was plotted against the days observed and is given in Fig. 21.

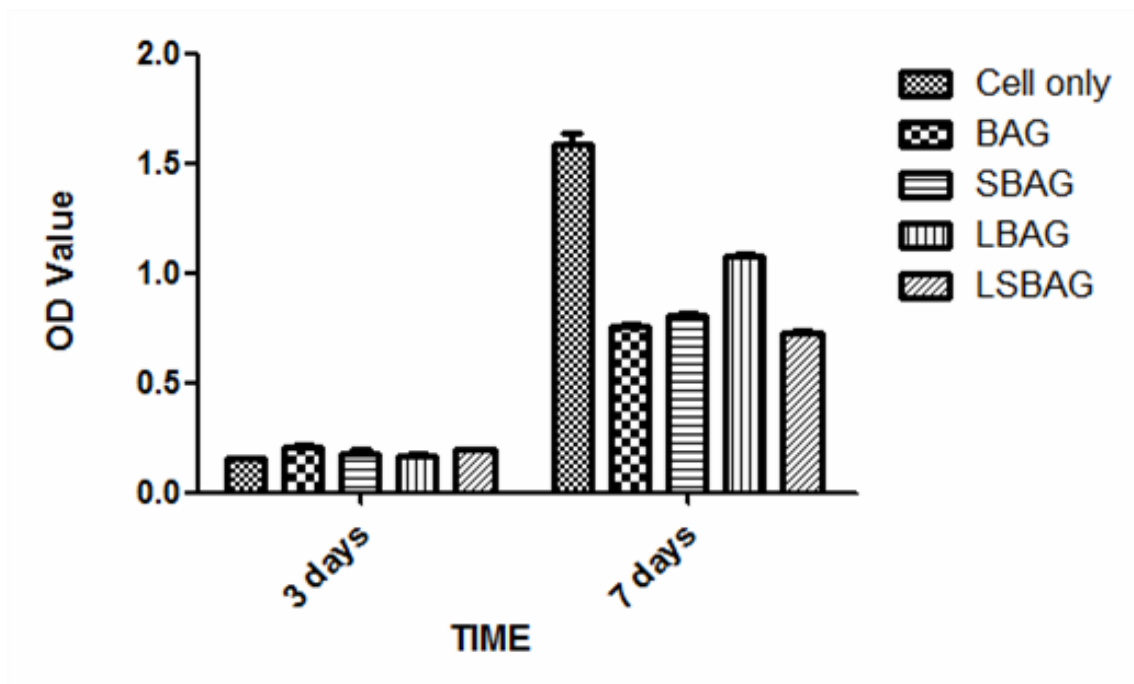


Fig. 21: MTT assay results; calculated OD values for NIH3T3 expressed on the samples of BAG, L-BAG, S-BAG and LS-BAG after days 3 and 7.

It was found that the initial proliferation of cells after day 3 was better than control due to initial attachment of cells. After 7 days, however, this was found to be better in case of L-BAG than the others. Cell growth rate was found to be reduced for all samples than control. All sample surface was considered as non-toxic and biocompatible. Cell morphology by SEM after day 7 was also revealed similar trend (Fig. 22) as L-BAG showed better NIH3T3 proliferation than other surfaces. Well-grown filopodia (microspikes) or cytoplasmic projections were seen and found to be more pronounced in this case. Filopodia contain actin filaments cross-linked into bundles by actin-binding proteins. Micropores present on the top of surface play pivotal role for better anchorage of the filopodia.

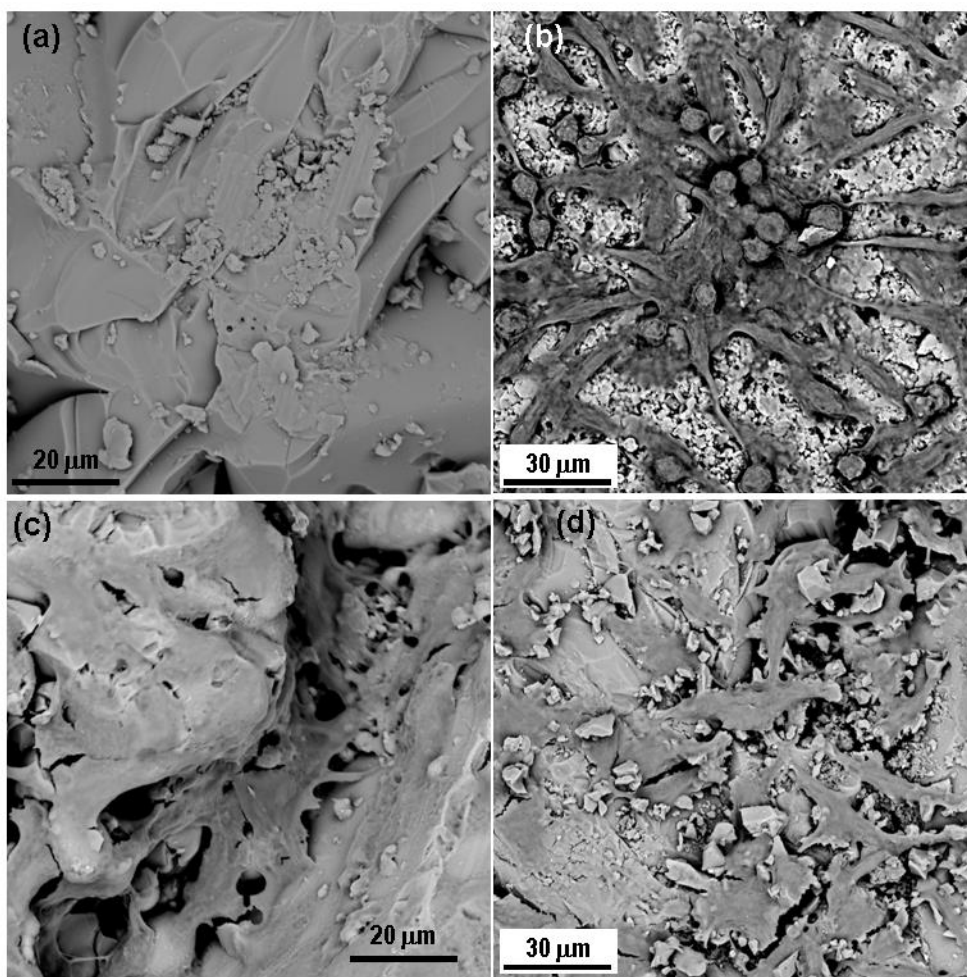


Fig. 22: SEM cell morphology on the samples of (a) BAG, (b) L-BAG, (c) S-BAG and (d) LS-BAG after 7 days.

NIH3T3 mouse embryo fibroblast cell lines are regularly used for MTT assay to assess cytotoxicity with respect to biomaterials' effects on cell growth metabolism [179]. These cells have branched cytoplasm surrounding an elliptical nucleus and can be recognized by abundant rough endoplasmic reticulum and also synthesizes extracellular matrix (ECM) and collagen. NIH3T3 has also capability to detect substrate rigidity beyond the cell border [180]. From the results of Figs. 21 and 22, it can be stated that there was substantial effect of Li alone to promote

fibroblasts which was found to be least in case of BAG. S-BAG on the other hand, was not contributing extensively towards ECM formation and the gross effect of Li and Sr on cell proliferation was found to be least in case of LS-BAG (Fig. 21). S-BAG however showed better bioactivity in terms of apatite like crystal formation which will be expected to contribute towards bone cell colonization in vivo. In this case, fibroblast cell extensions consolidated the pore site; ECM formed in situ along with  $\text{HCO}_3^-/\text{HPO}_4^{2-}$  deposition in contact with SBF after 7 days (Fig. 19) may help maturation of bone defect site faster in vivo. The combined effect of Li and Sr thus expected to generate both soft and hard tissue in vivo. Most plausible reason behind slower rate of growth of NIH3T3 after 3 days may be the presence of other ions (e.g.,  $\text{Ca}^{2+}$ ) which are also consistent with findings reported elsewhere stating that changes of extracellular calcium concentration can affect balance between proliferation and differentiation in fibroblasts. McNeil et al. demonstrated that elevation of extracellular calcium stimulates proliferation-associated signaling pathways in rat fibroblasts [181].

#### 5.2.5 Bone in-growth evaluation by micro-CT

Serial slices of X rays were carried out throughout Z-axis of a particular implanted bone section, images thus obtained were clubbed together and are given in Figs. 23a and b for BAG, 24a and b for L-BAG, 25a and b for S-BAG and 26a and b for LS-BAG after 2 and 4 months respectively. Serial images for BAG taken after 2 and 4 months showed that the porous scaffold has started degrading as revealed after 4 months but maintained its structure after 2 months. From the grey scale quantification, it can be shown that BAG samples had higher amount of mature bone tissue after 4 months than the 2 months when more soft tissue apposition was evident. Stability of the implant thus impaired after 4 months which is anticipated to be continued and simultaneously converted to hard cortical tissue. Effect of lithium and strontium



can be an interesting parameter which can dictate the degree of bone tissue conversion with time.

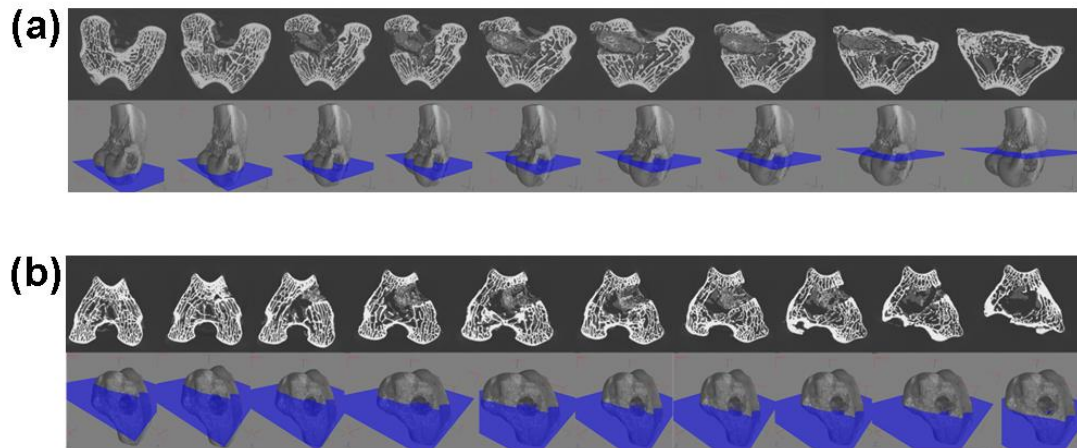


Fig. 23: Serial slices along the Z-axis in micro-CT. Images are obtained for implanted BAG scaffolds. (a) After 2 months; (b) After 4 months.

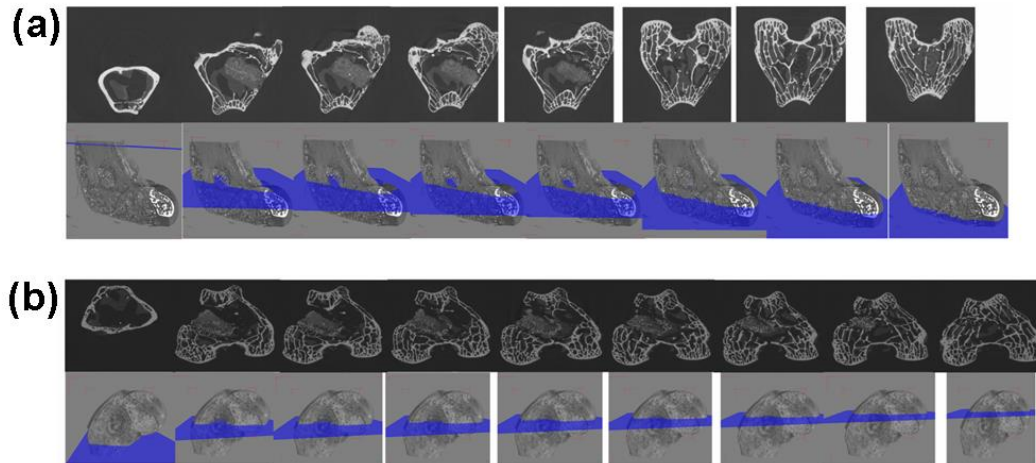


Fig. 24: Serial slices along the Z-axis in micro-CT. Images are obtained for implanted L-BAG scaffolds. (a) After 2 months; (b) After 4 months.

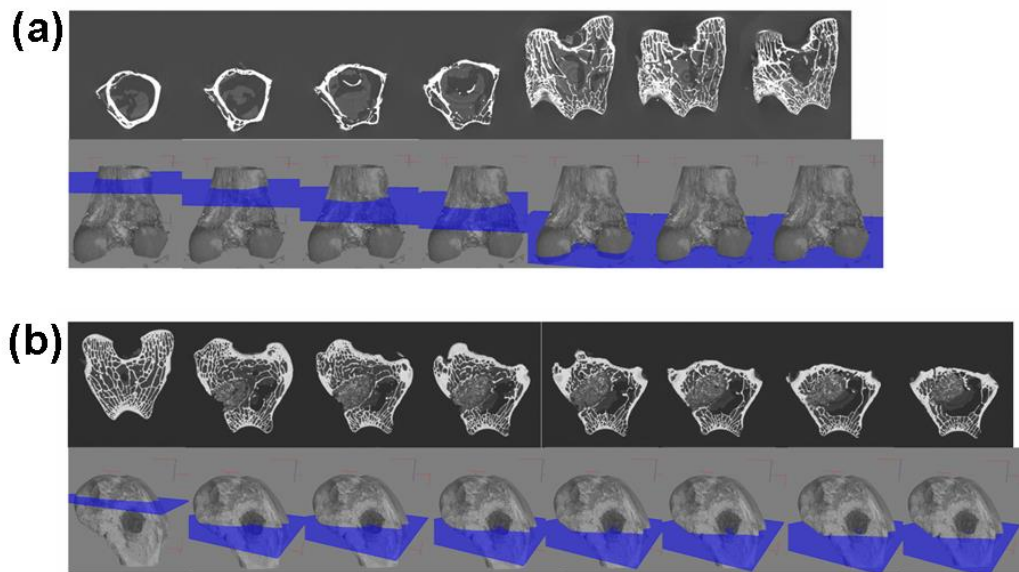


Fig. 25: Serial slices along the Z-axis in micro-CT. Images are obtained for implanted S-BAG scaffolds. (a) After 2 months; (b) After 4 months.

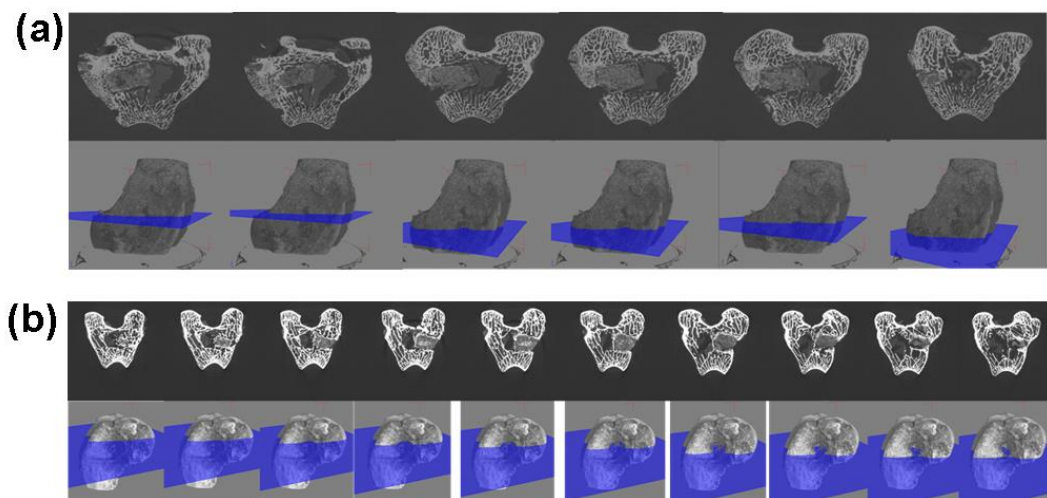


Fig. 26: Serial slices along the Z-axis in micro-CT. Images are obtained for implanted LS-BAG scaffolds. (a) After 2 months; (b) After 4 months.

Serial sectional images of L-BAG after 2 months showed tissue invasion more in the central part of the implant than the periphery with a clear interfacial gap with the surrounding tissue. Grey scale values were found to be in between of cortical and cancellous tissues after 2 months which indicates that the implant was in the process of being resorbed which was continued up to 4 months. But the degree of resorption was higher in case of L-BAG than the BAG alone. L-BAG samples after 4 months showed very similar grey scale values with that of the cortical part of the bone. However, degradation of the samples was lowered for L-BAG than BAG alone.

S-BAG samples had clearly shown its efficacy expressed towards conversion to more of cortical tissue than the cancellous one. Cortical tissue could be seen at the periphery of the inserted samples as seen after 4 months. LS-BAG samples after 2 months showed close resemblance of the cancellous tissue on the periphery and cortical tissue in the inside of the implanted samples. After 4 months, the same phenomenon continued, and the implanted samples were almost 60% converted to the surrounding bone. After 2 months, BAG samples only showed some interfacial gap which was absent for all doped samples.

3D images using micro-CT are given in “Supplementary Information” as Figs. 1a and b for BAG, 15a and b for L-BAG, 16a and b for S-BAG and 17a and b for LS-BAG after 2 and 4 months respectively. The extent to which both soft and hard tissue opposed to BAG samples when implanted, cannot be assessed quantitatively from radiography. Tissue and blood vessels could be seen in the 3D representation of the micro-CT. Porous nature both in and outside the medullary cavity were noticed in the 3D representation. Different grey scale values in the images represent quality of the bone and its degree of maturity. Implants could be seen from the 3D plots. It was found that mature bone tissue as well as blood vessels engulfed the implant

which indicates good vascularisation. Porous nature of the cortical bone was observed in some sections. In a comparison, LS-BAG samples showed highest degree of tissue impregnation and vascularity among the four compositions. Strontium doping synergistically affected bone tissue apposition than glass without any doping. BAG scaffolds without doping actually had lower vascularity potential than the doped ones.

#### 5.2.6 Radiological examination

Fig. 27a-d shows radiographs of defect surgery site and their interpretation is presented in Table 8. On the day of surgery, the distal metaphysis of femur showed presence of partial radiodense BAG implant (Fig. 27a) in the defect, which became moth-eaten on 1 month. The implant found to reduce in size gradually with implantation time and almost disappeared at 4 month with irregularly arranged bony tissue. In S-BAG samples (Fig. 27c), the defect radiodensity appeared to be unchanged after 1 month and the defect size shrunk at 2 months. At 3 months, only negligible amount of implant was present in the defect along with newly formed bony tissue and by the end of 4 months both the implant defects could be barely seen from the radiographs. L-BAG samples (Fig. 27b) also showed similar performance as that S-BAG, except that defect healing and new bone formation were enhanced. In LS-BAG samples (Fig. 27d), radiograph showed narrowing of bony defect and shrinkage of implant as early as one month post-operatively. Subsequent radiographs showed no traces of implant and defect. More importantly the radiodensity in defect area was almost identical to that of healthy bone.

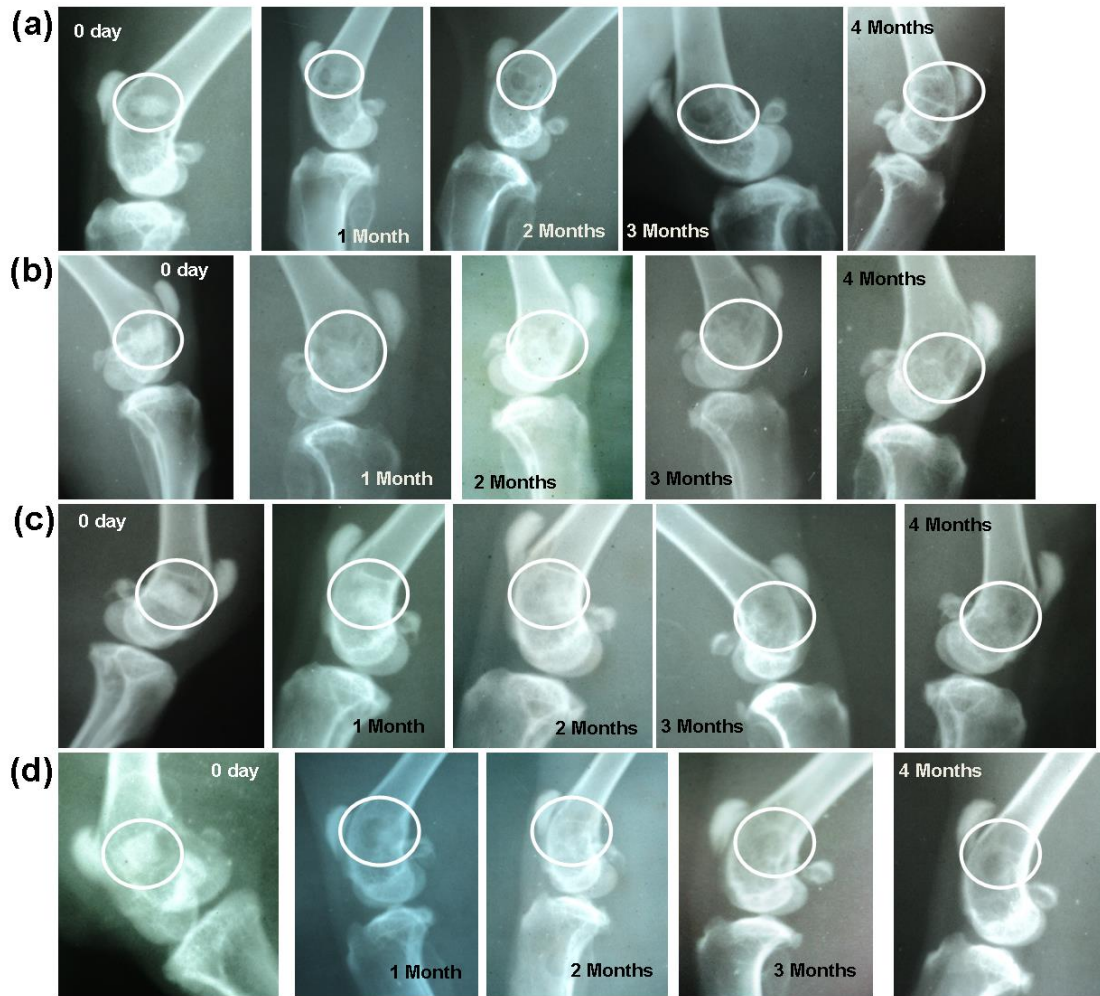


Fig. 27: Radiographs taken at '0' day, 1, 2, 3 and 4 months post-operatively implanted with (a) BAG, (b) L-BAG, (c) S-BAG and (d) LS-BAG.

Table 8: Radiological scoring values of different samples at different time intervals

<b>Group</b>	<b>1 month</b>	<b>2 month</b>	<b>3 month</b>	<b>4 month</b>	<b>SEM</b>
<b>S-BAG</b>	0.66 <sup>a</sup>	1.00 <sup>a</sup>	1.66 <sup>b</sup>	2.33 <sup>bc</sup>	0.28
<b>L-BAG</b>	0.66 <sup>a</sup>	0.66 <sup>a</sup>	1.33 <sup>b</sup>	2.33 <sup>c</sup>	0.28
<b>LS-BAG</b>	1.33 <sup>a</sup>	1.66 <sup>ab</sup>	2 <sup>bc</sup>	3 <sup>c</sup>	0.28
<b>BAG</b>	0.33 <sup>a</sup>	0.66 <sup>b</sup>	1 <sup>bc</sup>	1.66 <sup>c</sup>	0.28

Values are expressed as Mean  $\pm$  SE. Values with different superscript within a row differs significantly (P<0.001)

### 5.2.7 Histological evaluation

Fig. 28 and Table 9 show the histological section images and evaluation report of bone-implant interface at 2 and 4 months after observing different cellular events. BAG scaffolds (Fig. 28a) showed well-formed bony structure containing haversian system, canaliculi and sinusoidal spaces along with deposition of R.B.C., fat cells and scanty numbers of osteoblast in peri-medullary areas after 2 months. Strontium doped scaffolds (S-BAG: Fig. 28b) at 2 month showed prominent osteoblastic activity characterized by sufficient number of haversian canal, canaliculi, lacunae and osteoblastic cells with suitable cytoplasmic ratios. The bony matrix is invaded by highly proliferative branches of vessels containing sufficient amount of R.B.C, bony progenitor cells and focal calcified points. Similarly, L-BAG scaffolds (Fig. 28c) showed well developed bony structure with robust haversian system, osseous canaliculi and bony plates. The LS-BAG samples (Fig. 28d) depicted well-formed osseous structure containing haversian canal, lamellae and canaliculi which was invaded by numerous blood vessels along with prominent osteoblastic and osteoclastic activities in the margin of lesion.

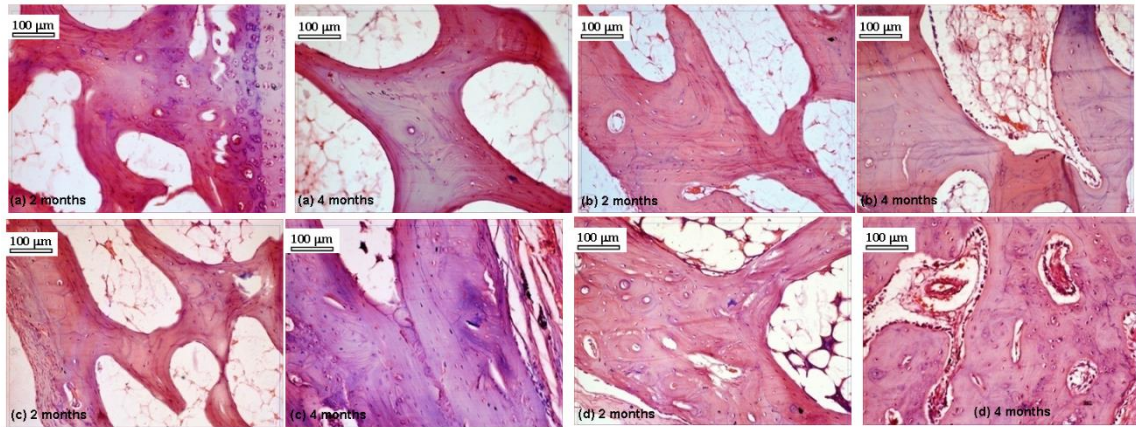


Fig. 28: Histological sections taken after 2 and 4 months post-operatively implanted with (a) BAG, (b) S-BAG, (c) L-BAG and (d) LS-BAG.

Table 9: Histological scoring values of different samples at 2 and 4 months

Cellular Response	Time Point (2 month)				Time Point (4month)			
	Group 1	Group 2	Group 3	Group 4	Group 1	Group 2	Group 3	Group 4
Fibro vascular proliferation	1 ± 0.3	1.66±0.3	1.33±0.3	1.66±0.3	1.33±0.3	1.66±0.3	1.33±0.3	1.66±0.3
Mononuclear cell	1 ± 0.23	1±0.23	1±0.23	1.33±0.23	1±0.23	1±0.23	1.33±0.23	1.33±0.23
Osteoclast activity	1±0.23	1.33±0.23	1±0.23	1.33±0.23	1±0.23	1±0.23	1.33±0.23	1.33±0.23
Mucin deposit	1.33±0.16	1±0.16	1±0.16	1.33±0.16	1±0.16	1±0.16	1±0.16	1±0.16
Vascularisation	1±0.26	1.33±0.26	1±0.26	1.66±0.26	1.33±0.26	1.66±0.26	1.33±0.26	2±0.26
Osteoblastic activity	1±0.31	1.66±0.31	1.33±0.31	1±0.31	1.33±0.31	1.66±0.31	1.66±0.31	2.3±0.31

Values are expressed as Mean ± SE.

Histological evaluations at 4 months for the doped and pure bioactive glasses are also shown in Figs. 28a-d. Compared to 2 months, apparently higher angiogenesis was observed in all doped samples. However, angiogenic proliferation was more in LS-BAG and L-BAG samples compared to other samples. All doped samples showed highly proliferative stage of osteoblast and osteoclast cells (progenitor cells) along with foci of calcification.



### 5.2.8 Fluorochrome labeling study

Fig. 29 shows images of samples after oxytetracycline marking, where golden yellow fluorescence represents new bone and dark sea green indicates matured old bone. After 2 months, BAG scaffolds depicted double tone golden yellow fluorescence in a narrow zone in the defect site and the host bone looked dark sea green homogenous color. Relatively, better intensity of new bone formation (golden yellow fluorescence) was observed in S-BAG and LS-BAG at this time point. L-BAG at this time point also showed more new bone formation as compared to pure sample. At 4 months, all the samples depicted more new bone formation as compared to 2 month. However, distinct new bone formation was exhibited in all doped bioactive glass implants. LS-BAG implanted bone showed wide regions of golden yellow fluorescence (new bone formation) indicating rapid bone regeneration. S-BAG bone samples showed scattered and multiple regions new bone formation in defect area demonstrating their effectiveness in bone regeneration. Based on the calculation, percentage of bone formation through fluorochrome labeling images at two time point of 2 and 4 months have been done and is given in Table 10.

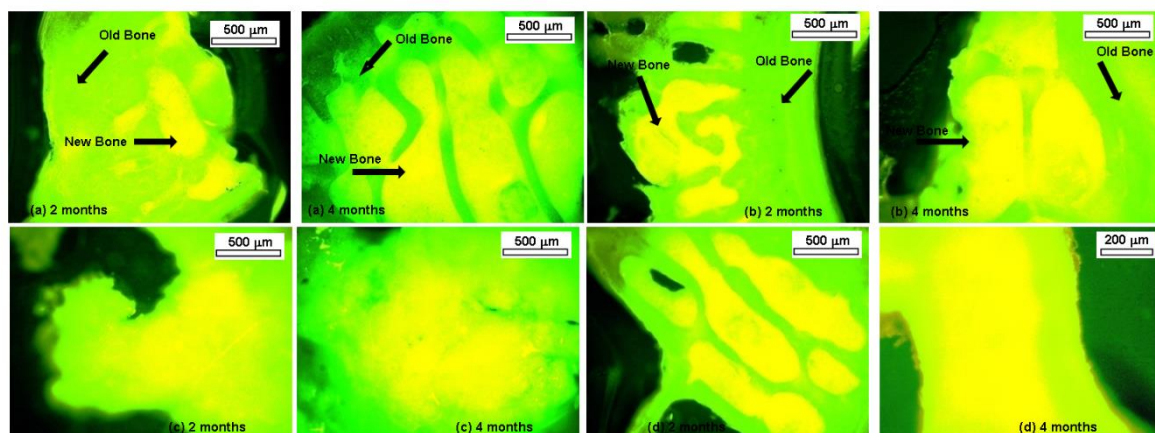


Fig. 29: Fluorochrome labelling study (after oxytetracycline markings) taken after 2 and 4 months post-operatively implanted with (a) BAG, (b) S-BAG, (c) L-BAG and (d) LS-BAG.

Table 10: Percentage of bone formation through fluorochrome labelling images at two time point of 2 and 4 months

Treatment	2 months	4 months
BAG	32.47 ± 0.439 <sup>bA</sup>	48.29 ± 0.541 <sup>bB</sup>
BAG-Sr	23.663 ± 0.513 <sup>aA</sup>	45.432 ± 0.573 <sup>aB</sup>
BAG-Li	39.459 ± 0.562 <sup>cA</sup>	51.466 ± 0.584 <sup>cB</sup>
BAG-Sr+Li	47.459 ± 0.513 <sup>dA</sup>	54.897 ± 0.588 <sup>dB</sup>

a, b, c, d means with different superscripts within a column differs significantly among the treatment ( $p < 0.01$ ).

A, B mean with different superscript within a row differs significantly between the month of sample within a treatment ( $p < 0.001$ ).

### 5.2.9 Scanning electron microscopic (SEM) study

Figs. 30 shows microstructural study of bone implant interface using SEM at two time point of 2 months (Figs. 30a-d) and 4 months (Figs. 30e-h). Effect of lithium and strontium could be established in SEM images and compared with the micro CT images. In all samples, with time, both soft and hard tissue got matured. L-BAG samples had a clear influence on soft tissue interaction with the sample (Figs. 30b, f). Collagenous network was prevalent in case of L-BAG while S-BAG samples (Figs. 30c, g) showed more of matured osteoblastic tissues opposed to the surface of the sample. LS-BAG on the other hand showed (Figs. 30d, h) both

collagenous network and mature bone tissues, which was not only covered the surface but also had invaded the porous network structure of the implant. Interestingly, BAG samples after 4 months showed matured osteoblastic tissues (Fig. 30e), but there was also sporadic presence of RBCs on the surface of samples. Interfacial gap between the implanted samples and the surrounding bone was found more in case of BAG than the other samples. Bony networks could be seen for BAG but no collagenous microstructure. Interfacial gap was absent in case of L-BAG and LS-BAG after 4 months but like the BAG samples, S-BAG also revealed slight interfacial gap after 2 months which however completely absent after 4 months. Granular nature of the porous scaffolds revealed before animal experimentation were absent when implanted. There were not any loose or unreacted glass particles after animal study.

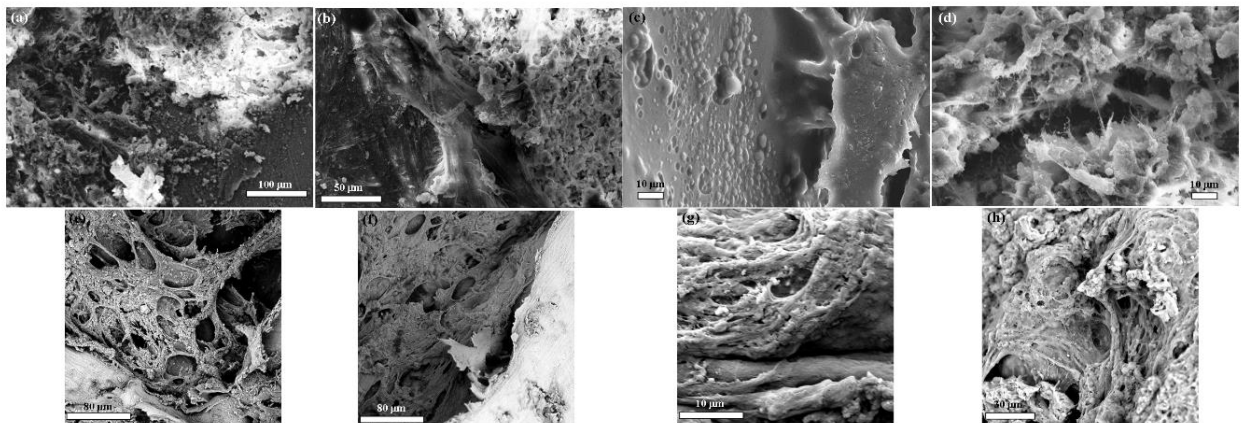


Fig. 30: SEM images of bone-material (BAG, L-BAG, S-BAG and LS-BAG) interface taken after 2 months (a-d) and 4 months (e-h) post-operatively respectively.

Earlier *in vitro* and *in vivo* studies on porous bioactive glass scaffolds demonstrated their potentiality towards bone tissue engineering due to inherent osteoconductive and osteogenic properties [182, 183]. Further improvement in biological properties of these scaffolds can be achieved via incorporation of suitable dopants that positively affect osteoblast activities thereby

enable early new bone formation [76]. Amalgamation of trace metallic elements into tissue engineering constructs offer low cost, longer shelf life with low regulatory burden and low risk as compared to biologics. Due to these added benefits, delivery of trace metallic element as biological agents is getting considerable attention in tissue engineering and regenerative medicine applications [184-186]. To achieve toward this goal of improving the performance of bioactive glasses, a simpler method was identified to develop lithium and strontium doped glass and to investigate the mechanism of how these next-generation biomaterials can enhance both osteogenesis and angiogenesis for faster patient healing times and high surgical success rates.

$\text{Li}^+$  is new additive ion of interest that brought attention due to its imminent role in osteogenesis. In a very recent study, Miguez-Pacheco et al. has shown that substitution of Na by different % of Li in 45S5 bioactive glasses cause decrease in  $T_g$  and  $T_m$  favoring sintering by viscous flow [187] which also consolidates our present finding in case of L-BAG. However, we have also completed cell viability and proliferation studies to further strengthen its potential application. In another study, it has been reported that 75 patients treated with lithium were found to exhibit significantly greater bone mass in several areas compared to 75 normal participants [188]. Similarly, strontium ( $\text{Sr}^{2+}$ ), a non-essential element accounts for 0.035% of the calcium content in our skeleton system and has been shown to boost bone regeneration when incorporated into synthetic bone grafts [189].

$\text{Li}^+$  doping in bioactive glasses may inhibit GSK3, a negative regulator of the Wnt signaling pathway [190]. Moreover, it activates  $\beta$ -catenin-mediated T cell factor (TCF)-dependent transcription during bone and cartilage fracture healing [191]. Similarly,  $\text{Sr}^{2+}$  enhances osteoclast apoptosis, increases pre-osteoblastic cell proliferation and collagen synthesis and thus decreases bone resorption and preserve bone formation[192, 193]. In our study,

radiological study revealed gradual replacement of scaffold with new bone after 2 months in all doped samples. Histological study revealed highly proliferative stage of osteoblast and osteoclast cells (progenitor cells) along with angio-proliferation component of bony tissue in doped samples compared to pure samples. This is presumably due to possible role of Sr and Li addition in bioactive glass.  $\text{Sr}^{2+}$  plays a vital role in overall bone turnover through early differentiation of osteoblast that helps in early expression of *cbfa1* gene, indispensable for osteoblast differentiation [194]. Sr can also stimulate the calcium sensing receptor and other equivalent signaling pathways to induce early osteoblast differentiation [192]. The Wnt signaling pathway is one of the most key signal cascades in bone formation and remodeling process [195, 196]. A direct link between BMP production and an activated Wnt signaling pathway in osteoblasts has been observed [197, 198]. The activation of  $\beta$ -catenin signaling by  $\text{Li}^+$  shows its paramount role for fracture healing [191]. Higher osteoblastic activity and lamellar bone formation are prominent in binary Sr-Li doped bioactive glass which is due to combining effects of both dopants on bone formation processes of resorption and mineral aggregation.

Fluorochrome labeling using tetracycline marker is an indicator for the new bone formation, bone mineralization and remodeling [199]. These stains when incorporated will directly bind to areas undergoing calcification at the bone/osteoid (unmineralized bone) interface. After administration, tetracycline generally follows ionized calcium and deposited to the areas of mineralized tissue [200, 201]. The labeled new bone and old bone emit bright golden-yellow and dark-sea green fluorescence respectively when observed under UV light. The method provides practical information in assessing the amount of new bone formation and bone healing [202]. In this study, at 2 month time point, the process of new bone formation was moderate in pure bioactive glass and relatively high in all three doped samples. In general, the activity of

new bone formation was increased in all samples after 4 months. This may be due to the significant effects of single or binary dopants which may in turn help in cellular proliferation and osteoblastic activity. Previous studies established that Sr can influence cellular activities via the membrane bound calcium sensing receptor, both in osteoblasts and in cells of the osteoclasts lineage [88, 203, 204]. Moreover, Sr may enhance the ability of MSCs as well as pre-osteoblasts proliferation and differentiation into bone-forming osteoblasts [205], through Wnt/b-catenin pathway by activating mitogenic signaling [206]. In a similar study using Sr doped HAp-based bioactive glasses implants, the sequential polychrome labeling of bone during *in vivo* osseointegration confirmed homogeneous bone formation around the test implants [207].

SEM examination revealed both collagenous network and mature bone tissues in L-BAG while S-BAG samples showed more of matured osteoblastic tissues apposed to the surface of the sample. Interfacial gap between the implanted samples and the surrounding bone was found more in pure BAG than the doped other samples. Bony networks could be seen for pure BAG but no collagenous microstructure could be noticed, which is an indirect estimation of poorer bone quality in case of BAG than the other samples. Interestingly, sporadic presence of RBCs on the surface of samples indicating the healing was still continuing. Sr controls key proteolytic enzymes, matrix metalloproteinase-2 (MMP-2) and matrix metalloproteinase-9 (MMP-9) along with osteoprotegrin (OPG) and receptor activator of nuclear factor  $\kappa$ - $\beta$  ligand (RANKL) that is produced by osteoblast cells and are key signaling mechanisms of osteoclast formation and its resorptive activity[208, 209]. The combining effect of Sr enhances overall bone turn over by reduced osteoclastic resorption and an enhanced osteoblastic activity.

Micro CT in scaffold research has enabled accurate morphological studies to be carried out, yielding comprehensive data sets [210, 211]. It also opened a new paradigm for investigations in tissue engineering [212]. Micro CT thus performed to understand the degree of vascularity as well as the interaction of soft and hard tissue with the material when implanted. In the present study, mature bone tissue as well as blood vessels engulfed the implant which indicates good vascularisation. In a comparison LS-BAG samples showed highest degree of tissue impregnation and vascularity among the four compositions probably due to the synergistic effect of lithium and strontium in particular. After 2 months, serial sectional images of L-BAG indicated that tissue invasion was more pronounced than in the central part of the implant than the periphery with a clear interfacial gap with the surrounding tissue. Grey scale values were found to be in between of cortical and cancellous tissues after 2 months which indicates that the implant was in the process of resorption. But the degree of resorption was higher in case of L-BAG than the BAG alone. S-BAG samples had clearly shown its efficacy expressed towards conversion to more of cortical tissue than the cancellous one. LS-BAG samples after 2 months showed close resemblance of the cancellous tissue on the periphery and cortical tissue in the inside of implanted samples. BAG samples only showed some interfacial gap which was absent for all doped samples. In a similar study, the bone regeneration ability of different bioactive glass particles has been observed in rabbit model [213, 214].

### 5.3. Calcium phosphate and bioactive glass coating on Magnesium alloy

#### 5.3.1. Material characterization

##### 5.3.1.1. Substrate characterization

SEM of bare substrate (BM) exhibited typical ground surface caused by mechanical grinding [Fig. 32A-a] having EDX [Figs. 32A-c and e] and XRF (not shown) confirming alloying materials Mg, Zn and Ca with impurities (like SiO<sub>2</sub>, Al<sub>2</sub>O<sub>3</sub>, SrO etc.). XRD [Fig. 31A-a] of BM indicated crystalline phase-pure magnesium, matched with JCPDS PDF #00-035-0821, while FTIR [Fig. 31B-a] supported the presence H<sub>2</sub>O and Mg-O as a result of environmental corrosion.

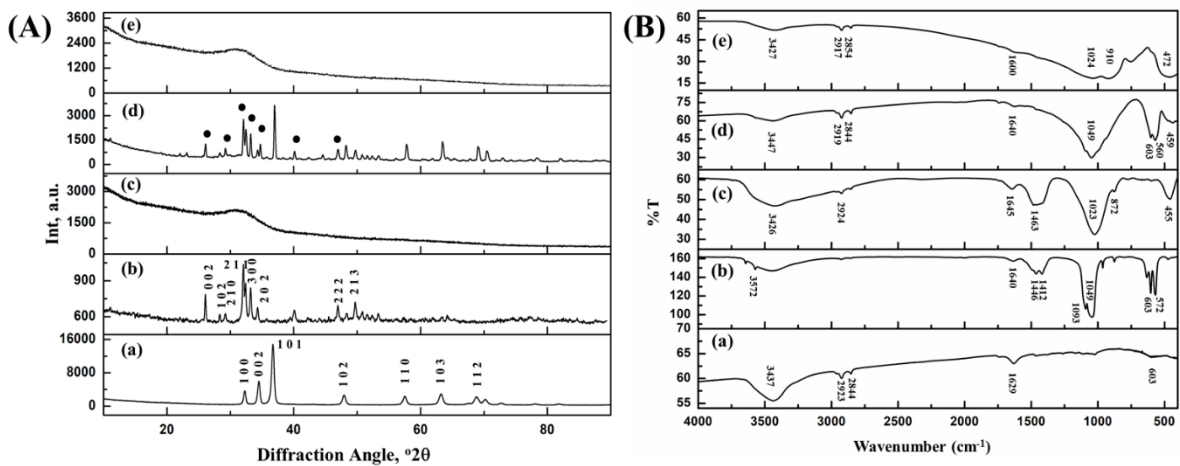


Fig. 31: (A)XRD pattern and (B) FTIR spectra of (a) BM, (b) HAp granules fired at 1250 °C, (c) bioactive glass, (d) BMH (• HAp phase) and (e) BMG.



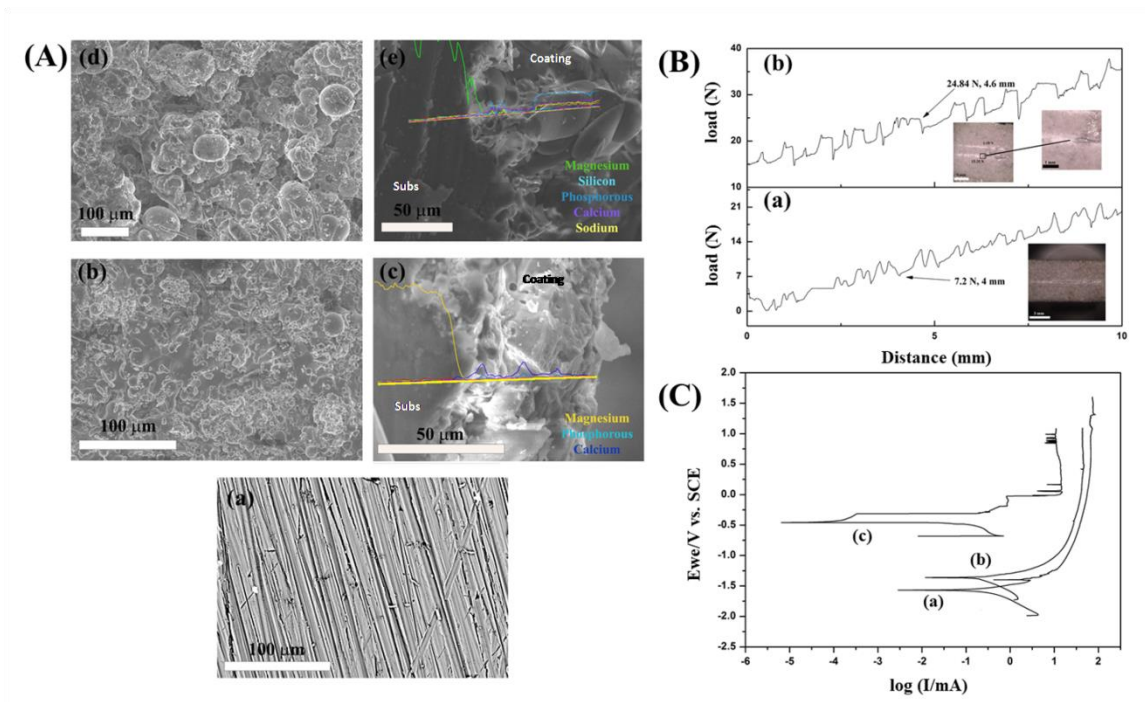


Fig. 32: (A) Top surface FESEM [(a), (b) and (d) for BM, BMH and BMG respectively] and interface FESEM-EDAX [(c) and (e) for BMH and BMG ]; (B) Scratch profile of (a) BMH and (b) BMG [Inset: optical microscope image of surface]; and (C) Tafel plot recorded during corrosion testing in contact with SBF for (a) BM, (b) BMH and (c) BMG samples.

### 5.3.1.2. Powder characterization

XRD of graded/ sieved (80-120  $\mu\text{m}$ ) HAp and bioactive glass powders confirmed crystalline hydroxyapatite phase [Fig. 31A-b] and amorphous glassy phase [Fig. 31A-c] from characteristic peaks [ $2\theta$  values  $31.7^\circ$ ,  $32.2^\circ$  and  $32.9^\circ$  corresponding to (211), (112) and (300) planes and matched with JCPDS PDF# 00-009-0432] and amorphous hump respectively. FTIR spectra [Fig. 31B-b] showed peaks related to vibrational and stretching of phosphate groups ( $603$ ,  $962$  and  $1093\text{ cm}^{-1}$ ) and apatite  $-\text{OH}$  group ( $3572\text{ cm}^{-1}$ ) supporting phase-purity of hydroxyapatite along with peaks corresponding to carbonate group ( $1640\text{ cm}^{-1}$ ) as well. FTIR

of bioactive glass sample [Fig. 31B-c] showed peaks at  $1023\text{ cm}^{-1}$  (stretching) and  $455\text{ cm}^{-1}$  (bending) corresponding to Si-O-Si vibrations and that at  $872\text{ cm}^{-1}$  corresponds to O-Si-O stretching. A broad absorption peak at  $3426\text{ cm}^{-1}$  corresponds to intermolecular hydrogen bonded OH whereas presence of molecular water is also evident by sharp peak at  $1645\text{ cm}^{-1}$  and  $2924\text{ cm}^{-1}$  and impurities like ionic nitrates at  $1463\text{ cm}^{-1}$ . Final composition of bioactive glass used for plasma spray coating was (approx. by wt.): 53%  $\text{SiO}_2$ , 23%  $\text{Na}_2\text{O}$ , 20%  $\text{CaO}$  and 4%  $\text{P}_2\text{O}_5$ .

### 5.3.1.3. Coating characterization

Figs. 31A-d and 31A-e shows the XRD of coated surface of BMH and BMG samples respectively. BMH samples showed phase mixture of HAp and Mg (73% and 27% respectively calculated from Reitveld analysis). Percentage of crystallinity (calculated by Landi's et al. method [215]) and average crystallite size (calculated by Scherrer's method [215]) of HAp phase is found to be about 74% and 19 nm respectively. Coating coverage was better in case of BMG compared to other samples with no formation of crystalline/ other amorphous phase. Amorphicity of S53P4 was increased after plasma spray process which is reflected by lower intensity of XRD pattern.

Figs. 31B-d and 31B-e show FTIR spectra of BMH and BMG respectively. Wider peaks in comparison with spectra of the HAp powder were found in case of BMH samples. Decrease in the crystallinity of BMH (as seen in XRD) has also been reflected in FTIR. No characteristic peaks were found due to carbonate bond as that of base HAp powder. Broadening of peaks at  $560$ ,  $603$  and  $1049\text{ cm}^{-1}$  and decrease in intensity at  $3752$  and  $632\text{ cm}^{-1}$  can be observed in case

of BMH samples. Peak broadening (at 472, 1024 and 1600  $\text{cm}^{-1}$ ) can be seen in case of BMG sample also after plasma spray coating.

Figs. 32A-b & c and 32A-d & e show FESEM microstructures of top surface and coating interfaces of plasma sprayed BMH and BMG, respectively. Layer-wise fish scale like morphology of melted and deformed splat can be seen near vicinity of substrate, whereas globular shaped splat along with some porosity ( $\sim 1\text{-}10\ \mu\text{m}$ ) was also found around outside/periphery of BMH samples together with some unmelted particles. Dimensions of pores for BMG was slightly higher (15-30  $\mu\text{m}$ ) with layer-wise globular shaped unmelted/ unreacted particles. The thickness of the coating was found to be 50-60  $\mu\text{m}$  for BMH and 90-100  $\mu\text{m}$  for BMG samples. There was sharp decrease in the Mg concentration which can be seen from the EDAX line scan at across the interface, Figs. 32A-c and 32A-e.

Load-displacement plot obtained after scratch test on BMH and BMG are shown in Figs. 32B-a and 32B-b, respectively; corresponding optical microscope images of the scratch are also provided. From these results, the delamination load was found to be 7.2 N at 3.8 mm for BMH, whereas in the case of BMG it was 24.84 N at 4.8 mm.

#### 5.3.1.4. Electrochemical properties:

Potentiodynamic polarization curves for BM, BMH and BMG samples are shown in Figs. 32C-a, b and c respectively. Corresponding data of corrosion potential ( $E_{\text{corr}}$ ) and corrosion current density ( $i_{\text{corr}}$ ) were evaluated from the curves. For BM, BMH and BMG,  $E_{\text{corr}}$  (mV) values were -1540, -1420 and -296, respectively with corresponding  $I_{\text{corr}}$  ( $\mu\text{A}$ ) values as 250, 297 and 68, respectively. The decrease in the  $E_{\text{corr}}$  of BMH and BMG clearly indicate that both coatings

have relatively better resistance to corrosion initiation than BM. However, the corrosion rate appears to be lowest for BMG due to their lowest  $I_{corr}$ .

#### 5.3.1.5. SBF immersion test:

Figs. 3A-a and b, 3B-a and b and 3C-a and b show the XRD pattern after 7 and 14 days of SBF immersion study of the BM, BMH and BMG samples, respectively. After 7 days of immersion, the XRD of BM showed 11% HAp (JCPDS PDF #00-19-0272) along with 89% Mg (JCPDS PDF #00-035-0821). Mg phase was found to increase up to 92.7% after day 14 confirming corrosion on the surface. XRD of BM samples also showed decrease in HAp phase crystallinity (11% to 7.3%) as well as average crystallite size (83 nm to 33nm) after day 14. Both BMH and BMG samples showed the formation of hydroxyapatite (JCPDS PDF #01-086-1201) and calcium phosphate hydroxide (JCPDS PDF #01-083-1887) along with  $Mg(OH)_2$  (JCPDS PDF #01-076-0667 and #00-044-1482 respectively). Percentage of phases in case of BMH samples was calculated using X'pert pro software and was found to be 7.5% (hydroxyapatite with average crystallite size 11 nm) and 92.5% (magnesium hydroxide). XRD taken after 14 days showed decrease in percentage (7.5% to 4.5%) of hydroxyapatite phase (with average crystallite size 4.7 nm). However, in case of BMG samples, Ca-P phase was found to increase from day 7 (31.3%) to day 14 (67.3%) along with average crystallite size of hydroxyapatite (9.3 nm to 11 nm).

FTIR spectra of BM, BMH and BMG samples after day 7 and 14 of SBF immersion study as shown in Figs. 33A-c and d, 33B-c and d and 33C-c and d supported XRD findings. BM samples showed peaks related to carbonated apatite at 563, 872, 1054, 1468 and 3435  $cm^{-1}$ . Based on FTIR result, after SBF study of BM samples, the layer obtained contains phosphates

and carbonates. A sharp P-O bending mode doublet at  $592\text{ cm}^{-1}$  is suggestive of hydroxyapatite [216]. However, decrease in C-O and P-O peak intensity supports the decrease in crystallinity as stated in XRD. BMH and BMG samples, on the other hand, showed fingerprints of apatite phase ( $563, 872, 1042, 1166, 1424, 1640, 2924$  and  $3700\text{ cm}^{-1}$  in case of BMH samples and  $872, 1042, 1468, 1640, 2924$  and  $3696\text{ cm}^{-1}$  in case of BMG samples) along with indication of Mg-O bonding at  $450$  to  $500\text{ cm}^{-1}$  wavenumbers. A detailed band interpretation is given in Table 11. BMG samples showed more apatite formation than BMH samples after SBF immersion study.

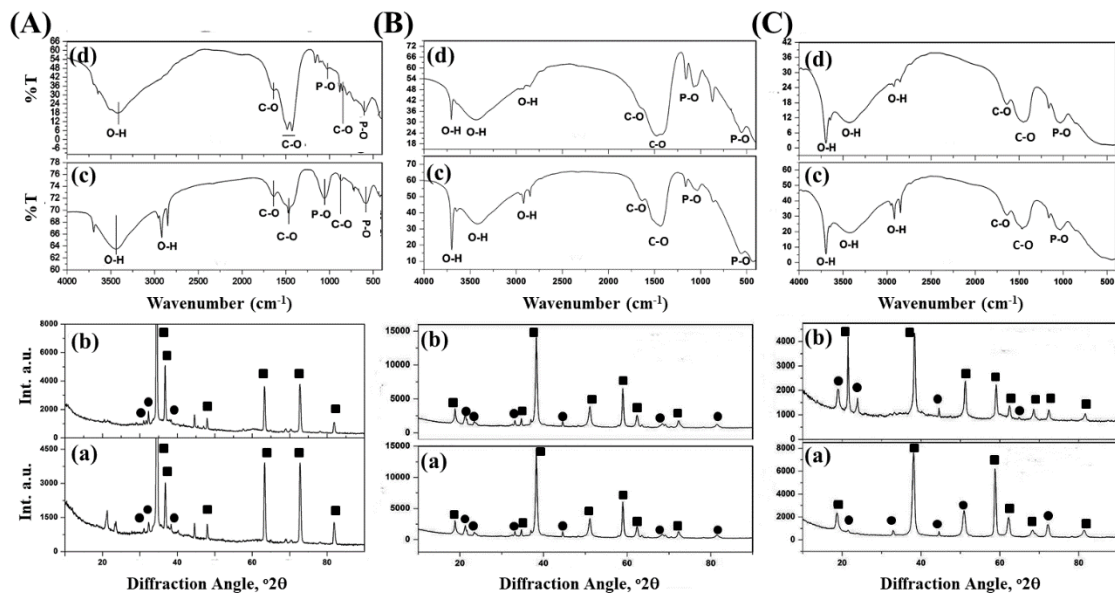


Fig. 33: XRD pattern and FTIR spectra of the samples after 7 and 14 days of SBF test; (A) for BM, (B) for BMH and (C) BMG; (a) & (b) are XRDs and (c) & (d) are FTIRs after 7 and 14 days respectively; [• HAp phase and ■ Mg phase].

Table 11: FTIR peak analysis after SBF immersion study

	BM (cm <sup>-1</sup> )		BMH (cm <sup>-1</sup> )		BMG (cm <sup>-1</sup> )	
	Day 7	Day 14	Day 7	Day 14	Day 7	Day 14
Mg-O	424	420	424	424	424	424
P-O			563	563		
P-O	585	592				
C-O/ HPO <sub>4</sub> <sup>3-</sup>	872	879	872	872		872
P-O			1042		1042	1042
P-O	1054			1054		
P-O		1166	1166	1166	1166	1166
C-O		1424	1424	1424		
C-O	1468	1476			1468	1468
H-O-H	1640	1640	1640	1640	1640	1640
Absorbed H <sub>2</sub> O	2851		2851	2851	2851	2851
Absorbed H <sub>2</sub> O	2924		2924	2924	2924	2924
H-O-H	3435	3426	3427	3427	3427	3427
O-H	3700	3694	3700	3700	3700	3696

After SBF immersion for 14 days, top surface of bare and coated Mg-alloy substrates was found to have different morphologies due to interaction with SBF. BM samples showed (Fig. 34A-a) flowerlike apatite deposition, primarily composed of needle shaped crystals covering the entire

surface. BMH samples (Fig. 34A-b) exhibited globular apatite microstructure composed of fine interconnected flakes with pores (0.1-1.5  $\mu\text{m}$ ). There was layer-wise apatite formation and when observed at higher magnification the precipitates revealed flake-like crystals with small pores in case of BMG (0.5-1.5  $\mu\text{m}$ ) (Fig. 34A-c and the inset) and the morphology was found to be denser and closely packed than others.

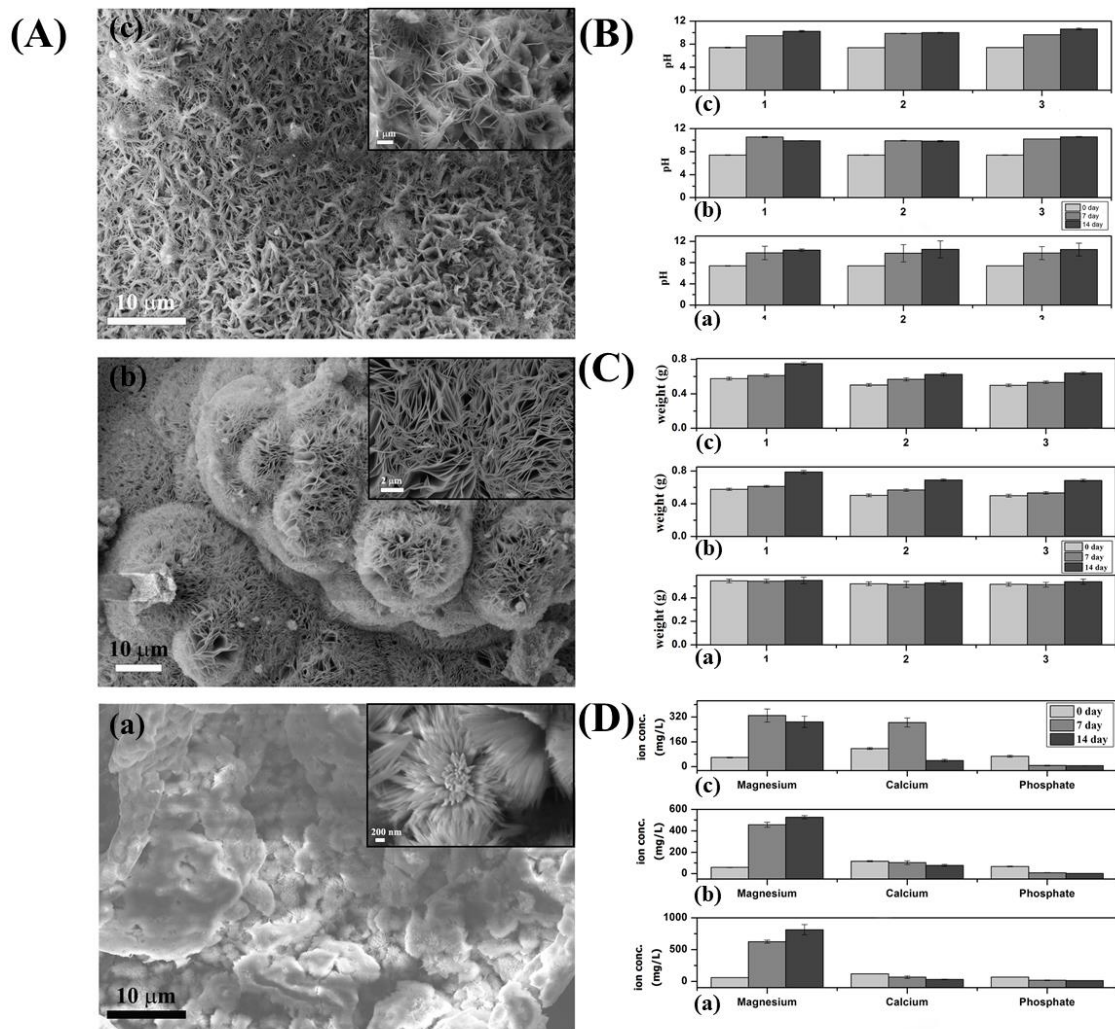


Fig. 34: (A) FESEM microstructures after 14 days of SBF study; change of (B) pH, (C) weight and (D) magnesium, calcium & phosphate ion concentration of supernatant of different samples

at day 0, 7 and 14; (a) is for BM, (b) is for BMH and (c) is for BMG; '1', '2', '3' stands for three samples of same type.

pH of supernatant solution collected from BM, BMH and BMG samples increased with time (Fig. 34B-a, b and c) with differing increased rates. Though, after initial 7 days, the increase in the pH was higher for BMH samples while that of BMG samples was found to be higher after day 14. Qualitatively, the change in the weight of the samples (Fig. 34C-a, b and c) was found to be directly proportional to the formation of apatite on these surfaces. Negligible weight change of BM samples (Fig. 34C-a) indicates its inability towards apatite formation, whereas the weight gain of BMH (Fig. 34C-b) (average increase after 7 day was ~ 3.4% and after 14 day it was ~ 12.9%) and BMG (Fig. 34C-c) (average increase in weight after 7 day was ~ 8.7%, after 14 days this was ~ 27.2%) demonstrates their apatite precipitation ability. The changes in the ion concentration of supernatant with immersion time is another way of correlating bioactivity (w.r.t. apatite formation) as well as corrosion (Fig. 34D-a, b and c). BM showed increase of Mg-ion concentration with time, whereas the solution of BMH samples showed initial increase of Mg-ions up to day 7 but the rate was decreased at day 14. In case of BMG samples, however, Mg ion was found to be decreased after day 7 to 14. Calcium ion concentration was decreased in case of BM and BMH after day 7 and 14, but the same increased in BMG after day 7 and eventually decreased at day 14. Supernatant corresponding to BMH and BMG showed lower concentration of phosphates which support higher bioactivity (w.r.t. apatite formation) of the samples.



#### 5.3.1.6. In vitro biocompatibility assessments

MTT and alamar blue assays were conducted to assess the cytotoxicity of present samples. Both results showed that these implants are non-toxic and provide favourable surfaces for cellular proliferation. MG-63 cell viability, cell proliferation and ALP expression on BM, BMH and BMG samples were measured on days 5, 7, 14 and 21 days. Maximum cell viability (\*\*p<0.01, \*\*\*p<0.001), proliferation (\*p<0.05\*\*\*p<0.001) and ALP expression (\*\*p<0.01,\*\*\*p<0.001) were recorded for BMH after 21 days of cell culture as shown in Figs. 6A, B and C respectively. Calcium (Ca<sup>2+</sup>) deposition, on the other hand, measured on day 14 and 21 days (Fig. 6D) showed maximum for BMH again after 21 days of cell culture (\*\*p<0.01, \*\*\*p<0.001).

#### 5.3.1.7. Cell morphology

Laser confocal helped to examine the cell morphology and spreading of cells on samples. Cell morphology on BM, BMH and BMG are presented in Figs.35E-a, b and c. Maximum number of cells present in BMH as compared to other compositions. Actin covers total surface of this sample and formed neo matrix which penetrated to sample as well. The actin filaments were stained with Alexa Fluor<sup>®</sup> 488 (green), nuclei with Hoechst 33342 (blue) and finally examined under confocal at 20X.

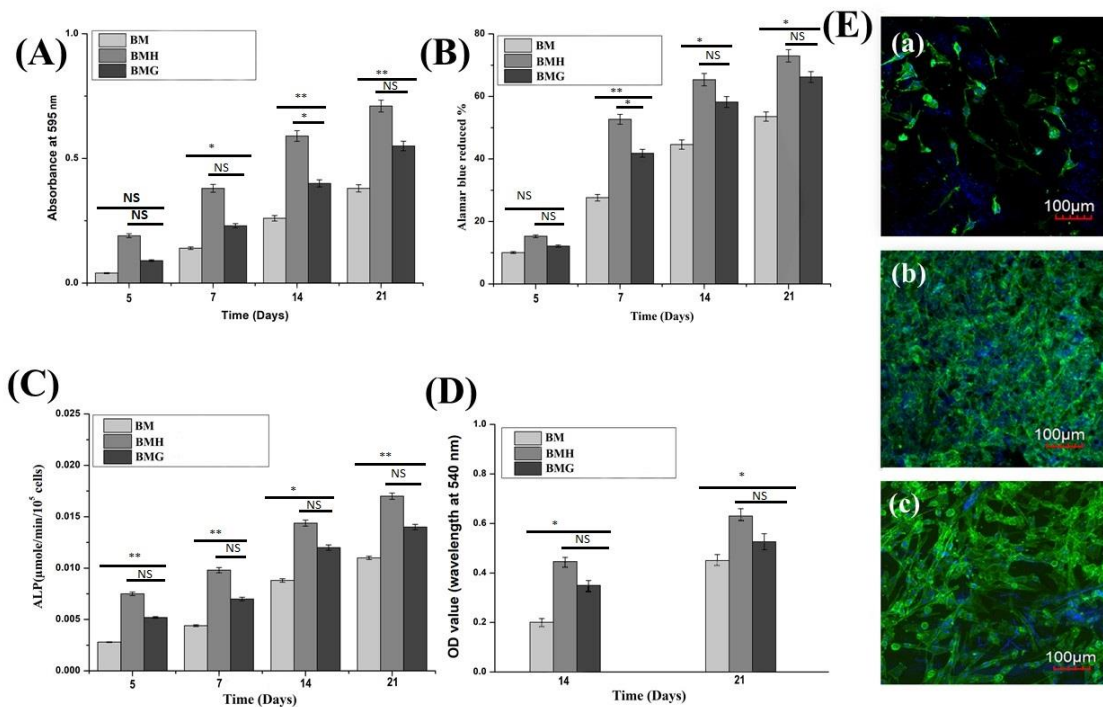


Fig. 35: MG-63 (A) Cell viability, (B) proliferation, (C) ALP expression and (D) mineralization assay of different samples; (E) cell morphology (by confocal laser microscopy) of (a) BM, (b) BMH and (c) BMG samples.

The cell growth upon different layers of 3D constructs was observed by Z-scanning during confocal microscopy and finally image was taken by merging the different layers. The image depicted abundance and homogeneously dispersed actin filaments on BMH and BMG implants compared to BM. BMH samples showed presence of abundance cells followed by BMG. However, actin sharing was meagre and secluded for BM to just around the cell nuclei.

mRNA expression of representative bone-associated genes, such as osteopontin (OPN), collagen I, osteocalcin (OCN) and Runx2 helps to investigate the osteogenic efficacy of different implants. Fig. 36 shows the comparison of the gene expression of cells on various implants after 21 days of culture. BMH and BMG samples exhibited relatively higher levels of

genes compared to BM samples. However, substantial difference in gene expression between BMH and BMG after 2 weeks of study was not observed.

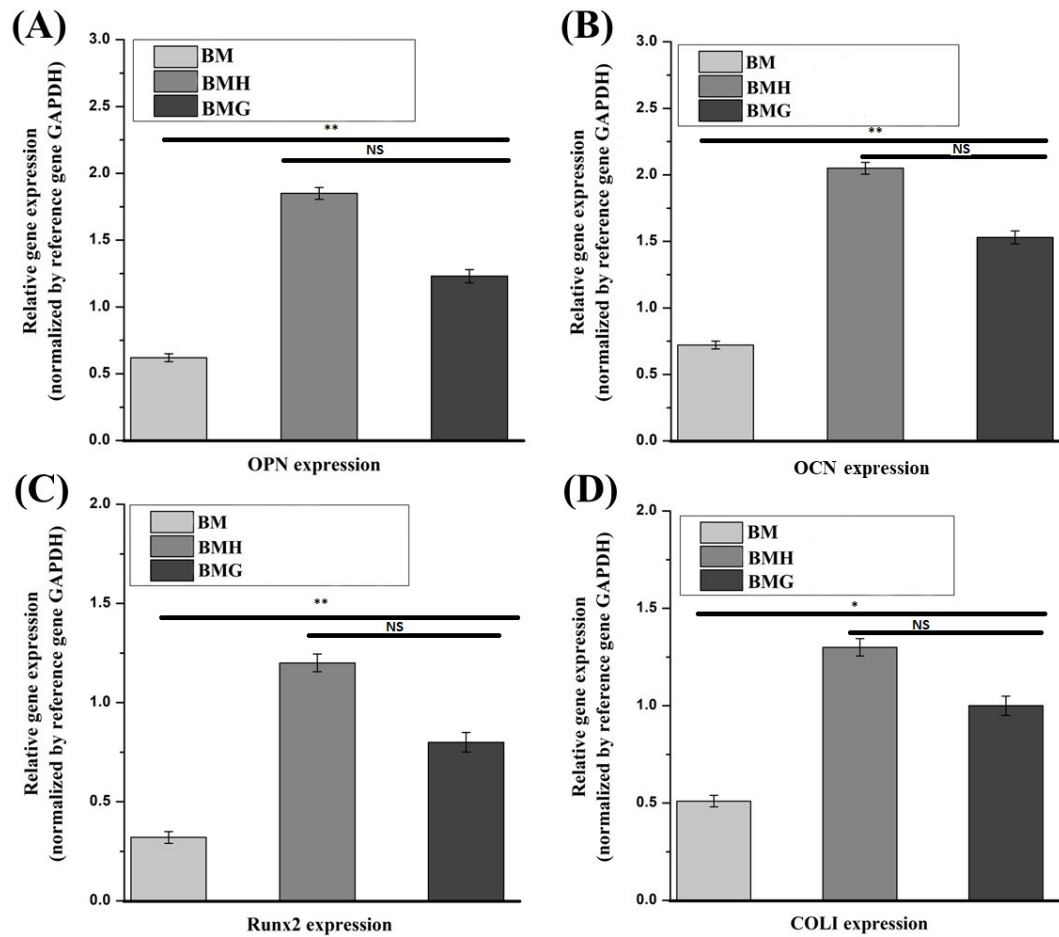


Fig. 36: Relative gene expressions (normalized by reference gene GAPDH) w.r.t. (A)OPN, (B) OCN, (C) Runx2 and (D) COLI expression of different samples.

### 5.3.1.8. *In vivo* studies

#### 5.3.1.8.1. Bone histology

Fig. 37A(a-c) shows histological picture of implanted bone at 2 months. As shown in Fig. 37A(a), BM implanted bone section depicted a well-developed bony matrix with sufficient number of Haversian canal, bony lacunae and few osteoclasts. Medullary portion was less avascular and occupied by few osteoclasts, osteocytes and scanty amount of mucin. Accumulation of osteocyte was prominent in cortical area. Angiogenesis towards medullary region was lesser in amount [Fig.37A(a)]. Bony section of BMH implant depicted bony lamellae characterized by well-developed Haversian system, canaliculi and resorption of bone in pericortical areas. Medullary region was occupied by RBC, scanty amount of mucin, few osteoblasts and numerous osteocytes. Bony lacunae in some places were invaded by few osteoclast cells. Angiogenesis was prominent in medullary portion although fibro-vascularization was sufficient in cortical mass [Fig. 37A(b)]. Fig. 37A(c) shows histological images of BMG implanted bone section. Section depicted presence of abundant osteocytes, osteoclasts and osteoblast. Fibro-vascularisation was prominent in cortical area and perimedullary area. Medullary cavity had adipose tissue, few RBC, moderate amount of mucin and osteoblast cell. Angiogenesis was fewer in cortical area than in medullary area [Fig. 37A(c)].

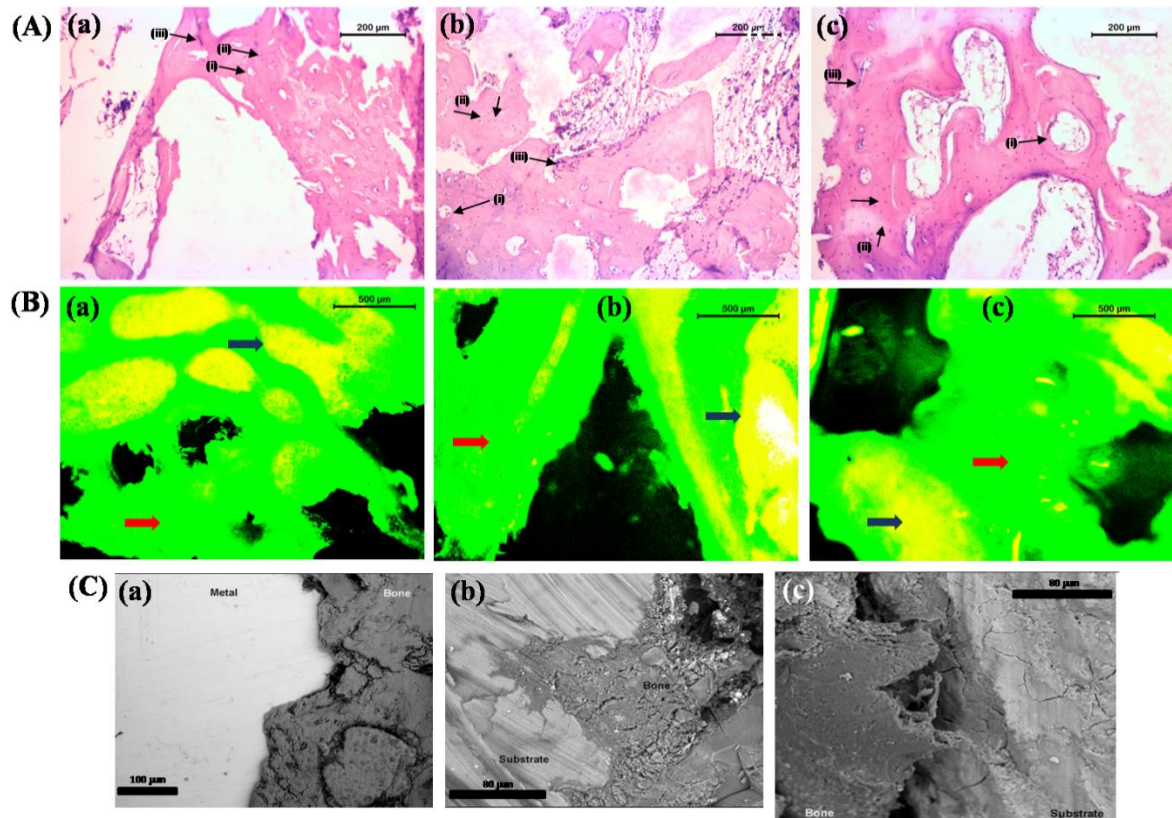


Fig. 37: (A) Histology [(i) Haversian canal, (ii) Osteoblasts, (iii) Osteoclasts] (B) Fluorochromelabelling [Blue arrow - new bone formation; Red arrow- old bone] and (C) SEM images of implanted bone samples after 2 months [(a) for BM, (b) for BMH and (c) for BMG].

### 5.3.1.8.2. Radiology

Fig. 38A shows sequential radiology of different implants in distal metaphysis of femur bone in rabbit model. In BM implant, day '0' (day of implantation) radiographs showed a radio dense circular material placed in metaphysis of the distal femur. After 1 month, the material radio density was reduced in comparison to earlier time point. A negligible impression of implant was found after 2 months indicating maximum degradation of material vis-à-vis moderate osseous growth in the defect site. Radiodensity of material and bone is comparable [Fig.38A(a-c)]. In BMH implant, "0" day radiograph showed radio-opaque material in the distal femoral

bone defect. By the end of 1 month, implant was visible in the defect region with comparable radiodensity of host bone although there was a distinct radiolucent gap between bone and implant. At 2 months, implant was visible with similar radio density of host bone but there was reduction in diameter of implant indicating degradation was under process. Radiolucent gap between implant and bone was reduced indicating new osseous tissue formation from the host bone [Fig. 38A (d-f)]. In BMG implant, “0” day radiograph showed presence of radiopaque implant in created defect of distal metaphysis of femur bone extending upto opposite cortex of bone. At 1 month, implant was visible with comparable radiodensity of host bone. Implant within the bone was under process of degradation as observed by reducing diameter of implant. Radiolucent gap in between implant and bone is negligible. The implant at 2 months showed moderate degradation as observed with loss of round shape of diameter within bony cavity. Radiodensity of implant is approaching to bone density and new bony tissue ingrowths over the defect area [Fig. 38A (g-i)].

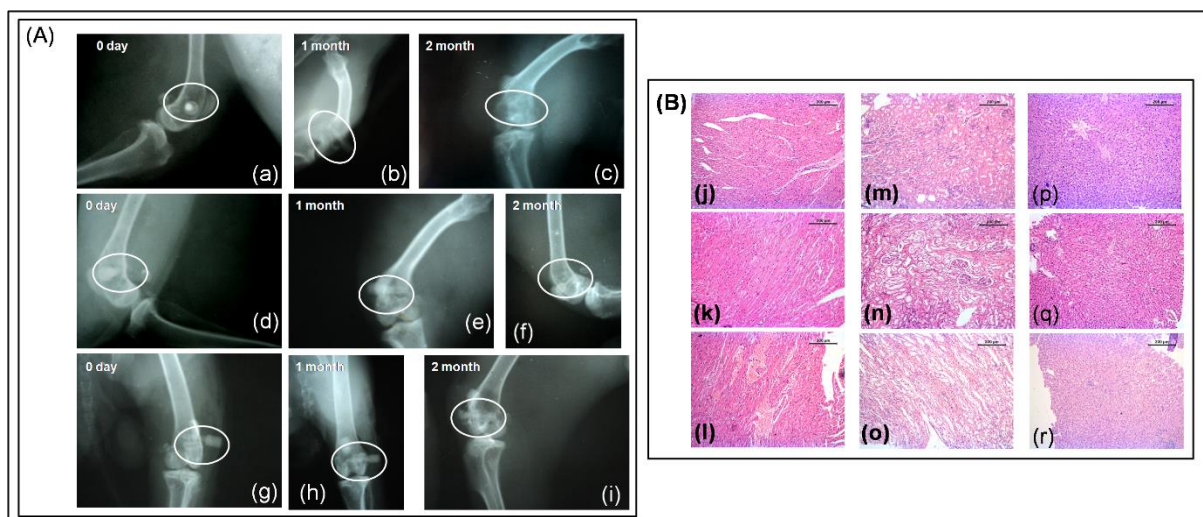


Fig. 38: (A) Radiographs of BM (a-c), BMH (d-f) and BMG (g-i) implanted bone immediately after implantation (day ‘0’), 1 month and 2 months post-surgery; (B) Histological images of

heart (j-l), kidney (m-o) and liver (p-r) of BM, BMH and BMG implanted at 2 months post-surgery.

#### 5.3.1.8.3. Fluorochrome labelling study

Golden yellow fluorescence in the section depicted new osseous tissue formation whereas dark sea green colour designates host bone. In the BM implant sample set 2 months showed new bone formation mainly at centre part and partially in edges, as pointed out by the presence of golden yellow fluorescence (Fig. 37B). New bone formation was nearly 23% in defect area. In BMH implant group depicted ample new osseous (~ 37%) in contrast to the other two groups. Although golden yellow fluorescence was mostly limited to peripheral side, a wide deep area of new bone formation was observed. Along this deep zone of golden fluorescence, a narrowband of fluorescence throughout the length was also observed nearly to the central part of section indicating bone formation both in central as well as in peripheral zone. In BMG implant group, new bone formation was nearly 29%, mostly in periphery. The new osseous tissue was measured using ImageJ software. The golden color pixels were calculated and changed to percentage taking data from three images each.

#### 5.3.1.8.4. SEM of bone-implant interface

Scanning electron microscopy of bone-implant interface of BM, BMH and BMG samples are given in [Fig. 37C]. It was found that BMH showed best bone apposition in due course of time with little or no interfacial gap, while BMG had also shown similar trend, but due to its conversion of apatite like layer, metal surface was found to be covered by apatite like layer with an apposition of bony soft tissue at interface. On the other hand, BM was found to be

replaced with associated interfacial bone with time, which is quite obvious for this alloy. Matured bony tissues were noticed in case of BMH with time.

#### 5.3.1.8.5. Toxicity study of vital organs

Heart: Fig. 38B(a-c) shows histological section at 2 months of implantation. Architectural detail of BM implanted heart myofibril retained its vitality with all processes including nuclear prominence, intact cytoplasm and fibrovascular network. Vascularisation of total structure was quite normal. Cellular details and infiltrating cells were within normal limit [Fig. 38B(a)]. In BMH implant group, section depicted almost normal structure of myocardial tissue characterized by well nuclear detail, cytoplasmic organelles and regularly arranged fibres. Mononuclear cells were predominant in some places without involving edema or other exudation [Fig. 38B(b)]. In BMG implant group, section depicted a normal architectural pattern of cardiac tissue without any presence of infiltrating cells [Fig. 38B(c)].

Kidney: In case of BM implant, kidney section depicted normal glomerular tufts, tubular architecture and well-maintained collecting ducts. Peri-glomerular spaces showed normal architectural detail with mild infiltrating cells. Few tubular lining epitheliums showed degeneration to some degree but within normal limit [Fig. 38B(d)]. Renal architecture of BMH implant was quite normal with glomerular tufts formation and different intact renal tubules. Oozing of RBCs in intertubular spaces was seen focally and some tubular epithelium showed necrosis and infiltration with mononuclear cells [Fig. 38B(e)]. In BMG implant, section showed normal architecture of kidney with glomerular tufts formation and different intact renal tubules [Fig. 38B(f)].



Liver: Section of BM implanted liver depicted normal limits of hepatocytes. Some portion of total portal triads showed few infiltration and RBC extravasations. Few hepatocytes showed focal changes with mild necrosis [Fig. 38B(g)]. In BMH, section depicted normal hepatic architectural detail characterized by well-formed hepatocytes, portal triads and well-made globules. Infiltration of mononuclear cells and von Kupffer cells were within normal limit [Fig. 38B(h)]. In BMG implant group, hepatic parenchyma showed presence of RBC, mononuclear cell, well-formed central veins and few von Kupffer cells [Fig. 3B(i)].

#### 5.3.1.8.6. *In vivo* immune response

TNF- $\alpha$ , IL-2 and IL-6 expression at 1, 2, 4 and 8 weeks showed that at 1st week, inflammatory response due to materials increased maximally followed by a gradual fall at 2nd, 3rd, 4th and finally at the end of 8th week where the immuno-reactivity of implanted animals returned to its baseline as compared to control (normal healthy) animals [Fig. 39(A-C)].

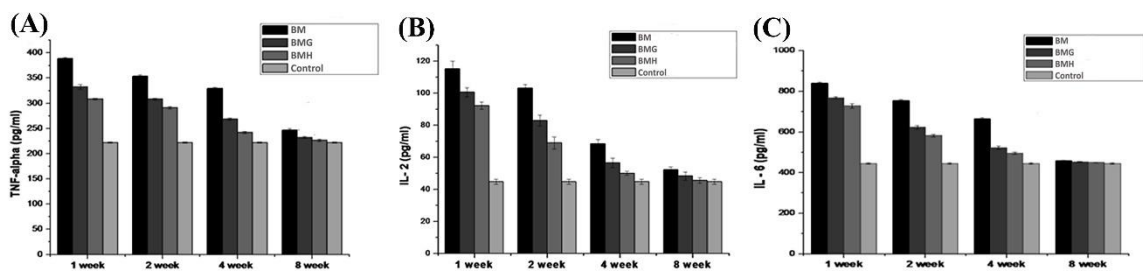
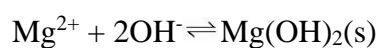
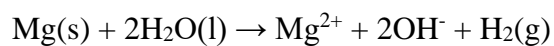


Fig. 39: Expressions of (A) TNF- $\alpha$ , (B) IL-2 and (C) IL-6 at 1, 2, 4 and 8 weeks for different samples with the reference of control (normal healthy animals).

Magnesium ion has diverse roles in numerous biological functions for instance in bone metabolism. The bivalent magnesium ions helps the formation of biological apatite as well as has stimulatory effect on the growth of marrow cells [217]. It was also reported that adding

magnesium helps in bone metabolism whereas, deficiency leads to lowered bone escalation and amplified bone resorption [218]. Faster degradation of Mg implant was observed within the bony environment especially in cancellous part of bone than cortical part [107]. Due to rapid degradation of bare Mg-based implants, attempts are to be made to trigger the mechanical integrity irrespective of the implantation site. Surface coating of Mg-based implant has obvious advantages of gradual degradation over a period of time along with superior corrosion consistency enabling the strength decay [219].

Mg-alloy mimics comparable elastic modulus and mechanical strength as cortical bone leading to bone regeneration [220]. In physiological environment, Mg-alloy decays in contact with water (body fluid) as shown below. Degradation of Mg-alloy in body fluids produces  $Mg^{2+}$  cations which are efficiently excreted by kidneys and eliminate them naturally through urine [221].

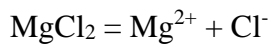
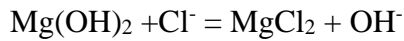


However, Mg and its alloys often retain their strength under physiological environment up to 6-8 weeks [222]. Their rapid degradation is a serious concern for degradable implant application. Therefore, several surface modification approaches have been attempted by different groups [223]. Surface modification not only ensures longer-time mechanical integrity by providing resistance against corrosion in biological fluids, but also improves bioactivity of these alloys depending on the type of coating material. Increasing mechanical integrity is essential as well as biodegradability of Mg as it can act as an advantage in temporary fracture

fixation devices. This could alleviate the necessity of second surgical operation for removal of implant vis-à-vis reduce the hospital cost as well as obvious surgical complications [221]. Among the various surface modification techniques, plasma spraying technique helps in chemical control, bio-corrosion resistance, as well as reduced substrate fatigue resistance [224]. Further, plasma spraying process enhanced surface properties and biocompatibility keeping excellent bulk properties unchanged. In particular, the technique have many advantages in biomedical application like exceptional film chemistry, sole substrates coating with superior adhesion, conformal and pin-hole free films and outstanding infiltration [225]. Hygroscopicity of substrates decrease many-fold after plasma spray coating, making the technique appropriate for coating corrosive materials like Mg-alloy.

Bioactive inorganic coatings, such as HAp and bioactive glass (BAG) on Mg/Mg-alloy can control corrosion and enhance bioactivity while providing a balance between time-dependant degradation and mechanical integrity [223, 226]. In the present investigation, plasma spraying was chosen in order to get a firm adhesion/ layer-wise formation of coating with porosity which would act as nucleation site for apatite formation and help different cell functions, ultimately increasing the biocompatibility of the sample. For the first time, plasma spray method using bioactive glass material has been employed for Mg-alloy. However, in plasma spray process using HAp, powders experience high flame temperature, which causes evaporation of water (trapped within pores or part of the HAp lattice structure), resulting decrease in crystallinity (Fig. 31A-d) and low adhesion strength (Fig. 32B-a) [227, 228]. Amorphous BAG powders showed firm apposition with the substrate surface after plasma spray coating [which reflected in better adhesions strength (Fig. 32B-b)] without any trace of magnesium phase in XRD (Fig. 31A-e). Microstructure of BMH showed melted and deformed splat in the inner side (nearer to the substrate surface) whereas globular shaped splat at the periphery of coating surface (Fig.

32A-c), which can be attributed to better surface cooling on outer surface as compared to inner layers; more cooling led them to more thermodynamically stable shape. Due to its amorphous nature, BAG forms less irregular and globular shaped splat on the surface (Fig. 32A-d). Pores having size ranging 1-10  $\mu\text{m}$  were seen in case of BMH samples whereas BMG showed interconnected pores ranging 15-30  $\mu\text{m}$ . Interface study confirmed presence of pores up to layers adjacent to BMH substrate which explains lower delamination strength as well as availability of Mg phase in XRD as an effect of Mg ion migration from substrate, on the other hand amorphous BMG showed absence of pores even upto layers adjacent to substrate confirming firm layer-wise formation of coating on surface of substrate. Better homogeneity and superior coverage of BAG coating (for BMG) ensured increase in resistance towards corrosion when immersed in SBF solution showing a very high  $E_{\text{corr}}$  value (-296.246 mV vs. SCE) compared to BM (-1540.824 mV vs. SCE) and BMH (-1420.479 mV vs. SCE) samples. Lower resistance of BMH was due to surface pores, which act as pitting corrosion sites [229]. Corrosion current densities ( $i_{\text{corr}}$ ) of coated and uncoated samples indicated that BMG samples exhibited lowest thermodynamic tendency to participate in anodic reaction thus effectively improving resistance followed by BMH and BM samples [230]. However, after initial corrosion, BMH samples tends to form inactive layer of  $\text{Mg}(\text{OH})_2$ , which reduced surface reactivity towards corrosion as stand-alone coating[231]. When immersed in ionic solutions consists of chloride ( $\text{Cl}^-$ ) ion (SBF), this passive layer converts from  $\text{Mg}(\text{OH})_2$  to soluble  $\text{MgCl}_2$  with time, weakening the surface as well as releasing  $\text{OH}^-$  ions in solution increasing the pH (Fig. 34B-b).  $\text{MgCl}_2$  dissolves easily in SBF and releases  $\text{Cl}^-$  to continue the chain of corrosion on surface [232].



SBF immersion study which also involves corrosion is a very complicated phenomenon where ion exchange occurs simultaneously for apatite formation as well as corrosion. When immersed in SBF, leaching of ions from substrate to solution occurs initially followed by apatite precipitation. Dissolution of calcium ion in case of BMH and BMG control formation of apatite phases on surface.  $\text{Ca}^{2+}$  ions of the coatings and ions from SBF solution underwent reduction reaction simultaneously with conversion of Mg to  $\text{MgCl}_2$  releasing  $\text{OH}^-$  in the solution, which increases the pH as well. Essentially, the reaction stages are outlined by following equations:

$\text{Mg} = \text{Mg}^{2+} + 2\text{e}^-$	$2\text{H}_2\text{PO}_4^- + 2\text{e}^- \rightarrow 2\text{H}_2\text{PO}_4^{2-} + \text{H}_2$
$2\text{H}_2\text{O} + 2\text{e}^- = \text{H}_2 + 2\text{OH}^-$	$2\text{H}_2\text{PO}_4^{2-} + 2\text{e}^- \rightarrow 2\text{PO}_4^{3-} + \text{H}_2$
$\text{Mg}^{2+} + 2\text{OH}^- = \text{Mg(OH)}_2$	$10\text{Ca}^{2+} + 6\text{PO}_4^{3-} + 2\text{OH}^- \rightarrow \text{Ca}_{10}(\text{PO}_4)_6(\text{OH})_2 \text{ (BMH)}$
$\text{Mg(OH)}_2 + \text{Cl}^- = \text{MgCl}_2 + \text{OH}^-$	$5\text{Ca}^{2+} + 3\text{PO}_4^{3-} + \text{OH}^- \rightarrow \text{Ca}_5(\text{PO}_4)_3(\text{OH}) \text{ (BMG)}$

Hence, more corrosion leads to higher pH as well as higher  $\text{Mg}^{2+}$  concentration after day 7 in case of BMH samples where porosities in the coating most probably let SBF penetrate to Mg-interface which gradually decreases with increasing apatite precipitation up to day 14 with increasing final weight as well. Slow increase in pH from day 0 to 7 until day 14 illustrated slower corrosion rate of BMG samples. Therefore, formation and crystallization of apatite layer retards aggressive corrosion during initial days. High calcium concentration of SBF related to BMG samples after day 7 supports leaching of bioactive glass which gradually react with phosphates to form apatite layer on surface of sample increasing final weight for this case

too[233]. Phase difference of apatite formed might be explained by the existence of different ions in solution at different concentrations in accordance with leaching of ions from sample [234]. However difference in average crystallite size of apatites formed in case of BM, BMH and BMG samples can be explained by the fact that more nucleation site decreases the average crystallite size. As HAp and BAG coatings are porous, they provide much more nucleation site than the uncoated substrate, hence lower average crystallite size which can be seen from XRD data. Decrease in average crystallite in case of BM and BMH samples from day 7 to 14 confirms presence of pores on surface created from corrosion. On the other hand, increase in average crystallite size for BMG samples proves better apatite formation on the surface than others. Apatite formation and corrosion is schematically represented in Fig. 40, where  $\text{Ca}^{2+}$ , originated from SBF and surface of sample react with  $\text{H}_2\text{PO}_4^-$  to form insoluble apatite. During the process,  $\text{OH}^-$  formed and reacts with leached  $\text{Mg}^{2+}$  to form  $\text{Mg}(\text{OH})_2$ , which also precipitates on surface increasing resistance of the coating. Depending upon  $\text{Ca}^{2+}$  concentration in SBF solution, different phases of Ca-P forms.  $\text{Ca}^{2+}$  concentration difference between supernatant of BMH and BMG after day 7 clearly gave an idea why two different apatite phases formed for BMH and BMG samples.

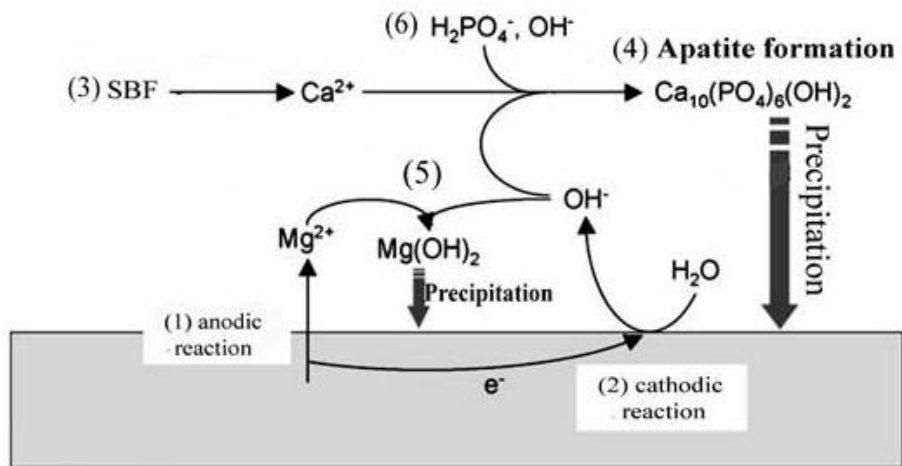


Fig. 40: Proposed mechanism of corrosion and apatite formation when immersed in SBF.

Cell-material interactions require initial attachment of cells which consecutively can influence ensuing cellular and tissue responses [235]. It is reported that the adhesion and viability cells depend on the culture setting and material surface features. However, rapid degradation of Mg and its alloys leads to constant increase in the pH, which can be detrimental to cell adhesion and survival. This can be seen from the in vitro results of BM with least corrosion resistance, which due to absence of coating, pH rapidly increases whereas, degradation of bioactive glass is more as compared to HAp resulting less attachment, viability and proliferation of cells in the order of the BM > BMG > BMH at different time intervals of 5, 7, 14 and 21 days post incubation. Further, coated Mg-alloys provide conducive atmosphere for cell connection and expansion. Any protective coatings prevents the entry of water and electrolyte [236], leading to slower the corrosion of Mg-alloy substrate vis-à-vis diminish the diffusion rate of  $OH^-$  from Mg surface to the medium. . As a result, the rise of pH of solution neighbouring the Mg sample, which in turn helps to surface attachment of numerous cells and subsequent proliferation.

Underlying principle of protective effect is that being a reactive metal, Mg will act in response with water, precipitation of  $Mg(OH)_2$  on the surface of Mg and consequent release of  $H_2$  gas.

It is assumed that the accrued  $\text{Mg}(\text{OH})_2$  layer on Mg prevents dissolution by avoiding mass diffusion between Mg and the solution [237]. . Resultant  $\text{Mg}(\text{OH})_2$  is changed to more soluble  $\text{MgCl}_2$  by  $\text{Cl}^-$  [238], which releases  $\text{Mg}^{2+}$  into the solution.  $\text{Mg}^{2+}$  release depends upon severity of Mg corrosion. Accordingly, in the present study, the release of  $\text{Mg}^{2+}$  in cell culture is used to judge the defensive effect of the HAp and bioactive glass coating on the Mg substrate. It has been observed that there was low release of  $\text{Mg}^{2+}$  from HAp and bioactive glass coating over the Mg substrate as compared to BM throughout the incubation period leading to less corrosion in coated samples. On the other hand, adhesion strength also plays a vital role as corrosion resistance [239]. In this study, plasma spray coating has been used for coating of HAp and bioactive glass on Mg surface, which helps in slow degradation of Mg.

ALP activity and ARS assay are the important tool to calculate mineralization upon implants. The cells resemble an orderly, sheet-like structure when there are considerable levels of mineralization. During the entire period of culture, the prerequisite nature of implants includes rising ALP activity, intensity of Alizarin Red staining, and stressed actin arrangement of cells upon the implants. In the present study, HAp and bioactive glass coated samples shows favourable results in comparison to bare Mg-implant. Likewise, images of BMH implant show unsystematic deposition of actin-stress fibers together with dense cell colony and to some extent on the BMG implant. In general, *in vitro* analysis illustrates considerable perfection of implant properties of HAp and bioactive glass coated samples in relation to biocompatibility, cell viability and proliferation, and osteoconductivity. Side by side, BMH implant is a notably better choice than BMG implant. *In vivo* biocompatibility can only be assessed by observing nature and magnitude of inflammation of neighbouring soft tissue reaction in presence of any foreign material. In the present study, although it is observed lesser vascularization, fibrous tissue, and presence of mononuclear cells in the histological figures, neither significant



inflammatory reaction is pronounced nor formation of gas cavities around the implantation site of bone. This advocates that the implants are well accepted *in vivo* indicating a promising biodegradable implant material.

Radiographic evaluation of implants is a non-invasive technique to assess the position of implant during the healing process. In the *in vivo* test, radiologically a significantly higher degradation of BM was observed as compared to BMH and BMG implant. There was moderate osseous growth in defect site in BM, whereas more bone formation was observed in coated implants. Enhanced bone formation might be owing to release of Mg ions, because high Mg concentration is essential for bone cell activation [240]. Similar experiment with Mg-Ca pins in bone defect model shows, better activity of osteoblasts and osteocytes around the implant[241]. Moreover, it could be expected that enhanced local pH surrounding the implanted area due to gradual corrosion of the Mg alloy provides a favourable environment for mineralization [155]. In both coated groups, implants within bone were under the process of gradual degradation as observed by reducing diameter of implant and new bony tissue ingrowths over defect area. This might be due to gradual degradation of Mg alloy from the coated implants. Moreover, during the entire healing process, no gas bubbles are observed, due to the gradual release of Mg ions from the coated implants during degradation [240, 241]. The radiological findings can be corroborated with the fluorochrome labelling results in the present study. Tetracycline, a bone specific marker was used for quantifying the amount of new bone formation in the defect area [242]. Tetracycline is deposited in any fracture site during the active mineralization process[243]. In the present study, BM implant at 2 months showed bone formation mainly at the middle and partially in peripheries, as marked by the presence of golden yellow fluorescence. In BMH and BMG implant group, the intensity of golden yellow fluorescence was more prominent at the periphery with new a wide deep area of new bone

formation. The findings of fluorochrome labelling can also be compared with histological results. No noticeable inflammatory effects are observed surrounding the implants indicating biocompatible nature of the implants. In bare Mg alloy, histological section depicted a bony matrix with abundance Haversian canal, bony lacunae and few osteoclasts along with lesser angiogenesis towards medullary region. In BMH, implant showed bony lamellae characterized by well-developed Haversian system, canaliculi and resorption of bone in pericortical areas signifying presence and delineation of osteogenic cells. In BMG, implant group depicted a large number of osteocytes, osteoclasts and osteoblast proliferation. New bone formation around the bare Mg implants at 2 months might be due to stimulating effect [240, 244]. At 2 months, HAp and bioactive glass coated samples depicted more presence of osteoid surface. The explanation for this improved osseous tissue regeneration rates adjacent to these coated implants are due to osteo- proliferative effect of calcium phosphate and bioactive glass coating of Mg implants [240]. As the corrosion of the coated implants happens relatively slowly, the corrosion products can be safely eliminated from the body system either through absorption by the adjacent tissues or local blood circulation which corroborated the findings of reduced bone growth caused by magnesium deficiency [245].

SEM examination during the post-surgical period demonstrates better amalgamation of material with the host bone while validating infiltration of osteogenic cells and ultimately resulting into evidence of mineralized matrix. There was no visible interfacial gap between the bone and implant in BMH group. This might be due to invasion of osteoblasts towards the implant structure. For the BMG implant, interfacial gap is more pronounced which might be due to slow invasion of osteoblasts.

The histology of heart, kidney and liver was carried out to assess whether any changes happen in cellular level or not. The results established that no apparent pathological lesions were seen after 2 months of experimentation, indicating safe degradation of implants *in vivo* and will not create any detrimental effects.

Immune reactivity of the animals implanted with the materials (BM, BMH and BMG) post-surgery and normal / control animals (without any implant) was verified by quantifying the amount of IL-2, IL-6 and TNF- $\alpha$  cytokine secretion. Study of host-implant inflammatory response was monitored for initial 2 months post-surgery and the results showed that at first 2 weeks, amount of IL-2, IL-6 and TNF- $\alpha$  cytokine secretion were increased preferably because of initial host-foreign body reactions but at the end of 8 weeks, it was comparatively decreased to its baseline quite similar to control group. Comparing with the positive control group, three types of materials showed a varied reactivity, starting from highest response against BM implant followed by BMG and BMH implant. In the first two weeks, concentrations of IL-2 , IL- 6 and TNF- $\alpha$  were found to be drastically higher than the control animals, likewise, from 4 weeks upto the end of the experiment (i.e., 8 weeks),secretions of cytokines (IL-2, IL-6 and TNF- $\alpha$ ) were reasonably decreased down to its normal range. Thus, at the end of 2 months, unlike BM, neither BMG nor BMH implant materials showed any kind of marked immune reactions post-surgery, in comparison to the control group.

## 6. CONCLUSIONS

- Three parts of our proposed objective has been successfully created and characterized.
- All parts were found to be bioactive, noncytotoxic, and helpful to the formation of new bone at the site.
- *In vivo* studies also proved the compatibility of the implants

### **HAp coated e-glass:**

- For the first time, graded pure HAp could be synthesized and applied to the E-glass substrate successfully (coating thickness ~ 5-10  $\mu\text{m}$ ).
- The system was found to be non-cytotoxic as assessed by NIH3T3 and MG-63 MTT data.
- This system has a potential for development of non-metallic craniofacial implants with high mechanical strength for benefit of the ailed patients.

### **Li-Sr doped bioactive glass scaffold:**

- All bioactive glass both doped and undoped showed *in vivo* new bone formation.
- Sr and/or Li doped bioactive glass showed acceleration of early-stage bone formation.
- Sr+Li doped prove to the most effective than the other two compositions.
- Incorporation of Sr and Li in bioactive glass can effectively enhance early stage *in vivo* osteointegration and bone remodelling.

### **HAp and bioactive glass coated Mg-alloy material:**

- Degradability could be decreased by coating HAp and bioactive glass.

- Early new bone formation and tough bone-implant bonding at interface as compared to bare Mg-alloy.
- HAp coated Mg-alloy implants show better osseointegration than bioactive glass coated implants in respect of in vitro and in vivo analysis

## 7. FUTURE SCOPE

1. Development of a fracture-fixation plate with optimized design and comprising of HAp coated e-glass, thus replacing the age-old concept of metallic plates and screws for the same purpose especially cranioplasty application.
2. Primary human trial of the cases of cranioplasty fracture fixation using HAp coated e-glass plates and screws.
3. The new Li-Sr doped bioactive glass material can be of very vital importance for soft and hard tissue generation which might be very useful as future wound dressing material for both orthopedic and fibroblastic tissue regeneration.
4. Li-doped bioactive glass material itself might be a new avenue for burn and diabetic wound healing, to be used either alone or as composite with other degradable and/ or non-degradable polymers.
5. Conventional magnesium alloy material has an inherent drawback of degradation in contact with moisture, thus the new magnesium alloy composition which were also coated with HAp and bioactive glass are extremely useful for development of another kind of fracture-fixation plates and screws for orthopedic and dental applications.
6. Primary human trial of such coated Mg-alloy plates and screws for the cases of cranioplasty fracture fixation and other applications.
7. Combination of HAp coated e-glass fibers, used alone or in combination with new bioactive glass material as secondary bone-regenerating suspended material, when combined in suitable polymer matrix, may give rise to a new implanting component, which could be a breakthrough as replacement of existing tailor-made cranioplasty implants.

## 8. REFERENCES

1. Goh, R.C., et al., *Customised fabricated implants after previous failed cranioplasty*. Journal of plastic, reconstructive & aesthetic surgery, 2010. **63**(9): p. 1479-1484.
2. Goiato, M.C., et al., *Reconstruction of skull defects: currently available materials*. Journal of Craniofacial Surgery, 2009. **20**(5): p. 1512-1518.
3. Lethaus, B., et al., *Cranioplasty with customized titanium and PEEK implants in a mechanical stress model*. Journal of neurotrauma, 2012. **29**(6): p. 1077-1083.
4. Honeybul, S. and K.M. Ho, *Long-term complications of decompressive craniectomy for head injury*. Journal of neurotrauma, 2011. **28**(6): p. 929-935.
5. Joseph, V. and P. Reilly, *Syndrome of the trephined: case report*. Journal of neurosurgery, 2009. **111**(4): p. 650-652.
6. Moin, H., P. Mohagheghzadeh, and A. Darbansheikh, *The use of frozen autogenous bone flap for cranioplasty*. 2005.
7. Zanotti, B., et al., *Cranioplasty: review of materials*. Journal of Craniofacial Surgery, 2016. **27**(8): p. 2061-2072.
8. Aydin, S., et al., *Cranioplasty: review of materials and techniques*. Journal of neurosciences in rural practice, 2011. **2**(02): p. 162-167.
9. Hatamleh, M.M., M. Cartmill, and J. Watson, *Management of extensive frontal cranioplasty defects*. Journal of Craniofacial Surgery, 2013. **24**(6): p. 2018-2022.
10. Kim, B.-J., et al., *Customized cranioplasty implants using three-dimensional printers and polymethyl-methacrylate casting*. Journal of Korean Neurosurgical Society, 2012. **52**(6): p. 541.
11. Scolozzi, P., A. Martinez, and B. Jaques, *Complex orbito-fronto-temporal reconstruction using computer-designed PEEK implant*. Journal of Craniofacial Surgery, 2007. **18**(1): p. 224-228.
12. Spetzger, U., V. Vougioukas, and J. Schipper, *Materials and techniques for osseous skull reconstruction*. Minimally invasive therapy & allied technologies, 2010. **19**(2): p. 110-121.
13. Staffa, G., et al., *Custom made bioceramic implants in complex and large cranial reconstruction: a two-year follow-up*. Journal of Cranio-Maxillofacial Surgery, 2012. **40**(3): p. e65-e70.
14. Wiggins, A., et al., *Cranioplasty with custom-made titanium plates—14 years experience*. Neurosurgery, 2013. **72**(2): p. 248-256.

15. Merlino, G. and S. Carlucci, *Role of systematic scalp expansion before cranioplasty in patients with craniectomy defects*. Journal of Cranio-Maxillofacial Surgery, 2015. **43**(8): p. 1416-1421.
16. De Bonis, P., et al., *Cranial repair: how complicated is filling a "hole"?* Journal of Neurotrauma, 2012. **29**(6): p. 1071-1076.
17. Shah, A.M., H. Jung, and S. Skirboll, *Materials used in cranioplasty: a history and analysis*. Neurosurgical Focus, 2014. **36**(4): p. E19.
18. Motherway, J.A., et al., *The mechanical properties of cranial bone: the effect of loading rate and cranial sampling position*. Journal of Biomechanics, 2009. **42**(13): p. 2129-2135.
19. Tyagi, S., *Glasses And Glass Ceramics As Biomaterials*. 2007, THAPAR UNIVERSITY, PATIALA.
20. Hench, L.L., *Bioceramics: from concept to clinic*. Journal of the american ceramic society, 1991. **74**(7): p. 1487-1510.
21. Hench, L.L., *Biomaterials: a forecast for the future*. Biomaterials, 1998. **19**(16): p. 1419-1423.
22. Hench, L.L. and J.M. Polak, *Third-generation biomedical materials*. Science, 2002. **295**(5557): p. 1014-1017.
23. Aydin, S., et al., *Cranioplasty: review of materials and techniques*. Journal of Neurosciences in Rural Practice, 2011. **2**(2): p. 162.
24. Courville, C.B., *Cranioplasty in prehistoric times*. Bulletin of the Los Angeles Neurological Society, 1959. **24**(1): p. 1-8.
25. Kennedy, K.A.R., *Primitive Surgery: Skills Before Science*. Spencer L. Rogers. American Anthropologist, 1987. **89**(1): p. 217-218.
26. Sanan, A. and S.J. Haines, *Repairing holes in the head: a history of cranioplasty*. Neurosurgery, 1997. **40**(3): p. 588-603.
27. Bowers, C.A., et al., *Risk factors and rates of bone flap resorption in pediatric patients after decompressive craniectomy for traumatic brain injury: clinical article*. Journal of Neurosurgery: Pediatrics, 2013. **11**(5): p. 526-532.
28. Stieglitz, L.H., et al., *What happens to the bone flap? Long-term outcome after reimplantation of cryoconserved bone flaps in a consecutive series of 92 patients*. Acta Neurochirurgica, 2015. **157**(2): p. 275-280.
29. Durand, J.-L., D. Renier, and D. Marchac. *The history of cranioplasty*. in *Annales de chirurgie plastique et esthétique*. 1997.
30. Matsuno, A., et al., *Analyses of the factors influencing bone graft infection after delayed cranioplasty*. Acta Neurochirurgica, 2006. **148**(5): p. 535-540.



31. Flanigan, P., V.R. Kshetry, and E.C. Benzel, *World War II, tantalum, and the evolution of modern cranioplasty technique*. Neurosurgical Focus, 2014. **36**(4): p. E22.
32. Blake, G.B., M.R. MacFarlane, and J.W. Hinton, *Titanium in reconstructive surgery of the skull and face*. British Journal of Plastic Surgery, 1990. **43**(5): p. 528-535.
33. Goldstein, J.A., J.T. Paliga, and S.P. Bartlett, *Cranioplasty: indications and advances*. Current Opinion in Otolaryngology and Head and Neck Surgery, 2013. **21**(4): p. 400-409.
34. Hill, C.S., et al., *Titanium cranioplasty and the prediction of complications*. British Journal of Neurosurgery, 2012. **26**(6): p. 832-837.
35. Marchac, D. and A. Greensmith, *Long-term experience with methylmethacrylate cranioplasty in craniofacial surgery*. Journal of Plastic, Reconstructive and Aesthetic Surgery, 2008. **61**(7): p. 744-752.
36. Alexander Jr, E. and P.H. Dillard, *The use of pure polyethylene plate for cranioplasty*. Journal of Neurosurgery, 1950. **7**(6): p. 492-498.
37. Klawitter, J.J., et al., *An evaluation of bone growth into porous high density polyethylene*. Journal of Biomedical Materials Research, 1976. **10**(2): p. 311-323.
38. Wang, J.-C., et al., *Clinical outcome of cranioplasty with high-density porous polyethylene*. Journal of Craniofacial Surgery, 2012. **23**(5): p. 1404-1406.
39. Hurel, S.J., et al., *The short Synacthen and insulin stress tests in the assessment of the hypothalamic–pituitary–adrenal axis*. Clinical Endocrinology, 1996. **44**(2): p. 141-146.
40. Chacón-Moya, E., et al., *Cranial vault reconstruction using computer-designed polyetheretherketone (PEEK) implant: case report*. Cir Cir, 2009. **77**: p. 437-440.
41. Uygur, S., et al., *Management of cranial bone defects: a reconstructive algorithm according to defect size*. Journal of Craniofacial Surgery, 2013. **24**(5): p. 1606-1609.
42. Hardy, W.N., et al., *Investigation of head injury mechanisms using neutral density technology and high-speed biplanar X-ray*. Stapp Car Crash Journal, 2001. **45**: p. 337-368.
43. Miller, K. and K. Chinzei, *Constitutive modelling of brain tissue: experiment and theory*. Journal of Biomechanics, 1997. **30**(11): p. 1115-1121.
44. Prange, M.T. and S.S. Margulies, *Regional, directional, and age-dependent properties of the brain undergoing large deformation*. Journal of Biomechanical Engineering, 2002. **124**(2): p. 244-252.
45. Gefen, A. and S.S. Margulies, *Are in vivo and in situ brain tissues mechanically similar?* Journal of Biomechanics, 2004. **37**(9): p. 1339-1352.

46. McPherson, G.K. and T.J. Kriewall, *The elastic modulus of fetal cranial bone: a first step towards an understanding of the biomechanics of fetal head molding*. Journal of Biomechanics, 1980. **13**(1): p. 9-16.
47. Bobyn, J.D., et al., *The optimum pore size for the fixation of porous-surfaced metal implants by the ingrowth of bone*. Clinical Orthopaedics and Related Research, 1980. **150**: p. 263-270.
48. Bauer, T.W. and G.F. Muschler, *Bone graft materials: an overview of the basic science*. Clinical Orthopaedics and Related Research®, 2000. **371**: p. 10-27.
49. Habal, M.B. and A.H. Reddi, *Bone grafts & bone substitutes*. 1992: Saunders.
50. Marx, R.E., *Bone and bone graft healing*. Oral and maxillofacial surgery clinics of North America, 2007. **19**(4): p. 455-466.
51. Kao, S.T. and D.D. Scott, *A review of bone substitutes*. Oral and maxillofacial surgery clinics of North America, 2007. **19**(4): p. 513-521.
52. Choi, H.J., *The thickness of parietal bones in a New Zealand sample of cadaveric skulls in relation to calvarial bone graft, 2007-2011*. 2011, University of Otago.
53. Zingale, A. and V. Albanese, *Cryopreservation of autogeneous bone flap in cranial surgical practice: what is the future? A grade B and evidence level 4 meta-analytic study*. Journal of neurosurgical sciences, 2003. **47**(3): p. 137.
54. Goldstein, J.A., J.T. Paliga, and S.P. Bartlett, *Cranioplasty: indications and advances*. Current opinion in otolaryngology & head and neck surgery, 2013. **21**(4): p. 400-409.
55. Chiarini, L., et al., *Cranioplasty using acrylic material: A new technical procedure*. Journal of Cranio-Maxillofacial Surgery, 2004. **32**(1): p. 5-9.
56. Fiaschi, P., et al., *Surgical results of cranioplasty with a polymethylmethacrylate customized cranial implant in pediatric patients: A single-center experience*. Journal of Neurosurgery: Pediatrics, 2016. **17**(6): p. 705-710.
57. Morales-Gomez, J.A., et al., *Cranioplasty with a low-cost customized polymethylmethacrylate implant using a desktop 3D printer*. Journal of Neurosurgery, 2018. **130**(5): p. 1721-1727.
58. Wallace, R.D., C. Salt, and P. Konofaos, *Comparison of autogenous and alloplastic cranioplasty materials following impact testing*. Journal of Craniofacial Surgery, 2015. **26**(5): p. 1551-1557.
59. Hanasono, M.M., N. Goel, and F. DeMonte, *Calvarial reconstruction with polyetheretherketone implants*. Annals of Plastic Surgery, 2009. **62**(6): p. 653-655.
60. Lethaus, B., et al., *Cranioplasty with customized titanium and PEEK implants in a mechanical stress model*. Journal of Neurotrauma, 2012. **29**(6): p. 1077-1083.

61. Kobayashi, S., et al., *Usefulness of ceramic implants in neurosurgery*. *Neurosurgery*, 1987. **21**(5): p. 751-755.
62. Hench, L.L. and O. Andersson, *Bioactive glasses*. *Advanced Series in Ceramics*, 1993. **1**: p. 41-62.
63. Stoor, P. and R. Grênman, *Bioactive glass and turbinate flaps in the repair of nasal septal perforations*. *Annals of Otolaryngology, Rhinology & Laryngology*, 2004. **113**(8): p. 655-661.
64. Zhang, D., et al. *Comparison of antibacterial effect of three bioactive glasses*. in *Key Engineering Materials*. 2006. Trans Tech Publication.
65. Zhang, D., et al. *Factors controlling antibacterial properties of bioactive glasses*. in *Key Engineering Materials*. 2007. Trans Tech Publication.
66. Munukka, E., et al., *Bactericidal effects of bioactive glasses on clinically important aerobic bacteria*. *Journal of Materials Science: Materials in Medicine*, 2008. **19**(1): p. 27-32.
67. Leppäranta, O., et al., *Antibacterial effect of bioactive glasses on clinically important anaerobic bacteria in vitro*. *Journal of Materials Science: Materials in Medicine*, 2008. **19**(2): p. 547-551.
68. Mengel, R., D. Schreiber, and L. Flores-de-Jacoby, *Bioabsorbable membrane and bioactive glass in the treatment of intrabony defects in patients with generalized aggressive periodontitis: results of a 5-year clinical and radiological study*. *Journal of Periodontology*, 2006. **77**(10): p. 1781-1787.
69. Sculean, A., et al., *Healing of human intrabony defects following regenerative periodontal therapy with an enamel matrix protein derivative alone or combined with a bioactive glass*. *Journal of Clinical Periodontology*, 2005. **32**(1): p. 111-117.
70. Tai, B.J., et al., *Anti-gingivitis effect of a dentifrice containing bioactive glass (NovaMin®) particulate*. *Journal of Clinical Periodontology*, 2006. **33**(2): p. 86-91.
71. Peltola, M., et al., *Bioactive glass S53P4 in frontal sinus obliteration: a long-term clinical experience*. *Head & Neck*, 2006. **28**(9): p. 834-841.
72. Aitasalo, K., et al., *Repair of orbital floor fractures with bioactive glass implants*. *Journal of Oral and Maxillofacial Surgery*, 2001. **59**(12): p. 1390-1395.
73. Della Santina, C.C. and S.C. Lee, *Ceravital reconstruction of canal wall down mastoidectomy: long-term results*. *Archives of Otolaryngology, Head & Neck Surgery*, 2006. **132**(6): p. 617-623.
74. Reck, R., S. Störkel, and A. Meyer, *Bioactive glass-ceramics in middle ear surgery an 8-Year review*. *Annals of the New York Academy of Sciences*, 1988. **523**(1): p. 100-106.

75. Kokubo, T. and H. Takadama, *How useful is SBF in predicting in vivo bone bioactivity?* *Biomaterials*, 2006. **27**(15): p. 2907-2915.
76. Isaac, J., et al., *Effects of strontium-doped bioactive glass on the differentiation of cultured osteogenic cells.* *European Cells and Materials*, 2011. **21**: p. 130-143.
77. Pina, S. and J.M.F. Ferreira, *Brushite-forming Mg-, Zn-and Sr-substituted bone cements for clinical applications.* *Materials*, 2010. **3**(1): p. 519-535.
78. Pina, S., et al., *Biological responses of brushite-forming Zn-and ZnSr-substituted  $\beta$ -tricalcium phosphate bone cements.* *European Cells and Materials*, 2010. **20**: p. 162-177.
79. Klammert, U., et al., *Phase composition, mechanical performance and in vitro biocompatibility of hydraulic setting calcium magnesium phosphate cement.* *Acta Biomaterialia*, 2010. **6**(4): p. 1529-1535.
80. Hoppe, A., N.S. Guldal, and A.R. Boccaccini, *A review of the biological response to ionic dissolution products from bioactive glasses and glass-ceramics.* *Biomaterials*, 2011. **32**(11): p. 2757-2774.
81. Liu, J., et al., *Strontium-substituted bioactive glasses in vitro osteogenic and antibacterial effects.* *Dental Materials*, 2016. **32**(3): p. 412-422.
82. Martin, R.A., et al., *An examination of the calcium and strontium site distribution in bioactive glasses through isomorphic neutron diffraction, X-ray diffraction, EXAFS and multinuclear solid state NMR.* *Journal of Materials Chemistry*, 2012. **22**(41): p. 22212-22223.
83. Massera, J. and L. Hupa, *Influence of SrO substitution for CaO on the properties of bioactive glass S53P4.* *Journal of Materials Science: Materials in Medicine*, 2014. **25**(3): p. 657-668.
84. Meunier, P.J., et al., *The effects of strontium ranelate on the risk of vertebral fracture in women with postmenopausal osteoporosis.* *New England Journal of Medicine*, 2004. **350**(5): p. 459-468.
85. Sila-asna, M. and A. Bunyaratvej, *Kobe University Repository: Kernel.* *Kobe J. Med. Sci*, 2007. **53**(1): p. 25-35.
86. Jensen, J.E.B., et al., *Relationship between trace element content and mechanical bone strength.* *Bone*, 1997. **20**(Suppl 4): p. 104.
87. Marie, P.J., *Strontium ranelate: a physiological approach for optimizing bone formation and resorption.* *Bone*, 2006. **38**(2): p. 10-14.
88. Bonnelye, E., et al., *Dual effect of strontium ranelate: Stimulation of osteoblast differentiation and inhibition of osteoclast formation and resorption in vitro.* *Bone*, 2008. **42**(1): p. 129-138.

89. Usuda, K., et al., *An overview of boron, lithium, and strontium in human health and profiles of these elements in urine of Japanese*. Environmental health and preventive medicine, 2007. **12**(6): p. 231-237.
90. Lao, J., E. Jallot, and J.M. Nedelec, *Strontium-delivering glasses with enhanced bioactivity: a new biomaterial for antiosteoporotic applications?* Chemistry of Materials, 2008. **20**(15): p. 4969-4973.
91. Isaac, J., et al., *Effects of strontium-doped bioactive glass on the differentiation of cultured osteogenic cells*. European Cells and Materials, 2011. **21**: p. 130-43.
92. Gentleman, E., et al., *The effects of strontium-substituted bioactive glasses on osteoblasts and osteoclasts in vitro*. Biomaterials, 2010. **31**(14): p. 3949-3956.
93. Hesaraki, S., et al., *The effect of Sr concentration on bioactivity and biocompatibility of sol-gel derived glasses based on CaO-SrO-SiO<sub>2</sub>-P<sub>2</sub>O<sub>5</sub> quaternary system*. Materials Science and Engineering: C, 2010. **30**(3): p. 383-390.
94. O'Donnell, M.D. and R.G. Hill, *Influence of strontium and the importance of glass chemistry and structure when designing bioactive glasses for bone regeneration*. Acta Biomaterialia. **6**(7): p. 2382-2385.
95. Sriranganathan, D., et al., *Strontium substituted bioactive glasses for tissue engineered scaffolds: the importance of octacalcium phosphate*. Journal of Materials Science: Materials in Medicine, 2016. **27**(2): p. 1-10.
96. Vacheron Trystram, M.N., et al., *Antipsychotics in bipolar disorders*. Encephale, 2003. **30**(5): p. 417-424.
97. Young, W., *Review of lithium effects on brain and blood*. Cell transplantation, 2009. **18**(9): p. 951-975.
98. Kallner, G. and U. Petterson, *Renal, thyroid and parathyroid function during lithium treatment: laboratory tests in 207 people treated for 1-30 years*. Acta Psychiatrica Scandinavica, 1995. **91**(1): p. 48-51.
99. Nordenstrom, J., et al., *Biochemical hyperparathyroidism and bone mineral status in patients treated long-term with lithium*. Metabolism, 1994. **43**(12): p. 1563-1567.
100. Davis, B.M., et al., *Lithium's effect on parathyroid hormone*. The American journal of psychiatry, 1981.
101. Khorami, M., et al., *In vitro bioactivity and biocompatibility of lithium substituted 45S5 bioglass*. Materials Science and Engineering: C, 2011. **31**(7): p. 1584-1592.

102. Miguez Pacheco, V., et al., *Development and characterization of lithium-releasing silicate bioactive glasses and their scaffolds for bone repair*. Journal of Non-Crystalline Solids, 2015.
103. Vallittu, P.K., T.O. Närhi, and L. Hupa, *Fiber glass–bioactive glass composite for bone replacing and bone anchoring implants*. Dental Materials, 2015. **31**(4): p. 371-381.
104. Aitasalo, K.M., et al., *Craniofacial bone reconstruction with bioactive fiber-reinforced composite implant*. Head & Neck, 2014. **36**(5): p. 722-728.
105. Witte, F., *The history of biodegradable magnesium implants: a review*. Acta biomaterialia, 2010. **6**(5): p. 1680-1692.
106. Staiger, M.P., et al., *Magnesium and its alloys as orthopedic biomaterials: a review*. Biomaterials, 2006. **27**(9): p. 1728-1734.
107. Erdmann, N., et al., *Biomechanical testing and degradation analysis of MgCa<sub>0.8</sub> alloy screws: a comparative in vivo study in rabbits*. Acta Biomaterialia, 2011. **7**(3): p. 1421-1428.
108. Wu, Q., et al., *The microstructure and properties of cyclic extrusion compression treated Mg–Zn–Y–Nd alloy for vascular stent application*. Journal of the mechanical behavior of biomedical materials, 2012. **8**: p. 1-7.
109. Grogan, J., et al., *A corrosion model for bioabsorbable metallic stents*. Acta biomaterialia, 2011. **7**(9): p. 3523-3533.
110. Hänzi, A.C., et al., *Biodegradable wound-closing devices for gastrointestinal interventions: degradation performance of the magnesium tip*. Materials Science and Engineering: C, 2011. **31**(5): p. 1098-1103.
111. Edwardá Moulton, S., et al., *Galvanic coupling conducting polymers to biodegradable Mg initiates autonomously powered drug release*. Journal of Materials Chemistry, 2008. **18**(30): p. 3608-3613.
112. Alvarez-Lopez, M., et al., *Corrosion behaviour of AZ31 magnesium alloy with different grain sizes in simulated biological fluids*. Acta Biomaterialia, 2010. **6**(5): p. 1763-1771.
113. Witte, F., et al., *In vitro and in vivo corrosion measurements of magnesium alloys*. Biomaterials, 2006. **27**(7): p. 1013-1018.
114. Kannan, M.B. and R.S. Raman, *Evaluating the stress corrosion cracking susceptibility of Mg–Al–Zn alloy in modified-simulated body fluid for orthopaedic implant application*. Scripta Materialia, 2008. **59**(2): p. 175-178.
115. Gu, X., et al., *Corrosion fatigue behaviors of two biomedical Mg alloys–AZ91D and WE43–in simulated body fluid*. Acta Biomaterialia, 2010. **6**(12): p. 4605-4613.

116. Smola, B., et al., *Microstructure, corrosion resistance and cytocompatibility of Mg–5Y–4Rare Earth–0.5 Zr (WE54) alloy*. Materials Science and Engineering: C, 2012. **32**(4): p. 659-664.
117. Jamesh, M., S. Kumar, and T.S. Narayanan, *Corrosion behavior of commercially pure Mg and ZM21 Mg alloy in Ringer's solution—Long term evaluation by EIS*. Corrosion Science, 2011. **53**(2): p. 645-654.
118. Song, Y., et al., *Biodegradable behaviors of AZ31 magnesium alloy in simulated body fluid*. Materials Science and Engineering: C, 2009. **29**(3): p. 1039-1045.
119. Xin, Y., T. Hu, and P.K. Chu, *Influence of test solutions on in vitro studies of biomedical magnesium alloys*. Journal of The Electrochemical Society, 2010. **157**(7): p. C238-C243.
120. Liu, X., P.K. Chu, and C. Ding, *Surface nano-functionalization of biomaterials*. Materials Science and Engineering: R: Reports, 2010. **70**(3-6): p. 275-302.
121. Zhang, S., et al., *Influence of heat treatments on In vitro degradation behavior of Mg–6Zn alloy studied by electrochemical measurements*. Advanced Engineering Materials, 2010. **12**(5).
122. Zhang, S., et al., *Research on an Mg–Zn alloy as a degradable biomaterial*. Acta biomaterialia, 2010. **6**(2): p. 626-640.
123. Gu, X., et al., *In vitro and in vivo studies on a Mg–Sr binary alloy system developed as a new kind of biodegradable metal*. Acta biomaterialia, 2012. **8**(6): p. 2360-2374.
124. Koleini, S., M.H. Idris, and H. Jafari, *Influence of hot rolling parameters on microstructure and biodegradability of Mg–1Ca alloy in simulated body fluid*. Materials & Design, 2012. **33**: p. 20-25.
125. Zberg, B., P.J. Uggowitzer, and J.F. Löffler, *MgZnCa glasses without clinically observable hydrogen evolution for biodegradable implants*. Nature Materials, 2009. **8**(11): p. 887.
126. Zhang, X., et al., *Biocorrosion properties of as-extruded Mg–Nd–Zn–Zr alloy compared with commercial AZ31 and WE43 alloys*. Materials Letters, 2012. **66**(1): p. 209-211.
127. Zong, Y., et al., *Comparison of biodegradable behaviors of AZ31 and Mg–Nd–Zn–Zr alloys in Hank's physiological solution*. Materials Science and Engineering: B, 2012. **177**(5): p. 395-401.
128. Gray, J. and B. Luan, *Protective coatings on magnesium and its alloys—a critical review*. Journal of alloys and compounds, 2002. **336**(1-2): p. 88-113.
129. Zhang, J., C. Yan, and F. Wang, *Electrodeposition of Al–Mn alloy on AZ31B magnesium alloy in molten salts*. Applied Surface Science, 2009. **255**(9): p. 4926-4932.
130. Zhang, S., et al., *Electrodeposition of high corrosion resistance Cu/Ni–P coating on AZ91D magnesium alloy*. Applied Surface Science, 2011. **257**(21): p. 9213-9220.

131. Iranipour, N., R.A. Khosroshahi, and N.P. Ahmadi, *A study on the electroless Ni–P deposition on WE43 magnesium alloy*. Surface and Coatings Technology, 2010. **205**(7): p. 2281-2286.
132. Jin, J., et al., *Electroless Ni-P plating on Mg-10Gd-4.8 Y-0.6 Zr magnesium alloy with a new pretreatment process*. Surface and Coatings Technology, 2011. **206**(2-3): p. 348-353.
133. Zhao, H. and J. Cui, *Electroless plating of silver on AZ31 magnesium alloy substrate*. Surface and Coatings Technology, 2007. **201**(8): p. 4512-4517.
134. Guo, H. and M. An, *Growth of ceramic coatings on AZ91D magnesium alloys by micro-arc oxidation in aluminate–fluoride solutions and evaluation of corrosion resistance*. Applied Surface Science, 2005. **246**(1-3): p. 229-238.
135. Blawert, C., et al., *Influence of process parameters on the corrosion properties of electrolytic conversion plasma coated magnesium alloys*. Surface and Coatings Technology, 2005. **200**(1-4): p. 68-72.
136. Liang, J., L. Hu, and J. Hao, *Characterization of microarc oxidation coatings formed on AM60B magnesium alloy in silicate and phosphate electrolytes*. Applied Surface Science, 2007. **253**(10): p. 4490-4496.
137. Song, Y., et al., *Plasma electrolytic oxidation coating on AZ91 magnesium alloy modified by neodymium and its corrosion resistance*. Applied Surface Science, 2008. **254**(10): p. 3014-3020.
138. Wu, G., et al., *Characterization of ceramic PVD thin films on AZ31 magnesium alloys*. Applied Surface Science, 2006. **252**(20): p. 7422-7429.
139. Wu, G., et al., *Improving corrosion resistance of titanium-coated magnesium alloy by modifying surface characteristics of magnesium alloy prior to titanium coating deposition*. Scripta Materialia, 2009. **61**(3): p. 269-272.
140. Wu, G., et al., *Corrosion behavior of Ti–Al–N/Ti–Al duplex coating on AZ31 magnesium alloy in NaCl aqueous solution*. Materials Characterization, 2009. **60**(8): p. 803-807.
141. Wu, G., et al., *Improving wear resistance and corrosion resistance of AZ31 magnesium alloy by DLC/AlN/Al coating*. Surface and Coatings Technology, 2010. **205**(7): p. 2067-2073.
142. Hoche, H., et al., *PVD coating and substrate pretreatment concepts for corrosion and wear protection of magnesium alloys*. Surface and Coatings Technology, 2011. **205**: p. S145-S150.
143. Wang, X., et al., *Effects of tantalum ion implantation on the corrosion behavior of AZ31 magnesium alloys*. Journal of alloys and compounds, 2007. **437**(1-2): p. 87-92.
144. Wang, X., et al., *Yttrium ion implantation on the surface properties of magnesium*. Applied Surface Science, 2006. **253**(5): p. 2437-2442.



145. Wang, X., et al., *The effects of cerium implantation on the oxidation behavior of AZ31 magnesium alloys*. Journal of Alloys and Compounds, 2008. **456**(1-2): p. 384-389.
146. Wan, Y., et al., *Influence of zinc ion implantation on surface nanomechanical performance and corrosion resistance of biomedical magnesium–calcium alloys*. Applied Surface Science, 2008. **254**(17): p. 5514-5516.
147. Höche, D., et al., *Magnesium nitride phase formation by means of ion beam implantation technique*. Applied Surface Science, 2011. **257**(13): p. 5626-5633.
148. Paital, S.R., et al., *Improved corrosion and wear resistance of Mg alloys via laser surface modification of Al on AZ31B*. Surface and Coatings Technology, 2012. **206**(8-9): p. 2308-2315.
149. Wu, G., J.M. Ibrahim, and P.K. Chu, *Surface design of biodegradable magnesium alloys—a review*. Surface and Coatings Technology, 2013. **233**: p. 2-12.
150. Kokubo, T., *Bioactive glass ceramics: properties and applications*. Biomaterials, 1991. **12**(2): p. 155-163.
151. Bhattacharjee, P., et al., *Nanofibrous nonmulberry silk/PVA scaffold for osteoinduction and osseointegration*. Biopolymers, 2015. **103**(5): p. 271-284.
152. Kokubo, T., et al., *Solutions able to reproduce in vivo surface-structure changes in bioactive glass-ceramic A-W*. Journal of the Biomedical Materials Research, 1990. **24**(6): p. 721-34.
153. Zhukauskas, R., et al., *Histological and radiographic evaluations of demineralized bone matrix and coralline hydroxyapatite in the rabbit tibia*. Journal of Biomaterials Applications, 2010. **24**(7): p. 639-656.
154. Suchanek, W. and M. Yoshimura, *Processing and properties of hydroxyapatite-based biomaterials for use as hard tissue replacement implants*. Journal of Materials Research, 1998. **13**(1): p. 94-117.
155. Kokubo, T., *Formation of biologically active bone-like apatite on metals and polymers by a biomimetic process*. Thermochemica Acta, 1996. **280**: p. 479-490.
156. Weng, W. and J.L. Baptista, *Sol–gel derived porous hydroxyapatite coatings*. Journal of materials science: materials in medicine, 1998. **9**(3): p. 159-163.
157. Gu, Y., K. Khor, and P. Cheang, *In vitro studies of plasma-sprayed hydroxyapatite/Ti-6Al-4V composite coatings in simulated body fluid (SBF)*. Biomaterials, 2003. **24**(9): p. 1603-1611.
158. Prevéy, P.S., *X-ray diffraction characterization of crystallinity and phase composition in plasma-sprayed hydroxyapatite coatings*. Journal of thermal spray technology, 2000. **9**(3): p. 369-376.

159. Landi, E., et al., *Densification behaviour and mechanisms of synthetic hydroxyapatites*. Journal of the European Ceramic Society, 2000. **20**(14-15): p. 2377-2387.
160. Panda, R., et al., *FTIR, XRD, SEM and solid state NMR investigations of carbonate-containing hydroxyapatite nano-particles synthesized by hydroxide-gel technique*. Journal of Physics and Chemistry of Solids, 2003. **64**(2): p. 193-199.
161. Berzina-Cimdina, L. and N. Borodajenko, *Research of calcium phosphates using Fourier transform infrared spectroscopy*. Infrared spectroscopy-materials science, engineering and technology, 2012. **12**(7): p. 251-263.
162. Koutsopoulos, S., *Synthesis and characterization of hydroxyapatite crystals: a review study on the analytical methods*. Journal of Biomedical Materials Research: An Official Journal of The Society for Biomaterials, The Japanese Society for Biomaterials, and The Australian Society for Biomaterials and the Korean Society for Biomaterials, 2002. **62**(4): p. 600-612.
163. Stanciu, G., et al., *Investigation of the hydroxyapatite growth on bioactive glass surface*. Journal of Biomedical & Pharmaceutical Engineering, 2007. **1**(1): p. 34-39.
164. Shi, D., G. Jiang, and J. Bauer, *The effect of structural characteristics on the in vitro bioactivity of hydroxyapatite*. Journal of Biomedical Materials Research: An Official Journal of The Society for Biomaterials, The Japanese Society for Biomaterials, and The Australian Society for Biomaterials and the Korean Society for Biomaterials, 2002. **63**(1): p. 71-78.
165. Fleet, M.E., X. Liu, and P.L. King, *Accommodation of the carbonate ion in apatite: An FTIR and X-ray structure study of crystals synthesized at 2–4 GPa*. American Mineralogist, 2004. **89**(10): p. 1422-1432.
166. Brauer, D.S., et al., *Fluoride-containing bioactive glasses: effect of glass design and structure on degradation, pH and apatite formation in simulated body fluid*. Acta Biomaterialia, 2010. **6**(8): p. 3275-3282.
167. Kim, H.-M., et al., *The mechanism of biomineralization of bone-like apatite on synthetic hydroxyapatite: an in vitro assessment*. Journal of the Royal Society Interface, 2004. **1**(1): p. 17-22.
168. Bagambisa, F.B., U. Joos, and W. Schilli, *Mechanisms and structure of the bond between bone and hydroxyapatite ceramics*. Journal of biomedical materials research, 1993. **27**(8): p. 1047-1055.
169. Oliver, W.C. and G.M. Pharr, *An improved technique for determining hardness and elastic modulus using load and displacement sensing indentation experiments*. Journal of materials research, 1992. **7**(6): p. 1564-1583.

170. El Hadad, A.A., et al., *Biocompatibility and corrosion protection behaviour of hydroxyapatite sol-gel-derived coatings on Ti6Al4V alloy*. *Materials*, 2017. **10**(2): p. 94.
171. Dias, A., et al., *In vitro studies of calcium phosphate glass ceramics with different solubility with the use of human bone marrow cells*. *Journal of Biomedical Materials Research Part A: An Official Journal of The Society for Biomaterials, The Japanese Society for Biomaterials, and The Australian Society for Biomaterials and the Korean Society for Biomaterials*, 2005. **74**(3): p. 347-355.
172. Liao, H., et al., *Response of rat osteoblast-like cells to microstructured model surfaces in vitro*. *Biomaterials*, 2003. **24**(4): p. 649-654.
173. Ravichandran, R., et al., *Precipitation of nanohydroxyapatite on PLLA/PBLG/Collagen nanofibrous structures for the differentiation of adipose derived stem cells to osteogenic lineage*. *Biomaterials*, 2012. **33**(3): p. 846-855.
174. do Prado, R.F., et al., *Osteoblast response to porous titanium and biomimetic surface: In vitro analysis*. *Materials Science and Engineering: C*, 2015. **52**: p. 194-203.
175. TV, K., et al., *CELL SURFACE INTERACTIONS IN THE STUDY OF BIOCOMPATIBILITY*. 2002.
176. Bhattacharjee, P., et al., *Non-mulberry silk fibroin grafted PCL nanofibrous scaffold: Promising ECM for bone tissue engineering*. *European Polymer Journal*, 2015. **71**: p. 490-509.
177. Baghbani, F., et al., *Synthesis, characterization and evaluation of bioactivity and antibacterial activity of quinary glass system (SiO<sub>2</sub>-CaO-P<sub>2</sub>O<sub>5</sub>-MgO-ZnO): In vitro study*. *Bulletin of Materials Science*, 2013. **36**(7): p. 1339-1346.
178. Soundrapandian, C., et al., *Porous bioactive glass scaffolds for local drug delivery in osteomyelitis: Development and in vitro characterization*. *AAPS PharmSciTech*, 2010. **11**(4): p. 1675-1683.
179. Todaro, G.J. and H. Green, *Quantitative studies of the growth of mouse embryo cells in culture and their development into established lines*. *The Journal of Cell Biology*, 1963. **17**(2): p. 299-313.
180. Wong, S., W.-H. Guo, and Y.-L. Wang, *Fibroblasts probe substrate rigidity with filopodia extensions before occupying an area*. *Proceedings of the National Academy of Sciences*, 2014. **111**(48): p. 17176-17181.
181. McNeil, S.E., et al., *Functional calcium-sensing receptors in rat fibroblasts are required for activation of SRC kinase and mitogen-activated protein kinase in response to extracellular calcium*. *Journal of Biological Chemistry*, 1998. **273**(2): p. 1114-1120.

182. Hench, L.L., et al., *Bonding mechanisms at the interface of ceramic prosthetic materials*. Journal of Biomedical Materials Research, 1971. **5**(6): p. 117-141.
183. Bosetti, M., et al., *Type I collagen production by osteoblast-like cells cultured in contact with different bioactive glasses*. Journal of Biomedical Materials Research Part A, 2003. **64**(1): p. 189-195.
184. Mourino, V., J.P. Cattalini, and A.R. Boccaccini, *Metallic ions as therapeutic agents in tissue engineering scaffolds: an overview of their biological applications and strategies for new developments*. Journal of the Royal Society Interface, 2012. **9**(68): p. 401-419.
185. Lakhkar, N.J., et al., *Bone formation controlled by biologically relevant inorganic ions: Role and controlled delivery from phosphate-based glasses*. Advanced Drug Delivery Reviews, 2013. **65**(4): p. 405-420.
186. Habibovic, P. and J.E. Barralet, *Bioinorganics and biomaterials: Bone repair*. Acta Biomaterialia, 2011. **7**(8): p. 3013-3026.
187. Miguez-Pacheco, V., et al., *Development and characterization of lithium-releasing silicate bioactive glasses and their scaffolds for bone repair*. Journal of Non-Crystalline Solids, 2016. **432**: p. 65-72.
188. Zamani, A., G.R. Omrani, and M.M. Nasab, *Lithium's effect on bone mineral density*. Bone, 2009. **44**(2): p. 331-334.
189. Nielsen, S.P., *The biological role of strontium*. Bone, 2004. **35**(3): p. 583-588.
190. Chalecka-Franaszek, E. and D.-M. Chuang, *Lithium activates the serine/threonine kinase Akt-1 and suppresses glutamate-induced inhibition of Akt-1 activity in neurons*. Proceedings of the National Academy of Sciences, 1999. **96**(15): p. 8745-8750.
191. Chen, Y., et al., *Beta-catenin signaling plays a disparate role in different phases of fracture repair: Implications for therapy to improve bone healing*. PLoS Medicine, 2007. **4**(7): p. e249.
192. Marie, P.J., *Strontium ranelate: a novel mode of action optimizing bone formation and resorption*. Osteoporosis International, 2005. **16**(1): p. S7-S10.
193. Roy, M., A. Bandyopadhyay, and S. Bose, *Induction plasma sprayed Sr and Mg doped nano hydroxyapatite coatings on Ti for bone implant*. Journal of Biomedical Materials Research Part B: Applied Biomaterials, 2011. **99**(2): p. 258-265.
194. Sila-Asna, M., et al., *Osteoblast differentiation and bone formation gene expression in strontium-inducing bone marrow mesenchymal stem cell*. Kobe Journal of Medical Sciences, 2007. **53**(1-2): p. 25-35.

195. Monroe, D.G., et al., *Update on Wnt signaling in bone cell biology and bone disease*. *Gene*, 2012. **492**(1): p. 1-18.
196. Milat, F. and K.W. Ng, *Is Wnt signalling the final common pathway leading to bone formation?* *Molecular and Cellular Endocrinology*, 2009. **310**(1): p. 52-62.
197. Lin, G.L. and K.D. Hankenson, *Integration of BMP, Wnt and notch signaling pathways in osteoblast differentiation*. *Journal of Cellular Biochemistry*, 2011. **112**(12): p. 3491-3501.
198. Zhang, R., et al., *Wnt/ $\beta$ -catenin signaling activates bone morphogenetic protein 2 expression in osteoblasts*. *Bone*, 2013. **52**(1): p. 145-156.
199. Kovar, J.L., et al., *Near-infrared-labeled tetracycline derivative is an effective marker of bone deposition in mice*. *Analytical Biochemistry*, 2011. **416**(2): p. 167-173.
200. Gibson, C.J., V.F. Thornton, and W.A.B. Brown, *Incorporation of tetracycline into impeded and unimpeded mandibular incisors of the mouse*. *Calcified Tissue Research*, 1978. **26**(1): p. 29-31.
201. Dahnert, L.E. and G.D. Bos, *Fluorescent tetracycline labeling as an aid to debridement of necrotic bone in the treatment of chronic osteomyelitis*. *Journal of Orthopaedic Trauma*, 2002. **16**(5): p. 345-346.
202. Nandi, S.K., et al., *Evaluation of new porous  $\beta$ -tri-calcium phosphate ceramic as bone substitute in goat model*. *Small Ruminant Research*, 2008. **75**(2): p. 144-153.
203. Chattopadhyay, N., et al., *The calcium-sensing receptor (CaR) is involved in strontium ranelate-induced osteoblast proliferation*. *Biochemical Pharmacology*, 2007. **74**(3): p. 438-447.
204. Hurtel-Lemaire, A.S., et al., *The calcium-sensing receptor is involved in strontium ranelate-induced osteoclast apoptosis: New Insights into the associated signaling pathways*. *Journal of Biological Chemistry*, 2009. **284**(1): p. 575-584.
205. Barbara, A., et al., *Normal matrix mineralization induced by strontium ranelate in MC3T3-E1 osteogenic cells*. *Metabolism*, 2004. **53**(4): p. 532-537.
206. Caverzasio, J., *Strontium ranelate promotes osteoblastic cell replication through at least two different mechanisms*. *Bone*, 2008. **42**(6): p. 1131-1136.
207. Basu, B., A. Sabareeswaran, and S.J. Shenoy, *Biocompatibility property of 100% strontium-substituted  $\text{SiO}_2\text{-Al}_2\text{O}_3\text{-P}_2\text{O}_5\text{-CaO-CaF}_2$  glass ceramics over 26 weeks implantation in rabbit model: Histology and micro-Computed Tomography analysis*. *Journal of Biomedical Materials Research Part B: Applied Biomaterials*, 2014. **103**(6): p. 1168-1179.

208. Tat, S.K., et al., *Strontium ranelate inhibits key factors affecting bone remodeling in human osteoarthritic subchondral bone osteoblasts*. *Bone*, 2011. **49**(3): p. 559-567.
209. Boyle, W.J., W.S. Simonet, and D.L. Lacey, *Osteoclast differentiation and activation*. *Nature*, 2003. **423**(6937): p. 337-342.
210. Mastrogiacomo, M., et al., *Synchrotron radiation microtomography of bone engineered from bone marrow stromal cells*. *Tissue Engineering*, 2004. **10**(11-12): p. 1767-1774.
211. Tuan, H.S. and D.W. Hutmacher, *Application of micro CT and computation modeling in bone tissue engineering*. *Computer-Aided Design*, 2005. **37**(11): p. 1151-1161.
212. Porter, B.D., et al., *Noninvasive image analysis of 3D construct mineralization in a perfusion bioreactor*. *Biomaterials*, 2007. **28**(15): p. 2525-2533.
213. Vogel, M., et al., *In vivo comparison of bioactive glass particles in rabbits*. *Biomaterials*, 2001. **22**(4): p. 357-362.
214. Sabareeswaran, A., et al., *Early osseointegration of a strontium containing glass ceramic in a rabbit model*. *Biomaterials*, 2013. **34**(37): p. 9278-9286.
215. Landi, E., et al., *Densification behaviour and mechanisms of synthetic hydroxyapatites*. *Journal of the European Ceramic Society*, 2000. **20**(14): p. 2377-2387.
216. Canham, L.T., et al., *Calcium phosphate nucleation on porous silicon: Factors influencing kinetics in acellular simulated body fluids*. *Thin Solid Films*, 1997. **297**(1-2): p. 304-307.
217. Li, L., J. Gao, and Y. Wang, *Evaluation of cyto-toxicity and corrosion behavior of alkali-heat-treated magnesium in simulated body fluid*. *Surface and Coatings Technology*, 2004. **185**(1): p. 92-98.
218. Rude, R.K., et al., *Dietary magnesium reduction to 25% of nutrient requirement disrupts bone and mineral metabolism in the rat*. *Bone*, 2005. **37**(2): p. 211-219.
219. Zheng, Y., X. Gu, and F. Witte, *Biodegradable metals*. *Materials Science and Engineering: R: Reports*, 2014. **77**: p. 1-34.
220. Brar, H.S., et al., *Magnesium as a biodegradable and bioabsorbable material for medical implants*. *JOM*, 2009. **61**(9): p. 31-34.
221. Liu, H. *Biodegradation and mechanical performance of Magnesium-based implants*. in *9th World Biomaterials Congress*. 2012. Chengdu, China: Curran Associates, Inc., NY.
222. Troitskii, V.V. and D.N. Tsitritin, *The resorbing metallic alloy Osteosinthezit<sup>TM</sup> as material for fastening broken bone*. *Khirurgiia*, 1944. **8**(1): p. 41-44.

223. Zhang, F., et al., *Corrosion behavior of mesoporous bioglass-ceramic coated magnesium alloy under applied forces*. Journal of the Mechanical Behavior of Biomedical Materials, 2016. **56**: p. 146-155.
224. Tsui, Y.C., C. Doyle, and T.W. Clyne, *Plasma sprayed hydroxyapatite coatings on titanium substrates Part 1: Mechanical properties and residual stress levels*. Biomaterials, 1998. **19**(22): p. 2015-2029.
225. Yang, J., et al., *Plasma surface modification of magnesium alloy for biomedical application*. Surface and Coatings Technology, 2010. **205**: p. S182-S187.
226. Jo, J.-H., et al., *Enhancing biocompatibility and corrosion resistance of Mg implants via surface treatments*. Journal of Biomaterials Applications, 2012. **27**(4): p. 469-476.
227. Levingstone, T.J., *Optimisation of plasma sprayed hydroxyapatite coatings (PhD Thesis)*. 2008, Dublin City University.
228. Liao, C.-J., et al., *Thermal decomposition and reconstitution of hydroxyapatite in air atmosphere*. Biomaterials, 1999. **20**(19): p. 1807-1813.
229. Song, G., A. Atrens, and M. Dargusch, *Influence of microstructure on the corrosion of diecast AZ91D*. Corrosion Science, 1998. **41**(2): p. 249-273.
230. Zeng, R.-C., et al., *In vitro corrosion and cytocompatibility of a microarc oxidation coating and poly (l-lactic acid) composite coating on Mg-1Li-1Ca alloy for orthopedic implants*. ACS Applied Materials and Interfaces, 2016. **8**(15): p. 10014-10028.
231. Ostrowski, N., et al., *Corrosion protection and improved cytocompatibility of biodegradable polymeric layer-by-layer coatings on AZ31 magnesium alloys*. Acta Biomaterialia, 2013. **9**(10): p. 8704-8713.
232. Assadian, M., et al., *Topography, wetting, and corrosion responses of electrodeposited hydroxyapatite and fluoridated hydroxyapatite on magnesium*. Biomedical Materials and Engineering, 2016. **27**(2-3): p. 287-303.
233. Varila, L., et al., *Surface reactions of bioactive glasses in buffered solutions*. Journal of the European Ceramic Society, 2012. **32**(11): p. 2757-2763.
234. Ducheyne, P. and Q. Qiu, *Bioactive ceramics: the effect of surface reactivity on bone formation and bone cell function*. Biomaterials, 1999. **20**(23-24): p. 2287-2303.
235. Kumari, T.V., et al., *Cell surface interactions in the study of biocompatibility*. Trends in Biomaterials and Artificial Organs, 2002. **15**(2).
236. Gray, J. and B. Luan, *Protective coatings on magnesium and its alloys - A critical review*. Journal of Alloys and Compounds, 2002. **336**(1-2): p. 88-113.

237. Yamamoto, A. and S. Hiromoto, *Effect of inorganic salts, amino acids and proteins on the degradation of pure magnesium in vitro*. Materials Science and Engineering: C, 2009. **29**(5): p. 1559-1568.
238. Altun, H. and S. Sen, *Studies on the influence of chloride ion concentration and pH on the corrosion and electrochemical behaviour of AZ63 magnesium alloy*. Materials and Design, 2004. **25**(7): p. 637-643.
239. Ahn, S., et al., *Localized corrosion mechanisms of the multilayered coatings related to growth defects*. Surface and Coatings Technology, 2004. **177**: p. 638-644.
240. Witte, F., et al., *In vivo corrosion of four magnesium alloys and the associated bone response*. Biomaterials, 2005. **26**(17): p. 3557-3563.
241. Li, Z., et al., *The development of binary Mg–Ca alloys for use as biodegradable materials within bone*. Biomaterials, 2008. **29**(10): p. 1329-1344.
242. Jacobs, J.J., J.L. Gilbert, and R.M. Urban, *Corrosion of metal orthopaedic implants*. Journal of Bone and Joint Surgery, 1998. **80**(2): p. 268-282.
243. Van Gaalen, S.M., et al., *Use of fluorochrome labels in in vivo bone tissue engineering research*. Tissue engineering Part B: Reviews, 2010. **16**(2): p. 209-217.
244. Yang, J., et al., *In vivo biocompatibility and degradation behavior of Mg alloy coated by calcium phosphate in a rabbit model*. Journal of Biomaterials Applications, 2012. **27**(2): p. 153-164.
245. Rude, R., et al., *Magnesium deficiency: effect on bone and mineral metabolism in the mouse*. Calcified Tissue International, 2003. **72**(1): p. 32-41.
246. Barua, P, et al., *Fiber nanobiocompositions for cranioplasty and other orthopedic applications*. In: Fiber-Reinforced Nanocomposites: Fundamentals and Applications, Elsevier 2020. p.525-558
247. Mahato, A, et al., *Bioactive Glass-Based Composites for Cranioplasty Implants*. In: Clinical Applications of Biomaterials, Springer 2017. p 337-355
248. Nandi, S, K, et al., *Doped bioactive glass materials in bone regeneration*. Advanced Techniques in Bone Regeneration 2016 Vol. **13** p 276-327
249. Mahato, A, et al., *Development of nano-porous hydroxyapatite coated e-glass for potential bone-tissue engineering application: An in vitro approach*. Materials Science and Engineering: C 2020 Vol. **111** p 110764
250. Mahato, A, et al. *Influence of single and binary doping of strontium and lithium on in vivo biological properties of bioactive glass scaffolds*. Scientific reports 2016 Vol. **6** Issue 1 p 1-18



251 Mahato, A, et al., *Role of calcium phosphate and bioactive glass coating on in vivo bone healing of new Mg–Zn–Ca implant*. Journal of Materials Science: Materials in Medicine 2021 Vol. **32** Issue 5 p 1-20

## 9. PUBLICATIONS

### 1) Book Chapters:

- a. **A. Mahato**, B. Kundu, Bioactive glass based composites for cranioplasty implants, in: G. Kaur (Ed.) Clinical Applications of Biomaterials: State-of-the-Art Progress, Trends, and Novel Approaches, **Springer**, Gewerbestrasse, Switzerland, 2017, pp. 337-356.
- b. S.K. Nandi, **A. Mahato**, B. Kundu, P. Mukherjee, Doped bioactive glass materials in bone regeneration, in: A.R. Zorzi, J.B. de Miranda (Eds.) Advanced Techniques in Bone Regeneration, **InTech Open**, Rijeka, Croatia, 2016, pp. 275.
- c. S.K. Nandi, **A. Mahato**, B. Kundu, P. Mukherjee, Organic-inorganic micro/nanofiber composites for biomedical applications, in: V. Grumezescu, A.M. Grumezescu (Eds.) Materials for Biomedical Engineering: Biopolymer Fibers, **Elsevier**, Bucharest, Romania, 2019, pp. 21-55.
- d. P. Barua, **A. Mahato**, P. Datta, S.K. Nandi, R. Sen, B. Kundu, Fiber-nano bio-compositions for cranioplasty and other orthopaedic applications, in: B. Han, S. Sharma, T.A. Nguyen, K. Subrahmanya Bhat, L. Longbiao (Eds.) Fiber-Reinforced Nanocomposites: Fundamentals and Applications, **Elsevier**, Amsterdam, Netherlands, 2020, pp. 525-558.

### 2) SCI Journals:

- a. **A. Mahato**, M. De, P. Bhattacharjee, V. Kumar, P. Mukherjee, G. Singh, B. Kundu, V.K. Balla, S.K. Nandi, Role of calcium phosphate and bioactive glass coating on in vivo bone healing of new Mg-Zn-Ca implant, **Journal of Materials Science: Materials in Medicine** 32 (2021) 55.
- b. **A. Mahato**, P.K. Khan, B. Kundu, S.K. Nandi, P. Mukherjee, S. Datta, S. Sarkar, J. Mukherjee, S. Nath, V.K. Balla, Influence of single and binary doping of strontium and lithium on in vivo biological properties of bioactive glass scaffolds, **Nature Scientific Reports** 6 (2016) 32964.
- c. **A. Mahato**, Z. Sandy, S. Bysakh, L. Hupa, I. Das, P. Bhattacharjee, B. Kundu, G. De, S.K. Nandi, P. Vallittu, Development of nano-porous hydroxyapatite coated e-glass for potential bone-tissue engineering application: An in vitro approach, **Materials Science and Engineering: C** 111 (2020) 110764.
- d. **A. Mahato**, B. Kundu, P. Mukherjee, S.K. Nandi, Applications of different bioactive glass and glass-ceramic materials for osteoconductivity and osteoinductivity, **Transactions of the Indian Ceramic Society** 76(3) (2017) 149-158.
- e. C. Soundrapandian, **A. Mahato**, B. Kundu, S. Datta, B. Sa, D. Basu, Development and effect of different bioactive silicate glass scaffolds: In vitro evaluation for use as a bone drug delivery system, **Journal of the Mechanical Behavior of Biomedical Materials** 40 (2014) 1-12.

Gurbinder Kaur *Editor*

# Clinical Applications of Biomaterials

State-of-the-Art Progress, Trends, and  
Novel Approaches

 Springer

# Chapter 10

## Bioactive Glass-Based Composites for Cranioplasty Implants

Arnab Mahato and Biswanath Kundu

**Abstract** Craniectomy is a very frequently used procedure in modern neurosurgical practice required secondary to a traumatic skull bone fracture, tumour extraction or severe infection. The craniofacial region is a complex zone, comprising bone, cartilage, soft tissue, nerves and blood vessels. The bones provide the support and protection for other elements, and hence their reconstruction is of a great importance to restore normal functionalities. The aim of this chapter is to summarise the advancement in the field of bioactive glass composites for the use as a craniofacial implant and their studies in surgical challenges. Our discussion broadly covers innovations in material development part and fine-tuning of the composites with structural and functional improvisations to draw the attention of scientists and researchers by summarising recent advancement of craniofacial implants based on composites of bioactive glass and their studies in craniofacial surgical challenges along with their aftermath. With the vast versatility of bioactive glass composite materials, current innovations in implant material development together with structural and functional modifications are waiting to be explored more and more. First, we have discussed the history and evolution of cranioplasty and its requirements in craniofacial surgery including origin, shape and size of the defect and mechanical properties of cranial bone. Subsequently, different craniofacial implant materials starting from bioactive glass, its composite with polymers, ceramics and other materials have been discussed. Finally, the future aspects have been briefly outlined.

**Keywords** Cranioplasty • Allografts • Autogenous bone graft • Synthetic materials • Bioactive glass • Bone defect • Mechanical properties • Polymers • Fabrication of composites • Ceramics • Hydroxyapatite • Fibres

---

A. Mahato • B. Kundu (✉)  
Bioceramics and Coating Division, CSIR-Central Glass and  
Ceramic Research Institute (CSIR-CGCRI), Kolkata 700032, India  
e-mail: [biswa\\_kundu@rediffmail.com](mailto:biswa_kundu@rediffmail.com); [biswa.kundun@gmail.com](mailto:biswa.kundun@gmail.com)

## 10.1 Introduction

Craniectomy is a very frequently used procedure in modern neurosurgical practice required secondary to a traumatic skull bone fracture, tumour extraction or severe infection. Conditions like intercranial haemorrhage, congenital malformations, progressively deforming skeletal diseases and the absence of intact cranial vault in children also can compromise the normal function and architectonics of craniofacial bones, which may require craniotomy followed by cranioplasty [1].

*Craniectomy:* A neurosurgical procedure in which a cranial bone flap is removed.

*Craniotomy:* When a cranial bone flap is removed temporarily to access the underlying brain.

*Cranioplasty:* A surgical procedure which restores the contour of cranial bone and corrects the bone defect.

The craniofacial region is a complex zone, comprising bone, cartilage, soft tissue, nerves and blood vessels. The bones provide the support and protection for other elements, and hence their reconstruction is of a great importance to restore normal functionalities [2]. But after craniectomy, syndrome of trephined, subdural effusion, seizures, etc., can be seen; diminishing these symptoms is one of the objectives of cranioplasty [3, 4]. Cranioplasty has been shown to improve electroencephalographic abnormalities, cerebral blood flow abnormalities and other neurological abnormalities [5, 6].

History of reconstruction of large skull bone defects dates back to antiquity. Till then autogenous bone grafts remained the gold standard, which were generally harvested from the calvarium, iliac crest, tibia or fibula [7], though the use of metal plates in 2000 BC was found where the material used was contingent upon the socio-economic rank of the patient [8]. With time and extended research, the disadvantages of different grafts were pointed out, and accordingly the use of grafts became more interesting topic of research. Problems like infection of the bone graft, donor-site morbidity, handling of bone graft and wastage of time reduced the usage of autogenous grafts. According to the source of the graft material, craniofacial implants are being called xenografts, allografts, autogenous bone graft and synthetic materials.

*Xenografts:* Grafts from different species transplanted into humans.

*Allografts:* Use of cartilage tissue in cranioplasty.

*Autogenous bone graft:* Implant taken from same species, from a different site.

*Synthetic materials:* Implant made synthetically in laboratories.

Along with the advantages and disadvantages of the said implants, an ideal craniofacial implant is yet to come. Depending on the research of craniofacial implants and subsequent case studies, the ideal material used for cranioplasty would be radiolucent, resistant to infections, not conductive of heat or cold, resistant to biochemical processes, malleable to fit defects and complete closure of the defect site [9]. The requirements and expectations from a synthetic graft material are quite high. An ideal graft material should be strong, lightweight, easily shaped, osteoinductive or osteoconductive and enable osteointegration. The best substitute should have the mechanical properties close to the surrounding bone. It was found that depending upon the species and age, a wide range of anisotropic elastic moduli of craniofacial bone can be obtained. The average elastic moduli of cranial bone, both foetal and matured, tested in a three-point bend set-up are  $7.467 \pm 5.39$  GPa (0.5 m/s),  $10.777 \pm 9.38$  GPa (1.0 m/s) and  $15.547 \pm 10.29$  GPa (2.5 m/s), whereas the average porosity of cranial bones was  $13.087 \pm 4.23\%$ , and the average percent bone volume (BV/TV) was  $70.847 \pm 10.13\%$  [10].

A number of synthetic biomaterials are available for craniofacial bone substitute, such as titanium, polymethyl methacrylate (PMMA), polyethylene (PE), polyetheretherketone (PEEK), hydroxyapatite (HAp) or combinations/ composites of these materials. The principal aim of the current clinical biomaterial research is to address the limitations of now-available materials. Bioactive glasses (BGs) are a group of non-metallic ceramic biomaterials with osteoconductive, osteoinductive and bacteriostatic properties, which was first introduced in the field by Prof. L. L. Hench and his team. Apart from the unique advantageous features of bioactive glass ceramics, their heterogeneous macrostructure restricts their versatility and mechanical strength [11]. Evolution of research in this field evolved the area, and the limitations are now taken care of by going interdisciplinary and making composites with other materials for particular purposes. The components of the composite are chosen very wisely and calculatedly to overcome certain limitations. Composites have an interesting aspect of high adaptiveness and tuneable properties by varying the component ratio which is helpful to fabricate patient-specific implants [12–14].

The aim of this chapter is to summarise the advancement in the field of bioactive glass composites for the use as a craniofacial implant and their studies in surgical challenges. Our discussion broadly covers innovations in material development part and fine-tuning of the composites with structural and functional improvisations to draw the attention of scientists and researchers by summarising recent advancement of craniofacial implants based on composites of bioactive glass and their studies in craniofacial surgical challenges along with their aftermath. With the vast versatility of bioactive glass composite materials, current innovations in implant material development together with structural and functional modifications are waiting to be explored more and more.

## 10.2 History and Evolution of Cranioplasty

The first ever report regarding craniofacial reconstruction was written in 1505, though evidence of cranioplasty dates back to 7000 BC [9]. Ancient civilisations like the Incans, the Britons, the Asiatics, the North Africans and the Polynesians

practised cranioplasty quite experimentally using mostly metals. Socioeconomic rank of the patient decided the type of material to be used. The first documented description of cranioplasty explains the technique used in the sixteenth century written by Fallopius. He proposed that bone could be replaced in cranial fractures if the dura stays intact. Another textbook from 1505 guides the physicians to treat the wounds with the help of xenograft obtained from a goat or a dog. Another well-known and successful cranioplasty published by Van Meekeren in 1668 illustrates a treatment of a Russian man after a word injury using canine xenograft, and the outcome was good [15–17]. Bone grafts from dog, ape, goose, rabbit, calf and eagle have been implanted into humans after boiling. Xenografts were diminished by the high rate of infections and the better outcome of the autografts. In 1821, Walther first successfully transplanted autologous bone graft where the removed bone flap has been attached again on the site. This procedure avoids host-tissue rejection, but the main disadvantage is related to donor-site morbidity [17–19]. In 1889, Seydel used pieces of tibia to cover a parietal defect as a plastic reconstruction. Many other bone harvest sites were experimented such as the ilium, ribs, sternum, scapula, fascia, etc.; however the need of two operative fields creates hesitation. The use of the cranium became more popular comparing other donor sites by the Miiller-Konig procedure [20]. These types of grafts can be preserved by cryopreservation or by placing in an abdominal pocket. The common disadvantage related to autologous bone grafts is bone flap resorption causing structural breakdown. In addition to it, Matsuno et al. showed that autologous bone grafts have very high rates of infection compared to other synthetic materials [21].

As we know that cranioplasty was started by using synthetic materials like metals which resurged in the early 1900s. Metals were experimented excessively till then as they are strong but malleable. Aluminium was the first metal used in cranioplasty but was prone to infect and irritate surrounding tissues. Although people with high status used gold, it is unfavourable for general use because of its high cost and softness. In the twentieth century, silver was tested along with gold before and during World War I but later made obsolete by other advanced materials. After World War I, different alloys were investigated and proved as a potential candidate for reconstruction of cranial defects. These included a wide range of metals like platinum, lead, aluminium, tantalum, cobalt, chromium, steel and their different alloys. During World War II, tantalum was largely used due to its bioinert, malleable and noncorrosive nature [22]. Based on the advances in research and case studies, more disadvantages came to notice, and alloying was readily accepted at that time due to their tuneable properties. Alloys are known to bend their properties according to the requirement by changing the metal proportions. This feature made them irresistible for a range of different types of cranial defects. Titanium was introduced in the late 1965 and found that it is better than other metals in biocompatibility and mechanical strength [23–25].

Celluloid, a synthetic plastic, was first used as an implant in the late nineteenth century; however it was not completely biocompatible. In the mid-twentieth century, more suitable alternatives of thermoplastic resins were introduced. Methyl methacrylate was discovered in 1939 and introduced in cranioplasty in 1940. It is a polymerised ester of acrylic acid with a compatible mechanical strength. However,

the difficulty in the preparation of the implant was a major limitation as it was brittle in nature as well [26]. Despite these drawbacks, PMMA was used widely in that span of time as a cranial bone graft. Polyethylene was developed in 1936 but used in this field in 1948 in case of smaller cranial defects. The low mechanical strength barred its use for reconstruction of large-size defects [17, 27]. Development of porous polyethylene made it more suitable to use as a bone graft by allowing soft-tissue ingrowth [28, 29]. In the beginning of the twenty-first century, modern era of cranioplasty has been initiated in search of patient-specific implant. In this era, with the specific requirement of the patients, like size, shape, bioactivity, biocompatibility, implantation period, etc., properties of the grafts have been chosen. In order to get grafts with such tuneable properties, horizon of this field increased tremendously, and different new types of implants have been introduced. Also different modifications of old implant materials like calcium phosphates, especially hydroxyapatite, and bioactive glasses came to the picture [30]. New polymer materials like PEEK were introduced to cranial reconstruction [31, 32]. Plates and screws of variety of new synthetic resorbable polymers with innovative design were introduced to clinical practice. Research related to bone-forming cell activity at the defect site has been prioritised using a combination of bone particles and growth factors. Also composites of different materials like calcium phosphates, bioactive glasses with a range of different elements, polymers and metals have been experimented extensively to reconstruct cranial defects.

The use of bioactive glass composites in craniofacial application is still limited, but the possibility is enormous as bioactive glass has all the required eligibility as a craniofacial implant. By making composites, possibility will increase further as the properties can be tailored.

### **10.3 Requirements of Craniofacial Surgery**

Depending upon the factors like size, shape and position of the defect, implantation time, mechanical properties of the surrounding bone and age of the patient, the requirements of cranioplastic implants differ. With the aim of making patient-specific implant, the factors are taken in consideration for the better future of craniofacial reconstruction. The desired properties of the implant can be achieved by making different composites, to use in unique surroundings of the respective patient.

#### ***10.3.1 Origin, Shape and Size of the Defect***

According to the origin, cranial bone defects may be of congenital or acquired. Congenital defects mostly come from craniosynostosis, whereas the acquired cranial bone defects mainly occur as a result from head injury or surgical action upon an intracranial lesion, cranial bone tumour, bone resorption or osteomyelitis. Tendency



**Table 10.1** Classification based on the size of a cranial bone defect [33–35]

	Defect	Size of the defect
Adult	Very small	Less than 4 cm <sup>2</sup>
	Small	4–25 cm <sup>2</sup>
	Medium	25–200 cm <sup>2</sup>
	Large	Larger than 200 cm <sup>2</sup>
Children	Small	Less than 4 cm <sup>2</sup>
	Medium	4–16 cm <sup>2</sup>
	Large	Larger than 16 cm <sup>2</sup>

of traumatic aetiology is higher in children and young people, mostly male. There are two types of bone tumour, primary and secondary, which can cause skull defect. Primary bone tumours like namely, fibrosarcomas, osteosarcomas, chondrosarcomas, osteomas, etc., and secondary bone tumours like dermoids, epidermoids and Ewing sarcomas may affect cranial bones by means of pressure, or they may force the bone out of its normal position, even sometimes destroying the bone.

However, the cranial bone defect size is not very significant for surgical purposes, but it is an important parameter for engineering the implant. The materials required and their properties are vastly dependent on the shape and size of the defect. Recently Uygur et al. proposed a classification from small-sized (smaller than 25 cm<sup>2</sup>), medium-sized (between 25 and 200 cm<sup>2</sup>) and large-sized (larger than 200 cm<sup>2</sup>) defect [33]. However, a standard classification of cranial bone defect size is not available yet (Table 10.1).

### 10.3.2 Mechanical Properties of Cranial Bone

The mechanical properties of skull bones have been extensively characterised, and it was found that cranial bone is comprised of a three-sandwich-type layered structure: external layers are made of compact, high-density cortical bone, whereas the central layer consists of a low-density, irregularly porous bone structure [10, 36–39]. Studies showed that foetal and adult cranial bones are vastly different in properties. Foetal cranial bone is thin and non-homogeneous which displays a highly directional fibre orientation [40]. With the maturity of the cranium, the bones structurally differentiate into a three-layered composite structure. With the structural development, the mechanical properties of the skull bones change diversely. The large variation of the mechanical properties can be attributed to the morphological differences between the subjects.

It was found that depending upon the species and age, a wide range of anisotropic elastic moduli of craniofacial bone have been obtained. The average elastic moduli of cranial bone, both foetal and matured, tested in a three-point bend set-up were found to be  $7.467 \pm 5.39$  GPa (with 0.5 m/s crosshead speed),  $10.777 \pm 9.38$  GPa (1.0 m/s) and  $15.547 \pm 10.29$  GPa (2.5 m/s), whereas the average porosity of cranial

bones was  $13.087 \pm 4.23\%$  with bone volume/total volume (BV/TV) was  $70.847 \pm 10.13\%$ . A correlation between percent BV and elastic modulus ( $r^2 = 0.1963$ ;  $p = 0.0004$ ) and maximum bending stress ( $r^2 = 0.2708$ ;  $p < 0.0001$ ) was found [10]. These results reported play very important role in the processing of patient-specific implant. The maximum force to failure, elastic modulus and maximum bending stress are very significant to make a suitable implant. Porosity and bone thickness are two other important variants, which also control the role of the bone graft.

## 10.4 Requirements for Craniofacial Implant Material

The requirements and expectations of an optimal graft material vary from patient to patient. Complexity of the required properties is increasing day by day. Optimal biomaterial should have better mechanical strength, lightweight, easily shaped, osteoinductive or osteoconductive and a structure which enables osteointegration. Density, surface area and porosity are some other properties, which also play significant part to make an implant appropriate for application. Depending upon the requirement, it can be biodegradable or biostable, and it may be bioinert or bioactive. The suitable structural design would support ingrowth of bone so that the implant could be integrated with the surrounding bone. Hence an implant with porous structure ranging 50–400  $\mu\text{m}$  is beneficial for osteointegration [41]. Porous structure works as a scaffold for osteoblast cells, which later forms bony ingrowth.

## 10.5 Bioactive Glass as a Craniofacial Implant

The maxillofacial area is a unique challenge for many decades to the surgeons because of its versatile properties (mechanical strength, thickness, bone structure) and infection sensitivity. Especially paranasal sinuses, upper respiratory tract and oral cavity are among the most sensitive areas, which need special attention. Since the first use of bioactive glass, it has attracted the attention of respective surgeons due to their osteoconductive as well as antimicrobial properties [42–47]. During the initial times, it was found to be very successful in dental applications with promising results. Bioactive glass has been used frequently in the treatment of intrabony defects and in dental extraction sites as filler before dental implant placement [48, 49]. Also the anti-gingivitis and antiplaque effects of bioactive glass (NovaMin®) have been studied with evident proof of gingival bleeding reduction and oral plaque formation [50]. The success in the dental field leads to the use of bioactive glass implant in other areas related to cranioplasty. Bioactive glass S53P4 was used in frontal sinus elimination and frontal bone reconstruction, nasal septum defect repair, orbital wall and nasal septum reconstruction and canal wall down mastoidectomy [51–53]. Middle ear implant made by bioactive glass for ossicular chain reconstruction also showed very good success rate even after 8 years [54].

However, bioactive glasses are very brittle and thus have limitations in shaping and flexibility for specific clinical requirements. These properties thus prevent the use of BG in load-bearing applications. Limitations led to the development of composite materials using bioactive glass to make use of its benefits up to full extent. Composite material is by definition a material composed of at least two different biomaterials. Over the last two decades, composites of bioactive glass have been used in different aspects and fields according to the properties of the composite materials. The arsenal of the application of bioactive glass has been increased enormously as the mechanical, biological and physiological properties of the composite materials can be tailored by changing the concentrations of base components.

### ***10.5.1 Bioactive Glass Composite with Polymer***

These composite materials consist of two phases, e.g. continuous phase, called the “matrix”, and dispersed phase, which can be fillers or fibres. The concept of making composites by using polymer and ceramic material was introduced by Bonfield et al. [55]. Composite structures are believed to add functionality to the biomedical composites, such as bioactivity, sustained release of drug moiety and typical biodegradation profile. In this way, composites of bioactive glass and polymers can be applied according to the demands of patients. There are several methods and types of composite materials, like particle composite or fibre composite or composite coatings. Though some methods are still in basic research level, some methods have been established, and with time, new methods are being introduced. Major manufacturing methods include melt extrusion, self-reinforcing and solvent casting.

Melt extrusion process is mostly used for making products with continuous cross sections such as rods, pipes, sheets, fibres, etc. Mixing of polymer and bioactive glass can also be done via this process, which can be used in other manufacturing processes. The extruder consists of a heated barrel with feeding hopper into which the raw materials are fed. The raw materials then come into contact with the rotating screw, which is responsible for the stirring and homogenising of the polymer. Heating elements are placed over the barrel. The polymer gradually melts, as it is conveyed forward in the barrel. At the end of barrel is the heated die that has an orifice with the specific profile needed for the extrudate. The melted polymer paste is then forced to run through an orifice with specific profile and after that cooled to get the final shape.

Another important and significant method to manufacture composites is solvent casting/particulate leaching (SCPL), in which the matrix polymer is dissolved in a volatile solvent to form a stable solution. Thus, the solubility of polymer in bioactive glass solution is the most important criteria for solvent casting technique. However, bioactive glass can be added up to a certain limit, above which it may make the composite more brittle than the requirement [56]. Viscosity is another factor to be considered important during this process. After getting clear solution, reinforcements can be added into the solution. The final solution is then cast to the mould to get the necessary structure. Solvent casting can also be used to form

porous structures by using selective porogens, which is soluble in the particular solvent. Depending upon the required pore size and interconnectivity, porogens can be varied with temperature.

Other methods like direct foaming/freeze drying, salt leaching, thermally induced phase separation, solid-liquid phase separation, rapid prototyping/solid freeform and slurry-dip in coating of scaffold are also used to manufacture composites, but they are still not accepted by the larger community of surgeons (Table 10.2).

Bioactive glass-polymers are relatively new in the class of bioactive materials for the treatment of maxillofacial defects, but during a very short span of time, BG-polymer composites proved their utility in the restoration of cranial vault. Due to the combination of BG's mechanical and biological properties and polymers' great flexibility, implants are applicable into various types of cranial defects with a very successful outcome. Initial applications of BG-polymer composites were mostly in dental application, but nowadays the use of this type of implant materials is increasing rapidly in different aspects of craniofacial reconstruction like orbital floor fractures, frontal bone defects, calvarial bone defects, etc.

In 2005, Niemela et al. reported advantageous effects of BG-poly-L/DL-lactide 70/30 composites with improved mechanical, biological and physiological properties; however they also confirmed that the increase in bioactive glass concentration may increase the brittleness along with decreased bioactivity [61]. After the first composite material, many variations with different components were tried, and after a thorough research subsequently, poly(methyl methacrylate) [PMMA] was found most compatible with bioactive glass particles for craniofacial application. Since then PMMA is one of the most widely researched alloplastic components in composite materials for craniofacial surgery. Low thermal conductivity and a density closer to bone make PMMA more acceptable by soft tissues. In 2006, Tuusa et al. fabricated

**Table 10.2** Advantages and disadvantages of different composite manufacturing methods [57–60]

Method	Advantages	Disadvantages
Melt extrusion	Useful of making continuous shaped composites Control over shape and size For making solid materials	Porous structure can't be done Use of temperature may hamper polymer Shear forces
Solvent casting/particulate leaching	Simple method Control over porous structure	Residual solvent Interconnectivity of pores Solubility of porogen materials
Thermally induced phase separation	High porosity Interconnected porous structure Uniform porosity	Processing duration
Solid-liquid phase separation	Control over porous structure, pore size and interconnectivity	Solvent residue
Rapid prototyping or solid freeform	Patient-specific implant Complex structure Control over pore size, distribution of pores	Limited polymer compatibility Expensive

an implant composed of fibre-reinforced composite (FRC) with bisphenol A-glycidyl methacrylate (BisGMA)-PMMA polymer matrix and a bioactive glass coating on the surface [62]. Though the results did not reveal a better bone formation than the controls, the procedure certainly made an impact and attracted researchers and surgeons to use composite materials in the arsenal of cranial reconstruction. Kessler et al. reported a successful production of filler material also made of BisGMA-PMMA matrix embedded with bioactive glass material with better outcomes [63]. In 2007, Ballo et al. experimented with a composition, which included BisGMA-TEGMA [tri(ethylene glycol) methacrylate], E-glass, PMMA and bioactive glass. Firstly, the E-glass fibre bundles were impregnated by BisGMA-TEGMA resin, followed by PMMA reinforcement. Three different types of specimens were fabricated: (a) unthreaded FRC with BG coating, (b) threaded FRC and (c) FRC coated with BG. They surprisingly found that the implant can withstand static load almost up to human maximal bite forces without fracture. Implant also showed better push-out force from dental plaster than a similar titanium implant [64]. Simultaneously, researchers found that BG-polymer composite implants can stimulate growth factor due to the effect of BG and nano-BG can adsorb proteins which ultimately favours bony ingrowth [65, 66]. Hautamaki et al. also found noticeable increase in osteoblast response of the specimens made of PMMA and bioactive glass in different ratios [67]. These findings supported and encouraged the application of BG-polymer composites in the areas never tried before. Another composite was made by impregnating E-glass FRC with MMA (methyl methacrylate)/BDDMA (butane-diol-di-methacrylate) copolymer system followed by BG granule coating and used as calvarial bone implant in rabbits. The implant seemed to promote bone healing process faster than the controls without any unwanted side effects [68]. Porous structure of the composite is found to mimic surrounding bone, while BG particles can enable new hard-tissue formation by osteoblasts on their surface. With the aim of mimicking Mother Nature, the use of natural polymer in composite implant materials was introduced. Peter et al. reported a novel composite implant fabricated by blending nano-bioactive glass with chitosan-gelatin biopolymer as a potential candidate for alveolar bone regeneration. Protein adsorption studies showed a significant increase of protein adsorption compared to control chitosan-gelatin scaffolds. Addition of bioactive glass nanoparticles also increased the cell attachment on the surface of the implant [69]. In 2010, four patients with pre-existing large calvarial (three patients) and midface (one patient) defects were operated by Dr. M. Peltola and his group by using implant containing BG and PMMA. After detecting the defects, implants were custom-made using powder-liquid PMMA bone cement matrix covered with 0.5–0.8 mm BG (BonAlive™) particles from both sides. The ratio of PMMA/BG was varied depending upon the requirements of the defects of concerning patient. Follow-up results proved a firm adhesion between the implant and skull, which may prevent long-term complications. Bone healing and new bone formation were seen between the implant and surrounding bone [70]. Another group reported successful periodontal tissue regeneration using biocompatible alginate/nano-bioactive glass composite material made by freeze drying method. The implants with pore size 100–300 µm showed good protein adsorption, cell attachment and cell proliferation [71]. BisGMA-

TEGDMA (triethylene glycol dimethacrylate) and BG composite material were used by Aitsalo et al. as an implant for 15 numbers of patients with defects as a consequence of craniotomies performed due to traumatic reasons. The implant material was composed of BisGMA-TEGDMA resin matrix reinforced by E-glass, and in between the layers, bioactive glass was used as a filler material [72]. The results were promising to the scientists which was also without infections or skin problems. In another study, Aitsalo et al. treated 12 patients (six male and six female) with skull bone defects after a tumour was surgically removed with pBisGMA-pTEGDMA (bisphenol A-glycidyl methacrylate/triethylene glycol dimethacrylate)/BG composite materials. The implants were composed of two FRC layers, supporting framework and porous layers. The porous layers containing bioactive glass were connected to each other by inter-connective elements. The standard size of the BG particles used was 500–800  $\mu\text{m}$ . The resin matrix materials were made of pBisGMA-pTEGDMA coupled with silanised E-glass. The mechanical strength of the implants was found to be very good in comparison to the similar type of implants used before. The bone-mimicking porous structure combined with BG particles enables new bone formation [73]. In 2012, Posti et al. operated a 33-year-old woman with severe traumatic brain injury in head-on collision with a custom-made FRC-BG implant fabricated in Turku Clinical Biomaterials Centre, Turku, Finland. The implant was fabricated by hand laminating two layers of dimethacrylate resin matrix keeping the bioactive glass particles (S53P4) in between them. Though some initial side effects were observed like swelling, but after more than 2 years of study, it was found that the mechanical integrity of the composite implant was not affected by the in vivo period. Formation of fibrous tissue with blood vessels, osteoblasts and collagen fibres was reported along with small clusters of more mature hard tissue [74]. At the same time, chitosan-bioactive glass composites were tried by Mota et al. with the aim of supporting periodontal regeneration. The composite was made by solvent casting method and used as bone regeneration membrane [GTR (guided tissue regeneration) membrane]. The implant showed adequate extensibility in wet conditions [75]. Recently Kulkova et al. reported a successful fabrication of a novel implant using FRC, E-glass fibres and bioactive glass (S53P4) granules. The composite was made by combining BisGMA-TEGDMA matrix and BG granules by the effect of excimer laser surface etching. The implant showed excellent fatigue resistance and the mechanical properties matching to bone [76]. However almost all the studies were done by using only S53P4 bioactive glass, which encouraged the researchers to use other bioactive glass composites in craniofacial reconstruction.

### ***10.5.2 Bioactive Glass Composite with Ceramic***

Ceramic composites are made with the aim of combining significant properties of the components, which were not achievable with the components alone. Another advantage of these composite materials is that the properties can be tailored according to the requirements using the same components, only by varying the combining

ratio. Sometimes composite can be made to cover up some disadvantages of bioactive glass, like high rate of ion leaching and brittleness, or to add special functionalities like increase of the bone formation rate or control over porosity. Though there are several methods for composite fabrication like melt quenching, milling and liquid phase sintering, sol-gel method is considered to be the most accepted one.

Generally melt quenching technique is followed by milling. Melt quenching method is famous for synthesising bioactive glass where glass frits can be made. In this method, raw materials are mixed thoroughly in solid form or in a solvent. The solvent is then dried to get powder of the mixture, which was then melted at required temperature followed by quenching in distilled water. After getting the frits, they were milled to get particles of bioactive glass, which was then mixed with other ceramic substances via ball milling. As melt quenching is the mostly used procedure for bioactive glass making, this process is more acceptable than the others. Control over porosity is another advantageous aspect of this technique.

The sol-gel method is a transition of inorganic/polymeric precursors in liquid phase into a solid inorganic material allowing the fabrication of new glasses and ceramics. The best part of this method is that the microstructure and properties of the material can be tailored with precision [77]. The method is so versatile that wide range of composition can be used and the composition can be varied in accordance with the requirement. Purity of the glass from this technique is found to be higher than other processes with a rare chance of getting unwanted products. In addition, the use of low temperature makes it preferable than melt quenching method.

In between the ceramic materials, hydroxyapatite (HAp) has long been used in dentistry owing to its ability to attach chemically to bone as it contains the minerals almost identical to bones. From the last decade with the tendency to tune the dissolution kinetics of calcium phosphate, a combination with bioactive glasses has been considered. Another disadvantage of HAp is its very low resorption rate, which increases the risk of infection [78]. The use of bioactive glass-ceramic composite materials increased in the modern era of craniofacial reconstruction. The first relevant work was reported by Duarte et al., where a combination of hydroxyapatite and  $P_2O_5$ -base bioactive glass ( $P_2O_5$  65%-CaO 15%-CaF<sub>2</sub> 10%-Na<sub>2</sub>O 10%) commercially named Bonelike® was applied as a bone graft in maxillofacial surgery to reconstruct a defected area after cyst excision. Sufficient new bone formation was observed in the defect area with resorption of the Bonelike® granules [79]. After the successful outcome of Bonelike® implants, it was studied extensively in different areas. Sousa et al. applied Bonelike® implants in maxillary cystic bone defects in 11 patients, aged between 24 and 53 years. After 48 weeks of implantation, the outcome was encouraging with high rate of bone formation. The patients were recovering from their bone lesions without any side effects or infections [80]. Pavan Kumar et al. tried Bonelike® implants in human intrabony periodontal angular defects, which showed promising bone filling and no adverse effects [81]. There are several other clinical trials that have been done using Bonelike®, which proved it as an effective composite material for craniofacial defect restoration [82–84]. Chatzistavrou et al. tried a different route and synthesised a sol-gel-based composite material made by combining a new glass ceramic (GC) ( $SiO_2$  60%- $P_2O_5$  3%- $Al_2O_3$

14%-CaO 6%-Na<sub>2</sub>O 7%-K<sub>2</sub>O 10%) system with 58S bioactive glass (GC 30 wt%-BG 70 wt%). They used the implant as sealing material to fix dental restorations with successful outcome of periodontal tissue attachment, providing complete sealing of the marginal gap [85]. In 2011, Pratibha et al. tried BG-HAp (BG: SiO<sub>2</sub>17%-CaO 53%-P<sub>2</sub>O<sub>5</sub> 30%) composite implant for periodontal defects with successful results [86]. More detailed clinical data was reported by Bhide et al. where a BG-HAp composite (50-50) was applied with autogenous cortical bone particulate in treatment of periodontal bone defects. The implant showed encouraging results of remarkable gain in probing attachment and depth reduction at 3 and 6 months [87]. A different approach was taken by Al-noaman, who made a composite of fluoro-apatite and bioactive glass (MgF<sub>2</sub> glass) with the aim of making a coating material for titanium dental implant [88, 89]. After that, no notable clinical research can be found in this area using bioactive glass-ceramic composites.

### ***10.5.3 Bioactive Glass Composite with Other Materials***

There are other materials also, which were used to make composites with bioactive glass which cannot be categorised. In 2001, maxillary sinus floor augmentation was done by using a composite of bioactive glass (45S5) and autogenous bone. The implant was used on 12 patients and observed that the implant successfully yielded sufficient volume of mineralised tissue with almost 3–5 mm of bone formation [90]. In another approach, enamel matrix protein derivative (EMD) was used with bioactive glass (45S5) to fabricate a bone graft for the treatment of intrabony periodontal defects in humans [91]. Turunen et al. compared the effect of adding bioactive glass in the treatment of maxillary sinus floor augmentation by making two compositions, one was autologous bone without BG and another was with BG (S53P4). The results showed that by incorporating BG, the need of autologous bone was decreased [92]. Another comparative study was done by Sculean et al. for the treatment of human intrabony defects following regenerative periodontal therapy. Among 30 patients, in each of the patient, one intrabony defect was randomly treated with either EMD + BG (test) (45S5) or with EMD alone (control), and the outcome confirmed almost similar results of two compositions with no additional improvement of clinical results in case of BG-incorporated implants [49, 93]. Demir et al. added bioactive glass with platelet-rich plasma (PRP) to evaluate the effect of BG on the clinical healing of intrabony defects. However the reports showed no advantageous effect of using bioactive glass [94]. Another work on bioactive glass-PRP composite was done by Carvalho et al. for the treatment of intrabony defects of dogs with no noticeable or advantageous differences [95]. A composite of bioactive glass and autogenous cortical bone (ACB) was also studied by Sumer et al. for the treatment of intra-osseous periodontal defects with the outcome of significant improvement of clinical and radiographic parameters. Bone heights were found to be increased in the patients treated with ACB-BG graft [96]. Recently Sandor et al. synthesised a



combination of bioactive glass (45S5) and adipose-derived stem cells to observe the effectiveness of bioactive glass in cranio-maxillofacial hard-tissue defects. The results came were sufficiently good even after 4 years of study [97].

## 10.6 Future Aspects

The field of bioactive glass composite for craniofacial reconstruction has been nurtured a lot in the last two decades, but there are still a lot of vacant spaces to fill up the store. A vast number of composites were tried with success, sometimes without success, but all the data made us more accurate in planning for the upcoming fabrication of composite materials. With the introduction of 3D scaffold designing in tissue engineering, a new door has opened; patient-specific implant got a new definition because of this technology. In the coming years, more emphasis will be given to make 3D implants based on bioactive glass or bioactive glass composites as bioactive glass can be used as to fabricate 3D scaffold. New ideas of adding stem cells and/or growth factors will get the attention of the researchers. The bioactive glass-based composites have been used in vitro using a wide range of cell types, and it's high time to use those data to apply the composites in clinical trials in vivo. The long-term understanding of in vivo in this field is still limited, specially related to the kinetics of degradation and ion release. The use of nano-scale composites will need to be investigated too. The results of these investigations will give a better insight of the synergistic effect of bioactive glass composites leading to more control over the strategies. The ongoing research efforts ensure that development of bioactive glass composite materials will remain a major area of application in the future.

**Acknowledgements** The authors gratefully acknowledge the support by the Director, CSIR-Central Glass and Ceramic Research Institute, Kolkata, India, and Council of Scientific and Industrial Research [through CSIR 12th 5 year plan programme (BIOCERAM)] for financial support.

## References

1. Piitulainen JM, Kauko T, Aitasalo KMJ, Vuorinen V, Vallittu PK, Posti JP. Outcomes of cranioplasty with synthetic materials and autologous bone grafts. *World Neurosurg.* 2015;83:708–14.
2. Petrovic V, Zivkovic P, Petrovic D, Stefanovic V. Craniofacial bone tissue engineering. *Oral Surg Oral Med Oral Pathol Oral Radiol.* 2012;114:1–9.
3. Honeybul S, Ho KM. Long-term complications of decompressive craniectomy for head injury. *J Neurotrauma.* 2011;28:929–35.
4. Joseph V, Reilly P. Syndrome of the trephined: case report. *J Neurosurg.* 2009;111:650–2.
5. Coelho F, Oliveira AM, Paiva WS, Freire FR, Calado VT, Amorim RL, Neville IS, de Andrade AF, Bor-Seng-Shu E, Anghinah R. Comprehensive cognitive and cerebral hemodynamic evaluation after cranioplasty. *Neuropsychiatr Dis Treat.* 2014;10:695.
6. Honeybul S, Janzen C, Kruger K, Ho KM. The impact of cranioplasty on neurological function. *Br J Neurosurg.* 2013;27:636–41.

7. De Bonis P, Frassanito P, Mangiola A, Nucci CG, Anile C, Pompucci A. Cranial repair: how complicated is filling a “hole”? *J Neurotrauma*. 2012;29:1071–6.
8. Shah AM, Jung H, Skirboll S. Materials used in cranioplasty: a history and analysis. *Neurosurg Focus*. 2014;36:E19.
9. Aydin S, Kucukyuruk B, Abuzayed B, Aydin S, Sanus GZ. Cranioplasty: review of materials and techniques. *J Neurosci Rural Pract*. 2011;2:162–7.
10. Motherway JA, Verschueren P, Van der Perre G, Vander Sloten J, Gilchrist MD. The mechanical properties of cranial bone: the effect of loading rate and cranial sampling position. *J Biomech*. 2009;42:2129–35.
11. Tyagi S. Glasses and glass ceramics as biomaterials. Patiala: Thapar University; 2007.
12. Hench LL. Bioceramics: from concept to clinic. *J Am Ceram Soc*. 1991;74:1487–510.
13. Hench LL. Biomaterials: a forecast for the future. *Biomaterials*. 1998;19:1419–23.
14. Hench LL, Polak JM. Third-generation biomedical materials. *Science*. 2002;295:1014–7.
15. Courville CB. Cranioplasty in prehistoric times. *Bull Los Angel Neurol Soc*. 1959;24:1–8.
16. Kennedy KAR. Primitive surgery: skills before science. Spencer L. Rogers. *Am Anthropol*. 1987;89:217–8.
17. Sanan A, Haines SJ. Repairing holes in the head: a history of cranioplasty. *Neurosurgery*. 1997;40:588–603.
18. Bowers CA, Riva-Cambrin J, Hertzler DA, Walker ML. Risk factors and rates of bone flap resorption in pediatric patients after decompressive craniectomy for traumatic brain injury: clinical article. *J Neurosurg Pediatr*. 2013;11:526–32.
19. Stieglitz LH, Fung C, Murek M, Fichtner J, Raabe A, Beck J. What happens to the bone flap? Long-term outcome after reimplantation of cryoconserved bone flaps in a consecutive series of 92 patients. *Acta Neurochir*. 2015;157:275–80.
20. Durand J-L, Renier D, Marchac D. The history of cranioplasty. *Ann Chir Plast Esthet*. 1997;42:75–83.
21. Matsuno A, Tanaka H, Iwamuro H, Takanashi S, Miyawaki S, Nakashima M, Nakaguchi H, Nagashima T. Analyses of the factors influencing bone graft infection after delayed cranioplasty. *Acta Neurochir*. 2006;148:535–40.
22. Flanigan P, Kshetry VR, Benzel EC. World War II, tantalum, and the evolution of modern cranioplasty technique. *Neurosurg Focus*. 2014;36:E22.
23. Blake GB, MacFarlane MR, Hinton JW. Titanium in reconstructive surgery of the skull and face. *Br J Plast Surg*. 1990;43:528–35.
24. Goldstein JA, Paliga JT, Bartlett SP. Cranioplasty: indications and advances. *Curr Opin Otolaryngol Head Neck Surg*. 2013;21:400–9.
25. Hill CS, Luoma AMV, Wilson SR, Kitchen N. Titanium cranioplasty and the prediction of complications. *Br J Neurosurg*. 2012;26:832–7.
26. Marchac D, Greensmith A. Long-term experience with methylmethacrylate cranioplasty in craniofacial surgery. *J Plast Reconstr Aesthet Surg*. 2008;61:744–52.
27. Alexander Jr E, Dillard PH. The use of pure polyethylene plate for cranioplasty. *J Neurosurg*. 1950;7:492–8.
28. Klawitter JJ, Bagwell JG, Weinstein AM, Sauer BW, Pruitt JR. An evaluation of bone growth into porous high density polyethylene. *J Biomed Mater Res*. 1976;10:311–23.
29. Wang J-C, Wei L, Xu J, Liu J-F, Gui L. Clinical outcome of cranioplasty with high-density porous polyethylene. *J Craniofac Surg*. 2012;23:1404–6.
30. Hurel SJ, Thompson CJ, Watson MJ, Harris MM, Baylis PH, Kendall-Taylor P. The short synacthen and insulin stress tests in the assessment of the hypothalamic–pituitary–adrenal axis. *Clin Endocrinol*. 1996;44:141–6.
31. Chacón-Moya E, Gallegos-Hernández JF, Piña-Cabrales S, Cohn-Zurita F, Goné-Fernández A. Cranial vault reconstruction using computer-designed polyetheretherketone (PEEK) implant: case report. *Cir Cir*. 2009;77:437–40.
32. Lethaus B, Safi Y, ter Laak-Poort M, Kloss-Brandstätter A, Banki F, Robbenmenke C, Steinseifer U, Kessler P. Cranioplasty with customized titanium and PEEK implants in a mechanical stress model. *J Neurotrauma*. 2012;29:1077–83.

33. Uygur S, Eryilmaz T, Cukurluoglu O, Ozmen S, Yavuzer R. Management of cranial bone defects: a reconstructive algorithm according to defect size. *J Craniofac Surg.* 2013;24:1606–9.
34. DeLuca L, Raszewski R, Tresser N, Guyuron B. The fate of preserved autogenous bone graft. *Plast Reconstr Surg.* 1997;99:1324–8.
35. Rogers GF, Greene AK. Autogenous bone graft: basic science and clinical implications. *J Craniofac Surg.* 2012;23:323–7.
36. Hardy WN, Foster CD, Mason MJ, Yang KH, King AI, Tashman S. Investigation of head injury mechanisms using neutral density technology and high-speed biplanar X-ray. *Stapp Car Crash J.* 2001;45:337–68.
37. Miller K, Chinzei K. Constitutive modelling of brain tissue: experiment and theory. *J Biomech.* 1997;30:1115–21.
38. Prange MT, Margulies SS. Regional, directional, and age-dependent properties of the brain undergoing large deformation. *J Biomech Eng.* 2002;124:244–52.
39. Gefen A, Margulies SS. Are in vivo and in situ brain tissues mechanically similar? *J Biomech.* 2004;37:1339–52.
40. McPherson GK, Kriewall TJ. The elastic modulus of fetal cranial bone: a first step towards an understanding of the biomechanics of fetal head molding. *J Biomech.* 1980;13:9–16.
41. Bobynd JD, Pilliar RM, Cameron HU, Weatherly GC. The optimum pore size for the fixation of porous-surfaced metal implants by the ingrowth of bone. *Clin Orthop Relat Res.* 1980;150:263–70.
42. Hench LL, Andersson O. Bioactive glasses. *Adv Ser Ceram.* 1993;1:41–62.
43. Stoor P, Grênman R. Bioactive glass and turbinate flaps in the repair of nasal septal perforations. *Ann Otol Rhinol Laryngol.* 2004;113:655–61.
44. Zhang D, Munukka E, Leppäranta O, Hupa L, Ylänen HO, Salonen JI, Eerola E, Viljanen MK, Hupa M. Comparison of antibacterial effect of three bioactive glasses. *Key Eng Mater.* 2006;309–311:345–8. Trans Tech Publication
45. Zhang D, Munukka E, Hupa L, Ylänen HO, Viljanen MK, Hupa M. Factors controlling antibacterial properties of bioactive glasses. *Key Eng Mater.* 2007;330–332:173–6. Trans Tech Publication
46. Munukka E, Leppäranta O, Korkeamäki M, Vaahtio M, Peltola T, Zhang D, Hupa L, Ylänen H, Salonen JI, Viljanen MK. Bactericidal effects of bioactive glasses on clinically important aerobic bacteria. *J Mater Sci Mater Med.* 2008;19:27–32.
47. Leppäranta O, Vaahtio M, Peltola T, Zhang D, Hupa L, Hupa M, Ylänen H, Salonen JI, Viljanen MK, Eerola E. Antibacterial effect of bioactive glasses on clinically important anaerobic bacteria in vitro. *J Mater Sci Mater Med.* 2008;19:547–51.
48. Mengel R, Schreiber D, Flores-de-Jacoby L. Bioabsorbable membrane and bioactive glass in the treatment of intrabony defects in patients with generalized aggressive periodontitis: results of a 5-year clinical and radiological study. *J Periodontol.* 2006;77:1781–7.
49. Sculean A, Pietruska M, Schwarz F, Willershausen B, Arweiler NB, Auschill TM. Healing of human intrabony defects following regenerative periodontal therapy with an enamel matrix protein derivative alone or combined with a bioactive glass. *J Clin Periodontol.* 2005;32:111–7.
50. Tai BJ, Bian Z, Jiang H, Greenspan DC, Zhong J, Clark AE, Du MQ. Anti-gingivitis effect of a dentifrice containing bioactive glass (NovaMin®) particulate. *J Clin Periodontol.* 2006;33:86–91.
51. Peltola M, Aitasalo K, Suonpää J, Varpula M, Yli-Urpo A. Bioactive glass S53P4 in frontal sinus obliteration: a long-term clinical experience. *Head Neck.* 2006;28:834–41.
52. Aitasalo K, Kinnunen I, Palmgren J, Varpula M. Repair of orbital floor fractures with bioactive glass implants. *J Oral Maxillofac Surg.* 2001;59:1390–5.
53. Della Santina CC, Lee SC. Ceravital reconstruction of canal wall down mastoidectomy: long-term results. *Arch Otolaryngol Head Neck Surg.* 2006;132:617–23.
54. Reck R, Störkel S, Meyer A. Bioactive glass-ceramics in middle ear surgery an 8-year review. *Ann N Y Acad Sci.* 1988;523:100–6.

55. Bonfield W, Grynepas MD, Tully AE, Bowman J, Abram J. Hydroxyapatite reinforced polyethylene—a mechanically compatible implant material for bone replacement. *Biomaterials*. 1981;2:185–6.
56. Cannillo V, Chiellini F, Fabbri P, Sola A. Production of Bioglass® 45S5–Polycaprolactone composite scaffolds via salt-leaching. *Compos Struct*. 2010;92:1823–32.
57. Ahmed I, Cronin PS, Abou Neel EA, Parsons AJ, Knowles JC, Rudd CD. Retention of mechanical properties and cytocompatibility of a phosphate-based glass fiber/poly(lactic acid) composite. *J Biomed Mater Res B Appl Biomater*. 2009;89:18–27.
58. Bonfield W. Design of bioactive ceramic-polymer composites. *Adv Ser Ceram*. 1993;1:299–304.
59. Peltola SM, Melchels FPW, Grijpma DW, Kellomäki M. A review of rapid prototyping techniques for tissue engineering purposes. *Ann Med*. 2008;40:268–80.
60. Puppi D, Chiellini F, Piras AM, Chiellini E. Polymeric materials for bone and cartilage repair. *Prog Polym Sci*. 2010;35:403–40.
61. Niemelä T, Niiranen H, Kellomäki M, Törmälä P. Self-reinforced composites of bioabsorbable polymer and bioactive glass with different bioactive glass contents. Part I: initial mechanical properties and bioactivity. *Acta Biomater*. 2005;1:235–42.
62. Tuusa SMR, Peltola MJ, Tirri T, Lassila LVJ, Vallittu PK. Frontal bone defect repair with experimental glass-fiber-reinforced composite with bioactive glass granule coating. *J Biomed Mater Res B Appl Biomater*. 2007;82:149–55.
63. Kessler S, Lee S. Use of bioactive glass in dental filling material, Google Patents. 2006.
64. Ballo AM, Lassila LV, Vallittu PK, Närhi TO. Load bearing capacity of bone anchored fiber-reinforced composite device. *J Mater Sci Mater Med*. 2007;18:2025–31.
65. Ehrlich H, Janussen D, Simon P, Bazhenov VV, Shapkin NP, Erler C, Mertig M, Born R, Heinemann S, Hanke T. Nanostructural organization of naturally occurring composites-part II: silica-chitin-based biocomposites. *J Nanomater*. 2008;2008:54.
66. Misra SK, Mohn D, Brunner TJ, Stark WJ, Philip SE, Roy I, Salih V, Knowles JC, Boccaccini AR. Comparison of nanoscale and microscale bioactive glass on the properties of P (3HB)/Bioglass® composites. *Biomaterials*. 2008;29:1750–61.
67. Hautamäki M, Meretoja VV, Mattila RH, Aho AJ, Vallittu PK. Osteoblast response to poly-methyl methacrylate bioactive glass composite. *J Mater Sci Mater Med*. 2010;21:1685–92.
68. Tuusa SMR, Peltola MJ, Tirri T, Puska MA, Rönttö M, Aho H, Sandholm J, Lassila LV, Vallittu PK. Reconstruction of critical size calvarial bone defects in rabbits with glass–fiber-reinforced composite with bioactive glass granule coating. *J Biomed Mater Res B Appl Biomater*. 2008;84:510–9.
69. Peter M, Binulal NS, Nair SV, Selvamurugan N, Tamura H, Jayakumar R. Novel biodegradable chitosan–gelatin/nano-bioactive glass ceramic composite scaffolds for alveolar bone tissue engineering. *Chem Eng J*. 2010;158:353–61.
70. Peltola MJ, Vallittu PK, Vuorinen V, Aho AAJ, Puntala A, Aitasalo KMJ. Novel composite implant in craniofacial bone reconstruction. *Eur Arch Otorhinolaryngol*. 2012;269:623–8.
71. Srinivasan S, Jayasree R, Chennazhi KP, Nair SV, Jayakumar R. Biocompatible alginate/nano bioactive glass ceramic composite scaffolds for periodontal tissue regeneration. *Carbohydr Polym*. 2012;87:274–83.
72. Aitasalo K, Rekola J, Piitulainen J, Vallittu PK. Craniofacial bone reconstruction with a novel bioactive composite implant. *J Neurol Surg Part B: Skull Base*. 2012;73:A099.
73. Aitasalo KMJ, Piitulainen JM, Rekola J, Vallittu PK. Craniofacial bone reconstruction with bioactive fiber-reinforced composite implant. *Head Neck*. 2014;36:722–8.
74. Posti JP, Piitulainen JM, Hupa L, Fagerlund S, Frantzén J, Aitasalo KMJ, Vuorinen V, Serlo W, Syrjänen S, Vallittu PK. A glass fiber-reinforced composite–bioactive glass cranioplasty implant: a case study of an early development stage implant removed due to a late infection. *J Mech Behav Biomed Mater*. 2015;55:191–200.
75. Mota J, Yu N, Caridade SG, Luz GM, Gomes ME, Reis RL, Jansen JA, Walboomers XF, Mano JF. Chitosan/bioactive glass nanoparticle composite membranes for periodontal regeneration. *Acta Biomater*. 2012;8:4173–80.

76. Kulkova J, Moritz N, Huhtinen H, Mattila R, Donati I, Marsich E, Paoletti S, Vallittu PK. Bioactive glass surface for fiber reinforced composite implants via surface etching by excimer laser. *Med Eng Phys*. 2016;38:664–70.
77. Scherer GW, Brinker CJ. Sol-gel science: the physics and chemistry of sol-gel processing. USA: Academic Press; 1990.
78. Szpalski C, Barr J, Wetterau M, Saadeh PB, Warren SM. Cranial bone defects: current and future strategies. *Neurosurg Focus*. 2010;29:E8.
79. Duarte F, Santos JD, Afonso A. Medical applications of bonelike® in maxillofacial surgery. *Mater Sci Forum*. 2004;455:370–3.
80. Sousa RC, Lobato JV, Maurício AC, Hussain NS, Botelho CM, Lopes MA, Santos JD. A clinical report of bone regeneration in maxillofacial surgery using Bonelike® synthetic bone graft. *J Biomater Appl*. 2007;22:373–85.
81. Pavan Kumar G, Jaya Kumar A, Krishnanjaneya Reddy P, Nandyala SH, Lopes MA, Santos JD. Application of glass reinforced hydroxyapatite composite in the treatment of human intrabony periodontal angular defects—two case reports. *Solid State Phenom*. 2010;161:93–101.
82. Lobato JV, Sooraj Hussain N, Sousa RC, Mauricio AC, S.J. D. Bone regeneration in maxillofacial surgery using novel Bonelike® synthetic bone graft – radiological and histological analysis. *J Biomater Appl*. 2008;22:373–85.
83. Lobato JV, Hussain NS, Lopes MA, Lobato JM, Mauricio AC, Afonso A, Ali N, Santos JD. Clinical applications of titanium dental implants coated with glass-reinforced hydroxyapatite composite (bonelike). *Int J Nanomanufacturing*. 2008;2:135–48.
84. Kumar PG, Kumar JA, Anumala N, Reddy KP, Avula H, Hussain SN. Volumetric analysis of intrabony defects in aggressive periodontitis patients following use of a novel composite alloplast: a pilot study. *Quintessence Int*. 2011;42:375–84.
85. Chatzistavrou X, Esteve D, Hatzistavrou E, Kontonasaki E, Paraskevopoulos KM, Boccaccini A. Sol-gel based fabrication of novel glass-ceramics and composites for dental applications. *Mater Sci Eng C*. 2010;30:730–9.
86. Pratibha PK, Bhide A, Bhat GS. Comparison of bioactive glass-hydroxyapatite alone and in combination with autogenous bone particulate in the management of periodontal defects, international conference on biology, environment and chemistry, IACSIT, Singapore. 2011.
87. Bhide A, Pratibha PK, Bhat GS. Evaluation of autogenous cortical bone particulate with bioactive glass-synthetic hydroxyapatite in treatment of periodontal bone defects. *Int J Biosci Biochem Bioinforma*. 2012;2:36.
88. Al-Noaman A, Karpukhina N, Rawlinson SCF, Hill RG. Effect of FA on bioactivity of bioactive glass coating for titanium dental implant. Part I: composite powder. *J Non-Cryst Solids*. 2013;364:92–8.
89. Al-Noaman A, Karpukhina N, Rawlinson SCF, Hill RG. Effect of FA addition on bioactivity of bioactive glass coating for titanium dental implant: part II—composite coating. *J Non-Cryst Solids*. 2013;364:99–106.
90. Cordioli G, Mazzocco C, Schepers E, Brugnolo E, Majzoub Z. Maxillary sinus floor augmentation using bioactive glass granules and autogenous bone with simultaneous implant placement. *Clin Oral Implants Res*. 2001;12:270–8.
91. Sculean A, Barbé G, Chiantella GC, Arweiler NB, Berakdar M, Brex M. Clinical evaluation of an enamel matrix protein derivative combined with a bioactive glass for the treatment of intrabony periodontal defects in humans. *J Periodontol*. 2002;73:401–8.
92. Turunen T, Peltola J, Yli-Urpo A, Happonen RP. Bioactive glass granules as a bone adjunctive material in maxillary sinus floor augmentation. *Clin Oral Implants Res*. 2004;15:135–41.
93. Sculean A, Pietruska M, Arweiler NB, Auschill TM, Nemcovsky C. Four-year results of a prospective-controlled clinical study evaluating healing of intra-bony defects following treatment with an enamel matrix protein derivative alone or combined with a bioactive glass. *J Clin Periodontol*. 2007;34:507–13.
94. Demir B, Şengün D, Berberoğlu A. Clinical evaluation of platelet-rich plasma and bioactive glass in the treatment of intra-bony defects. *J Clin Periodontol*. 2007;34:709–15.

95. Carvalho MD, Suaid FF, Santamaria MP, Casati MZ, Nociti Jr FH, Sallum AW, Sallum EA. Platelet-rich plasma plus bioactive glass in the treatment of intra-bony defects: a study in dogs. *J Appl Oral Sci.* 2011;19:82–9.
96. Sumer M, Keles GC, Cetinkaya BO, Balli U, Pamuk F, Uckan S. Autogenous cortical bone and bioactive glass grafting for treatment of intraosseous periodontal defects. *Eur J Dent.* 2013;7:6–14.
97. Sándor GK, Numminen J, Wolff J, Thesleff T, Miettinen A, Tuovinen VJ, Mannerstrom B, Patrikoski M, Seppanen R, Miettinen S. Adipose stem cells used to reconstruct 13 cases with cranio-maxillofacial hard-tissue defects. *Stem Cells Transl Med.* 2014;3:530–40.

IntechOpen

# Advanced Techniques in Bone Regeneration

*Edited by Alessandro Rozim Zorzi  
and Joao Batista de Miranda*



---

## Doped Bioactive Glass Materials in Bone Regeneration

---

Samit Kumar Nandi, Arnab Mahato,  
Biswanath Kundu and Prasenjit Mukherjee

Additional information is available at the end of the chapter

<http://dx.doi.org/10.5772/63266>

---

### Abstract

In the arena of orthopaedic surgery, autograft is considered to be the gold standard for correction of fracture repair or other bone pathologies. But, it has some limitations such as donor site morbidity and shortage of supply, which evolved the use of allograft that also has some disadvantages such as immunogenic response to the host, low osteogenicity as well as possibilities of disease transmission. Despite the benefits of autografts and allografts, the limitations of each have necessitated the pursuit of alternatives biomaterials that has the ability to initiate osteogenesis, and the graft should closely mimic the natural bone along with regeneration of fibroblasts. A variety of artificial materials such as demineralised bone matrix, coralline hydroxyapatite and calcium phosphate-based ceramics such as hydroxyapatite (HA),  $\beta$ -tricalcium phosphate ( $\beta$ -TCP) and bioactive glass have been used over the decades to fill bone defects almost without associated soft tissue development. Most of them were having only the properties of osteointegration and osteoconduction. Only bioactive glass possesses osteogenic property that stimulates proliferation and differentiation of osteoprogenitor cells and in some cases influencing the fibroblastic properties. But, this material has also some disadvantages such as short-term and low mechanical strength along with decreased fracture resistance; but, this was further minimised by ion doping that positively enhanced new bone formation. There are many metal ions such as magnesium (Mg), strontium (Sr), manganese (Mn), iron (Fe), zinc (Zn), silver (Ag) and some rare earths that have been doped successfully into bioactive glass to enhance their mechanical and biological properties. In some of the cases, mesoporous bioactive glass materials with or without such doping have also been employed (with homogeneous distribution of pores in the size ranging between 2 and 50 nm). These biomaterials can be served as scaffold for bone regeneration with adequate mechanical properties to restore bone defects and facilitate healing process by regeneration of soft tissues as well. This chapter encompasses the use of bioactive glass in bulk and mesoporous form with doped therapeutic ions, their role in bone tissue regeneration, use as delivery of growth factors as well as coating material for orthopaedic implants.



## 1. Introduction

Bone tissue repair and regeneration have made considerable strides in the modern era. An in-depth perceptiveness of the underlying principles has been achieved, new methods and materials developed and a multidisciplinary approach was used to accomplish successful bone tissue regeneration. Many scaffold systems have been planned for hard tissue engineering. Novelty has been worked out in terms of scaffold design, material selection, inclusion of drugs and growth factors, mechanical stability and bone regeneration competence. Nevertheless, autografts are still considered as 'gold standard' for bone tissue repair; equivalent osteogenic or osteoinductive performance is not obtained by the synthetic bone graft substitutes. Due to limitations of autografts in sufficient quantities to meet the overall medical demand for orthopaedic implants, allografts and xenografts are alternative sources to overcome such problems, but are having the risks of disease transmission and immune rejection. As a result, synthetic bone graft substitutes are the rational choice to meet the huge demand for orthopaedic implants, even though its inherent limitations in terms of strength, osteoconduction, osteoinduction, osseointegration and biodegradation. Accordingly, modern research area has been focussed on development of new biomaterials, modification of mechanical and structural features, improvement of biocompatibility, osteoinductivity and to incorporate growth factors and stem cells onto scaffolds to encourage bone regeneration.

Bone tissue regeneration strategies intend to use synthetic temporary templates to assist the natural healing of bone defects. Bone extracellular matrix (ECM) containing collagen fibrous structure, with mineralised calcium phosphate, is secreted from osteoblasts [1, 2]. For effective bone regeneration in non-load-bearing defects require a biomaterial scaffold that might have a three-dimensional (3D) fibrous structure mimicking the ECM [3–5] and can be easily placed into position during surgery. The scaffolds are also required to be biocompatible (should not elicit an inflammatory response nor exhibit immunogenicity or cytotoxicity), bioactive (bond with bone), bioresorbable, allow new bone formation at an acceptable rate, be economical to make and allow easy fabrication into the final preforms [6–8]. The scaffolds must be easily sterilisable to prevent infection especially for bulk degradable scaffolds [9]. Additionally, the mechanical properties of the scaffold must be optimal to prevent structural failure during handling and patient's normal activities. Furthermore, controllable interconnected porosity is of paramount necessity for cells to grow into the scaffold and to support angiogenesis. The scaffolds should also have porosity of 90% with pore diameter of at least 100  $\mu\text{m}$  for proper cell penetration and vascularisation of the ingrown tissue [10–12].

A number of inorganic and organic materials are being used as bone substitutes that include calcium phosphate ceramics, phosphates of magnesium, sulphate, carbonate and silicate of calcium and collagen with positive cell-material interactions. Inert inorganic materials, such as alumina, zirconia, titanium alloy and cobalt-chromium alloy, are also used in hard tissue applications, but lack resorbability and absence of osseointegration at the bone-implant interface. Positive interaction with cells was established using synthetic biodegradable polymers, such as polylactic-co-glycolic acid (PLGA), polycaprolactone (PCL) and polyethylene glycol (PEG) [13, 14]. The degradation products of these materials have no detrimental

effects in body system. Furthermore, degradation rate, hydrophilicity and mechanical strength can be controlled by changing the chemical composition. Many natural biopolymers are also available and are very suitable bone substitutes in terms of cell-material interactions. Large polymers of very high molecular weight such as chitosan, alginate, cellulose, gelatin, collagen, keratin and hyaluronic acid also exhibit favourable cell-material interactions. Additional biocompatibility to a structurally stable scaffold is the selection criteria for bone substitute materials currently in vogue [15, 16].

In bone tissue engineering, commonly used materials are ceramic and glass due to their superior biocompatibility. Poor mechanical strength and stability are the major deficits rendering them unsuitable as porous scaffolds. In addition, processing defects such as irregularly shaped pores, surface defects and residual stress, all reduce the mechanical strength of the scaffold systems. These limitations compelled the researchers to find out the solutions for the improvement of biological performance of these materials by combinations of various strategies to augment cell-material interactions and stimulation of cells to ensure rapid but controlled bone regeneration. One of the alternate strategies is metallic ion doping for improving biological performance enhancement.

The aim of this chapter is to summarise the recent advancement of metallic ion dopants in addition to bioactive glass scaffold and their studies in orthopaedic surgical challenges. Our discussion broadly covers innovations in materials development and fine tuning together with structural and functional improvisations.

## 2. Bioactive glass materials

“Bioactive” glass can be defined by its name itself, which include “Bioactive”, means *One that elicits a specific biological response at the interface of the material which results in the formation of a bond between the tissues and the material*, and “glass”, often defined as *solid that possesses a non-crystalline (that is, amorphous) structure at the atomic scale and that exhibits a glass transition when heated towards the liquid state* [17]. In short, bioactive glass has been designed to elicit a particular biological reaction at the interface of the material, which stimulates cell proliferation, gene response and the formation of a bond between living tissues and the material [17–20]. Its surface develops a biologically active apatite layer (HCA), which initiates bonding with bone. The apatite phase formed chemically and structurally mimics the mineral phase of bone [21]. Among other essential qualities of bioactive glass are that they should be non-mutagenic, non-carcinogenic and non-antigenic so that they do not have any adverse effect on the cells [22]. With these typical properties, bioactive glasses are reported to be capable of more bone regeneration than other bioactive ceramics available. However, in the case of bioactive glass there are many areas to improve as it has not yet reached its true potential.

The invention of bioactive glass was not by accident, in contrary it was being invented through a series of curious set of events. The first bioactive glass as an alternative to nearly inert implant materials was invented by Prof. Larry Hench at the University of Florida in 1969. A US army colonel, returned from Vietnam war, asked him if material could be developed that could

survive the aggressive environment of human body. All available materials at that time, such as metals and polymers, were designed to be bio-inert, which were found to trigger fibrous encapsulation after implantation rather than forming a stable interface or bond with the tissues [23]. The melt-derived bioactive glass invented by professor L. Hench was composed of 46.1 mol%  $\text{SiO}_2$ , 24.4 mol%  $\text{Na}_2\text{O}$ , 26.9 mol%  $\text{CaO}$  and 2.6 mol%  $\text{P}_2\text{O}_5$ , later termed as 45S5 and Bioglass<sup>®</sup>, which forms a bond with bone strong enough so that it could not be removed without breaking the bone [24]. It is now almost 50 years since the discovery of bonding of bioactive glass with living bone and over time many advances have been made in this field, understanding the mechanism of bone bonding, and respectively modifying the properties of bioactive glass by adjustment of the composition [25–28]. The most interesting aspect of bioactive glass is the high adaptiveness to the biological environment and the tuneable properties, by which the rate of bonding with bone can be controlled, thus the fabrication of patient-specific implants is possible. Today, new bioactive glasses can be made specifically for different types of clinical applications, in different forms such as fibres, microspheres and to show required bioactivity at when implanted.

## 2.1. Synthesis

According to process method used, bioactive glasses can be classified into two different categories: (1) melt derived, (2) sol-gel derived. In these fabrication techniques, melting method is traditional [27, 29–32]; however, the latter appealed the scientists in the last two decades [33, 34]. The synthesis route of bioactive glass has eminent effect on the specific surface area as well as degradability of the material.

## 2.2. Melt derived

The first bioactive glass itself made by Professor Larry Hench in the 1970s was made through melt-quenched method. The idea behind the invention was to make an implant material which can form a hydroxyapatite (HA) layer on its surface when implanted, which can develop a living bond with the host [35]. As the main aim was to mimic bone and bone contains hydroxyapatite [ $\text{Ca}_5(\text{PO}_4)_3\text{OH}$ ],  $\text{Ca}^+$  and  $\text{PO}_4^{3-}$  were taken as a component of glass. The other main components of glass  $\text{Si}^{4+}$  and  $\text{Na}^{2+}$  can also be found in human body. Among the compositions Hench and co-workers made, 45S5 were found to bond with rat femur. The selection of the components of this glass, named as Bioglass<sup>®</sup>, was ideal. The low silica content compared to the previous soda-lime-silicate glasses forms a layer of silica and amorphous calcium phosphate on the surface of the implant. Since then the research on bioactive glass somehow concentrated mostly compositions similar to 45S5 bioactive glass.

Most of those bioactive glasses were produced by melting raw materials at an elevated temperature because it is a simple, low-cost technique and does not take much time to complete. It typically involves raw materials selection, weighing, mixing of components in appropriate proportion and removal of impurities to get a homogeneous melt. The reactivity of a glass in aqueous solutions is strongly dependent on the composition of the glass and thus the choice of composition is very important. Because the limited range of glass composition shows bioactivity, the glass composition should be chosen in a way so that it can be melted

and formed into required shapes with available methods. The raw materials can be divided into five different categories according to their role: glass former, flux, modifier, colourant and fining agent. Glass formers are the most important components of glass as they form the matrix of the glass structure. Silica ( $\text{SiO}_2$ ), boric acid ( $\text{B}_2\text{O}_3$ ) and phosphoric acid ( $\text{P}_2\text{O}_5$ ) are the most common type of glass former normally present in oxide glass. In between these silica is widely used; however, the melting temperature of silica is too high ( $1600\text{--}1725^\circ\text{C}$ ) and so different types of flux such as  $\text{Na}_2\text{O}$  and  $\text{PbO}$  can be used to decrease the melting temperature of the mixture. The addition of flux sometime degrades the properties of glass, which can be overcome by introducing different property modifier or intermediates such as boron, sodium, magnesium, titanium and calcium. Colourants are used to control the colour in the final product. Finally, fining agents such as arsenic, antimony oxides, potassium and sodium nitrates are added to raw materials to remove bubbles from the melt. During melting of the raw materials inside the furnace, they react with each other and carbon dioxide and Water-vapour emission takes place, which causes the formation of bubbles. To raise the bubbles up to the upper surface of the melt, low viscosity is maintained. Batch particle size and their mixing in proper proportion are other factors that provide homogeneity in glass structure. Glass forming is an intermediate stage in between glass melting and annealing. The stages of glass synthesis are illustrated schematically in **Figure 1**.

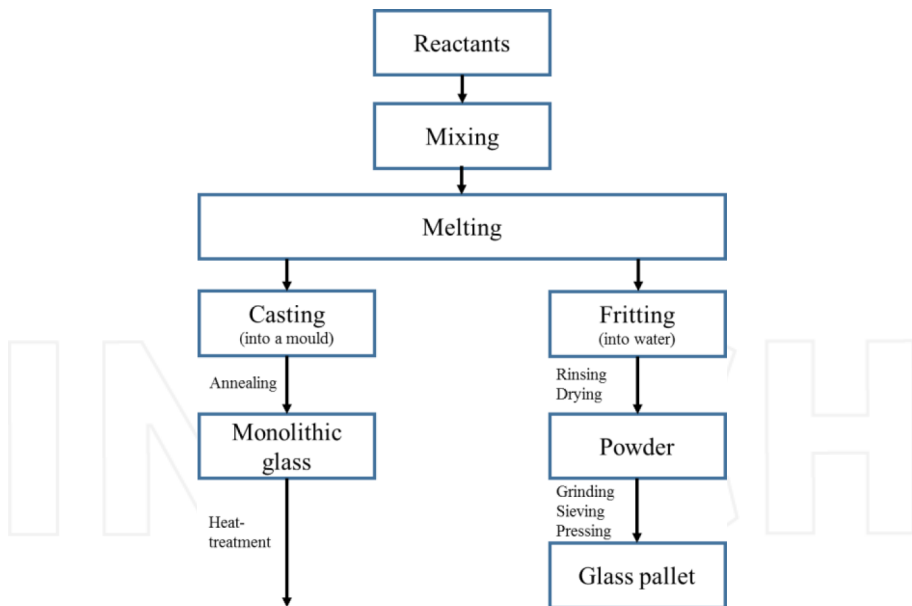


**Figure 1.** Schematic representation of melt-derived glass synthesis.

Practically appropriate amount (mole/weight fraction) of initial ingredients is mixed, followed by grinding, to break agglomerated particles. In order to obtain more uniform powder, the

mixture of ingredients is ground in ball mill using acetone (water can also be used unless some ingredient is hygroscopic). After drying the mixture in air, the powder can be transferred in platinum crucible and melted in a high-temperature furnace. Generally, around 500°C, the gaseous substances (moisture and gas) come out of the composition. Hence, it is better to calcine the mixture at 500°C for at least 2 h. Before taking out the melt, it must be confirmed that the glass mixture is held at the melting temperature for at least an hour to achieve homogeneous, bubble-free molten materials. Then, the molten glass can be quenched in liquid such as water, liquid nitrogen, etc. Granules of different sizes formed collectively known as frits can be collected and milled to get glass powder. Desirable size and shapes can be made by pouring the molten mixture into moulds of particular shapes. In the case of preparation of glass with particular shape, the poured glass is annealed slightly below the glass transition temperature of the corresponding glass for 12 h in air in pit furnace.

### 2.2.1. Important factors

Important factors to remember while melting a glass are viscosity, thermal expansion and crystallisation characteristics. Low viscosity helps the melt to be bubble free and homogeneous and also facilitates easy elimination from the platinum pot. It is a crucial factor in determining the best possible procedure for a particular composition. Viscosity values at high temperatures can be linked with melt-forming processes and low-temperature values indicate the suitability of the glass, whether for sintering into porous bodies or coating on metal implants. The approximate viscosity values for a bioactive-glass-forming process are given in **Table 1**.

Processing	Viscosity ( $\eta$ ) (dPa s)
Melting	$10^{-10}^2$
Pressing	$10^4\text{-}10^6$
Drawing of continuous fibres	$10^{2.5}\text{-}10^{3.5}$
Sinter glass powder to porous body	$10^8\text{-}10^9$
Annealing	$10^{12}\text{-}10^{13}$

**Table 1.** Approximate viscosity values (dPa s) for bioactive-glass-forming process.

Bioactive glass coating provides better bone-implant connection when coated on metal prostheses [36–41]. According to the implantation area, lower surface reactivity may be preferred and in such cases glass composition with less bioactivity are favoured. Whatever be the case the thermal expansion of the glass must be compatible with the metal otherwise cracks may appear on the coating leading to peeling off of the coating.

Another important factor is that the melting temperature should be higher than liquidus temperature of the compositions. Recent development of bioactive glasses focuses on the change of chemical composition and different heat treatment condition [42, 43]. Aboud et al. analysed the effect of increasing temperature on the crystallisation behaviour and the phase formation order of different crystals of  $\text{SiO}_2\text{-P}_2\text{O}_5\text{-Al}_2\text{O}_3\text{-MgO-Na}_2\text{O}$  glasses [44]. The changes

in microstructure, mechanical and chemical properties of this glass with different heat treatment conditions result in an important application in dental restoration [45]. Also, thermal treatments of bioactive glass tend to enable the glass to attain different elastic properties and a range of bioactivity, which could be helpful for making patient-specific implant [46].

### 2.3. Sol-gel derived

Sol-gel glasses are made by a chemical-based process at much lower temperatures than the traditional processing methods [47–51]. The method has been recently accepted by a number of research groups to make a new generation of bioactive glass and offers assurance for tailoring the composition to match the specific requirements. Recently, scientists have preferred the sol-gel method in order to increase the specific surface area, and thus, the surface reactivity and degradability of the material [52]. It also provides better control over homogeneity and purity [53].

A sol is a colloidal suspension of solid particles (with a diameter of 1–100 nm) in a liquid, where the colloids exhibit *Brownian motion*, a random walk driven by momentum imparted by collisions with molecules of the suspending medium. Gel can be described as a rigid network of covalently bonded silica comprised of interconnected pores [54, 55]. Three methods can be used to make sol-gel materials: gelation of colloidal particles, hypercritical drying or controlled hydrolysis and condensation of metal alkoxide precursors followed by drying at ambient pressure. All the three methods create a three-dimensional, interconnected network. Gels can be categorised into three types, such as alcogels, xerogels and aerogels [53]. Alkogels are generally alcohol based, whereas xerogels are formed from thermal removal of pore liquid. Gels with low density ( $80 \text{ kg m}^{-3}$ ) and large pore volumes (up to 98%) are called aerogels, which are the result of removal of pore liquid from the rigid network without collapsing it.

Preparation of gel glasses by a sol-gel method composed of seven steps. First, the alkoxide or organometallic precursors are mixed to form the low-viscosity sol, followed by hydrolysis of liquid alkoxide precursors with de-ionised water [56, 57]. Hydrolysis of silicon alkoxide forms silanol groups  $[\text{Si}(\text{OH})_4]$ , eventually interact with each other to make the Si-O-Si bond and increase the viscosity of the sol (**Figure 2**). This is the time where the sol can be applied as a coating, be pulled into fibre, electrospun, impregnated into a composite or formed into powders. During the process of gelation, the viscosity of the solution sharply increases [58]. The gelation time depends upon the concentration of the solvent, nature of the oxide group and the amount of water used for the hydrolysis [59, 60]. While aging of a gel for several hours at 25–80°C, decrease in porosity and increase in the strength can be observed due to polycondensation and reprecipitation of the gel network [61–63]. Aging process also affects the pore volume, surface area and density of the gel. The removal of pore liquid has different effect on arising stress for colloidal gels (pore size > 100 nm) and alkoxide-based gels with pore size 1–10 nm. Colloidal gels can be dried easily; however, in the case of alkoxide-based gels, large capillary stress may arise during drying. Hypercritical drying at elevated temperature and pressure, above the pore-liquid-solid critical point, avoids the solid-liquid interface and eliminates drying stress [17].

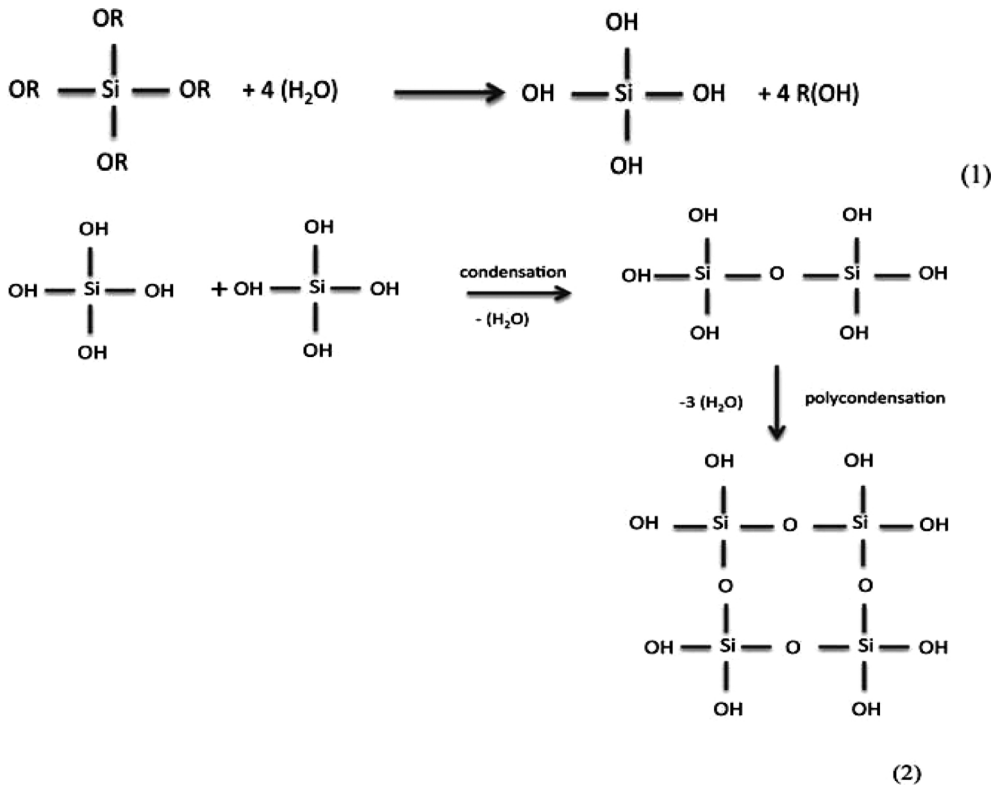


Figure 2. (1) Hydrolysis of  $\text{Si}(\text{OH})_4$ ; (2) formation of Si-O-Si bond.

In order to control the stability of the material, chemical stabilisation of the dried gel is required. Sintering of the gel at 500-900°C desorbs silanol groups from the surface and eliminates 3-Si rings from the gel. It also increases the density, strength and hardness of the gel. The sintering temperature of alkoxide-based gels is in the range of 900-1150°C depending upon composition. The schematic diagram of the sol-gel process is provided in Figure 3.

The physical differences between the two synthesis routes are that sol-gel glasses tend to have an inherent nanoporosity whereas melt-derived glasses are dense in nature [64]. The surface area of sol-gel glasses is also higher than melt-quenched glass, which results in greater dissolution rate, and hence higher cellular response. The hierarchical pore structure consisting of interconnected macropores (>100  $\mu\text{m}$ ) and nanopores is beneficial for interaction and stimulation with cells as it mimics the hierarchical structure of natural tissues. Also bioactive glasses in the form of nanoporous powders or monoliths or as nanoparticles can be made by changing the pH of the sol-gel process [65]. However, the sol-gel made scaffolds have lower strengths than melt-quenched glasses, and thus inappropriate to use in hard tissue engineering (Figures 4 and 5).

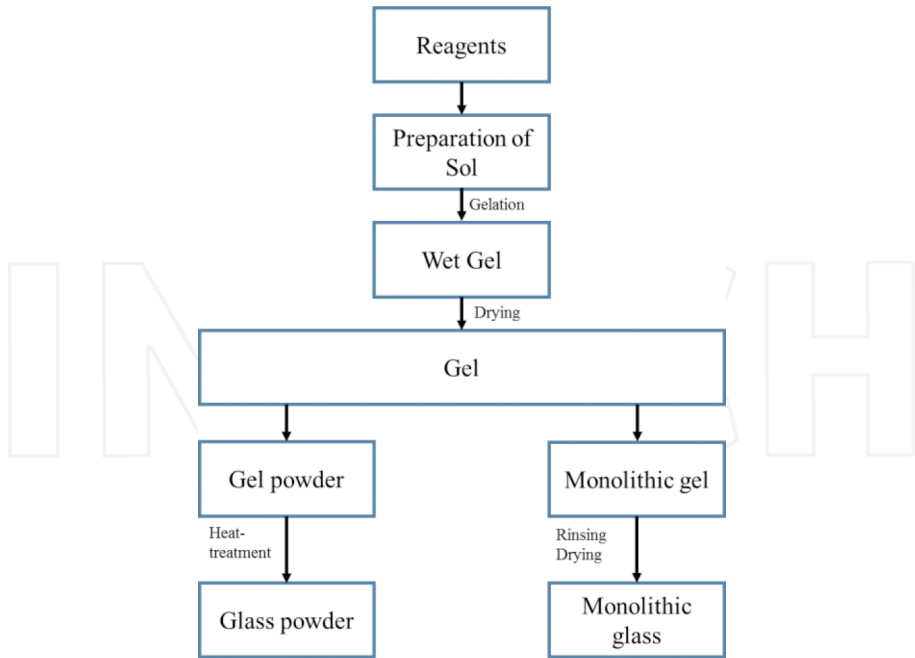


Figure 3. Schematic representation of sol-gel glass synthesis.

### 2.3.1. Important factor

The physical and chemical properties of sol-gel bioactive glass mainly depend upon silica and so the hydrolysis and condensation of silica plays an important role. The kinetics of hydrolysis and condensation of silica depend upon several factors such as pH, composition, temperature, precursor, catalysis and concentration of ions and the ratio of moles of water/moles of tetraethyl orthosilicate (TEOS). Iler divides the polymerisation of silica in between three pH ranges: <pH 2, pH 2-7 and >pH 7. pH 2 and pH 7 appear to be boundaries because at pH 2 the surface charge (PZC) and the electrical mobility of silica (isoelectric point, IEP) are zero, whereas above pH 7 the solubility and dissolution rates of silica are maximised leading to particle growth without gelation [65].

### 2.4. Composition of bioactive glasses and their effects on bioactivity

Since the report of bone-bonding properties of bioactive glass, silica has been used as the major component of glass composition and also most widely researched with changing its amount. Silicate glasses comprise an amorphous network structure based on  $\text{SiO}^+$  tetrahedron, which are linked to each other at the oxygen centres. Silicate glasses have open structure of silica due to the presence of non-bridging oxygen ions attached with silicon. Addition of network modifiers such as  $\text{Na}^+$ ,  $\text{K}^+$ ,  $\text{Ca}^+$  also causes the opening of silica network structures. These ions



replace bridging oxygens of the network with non-bridging oxygens, hence opening of the glass structure. The number of modifier ion-oxygen bonds and non-bridging oxygen bonds determines several properties of the corresponding glass [66]. Detailed structural features of silicate glasses and their effect on different physical and chemical properties have been reported by various research groups [67–69]. In the case of bioactive silicate ( $\text{SiO}_2$  less than 60 wt%) glasses, each silica tetrahedron contains more than 2.6 number of non-bridging oxygen ions, which is necessary in order to be bioactive [70].

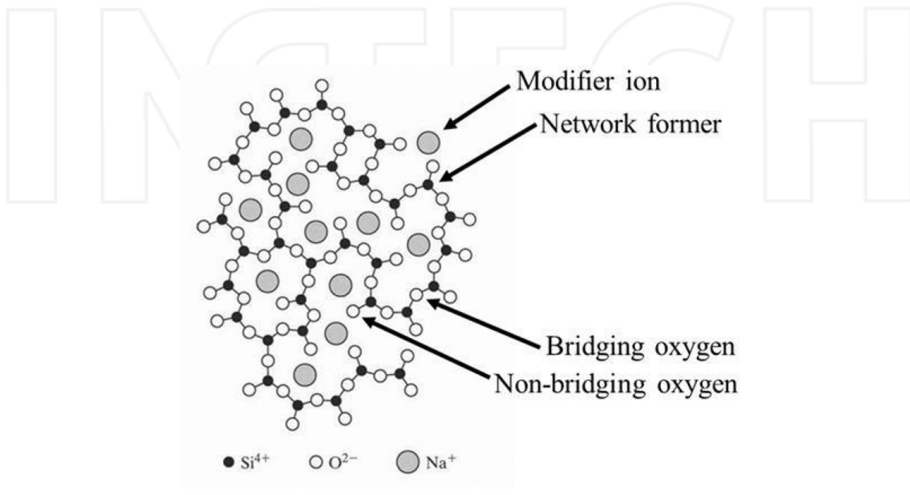


Figure 4. 2D presentation of random glass network modifiers and network formers [70].

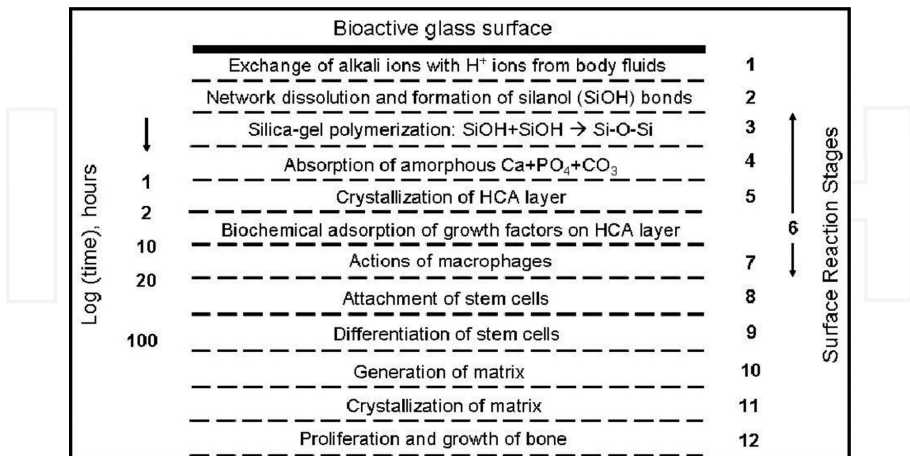


Figure 5. Sequence of interfacial reactions kinetics involved in forming a bond between bone and a bioactive glass [87].

The composition of bioactive glass is different from the traditional soda-lime-silica glasses that consist more than 65 wt% of silica. Basic components required for a glass to obtain bioactivity are  $\text{SiO}_2$ ,  $\text{Na}_2\text{O}$ ,  $\text{CaO}$  and  $\text{P}_2\text{O}_5$ , which can be distinguished in three main features according to Hench and Anderson [71]; the amount of  $\text{SiO}_2$  should be in between 45 and 60 wt%,  $\text{Na}_2\text{O}$  and  $\text{CaO}$  content must be high and a high  $\text{CaO}/\text{P}_2\text{O}_5$  ratio. Higher content of  $\text{SiO}_2$  decrease the dissolution rate of the glass ions from the surface, leading to decrease of bioactivity. Very low content of silica also leads to totally dissolvable monomeric  $\text{SiO}^4$  units. Silica content also plays an important role to form hydroxyapatite carbonate (HCA) upon contact with physiological fluids, thus leading to the chemical attachment to soft/hard tissues. As a result, the interfacial bonding strength with bone increases, and a stable bond with strength equivalent to or greater than bone forms. High  $\text{CaO}/\text{P}_2\text{O}_5$  ratio tends to enable the release of ions from the surface of the material when soaked in body fluid, forming a surface layer of HCA in a very short time span. It also supports cell proliferation on the surface of the implant by maintaining the ion concentration [35]. Previously, Hench and co-workers assumed that a typical range (2–6 wt%) of  $\text{P}_2\text{O}_5$  is required for a glass to be bioactive as it aid the formation of calcium phosphate phase on the surface, but later Hench and Andersson observed that bioactivity can be independent of  $\text{P}_2\text{O}_5$  as phosphate ion is also available in physiological fluids.

In the last two decades, a number of different oxide systems have been studied to understand the effect on glass bioactivity and to increase its mechanical strength, still a complete understanding of the correlation between composition and bioactivity is insufficient but mechanical improvement can be possible. Different partial substitutions in the already approved glass compositions have been made, as  $\text{CaO}$  by 12.5 wt%  $\text{CaF}_2$ ,  $\text{SiO}_2$  by 5-15 wt%  $\text{B}_2\text{O}_3$ , but no significant effects were found. Even fluoride substitution reduced the bone bonding capability of the glass [72]. The substitution of  $\text{MgO}$  for  $\text{CaO}$  or  $\text{K}_2\text{O}$  for  $\text{Na}_2\text{O}$  showed slight increase in bioactivity. During 1990s glasses with alumina and boron oxide gained enormous interest. Sadly, the addition of small 3 wt%  $\text{Al}_2\text{O}_3$  to the 45S5 formula was found to prevent bonding with bone. Andersson proved that substitution by  $\text{Al}_2\text{O}_3$  (1-1.5 wt%) can reduce the bioactivity of glass because of its carcinogenicity [71]. Osaka et al. and Saranti et al. studied glasses with  $\text{B}_2\text{O}_3$  content and found that the presence of boron has a positive impact on the bioactivity of the glass [73, 74]. In the case of only  $\text{B}_2\text{O}_3$ -substituted glass, the ratio between  $\text{B}_2\text{O}_3$  and  $\text{SiO}_2$  plays an important role in the rate of formation of calcium phosphate layer on the surface of the implant [75]. Later, de Arenes proposed to control the  $\text{B}_2\text{O}_3/\text{Al}_2\text{O}_3$  ratio in  $\text{B}_2\text{O}_3$  and  $\text{Al}_2\text{O}_3$  containing glasses in order to show bioactivity [76]. In recent years, researchers tend to play with the composition of glass incorporating the ions that are abundant in human bone, such as  $\text{Mg}$ ,  $\text{Zn}$ ,  $\text{Cu}$  etc. [77–83]. Xia Li et al. found that by incorporating  $\text{Mg}$ ,  $\text{Zn}$  or  $\text{Cu}$  in different amounts in place of  $\text{Ca}^{2+}$  can affect the bioactivity of the glass to different extent in a sequence of  $\text{Cu} < \text{Mg} < \text{Zn}$  [84]. Potassium substitution in place of  $\text{Na}^+$  reduces the viscosity of silicate glasses and their susceptibility of crystallisation [85]. Even now, a lot of research is going on to find a relation between the composition of the glasses, which have more than four components and tissue connectivity through phase diagram, but relation between these two factors is yet to come. Some researchers such as Andersson et al. and Brink et al. predicted the *in vivo* reactivity of glasses with six or seven oxides as a function of their composition with phenomenological models suggested by regression analysis [71, 86].

## 2.5. Surface reaction kinetics

Chemical reactivity of a glass in contact with body fluid holds the key of the bone bonding properties of the glass. Due to the chemical reactions, a layer of hydroxycarbonate apatite forms on the surface to which bone can connect. When immersed in an aqueous solution, such as SBF (simulated body fluid) or PBS (phosphate-buffer solution), three general processes occur: leaching, dissolution and precipitation. Leaching can be characterised as release of ions, generally by exchange of alkali or alkaline earth metals ions with  $H^+$  or  $H_3O^+$  ions of the solution. Glass modifier ions leach very easily from the surface of the glass when immersed in an aqueous solution, as they are not part of the glass network. The ion exchange process leads to increase in the hydroxide ion concentration, i.e., the basicity of the solution increases to  $pH > 7$ . Network dissolution occurs simultaneously by breaking of the network forming silica bonds (-Si-O-Si-O-Si-) by the attack of hydroxyl ions ( $OH^-$ ). It releases silica into the solution in the form of silicic acid ( $Si(OH)_4$ ). In this step, glass composition plays an important role as the rate of silica dissolution depends very much on glass composition. Silica dissolution rate rapidly decreases if the weight percentage of  $SiO_2$  goes beyond 60% because of the increase of bridging oxygen, which can hold the network very strongly. Hydrated silica then undergoes polycondensation with neighbouring silanols to form silica-rich layer. In the precipitation part, calcium and phosphate ions released from the glass together with those from solution to form a calcium-phosphate-rich layer on the glass surface. Slowly, it crystallises to form HCA by incorporating carbonate ions from solution. Generally, there are five reaction stages on the implant side of the interface with a bioactive glass [72].

Stage 1: Leaching and formation of silanols ( $SiOH$ ).

Stage 2: Loss of soluble silica and formation of silanols.

Stage 3: Polycondensation of silanols to form a hydrated silica gel.

Stage 4: Formation of an amorphous calcium phosphate layer.

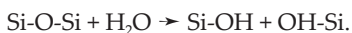
Stage 5: Crystallisation of a hydroxycarbonate apatite layer.

Hench et al. have been extensively described the reaction processes [25, 72, 87–89].

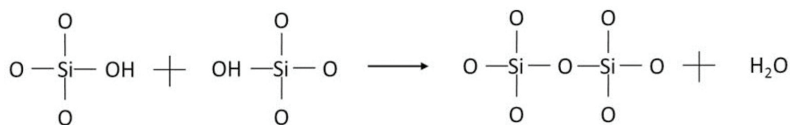
1. Rapid exchange of alkali or alkaline earth metal ions  $Na^+$  or  $K^+$  with  $H^+$  or  $H_3O^+$  from solution



2. -Si-O-Si-O-Si- bonds break through the action of hydroxyl ions and form Si-OH (silanols)



3. Condensation of Si-OH groups near the glass surface: re-polymerisation of the silica rich layer



4. Migration of  $\text{Ca}^+$  and  $\text{PO}_4^{3-}$  groups to the surface through the  $\text{SiO}_2$ -rich layer forming a  $\text{CaO-P}_2\text{O}_5$ -rich film on top of the  $\text{SiO}_2$ -rich layer, followed by growth of the amorphous  $\text{CaO-P}_2\text{O}_5$ -rich film by incorporation of soluble calcium and phosphate ions from solution.
5. Incorporation of hydrolysis and carbonate from solution and crystallisation of the  $\text{CaO-P}_2\text{O}_5$  film to HCA.

As these stages were proposed many years ago, they are proved through time by various types of characterisation techniques.  $^{17}\text{O}$  nuclear magnetic resonance (NMR) confirmed the increase of bridging oxygen bonds during leaching, which indicates the repolymerisation of  $\text{Si-OH}$  groups in the silica-rich layer [90]. The formation of crystallise HCA layer on the surface was confirmed by surface-sensitive-small-angle X-ray diffraction (XRD) [91]. Calcium phosphate nucleate on the  $\text{Si-OH}$  groups as they have negative charge in solution and the separation of the  $\text{Si-OH}$  groups is thought to dictate the orientation of the apatite crystals, which grow with a preferred orientation in the 001 plane on Bioglass 45S5 [23, 92–95].

## 2.6. Bioactive glass *in vivo*

The bioactivity of glasses can only be investigated and confirmed after testing with living tissues. If a calcium phosphate layer can be found on a silica gel layer at the surface of the implants, the glass can be called bioactive. The extent of bioactivity of the glass is directly dependent on the ability of the glass to form calcium apatite layer. The above-mentioned five stages on the surface of bioactive glass do not depend on the presence of tissues. The sequence of *in-vivo* reactivity of bioactivity glass with tissues has been investigated by Hench and Andersson [37, 87, 96].

Stage 6: Adsorption of biological moieties in the  $\text{SiO}_2$ -hydroxycarbonate apatite layer

Stage 7: Action of macrophases

Stage 8: Attachment of stem cells

Stage 9: Differentiation of stem cells

Stage 10: Generation of matrix

Stage 11: Mineralisation of matrix

Through the 11 stages, a bioactive glass bonds with the bone. Gradually, the bioactive glass will be absorbed with increasing bone ingrowth.

45S5 Bioglass<sup>®</sup> was the first bioactive glass successfully investigated *in vivo* by many researchers [17]. After that another bioactive glass S53P4 was developed by Andersson and Karlsson

and has been successfully used in clinical applications [97–99]. Later, glass 13-93 and glass 1-98 also showed good bioactivity *in vivo* [86, 100–102].

Extensive research in this field in recent years comes out with some limitations of the model of reaction kinetics proposed by Prof. Hench. Hench proposed that in the first stage of the reaction a rapid exchange of  $\text{Na}^+$  ions released from the glass with the protons ( $\text{H}^+$ ) of the solution occur, although in the modern era bioactive glass has been synthesised without sodium. Influence of the mole fraction of silica on the bioactivity is still not clear. Also, it was observed that if the implant is broken and the broken surfaces stay in contact with SBF, they tend to self-repair by fusing themselves through their apatite surface layers [103].

In the case of clinical trial, the main problem is to make patient-specific implants because every patient is different. To study the implant specificity and implant site adjustment *in vivo* animal model, studies can be compared if the same models are used. The first *in vivo* study was completed for Bioglass monoliths on the rat femurs, and after 6 weeks the interfacial shear strength of the bond between the glass and the cortical bone was equal or greater than the strength of the host bone [24, 104]. Bioglass 45S5 also degrades more rapidly than hydroxyapatite, and the degeneration was because of solution-mediated dissolution. The model of the study later named as Oonishi model was completed by drilling 6 mm diameter into the femoral condyle of rabbits. Bleeding was stopped before inserting the particles [105–107]. Recently, it was found that initially the bone grew into the particles that were on the outer periphery in contact with the host bone, but within 2 months of implantation bone also formed inside the isolated Bioglass particles. This study indicates that the Bioglass particles can trigger stem cell differentiation and convert it into osteoblasts [108]. Hands-on experience by various surgeons points out the advantage of making a putty-like material by mixing the particles with blood prior to implantation, which later encourages the development of Nova bone [109]. The explanation behind this advantage of putty-like material is either it can separate the particles to allow new bone to grow between them or the pH environment created was more suitable for bone ingrowth. Fujibayashi et al. used the Oonishi model to test phosphate-free glass particles and for one of his compositions almost similar amount of bone ingrowth to Bioglass was found. But with increasing  $\text{SiO}_2$  content the bone ingrowth reduce rapidly [110]. Wheeler et al. compared Bioglass 45S5 with sol-gel glasses 77S and 58S using the Oonishi model and observed that up to 8 weeks the bone ingrowth was more in the case of Bioglass, but after 12 weeks the amounts were equivalent. The procedure of bone ingrowth, *viz.* formation of silica layer, apatite formation and finally bone formation via HCA was found to be same as Bioglass [111]. The initial slower rate can be result in the rapid release of calcium in the case of sol-gel glasses causing increase in pH at the site.

## 2.7. Bioactivity *in vitro*

Before going to *in vivo* trials, a glass material has to be passed *in vitro* tests. The *in vitro* test helps us both ethically and economically as they reduce the number of animals necessary for *in vivo* tests. Earlier *in vitro* test was performed by immersing the glass in either distilled water or tris-buffered solutions, but after development of SBF by Kokubo et al. it has become the most widely used solution for *in vitro* investigation. SBF contains all the essential inorganic

components of human blood, and proportions are also almost similar to human blood plasma [112]. During *in vitro* studies, pH of the solution is buffered between 7.25 and 7.4 at 37°C.

	Na <sup>+</sup>	K <sup>+</sup>	Mg <sup>2+</sup>	Ca <sup>2+</sup>	Cl <sup>-</sup>	HCO <sub>3</sub> <sup>-</sup>	HPO <sub>4</sub> <sup>2-</sup>	SO <sub>4</sub> <sup>2-</sup>
Plasma	142.0	5.0	1.5	2.5	103.0	27.0	1.0	0.5
SBF	142.0	5.0	1.5	2.5	147.8	4.2	1.0	0.5

**Table 2.** Ion concentrations of SBF and human blood plasma (mM) [112].

SBF is a supersaturated solution and hence precipitation of calcium phosphate can easily take place during preparation, storage and *in vitro* test. Many researchers have tried to correct the difference of ion concentrations of Cl<sup>-</sup> and HCO<sub>3</sub><sup>-</sup>. Oyane et al. made a revised SBF (r-SBF) in which the concentrations were matched, but the solution shows a strong tendency to precipitate calcium carbonate [113]. In 2004, Takadama proposed a modified SBF (n-SBF) in which only Cl<sup>-</sup> ion concentration was increased [114]. Several properties of bioactive glasses have been studied in SBF by observing the changes in weight and surface morphology of the glass and also observing the change of pH and ionic concentrations of the solution. Some research groups focussed on the physical and mechanical properties whereas some groups are interested in knowing chemical and bioactive properties of glass [115–118]. It was observed that the extent of bone ingrowth among glass particles increased according to their ability to form apatite in SBF. Thus, it can be said that the *in vivo* bioactivity of a glass can be assumed precisely from its nature in SBF.

Five typical reaction stages, as described in surface reaction kinetics part, occur when *in vitro* bioactivity test is performed. Initially, due to ion exchange of alkali or alkaline earth metal ions with H<sup>+</sup> ions of the SBF solution, pH of the solution increases. By the action of OH<sup>-</sup> ions network, dissolution occurs with the formation of Si(OH)<sub>4</sub>. The dependency of dissolution rate is more or less same as described before. The leaching and dissolution phenomenon is followed by a formation of silica-rich layer on the surface by polycondensation of neighbouring silanols, which ultimately form a calcium-phosphate-rich layer by incorporating Ca<sup>+</sup> and PO<sub>4</sub><sup>3-</sup> ions. The layer increases by including soluble calcium and phosphates from the SBF, forming an amorphous CaP-rich layer. Finally, the CaP-rich layer crystallises to a hydroxycarbonate apatite structure.

With changes in composition, differences in sample dosage, shape and size, sample porosity and surface morphology also affect the bioactivity of a glass [117, 119–123]. Most studies of bioactive glasses have used samples in the form of discs or plates, however in accordance with their applications other forms are also of interest.

## 2.8. Mesoporous bioactive glass (MBG)

For treatment of bone defects resulting from trauma, infections, tumours or genetic malformations, bioactive glass scaffolds have been extensively studied. In the case of bone regeneration, combination of osteoconductive, osteostimulative and angiogenic factors with bioactive

glass are proved to be useful [124–126]. This advantage of bioactive glass made it a subject of interest for almost 50 years and day by day according to rise in life expectancy, the field of its application is increasing. Extensive research in this topic comes out with a handful of modifications for the last two to three decades. Recently, it was found that kinetic deposition process of HCA on bioactive glass can be enhanced by increasing the surface area and pore volume [127]. Therefore, control over porosity, pore size and internal pore connectivity of bioactive glasses is essential to understand and design better bone forming biomaterials. A new field of application was started when surgeons found that in the case of bone reconstruction surgery, bacterial infection may cause osteomyelitis. Traditionally, techniques such as systemic antibiotic administration, surgical debridement, wound drainage and implant removal have limitations and may lead to additional surgical interventions for the patients [128]. Conventional drug delivery options, such as injection or taking a pill, increase the concentration of drug in blood up to peaks and then suddenly decline [129]. Hence, to improve drug delivery efficacy, continuous action, reduce toxicity and convenience to patients a lot of work has done. In addition, the procedure was also considered for treating malignant bone disease in which drug will be effectively released at the sites of bone disease from loaded biomaterials [130, 131]. Since the invention of first bioactive glass, in the last 40 years it has shown various attractive properties for bone tissue regeneration application by virtue of their osteoconductivity and degradability [124, 132, 133]. In 2004, Yu et al. for the first time prepared mesoporous bioactive glasses (MBG) by the sol-gel method using surfactants, which opened a new direction in the field of regenerative medicine [134]. The materials were composed of highly ordered mesopore channel structure with a pore size ranging from 5 to 20 nm. MBG has gained the interest of researchers very rapidly for its drug loading and release properties, which depend on the mesoporous structure of the materials. Due to its tuneable pore size, large specific surface area and pore volume, the materials can be used in bone-forming activity and can be loaded with osteogenic or therapeutic agents [125, 126, 128, 131, 135, 136].

### *2.8.1. Preparation of different types of mesoporous bioactive glasses and their in vitro bioactivity*

Mesoporous bioactive glasses were emerged when the supramolecular chemistry of surfactants was incorporated into the bioactive glasses field. These materials have the composition of bioactive glasses but with designed mesoporosity and textural parameters. MBGs are generally prepared by combining non-ionic surfactants (triblock copolymers, CTAB, P123, F127, PEO, PU, etc.) into the reaction system, which are essential for obtaining well-ordered structures [134, 137]. The most well-known and accepted procedure of making mesoporous bioactive glass is evaporation-induced self-assembly (EISA) method [138]. The initial homogeneous mixture is obtained by dissolving precursors in a common medium such as ethanol-water mixed solvent system. The surfactants can act as micelles and are able to link with the hydrolysed precursors (e.g., TEOS and TEP) to form an ordered mesophase, where a constant ratio of network former and precursors and the surfactant was kept [139]. After that, following the process of sol-gel, gelling and drying takes place, and by the removal of surfactant through calcination finally gives MBG with a well-ordered mesoporous structure. The order of porosity of the material depends on surfactant chemistry (ionic, non-ionic, polymeric, etc.), surfactant concentration, organic/inorganic phase volume ratio, temperature and pH of the sol.

Recent studies on mesoporous bioactive glass show increasing use of MBG in different fields of tissue engineering and drug delivery. The types of MBG used in these fields may be particle, sphere, fibres or 3D scaffolds. The first MBG powders or particles were prepared by using P123 and F127 as a surfactant, with the composition of 80Si-15Ca-5P, 70Si-25Ca-5P and 60Si-35Ca-5P. Calcination at 700°C gives a highly ordered MBG powder. The bioactive characteristics of a scaffold can be assumed from their ability to form apatite layer on their surface *in vitro*. Zhu and Kaskel reported that the rate of apatite formation in the case of MBG is noticeably higher than its contemporary bioactive glass scaffolds [140]. Other than the mesoporous structure, the chemical composition of the mesoporous bioactive glass is the other factor to influence *in vitro* bioactivity. Now a days, scientists are focussing on modifying the basic properties of MBGs, which are high specific surface area, porosity etc. and found that upon changing these properties the apatite-formation ability of MBG could be fine-tuned [49, 141–143]. Lei et al. prepared MBG microspheres through the sol-gel process with uniform diameter range of 2-5  $\mu\text{m}$  and a mesoporous shell [144]. Zhao et al. prepared MBG microspheres with high  $\text{P}_2\text{O}_5$  contents (up to 15%) and studied the apatite formation *in vitro* [145]. Studies indicate that the diameter of the microspheres has a positive effect on the bioactivity. Moreover, MBG microspheres with higher  $\text{P}_2\text{O}_5$  content were found to be more bioactive due to their different ion diffusion rates from the glass network. MBG can also be prepared as ultrathin fibres by electro-spinning techniques with high matrix homogeneities. By controlling the parameters of electro-spinning, the properties of the fibres such as pore volume, surface area and diameter of the hollow core can be tuned. These fibres were found to be highly bioactive when tested *in vitro* [146, 147].

## 2.9. Ion-doped bioactive glass with and without mesoporosity

### 2.9.1. Introduction

The clinical demand of bioactive glass is increasing rapidly day by day due to its versatile properties *viz.* bioactivity, resorbability, ostioproductive, osteoconductive and osteoinductive nature, depending upon its flexible compositional range. With increasing population, the diversity of required implants is also expanding. The wide range of application of bioactive glasses include implants for bone defects, repairing or replacing damaged diseased tissues, scaffolds for bone grafting, preparing bone cement, as novel drug carrier and coating material for implants [26, 37]. When implanted in human body, a hydroxyapatite carbonate layer forms on the implant-bone interface which is chemically and structurally similar to the mineral phase of human bone. In the last two decades, researchers found that the sites of implantation of different parts of our body require different chemical and physical properties, and hence bioactive glass with different or modified compositions. Bioactivity of a glass is mainly dependent on its surface reactivity and composition and by modifying those, improvement of the system can be possible. Sometimes modification also needed in order to overcome the disadvantages of traditional bioactive glasses such as high solubility and low fracture toughness.



Recent trends in literature suggest that ionic dissolution products from inorganic materials are keys to understand and assume the behaviour of bioactive glasses *in vitro* and *in vivo*. Since many trace elements such as Sr, Cu, Zn, Mg or Co present in the human body are known for their anabolic effects in bone metabolism, in order to mimic the natural system new approaches for enhancing bioactivity, beneficial and appropriate ions are being introduced [148–151]. It is believed that more similar system such as the host body will increase the bioactivity of the implant. The release of these ions after exposure to a physiological environment tends to improve the bioactive activities of the implant related to both osteogenesis and angiogenesis. Thus, recent trend is to incorporate different ions into the composition of bioactive glasses to enhance their physical characteristics and therapeutic benefit.

This incorporation of different ions in the composition of glass is called doping and it is very crucial for production of functional materials. By definition, a doping element is an additional incorporation in the main composition at a very low concentration compared to the main constituents ranging from a few ppm to a few percent. In many cases, it was found that the functionality of the material is directly dependent on the doping elements. In some other cases, doping may improve surface structure of the implant or the physical attributes of it. In particular, the points related to doping can be listed as follows [152]:

1. The functionality is directly associated with doping.
2. Doping provides a structural control over the material.
3. Doping provokes unexpected structural modifications.
4. Doping brings new unexpected functionality to the material.

It is hard to identify the particular time when doping was first started, but around late 1985 the trend of incorporating different ions were started. First, a number of different ions such as Al, Ag, Fe, Ni, Cr, Cu, Co, Ta, Sb, La, etc. were doped and then tested *in vitro* and *in vivo* [153]. Initially, the dopants were chosen according to their similarity in valence with the elements already present, but with time and following the literature about the essential trace elements required in our body, the interest about dopants has been focussed on some specific elements and their affects [149, 150].

### 2.9.2. Role of inorganic ions present in human body

Human bone is a highly vascularised tissue which can remodel throughout the life by regulated activity of osteoblasts (bone-forming cells) and osteoclasts (bone-resorbing cells) [154]. The process of bone remodelling is dependent on a variety of local regulatory agents such as growth factors, hormones, etc. [155]. Inorganic ions such as calcium [156–158], phosphorous [159], silicon [160, 161], strontium [162–164], zinc [165], boron [166] and magnesium [167] are also affect the bone metabolism. The acts of the inorganic ions in this context are given in **Table 3**.

Ion	Biological activity	Reference
Si	• Metabolic processes, formation of bone tissue	[160, 168]
	• Intake of Si increase bone mineral density	[169]
	• HAP precipitation	[170]
	• HAP precipitation	[161]
	• Help to stimulate collagen I formation and osteoblastic differentiation	
Ca	• Favours osteoblast proliferation, differentiation and mineralisation	[156]
	• Activates Ca-sensing receptors in osteoblast cells	[155]
P	• Matrix gla protein (MGP) stimulation	[159]
Zn	• Shows anti-inflammatory effect	[171]
	• Bone formation <i>in vitro</i> by activation of protein synthesis in osteoblasts	[172]
	• Increase ATP's activity	
Mg	• Help to form new bone	[173]
	• Increase bone-cell adhesion and stability	[174]
Sr	• Beneficial effects on bone formation <i>in vivo</i>	[155]
	• For treating osteoporosis	[175]
Cu	• Promote synergic stimulating effects on angiogenesis when associated with angiogenic growth factor FGF-2	[176]
	• Stimulates proliferation of human endothelial cells	[177]
B	• Stimulates RNA synthesis in fibroblast cells	[178]
	• Stimulates bone formation	[179]
Li	• treatment of both bipolar and unipolar depressive disorder	[180, 181]
	• effects on blood and brain	[182]
	• enhance immunological activities of monocytes and lymphocytes	

**Table 3.** Acts of different inorganic ions in human body.

By acting as an enzyme cofactors, metal ions influence signalling pathways and stimulate tissue formation [150, 183]. These effects make metal ions interesting for use as doping materials in the field of hard and soft tissue engineering. Several ions, such as Sr, Zn, Cu, Mg, B, etc. have been considered to be promising in enhancing the bioactivity of implant materials by controlling the release of specific ions during *in vivo* dissolution.

### 2.9.3. Ion-doped bioactive silicate-based glasses

In order to improve the bioactivity, stimulating effects on osteogenesis, angiogenesis and antibacterial effects of bioactive glasses in a specific physiological environment, many methods

have been studied incorporating various metal ions in the silicate network. Different substituted silicate glasses exhibit a certain level of acellular bioactivity when tested *in vitro* by standard SBF test, according to Kokubo et al. [21]. The formation of HCA layer on the surface has been the unit of bioactivity measurement as from these results one can assume the bioactivity *in vivo*.

#### 2.9.3.1. Zinc-bioactive glass

Zinc is an essential trace element in our body as it is a cofactor for many enzymes. It also helps to stimulate protein synthesis which is essential for DNA replication and also has an important role in the growth, development and differentiation of bone cell [184–187]. In addition, zinc also has antibacterial properties against *Staphylococcus aureus* [188].

Balamurugan et al. synthesised a bioactive glass in CaO-P<sub>2</sub>O<sub>5</sub>-SiO<sub>2</sub>-ZnO system by the sol-gel method containing 5 mol% ZnO which increased ALP activity and osteoblast proliferation [189]. They also examined that incorporation of zinc does not reduce the bioactivity of the bioactive glass. Higher surface area of Zn-substituted glass can be a better nucleation site when immersed in SBF solution making the calcium phosphate phase more crystalline [190, 191]. Recently, Atkinson et al. found that up to 5 mol% of zinc substitution in a sodium-free bioactive glass composition has the ability to induce apatite formation alongside a calcite phase. Increase in Zn content has a tendency to decrease the calcite phase, however it does not affect the apatite deposition [187]. This calcite phase can also bond with bone without the formation of an appetite layer [192]. Du et al. observed that initially Zn retarded the nucleation of HCA at the early stage of SBF soaking, but did not affect the HCA formation in long-term immersion [193]. Scientists have also reported that more than 10 mol% of Zn has a negative effect on bioactivity and after 20% an excessive drop can be seen [194]. ZnO can act as a network modifier or an intermediate oxide or both in the glass structure. It is found that up to a certain amount ZnO works as a network modifier, but with increasing ZnO content it switched from network modifier to an intermediate oxide [191]. Shahrabi et al. found that 5 mol% ZnO may reduce the number of non-bridging oxygen atoms, resulting in a decrease in glass bioactivity [195]. Zinc has the ability to remove cations from silica network and the new bond formed (Si-O-Zn) have considerably lower bond strength than Si-O-Si bond, which leads to decline in glass transition temperature. As observed, zinc can show very good antibacterial activity for the *Bacillus subtilis* and *Pseudomonas aeruginosa* strains [187].

#### 2.9.3.2. Strontium-bioactive glass

Strontium (Sr) is a naturally occurring mineral found in water and food. It is also an essential trace element of human body. The total amount of Sr in human body of a 70 kg standard man is around 0.32 g. Recently, researchers have found that Sr positively affects bone metabolism to promote bone formation and osteoblast replication while inhibiting bone resorption by osteoclasts [196]. Evidence also showed that strontium not only enhances osteogenic differentiation, but also helps to stabilise the bone structure [197]. However, too much Sr may

increase the number of osteoclast cells which can inhibit bone regeneration and remodelling, leading to osteonecrosis. Thus, strontium has very good effects up to an optimum level. Among the trace elements human body have, only Sr was correlated with bone compression strength [198]. *In vitro* and *in vivo* studies showed that strontium ions upregulate osteoblasts and downregulate osteoclasts [175, 199]. The presence of Sr on the surface of a biomaterial decreases the rate of ion-release at the defect site, which is therapeutically beneficial [200]. Sr-substituted boron glasses show a good adhesion with osteoblast-like cells, Saos-2, thus enhances the cytocompatibility of borate glass. Lao et al. confirmed that Sr-doped bioactive glasses are more bioactive *in vitro* than their original counterparts. Sr-doped glasses are also able to increase the rate of bone-like apatite layer formation on their surface. Moreover, it also decreases the Ca/P ratio very rapidly, which leads to faster stability of apatite layer, and hence greater bioactivity [201]. Substitution of 5 wt% strontium in place of calcium shows advantageous effect on foetal mouse calvarial bone cells [202].

Strontium-based bioactive glasses has a tendency to increase metabolic activity in osteoblasts and to decrease osteoclast activity. The decrease of osteoclasts is may be caused by decreasing tartrate resistant acid phosphate activity and inhibiting resorption of calcium phosphate films [203]. In some cases, it was found that substitution of Sr in place of Ca is more effective strategy for building materials suitable for bone regeneration therapies [203]. The substitution of Ca by Sr (in mol%) sometimes increases silica content as Sr is heavier than Ca, which results in reduced solubility and hence bioactivity. Though replacing by wt% sometimes increases the rate of HCA formation [201, 204]. In comparison, Sr is slightly larger than Ca, which expands the silica network and increases ion dissolution rates, leading to significantly increased *in vitro* and *in vivo* reactivity. The *in vivo* bioactivity is greater in the case of Sr-doped bioactive glasses due to the biological effects of Sr on bone-forming cells [205].

In corporation of mesoporosity in bioactive glass was found to enhance bone-forming ability, degradation and drug delivery properties compared with traditional bioactive glasses. Therefore, there has been a growing interest on ion-doped mesoporous bioactive glasses and their properties. Zhang et al. found that Sr-MBG shows very good mechanical stability from the viewpoint of its original counterpart, which is required for bone repair [206]. They also observed good apatite forming ability of the Sr-doped MBG. Further study of Sr-MBG scaffolds showed that substitution of Sr for Ca stimulated the proliferation, ALP activity, osteogenic-related gene expression and ECM mineralisation of MC3T3-E1 cells [206].

Zhao et al. tested Sr-MBG scaffold in restoration of the rat critical-sized calvarial defects model and found that Sr-MBG scaffolds have superior osteoconductive property in course to normal MBG scaffolds. Moreover, it was found that Sr-MBG scaffolds has a tendency to stimulate new blood vessel formation in bone defect areas [207]. Very recently, Sriranganathan et al. reported that with increase of the Sr substitution for Ca in high phosphate bioactive glasses decreases the formation of apatite layer directly. They proposed that the apatite formation proceeds via the formation of an octacalcium phosphate ( $\text{Ca}_8(\text{PO}_4)_6\text{H}_2 \cdot 5\text{H}_2\text{O}$ ) phase, which then transforms into hydroxyl-carbonate apatite. Above a certain concentration of strontium, the octacalcium phosphate phase is unable to form, which ultimately delays the HCA formation [208].

### 2.9.3.3. Lithium-bioactive glass

Lithium has a prolonged medical history as it has been used for over 100 years to treat manic depression [180]. Lithium also marked its importance in the treatment of both bipolar and unipolar depressive disorders. Along with that lithium also has several other effects on blood and brain [181]. Clinicians also observed that lithium often increases the white blood cell counts (granulocytosis) and reduces blood lymphocyte counts (lymphopenia). Lithium also has a tendency to enhance immunological activities of monocytes and lymphocytes. Researchers have also found evidence of lithium in bone mineral metabolism [182, 209, 210].

*In vitro* bioactivity test indicates a decrease in bioactivity with increase in lithium-ion concentration. The theory behind it is that lithium forms lithium oxide groups by reacting with the hydroxyl groups present in the pure sol-gel, which limits crystal formation. Recently, Khorami et al. observed the *in vitro* bioactivity of lithium substituted 45S5 glasses and found no certain advantage of lithium in the reactivity of the bioactive glass composition. A theory based on observations state that *in vitro* reactivity increases with increasing glass solubility. In this study, lithium was replaced for sodium (in wt%) and hence a little decrease in the molar concentration of glass network formers ( $\text{SiO}_2$  and  $\text{P}_2\text{O}_5$ ) takes place, which may result in an increase in glass solubility. However, the ionic radius of  $\text{Li}^+$  is lower than  $\text{Na}^+$ . Thus, lithium has a strong affinity for bonding to oxygen and tends to contract the free spaces in the silicate network. This phenomenon reduces the rate of glass dissolution and improves chemical durability [211].

The release of lithium ions in SBF is higher for sample with higher lithium content, with an initial burst in the first 24 h followed by more sustained release. Lithium also shows ALP activity and mineralisation in a dose-dependent manner from 0.2 to 0.85 ppm when exposed to murine osteoblast cells [212].

### 2.9.3.4. Magnesium-bioactive glass

Magnesium naturally exists in human body and it is amongst the most important elements in the bone matrix. Enamel, dentin and bone contain 0.44, 1.23 and 0.72 wt% magnesium, respectively [213]. Magnesium is involved in over 300 chemical reactions inside human body. It is also known to activate phagocytosis and regulate active calcium transport. Magnesium also has positive effect in wound healing, bone metabolism, fracture prevention and bone density [214, 215].

When doped, Mg can act as a network former or network modifier. This indicates that an increase in Mg content may lead to more  $\text{Mg}^{2+}$  ions participating in the silica network by making weaker Si-O-Mg bond rather than stronger Si-O-Si bonds, leading to weakening of overall glass network [216]. With increasing MgO content glass degradation gradually decreases, and the formation of apatite layer is hampered [213, 217].

MgO can affect the surface reactivity of Mg-doped bioactive glasses by indirectly influencing the early stage of mineralisation by favouring the silica atom with non-bridging oxygen speciation [116]. Surface reactivity of Mg-BG increases with increasing MgO/CaO ratio, which can play an important role in glass bioactivity. Based on another study, it was found that the

role of  $Mg^{2+}$  in the formation of HCA apatite layer in  $SiO_2$ -CaO- $Na_2O$ - $P_2O_5$  system was insignificant. These contradictory observations created a variety of theories based on ionic potential [218], structural parameter [66] or network connectivity [219]. However, all these theories failed to explain glass bioactivity properly. Varanasi et al. observed significant effect of MgO on the osteoblast differentiation [220]. Other studies also support the increased osteoblast proliferation and differentiation. These findings proved the positive effect of magnesium doping in the bioactivity of bioactive glass.

#### 2.9.3.5. Silver-bioactive glass

In bone reconstruction surgeries, there are two main factors that should be considered: (1) chemical bond with living bone; (2) prevents bacterial infection. As we know that bioactive glasses show well bioactivity and bond with living bone, but a colonisation of bacteria on the surface of the implant can lead to failure of the treatment. The consequences of implant infections are serious and sometimes it leads to second surgery with a lot of suffering [221].

Due to the antimicrobial properties of silver, the recent focus on development of silver-doped implants is increasing. The antibacterial properties of bioactive glasses containing silver have been investigated by several researchers [222, 223]. The main advantage of incorporating silver ions in a gel-glass system is that the porous glass matrix enables a controlled, sustained delivery of antibacterial agent. Some researchers found that high concentration (2 wt%) of silver ions show cytotoxicity, but in the range of 0.75-1 wt% silver has no toxic influence [224]. Due to the higher efficacy of silver, it has gained the interest of scientists, and after extensive research different mechanisms have been proposed for its antimicrobial activities:

1. Interface with electron transport.
2. Binding to DNA.
3. Interaction with the cell components [225, 226].

Silver incorporation has no significant effect over the bioactivity of the glass [222]. However, silver has a tendency to reduce the dissolution of silica when replaced in place of calcium. As silver is monovalent in comparison with bivalent calcium ion, it takes two silver ions to make two non-bridging oxygen groups in place of one calcium ion. Thus, replacement of calcium by silver lessens the number of non-bridging oxygen groups, and reduces the glass dissolution [191]. Due to its highly promising antibacterial and anti-inflammatory properties, silver-doped bioactive glasses are considered to be very useful for wound healing applications alongside tissue engineering.

### 3. Clinical relevance of doped bioactive glass

Bioactive glasses are that bone substitutes which possess the unique property of osteoconduction as well as osteoproduction by stimulating proliferation and differentiation of osteoprogenitor cells through a direct genetic control [24,

227]. The discovery of these new materials led Hench and Wilson to propose the concept of osteostimulation or osteopromotion to define this class of bioactive materials and their effects on the genetic activation of bone cells [228]. Bioactive glasses are surface reactive biomaterials that, when in contact with physiological fluids, release soluble ionic products that have been suggested to stimulate *in vitro* osteogenesis [227, 229]. On critical analysis, Young's modulus of bioactive glass being between 30 and 50 GPa, nearly that of natural bone, is a great advantage. One disadvantage is the low mechanical strength and decreased fracture resistance [230]. This can be easily overcome by altering the composition, using it in low load-bearing areas, and using it for the bioactive stage. Furthermore, bioactive glass manufactured via the sol-gel technique permits the synthesis of material with higher purity and homogeneity at low temperatures [52]. Additives can be easily introduced during the sol-gel process to improve the bioactivity of such glasses. Indeed, improvement of the biological properties of bioactive materials can be achieved by the incorporation of ions (doping) that positively affect osteoblast behaviour and consequently enhance new bone formation [202].

In addition, *in vivo* studies have demonstrated beneficial results from their use in various clinical situations [231–234]. After implantation, interaction with surrounding tissues results in a time-dependent alteration of the material's surface and the formation of a hydroxyl carbonate apatite layer that is very similar to the mineral phase of bone [235]. More recently, a new category of sol-gel glasses has been manufactured with enhanced bioactivity and open pores enclosed in a mesoporous matrix [134, 236]. Furthermore, bioactive glass manufactured via the sol-gel technique permits the synthesis of materials with higher purity and homogeneity at low temperatures [52]. Additives can be easily introduced during the sol-gel process to improve the bioactivity of such glasses. Indeed, improvement of the biological properties of bioactive materials can be achieved by the incorporation of ions that positively affect osteoblast behaviour and consequently enhance *de novo* bone formation.

Metallic ions in body play a crucial role as cofactors of enzymes and excite a chain of reactions related to cell signalling pathways [176]. A number of literatures have been cited on the interaction of metallic ions in various diseases and metabolic disorders such as cancer, CNS disorders, infectious diseases and hormonal disorders [237, 238]. Hence, the effectiveness and selectivity of the beneficial effect of metallic ions can be enhanced by controlling the exact level in the body. Additionally, due to unstable ionic states of certain metallic ions, toxic effects may follow while directly ingested. Hence, wide spread research is underway to develop matrices to control the local release of metallic ions with less systemic toxicity as well as availability of relatively high concentrations of metallic-ion-based drugs to target tissues. The degree of metallic ion loading into matrices for local delivery as well as their controlled and sustained release is of paramount importance for optimal therapeutic use. Common strategy is to load metallic ions into matrices such as hydroxyapatite, bioactive glass, silica and carbon fibres to improve ionic stability and to release for a prolong period of time [148, 239–248]. Due to these superior characteristics, metallic ion doping in biomaterials is an alternative, cost-effective, safe strategy than use of recombinant proteins or genetic engineering approaches [249].

### 3.1. Doped bioactive glass in bone regeneration

In bone tissue engineering, bioceramics or bioactive glasses and biodegradable polymers [15], often comprise metallic ions as part of the bioceramic or bioactive glass structural composition. The metal ion is generally released during their degradation *in vitro* or *in vivo* [148, 250]. For instance, when bioactive glass (e.g., 45S5 Bioglass) [26, 251] is used as scaffolds to fill a bone defect, critical concentrations of soluble Si, Ca, P and Na ions are released, with the capacity to generate both intracellular and extracellular effects at the interface between the glass and the cellular environment [124, 133, 148, 227, 252–261]. It has also been observed that released ions from bioactive glasses can induce gene expression which in turn helps in bone metabolism by signal transduction as well as enhance cell differentiation and osteogenesis [27, 124, 227, 254]. Furthermore, the ionic dissolution products of bioactive glasses can also encourage angiogenesis [262]. Other metallic ions which may have significant role in bone tissue engineering include copper, magnesium, strontium, manganese, iron, zinc and silver owing to their imminent role as cofactors in metabolic processes in bone, articular tissues and immune system functions [149, 263].

The application of chitosan-doped bioactive glass (BG-CH) was assessed in the guided bone regeneration in ovariectomised rats. The histomorphometric analysis showed increased bone/tissue volume, osteoblast number and osteoblast surface/bone surface and trace elements such as Sr and Fe were detected in the newly formed bone may be responsible for enhanced bone healing and found clinically useful as a therapeutic and implantable material [264].

Zinc being a trace mineral in human body performs a variety of functions in relation to the immune system, cell division, fertility and the body growth and maintenance. Moreover, zinc is also a necessary element for the formation, mineralisation, development and maintenance of healthy bones. These unique properties of zinc evoked the interest of researchers to use it along with silicate-based bioactive glasses for bone tissue engineering and found to have significant ability to enhance antibacterial effects, bioactivity and distinct physical, structural and mechanical properties of bioactive glasses [265]. Zinc also stimulates bone formation and mineralisation by activating aminoacyl-tRNA synthetase in osteoblastic cells, and it stimulates cellular protein synthesis. Zinc plays a role in the preservation of bone mass by inhibiting osteoclast-like cell formation from marrow cells [171]. It also promotes attachment, proliferation of osteoblast and increase ALP expression that is responsible for laying down the bone callus. The doping of Zn into bioactive glasses produces higher chemical stability and densification of glasses matrices. Zinc doping in bioglass for repair of diaphyseal defect creates a good link of interface between bone and Zn-BG during the first speeds, whereas during the last speeds osseointegration, resorption and degradation of bioactive glass and their replacement by bone cells occurs [266].

Strontium (Sr) is a naturally occurring trace element often acts similarly to Ca in the human body; both have strong bone-seeking properties, and Sr can be substituted with Ca in the apatitic phase of bone mineral [267]. Administration of Sr in moderate doses prevented caries in rats [268]. Among the trace metals present in human bone, Sr was the only that was correlated with bone compression strength [198]. Furthermore, over the past few years, Sr has attracted attention through its beneficial effects on bone healing. Indeed, both *in vitro* and *in*



*in vivo* studies have demonstrated stimulatory effects of Sr on osteoblasts and an inhibitory effect on osteoclasts, associated with an increase in bone density and resistance [199, 269–271]. Nowadays, strontium ranelate is used as a commercial antiosteoporotic oral drug that has been proven to reduce the incidence of fractures in osteoporotic patients [196, 272]. Addition of strontium-substituted bioactive glass (SrBG) into PCL and fabricating into 3D bioactive composite scaffolds utilising additive manufacturing technology yield higher compressive Young's modulus [273]. Oxidative stress, a pivotal pathological factor inducing bone osteoporosis, can also be reduced by Zn doping of bioglass in ovariectomised Wistar rats as Zn significantly enhances superoxide dismutase (SOD), catalase (CAT) and glutathione peroxidase (GPx) and the Ca/P ratio whereas decreases thiobarbituric acid-reactive substances and thus improves bone mineralisation [274]. The study on effects of the substitution of calcium oxide with Sr on bioactive glass also shows promotion of osteogenesis in a differentiating bone cell culture model using mesenchymal stromal cells obtained from rat bone marrow and proved to be potential for bone tissue regeneration [275]. Sr-doped bioglass implant enhances bone regeneration in patients suffering from osteoporosis [276]. The growing evidence of the beneficial effects of strontium on bone justifies the increasing interest in Sr incorporation into biomaterials for hard tissue repair. Thus, strontium-doped bioactive glasses have been recently developed via a sol-gel method that enables a better control of the reaction kinetics [201, 277].

A multifunctional bioactive scaffold should combine angiogenesis capacity, and osteostimulation, for regenerating lost bone tissues. To achieve these objectives when copper (Cu)-containing mesoporous bioactive glass (Cu-MBG) scaffolds with interconnective large pores are used *in vitro* both Cu-MBG scaffolds and their ionic extracts stimulates hypoxia-inducible factor (HIF)-1 $\alpha$  and vascular endothelial growth factor (VEGF) expression in human bone marrow stromal cells (hBMSCs). Thus, incorporation of Cu<sup>2+</sup> ions into MBG scaffolds increase hypoxia-like tissue reaction which enhance angiogenesis and osteogenesis and has promising scope for the treatment of large bone defect [278]. Controlled delivery of 3 wt% CuO from borate bioactive glass scaffolds implanted in rat calverial defect shows significantly better capacity to stimulate angiogenesis and regenerate bone when compared to the undoped glass scaffolds [279]. It is also evident that copper-doped bioglass scaffold *in vivo* acts on BMSCs ((bone-marrow derived mesenchymal stem cells) to stimulate secretion of VEGF which in turn enhances the angiogenic growth into the scaffolds [280]. Copper (Cu) has the property to stimulate vascularisation/angiogenesis and silicate bioceramics have also stimulatory effects on vascularisation *in vitro* due to the release of silicon (Si) ions. Hence, when combined in bioceramic implant Cu and Si have synergistic effects [281].

Biomaterial-centred bacterial infection, one of the major reasons for revision surgery [282], led the researchers to explore such material that could control infection as well as promote bone healing. Incorporation of silver oxide (Ag<sub>2</sub>O) proved its promising future to combat against microbial infection on biomedical materials and devices [241, 242, 283–285]. The introduction of Ag<sub>2</sub>O into the bioactive glass shows promising bactericidal efficacy against *Escherichia coli*, *P. aeruginosa* and *S. aureus* *in vitro* by leaching of Ag<sup>+</sup> ions from bioglass matrix [223, 286–288]. Doping of Ag<sup>+</sup> ions in 45S5 bioglass based scaffolds even proves to be effective against MRSA (methicillin-resistant *S. aureus*) *in vitro* [289]. Silver-doped bioactive gel-glass Ag-S70C30 has

beneficial role as antimicrobial wound healing agent in inflammatory response in a local body compartment such as in acne lesions and in non-healing dermal wounds as it has no cytotoxicity against human epidermal keratinocytes [290]. Mesoporous bioactive glasses doped with Ti/Ag have improved hydroxyapatite- (HAP) induced growth and antimicrobial properties and more potency than pure MBGs in bone-tissue regeneration and surgery [291]. Very recently, scaffolds of a borosilicate bioactive glass (composition: 6Na<sub>2</sub>O, 8K<sub>2</sub>O, 8MgO, 22CaO, 36B<sub>2</sub>O<sub>3</sub>, 18SiO<sub>2</sub>, 2P<sub>2</sub>O<sub>5</sub>; mol%) doped with varying amounts of Ag<sub>2</sub>O (0.05, 0.5 and 1.0 wt%) is being used for bone defect repair and as well as to control infection caused by *E. coli* and *S. aureus*. Better adhesion, proliferation and alkaline phosphatase activity of murine osteoblastic MC3T3-E1 cells on the Ag<sub>2</sub>O-doped bioactive glass scaffolds is found than on the undoped scaffolds *in vitro* [292].

Wnt pathway has been found to play a central role in controlling embryonic bone development and bone mass [293] during the past decade. In the developing skeletogenesis, Wnt signalling is required for limb bud initiation, early limb patterning, and, finally, late limb morphogenesis events. It has been reported that Wnt-3a and Wnt-7a are expressed in the limb bud and have roles in skeletal pattern determination [294], and that Wnt-14 is involved in joint formation [295]. In addition, Wnt-3a, Wnt-4, Wnt-5a and Wnt-7a all influence cartilage development [295]. Wnt are 39-46 kDa cysteine-rich, secreted glycoproteins that have been identified in organisms ranging from hydra to humans [296]. Recently, it has been suggested that canonical Wnt signalling plays an important role in fracture healing [297]. Lithium (Li) is an element known to mimic the Wnt signalling pathway, which plays a central role in osteoblast proliferation and differentiation [298]. Expression of various Wnts has been reported to be upregulated during fracture repair, and increased  $\beta$ -catenin signalling by lithium administration has been shown to improve fracture healing [299]. Edgington et al. reported that lithium-based dopants to  $\beta$ -TCP induced an effect on the cell-material interaction of osteoblast cells as well as the study exhibited increased proliferative activity at the lower concentration of Li-doping, while the higher concentration showed a decrease in activity, indicating a toxic effect of Li at elevated doses *in vitro* [300]. Lithium activates  $\beta$ -catenin signalling by inhibiting GSK3 $\beta$  [301–303]. It is also reported that lithium enhances bone formation and improves bone mass in mice [304]. Bioactive glasses with Li-containing composition (55% SiO<sub>2</sub>-36% CaO-4% P<sub>2</sub>O<sub>5</sub>-5% Li<sub>2</sub>O) synthesised through a quick alkali sol-gel process stimulate apatite formation after immersion in SBF. Furthermore, addition of Li enhances chemical durability and antibacterial activity against *Enterococcus faecalis*. Li-doped bioglass has excellent antibacterial property against tooth infections for the treatment of root canal, other dental applications [305]. Researches reveal that different concentrations of Li<sub>2</sub>O (0-12 wt%) substitution for Na<sub>2</sub>O in 45S5 bioglass causes *in vitro* more apatite formation and osteoblastic cell responses than non-substituted 45S5 bioglass thus prove its efficacy for bone defect filler [211]. Another study shows that Li doping in therapeutic range (<8.3 ppm) in 45S5 Bioglass causes more HA deposition than non-doped bioglass *in vitro* [306].

There are even some more ions or materials, doping of which positively improve the quality, bioactivity or bone regeneration. Study with boron modified bioactive glass particle shows significantly more thickness of osseointegrated tissue and more area of neoformed bone tissue

than non-doped 45S5 glass along with increase in the Ca:P ratio. Boron modification enhances bone formation more than 45S5 glass when implanted into the intramedullary canal of rat tibiae [307]. Modification of bioactive glass by substitution of Na<sub>2</sub>O with doping of fluorides, such as CaF<sub>2</sub> and MgF<sub>2</sub> or B<sub>2</sub>O<sub>3</sub>, increases its mechanical property [308]. Nickel and cobalt both stimulate the hypoxia-inducible factor-1 (HIF-1 $\alpha$ ), which significantly improving blood vessel formation in tissue engineering applications. No significant structural differences or dissolution rate occur when nickel and cobalt are doped in bioactive glasses [309]. Magnesium-doped melt-derived glasses in the system SiO<sub>2</sub>-CaO-Na<sub>2</sub>O-P<sub>2</sub>O<sub>5</sub> influences the formation and the evolution of the newly formed layers, promotes the dissolution of the silica network, increases the thickness of the silica gel layer as well as slows down the crystallisation of the apatite layer [310]. Silica- and phosphate-based bioactive glass nanoparticles (58SiO<sub>2</sub>-33CaO-9P<sub>2</sub>O<sub>5</sub>) doped with neem (*Azadirachta indica*) leaf powder and silver nanoparticles show good antimicrobial activity against *S. aureus* and *E. coli* and less bioactivity compared with silver-doped glass particles [311].

### 3.2. Doped bioactive glass as coating of orthopaedic implants

Since the discovery of bioglass it had mainly been used for coating of metallic implant which are bioinert in nature, i.e. bonding ability to bone tissue is poor [312]. On the other hand, bioglass being an excellent osteogenic agent it has also some inherent disadvantages such as poor mechanical properties leading to its limited application in load-bearing implants where metallic alloys are still the materials of choice. Hence, coatings have drawn attention of researchers as a method to improve adherence of bone tissue to metallic alloy to be used as load-bearing implant in orthopaedic surgery. For this purpose, coating material should have thermal coefficient similar to that have bioglass, as well as, has some other properties such as firing cycle during preparation of coating should not degrade the quality of metal and optimum adherence should be achieved with hydroxyapatite formation in contact with body fluid.

To achieve the goal researchers embedded bioglass or hydroxyapatite particles on coating of Ti6Al4V by a simple enamelling technique to enhance their bioactivity and found excellent glass/metal adhesion with well-attached bioactive particles on the surface that can withstand substantial chemical and mechanical stresses [313]. Another family of glasses in the SiO<sub>2</sub>-Na<sub>2</sub>O-K<sub>2</sub>O-CaO-MgO-P<sub>2</sub>O<sub>5</sub> system has been synthesised for coatings on Ti-based and Co-Cr alloys by the scientists, where desired achievement were observed to alloys by formation of 100–200 nm thick interfacial layers (Ti<sub>5</sub>Si<sub>3</sub> on Ti-based alloys and CrO<sub>x</sub> on Co-Cr) and commercially Ti alloy-based dental implants were fabricated with 100  $\mu$ m thick glass coatings successfully [314]. Surgical suture materials such as absorbable polyglactin 910 and non-resorbable Mersilk when coated with silver-doped bioactive glass powder (AgBG) and tested *in vitro*, after 3 days of immersion in SBF, hydroxyapatite forms on the coated suture surfaces and thus their bioactive behaviour is enhanced as a result their use in body wall repair and wound healing property is also enhanced [243] it also limits bacterial attachment [315]. *In vivo* histologic and histomorphometric study on osteointegration of gradient coatings composed of bioactive glass and nanohydroxyapatite (BG-nHA) on titanium-alloy orthopaedic implants and surrounding

bone tissue. Fluorescence micrograph shows better osteointegration of orthopaedic implant in BG-nHA than uncoated implant [316].

Mesoporous bioactive glass coatings immobilised with L-ascorbic acid phosphate magnesium salt *n*-hydrate (AsMg) on stainless steel plate causes osteoblast MC3T3-E1 cells stimulation by the MBG with enhanced cell attachment, proliferation, differentiation and better developed cytoskeleton as well as, enhanced fibroblast NIH3T3 proliferation *in vitro* [317]. To compare the behaviour of hydroxyapatite and the bioactive glass coated titanium dental implants different clinical and radiological parameters were studied for 12 months in 31 patients. The study revealed equal potency of bioglass as hydroxyapatite to achieve osteointegration in dental implants [318]. Similarly, nanoparticulate bioactive glass coating on the porous titanium implants promotes better osteointegration and stimulates the formation of bone within the pores than non-coated implants [319]. Incorporation of nanosized HAP into ZnO containing bioglass coating on Ti-6Al-4V substrate improves mechanical properties of the coating but do not hamper *in vitro* bioactivity [320]. Composite orthopaedic coatings with antibacterial capability containing chitosan, Bioglass particles (9.8 µm) and silver nanoparticles (Ag-np) were coated in stainless steel 316 substrate and studied *in vitro* in SBF. Result showed low released concentration of Ag ions (<2.5 ppm) was efficiently antibacterial against *S. aureus* up to 10 days and coating enhanced proliferation of MG-63 osteoblast-like cells up to 7 days in culture and it was also found that high concentration of Ag-np (342 µg) have cytotoxic effect [321]. 45S5 bioglass-silica coatings on 316L stainless steel also causes good osteointegration as well as prevents the metallic implant from corrosion in presence of body fluid [322].

### 3.3. Doped bioactive glass for delivery of growth factors in bone healing

Growth factors are proteins secreted by cells, act on the appropriate target cell or cells to carry out specific action and thereby their over expression have also been shown in different stages of fracture healing. This phenomenon has led the researchers to study their role as well as the potential to be used as therapeutic agent to accelerate fracture healing. Hence, growth factors are also incorporated into bioactive glass implant, scaffold or coating materials to enhance osteogenic property. Incorporation of bioactive glass and fibroblasts into alginate beads stimulates VEGF as a result potentially it can be used for therapeutic angiogenesis [323]. Combination of prolonged localised VEGF presentation from a matrix coated with a bioactive glass enhances bone regeneration as VEGF has beneficial role in osteogenesis [324]. The combination of novel MBG/silk fibrin scaffold and BMP7 and/or PDGF-B adenovirus synergistically promotes wound healing in acute buccal periodontal defects and osteoporosis related fracture by recruitment of recruitment of mesenchymal progenitor cells [325, 326]. Borate bioactive glass microfibrils doped with 0-3.0 wt% CuO has remarkable ability to stimulate angiogenesis which help to heal full-thickness skin defects in rodents and promotes human umbilical vein endothelial cells (HUVEC) migration, tubule formation and secretion of vascular endothelial growth factor, as well as the expression of angiogenic-related genes of the fibroblasts *in vitro* [327].

## 4. Conclusion and final remarks

Innovative research on bone tissue engineering has made considerable strides over the few decades in the development of new materials, processing techniques and their evaluation and applications. Bioresorbable scaffolds with controlled porosity and tailored properties are of paramount necessity in the successful outcome of bone healing. Silicate bioactive glasses have been extensively investigated over last 40 years. Borate and borosilicate bioactive glass compositions are promising and currently being used in tissue engineering. Although the ability of bioactive glass to support osteogenesis has been proved, recent work has shown the angiogenic potential which may be utilised for the benefits of bioactive glass to soft tissue repair. Due to its biodegradable properties, it may release ions during the degradation process. Apart from doping the bioactive glass with several metallic ions, the degrading ions of its own are known to have a beneficial effect on osteogenesis and on angiogenesis. Current findings show that they may also have a favourable effect on chondrogenesis. Metallic ion doping with the presently available bioactive glass may further improve the biological performance of the material that may open a new vista in bone tissue engineering. Future research will take benefit of the advantageous properties of doped bioactive glass in bone healing as well as coating of several metallic implants.

## Author details

Samit Kumar Nandi<sup>1\*</sup>, Arnab Mahato<sup>2</sup>, Biswanath Kundu<sup>2</sup> and Prasenjit Mukherjee<sup>3</sup>

\*Address all correspondence to: samitnandi1967@gmail.com

1 Department of Veterinary Surgery and Radiology, West Bengal University of Animal and Fishery Sciences, Kolkata, India

2 Bioceramics and Coating Division, CSIR-Central Glass and Ceramic Research Institute, Kolkata, India

3 Teaching Veterinary Clinical complex, West Bengal University of Animal and Fishery Sciences, Kolkata, India

## References

- [1] Marastoni S, Ligresti G, Lorenzon E, Colombatti A, Mongiat M. Extracellular matrix: a matter of life and death. *Connective Tissue Research*. 2008;49(3–4):203–6.
- [2] Cancedda R. Cartilage and bone extracellular matrix. *Current Pharmaceutical Design*. 2009;15(12):1334–48.

- [3] Brightman AO, Rajwa BP, Sturgis JE, McCallister ME, Robinson JP, Voytik-Harbin SL. Time-lapse confocal reflection microscopy of collagen fibrillogenesis and extracellular matrix assembly in vitro. *Biopolymers*. 2000;54(3):222–34.
- [4] Xiao G, Gopalakrishnan R, Jiang D, Reith E, Benson MD, Franceschi RT. Bone morphogenetic proteins, extracellular matrix and mitogen-activated protein kinase signaling pathways are required for osteoblast-Specific gene expression and differentiation in MC3T3-E1 Cells. *Journal of Bone and Mineral Research*. 2002;17(1):101–10.
- [5] Benders KEM, van Weeren PR, Badylak SF, Saris DBF, Dhert WJA, Malda J. Extracellular matrix scaffolds for cartilage and bone regeneration. *Trends in Biotechnology*. 2013;31(3):169–76.
- [6] Jones JR, Lee PD, Hench LL. Hierarchical porous materials for tissue engineering. *Philosophical Transactions of the Royal Society of London A: Mathematical, Physical and Engineering Sciences*. 2006;364(1838):263–81.
- [7] Goff T, Kanakaris NK, Giannoudis PV. Use of bone graft substitutes in the management of tibial plateau fractures. *Injury*. 2013;44:S86–S94.
- [8] Ricciardi BF, Bostrom MP, editors. *Bone graft substitutes: Claims and credibility*. *Seminars in Arthroplasty*; 2013. Elsevier.
- [9] Chaikof EL, Matthew H, Kohn J, Mikos AG, Prestwich GD, Yip CM. Biomaterials and scaffolds in reparative medicine. *Annals of the New York Academy of Sciences*. 2002;961(1):96–105.
- [10] Griffith LG. Emerging design principles in biomaterials and scaffolds for tissue engineering. *Annals of the New York Academy of Sciences*. 2002;961(1):83–95.
- [11] Karageorgiou V, Kaplan D. Porosity of 3D biomaterial scaffolds and osteogenesis. *Biomaterials*. 2005;26(27):5474–91.
- [12] Levenberg S, Langer R. Advances in tissue engineering. *Current Topics in Developmental Biology*. 2004;61:113–34.
- [13] Hutmacher DW. Scaffolds in tissue engineering bone and cartilage. *Biomaterials*. 2000;21(24):2529–43.
- [14] Kellomaki M, Niiranen H, Puumanen K, Ashammakhi N, Waris T, Tormala P. Bioabsorbable scaffolds for guided bone regeneration and generation. *Biomaterials*. 2000;21(24):2495–505.
- [15] Rezwani K, Chen QZ, Blaker JJ, Boccaccini AR. Biodegradable and bioactive porous polymer/inorganic composite scaffolds for bone tissue engineering. *Biomaterials*. 2006;27(18):3413–31.
- [16] Torres AL, Gaspar VM, Serra IR, Diogo GS, Fradique R, Silva AP, et al. Bioactive polymeric-ceramic hybrid 3D scaffold for application in bone tissue regeneration. *Materials Science and Engineering: C*. 2013;33(7):4460–9.

- [17] Hench LL, Wilson J. An introduction to bioceramics. World Scientific; Singapore, 1993.
- [18] Kokubo T. Bioceramics and their clinical applications. Elsevier; England, 2008.
- [19] Hench LL. The future of bioactive ceramics. *Journal of Materials Science: Materials in Medicine*. 2015;26(2):1–4.
- [20] Salinas AJ, Vallet-Regi M. Bioactive ceramics: from bone grafts to tissue engineering. *RSC Advances*. 2013;3(28):11116–31.
- [21] Kokubo T, Takadama H. How useful is SBF in predicting in vivo bone bioactivity? *Biomaterials*. 2006;27(15):2907–15.
- [22] Williams D. Consensus and definitions in biomaterials. *Advances in Biomaterials*. 1988;8:11–6.
- [23] Jones JR. Review of bioactive glass: from Hench to hybrids. *Acta Biomaterialia*. 2013;9(1):4457–86.
- [24] Hench LL, Splinter RJ, Allen WC, Greenlee TK. Bonding mechanisms at the interface of ceramic prosthetic materials. *Journal of Biomedical Materials Research*. 1971;5(6): 117–41.
- [25] Hench LL. Bioceramics: from concept to clinic. *Journal of the American Ceramic Society*. 1991;74(7):1487–510.
- [26] Hench LL. Biomaterials: a forecast for the future. *Biomaterials*. 1998;19(16):1419–23.
- [27] Hench LL, Polak JM. Third-generation biomedical materials. *Science*. 2002;295(5557): 1014–7.
- [28] Hench LL, Hench JW, Greenspan DC. Bioglass: a short history and bibliography. *Journal of the Australasian Ceramic Society*. 2004;40(1):1–42.
- [29] Guarino V, Causa F, Ambrosio L. Bioactive scaffolds for bone and ligament tissue. *Expert Review of Medical Devices*. 2007;4(3):405–18.
- [30] Hutmacher DW, Schantz JT, Lam CXF, Tan KC, Lim TC. State of the art and future directions of scaffold-based bone engineering from a biomaterials perspective. *Journal of Tissue Engineering and Regenerative Medicine*. 2007;1(4):245–60.
- [31] Jones JR. New trends in bioactive scaffolds: the importance of nanostructure. *Journal of the European Ceramic Society*. 2009;29(7):1275–81.
- [32] Jones JR. Bioactive ceramics and glasses. In *Tissue engineering using ceramics and polymers*. Cambridge, UK: Woodhead Publishing Limited; 2007.
- [33] Chen X, Meng Y, Li Y, Zhao N. Investigation on bio-mineralization of melt and sol-gel derived bioactive glasses. *Applied Surface Science*. 2008;255(2):562–4.
- [34] Gupta R, Kumar A. Bioactive materials for biomedical applications using sol-gel technology. *Biomedical Materials*. 2008;3(3):034005.

- [35] Hench LL. The story of Bioglass®. *Journal of Materials Science: Materials in Medicine*. 2006;17(11):967–78.
- [36] Lacefield W, Hench L. The bonding of Bioglass® to a cobalt–chromium surgical implant alloy. *Biomaterials*. 1986;7(2):104–8.
- [37] Hench LL, Andersson O. Bioactive glass coatings. *Advanced Series in Ceramics*. 1993;1:239–60.
- [38] Bloyer DR, Gomez-Vega JM, Saiz E, McNaney JM, Cannon RM, Tomsia AP. Fabrication and characterization of a bioactive glass coating on titanium implant alloys. *Acta Materialia*. 1999;47(15):4221–4.
- [39] Moritz N, Vedel E, Ylänen H, Jokinen M, Hupa M, Yli-Urpo A. Characterisation of bioactive glass coatings on titanium substrates produced using a CO<sub>2</sub> laser. *Journal of Materials Science: Materials in Medicine*. 2004;15(7):787–94.
- [40] Borrajo JP, Serra J, González P, León B, Muñoz FM, Lopez M. In vivo evaluation of titanium implants coated with bioactive glass by pulsed laser deposition. *Journal of Materials Science: Materials in Medicine*. 2007;18(12):2371–6.
- [41] Lopez-Esteban S, Gutierrez-Gonzalez CF, Gremillard L, Saiz E, Tomsia AP. Interfaces in graded coatings on titanium-based implants. *Journal of Biomedical Materials Research Part A*. 2009;88(4):1010–21.
- [42] James P. Glass ceramics: new compositions and uses. *Journal of Non-Crystalline Solids*. 1995;181(1):1–15.
- [43] Lockyer MWG, Holland D, Dupree R. NMR investigation of the structure of some bioactive and related glasses. *Journal of Non-Crystalline Solids*. 1995;188(3):207–19.
- [44] Aboud T, Stoch L. Crystallization behavior in the glass system SiO<sub>2</sub>–P<sub>2</sub>O<sub>5</sub>–Al<sub>2</sub>O<sub>3</sub>–MgO–Na<sub>2</sub>O. *Journal of Non-Crystalline Solids*. 1997;219:149–54.
- [45] Szabo I, Nagy B, Völksch G, Höland W. Structure, chemical durability and microhardness of glass–ceramics containing apatite and leucite crystals. *Journal of Non-Crystalline Solids*. 2000;272(2):191–9.
- [46] Begum AN, Rajendran V, Ylänen H. Effect of thermal treatment on physical properties of bioactive glass. *Materials Chemistry and Physics*. 2006;96(2):409–17.
- [47] Liu J, Miao X. Sol–gel derived bioglass as a coating material for porous alumina scaffolds. *Ceramics International*. 2004;30(7):1781–5.
- [48] Li N, Jie Q, Zhu S, Wang R. Preparation and characterization of macroporous sol–gel bioglass. *Ceramics International*. 2005;31(5):641–6.
- [49] Xia W, Chang J. Well-ordered mesoporous bioactive glasses (MBG): a promising bioactive drug delivery system. *Journal of Controlled Release*. 2006;110(3):522–30.



- [50] Balamurugan A, Sockalingum G, Michel J, Fauré J, Banchet V, Wortham L, et al. Synthesis and characterisation of sol gel derived bioactive glass for biomedical applications. *Materials Letters*. 2006;60(29):3752–7.
- [51] Balamurugan A, Balossier G, Michel J, Kannan S, Benhayoune H, Rebelo A, et al. Sol-gel derived  $\text{SiO}_2\text{-CaO-MgO-P}_2\text{O}_5$  bioglass system—preparation and in vitro characterization. *Journal of Biomedical Materials Research Part B: Applied Biomaterials*. 2007;83(2):546–53.
- [52] Li R, Clark A, Hench L. An investigation of bioactive glass powders by sol-gel processing. *Journal of Applied Biomaterials*. 1991;2(4):231–9.
- [53] Hench LL, West JK. The sol-gel process. *Chemical Reviews*. 1990;90(1):33–72.
- [54] Rideal E, Davies J. *Interfacial phenomena*. New York: Academic Press; 1963.
- [55] Kaur G, Pandey OP, Singh K, Homa D, Scott B, Pickrell G. A review of bioactive glasses: their structure, properties, fabrication and apatite formation. *Journal of Biomedical Materials Research Part A*. 2014;102(1):254–74.
- [56] Vallet-Regí M. Ceramics for medical applications. *Journal of the Chemical Society, Dalton Transactions*. 2001(2):97–108.
- [57] R.K. Iler, *The colloid chemistry of silica and silicates*, *Soil Science*, 80 (1955) 86.
- [58] Brinker CJ, Scherer GW, Roth E. Sol→ gel→ glass. II. Physical and structural evolution during constant heating rate experiments. *Journal of Non-Crystalline Solids*. 1985;72(2):345–68.
- [59] Hench LL, Ulrich DR. *Science of ceramic chemical processing*. Wiley-Interscience; 1986.
- [60] Colby MW, Osaka A, Mackenzie JD. Temperature dependence of the gelation of silicon alkoxides. *Journal of Non-Crystalline Solids*. 1988;99(1):129–39.
- [61] Falcone JS. *Soluble silicates*. American Chemical Society; 1982.
- [62] Iler RK. *The chemistry of silica*. New York: Wiley; 1979.
- [63] Liu S. *Aging of gels*. University of Florida, Internal report; 1989.
- [64] Sepulveda P, Jones JR, Hench LL. Characterization of melt-derived 45S5 and sol-gel-derived 58S bioactive glasses. *Journal of Biomedical Materials Research*. 2001;58(6):734–40.
- [65] Brinker CJ, Scherer GW. *Sol-gel science: the physics and chemistry of sol-gel processing*. Academic Press; London, 2013.
- [66] Strnad Z. Role of the glass phase in bioactive glass–ceramics. *Biomaterials*. 1992;13(5):317–21.
- [67] Shelby JE. *Introduction to glass science and technology*. UK: Royal Society of Chemistry; 2005.

- [68] Cormack AN, Tilocca A. Structure and biological activity of glasses and ceramics. *Philosophical Transactions of the Royal Society of London A: Mathematical, Physical and Engineering Sciences*. 2012;370(1963):1271–80.
- [69] Elgayar I, Aliev AE, Boccaccini AR, Hill RG. Structural analysis of bioactive glasses. *Journal of Non-Crystalline Solids*. 2005;351(2):173–83.
- [70] Ylänen H. Bone ingrowth into porous bodies made by sintering bioactive glass microspheres. Åbo Akademi Process Chemistry Group, Combustion and Materials Chemistry; 2000.
- [71] Andersson Ö, Liu G, Karlsson K, Niemi L, Miettinen J, Juhanoja J. In vivo behaviour of glasses in the  $\text{SiO}_2\text{-Na}_2\text{O-CaO-P}_2\text{O}_5\text{-Al}_2\text{O}_3\text{-B}_2\text{O}_3$  system. *Journal of Materials Science: Materials in Medicine*. 1990;1(4):219–27.
- [72] Hench LL, Andersson Å. An introduction to bioceramics. Singapore: World Scientific; 1993.
- [73] Osaka A, Hayakawa S, Tsuru K, Ohtsuki C. Bioactivity of alkali and alkaline earth borosilicate glasses. *Borate Glasses, Crystals and Melts*. 1997:490–7.
- [74] Saranti A, Koutselas I, Karakassides MA. Bioactive glasses in the system  $\text{CaO-B}_2\text{O}_3\text{-P}_2\text{O}_5$ : preparation, structural study and in vitro evaluation. *Journal of Non-Crystalline Solids*. 2006;352(5):390–8.
- [75] Yao A, Wang D, Huang W, Fu Q, Rahaman MN, Day DE. In vitro bioactive characteristics of borate-based glasses with controllable degradation behavior. *Journal of the American Ceramic Society*. 2007;90(1):303–6.
- [76] Barrios de Arenas I, Schattner C, Vásquez M. Bioactivity and mechanical properties of  $\text{Na}_2\text{O-CaO-SiO}_2\text{-P}_2\text{O}_5$  modified glasses. *Ceramics International*. 2005;32(5):515–20.
- [77] Rude RK, Gruber HE. Magnesium deficiency and osteoporosis: animal and human observations. *The Journal of Nutritional Biochemistry*. 2004;15(12):710–6.
- [78] Okuma T. Magnesium and bone strength. *Nutrition*. 2001;17(7–8):679–80.
- [79] Cowan JA. Structural and catalytic chemistry of magnesium-dependent enzymes. *Biometals: An International Journal on the Role of Metal Ions in Biology, Biochemistry, and Medicine*. 2002;15(3):225–35.
- [80] Gomez S, Rizzo R, Pozzi-Mucelli M, Bonucci E, Vittur F. Zinc mapping in bone tissues by histochemistry and synchrotron radiation-induced X-ray emission: correlation with the distribution of alkaline phosphatase. *Bone*. 1999;25(1):33–8.
- [81] Peretz A, Papadopoulos T, Willems D, Hotimsky A, Michiels N, Siderova V, et al. Zinc supplementation increases bone alkaline phosphatase in healthy men. *Journal of Trace Elements in Medicine and Biology*. 2001;15(2–3):175–8.

- [82] Nishi Y. Zinc and growth. *Journal of the American College of Nutrition*. 1996;15(4):340–4.
- [83] Tapiero H, Townsend DM, Tew KD. Trace elements in human physiology and pathology. Copper. *Biomedicine and Pharmacotherapy*. 2003;57(9):386–98.
- [84] Li X, Wang X, He D, Shi J. Synthesis and characterization of mesoporous CaO–MO–SiO<sub>2</sub>–P<sub>2</sub>O<sub>5</sub> (M = Mg, Zn, Cu) bioactive glasses/composites. *Journal of Materials Chemistry*. 2008;18(34):4103–9.
- [85] Sitarz M, Bulat K, Szumera M. Influence of modifiers and glass-forming ions on the crystallization of glasses of the NaCaPO<sub>4</sub>–SiO<sub>2</sub> system. *Journal of Thermal Analysis and Calorimetry*. 2012;109(2):577–84.
- [86] Brink M. *Bioactive glasses with a large working range*. Abo Akademi University; 1997.
- [87] Hench LL, Andersson OH, LaTorre GP. The kinetics of bioactive ceramics. Part III. Surface reactions for bioactive glasses compared with an inactive glass. *Bioceramics*. 1991;4:156–62.
- [88] Hench LL, Andersson OH, LaTorre GP. The kinetics of bioactive ceramics. *Bioceramics, USA*. 1991:43.
- [89] Hench LL, West JK. Biological applications of bioactive glasses. *Life Chemistry Reports*. 1996;13:187–241.
- [90] Skipper LJ, Sowrey FE, Pickup DM, Drake KO, Smith ME, Saravanapavan P, et al. The structure of a bioactive calcia–silica sol–gel glass. *Journal of Materials Chemistry*. 2005;15(24):2369–74.
- [91] Martin RA, Twyman H, Qiu D, Knowles JC, Newport RJ. A study of the formation of amorphous calcium phosphate and hydroxyapatite on melt quenched Bioglass<sup>®</sup> using surface sensitive shallow angle X-ray diffraction. *Journal of Materials Science: Materials in Medicine*. 2009;20(4):883–8.
- [92] Li P, Zhang F. The electrochemistry of a glass surface and its application to bioactive glass in solution. *Journal of Non-Crystalline Solids*. 1990;119(1):112–8.
- [93] Doostmohammadi A, Monshi A, Fathi MH, Braissant O. A comparative physico-chemical study of bioactive glass and bone-derived hydroxyapatite. *Ceramics International*. 2011;37(5):1601–7.
- [94] Karlsson KH, Fröberg K, Ringbom T. A structural approach to bone adhering of bioactive glasses. *Journal of Non-Crystalline Solids*. 1989;112(1):69–72.
- [95] FitzGerald V, Pickup DM, Greenspan D, Wetherall KM, Moss RM, Jones JR, et al. An atomic scale comparison of the reaction of Bioglass<sup>®</sup> in two types of simulated body fluid. *Physics and Chemistry of Glasses-European Journal of Glass Science and Technology Part B*. 2009;50(3):137–43.

- [96] Hench LL. Bioactive ceramics: theory and clinical applications. *Bioceramics*. 1994;7:3–14.
- [97] Andersson ÖH, Karlsson KH, Kangasniemi K. Calcium phosphate formation at the surface of bioactive glass in vivo. *Journal of Non-Crystalline Solids*. 1990;119(3):290–6.
- [98] Aitasalo K, Peltola M, Suonpää J, Yli-Urpo A, editors. Bioactive glass S53P4 in frontal sinus obliteration. In A 9-year experience. 13th International Symposium on Ceramics in Medicine; 2000; Bologna, Italy.
- [99] Peltola M. Experimental follow-up model for clinical frontal sinus obliteration with bioactive glass (S53P4). *Acta Oto-Laryngologica*. 2000;120(543):167–9.
- [100] Brink M, Turunen T, Happonen RP, Yli-Urpo A. Compositional dependence of bioactivity of glasses in the system  $\text{Na}_2\text{O}-\text{K}_2\text{O}-\text{MgO}-\text{CaO}-\text{B}_2\text{O}_3-\text{P}_2\text{O}_5-\text{SiO}_2$ . *Journal of Biomedical Materials Research*. 1997;37(1):114–21.
- [101] Ylänen H, Karlsson KH, Itälä A, Aro HT. Effect of immersion in SBF on porous bioactive bodies made by sintering bioactive glass microspheres. *Journal of Non-Crystalline Solids*. 2000;275(1):107–15.
- [102] Itälä A, Nordström EG, Ylänen H, Aro HT, Hupa M. Creation of microrough surface on sintered bioactive glass microspheres. *Journal of Biomedical Materials Research*. 2001;56(2):282–8.
- [103] Bovo N. Structure-properties relationships in bioactive glasses for PAA-based polyalkenoate cements. *Enginyeria Metallurgica: Universitat Politècnica de Catalunya, Barcelona, Spain*; 2007.
- [104] Hench LL, Pantano CG, Buscemi PJ, Greenspan DC. Analysis of bioglass fixation of hip prostheses. *Journal of Biomedical Materials Research*. 1977;11(2):267–82.
- [105] Oonishi H, Hench LL, Wilson J, Sugihara F, Tsuji E, Matsuura M, et al. Quantitative comparison of bone growth behavior in granules of Bioglass, A-W glass-ceramic, and hydroxyapatite. *Journal of Biomedical Materials Research*. 2000;51(1):37–46.
- [106] Oonishi H, Kushitani S, Yasukawa E, Iwaki H, Hench LL, Wilson J, et al. Particulate bioglass compared with hydroxyapatite as a bone graft substitute. *Clinical Orthopaedics and Related Research*. 1997;334:316–25.
- [107] Oonishi H, Hench LL, Wilson J, Sugihara F, Tsuji E, Kushitani S, et al. Comparative bone growth behavior in granules of bioceramic materials of various sizes. *Journal of Biomedical Materials Research*. 1999;44(1):31–43.
- [108] Schepers EJG, Ducheyne P. Bioactive glass particles of narrow size range for the treatment of oral bone defects: a 1–24 month experiment with several materials and particle sizes and size ranges. *Journal of Oral Rehabilitation*. 1997;24(3):171–81.
- [109] Wang Z, Lu B, Chen L, Chang J. Evaluation of an osteostimulative putty in the sheep spine. *Journal of Materials Science: Materials in Medicine*. 2011;22(1):185–91.

- [110] Fujibayashi S, Neo M, Kim H-M, Kokubo T, Nakamura T. A comparative study between in vivo bone ingrowth and in vitro apatite formation on  $\text{Na}_2\text{O}-\text{CaO}-\text{SiO}_2$  glasses. *Biomaterials*. 2003;24(8):1349–56.
- [111] Wheeler DL, Eschbach EJ, Hoellrich RG, Montfort MJ, Chamberland DL. Assessment of resorbable bioactive material for grafting of critical-size cancellous defects. *Journal of Orthopaedic Research*. 2000;18(1):140–8.
- [112] Kokubo T, Kushitani H, Ohtsuki C, Sakka S, Yamamuro T. Chemical reaction of bioactive glass and glass-ceramics with a simulated body fluid. *Journal of Materials science: Materials in Medicine*. 1992;3(2):79–83.
- [113] Oyane A, Kim HM, Furuya T, Kokubo T, Miyazaki T, Nakamura T. Preparation and assessment of revised simulated body fluids. *Journal of Biomedical Materials Research Part A*. 2003;65(2):188–95.
- [114] Takadama H, Hashimoto M, Mizuno M, Kokubo T. Round-robin test of SBF for in vitro measurement of apatite-forming ability of synthetic materials. *Phosphorus Research Bulletin*. 2004;17(0):119–25.
- [115] Clément J, Ekeberg L, Martinez S, Ginebra M, Gil F, Planell J, editors. Influence of the Chemical Composition on the Mechanical Properties and In Vitro Solubility of Phosphate Glasses in the System  $\text{P}_2\text{O}_5-\text{CaO}-\text{Na}_2\text{O}$ . *Bioceramics*; 1998.
- [116] Oliveira JM, Correia RN, Fernandes MH. Effects of Si speciation on the in vitro bioactivity of glasses. *Biomaterials*. 2002;23(2):371–9.
- [117] Lukito D, Xue JM, Wang J. In vitro bioactivity assessment of 70 (wt.%)  $\text{SiO}_2$ -30 (wt.%)  $\text{CaO}$  bioactive glasses in simulated body fluid. *Materials Letters*. 2005;59(26):3267–71.
- [118] Agathopoulos S, Tulyaganov DU, Ventura JMG, Kannan S, Karakassides MA, Ferreira JMF. Formation of hydroxyapatite onto glasses of the  $\text{CaO}-\text{MgO}-\text{SiO}_2$  system with  $\text{B}_2\text{O}_3$ ,  $\text{Na}_2\text{O}$ ,  $\text{CaF}_2$  and  $\text{P}_2\text{O}_5$  additives. *Biomaterials*. 2006;27(9):1832–40.
- [119] Jones JR, Sepulveda P, Hench LL. Dose-dependent behavior of bioactive glass dissolution. *Journal of Biomedical Materials Research*. 2001;58(6):720–6.
- [120] Greenspan DC, Zhong JP, LaTorre GP. Effect of surface area to volume ratio on in vitro surface reactions of bioactive glass particulates. *Bioceramics*. 1994;7:55–60.
- [121] Greenspan DC, Zhong JP, LaTorre GP. Evaluation of surface structure of bioactive glasses *in-vitro*. *Bioceramics*. 1995;8:477–82.
- [122] Balas F, Pérez-Pariente J, Vallet-Regí M, editors. Relationship between bioactivity and textural parameters in glasses. *Bioceramics*; 1998.
- [123] Andrade ÂL, Valério P, Goes AM, de Fátima Leite M, Domingues RZ. Influence of morphology on in vitro compatibility of bioactive glasses. *Journal of Non-Crystalline Solids*. 2006;352(32):3508–11.

- [124] Hench LL, Thompson I. Twenty-first century challenges for biomaterials. *Journal of the Royal Society Interface*. 2010;7(Suppl 4):S379–91.
- [125] Wang C, Xue Y, Lin K, Lu J, Chang J, Sun J. The enhancement of bone regeneration by a combination of osteoconductivity and osteostimulation using  $\beta$ -CaSiO<sub>3</sub>/ $\beta$ -Ca<sub>3</sub>(PO<sub>4</sub>)<sub>2</sub> composite bioceramics. *Acta Biomaterialia*. 2012;8(1):350–60.
- [126] Yong Cheng H, Zhong Jp. Osteostimulation of bioglass. *Chinese Medical Journal (England)*. 2009;122(19):2386–9.
- [127] Vallet-Regí M, Ragel C, Salinas AJ. Glasses with medical applications. *European Journal of Inorganic Chemistry*. 2003;2003(6):1029–42.
- [128] Zhao L, Yan X, Zhou X, Zhou L, Wang H, Tang J, et al. Mesoporous bioactive glasses for controlled drug release. *Microporous and Mesoporous Materials*. 2008;109(1):210–5.
- [129] Xue JM, Shi M. PLGA/mesoporous silica hybrid structure for controlled drug release. *Journal of Controlled Release*. 2004;98(2):209–17.
- [130] Li J, Song Y, Zhang S, Zhao C, Zhang F, Zhang X, et al. In vitro responses of human bone marrow stromal cells to a fluoridated hydroxyapatite coated biodegradable Mg–Zn alloy. *Biomaterials*. 2010;31(22):5782–8.
- [131] Zhu Y, Ikoma T, Hanagata N, Kaskel S. Rattle-type Fe<sub>3</sub>O<sub>4</sub>@ SiO<sub>2</sub> hollow mesoporous spheres as carriers for drug delivery. *Small*. 2010;6(3):471–8.
- [132] Chen QZ, Thompson ID, Boccaccini AR. 45S5 Bioglass®-derived glass–ceramic scaffolds for bone tissue engineering. *Biomaterials*. 2006;27(11):2414–25.
- [133] Jones JR, Ehrenfried LM, Hench LL. Optimising bioactive glass scaffolds for bone tissue engineering. *Biomaterials*. 2006;27(7):964–73.
- [134] Yan X, Yu C, Zhou X, Tang J, Zhao D. Highly ordered mesoporous bioactive glasses with superior in vitro bone-forming bioactivities. *Angewandte Chemie International Edition*. 2004;43(44):5980–4.
- [135] Kim TG, Shin H, Lim DW. Biomimetic scaffolds for tissue engineering. *Advanced Functional Materials*. 2012;22(12):2446–68.
- [136] Wu C, Chang J. Mesoporous bioactive glasses: structure characteristics, drug/growth factor delivery and bone regeneration application. *Interface Focus*. 2012;2:292–306.
- [137] Yan X, Huang X, Yu C, Deng H, Wang Y, Zhang Z, et al. The in-vitro bioactivity of mesoporous bioactive glasses. *Biomaterials*. 2006;27(18):3396–403.
- [138] Brinker CJ, Lu Y, Sellinger A, Fan H. Evaporation-induced self-assembly: nanostructures made easy. *Advanced Materials*. 1999;11(7):579–85.
- [139] Vallet-Regí M, Garcia MM, Colilla M. Biomedical applications of mesoporous ceramics: drug delivery, smart materials and bone tissue engineering. CRC Press; USA, 2012.

- [140] Zhu Y, Kaskel S. Comparison of the in vitro bioactivity and drug release property of mesoporous bioactive glasses (MBGs) and bioactive glasses (BGs) scaffolds. *Microporous and Mesoporous Materials*. 2009;118(1):176–82.
- [141] Lei B, Chen X, Wang Y, Zhao N, Du C, Zhang L. Acetic acid derived mesoporous bioactive glasses with an enhanced in vitro bioactivity. *Journal of Non-Crystalline Solids*. 2009;355(52):2583–7.
- [142] Xia W, Chang J. Preparation, in vitro bioactivity and drug release property of well-ordered mesoporous 58S bioactive glass. *Journal of Non-Crystalline Solids*. 2008;354(12):1338–41.
- [143] Li X, Wang X, He D, Shi J. Synthesis and characterization of mesoporous CaO–MO–SiO<sub>2</sub>–P<sub>2</sub>O<sub>5</sub> (M = Mg, Zn, Cu) bioactive glasses/composites. *Journal of Materials Chemistry*. 2008;18(34):4103–9.
- [144] Lei B, Chen X, Wang Y, Zhao N. Synthesis and in vitro bioactivity of novel mesoporous hollow bioactive glass microspheres. *Materials Letters*. 2009;63(20):1719–21.
- [145] Zhao S, Li Y, Li D. Synthesis and in vitro bioactivity of CaO–SiO<sub>2</sub>–P<sub>2</sub>O<sub>5</sub> mesoporous microspheres. *Microporous and Mesoporous Materials*. 2010;135(1):67–73.
- [146] Hong Y, Chen X, Jing X, Fan H, Guo B, Gu Z, et al. Preparation, bioactivity, and drug release of hierarchical nanoporous bioactive glass ultrathin fibers. *Advanced Materials*. 2010;22(6):754–8.
- [147] Hong Y, Chen X, Jing X, Fan H, Gu Z, Zhang X. Fabrication and drug delivery of ultrathin mesoporous bioactive glass hollow fibers. *Advanced Functional Materials*. 2010;20(9):1503–10.
- [148] Hoppe A, Güldal NS, Boccaccini AR. A review of the biological response to ionic dissolution products from bioactive glasses and glass–ceramics. *Biomaterials*. 2011;32(11):2757–74.
- [149] Saltman PD, Strause LG. The role of trace minerals in osteoporosis. *Journal of the American College of Nutrition*. 1993;12(4):384–9.
- [150] Beattie JH, Avenell A. Trace element nutrition and bone metabolism. *Nutrition Research Reviews*. 1992;5(01):167–88.
- [151] Nielsen FH. New essential trace elements for the life sciences. *Biological Trace Element Research*. 1990;26(1):599–611.
- [152] Nedelec JM, Courthéoux L, Jallot E, Kinowski C, Lao J, Laquerriere P, et al. Materials doping through sol–gel chemistry: a little something can make a big difference. *Journal of Sol-Gel Science and Technology*. 2008;46(3):259–71.
- [153] Krajewski A, Ravaglioli A, Fabbri B, Azzoni CB. Doping influence on the interaction between a bioactive glass and a simulated physiological solution: chemical and EPR tests. *Journal of Materials Science*. 1987;22(4):1228–34.

- [154] Cortizo AM, Molinuevo MS, Barrio DA, Bruzzone L. Osteogenic activity of vanadyl (IV)-ascorbate complex: evaluation of its mechanism of action. *The International Journal of Biochemistry & Cell Biology*. 2006;38(7):1171–80.
- [155] Marie PJ, Ammann P, Boivin G, Rey C. Mechanisms of action and therapeutic potential of strontium in bone. *Calcified Tissue International*. 2001;69(3):121–9.
- [156] Maeno S, Niki Y, Matsumoto H, Morioka H, Yatabe T, Funayama A, et al. The effect of calcium ion concentration on osteoblast viability, proliferation and differentiation in monolayer and 3D culture. *Biomaterials*. 2005;26(23):4847–55.
- [157] Marie PJ. The calcium-sensing receptor in bone cells: a potential therapeutic target in osteoporosis. *Bone*. 2010;46(3):571–6.
- [158] Valerio P, Pereira MM, Goes AM, Leite MF. Effects of extracellular calcium concentration on the glutamate release by bioactive glass (BG60S) preincubated osteoblasts. *Biomedical Materials*. 2009;4(4):045011.
- [159] Julien M, Khoshniat S, Lacreusette A, Gatius M, Bozec A, Wagner EF, et al. Phosphate-dependent regulation of MGP in osteoblasts: Role of ERK1/2 and Fra-1. *Journal of Bone and Mineral Research*. 2009;24(11):1856–68.
- [160] Carlisle EM. Silicon: a requirement in bone formation independent of vitamin D1. *Calcified Tissue International*. 1981;33(1):27–34.
- [161] Reffitt DM, Ogston N, Jugdaohsingh R, Cheung HFJ, Evans BAJ, Thompson RPH, et al. Orthosilicic acid stimulates collagen type 1 synthesis and osteoblastic differentiation in human osteoblast-like cells in vitro. *Bone*. 2003;32(2):127–35.
- [162] Delannoy PH, Bazot D, Marie PJ. Long-term treatment with strontium ranelate increases vertebral bone mass without deleterious effect in mice. *Metabolism*. 2002;51(7):906–11.
- [163] Shahnazari M, Sharkey NA, Fosmire GJ, Leach RM. Effects of strontium on bone strength, density, volume, and microarchitecture in laying hens. *Journal of Bone and Mineral Research*. 2006;21(11):1696–703.
- [164] Grynepas MD, Marie PJ. Effects of low doses of strontium on bone quality and quantity in rats. *Bone*. 1990;11(5):313–9.
- [165] Brandão-Neto J, Stefan V, Mendonça BB, Bloise W, Castro AVB. The essential role of zinc in growth. *Nutrition Research*. 1995;15(3):335–58.
- [166] Choi MK, Kim MH, Kang MH. The effect of boron supplementation on bone strength in ovariectomized rats fed with diets containing different calcium levels. *Food Science and Biotechnology*. 2005;14(2):242–8.
- [167] Hartwig A. Role of magnesium in genomic stability. *Mutation Research Fundamental and Molecular Mechanisms of Mutagenesis*. 2001;475(1):113–21.



- [168] Carlisle EM. Silicon: a possible factor in bone calcification. *Science*. 1970;167(3916):279–80.
- [169] Jugdaohsingh R, Tucker KL, Qiao N, Cupples LA, Kiel DP, Powell JJ. Dietary silicon intake is positively associated with bone mineral density in men and premenopausal women of the Framingham offspring cohort. *Journal of Bone and Mineral Research*. 2004;19(2):297–307.
- [170] Damen JJM, Ten Cate JM. Silica-induced precipitation of calcium phosphate in the presence of inhibitors of hydroxyapatite formation. *Journal of dental Research*. 1992;71(3):453–7.
- [171] Yamaguchi M. Role of zinc in bone formation and bone resorption. *The Journal of Trace Elements in Experimental Medicine*. 1998;11(2–3):119–35.
- [172] Kwun IS, Cho YE, Lomeda RAR, Shin HI, Choi JY, Kang YH, et al. Zinc deficiency suppresses matrix mineralization and retards osteogenesis transiently with catch-up possibly through Runx 2 modulation. *Bone*. 2010;46(3):732–41.
- [173] Zreiqat H, Howlett CR, Zannettino A, Evans P, Schulze-Tanzil G, Knabe C, et al. Mechanisms of magnesium-stimulated adhesion of osteoblastic cells to commonly used orthopaedic implants. *Journal of Biomedical Materials Research*. 2002;62(2):175–84.
- [174] Yamasaki Y, Yoshida Y, Okazaki M, Shimazu A, Uchida T, Kubo T, et al. Synthesis of functionally graded MgCO<sub>3</sub> apatite accelerating osteoblast adhesion. *Journal of Biomedical Materials Research*. 2002;62(1):99–105.
- [175] Marie PJ. Strontium ranelate: a physiological approach for optimizing bone formation and resorption. *Bone*. 2006;38(2):10–4.
- [176] Gérard C, Bordeleau LJ, Barralet J, Doillon CJ. The stimulation of angiogenesis and collagen deposition by copper. *Biomaterials*. 2010;31(5):824–31.
- [177] Hu Gf. Copper stimulates proliferation of human endothelial cells under culture. *Journal of Cellular Biochemistry*. 1998;69(3):326–35.
- [178] Nielsen FH. Is boron nutritionally relevant? *Nutrition Reviews*. 2008;66(4):183–91.
- [179] Uysal T, Ustdal A, Sonmez MF, Ozturk F. Stimulation of bone formation by dietary boron in an orthopedically expanded suture in rabbits. *The Angle Orthodontist*. 2009;79(5):984–90.
- [180] Vacheron Trystram MN, Braitman A, Cheref S, Auffray L. Antipsychotics in bipolar disorders. *Encephale*. 2003;30(5):417–24.
- [181] Young W. Review of lithium effects on brain and blood. *Cell Transplantation*. 2009;18(9):951–75.

- [182] Kallner G, Petterson U. Renal, thyroid and parathyroid function during lithium treatment: laboratory tests in 207 people treated for 1–30 years. *Acta Psychiatrica Scandinavica*. 1995;91(1):48–51.
- [183] Sun ZL, Wataha JC, Hanks CT. Effects of metal ions on osteoblast-like cell metabolism and differentiation. *Journal of Biomedical Material Research*. 1997;34(1):29–37.
- [184] Lázaro GS, Santos SC, Resende CX, dos Santos EA. Individual and combined effects of the elements Zn, Mg and Sr on the surface reactivity of a  $\text{SiO}_2 \cdot \text{CaO} \cdot \text{Na}_2\text{O} \cdot \text{P}_2\text{O}_5$  bioglass system. *Journal of Non-Crystalline Solids*. 2014;386:19–28.
- [185] Li HC, Wang DG, Chen CZ. Effect of zinc oxide and zirconia on structure, degradability and in vitro bioactivity of wollastonite. *Ceramics International*. 2015;41:10160–9.
- [186] Popp JR, Love BJ, Goldstein AS. Effect of soluble zinc on differentiation of osteoprogenitor cells. *Journal of Biomedical Materials Research Part A*. 2007;81(3):766–9.
- [187] Atkinson I, Anghel EM, Predoana L, Mocioiu OC, Jecu L, Raut I, et al. Influence of ZnO addition on the structural, in vitro behavior and antimicrobial activity of sol–gel derived  $\text{CaO-P}_2\text{O}_5\text{-SiO}_2$  bioactive glasses. *Ceramics International*. 2016;42(2):3033–45.
- [188] Sánchez-Salcedo S, Shruti S, Salinas AJ, Malavasi G, Menabue L, Vallet-Regi M. In vitro antibacterial capacity and cytocompatibility of  $\text{SiO}_2\text{-CaO-P}_2\text{O}_5$  meso-macroporous glass scaffolds enriched with ZnO. *Journal of Materials Chemistry B*. 2014;2(30):4836–47.
- [189] Balamurugan A, Balossier G, Kannan S, Michel J, Rebelo AH, Ferreira JM. Development and in vitro characterization of sol–gel derived  $\text{CaO-P}_2\text{O}_5\text{-SiO}_2\text{-ZnO}$  bioglass. *Acta Biomaterialia*. 2007;3(2):255–62.
- [190] Courthéoux L, Lao J, Nedelec JM, Jallot E. Controlled bioactivity in zinc-doped sol–gel-derived binary bioactive glasses. *The Journal of Physical Chemistry C*. 2008;112(35):13663–7.
- [191] El-Kady AM, Ali AF. Fabrication and characterization of ZnO modified bioactive glass nanoparticles. *Ceramics International*. 2012;38(2):1195–204.
- [192] Fujita Y, Yamamuro T, Nakamura T, Kotani S, Ohtsuki C, Kokubo T. The bonding behavior of calcite to bone. *Journal of Biomedical Materials Research*. 1991;25(8):991–1003.
- [193] Du RL, Chang J, Ni SY, Zhai WY, Wang JY. Characterization and in vitro bioactivity of zinc-containing bioactive glass and glass-ceramics. *Journal of biomaterials applications*. 2006;20(4):341–60.
- [194] Aina V, Malavasi G, Pla AF, Munaron L, Morterra C. Zinc-containing bioactive glasses: surface reactivity and behaviour towards endothelial cells. *Acta Biomaterialia*. 2009;5(4):1211–22.

- [195] Shahrabi S, Hesaraki S, Moemeni S, Khorami M. Structural discrepancies and in vitro nanoapatite formation ability of sol-gel derived glasses doped with different bone stimulator ions. *Ceramics International*. 2011;37(7):2737–46.
- [196] Meunier PJ, Roux C, Seeman E, Ortolani S, Badurski JE, Spector TD, et al. The effects of strontium ranelate on the risk of vertebral fracture in women with postmenopausal osteoporosis. *New England Journal of Medicine*. 2004;350(5):459–68.
- [197] Sila-asna M, Bunyaratvej A. Kobe University Repository: Kernel. *Kobe Journal of Medical Sciences*. 2007;53(1):25–35.
- [198] Jensen JEB, Stang H, Kringsholm B, Pritzl G, Sorensen OH. Relationship between trace element content and mechanical bone strength. *Bone*. 1997;20(Suppl 4):104.
- [199] Bonnelye E, Chabadel A, Saltel F, Jurdic P. Dual effect of strontium ranelate: stimulation of osteoblast differentiation and inhibition of osteoclast formation and resorption in vitro. *Bone*. 2008;42(1):129–38.
- [200] Usuda K, Kono K, Dote T, Watanabe M, Shimizu H, Tanimoto Y, et al. An overview of boron, lithium, and strontium in human health and profiles of these elements in urine of Japanese. *Environmental Health and Preventive Medicine*. 2007;12(6):231–7.
- [201] Lao J, Jallot E, Nedelec JM. Strontium-delivering glasses with enhanced bioactivity: a new biomaterial for antiosteoporotic applications? *Chemistry of Materials*. 2008;20(15):4969–73.
- [202] Isaac J, Nohra J, Lao J, Jallot E, Nedelec JM, Berdal A, et al. Effects of strontium-doped bioactive glass on the differentiation of cultured osteogenic cells. *European Cells and Materials*. 2011;21:130–43.
- [203] Gentleman E, Fredholm YC, Jell G, Lotfibakhshaiesh N, O'Donnell MD, Hill RG, et al. The effects of strontium-substituted bioactive glasses on osteoblasts and osteoclasts in vitro. *Biomaterials*. 2010;31(14):3949–56.
- [204] Hesaraki S, Gholami M, Vazehrad S, Shahrabi S. The effect of Sr concentration on bioactivity and biocompatibility of sol-gel derived glasses based on CaO–SrO–SiO<sub>2</sub>–P<sub>2</sub>O<sub>5</sub> quaternary system. *Materials Science and Engineering: C*. 2010;30(3):383–90.
- [205] O'Donnell MD, Hill RG. Influence of strontium and the importance of glass chemistry and structure when designing bioactive glasses for bone regeneration. *Acta Biomaterialia*. 6(7):2382–5.
- [206] Zhang J, Zhao S, Zhu Y, Huang Y, Zhu M, Tao C, et al. Three-dimensional printing of strontium-containing mesoporous bioactive glass scaffolds for bone regeneration. *Acta Biomaterialia*. 2014;10(5):2269–81.
- [207] Zhao S, Zhang J, Zhu M, Zhang Y, Liu Z, Tao C, et al. Three-dimensional printed strontium-containing mesoporous bioactive glass scaffolds for repairing rat critical-sized calvarial defects. *Acta Biomaterialia*. 2015;12:270–80.

- [208] Sriranganathan D, Kanwal N, Hing KA, Hill RG. Strontium substituted bioactive glasses for tissue engineered scaffolds: the importance of octacalcium phosphate. *Journal of Materials Science: Materials in Medicine*. 2016;27(2):1–10.
- [209] Nordenstrom J, Elvius M, Bagedahl-Strindlund M, Zhao B, Topping O. Biochemical hyperparathyroidism and bone mineral status in patients treated long-term with lithium. *Metabolism*. 1994;43(12):1563–7.
- [210] Davis BM, Pfefferbaum A, Krutzik S, Davis KL. Lithium's effect of parathyroid hormone. *American Journal of Psychiatry*. 1981;138(4):489–92.
- [211] Khorami M, Hesarak S, Behnamghader A, Nazarian H, Shahabi S. In vitro bioactivity and biocompatibility of lithium substituted 45S5 bioglass. *Materials Science and Engineering: C*. 2011;31(7):1584–92.
- [212] Miguez-Pacheco V, Büttner T, Maçon ALB., Jones JR, T. Fey D. de Ligny, Greil P, Chevalier J, Malchere A, Boccaccini AR. Development and characterization of lithium-releasing silicate bioactive glasses and their scaffolds for bone repair, *Journal of Non-Crystalline Solids*. 2016;432:65–72
- [213] Ma J, Chen CZ, Wang DG, Hu JH. Synthesis, characterization and in vitro bioactivity of magnesium-doped sol-gel glass and glass-ceramics. *Ceramics International*. 2011;37(5):1637–44.
- [214] Spasov AA, Fomichev EV, Guseva TN, Mazanova LS, Shchava SN. Efficiency of magnesium-containing preparation polykatan in therapy of purulent wounds. *Bulletin of Experimental Biology and Medicine*. 2001;131(2):132–5.
- [215] Sojka JE. Magnesium supplementation and osteoporosis. *Nutrition Reviews*. 1995;53(3):71–4.
- [216] Watts SJ, Hill RG, O'Donnell MD, Law RV. Influence of magnesia on the structure and properties of bioactive glasses. *Journal of Non-Crystalline Solids*. 2010;356(9):517–24.
- [217] Ma J, Chen CZ, Wang DG, Shao X, Wang CZ, Zhang HM. Effect of MgO addition on the crystallization and in vitro bioactivity of glass ceramics in the CaO–MgO–SiO<sub>2</sub>–P<sub>2</sub>O<sub>5</sub> system. *Ceramics International*. 2012;38(8):6677–84.
- [218] Rawlings RD. Bioactive glasses and glass-ceramics. *Clinical Materials*. 1993;14(2):155–79.
- [219] Hill R. An alternative view of the degradation of bioglass. *Journal of Materials Science Letters*. 1996;15(13):1122–5.
- [220] Varanasi VG, Saiz E, Loomer PM, Ancheta B, Uritani N, Ho SP, et al. Enhanced osteocalcin expression by osteoblast-like cells (MC3T3-E1) exposed to bioactive coating glass (SiO<sub>2</sub>–CaO–P<sub>2</sub>O<sub>5</sub>–MgO–K<sub>2</sub>O–Na<sub>2</sub>O system) ions. *Acta Biomaterialia*. 2009;5(9): 3536–47.

- [221] Balamurugan A, Balossier G, Laurent-Maquin D, Pina S, Rebelo AHS, Faure J, et al. An in vitro biological and anti-bacterial study on a sol-gel derived silver-incorporated bioglass system. *dental materials*. 2008;24(10):1343–51.
- [222] Bellantone M, Coleman NJ, Hench LL. Bacteriostatic action of a novel four-component bioactive glass. *Journal of biomedical Materials Research*. 2000;51(3):484–90.
- [223] Bellantone M, Williams HD, Hench LL. Broad-spectrum bactericidal activity of Ag<sub>2</sub>O-doped bioactive glass. *Antimicrobial Agents and Chemotherapy*. 2002;46(6):1940–5.
- [224] Luo SH, Xiao W, Wei XJ, Jia WT, Zhang CQ, Huang WH, et al. In vitro evaluation of cytotoxicity of silver-containing borate bioactive glass. *Journal of Biomedical Materials Research Part B: Applied Biomaterials*. 2010;95(2):441–8.
- [225] Efrima S, Bronk BV. Silver colloids impregnating or coating bacteria. *The Journal of Physical Chemistry B*. 1998;102(31):5947–50.
- [226] Liao SY, Read DC, Pugh WJ, Furr JR, Russell AD. Interaction of silver nitrate with readily identifiable groups: relationship to the antibacterial action of silver ions. *Letters in Applied Microbiology*. 1997;25(4):279–83.
- [227] Xynos ID, Edgar AJ, Buttery LDK, Hench LL, Polak JM. Ionic products of bioactive glass dissolution increase proliferation of human osteoblasts and induce insulin-like growth factor II mRNA expression and protein synthesis. *Biochemical and Biophysical Research Communications*. 2000;276(2):461–5.
- [228] Hench LL, Wilson J. Surface-active biomaterials. *Science*. 1984;226(4675):630–6.
- [229] Tsigkou O, Jones JR, Polak JM, Stevens MM. Differentiation of fetal osteoblasts and formation of mineralized bone nodules by 45S5 Bioglass<sup>®</sup> conditioned medium in the absence of osteogenic supplements. *Biomaterials*. 2009;30(21):3542–50.
- [230] Krishnan V, Lakshmi T. Bioglass: a novel biocompatible innovation. *Journal of Advanced Pharmaceutical Technology and Research*. 2013;4(2):78–83.
- [231] Froum SJ, Weinberg MA, Tarnow D. Comparison of bioactive glass synthetic bone graft particles and open debridement in the treatment of human periodontal defects. A clinical study. *Journal of Periodontology*. 1998;69(6):698–709.
- [232] Anderegg CR, Alexander DC, Freidman M. A bioactive glass particulate in the treatment of molar furcation invasions. *Journal of Periodontology*. 1999;70(4):384–7.
- [233] Froum S, Cho S-C, Rosenberg E, Rohrer M, Tarnow D. Histological comparison of healing extraction sockets implanted with bioactive glass or demineralized freeze-dried bone allograft: a pilot study. *Journal of Periodontology*. 2002;73(1):94–102.
- [234] Peltola M, Aitasalo K, Suonpaa J, Varpula M, Yli-Urpo A. Bioactive glass S53P4 in frontal sinus obliteration: A long-term clinical experience. *Head and Neck*. 2006;28(9):834–41.

- [235] Hench LL, Paschall HA. Histochemical responses at a biomaterial's interface. *Journal of Biomedical Materials Research*. 1974;8(3):49–64.
- [236] Izquierdo-Barba I, Arcos D, Sakamoto Y, Terasaki O, Lopez-Noriega A, Vallet-Regí Ma. High-performance mesoporous bioceramics mimicking bone mineralization. *Chemistry of Materials*. 2008;20(9):3191–8.
- [237] Taylor A. 9 Therapeutic uses of trace elements. *Clinics in Endocrinology and Metabolism*. 1985;14(3):703–24.
- [238] Gielen M, Tiekink ERT. *Metallotherapeutic drugs and metal-based diagnostic agents: the use of metals in medicine*. Chichester, UK: John Wiley & Sons; 2005.
- [239] Dueland R, Spadaro JA, Rahn BA. Silver antibacterial bone cement: comparison with gentamicin in experimental osteomyelitis. *Clinical Orthopaedics and Related Research*. 1982;169:264–8.
- [240] Yamamoto K, Ohashi S, Aono M, Kokubo T, Yamada I, Yamauchi J. Antibacterial activity of silver ions implanted in SiO<sub>2</sub> filler on oral streptococci. *Dental Materials*. 1996;12(4):227–9.
- [241] Kim TN, Feng QL, Kim JO, Wu J, Wang H, Chen GC, et al. Antimicrobial effects of metal ions (Ag<sup>+</sup>, Cu<sup>2+</sup>, Zn<sup>2+</sup>) in hydroxyapatite. *Journal of Materials Science: Materials in Medicine*. 1998;9(3):129–34.
- [242] Kawashita M, Tsuneyama S, Miyaji F, Kokubo T, Kozuka H, Yamamoto K. Antibacterial silver-containing silica glass prepared by sol-gel method. *Biomaterials*. 2000;21(4):393–8.
- [243] Blaker JJ, Nazhat SN, Boccaccini AR. Development and characterisation of silver-doped bioactive-glass-coated sutures for tissue engineering and wound healing applications. *Biomaterials*. 2004;25(7):1319–29.
- [244] Rupp ME, Fitzgerald T, Marion N, Helget V, Puumala S, Anderson JR, et al. Effect of silver-coated urinary catheters: efficacy, cost-effectiveness, and antimicrobial resistance. *American Journal of Infection Control*. 2004;32(8):445–50.
- [245] Dubas ST, Kumlangdudsana P, Potiyaraj P. Layer-by-layer deposition of antimicrobial silver nanoparticles on textile fibers. *Colloids and Surfaces A: Physicochemical and Engineering Aspects*. 2006;289(1):105–9.
- [246] Rivera-Garza M, Olguin MT, Garcia-Sosa I, Alcantara D, Rodriguez-Fuentes G. Silver supported on natural Mexican zeolite as an antibacterial material. *Microporous and Mesoporous Materials*. 2000;39(3):431–44.
- [247] Park S-J, Jang Y-S. Preparation and characterization of activated carbon fibers supported with silver metal for antibacterial behavior. *Journal of Colloid and Interface Science*. 2003;261(2):238–43.

- [248] Alt V, Bechert T, Steinrucke P, Wagener M, Seidel P, Dingeldein E, et al. An in vitro assessment of the antibacterial properties and cytotoxicity of nanoparticulate silver bone cement. *Biomaterials*. 2004;25(18):4383–91.
- [249] Barralet J, Gbureck U, Habibovic P, Vorndran E, Gerard C, Doillon CJ. Angiogenesis in calcium phosphate scaffolds by inorganic copper ion release. *Tissue Engineering Part A*. 2009;15(7):1601–9.
- [250] Habibovic P, Barralet JE. Bioinorganics and biomaterials: bone repair. *Acta Biomaterialia*. 2011;7(8):3013–26.
- [251] Hench LL. Bioceramics. *Journal of the American Ceramic Society*. 1998;81(7):1705–28.
- [252] Wilson J, Low SB. Bioactive ceramics for periodontal treatment: comparative studies in the Patus monkey. *Journal of Applied Biomaterials*. 1992;3(2):123–9.
- [253] Hench LL, Polak JM, Xynos ID, Buttery LDK. Bioactive materials to control cell cycle. *Material Research Innovations*. 2000;3(6):313–23.
- [254] Xynos ID, Edgar AJ, Buttery LDK, Hench LL, Polak JM. Gene-expression profiling of human osteoblasts following treatment with the ionic products of Bioglass® 45S5 dissolution. *Journal of Biomedical Materials Research*. 2001;55(2):151–7.
- [255] Bielby RC, Christodoulou IS, Pryce RS, Radford WJP, Hench LL, Polak JM. Time- and concentration-dependent effects of dissolution products of 58S sol-gel bioactive glass on proliferation and differentiation of murine and human osteoblasts. *Tissue Engineering*. 2004;10(7–8):1018–26.
- [256] Gough JE, Jones JR, Hench LL. Nodule formation and mineralisation of human primary osteoblasts cultured on a porous bioactive glass scaffold. *Biomaterials*. 2004;25(11):2039–46.
- [257] Bielby RC, Pryce RS, Hench LL, Polak JM. Enhanced derivation of osteogenic cells from murine embryonic stem cells after treatment with ionic dissolution products of 58S bioactive sol-gel glass. *Tissue Engineering*. 2005;11(3–4):479–88.
- [258] Christodoulou I, Buttery LDK, Saravanapavan P, Tai G, Hench LL, Polak JM. Dose- and time-dependent effect of bioactive gel-glass ionic-dissolution products on human fetal osteoblast-specific gene expression. *Journal of Biomedical Materials Research Part B: Applied Biomaterials*. 2005;74(1):529–37.
- [259] Christodoulou I, Buttery LDK, Tai G, Hench LL, Polak JM. Characterization of human fetal osteoblasts by microarray analysis following stimulation with 58S bioactive gel-glass ionic dissolution products. *Journal of Biomedical Materials Research Part B: Applied Biomaterials*. 2006;77(2):431–46.
- [260] Day RM, Boccaccini AR, Shurey S, Roether JA, Forbes A, Hench LL, et al. Assessment of polyglycolic acid mesh and bioactive glass for soft-tissue engineering scaffolds. *Biomaterials*. 2004;25(27):5857–66.

- [261] Jones JR, Ehrenfried LM, Saravanapavan P, Hench LL. Controlling ion release from bioactive glass foam scaffolds with antibacterial properties. *Journal of Materials Science: Materials in Medicine*. 2006;17(11):989–96.
- [262] Gorustovich AA, Roether JA, Boccaccini AR. Effect of bioactive glasses on angiogenesis: a review of in vitro and in vivo evidences. *Tissue Engineering Part B: Reviews*. 2009;16(2):199–207.
- [263] Yazar M, Sarban S, Kocyigit A, Isikan UE. Synovial fluid and plasma selenium, copper, zinc, and iron concentrations in patients with rheumatoid arthritis and osteoarthritis. *Biological Trace Element Research*. 2005;106(2):123–32.
- [264] Jebahi S, Oudadesse H, Saleh GB, Saoudi M, Mesadhi S, Rebai T, et al. Chitosan-based bioglass composite for bone tissue healing: oxidative stress status and antiosteoporotic performance in a ovariectomized rat model. *Korean Journal of Chemical Engineering*. 2014;31(9):1616–23.
- [265] Balasubramanian P, Strobel LA, Kneser U, Boccaccini AR. Zinc-containing bioactive glasses for bone regeneration, dental and orthopedic applications. *Biomedical Glasses*. 2015;1(1):51–69.
- [266] Mosbahi S, Oudadesse H, Wers E, Trigui M, Lefevre B, Roiland C, et al. Study of bioactive glass ceramic for use as bone biomaterial in vivo: investigation by nuclear magnetic resonance and histology. *Ceramics International*. 2016;42(4):4827–36.
- [267] Vaughan J. *The physiology of bone*. 3rd ed. Oxford: Clarendon Press; 1981.
- [268] Curzon MEJ. The relation between caries prevalence and strontium concentrations in drinking water, plaque, and surface enamel. *Journal of Dental Research*. 1985;64(12):1386–8.
- [269] Marie PJ, Hott M, Modrowski D, De Pollak C, Guillemain J, Deloffre P, et al. An uncoupling agent containing strontium prevents bone loss by depressing bone resorption and maintaining bone formation in estrogen-deficient rats. *Journal of Bone and Mineral Research*. 2005;20(6):1065–74.
- [270] Canalis E, Hott M, Deloffre P, Tsouderos Y, Marie PJ. The divalent strontium salt S12911 enhances bone cell replication and bone formation in vitro. *Bone*. 1996;18(6):517–23.
- [271] Baron R, Tsouderos Y. In vitro effects of S12911-2 on osteoclast function and bone marrow macrophage differentiation. *European Journal of Pharmacology*. 2002;450(1):11–7.
- [272] Reginster J-Y, Felsenberg D, Boonen S, Diez-Perez A, Rizzoli R, Brandi M-L, et al. Effects of long-term strontium ranelate treatment on the risk of nonvertebral and vertebral fractures in postmenopausal osteoporosis: results of a five-year, randomized, placebo-controlled trial. *Arthritis and Rheumatism*. 2008;58(6):1687–95.



- [273] Poh PSP, Hutmacher DW, Stevens MM, Woodruff MA. Fabrication and in vitro characterization of bioactive glass composite scaffolds for bone regeneration. *Biofabrication*. 2013;5(4):045005.
- [274] Jebahi S, Oudadesse H, El Feki H, Rebai T, Keskes H, Pellen P, et al. Antioxidative/oxidative effects of strontium-doped bioactive glass as bone graft. In vivo assays in ovariectomised rats. *Journal of Applied Biomedicine*. 2012;10(4):195–209.
- [275] Santocildes-Romero ME, Crawford A, Hatton PV, Goodchild RL, Reaney IM, Miller CA. The osteogenic response of mesenchymal stromal cells to strontium-substituted bioactive glasses. *Journal of Tissue Engineering and Regenerative Medicine*. 2015;9(5):619–31.
- [276] Jebahi S, Oudadesse H, Abdessalem N, Keskes H, Rebai T, el Feki H, et al. Comparative study of bone microarchitectural structure after porous bioglass and Strontium doped bioactive glass bone graft in Wistar rat model. *Journal of Scientific and Innovative Research*. 2014;3(1):16–20.
- [277] Lao J, Nedelec J-M, Jallot E. New strontium-based bioactive glasses: physicochemical reactivity and delivering capability of biologically active dissolution products. *Journal of Materials Chemistry*. 2009;19(19):2940–9.
- [278] Wu C, Zhou Y, Xu M, Han P, Chen L, Chang J, et al. Copper-containing mesoporous bioactive glass scaffolds with multifunctional properties of angiogenesis capacity, osteostimulation and antibacterial activity. *Biomaterials*. 2013;34(2):422–33.
- [279] Wang H, Zhao S, Zhou J, Shen Y, Huang W, Zhang C, et al. Evaluation of borate bioactive glass scaffolds as a controlled delivery system for copper ions in stimulating osteogenesis and angiogenesis in bone healing. *Journal of Materials Chemistry B*. 2014;2(48):8547–57.
- [280] Rath SN, Brandl A, Hiller D, Hoppe A, Gbureck U, Horch RE, et al. Bioactive copper-doped glass scaffolds can stimulate endothelial cells in co-culture in combination with mesenchymal stem cells. *PLoS One*. 2014;9(12):e113319.
- [281] Kong N, Lin K, Li H, Chang J. Synergy effects of copper and silicon ions on stimulation of vascularization by copper-doped calcium silicate. *Journal of Materials Chemistry B*. 2014;2(8):1100–10.
- [282] Gristina AG. Biomaterial-centered infection: microbial adhesion versus tissue integration. *Science*. 1987;237(4822):1588–95.
- [283] Matsuura T, Abe Y, Sato Y, Okamoto K, Ueshige M, Akagawa Y. Prolonged antimicrobial effect of tissue conditioners containing silver-zeolite. *Journal of Dentistry*. 1997;25(5):373–7.
- [284] Gatter N, Kohnen W, Jansen B. In vitro efficacy of a hydrophilic central venous catheter loaded with silver to prevent microbial colonization. *Zentralblatt für Bakteriologie*. 1998;287(1):157–69.

- [285] Adams AP, Santschi EM, Mellencamp MA. Antibacterial properties of a silver chloride-coated nylon wound dressing. *Veterinary Surgery*. 1999;28(4):219–25.
- [286] George N, Faoagali J, Muller M. Silvazine<sup>TM</sup> (silver sulfadiazine and chlorhexidine) activity against 200 clinical isolates. *Burns*. 1997;23(6):493–5.
- [287] Gupta A, Silver S. Molecular genetics: silver as a biocide: will resistance become a problem? *Nature Biotechnology*. 1998;16(10):888.
- [288] El-Kady AM, Ali AF, Rizk RA, Ahmed MM. Synthesis, characterization and microbiological response of silver doped bioactive glass nanoparticles. *Ceramics International*. 2012;38(1):177–88.
- [289] Newby PJ, El-Gendy R, Kirkham J, Yang XB, Thompson ID, Boccaccini AR. Ag-doped 45S5 Bioglass<sup>®</sup>-based bone scaffolds by molten salt ion exchange: processing and characterisation. *Journal of Materials Science: Materials in Medicine*. 2011;22(3):557–69.
- [290] Lohbauer U, Jell G, Saravanapavan P, Jones JR, Hench LL. Indirect cytotoxicity evaluation of silver doped bioglass Ag-S70C30 on human primary keratinocytes. *Key Engineering Materials*. 2005;284:431–4.
- [291] Lin H, Zhang J, Qu F, Jiang J, Jiang P. In vitro hydroxyapatite-forming ability and antimicrobial properties of mesoporous bioactive glasses doped with Ti/Ag. *Journal of Nanomaterials*. 2013;2013:24.
- [292] Wang H, Zhao S, Cui X, Pan Y, Huang W, Ye S, et al. Evaluation of three-dimensional silver-doped borate bioactive glass scaffolds for bone repair: biodegradability, biocompatibility, and antibacterial activity. *Journal of Materials Research*. 2015;30(18):2722–35.
- [293] Westendorf JJ, Kahler RA, Schroeder TM. Wnt signaling in osteoblasts and bone diseases. *Gene*. 2004;341:19–39.
- [294] Kengaku M, Capdevila J, Rodriguez-Esteban C, De La Pena J, Johnson RL, Belmonte JCI, et al. Distinct WNT pathways regulating AER formation and dorsoventral polarity in the chick limb bud. *Science*. 1998;280(5367):1274–7.
- [295] Hartmann C, Tabin CJ. Dual roles of Wnt signaling during chondrogenesis in the chicken limb. *Development*. 2000;127(14):3141–59.
- [296] Katoh M. WNT and FGF gene clusters (review). *International Journal of Oncology*. 2002;21(6):1269–73.
- [297] Sretero FJ, Hoepfner LH, Westendorf JJ. Wnt signaling during fracture repair. *Current Osteoporosis Reports*. 2009;7(2):64–9.
- [298] Spencer GJ, Utting JC, Etheridge SL, Arnett TR, Genever PG. Wnt signalling in osteoblasts regulates expression of the receptor activator of NF $\kappa$ B ligand and inhibits osteoclastogenesis in vitro. *Journal of Cell Science*. 2006;119(7):1283–96.

- [299] Chen Q-Z, Rezwan K, Francon V, Armitage D, Nazhat SN, Jones FH, et al. Surface functionalization of Bioglass®-derived porous scaffolds. *Acta Biomaterialia*. 2007;3(4): 551–62.
- [300] Edgington JM, Bandyopadhyay A, Bose S. In vitro characterization of lithium-doped tricalcium phosphate for bone graft. Society for Biomaterials. 2011:Abstract #727.
- [301] Phiel CJ, Klein PS. Molecular targets of lithium action. *Annual Review of Pharmacology and Toxicology*. 2001;41(1):789–813.
- [302] Zhang F, Phiel CJ, Spece L, Gurvich N, Klein PS. Inhibitory phosphorylation of glycogen synthase kinase-3 (GSK-3) in response to lithium Evidence for autoregulation of GSK-3. *Journal of Biological Chemistry*. 2003;278(35):33067–77.
- [303] Noble W, Planel E, Zehr C, Olm V, Meyerson J, Suleman F, et al. Inhibition of glycogen synthase kinase-3 by lithium correlates with reduced tauopathy and degeneration in vivo. *Proceedings of the National Academy of Sciences of the United States of America*. 2005;102(19):6990–5.
- [304] Clement-Lacroix P, Ai M, Morvan F, Roman-Roman S, Vayssiere B, Belleville C, et al. Lrp5-independent activation of Wnt signaling by lithium chloride increases bone formation and bone mass in mice. *Proceedings of the National Academy of Sciences of the United States of America*. 2005;102(48):17406–11.
- [305] Kavitha RJ, Subha B, Shanmugam S, Ravichandran K. Synthesis and in vitro characterisation of lithium doped bioactive glass through quick alkali sol-gel method. *International Journal of Innovative Research in Science and Engineering*. 2014;1(2): 2347–3207.
- [306] Miguez-Pacheco V, Buttner T, Macon ALB, Jones JR, Fey T, de Ligny D, et al. Development and characterization of lithium-releasing silicate bioactive glasses and their scaffolds for bone repair. *Journal of Non-Crystalline Solids*. 2016;432:65–72.
- [307] Gorustovich AA, Lopez JMP, Guglielmotti MB, Cabrini RL. Biological performance of boron-modified bioactive glass particles implanted in rat tibia bone marrow. *Biomedical Materials*. 2006;1(3):100.
- [308] Floroian L. Biocompatibility and physical properties of doped bioactive glass ceramics. *Bulletin of the Transilvania University of Brasov*. 2010;3:52.
- [309] Smith JM, Martin RA, Cuello GJ, Newport RJ. Structural characterisation of hypoxia-mimicking bioactive glasses. *Journal of Materials Chemistry B*. 2013;1(9):1296–303.
- [310] Dietrich E, Oudadesse H, Lucas-Girot A, Mami M. In vitro bioactivity of melt-derived glass 46S6 doped with magnesium. *Journal of Biomedical Materials Research Part A*. 2009;88(4):1087–96.
- [311] Prabhu M, Ruby Priscilla S, Kavitha K, Manivasakan P, Rajendran V, Kulandaivelu P. In vitro bioactivity and antimicrobial tuning of bioactive glass nanoparticles added

- with neem (*Azadirachta indica*) leaf powder. *BioMed Research International*. 2014;2014:Article ID 950691.
- [312] Hench LL, Andersson OG. Bioactive glass coatings. In: Hench LL, Wilson J, editors. *An introduction to bioceramics*. Singapore: World Scientific; 1993. p. 239–59.
- [313] Gomez-Vega JM, Saiz E, Tomsia AP, Marshall GW, Marshall SJ. Bioactive glass coatings with hydroxyapatite and Bioglass® particles on Ti-based implants. 1. Processing. *Biomaterials*. 2000;21(2):105–11.
- [314] Lopez-Esteban S, Saiz E, Fujino S, Oku T, Sukanuma K, Tomsia AP. Bioactive glass coatings for orthopedic metallic implants. *Journal of the European Ceramic Society*. 2003;23(15):2921–30.
- [315] Pratten J, Nazhat SN, Blaker JJ, Boccaccini AR. In vitro attachment of *Staphylococcus epidermidis* to surgical sutures with and without Ag-containing bioactive glass coating. *Journal of Biomaterials Applications*. 2004;19(1):47–57.
- [316] Xie X-H, Yu X-W, Zeng S-X, Du R-L, Hu Y-H, Yuan Z, et al. Enhanced osteointegration of orthopaedic implant gradient coating composed of bioactive glass and nano-hydroxyapatite. *Journal of Materials Science: Materials in Medicine*. 2010;21(7):2165–73.
- [317] Wang X, Li X, Onuma K, Ito A, Sogo Y, Kosuge K, et al. Mesoporous bioactive glass coatings on stainless steel for enhanced cell activity, cytoskeletal organization and AsMg immobilization. *Journal of Materials Chemistry*. 2010;20(31):6437–45.
- [318] Mistry S, Kundu D, Datta S, Basu D. Comparison of bioactive glass coated and hydroxyapatite coated titanium dental implants in the human jaw bone. *Australian Dental Journal*. 2011;56(1):68–75.
- [319] Drnovsek N, Novak S, Dragin U, Ceh M, Gorenssek M, Gradisar M. Bioactive glass enhances bone ingrowth into the porous titanium coating on orthopaedic implants. *International Orthopaedics*. 2012;36(8):1739–45.
- [320] Soundrapandian C, Bharati S, Basu D, Datta S. Studies on novel bioactive glasses and bioactive glass-nano-HAp composites suitable for coating on metallic implants. *Ceramics International*. 2011;37(3):759–69.
- [321] Pishbin F, Mourino V, Gilchrist JB, McComb DW, Kreppel S, Salih V, et al. Single-step electrochemical deposition of antimicrobial orthopaedic coatings based on a bioactive glass/chitosan/nano-silver composite system. *Acta Biomaterialia*. 2013;9(7):7469–79.
- [322] Pourhashem S, Afshar A. Double layer bioglass-silica coatings on 316L stainless steel by sol-gel method. *Ceramics International*. 2014;40(1):993–1000.
- [323] Keshaw H, Forbes A, Day RM. Release of angiogenic growth factors from cells encapsulated in alginate beads with bioactive glass. *Biomaterials*. 2005;26(19):4171–9.

- [324] Leach JK, Kaigler D, Wang Z, Krebsbach PH, Mooney DJ. Coating of VEGF-releasing scaffolds with bioactive glass for angiogenesis and bone regeneration. *Biomaterials*. 2006;27(17):3249–55.
- [325] Zhang Y, Cheng N, Miron R, Shi B, Cheng X. Delivery of PDGF-B and BMP-7 by mesoporous bioglass/silk fibrin scaffolds for the repair of osteoporotic defects. *Biomaterials*. 2012;33(28):6698–708.
- [326] Zhang Y, Miron RJ, Li S, Shi B, Sculean A, Cheng X. Novel mesoporous bioGlass/silk scaffold containing adPDGF-B and adBMP7 for the repair of periodontal defects in beagle dogs. *Journal of Clinical Periodontology*. 2015;42(3):262–71.
- [327] Zhao S, Li L, Wang H, Zhang Y, Cheng X, Zhou N, et al. Wound dressings composed of copper-doped borate bioactive glass microfibers stimulate angiogenesis and heal full-thickness skin defects in a rodent model. *Biomaterials*. 2015;53:379–91.

INTECH

Edited by  
VALENTINA GRUMEZESCU  
ALEXANDRU MIHAI GRUMEZESCU

# MATERIALS FOR BIOMEDICAL ENGINEERING

BIOPOLYMER FIBERS



# Organic–inorganic micro/nanofiber composites for biomedical applications

Samit Kumar Nandi<sup>1,\*</sup>, Arnab Mahato<sup>2,\*</sup>, Biswanath Kundu<sup>2</sup> and Prasenjit Mukherjee<sup>3</sup>

<sup>1</sup>*Department of Veterinary Surgery and Radiology, West Bengal University of Animal and Fishery Sciences, Kolkata, India* <sup>2</sup>*Bioceramics and Coating Division, CSIR-Central Glass and Ceramic Research Institute, Kolkata, India* <sup>3</sup>*Veterinary Clinical Complex, West Bengal University of Animal and Fishery Sciences, Kolkata, India*

## 2.1 INTRODUCTION

Tissue engineering is an emerging and interdisciplinary field of research focused on the fabrication of artificial tissue and organs. The primary aim of tissue engineering is to mimic the physiological environment including the different structural and physical features of native tissues (Khademhosseini et al., 2009). However, according to biologists it is better to help the body repair its own defects than to use replacement devices. To help the body restore its own defects a scaffold can be used as a support for tissue construction. It is challenging to achieve this goal and involves three main element: cells, scaffolds and signals for better understanding and planning. Cells are first extracted from either a small biopsy of healthy organs or from adult/embryonic stem cells, followed by cultivation in a sterile environment keeping functions normal (Hench and Polak, 2002). Scaffolds are the mechanical platform for cell adhesion, proliferation and differentiation (Shin, 2007). Scaffolds also provide an artificial but appropriate environment for cell infiltration with constant supplies of oxygen and nutrients. After the regeneration of native tissues, the scaffolds degrade naturally to provide space for mature tissue. Finally the signaling molecules play an important role in the further differentiation of the target cells.

Tissue engineering is categorized as “top down” or “bottom up.” In the first type, typically porous biocompatible scaffold is seeded by cells and then incubated in a suitable environment until the ECM forms, which eventually resembles native tissue (Nichol and Khademhosseini, 2009). The bottom-up approach

\*Equally contributed.

depends on small cell modules that are assembled to form larger constructs (Hasan et al., 2009).

Despite the fact that metal implants have been used for decades, metals do not meet all biomechanical requirements, such as isoelasticity of skeleton and bone. Metal implants can also lead to insufficient or over loading around the defect site. Corrosion of metals may also cause infection or cytotoxic reactions that lead to itching or pain. In addition, metal implants interfere with magnetic resonance imaging and prevent possible postoperative radiation therapy (Sawyer-Glover and Shellock, 2000; Shellock, 2001). The problems related to metal implants can be addressed by using durable and tough nonmetallic implants. For example, fiber-embedded polymer matrix implants have been found to be more appropriate than other nonmetallic implants. The first studies on nonmetallic fiber-based implants was done in the early 1960s, but extensive research in this field started in the 1990s. Fiber-based implants were first used clinically in the field of dentistry and eventually in orthodontics and periodontology (Vallittu and Sevelius, 2000). Research to develop implants for other areas is ongoing, utilizing the advantageous properties of fibers. Reasonability of their properties as implant applications have made them more favorable.

---

## 2.2 GLOBAL PERSPECTIVE ON HARD AND SOFT TISSUE ENGINEERING

The term tissue engineering is a newer concept in the arsenal of regenerative medicine, and is a combination of replacement, repair and regeneration of tissues both hard and soft. In between the three concepts, replacement is the oldest and refers to replacement tissue or organs implanted within the defect site of the body. The field of tissue engineering actually began in response to tissue lost as a result of trauma or disease. While tissue replacement is the oldest known practice, in 1996, the Food & Drug Administration approved a skin substitute known as Integra. The aim of tissue engineering is to study the principles of *in vivo* tissue growth and regeneration and then create suitable implants accordingly. Tissue regeneration is a complex process and includes multiple biological, chemical, and physical processes and decoding (Smith et al., 2011). Thus, tissue engineering is an interdisciplinary field comprised combining principles and methods of engineering and life sciences. Thus, understanding both soft and hard tissue engineering is required.

### 2.2.1 SOFT TISSUE ENGINEERING

In general, “soft tissue” refers to the tissues that connect, support or surround the structures and organs of the body. Tendons, ligaments, fascia, skin, fibrous



tissues and muscles are some examples of soft tissues. Soft tissue replacements may be needed due to tissue damage from congenital or chronic diseases (infections, inflammatory diseases, cystic fibrosis, ciliary dyskinesia, cardiovascular, congenital, or acquired diseases), tumor rejection or traumatic lesions (e.g., corneal scars, severe burns). Until now autologous bone grafts were considered as the gold standard, though the use of allografts, xenografts, and synthetic materials have also been extensively tested in recent decades (Stosich et al., 2009). The complexity of the tissue (cartilage, muscle, blood vessels, nerves, etc.) makes the task of achieving adequate vascularization and particular shapes and sizes difficult (Johnson et al., 2007; Stosich et al., 2007). In last few decades, number of strategies have been developed, for example, use of microchannel network to facilitate cell seeding and diffusion of soluble molecules stimulating vascular growth, generation of blood vessel analogs that can be connected to vascular network during surgery to obtain optimal mechanical and physiological properties (Garfein et al., 2003; Guangyuan et al., 2008; Hong et al., 2010). In addition to biological factors, other three main factors are: base biomaterial of the scaffold, stem or progenitor cells and bioactive substances catalyzing proliferation and differentiation of respective cells.

Biomaterials suitable as scaffolds in soft tissue engineering include natural polymers (derivatives of hyaluronic acid, chitosan, amylose/amylopectin, heparin, dextran, collagen types I and IV, fibrin, fibronectin, silk, elastin, gelatin, and adipose-derived ECM), matrigel (laminin, collagen-IV, entactin, and perlecan), decellularized human placenta, laminin, keratin, mussel adhesive proteins bearing the amino acid 3,4-dihydroxyphenyl-L-alanine residues that mediate underwater chemisorption to different substrata, synthetic polymers [poly(lactic acid) (PLA), polycaprolactone (PCL), elastic biodegradable poly(L-lactide-*co*-caprolactone)], polyethylene glycol, polyglutamic acid, poly(L-lactide-*co*-glycolic acid) (PLGA), poly(L-lactic acid) (PLLA), poly(propylene) fumarate,  $\beta$ -tricalcium phosphate, poly(propylene fumarate-*co*-ethylene glycol), oligo (poly(ethylene glycol) fumarate, polyethylene terephthalate, polytetrafluoroethylene, polyethylene glycol diacrylate, and polyethylene oxide (Waite, 1992; Flynn et al., 2007; Mano et al., 2007; Vashi et al., 2008; Heim et al., 2010; Connelly et al., 2011; Sapir et al., 2011; Wang et al., 2011a,b; Zhu and Marchant, 2011; Zakhem et al., 2012; Peter et al., 1997; Lu et al., 1998; Suggs et al., 1998; Jo et al., 2001; Hemmrich and Von Heimburg, 2006; Kretlow et al., 2007; Speer et al., 2011; Zhu et al., 2007; Zhu and Ong, 2009; Choi et al., 2010; Sala et al., 2011; Bitar and Zakhem, 2013). Researchers have found that combination of synthetic and natural fibers with other bioactive materials are prone to show promising results when used in soft tissue engineering applications (Wang et al., 1999; Wang et al., 2001; Shachar et al., 2011).

Further research in this area is needed to determine the biomaterial scaffold that can regenerate tissue structurally and biologically by mimicking natural growth of the corresponding tissues.

### 2.2.2 HARD TISSUE ENGINEERING

Hard tissue engineering deals with issues related to bone where a repair or restoration is required. Bone tissue engineering requires understanding of bone structure, bone mechanics, and the process of tissue formation. Bones provide load-bearing capacity to our skeleton and protection of our internal organs. In addition, bone is engaged in a constant cycle of chemical exchange and structural remodeling due to both internal mediators and external mechanical demands. Bone has been referred to as a *smart material* due to its scar-less regenerative capacity (Fazzalari, 2011). Hence, newly restored bone should be fully integrated with neighboring host tissues and perform as native bone. Due to the different loading conditions at different sites, the structural and functional characteristics of bone differ from place to place. Skeletal structures range from long (tibia, ulnar, etc.) to short (phalanges), flat (skull) and irregular (pelvic, vertebrae). While the features of bone are complex, hierarchically they have a very simple architecture. Bone ECM is comprised of both an organic component (type-1 collagen) and an inorganic component (carbonated apatite). The nanocomposite structure (tough and flexible collagen fibers reinforced by hydroxyapatite crystals) is integral to the requisite compressive strength and high fracture toughness of bone (Amini et al., 2012).

There are two ways bone tissue formation can occur: intramembraneously and endochondrally. In both cases, mesenchymal cellular condensation occurs and acts as a template for bone formation followed by differentiation of the progenitor cells. Most bone of the body is formed via endochondral path, and involves differentiation of mesenchymal progenitor cells to form chondrocytes followed by mineralization and replacement by new bone (Shapiro, 2008). Upon fracture, hematoma is formed, accompanied by an inflammatory response. Signaling molecules, such as ionic liquids, tumor necrosis factor alpha (TNF- $\alpha$ ), fibroblast growth factors, bone morphogenetic proteins, etc., play an important role in the formation of new bone. External soft tissues stabilize fractures mainly by forming callus, which subsequently undergoes chondrogenesis. With the maturity of the newly formed tissues chondrocyte proliferation is decreased. The mechanical stability of the cortex is achieved through subsequent remodeling of the newly formed bone.

An array of different osteoconductive biomaterials has been studied including polymers (natural and synthetic), ceramics (natural and synthetic), metals and their composites (Ripamonti, 1991; Pollick et al., 1995; Ripamonti, 1996; Barrere et al., 2003; Ripamonti et al., 2009; Yuan et al., 2001). Polymers can be used as individual or copolymers or polymer-ceramic composites. Some of the polymers in use today include PLGA, PLGA-poly( $\epsilon$ -caprolactone) (PCL), PLGA-PLL, etc. Polymers can be used as a cosystem with ceramics like hydroxyapatite, calcium phosphates or bioactive glasses (BGs) to make polymer/ceramic composite materials that have shown good results and acceptability over other materials currently available (Khan et al., 2004; Hasegawa et al., 2007; Khan et al., 2006). Ceramics

can also be used as individual biomaterial as it is composed of minerals, found in our bone. Thus they tend to have good acceptance from surrounding tissues of defect site when implanted. Sometime, ceramics are combined with different metal ions to make the implant, specifically suitable for its application in certain areas. Ion-doped ceramic implants are still being researched but more researchers are becoming interested in this type of material.

Research to find the optimal implant is ongoing.

---

## 2.3 ORGANIC–INORGANIC MICRO/NANOFIBER COMPOSITES IN HARD AND SOFT TISSUE ENGINEERING

Fibers are widely used for the fabrication of scaffolds in hard and soft tissue engineering and regenerative medicine. The application of fibers in tissue engineering is not limited to only the top-down approach. Tunable properties of fibers which depend on different synthesis methods, actually make them more approachable. Applications of fiber-based implants are growing and research is ongoing. Due to the possibility of different mechanical properties fiber can be used in soft tissue engineering as well as in hard tissue engineering ([Table 2.1](#)).

---

## 2.4 FIBER FABRICATION TECHNIQUES

One-dimensional fibers are rich in useful properties for a variety of applications due to their unique geometry and high aspect ratio. Their high-surface-to-volume ratio makes them favorable for absorption and release phenomenon. Synthetic polymer fibers have been fabricated using a range of different techniques but in comparison production of functional biological fibers are more recent and less known, though we do know that in terms of application biological fibers rapidly spread over a large and diverse area. The most common and widely accepted fabrication techniques include wet spinning, electro-spinning, drawing, extrusion, solvent casting and microfluidic spinning ([Fig. 2.1](#)). The potential area of application is broad and the fibers are chosen according to the properties incorporated with different fabrication techniques. Ongoing efforts are concentrated in generating biological fibers by mimicking the structural and functional features present in natural fibers. It has also been found that utilizing natural fibers can improve the biological properties. Depending on the fabrication technique diverse structures including membranes, weaves, meshes, gels and even free-form architectures can be made with specific properties ([Ang-atikarnkul et al., 2014](#)) (cf. [Fig. 2.2](#)). Incorporation of biologically active surfaces provides significant value as an important material in the biomedical field. Fibers with either continuous or discontinuous arrangement can provide distinct advantages for different fields of application ([Iftekhhar, 2003](#)).

**Table 2.1** Tissue Engineering Studies Using Scaffolds Formed by Fiber-Based Techniques

Material	Method	Properties	Application	Remarks	References
Polyglycolic acid (PGA) reinforced agarose and fibrin	Vacuum-assisted infusion	Ultimate tensile stress: 67–85 MPa Young's modulus: 0.068–0.077 MPa	Articular cartilage (chondrocytes)	The mechanical properties of the composite scaffold were comparable to native tissue <ul style="list-style-type: none"> <li>• Composite scaffolds mimics the anisotropic, nonlinear and viscoelastic biomechanical of cartilage</li> <li>• Use of reinforcement improved the aggregate and Young's moduli by 4 and 15 folds, respectively</li> </ul>	<a href="#">Moutos et al. (2007)</a>
PCL supporting fibrin	Vacuum-assisted infusion	Ultimate tensile stress: 22.9–35.3 MPa Young's modulus: 0.74 MPa	Articular cartilage (human adipose-derived stem cells)	<ul style="list-style-type: none"> <li>• 1.4 mm thick scaffolds were formed by adopting a 3D weaving technique</li> <li>• Anisotropic properties in the in-plane direction</li> </ul>	<a href="#">Moutos and Guilak (2009)</a>
PCL supporting fibrin	3D weaving	0.18–0.56 MPa Young's modulus: 0.05–0.4 MPa	Articular cartilage (human adipose-derived stem cells)	<ul style="list-style-type: none"> <li>• Weaving properties of the scaffolds significantly affected the mechanical properties</li> </ul>	<a href="#">Valonen et al. (2010)</a>
Poly(D,L-lactide-co-glycolide) PLGA	Weaving	Failure load: 97.2 N Elastic stiffness: 16.8 N/mm	Tendon and ligament (bone marrow stromal cells)	<ul style="list-style-type: none"> <li>• Woven structures were stronger than knitted and hybrid scaffolds</li> </ul>	<a href="#">Sahoo et al. (2007)</a>
PLGA knitted scaffold PLGA knitted scaffold coated with PCL PLGA knitted scaffold coated with PLGA nanofibers PLGA knitted scaffold coated with collagen	Knitting	Failure load: 56.3–68.4 N Elastic stiffness: 4.3–9.1 N/mm	Tendon and ligament (bone marrow stromal cells)	<ul style="list-style-type: none"> <li>• The stem cell-seeded rolled up scaffolds were 11% stronger than their unseeded counterparts after 3 weeks of culture</li> <li>• Cell proliferation and viability on the hybrid scaffolds increased during the third week</li> <li>• Viable cells were uniformly distributed on the seeded nanofibrous surfaces and also on the knitted silk microfibers in the depths of the hybrid scaffold</li> <li>• Hybrid knitted scaffolds showed a lower stiffness while improved cell attachment</li> </ul>	<a href="#">Sahoo et al. (2007)</a>

Poly(lactic acid-co-caprolactone) (PLACL) supporting cell encapsulated collagen	Knitting		Skin, bladder wall, and blood vessel (neonatal fibroblasts)	<ul style="list-style-type: none"> <li>Position of cells in the through-plane direction was controlled in the fabrication process</li> </ul>	<a href="#">Ananta et al. (2008)</a>
PLGA knitted with collagen nanofibers	Knitting		Skin (human foreskin fibroblasts)	<ul style="list-style-type: none"> <li>Hybrid scaffolds improved cell proliferation</li> <li>In vivo experiments confirmed the formation of dermal tissues after 2 weeks</li> </ul>	<a href="#">Chen et al. (2005)</a>
PLA	Wet spun	Tensile strength: 0.03–0.33 MPa Porosity: 0.8–0.93	Urinary bladder	<ul style="list-style-type: none"> <li>The mechanical properties varies with the number of plies used in the yarn</li> <li>The fabricated structures had higher mechanical properties than the targeted tissue</li> </ul>	<a href="#">Gupta and Revagade (2009)</a>
Raw <i>Bombyx mori</i> silk supporting collagen sponge	Knitting	Tensile strength: 6.72 MPa Stiffness: 28.26 N/mm	Tendon (human embryonic stem cells-derived mesenchymal stem cells)	<ul style="list-style-type: none"> <li>The mechanical properties of the engineering tendons were lower but comparable with the original tissue</li> </ul>	<a href="#">Chen et al. (2010)</a>
PCL embroidered structure covered with collagen or collagen and chondroitin sulfate (CS)	Knitting	Porosity: 0.8 Pore size: 200–900 $\mu\text{m}$	Bone (human mesenchymal stem cells, ovine mesenchymal stem cells)	<ul style="list-style-type: none"> <li>In the presence of osteogenic supplements the hMSC showed increasing alkaline phosphatase (ALP) activity up to day 14 and produced large amounts of calcified matrix after 28 days</li> <li>Composite scaffolds enhanced cell proliferation and ALP activity</li> <li>Effectively induced the osteogenic differentiation</li> </ul>	<a href="#">Rentsch et al. (2009)</a>
Poly(L/D)lactide 96/4	Knitting	Porosity: 0.8–0.87 Tensile strength: 3.3–5.4 MPa		<ul style="list-style-type: none"> <li>The mechanical properties were a function of the number of ply in the yarn</li> <li>The degradation rate of the knitted geometries was reported over a period of 52 weeks</li> </ul>	<a href="#">Ellä et al. (2011)</a>

(Continued)

**Table 2.1** Tissue Engineering Studies Using Scaffolds Formed by Fiber-Based Techniques *Continued*

Material	Method	Properties	Application	Remarks	References
Polyester filament covered with polyurethane and <i>N,N</i> -dimethyl formamide	Knitting	Tensile strength (load): 92–145 MPa	Vascular graft	<ul style="list-style-type: none"> <li>Composite grafts showed higher ultimate strength and strain than the knitted structure</li> </ul>	<a href="#">Xu et al. (2010a)</a>
Microsponge	Knitting	Young's modulus: 7.24–14.62 MPa Stiffness: 50.5–55.2 N/mm	Articular cartilage (bovine chondrocytes)	<ul style="list-style-type: none"> <li>Three PLGA/collagen hybrid scaffolds of different structural design: "thin," "semi" and "sandwich" were prepared in this study</li> <li>Semi and sandwich offered better mechanical properties</li> <li>The mechanical properties were lower but comparable with bovine articular cartilage</li> </ul>	<a href="#">Dai et al. (2010)</a>
Silk fibroin coated with PLGA electrospun nanofibers	Knitting	Scaffold ultimate strength (load): 95.6 N Composite scaffold: 61.5–75.3 N	Ligament and tendon (bone marrow-derived stem cell)	<ul style="list-style-type: none"> <li>The stem cell-seeded rolled up scaffolds were 11% stronger than their unseeded counterparts after 3 weeks of culture</li> <li>Cell proliferation and viability on the hybrid scaffolds increased during the third week</li> <li>Viable cells were uniformly distributed on the seeded nanofibrous surfaces and also on the knitted silk microfibers</li> </ul>	<a href="#">Sahoo et al. (2007)</a>
Raw <i>Bombyx mori</i> silk fibers knitted fibers combined with silk sponge	Knitting	Pore diameter of knitted structure: 1 mm Tensile strength (load): 250 N Tensile stiffness: 40 N/mm	Anterior cruciate ligament (human bone marrow-derived mesenchymal stem cells)	<ul style="list-style-type: none"> <li>Composite scaffolds improved cell attachment and proliferation</li> <li>Composite scaffolds had similar mechanical properties with the knitted structure but they maintained their mechanical properties over a 2-week period</li> </ul>	<a href="#">Liu et al. (2008)</a>

PLGA supporting collagen–chitosan hydrogel	Knitting	Surface area: 2.01 after 1 week–2.74 after 4 weeks Tensile strength: 3.6 MPa	Skin	<ul style="list-style-type: none"> <li>• Implantation in rats indicated angiogenesis start from early stages of implantation</li> <li>• Angiogenesis rate was faster in the hybrid scaffold in comparison with pure knitted PLGA construct</li> </ul>	Wang et al. (2012)
PLGA and PLLA fibers	Knitting	Tensile strength (load): 332 N reduced to 92.8 N in 12 weeks Young’s modulus: 354.4 MPa reduced to 53.8 N in 12 weeks	Anterior cruciate ligament (rabbit and mouse anterior cruciate ligament fibroblasts)	<ul style="list-style-type: none"> <li>• Increasing braiding angle increases surface pore area</li> <li>• Braids comprised of the same number and type of yarns differ in strength due to differences in strain rate and geometry</li> <li>• The mechanical properties of the seeded structure degraded over time</li> <li>• The stress–strain curve was similar to the values for natural ligament tissue</li> <li>• The 3D circular fibrous scaffold could withstand the tensile load applied on native ligament</li> <li>• 100–300 μm pore diameters showed best results</li> <li>• In vivo performance of the developed cell-seeded, tissue-engineered ligament construct demonstrated excellent healing and regeneration potential</li> </ul>	Cooper et al. (2005), Cooper et al. (2007)
Collagen fiber cross-linked with and without gelating using either UV or 1-ethyl-3-(3-dimethylaminopropyl) carbodiimide (EDC)		Tensile strength: 1.07–19.3 MPa Young’s modulus: 6.32–148 MPa Tensile strain: 18–20%	Anterior cruciate ligament (primary mouse anterior cruciate ligament fibroblasts)	<ul style="list-style-type: none"> <li>• The mechanical properties of EDC cross-linked collagen fiber braid twist scaffolds without gelatin are similar to native anterior cruciate ligament</li> <li>• Adding gelatin lowered the mechanical properties</li> </ul>	Walters et al. (2012)

(Continued)

**Table 2.1** Tissue Engineering Studies Using Scaffolds Formed by Fiber-Based Techniques *Continued*

Material	Method	Properties	Application	Remarks	References
<i>Antheraea pernyi</i> silk fibroin		Tensile strength (load): 50 N after 12 weeks implantation 16 N after 12	Tendon (tenocytes)	<ul style="list-style-type: none"> <li>Enhanced adhesion and propagation of the tenocytes on the scaffold</li> <li>In vivo data confirm efficient neotendon formation</li> <li>Bundles of collagen fibers in the neo-tendons were uniform with well-oriented implantation</li> </ul>	<a href="#">Fang et al. (2009)</a>
Poly(L-lactic acid) (PLLA)		Tensile strength: 6.57–7.62 MPa Young's modulus: 47.6–55.0 MPa	Tendon and ligament (human mesenchymal stem cells)	<ul style="list-style-type: none"> <li>The mechanical properties of the braided scaffold depended on the number of bundles involved in the construct</li> <li>Three-bundle scaffold had a higher mechanical strength than the four and five bundle scaffolds</li> </ul>	<a href="#">Barber et al. (2011)</a>
Deposition of a layer of PCL fibers on PCL fibers	Melt plotting	Porosity: 0.5–0.68 Tensile strength: 1.7–4.1 MPa Young's modulus: 14.6–41.3 MPa	Bone (osteoblast-like cells (MG63))	<ul style="list-style-type: none"> <li>Hybrid scaffold displayed higher viability and calcium deposition compared with the normally fabricated scaffold</li> <li>Hybrid scaffolds had lower mechanical strength in comparison with the pure melt-plotted PCL scaffold</li> </ul>	<a href="#">Kim et al. (2011)</a>
Poly(L-lactide), poly(D,L-lactide), poly(D,L-lactide-co-glycolide) and PCL	Direct writing		Microvascular network (human umbilical vein endothelial cells)	<ul style="list-style-type: none"> <li>Endothelial cells adhered to the surface of all the fabricated scaffolds</li> <li>Cultured cells proliferated on fibrous scaffolds both along axis and around circumference of fibers</li> <li>Cells cultured on nonsuspended fibers did not follow the pattern and attached to the substrate</li> </ul>	<a href="#">Berry et al. (2011)</a>
Titanium fiber-reinforced 13-93 bioactive glass (BG)	Extrusion	Pore sizes ranging from 400 to 800 $\mu\text{m}$ and a porosity of $\sim 50\%$ fracture toughness $\sim 0.8 \text{ MPa}^{1/2}$ and a flexural strength of $\sim 15 \text{ MPa}$	In vitro	Addition of Ti fibers increased the fracture toughness of the scaffolds by $\sim 70\%$ and flexural strength by $\sim 40\%$	<a href="#">Thomas et al. (2016)</a>



Poly(ester-urethane) urea	Electro-spinning		Skin tissue engineering	<ul style="list-style-type: none"> <li>Fiber morphology did not change after the embedding</li> <li>Sustained drug- release property</li> </ul>	Yu et al. (2016), Kishan et al. (2016)
Polyurethane	Electro-spinning	Fiber diameter approximately 20 $\mu\text{m}$	In vitro	<ul style="list-style-type: none"> <li>Attractive architecture that provides adequate porosity</li> <li>Interconnectivity of pores ideal for cell adhesion and proliferation</li> </ul>	Gabriel et al. (2017)
PLLA	Thermal-induced phase separation and thermal-induced phase separation	Diameter in the range of 50–350 $\mu\text{m}$ macropores (50–350 $\mu\text{m}$ ) micropores (100 nm to 10 $\mu\text{m}$ )	In vitro	Microenvironment more ideal for protein adsorption, cell proliferation and cell infiltration	Wang et al. (2016)
Polycaprolactone (PCL)/gelatin	Electro-spinning	Tensile strength 1.55 $\pm$ 0.49 MPa	Tendon tissue engineering	<ul style="list-style-type: none"> <li>Compatible with simultaneous, sufficient cell encapsulation</li> </ul>	Yang et al. (2016)
Hydroxyapatite-tussah silk fibroin	Electro-spinning	Breaking stress 2.7 MPa	Bone tissue engineering	<ul style="list-style-type: none"> <li>Good mechanical properties of composite elicited</li> <li>Effective cell adhesion, proliferation and bone formation</li> </ul>	Shao et al. (2016)
Poly(glycerol sebacate) (PGS)-poly( $\epsilon$ -caprolactone) (PCL)	Electro-spinning	Elastic modulus is 6.7 $\pm$ 1.1 MPa Tensile Strength 1.0 $\pm$ 0.21 MPa	Heart valve tissue engineering	<ul style="list-style-type: none"> <li>Mimicking environment</li> <li>Allows the cells to spread and distribute themselves within the hydrogel by providing appropriate mechanical properties</li> </ul>	Eslami et al. (2014)
Collagen	Electro-spinning	Young's modulus: 52.1–348 MPa	Ligament tissue engineering	Sufficiently porous to facilitate cell perfusion and nutrient distribution of seeded cells	Full et al. (2015)
Sodium alginate	Coaxial fluid cross-link		Vascularized tissue engineering	<ul style="list-style-type: none"> <li>Strong bonding strength</li> <li>Mechanical support to cellular assembly</li> </ul>	Li et al. (2016)
Poly(glycerol-dodecanedioate)/gelatin	Electro-spinning		Soft tissue engineering	<ul style="list-style-type: none"> <li>Controllable fiber diameter</li> <li>Fiber stability</li> </ul>	Dai et al. (2014)

(Continued)

**Table 2.1** Tissue Engineering Studies Using Scaffolds Formed by Fiber-Based Techniques *Continued*

Material	Method	Properties	Application	Remarks	References
Hyaluronic acid/poly(lactic-co-glycolic acid)/epigallocatechin-3-O-gallate	Electro-spinning	Fiber diameter: 1270 ± 510 nm Tensile strength 1.46 MPa Elastic moduli 28.00 MPa	Skin tissue engineering	<ul style="list-style-type: none"> <li>Sustained release patterns controlled degradation</li> </ul>	<a href="#">Lee et al. (2014)</a>
Poly(ethylene glycol)/PCL	Electro-spinning	Elastic moduli 3.79 ± 0.90 MPa	Heart valve tissue engineering	Matches the anisotropy of the native aortic valve leaflet	<a href="#">Tseng et al. (2014)</a>
Poly(L-lactide-co-acryloyl carbonate)	Electro-spinning	Diameter 0.8 – 0.9 μm Young modulus 30.1 ± 10 MPa	Ligament tissue engineering	Similar to that of native anterior cruciate ligament	<a href="#">Chen et al. (2014)</a>
Keratin	Electro-spinning	Diameters 4.8 ± 4.0 μm	Cartilage tissue engineering	Better support to the development, and chondrogenic differentiation of adipose-derived mesenchymal stem cells	<a href="#">Xu et al. (2014)</a>
PCL/oligomer	Electro-spinning	Ultimate tensile strength of 2.8 ± 1 MPa Elastic modulus of 30 ± 15 MPa	Cardiac tissue engineering	Fiber meshes resemble the fibrillar structural organization of ECM	<a href="#">Reddy et al. (2014)</a>
Poly(ε-caprolactone)/human adipose-derived stem cells	Electro-spinning	Diameter 0.43 ± 0.18 mm	Cuff tendon tissue engineering	Increased expression of tenomodulin	<a href="#">Orr et al. (2015)</a>
Human-like collagen/chitosan and polylactic acid	Electro-spinning		Vascular tissue engineering	Improved mechanical properties	<a href="#">Zhu et al. (2014)</a>
PCL/gelatin and collagen type I	Electro-spinning	Diameter 481–858 nm	Skin tissue engineering	Good cell adhesion	<a href="#">Gautam et al. (2014)</a>
Copolymer-poly(ethylene oxide terephthalate)-poly(butylene terephthalate)/calcium phosphate coating	Electro-spinning	Diameter 6.5 μm	Bone tissue engineering	Osteogenic ability	<a href="#">Nandakumar et al. (2010)</a>
Polyurethane/hydroxyapatite	Electro-spinning		Bone tissue engineering	<ul style="list-style-type: none"> <li>Decreased electrospun fiber diameter</li> <li>Better proliferation</li> </ul>	<a href="#">Mi et al. (2014)</a>
Poly(ε-caprolactone)-polydimethylsiloxane	Electro-spinning	Tensile Strength 3.86–10.51 MPa Young modulus 14.0–32.5 MPa	Bone tissue engineering	Excellent mechanical and shape memory properties	<a href="#">Kai et al. (2016)</a>

Poly(glycerol sebacate) PGS/fibrinogen	Electro-spinning	Diameter $1076 \pm 212$ nm Young's modulus $22.31 \pm 3.1$ MPa	Cardiac tissue engineering	<ul style="list-style-type: none"> <li>• Provide internal structures and mechanical support desired</li> <li>• Form gap junctions with the host cardiomyocytes and enhance the regeneration process</li> </ul>	<a href="#">Ravichandran et al. (2013)</a>
Poly(L-lactic acid)/gelatin	Electro-spinning	Diameter 100–500 nm	Vascular tissue engineering	Highly supported the SMCs and improved the proliferation of cells	<a href="#">Shalumon et al. (2015)</a>
Poly(lactide-co-glycolide)/ BG	Freeze-drying		Tissue engineering	Superior pore structure	<a href="#">Haaparanta et al. (2015)</a>
Chitosan-poly(butylene succinate)	Melt-drawing	Porosity $59.0 \pm 11.4\%$ Pore size $144.9 \pm 33.4$ mm	Bone marrow	High levels of cell viability	<a href="#">Costa-Pinto et al. (2012)</a>

*With permission from Elsevier.*

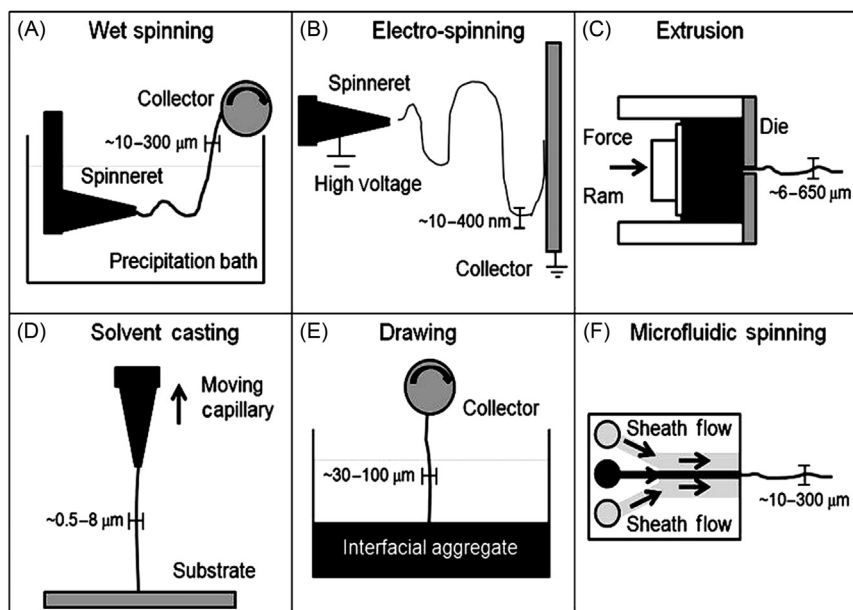


FIGURE 2.1

Different fiber fabrication techniques; (A) wet spinning, (B) electro-spinning, (C) extrusion, (D) solvent casting, (E) drawing and (F) microfluidic spinning.

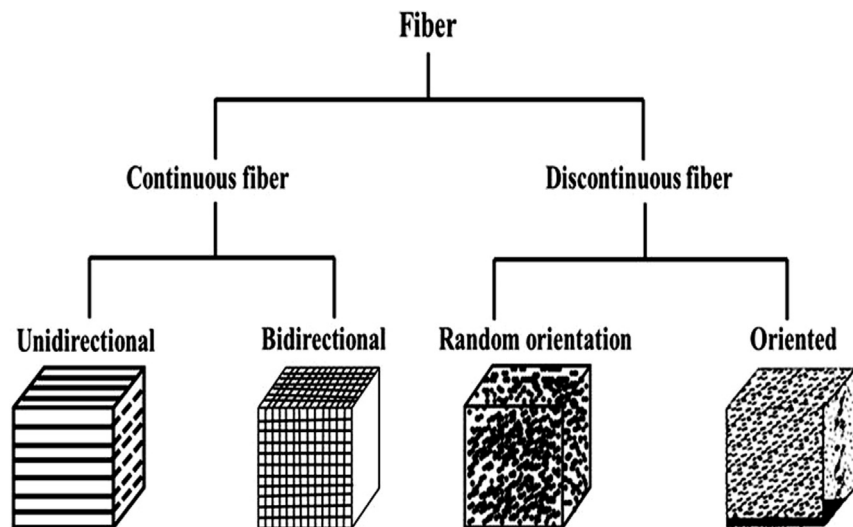


FIGURE 2.2

Classifications of fibers.

### 2.4.1 WET SPINNING

In wet spinning, biological moieties are injected as solutions for the formation of fibers. A variety of fibers can be produced by this technique. This process generally involves the use of spinnerets or capillaries of 10–50  $\mu\text{m}$  in which the solution is driven by syringe pumps for the extrusion of the fibers inside a coagulant bath. The coagulant bath generally consists of a solution in which the biological moieties are nonsoluble or very poorly soluble. The collected fibers are then washed, followed by air-drying using a spinning carrier cylinder (Qiu et al., 2009). The mechanical and physical properties of the fibers can be tuned by changing the parameters used in this process, such as flow rate, solution concentration, spinneret diameter, etc. According to the requirements, the parameters should be optimized to minimize bead formation or any discontinuities. Recent research also suggests molecular weight and osmotic stress are important parameters for construction of fibers (Cho et al., 2012; Sohn and Gido, 2009). Wet spinning of protein solution is also helpful. Even plant protein fibers like soy and wheat protein have been produced for use in tissue engineering (implants as well as for controlled drug delivery; Reddy and Yang, 2011). Traditional natural ECMs like collagen can also be used to make implants for biomedical applications.

### 2.4.2 ELECTRO-SPINNING

Fibers with the smallest diameters (10 nm to few microns) can be achieved by electro-spinning (Huang and You, 2013). Fibers with smaller diameters (2–6 nm) have been reported by different research groups (Bhardwaj and Kundu, 2010; Zarkoob et al., 2004). The basic components of the electro-spinning process are a high voltage power supply, a spinneret and a collector (a counter electrode). In this process, applied voltage causes formation of cone-shaped droplet of the solution at tip of nozzle. Once the strength of the electric field overcomes the threshold value of the particular solution, the electrostatic force on the deformed drop can overcome the surface tension and thus a continuous liquid jet is formed. When the solution evaporates, solid fibers can be collected from the collector (Huang et al., 2000). The main parameters of this technique include solution properties such as conductivity, volatility, viscosity and processing parameters like flow rate, voltage, distance between the spinneret and the collector (Huang et al., 2003; Sill and von Recum, 2008; Li and Xia, 2004). Using extended experimental investigations, a trend is usually calculated between parameters and corresponding fiber morphology, which however, are not always constant in every cycle. For example, it is known that more applied voltage will lead to larger fiber diameter, and faster flow rate also can make the diameter larger. Electrospun fibers of different biological moieties have also been created, aimed at improving application in the field of biomaterials (Raveendran et al., 2013; Schmucker et al., 2014; Mi et al., 2014; Lee and Belcher, 2004). The

small diameter of electrospun fibers gives them a very high surface area, which is useful for many applications such as absorption and release of reagents/drugs. Electro-spinning has gained acceptance, but it is worth noting that the formation of electrospun fibers with controlled inhomogeneity and nonuniformity remains a challenge.

### 2.4.3 EXTRUSION

Extrusion is a popular way to make fibers from biological materials due to its very low consumption of energy. However, the fibers synthesized by this route are found to have large diameter (in the hundreds of micrometers). The diameter of the fiber depends on the postprocessing methods, that is, cross-linking, dehydration or solvent immersion. In this process, a solution/gel-like substance is pushed through a syringe pump with an appropriate flow rate followed by washing and drying. Lack of mechanical strength is a hurdle for this process and thus cross-linking treatment is required before application as a biomaterial for soft or hard tissue repair (Zeugolis et al., 2010).

In the case of melt-spinning extrusion, the material is first heated until melted and then extruded. However, this process has not evolved much in this field due to its high-temperature requirement.

### 2.4.4 SOLVENT CASTING

Solvent casting is based on the evaporation phenomenon of liquid solvent for the generation of fibers. The technique involves submersion of an existing fiber or rod into a mixture containing the biomaterial of interest followed by drying/heating. To get the preferred diameter or thickness the process is generally repeated several times. Thus, the process is slow and time consuming, leading to less acceptance among the researchers. Depending on the pulling speed, surface morphology and diameter of the fiber can be varied.

### 2.4.5 DRAWING

In this process, fibers drawn from the interfaces of two oppositely charged solutions are collected in a carrier cylinder. The creation of a complex interface is possible only with some biomaterials. Hence, the range of materials that can be used in this technique is limited. However, electrostatic assembly of chosen materials can produce sufficiently strong fibers. These charged, multidomain fibers are useful for pH-triggered drug delivery, and due to their high strength they can be utilized for hard tissue engineering applications. Recently researchers also fabricated fibers drawn from multiple interfaces with impressive results. These multidomain fiber structures enable cell coculture, which is required to understand the growth and differentiation needed for tissue regeneration applications. The

diameter of the fibers fabricated through this technique vary from 8 to 50  $\mu\text{m}$  (Wan et al., 2012; Tentori and Jaworski, 2014).

### 2.4.6 MICROFLUIDIC SPINNING

Microfluidic devices are popular in cases where formation of fibers with particular sizes in the micron scale are required. Microfluidics allows tunability in the fiber properties (such as fiber diameter) by varying parameters like flow rate, solution viscosity, and channel geometries. The tunability is achieved by the laminar flow arising from the low Reynolds numbers typical in microfluidics, which provides good control over kinetics and reproducible flow patterns. This technique also allows different multiphase flows, coaxial flows, and parallel flows that can be utilized to fabricate complex and requirement-based fiber structures (Chung et al., 2012).

In the arsenal of tissue engineering the use of fiber has increased enormously in recent decades and with it fabrication techniques have become increasingly able to control the mechanical and physiochemical properties. As discussed, all the fabrication processes have advantages and disadvantages (Table 2.2).

**Table 2.2** Advantages and Disadvantages of Common Fiber Processing Techniques

Processing Technique	Benefits	Drawbacks
Wet spinning Electro-spinning	<ul style="list-style-type: none"> <li>Controlled fiber diameters</li> <li>Straightforward setup</li> <li>The range of materials can be used is high</li> <li>Cheap procedure</li> <li>Size control</li> </ul>	<ul style="list-style-type: none"> <li>Extensive setup</li> <li>Hard to make multidomain fibers</li> </ul>
Extrusion	<ul style="list-style-type: none"> <li>Low cost</li> <li>Straightforward setup</li> </ul>	<ul style="list-style-type: none"> <li>May require wet-extrusion or cross-linking</li> <li>Smaller fiber diameter is not possible</li> </ul>
Solvent casting	<ul style="list-style-type: none"> <li>Unique surface textures</li> <li>Controlled shapes</li> </ul>	<ul style="list-style-type: none"> <li>Low throughput</li> <li>Limited solvent choices</li> <li>Limited fiber dimensions</li> </ul>
Microfluidic spinning	<ul style="list-style-type: none"> <li>Possible to generate multidomain fibers (i.e., laminar, coaxial, hollow, embedded)</li> <li>Low sample consumption</li> </ul>	<ul style="list-style-type: none"> <li>Limited number of commercial setups available</li> <li>Potential clogging</li> <li>Extensive setup if built in-house</li> </ul>

*With permission from Biodesign.*

---

## 2.5 CERAMIC/GLASS MATERIALS FIBERS FOR BIOMEDICAL APPLICATIONS

### 2.5.1 CERAMIC AND GLASS FIBERS AS BONE GRAFT SUBSTITUTE

BG plays a unique role in bone regeneration due to its excellent bioactivity, osteoconductivity and osteoinductivity. However, most studies in this field have focused on melt-derived glasses, either in bulk or granular form. Glass fibers have the potential to act as cell supporters for ECM production and tissue regeneration, with a mechanical strength superior to that of equivalent bulk glasses (De Diego et al., 2000). Kim et al. (2006) studied the bioactivity of nanofiber in vitro within a simulated body fluid and found rapid induction of bone-like minerals onto the nanofiber surface. The bone marrow-derived cells were found to attach and proliferate actively on the nanofiber mesh and differentiate into osteoblastic cells with excellent osteogenic potential. The bioactive nanofibers have been further exploited in various forms, such as bundled filament, nanofibrous membrane, 3D macroporous scaffold and nanocomposite with biopolymer, suggesting their versatility and potential applications in bone tissue engineering. A novel nanocomposite biomaterial consisting of bioactive glass nanofiber (BGNF) and collagen-reconstituted fibrous matrix for bone regenerative medicine has also been developed. The BGNF was distributed uniformly within the collagen-reconstituted nanofibrous matrix. The nanocomposite matrices induced rapid bone-like apatite minerals formation on their surfaces upon incubation in simulated body fluid, exhibiting excellent bioactivity in vitro. Osteoblastic cells showed favorable growth on the BGNF-collagen nanocomposite. In particular, the alkaline phosphatase activity of the cells on the nanocomposite was significantly higher than that on the collagen. This novel BGNF-collagen nanocomposite is believed to have significant potential in bone regeneration and tissue engineering applications (Kim et al., 2006). Glass fiber scaffolds can get completely resorbed and become osteoconductive. Structural and morphological characteristics also become like a bone substitute (Moimas et al., 2006).

Fiber-reinforced composite (FRC) made of E-glass fiber veil with the bisphenol-a-glycidyl methacrylate-polymethylmethacrylate (BisGMA-PMMA) resin system improves has improved bone adhesion with mechanical roughening and special chemical treatments like dental primers, or treated with an experimental silane mixture, or with a mixture of the experimental silane liquid and Clearfil Se Bond Primer (Tuusa et al., 2005). FRC made of E-glass fiber and BisGMA-PMMA resin matrix has also been used for frontal bone defect in rabbits experimentally, showing its potential as an alternative for bone defect reconstruction (Tuusa et al., 2007).

Biomedical nanocompositions of bioceramic and resorbable polymers have potential for the successful regeneration of bone tissues. Many researchers have developed novel nanocomposite made of BG in a nanofibrous form and a degradable synthetic polymer, PLA. The nanocomposites induce rapid formation of a



hydroxycarbonate apatite layer on the surface under a simulated physiological medium. Increasing the amount of bioactive nanofiber (from 5% to 25%) improves the in vitro bioactivity of the nanocomposite. Osteoblasts attach and grow well on the nanocomposites and secrete collagen protein at initial culturing periods. Significant differentiation of cells was found to be improved on nanocomposites than pure PLA. Moreover, the mineralized product by the cells was observed to be significantly higher on the nanocomposites with respect to pure PLA. Nanocomposites comprised of bioactive nanofiber and degradable polymer are a promising bone regeneration matrix due to their excellent bioactivity and osteoblast response (Kim et al., 2008).

An in vitro study was conducted by Brown et al. (2008) to evaluate the ability of two types of constructs of bioactive, silica-based 13-93 glass fibers scaffold to support the growth and differentiation of MC3T3-E1 osteoblastic cells and concluded that 13-93 glass fiber scaffolds are a favorable substrate for the growth and differentiation of osteoblasts and a promising material for bone tissue engineering and repair of bone defects. Surgeons dealing with patients with cranio-maxillofacial defects have to face both psychological and functional aspects of treatment. Efeoglu et al. (2009) used PCL with phosphate glass fiber that showed promising results for nonload-bearing applications in the craniomaxillofacial region. Moreover, new micro-CT measurement of temporal characterization of mineralization of bone has shown its efficacy for prediction of bony healing and its quality. A study with submicron BG fibers 70S30C (70 mol% SiO (Hench and Polak, 2002), 30 mol% CaO) fabricated by electro-spinning showed similar elastic modulus with bone when used as bone tissue scaffold (Lu et al., 2009). When bone-to-implant contact and the osteoconductive capacity of bioactive FRC implant were evaluated in vivo it was found that addition of bioactive glass (BAG) to the FRC implant increases peri-implant osteogenesis and bone maturation (Ballo et al., 2009). FRC implants also promoted the healing process of critical size calvarial bone defects in rabbits, showing its efficacy in the reconstruction of bone defects in the head and neck (Tuusa et al., 2008). Another recent study reported on an implant material consisting of a supporting fiber-reinforced framework and porous inner layers of bisphenol-a-glycidyl methacrylate and triethyleneglycoldi-methacrylate resin matrix reinforced with silanized E-glass filled with a BG (S53P4) that may fill a potential role in craniofacial bone reconstruction (Aitasalo et al., 2014).

### 2.5.2 ROLE IN SOFT TISSUE (WOUND) HEALING

Ideally bioactive wound dressings should contain antimicrobial drugs, growth-promoting factors, nanosilver and other bioactive ingredients that promote tissue growth in the wounded area (Zahedi et al., 2010). Bunting et al. (2005) found that bioglass 45S5 fibers form a biocompatible scaffold that helps to regenerate peripheral axons in vivo and thus have potential for use in clinical cases, where there are long inter-stump gaps to be bridged. Nanofibers have a high

surface-area-to-volume ratio and surface molecular chains ready to bind with desirable drugs. Wound dressing material should contain active agents like antibiotics, antiinflammatory agents, growth-promoting factors, vitamins, minerals and inorganic ions like silver (Lakshman et al., 2010) and iodine. El-Newehy et al. (2012) developed PVA/PEO/metronidazole composite nanofibers using nanospider technology. The fibers were effective against *Escherichia coli*, *Pseudomonas aeruginosa*, *Aspergillus niger*, *Penicillium notatum*, and *Aspergillus flavus* and the stabilized fibers also had a controlled release rate compared to nonstabilized fibers. Zahedi et al. (2013) synthesized, used phenytoin sodium (PHT-Na) (an antiepileptic drug with known properties of wound healing) and loaded in electrospun PVA/PCL nanofibers; histological assessment of PVA + PHT-Na fibers of which showed re-epithelialization, low tissue necrosis and a high degree of wound healing. Babaeijandaghi et al. (2010) electrospun polyethersulfone (PES), a synthetic and biocompatible polymer, into nanofibers and applied it as an epidermal wound dressing. It proved to be effective in improving skin healing. Yan et al. (2011) reported electrospun polyurethane/nanoTiO<sub>2</sub> nanofibers as wound dressing that showed antibacterial efficiency as well as good water vapor transmission, which are critical to prevent the wound bed from exudate accumulation. Dubsky et al. (2012) prepared gelatin nanofibers with needleless nanospider technology and performed a comparative study between gelatin nanofibers and PCL nanofibers and concluded that gelatin improved wound closure by increased granular tissue formation and reepithelialization.

### 2.5.3 ROLE AS SUSTAINED LOCAL DELIVERY OF ANTIBIOTICS IN TREATING BONE INFECTION

The usual treatment regimen for osteomyelitis or bone infection has various challenges such as the fact that the desired concentration of parenteral antibiotic cannot reach the infection site due to presence of the blood bone barrier. Various factors to control infection and many pathogens as well as antibiotics have been identified in recent years (Trampuz and Zimmerli, 2006; Crowley et al., 2007; Struijs et al., 2007).

A study of PCL nanofibers fabricated by incorporating calcium peroxide showed inhibitory properties of the nanofibers on the growth of *E. coli* and *Staphylococcus epidermidis* due to burst release of calcium peroxide from the nanofibers. The results showed that oxygen-generating nanofibers provide a short-term peroxide-based antimicrobial response with viable and morphologically healthy osteoblasts in tissue culture except initial toxic effect over first 24 hours (Wang et al., 2010).

Hsu et al. (2014) studied the effect of biodegradable drug-eluting nanofiber-enveloped implants made of poly(D,L)-lactide-co-glycolide and incorporated vancomycin and ceftazidime, which were electrospun into biodegradable drug-eluting membranes and enveloped on the surface of stainless plates. The result showed

nanofiber-enveloped plates released vancomycin and ceftazidime above the minimum inhibitory concentration for more than 3 and 8 weeks in vitro and in vivo, respectively, and proved to be very effective at eluting antibiotic in biodegradable implants for sustained release.

#### 2.5.4 AS CARRIER FOR DELIVERY OF ANTICANCER DRUGS AND GROWTH FACTORS

At a molecular level cancer develops due to genetic alterations of multiple subsets of genes, either activation of oncogenes or inactivation of tumor suppressor genes, and ultimately leading to malignant proliferation of cancer cells, tissue infiltration and dysfunction of organs (Sarkar et al., 2007). In general, there is dynamic angiogenesis and high vascular density in tumor tissue, but with a malfunctioning of vascular design. The situation is compounded due to poor lymphatic drainage, known as the enhanced permeation and retention effect (Byrne et al., 2008; Iyer et al., 2006). Traditional chemotherapy (both orally and intravenously) fails to direct sufficient concentration of drugs at the tumor site due to intrinsic convolution of tumor microenvironment and the existence of P-glycoprotein. The therapeutic drugs also affect in vivo hepatic and renal clearance, enzymolysis and hydrolysis, as well as endosomal/lysosomal degradation (Wiradharma et al., 2009; Jabr-Milane et al., 2008). Additionally, the effectiveness of anticancer drugs is restricted due to properties such poor solubility, narrow therapeutic concentration around the tumor site as well as low efficacy for solid tumors and severe cytotoxicity to healthy body tissue, leading to treatment failure in cancer (Pulkkinen et al., 2008; Xie et al., 2010).

Considering the above facts, there is a paramount necessity to develop an ideal therapeutic approach capable of delivering chemotherapeutic agents directly to tumor sites (Panyala et al., 2009). With the advent of new modalities of delivery of drugs through organic/inorganic fibers, the treatment of cancer may take a new path in the coming years.

The nanofibers developed by electro-spinning have gained considerable attention as this technique can produce ultrafine polymer fibers for drug delivery applications. As a fibrous material, it has the ability to entrap drugs with a high loading capacity and high encapsulation efficiency because of their low weight and inherent high surface-to-volume ratio. Delivery of anticancer drugs can be successfully carried out with this fiber, especially in postoperative local chemotherapy via surgical implantation of the scaffold (Xu et al., 2008). The electro-spun PLGA-based micro- and nanofibers may have the ability to deliver paclitaxel to treat C6 glioma in a sustained way in vitro (Xie and Wang, 2006). In another study, controlled release of 1, 3-bis (2-chloroethyl)-1-nitrosourea was carried out from an implantable poly(ethylene glycol)-poly(L-lactic acid) diblock copolymer fiber for postoperative chemotherapy of cancer against rat Glioma C6 cells showing increased antitumor activity (Xu et al., 2006). A new approach for

multidrug delivery of both paclitaxel and doxorubicin hydrochloride (DOX) through nanofibers prepared by “emulsion electro-spinning” has also been developed (Xu et al., 2009).

Another recent study showed the inhibitory effect of released dichloroacetate from PLA electrospun mats to suppress cervical carcinoma in an in vivo mice model within 3 months. The significant reduction of tumor volume and weight may be due to synergistic necrosis of the tumor cells, caused by multiple adenosine-5'-triphosphate depletion promoted by high dosage of dichloroacetate (Liu et al., 2012). The cell-culture study using coated paclitaxel-loaded CS nanofibers with hyaluronic acid confirmed the ability of released paclitaxel to inhibit the attachment and proliferation of DU145 prostate cancer cells even with a small amount of the drug (Ma et al., 2011).

Although inorganic compounds such as cisplatin have antitumor activities, they have a short half-life in the biological system. To overcome this limitation, titanocene dichloride was incorporated in PLLA nanofibers and showed inhibitory activity against lung tumor cells (Chen et al., 2010). Hydroxycamptothecin (HCPT), an insoluble and unstable anticancer drug, was loaded in poly(D,L-lactic acid)-PEG electrospun nanofibers using 2-hydroxypropyl- $\beta$ -cyclodextrin as solubilizer. This showed much higher inhibitory activity against human mammary gland MCF-7 cancer cells (Xie et al., 2010). In another study, the core–shell HCPT-loaded fibers showed higher inhibitory activity (> 20 times) against human hepatocellular carcinoma cells (Hep G2) than free HCPT during 72 hours' incubation (Luo et al., 2012). For long-term anticancer efficacy, a doxorubicin drug molecule was used for sustained release through PLGA/CNTs composite nanofibers. The results showed that the prepared PLGA/DOX@CNTs nanofibers platform could effectively inhibit the cell viability of HeLa cells in vitro (Yu et al., 2015). The doxorubicin-loaded electrospun hybrid nanofibers comprising n-HA particles and PLGA showed anticancerous effects by sustained release of the drugs (Zheng et al., 2013).

### 2.5.5 ROLE IN DENTAL APPLICATIONS

The first implants used to replace missing teeth possibly date back to the end of the first century AD. A piece of metal (wrought iron or nonalloy steel) was found in the maxilla of a male over 30 years of age from that period (Becker, 1999). Modern implants emerged in the 1960s with osseointegration. Endosseous implants are now being used for single tooth replacement, bridgework, complete-arch reconstructions and complete removable overdentures or to reconstruct maxillofacial defects (Sabri, 1998; Knabe and Hoffmeister, 1998; Balshi et al., 1999; Mericske-Stern, 1998). Implant dentistry is constantly growing as new levels of biological technology emerge.

In the last five decades, polymer-based composites have been used as dental restorative materials (Alsharif et al., 2014) due to their ability to preserve teeth better and because of the low risk of leakage during bonding to enamel

(Leprince et al., 2013; Ferracane, 2011). However, these types of materials have limitations: (1) weakness in mechanical properties (Mahn, 2013) and (2) high polymerization shrinkage (Pires de Souza et al., 2009). These weaknesses lead to shorter lifespan of dental resin-based composite (5–7 years) compared to dental amalgam (13 years) (Zhang and Darvell, 2012; Chen et al., 2011). Recently, a number of materials have been developed with improved aesthetic quality and the ability to bond better with the enamel surface (Leloup et al., 2001; Atai et al., 2009). One of the materials is polydimethacrylate monomer, a reinforcement that interacts chemically or mechanically with the matrix (Sideridou et al., 2003). Bisphenol A-glycol dimethacrylate (Bis-GMA) monomer has been extensively used as a matrix due to its low polymerization shrinkage, low thermal expansion, acceptable clinical handling and low volatility (Khatri et al., 2003). Triethylene glycol dimethacrylate is used to diminish viscosity of the Bis-GMA and eventually improve dispersion of reinforcements following dilution (Antonucci et al., 2012; Zhang and Darvell, 2010).

Regardless of advancements of dental composites, improving their mechanical properties remains a challenge. Adequate mechanical properties of dental composites such as tensile, flexural and hardness are paramount. To minimize these shortcomings, various reinforcements have been used such as silica, glass fiber (van Heumen et al., 2008; Lin et al., 2008; Fong, 2004), organic polymer fiber (Sun et al., 2010) and ceramic whiskers (Xu et al., 2010b) with successful outcomes for dental applications. However, these fillers did not add to the bioactivity of the composites or prevent caries (Sideridou and Karabela, 2009; Yousif et al., 2012).

In order to increase the mineral content of the tooth, enhance the mechanical properties of composites and reduce polymerization, bionanocomposites were developed with nanoparticles or nanofibers as reinforcement. Tetracycline-incorporated nanofibers were successfully synthesized via electro-spinning and functioned as an antimicrobial surface modifier and osteogenic inducer for titanium dental implants (Bottino Marco et al., 2017). In a recent study, resin-based dental sealants modified with nylon-6 and chitosan nanofibers were prepared to provide an antibacterial effect (Hamilton et al., 2015). Poly( $\epsilon$ -caprolactone)-poly(ethylene glycol) copolymer nanofibrous mats incorporated into chitosan for the regeneration of periodontum were developed (Jiang et al., 2015).

---

## 2.6 CONCLUSIONS

Research in biomedical engineering has drawn considerable attention over the last few decades on the development of new materials, processing and their assessment and possible applications. Organic/inorganic micro/nanofibers are paramount to successful outcomes in biomedical engineering. A broad range of fibers of polymers including engineering plastics, biopolymers, conducting polymers,

block copolymers, and polymer blends have been explored. Today ceramic/glass fiber is playing a crucial role in bone and soft tissue engineering due to its high surface-to-volume ratio, high porosity, adjustable pore size and morphological similarity to the ECM. More importantly, nanofibers appear to interact with cells, for example, selective endocytosis, adhesion and orientation. Organic/inorganic micro/nanofibers may also prove to be a suitable carrier system in drug delivery applications in a wide variety of situations such as bone tissue engineering and cancer therapy. Future research should take advantage of these properties of fibers.

---

## REFERENCES

- Aitasalo, K.M.J., Piitulainen, J.M., Rekola, J., Vallittu, P.K., 2014. Craniofacial bone reconstruction with bioactive fiber reinforced composite implant. *Head Neck* 36 (5), 722–728.
- Alsharif, S.O., Akil, H.B.M., El-Aziz, N.A.A., Ahmad, Z.A.B., 2014. Effect of alumina particles loading on the mechanical properties of light-cured dental resin composites. *Mater. Des. (1980–2015)* 54, 430–435.
- Amini, A.R., Laurencin, C.T., Nukavarapu, S.P., 2012. Bone tissue engineering: recent advances and challenges. *Crit. Rev. Biomed. Eng.* 40 (5).
- Ananta, M., Aulin, C.E., Hilborn, J., Aibibu, D., Houis, S., Brown, R.A., et al., 2008. A poly(lactic acid-*co*-caprolactone)–collagen hybrid for tissue engineering applications. *Tissue Eng. Part A* 15 (7), 1667–1675.
- Ang-atikarnkul, P., Watthanaphanit, A., Rujiravanit, R., 2014. Fabrication of cellulose nanofiber/chitin whisker/silk sericin bionanocomposite sponges and characterizations of their physical and biological properties. *Compos. Sci. Technol.* 96, 88–96.
- Antonucci, J.M., Zeiger, D.N., Tang, K., Lin-Gibson, S., Fowler, B.O., Lin, N.J., 2012. Synthesis and characterization of dimethacrylates containing quaternary ammonium functionalities for dental applications. *Dental Mater.* 28 (2), 219–228. 2018/06/22.
- Atai, M., Solhi, L., Nodehi, A., Mirabedini, S.M., Kasraei, S., Akbari, K., et al., 2009. PMMA-grafted nanoclay as novel filler for dental adhesives. *Dental Mater.* 25 (3), 339–347. 2018/06/22.
- Babaeijandaghi, F., Shabani, I., Seyedjafari, E., Naraghi, Z.S., Vasei, M., Haddadi-Asl, V., et al., 2010. Accelerated epidermal regeneration and improved dermal reconstruction achieved by polyethersulfone nanofibers. *Tissue Eng. Part A* 16 (11), 3527–3536.
- Ballo, A.M., Akca, E.A., Ozen, T., Lassila, L., Vallittu, P.K., Narhi, T.O., 2009. Bone tissue responses to glass fiber-reinforced composite implants—a histomorphometric study. *Clin. Oral Implants Res.* 20 (6), 608–615.
- Balshi, T.J., Wolfinger, G.J., Balshi, S.F., 1999. Analysis of 356 pterygomaxillary implants in edentulous arches for fixed prosthesis anchorage. *Int. J. Oral Maxillofac. Implants* 14 (3), 398–406.
- Barber, J.G., Handorf, A.M., Allee, T.J., Li, W.-J., 2011. Braided nanofibrous scaffold for tendon and ligament tissue engineering. *Tissue Eng. Part A* 19 (11-12), 1265–1274.
- Barrere, F., van der Valk, C.M., Dalmeijer, R.A.J., Meijer, G., van Blitterswijk, C.A., de Groot, K., et al., 2003. Osteogenicity of octacalcium phosphate coatings applied on porous metal implants. *J. Biomed. Mater. Res. Part A* 66 (4), 779–788.

- Becker, M.J., 1999. Ancient "dental implants": a recently proposed example from France evaluated with other spurious examples. *Int. J. Oral Maxillofac. Implants* 14 (1).
- Berry, S.M., Warren, S.P., Hilgart, D.A., Schworer, A.T., Pabba, S., Gobin, A.S., et al., 2011. Endothelial cell scaffolds generated by 3D direct writing of biodegradable polymer microfibers. *Biomaterials* 32 (7), 1872–1879.
- Bhardwaj, N., Kundu, S.C., 2010. Electrospinning: a fascinating fiber fabrication technique. *Biotechnol. Adv.* 28 (3), 325–347.
- Bitar, K.N., Zakhem, E., 2013. Tissue engineering and regenerative medicine as applied to the gastrointestinal tract. *Curr. Opin. Biotechnol.* 24 (5), 909–915.
- Bottino Marco, C., Munchow Eliseu, A., Albuquerque Maria, T.P., Kamocki, K., Shahi, R., Gregory Richard, L., et al., 2017. Tetracycline incorporated polymer nanofibers as a potential dental implant surface modifier. *J. Biomed. Mater. Res. Part B: Appl. Biomater.* 105 (7), 2085–2092.
- Brown, R.F., Day, D.E., Day, T.E., Jung, S., Rahaman, M.N., Fu, Q., 2008. Growth and differentiation of osteoblastic cells on 13-93 bioactive glass fibers and scaffolds. *Acta Biomater.* 4 (2), 387–396.
- Bunting, S., Di Silvio, L., Deb, S., Hall, S., 2005. Bioresorbable glass fibres facilitate peripheral nerve regeneration. *J. Hand Surg.* 30 (3), 242–247.
- Byrne, J.D., Betancourt, T., BrannonPeppas, L., 2008. Active targeting schemes for nanoparticle systems in cancer therapeutics. *Adv. Drug Deliv. Rev.* 60 (15), 1615–1626.
- Chen, G., Sato, T., Ohgushi, H., Ushida, T., Tateishi, T., Tanaka, J., 2005. Culturing of skin fibroblasts in a thin PLGA–collagen hybrid mesh. *Biomaterials* 26 (15), 2559–2566.
- Chen, J.L., Yin, Z., Shen, W.L., Chen, X., Heng, B.C., Zou, X.H., et al., 2010. Efficacy of hESC-MSCs in knitted silk–collagen scaffold for tendon tissue engineering and their roles. *Biomaterials* 31 (36), 9438–9451.
- Chen, L., Yu, Q., Wang, Y., Li, H., 2011. BisGMA/TEGDMA dental composite containing high aspect-ratio hydroxyapatite nanofibers. *Dental Mater.* 27 (11), 1187–1195. 2018/06/22.
- Chen, F., Hayami, J.W., Amsden, B.G., 2014. Electrospun poly(L-lactide-co-acryloyl carbonate) fiber scaffolds with a mechanically stable crimp structure for ligament tissue engineering. *Biomacromolecules* 15 (5), 1593–1601.
- Cho, H.J., Yoo, Y.J., Kim, J.W., Park, Y.H., Bae, D.G., Um, I.C., 2012. Effect of molecular weight and storage time on the wet-and electro-spinning of regenerated silk fibroin. *Polym. Degrad. Stab.* 97 (6), 1060–1066.
- Choi, J.H., Gimble, J.M., Lee, K., Marra, K.G., Rubin, J.P., Yoo, J.J., et al., 2010. Adipose tissue engineering for soft tissue regeneration. *Tissue Eng. Part B: Rev.* 16 (4), 413–426.
- Chung, B.G., Lee, K.-H., Khademhosseini, A., Lee, S.-H., 2012. Microfluidic fabrication of microengineered hydrogels and their application in tissue engineering. *Lab Chip* 12 (1), 45–59.
- Connelly, J.T., Petrie, T.A., García, A.J., Levenston, M.E., 2011. Fibronectin-and collagen-mimetic ligands regulate bone marrow stromal cell chondrogenesis in three-dimensional hydrogels. *Eur. Cell Mater.* 22, 168–176.
- Cooper, J.A., Lu, H.H., Ko, F.K., Freeman, J.W., Laurencin, C.T., 2005. Fiber-based tissue-engineered scaffold for ligament replacement: design considerations and in vitro evaluation. *Biomaterials* 26 (13), 1523–1532.

- Cooper, J.A., Sahota, J.S., Gorum, W.J., Carter, J., Doty, S.B., Laurencin, C.T., 2007. Biomimetic tissue-engineered anterior cruciate ligament replacement. *Proc. Natl. Acad. Sci.* 104 (9), 3049–3054.
- Costa-Pinto, A.R., Correlo, V.M., Sol, P.C., Bhattacharya, M., Srouji, S., Livne, E., et al., 2012. Chitosan-poly(butylene succinate) scaffolds and human bone marrow stromal cells induce bone repair in a mouse calvaria model. *J. Tissue Eng. Regen. Med.* 6 (1), 21–28.
- Crowley, D.J., Kanakaris, N.K., Giannoudis, P.V., 2007. Debridement and wound closure of open fractures: the impact of the time factor on infection rates. *Injury* 38 (8), 879–889.
- Dai, W., Kawazoe, N., Lin, X., Dong, J., Chen, G., 2010. The influence of structural design of PLGA/collagen hybrid scaffolds in cartilage tissue engineering. *Biomaterials* 31 (8), 2141–2152.
- Dai, X., Kathiria, K., Huang, Y.C., 2014. Electrospun fiber scaffolds of poly(glycerol-dodecanedioate) and its gelatin blended polymers for soft tissue engineering. *Biofabrication* 6 (3), 5003–5005.
- De Diego, M.A., Coleman, N.J., Hench, L.L., 2000. Tensile properties of bioactive fibers for tissue engineering applications. *J. Biomed. Mater. Res.* 53 (3), 199–203.
- Dubsky, M., Kubinova, S., Sirc, J., Voska, L., Zajicek, R., Zajicova, A., et al., 2012. Nanofibers prepared by needleless electrospinning technology as scaffolds for wound healing. *J. Mater. Sci.: Mater. Med.* 23 (4), 931–941.
- Efeoglu, C., Burke, J.L., Parsons, A.J., Aitchison, G.A., Scotchford, C., Rudd, C., et al., 2009. Analysis of calvarial bone defects in rats using microcomputed tomography: potential for a novel composite material and a new quantitative measurement. *Br. J. Oral Maxillofac. Surg.* 616–621.
- Ellä, V., Annala, T., Länsman, S., Nurminen, M., Kellomäki, M., 2011. Knitted polylactide 96/4 L/D structures and scaffolds for tissue engineering: shelf life, in vitro and in vivo studies. *Biomater* 1 (1), 102–113.
- El-Newehy, M.H., Al-Deyab, S.S., Kenawy, E.-R., Abdel-Megeed, A., 2012. Fabrication of electrospun antimicrobial nanofibers containing metronidazole using nanospider technology. *Fibers Polym.* 13 (6), 709–717.
- Eslami, M., Vrana, N.E., Zorlutuna, P., Sant, S., Jung, S., Masoumi, N., et al., 2014. Fiber-reinforced hydrogel scaffolds for heart valve tissue engineering. *J. Biomater. Appl.* 29 (3), 399–410.
- Fang, Q., Chen, D., Yang, Z., Li, M., 2009. In vitro and in vivo research on using *Antheraea pernyi* silk fibroin as tissue engineering tendon scaffolds. *Mater. Sci. Eng.: C* 29 (5), 1527–1534.
- Fazzalari, N.L., 2011. Bone fracture and bone fracture repair. *Osteoporosis Int.* 22 (6), 2003–2006.
- Ferracane, J.L., 2011. Resin composite--state of the art. *Dental Mater.* 27 (1), 29–38.
- Flynn, L., Prestwich, G.D., Semple, J.L., Woodhouse, K.A., 2007. Adipose tissue engineering with naturally derived scaffolds and adipose-derived stem cells. *Biomaterials* 28 (26), 3834–3842.
- Fong, H., 2004. Electrospun nylon 6 nanofiber reinforced BIS-GMA/TEGDMA dental restorative composite resins. *Polymer* 45 (7), 2427–2432.
- Full, S.M., Delman, C., Gluck, J.M., Abdmaulen, R., Shemin, R.J., Heydarkhan-Hagvall, S., 2015. Effect of fiber orientation of collagen-based electrospun meshes on human



- fibroblasts for ligament tissue engineering applications. *J. Biomed. Mater. Res. B Appl. Biomater.* 103 (1), 39–46.
- Gabriel, L.P., Rodrigues, A.A., Macedo, M., Jardini, A.L., Maciel Filho, R., 2017. Electrospun polyurethane membranes for tissue engineering applications. *Mater. Sci. Eng. C, Mater. Biol. Appl.* 72, 113–117.
- Garfein, E.S., Orgill, D.P., Pribaz, J.J., 2003. Clinical applications of tissue engineered constructs. *Clin. Plast. Surg.* 30 (4), 485–498.
- Gautam, S., Chou, C.F., Dinda, A.K., Potdar, P.D., Mishra, N.C., 2014. Surface modification of nanofibrous polycaprolactone/gelatin composite scaffold by collagen type I grafting for skin tissue engineering. *Mater. Sci. Eng. C, Mater. Biol. Appl.* 34, 402–409.
- Guangyuan, L., Baiyang, S., Gan, W., Yujun, W., Yandao, G., Xiufang, Z., et al., 2008. Controlling the degradation of covalently cross-linked carboxymethyl chitosan utilizing bimodal molecular weight distribution. *J. Biomater. Appl.* 23 (5), 435–451.
- Gupta, B., Revagade, N., 2009. Development and structural evaluation of poly(lactic acid) based knitted scaffold for human urinary bladder reconstruction. *Indian J. Fibre Textile Res.* 34 (2), 115.
- Haaparanta, A.M., Uppstu, P., Hannula, M., Ella, V., Rosling, A., Kellomaki, M., 2015. Improved dimensional stability with bioactive glass fibre skeleton in poly(lactide-co-glycolide) porous scaffolds for tissue engineering. *Mater. Sci. Eng. C, Mater. Biol. Appl.* 56, 457–466.
- Hamilton, M., Otte Andrew, D., Gregory Richard, L., Pinal, R., Ferreira-Zandona, A., Bottino Marco, C., 2015. Physicomechanical and antibacterial properties of experimental resin-based dental sealants modified with nylon-6 and chitosan nanofibers. *J. Biomed. Mater. Res. Part B: Appl. Biomater* 103 (8), 1560–1568.
- Hasan, S.K., Moon, S., Song, Y.S., Keles, H.O., Manzur, F., Mikkilineni, S., et al., 2009. Layer by layer 3D tissue epitaxy by cell laden hydrogel droplets. *IEEE 35th Annual Northeast Bioengineering Conference. IEEE, Boston, MA.*
- Hasegawa, S., Neo, M., Tamura, J., Fujibayashi, S., Takemoto, M., Shikinami, Y., et al., 2007. In vivo evaluation of a porous hydroxyapatite/poly-DL-lactide composite for bone tissue engineering. *J. Biomed. Mater. Res. Part A* 81 (4), 930–938.
- Heim, M., Römer, L., Scheibel, T., 2010. Hierarchical structures made of proteins. The complex architecture of spider webs and their constituent silk proteins. *Chem. Soc. Rev.* 39 (1), 156–164.
- Hemrich, K., Von Heimburg, D., 2006. Biomaterials for adipose tissue engineering. *Expert Rev. Med. Devices* 3 (5), 635–645.
- Hench, L.L., Polak, J.M., 2002. Third-generation biomedical materials. *Science* 295 (5557), 1014–1017.
- van Heumen, Cl.C.M., Kreulen, C.M., Bronkhorst, E.M., Lesaffre, E., Creugers, N.H.J., 2008. Fiber-reinforced dental composites in beam testing. *Dental Mater.* 24 (11), 1435–1443. 2018/06/22.
- Hong, Y., Guan, J., Fujimoto, K.L., Hashizume, R., Pelinescu, A.L., Wagner, W.R., 2010. Tailoring the degradation kinetics of poly(ester carbonate urethane) urea thermoplastic elastomers for tissue engineering scaffolds. *Biomaterials* 31 (15), 4249–4258.
- Hsu, Y.-H., Chen, D.W.-C., Tai, C.-D., Chou, Y.-C., Liu, S.-J., Ueng, S.W.-N., et al., 2014. Biodegradable drug-eluting nanofiber-enveloped implants for sustained release of high bactericidal concentrations of vancomycin and ceftazidime: in vitro and in vivo studies. *Int. J. Nanomed.* 9, 4347.

- Huang, L., McMillan, R.A., Apkarian, R.P., Pourdeyhimi, B., Conticello, V.P., Chaikof, E. L., 2000. Generation of synthetic elastin-mimetic small diameter fibers and fiber networks. *Macromolecules* 33 (8), 2989–2997.
- Huang, J., You, T., 2013. Electrospun nanofibers: from rational design, fabrication to electrochemical sensing applications. *Intech Open*.
- Huang, Z.-M., Zhang, Y.-Z., Kotaki, M., Ramakrishna, S., 2003. A review on polymer nanofibers by electrospinning and their applications in nanocomposites. *Compos. Sci. Technol.* 63 (15), 2223–2253.
- Iftekhar, A., 2003. *Biomedical Composites. Standard Handbook of Biomedical Engineering and Design.* McGraw-Hill, New York.
- Iyer, A.K., Khaled, G., Fang, J., Maeda, H., 2006. Exploiting the enhanced permeability and retention effect for tumor targeting. *Drug Discovery Today* 11 (17-18), 812–818.
- Jabr-Milane, L., van Vlerken, L., Devalapally, H., Shenoy, D., Komareddy, S., Bhavsar, M., et al., 2008. Multi-functional nanocarriers for targeted delivery of drugs and genes. *J. Controlled Release* 130 (2), 121–128.
- Jiang, W., Li, L., Zhang, D., Huang, S., Jing, Z., Wu, Y., et al., 2015. Incorporation of aligned PCL–PEG nanofibers into porous chitosan scaffolds improved the orientation of collagen fibers in regenerated periodontium. *Acta Biomater.* 25, 240–252.
- Jo, S., Shin, H., Shung, A.K., Fisher, J.P., Mikos, A.G., 2001. Synthesis and characterization of oligo (poly(ethylene glycol) fumarate) macromer. *Macromolecules* 34 (9), 2839–2844.
- Johnson, P.C., Mikos, A.G., Fisher, J.P., Jansen, J.A., 2007. Strategic directions in tissue engineering. *Tissue Eng.* 13 (12), 2827–2837.
- Kai, D., Prabhakaran, M.P., Chan, B.Q., Liow, S.S., Ramakrishna, S., Xu, F., et al., 2016. Elastic poly(epsilon-caprolactone)-polydimethylsiloxane copolymer fibers with shape memory effect for bone tissue engineering. *Biomed. Mater.* 11 (1), 015007.
- Khademhosseini, A., Vacanti, J.P., Langer, R., 2009. Progress in tissue engineering. *Sci. Am.* 300 (5), 64–71.
- Khan, Y.M., Katti, D.S., Laurencin, C.T., 2004. Novel polymer-synthesized ceramic composite-based system for bone repair: an in vitro evaluation. *J. Biomed. Mater. Res. Part A* 69 (4), 728–737.
- Khan, Y., Saadiq, F.E.-A., Laurencin, C.T., 2006. In vitro and in vivo evaluation of a novel polymer-ceramic composite scaffold for bone tissue engineering. *Engineering in Medicine and Biology Society, 2006 EMBS'06 28th Annual International Conference of the IEEE.* IEEE.
- Khatri, C.A., Stansbury, J.W., Schultheisz, C.R., Antonucci, J.M., 2003. Synthesis, characterization and evaluation of urethane derivatives of Bis-GMA. *Dental Mater.* 19 (7), 584–588. 2018/06/22.
- Kim, H., Kim, H., Knowles, J.C., 2006. Production and potential of bioactive glass nanofibers as a Next generation biomaterial. *Adv. Funct. Mater.* 16 (12), 1529–1535.
- Kim, H.-W., Lee, H.-H., Chun, G.-S., 2008. Bioactivity and osteoblast responses of novel biomedical nanocomposites of bioactive glass nanofiber filled poly(lactic acid). *J. Biomed. Mater. Res. Part A* 85 (3), 651–663.
- Kim, G.H., Ahn, S.H., Lee, H.J., Lee, S., Cho, Y., Chun, W., 2011. A new hybrid scaffold using rapid prototyping and electrohydrodynamic direct writing for bone tissue regeneration. *J. Mater. Chem.* 21 (47), 19138–19143.

- Kishan, A.P., Robbins, A.B., Mohiuddin, S.F., Jiang, M., Moreno, M.R., Cosgriff-Hernandez, E.M., 2016. Fabrication of macromolecular gradients in aligned fiber scaffolds using a combination of in-line blending and air-gap electrospinning. *Acta Biomater.* 30, 703–706.
- Knabe, C., Hoffmeister, B., 1998. The use of implant-supported ceramometal titanium prostheses following sinus lift and augmentation procedures: a clinical report. *Int. J. Oral Maxillofac. Implants* 13 (1).
- Kretlow, J.D., Klouda, L., Mikos, A.G., 2007. Injectable matrices and scaffolds for drug delivery in tissue engineering. *Adv. Drug Delivery Rev.* 59 (4), 263–273.
- Lakshman, L.R., Shalumon, K.T., Nair, S.V., Jayakumar, R., Nair, S.V., 2010. Preparation of silver nanoparticles incorporated electrospun polyurethane nanofibrous mat for wound dressing. *Journal of Macromolecular Science, Part A: Pure Appl. Chem.* 47 (10), 1012–1018.
- Lee, S.-W., Belcher, A.M., 2004. Virus-based fabrication of micro-and nanofibers using electrospinning. *Nano Lett.* 4 (3), 387–390.
- Lee, E.J., Lee, J.H., Jin, L., Jin, O.S., Shin, Y.C., Sang, J.O., et al., 2014. Hyaluronic acid/poly(lactic-co-glycolic acid) core/shell fiber meshes loaded with epigallocatechin-3-O-gallate as skin tissue engineering scaffolds. *J. Nanosci. Nanotechnol.* 14 (11), 8458–8463.
- Leloup, G., D’Hoore, W., Bouter, D., Degrange, M., Vreven, J., 2001. Concise review biomaterials & bioengineering: meta-analytical review of factors involved in dentin adherence. *J. Dental Res.* 80 (7), 1605–1614.
- Leprince, J.G., Palin, W.M., Hadis, M.A., Devaux, J., Leloup, G., 2013. Progress in dimethacrylate-based dental composite technology and curing efficiency. *Dental Mater.* 29 (2), 139–156.
- Lin, S., Cai, Q., Ji, J., Sui, G., Yu, Y., Yang, X., et al., 2008. Electrospun nanofiber reinforced and toughened composites through in situ nano-interface formation. *Compos. Sci. Technol.* 68 (15), 3322–3329.
- Liu, H., Fan, H., Wang, Y., Toh, S.L., Goh, J.C., 2008. The interaction between a combined knitted silk scaffold and microporous silk sponge with human mesenchymal stem cells for ligament tissue engineering. *Biomaterials* 29 (6), 662–674.
- Liu, D., Liu, S., Jing, X., Li, X., Li, W., Huang, Y., 2012. Necrosis of cervical carcinoma by dichloroacetate released from electrospun polylactide mats. *Biomaterials* 33 (17), 4362–4369.
- Li, Y., Liu, Y., Li, S., Liang, G., Jiang, C., Hu, Q., 2016. Novel control of gel fraction and enhancement of bonding strength for constructing 3D architecture of tissue engineering scaffold with alginate tubular fiber. *J. Biosci. Bioeng.* 121 (1), 111–116.
- Li, D., Xia, Y., 2004. Electrospinning of nanofibers: reinventing the wheel? *Adv. Mater.* 16 (14), 1151–1170.
- Lu, L., Garcia, C.A., Mikos, A.G., 1998. Retinal pigment epithelium cell culture on thin biodegradable poly(D,L-lactic-co-glycolic acid) films. *J. Biomater. Sci., Polym. Ed.* 9 (11), 1187–1205.
- Lu, H., Zhang, T., Wang, X.P., Fang, Q.F., 2009. Electrospun submicron bioactive glass fibers for bone tissue scaffold. *J. Mater. Sci.: Mater. Med.* 20 (3), 793–798.
- Luo, X., Xie, C., Wang, H., Liu, C., Yan, S., Li, X., 2012. Antitumor activities of emulsion electrospun fibers with core loading of hydroxycamptothecin via intratumoral implantation. *Int. J. Pharm.* 425 (1-2), 19–28.

- Ma, G., Liu, Y., Peng, C., Fang, D., He, B., Nie, J., 2011. Paclitaxel loaded electrospun porous nanofibers as mat potential application for chemotherapy against prostate cancer. *Carbohydr. Polym.* 86 (2), 505–512.
- Mahn, E., 2013. Clinical criteria for the successful curing of composite materials. *Revista Clinica de Periodoncia, Implantologia y Rehabilitacion Oral* 6 (3), 148–153.
- Mano, J.F., Silva, G.A., Azevedo, H.S., Malafaya, P.B., Sousa, R.A., Silva, S.S., et al., 2007. Natural origin biodegradable systems in tissue engineering and regenerative medicine: present status and some moving trends. *J. R. Soc. Interface* 4 (17), 999–1030.
- Mericske-Stern, R., 1998. Treatment outcomes with implant-supported overdentures: clinical considerations. *J. Prosthet. Dent.* 79 (1), 66–73.
- Mi, H.Y., Palumbo, S., Jing, X., Turng, L.S., Li, W.J., Peng, X.F., 2014. Thermoplastic polyurethane/hydroxyapatite electrospun scaffolds for bone tissue engineering: effects of polymer properties and particle size. *J. Biomed. Mater. Res. Part B, Appl. Biomater.* 102 (7), 1434–1444.
- Mi, X., Vijayaragavan, K.S., Heldt, C.L., 2014. Virus adsorption of water-stable quaternized chitosan nanofibers. *Carbohydr. Res.* 387, 24–29.
- Moimas, L., Biasotto, M., Di Lenarda, R., Olivo, A., Schmid, C., 2006. Rabbit pilot study on the resorbability of three-dimensional bioactive glass fibre scaffolds. *Acta Biomater.* 2 (2), 191–199.
- Moutos, F.T., Guilak, F., 2009. Functional properties of cell-seeded three-dimensionally woven poly( $\epsilon$ -caprolactone) scaffolds for cartilage tissue engineering. *Tissue Eng. Part A* 16 (4), 1291–1301.
- Moutos, F.T., Freed, L.E., Guilak, F., 2007. A biomimetic three-dimensional woven composite scaffold for functional tissue engineering of cartilage. *Nat. Mater.* 6 (2), 162–167.
- Nandakumar, A., Yang, L., Habibovic, P., van Blitterswijk, C., 2010. Calcium phosphate coated electrospun fiber matrices as scaffolds for bone tissue engineering. *Langmuir* 26 (10), 7380–7387.
- Nichol, J.W., Khademhosseini, A., 2009. Modular tissue engineering: engineering biological tissues from the bottom up. *Soft Matter* 5 (7), 1312–1319.
- Orr, S.B., Chainani, A., Hippensteel, K.J., Kishan, A., Gilchrist, C., Garrigues, N.W., et al., 2015. Aligned multilayered electrospun scaffolds for rotator cuff tendon tissue engineering. *Acta Biomater.* 24, 117–126.
- Panyala, N.R., Pena-Mendez, E.M., Havel, J., 2009. Gold and nanogold in medicine: overview, toxicology and perspectives. *J. Appl. Biomed. (De Gruyter Open)* 7 (2).
- Peter, S.J., Yaszemski, M.J., Suggs, L.J., Payne, R.G., Langer, R., Hayes, W.C., et al., 1997. Characterization of partially saturated poly(propylene fumarate) for orthopaedic application. *J. Biomater. Sci., Polym. Ed.* 8 (11), 893–904.
- Pires de Souza, Fd.C.P., Drubi Filho, B., Casemiro, L.A., Garcia, Ld.F.R., Consani, S., 2009. Polymerization shrinkage stress of composites photoactivated by different light sources. *Braz. Dental J.* 20, 319–324.
- Pollick, S., Shors, E.C., Holmes, R.E., Kraut, R.A., 1995. Bone formation and implant degradation of coralline porous ceramics placed in bone and ectopic sites. *J. Oral Maxillofac. Surg.* 53 (8), 915–922.
- Pulkkinen, M., Pikkarainen, J., Wirth, T., Tarvainen, T., Haapa-aho, V., Korhonen, H., et al., 2008. Three-step tumor targeting of paclitaxel using biotinylated PLA-PEG nanoparticles and avidin-biotin technology: formulation development and in vitro anticancer activity. *Eur. J. Pharm. Biopharm.* 70 (1), 66–74.

- Qiu, W., Teng, W., Cappello, J., Wu, X., 2009. Wet-spinning of recombinant silk-elastin-like protein polymer fibers with high tensile strength and high deformability. *Biomacromolecules* 10 (3), 602–608.
- Raveendran, S., Dhandayuthapani, B., Nagaoka, Y., Yoshida, Y., Maekawa, T., Kumar, D. S., 2013. Biocompatible nanofibers based on extremophilic bacterial polysaccharide, Mauran from *Halomonas maura*. *Carbohydr. Polym.* 92 (2), 1225–1233.
- Ravichandran, R., Venugopal, J.R., Sundarajan, S., Mukherjee, S., Sridhar, R., Ramakrishna, S., 2013. Expression of cardiac proteins in neonatal cardiomyocytes on PGS/fibrinogen core/shell substrate for cardiac tissue engineering. *Int. J. Cardiol.* 167 (4), 1461–1468.
- Reddy, C.S., Venugopal, J.R., Ramakrishna, S., Zussman, E., 2014. Polycaprolactone/oligomer compound scaffolds for cardiac tissue engineering. *J. Biomed. Mater. Res. Part A* 102 (10), 3713–3725.
- Reddy, N., Yang, Y., 2011. Potential of plant proteins for medical applications. *Trends Biotechnol.* 29 (10), 490–498.
- Rentsch, B., Hofmann, A., Breier, A., Rentsch, C., Scharnweber, D., 2009. Embroidered and surface modified polycaprolactone-co-lactide scaffolds as bone substitute: in vitro characterization. *Ann. Biomed. Eng.* 37 (10), 2118–2128.
- Ripamonti, U., 1991. The induction of bone in osteogenic composites of bone matrix and porous hydroxyapatite replicas: an experimental study on the baboon (*Papio ursinus*). *J. Oral Maxillofac. Surg.* 49 (8), 817–830.
- Ripamonti, U., 1996. Osteoinduction in porous hydroxyapatite implanted in heterotopic sites of different animal models. *Biomaterials* 17 (1), 31–35.
- Ripamonti, U., Crooks, J., Khoali, L., Roden, L., 2009. The induction of bone formation by coral-derived calcium carbonate/hydroxyapatite constructs. *Biomaterials* 30 (7), 1428–1439.
- Sabri, R., 1998. Four single-tooth implants as supernumerary premolars in the treatment of diastemas and microdontia: report of a case. *Int. J. Oral Maxillofac. Implants* 13 (5).
- Sahoo, S., Cho-Hong, J.G., Siew-Lok, T., 2007. Development of hybrid polymer scaffolds for potential applications in ligament and tendon tissue engineering. *Biomed. Mater.* 2 (3), 169.
- Sala, F.G., Matthews, J.A., Speer, A.L., Torashima, Y., Barthel, E.R., Grikscheit, T.C., 2011. A multicellular approach forms a significant amount of tissue-engineered small intestine in the mouse. *Tissue Eng. Part A* 17 (13-14), 1841–1850.
- Sapir, Y., Kryukov, O., Cohen, S., 2011. Integration of multiple cell-matrix interactions into alginate scaffolds for promoting cardiac tissue regeneration. *Biomaterials* 32 (7), 1838–1847.
- Sarkar, F.H., Banerjee, S., Li, Y., 2007. Pancreatic cancer: pathogenesis, prevention and treatment. *Toxicol. Appl. Pharmacol.* 224 (3), 326–336.
- Sawyer-Glover, A.M., Shellock, F.G., 2000. Pre-MRI procedure screening: recommendations and safety considerations for biomedical implants and devices. *J. Magn. Reson. Imaging* 12 (1), 92–106.
- Schmucker, A.L., Dickerson, M.B., Rycenga, M., Mangelson, B.F., Brown, K.A., Naik, R. R., et al., 2014. Combined chemical and physical encoding with silk fibroin-embedded nanostructures. *Small* 10 (8), 1485–1489.
- Shachar, M., Tsur-Gang, O., Dvir, T., Leor, J., Cohen, S., 2011. The effect of immobilized RGD peptide in alginate scaffolds on cardiac tissue engineering. *Acta Biomater.* 7 (1), 152–162.

- Shalumon, K.T., Deepthi, S., Anupama, M.S., Nair, S.V., Jayakumar, R., Chennazhi, K.P., 2015. Fabrication of poly(L-lactic acid)/gelatin composite tubular scaffolds for vascular tissue engineering. *Int. J. Biol. Macromol.* 72, 1048–1055.
- Shao, W., He, J., Sang, F., Ding, B., Chen, L., Cui, S., et al., 2016. Coaxial electrospun aligned tussah silk fibroin nanostructured fiber scaffolds embedded with hydroxyapatite-tussah silk fibroin nanoparticles for bone tissue engineering. *Mater. Sci. Eng. C, Mater. Biol. Appl.* 58, 342–351.
- Shapiro, F., 2008. Bone development and its relation to fracture repair. The role of mesenchymal osteoblasts and surface osteoblasts. *Eur. Cell Mater.* 15, 53–76.
- Shellock, F.G., 2001. Metallic neurosurgical implants: evaluation of magnetic field interactions, heating, and artifacts at 1.5-Tesla. *J. Magn. Reson. Imaging* 14 (3), 295–299.
- Shin, H., 2007. Fabrication methods of an engineered microenvironment for analysis of cell–biomaterial interactions. *Biomaterials* 28 (2), 126–133.
- Sideridou, I., Tserki, V., Papanastasiou, G., 2003. Study of water sorption, solubility and modulus of elasticity of light-cured dimethacrylate-based dental resins. *Biomaterials* 24 (4), 655–665.
- Sideridou, I.D., Karabela, M.M., 2009. Effect of the amount of 3-methacyloxypropyltrimethoxysilane coupling agent on physical properties of dental resin nanocomposites. *Dental Mater.* 25 (11), 1315–1324. 2018/06/22.
- Sill, T.J., von Recum, H.A., 2008. Electrospinning: applications in drug delivery and tissue engineering. *Biomaterials* 29 (13), 1989–2006.
- Smith, J.O., Aarvold, A., Tayton, E.R., Dunlop, D.G., Oreffo, R.O.C., 2011. Skeletal tissue regeneration: current approaches, challenges, and novel reconstructive strategies for an aging population. *Tissue Eng. Part B: Rev.* 17 (5), 307–320.
- Sohn, S., Gido, S.P., 2009. Wet-spinning of osmotically stressed silk fibroin. *Biomacromolecules* 10 (8), 2086–2091.
- Speer, A.L., Sala, F.G., Matthews, J.A., Grikscheit, T.C., 2011. Murine tissue-engineered stomach demonstrates epithelial differentiation. *J. Surg. Res.* 171 (1), 6–14.
- Stosich, M.S., Bastian, B., Marion, N.W., Clark, P.A., Reilly, G., Mao, J.J., 2007. Vascularized adipose tissue grafts from human mesenchymal stem cells with bioactive cues and microchannel conduits. *Tissue Eng.* 13 (12), 2881–2890.
- Stosich, M.S., Muioli, E.K., Wu, J.K., Lee, C.H., Rohde, C., Yoursef, A.M., et al., 2009. Bioengineering strategies to generate vascularized soft tissue grafts with sustained shape. *Methods* 47 (2), 116–121.
- Struijs, P.A.A., Poolman, R.W., Bhandari, M., 2007. Infected nonunion of the long bones. *J. Orthop. Trauma* 21 (7), 507–511.
- Suggs, L.J., Krishnan, R.S., Garcia, C.A., Peter, S.J., Anderson, J.M., Mikos, A.G., 1998. In vitro and in vivo degradation of poly(propylene fumarate-co-ethylene glycol) hydrogels. *J. Biomed. Mater. Res.* 42 (2), 312–320.
- Sun, W., Cai, Q., Li, P., Deng, X., Wei, Y., Xu, M., et al., 2010. Post-draw PAN–PMMA nanofiber reinforced and toughened Bis-GMA dental restorative composite. *Dental Mater.* 26 (9), 873–880. 2018/06/22.
- Tentori, A.M., Jaworski, J., 2014. Fabrication and applications of biological fibers. *Bio Des.* 2 (3), 69–80.
- Thomas, A., Kolan, K.C., Leu, M.C., Hilmas, G.E., 2016. Freeform extrusion fabrication of titanium fiber reinforced 13-93 bioactive glass scaffolds. *J. Mech. Behav. Biomed. Mater.* 69, 153–162.

- Trampuz, A., Zimmerli, W., 2006. Diagnosis and treatment of infections associated with fracture-fixation devices. *Injury* 37 (2), S59–S66.
- Tseng, H., Puperi, D.S., Kim, E.J., Ayoub, S., Shah, J.V., Cuchiara, M.L., et al., 2014. Anisotropic poly(ethylene glycol)/polycaprolactone hydrogel-fiber composites for heart valve tissue engineering. *Tissue Eng. Part A* 20 (19-20), 2634–2645.
- Tuusa, S.M.R., Lassila, L.V.J., Matinlinna, J.P., Peltola, M.J., Vallittu, P.K., 2005. Initial adhesion of glass fiber reinforced composite to the surface of porcine calvarial bone. *J. Biomed. Mater. Res. Part B: Appl. Biomater.* 75 (2), 334–342.
- Tuusa, S., Peltola, M.J., Tirri, T., Lassila, L.V.J., Vallittu, P.K., 2007. Frontal bone defect repair with experimental glass fiber reinforced composite with bioactive glass granule coating. *J. Biomed. Mater. Res. Part B: Appl. Biomater.* 82 (1), 149–155.
- Tuusa, S., Peltola, M.J., Tirri, T., Puska, M.A., Roytta, M., Aho, H., et al., 2008. Reconstruction of critical size calvarial bone defects in rabbits with glass-fiber reinforced composite with bioactive glass granule coating. *J. Biomed. Mater. Res. Part B: Appl. Biomater.* 84 (2), 510–519.
- Vallittu, P.K., Sevelius, C., 2000. Resin-bonded, glass fiber-reinforced composite fixed partial dentures: a clinical study. *J. Prosthet. Dent.* 84 (4), 413–418.
- Valonen, P.K., Moutos, F.T., Kusanagi, A., Moretti, M.G., Diekmann, B.O., Welter, J.F., et al., 2010. In vitro generation of mechanically functional cartilage grafts based on adult human stem cells and 3D-woven poly( $\epsilon$ -caprolactone) scaffolds. *Biomaterials* 31 (8), 2193–2200.
- Vashi, A.V., Keramidas, E., Abberton, K.M., Morrison, W.A., Wilson, J.L., O'Connor, A. J., et al., 2008. Adipose differentiation of bone marrow-derived mesenchymal stem cells using Pluronic F-127 hydrogel in vitro. *Biomaterials* 29 (5), 573–579.
- Waite, J.H., 1992. The DOPA ephemera: a recurrent motif in invertebrates. *Biol. Bull.* 183 (1), 178–184.
- Walters, V.I., Kwansa, A.L., Freeman, J.W., 2012. Design and analysis of braid-twist collagen scaffolds. *Connect. Tissue Res.* 53 (3), 255–266.
- Wan, A.C.A., Leong, M.F., Toh, J.K.C., Zheng, Y., Ying, J.Y., 2012. Multicomponent fibers by multi-interfacial polyelectrolyte complexation. *Adv. Healthc. Mater.* 1 (1), 101–105.
- Wang, C., Stewart, R.J., Kopeček, J., 1999. Hybrid hydrogels assembled from synthetic polymers and coiled-coil protein domains. *Nature* 397 (6718), 417–420.
- Wang, C., Kopeček, J., Stewart, R.J., 2001. Hybrid hydrogels cross-linked by genetically engineered coiled-coil block proteins. *Biomacromolecules* 2 (3), 912–920.
- Wang, J., Zhu, Y., Bawa, H.K., Ng, G., Wu, Y., Libera, M., et al., 2010. Oxygen-generating nanofiber cell scaffolds with antimicrobial properties. *ACS Appl. Mater. Interfaces* 3 (1), 67–73.
- Wang, J., Hu, W., Liu, Q., Zhang, S., 2011a. Dual-functional composite with anticoagulant and antibacterial properties based on heparinized silk fibroin and chitosan. *Colloids Surf. B: Biointerfaces* 85 (2), 241–247.
- Wang, C.-C., Yang, K.-C., Lin, K.-H., Liu, H.-C., Lin, F.-H., 2011b. A highly organized three-dimensional alginate scaffold for cartilage tissue engineering prepared by microfluidic technology. *Biomaterials* 32 (29), 7118–7126.
- Wang, J., Ye, R., Wei, Y., Wang, H., Xu, X., Zhang, F., et al., 2012. The effects of electrospun TSF nanofiber diameter and alignment on neuronal differentiation of human embryonic stem cells. *J. Biomed. Mater. Res. Part A* 100 (3), 632–645.

- Wang, X., Lou, T., Zhao, W., Song, G., Li, C., Cui, G., 2016. The effect of fiber size and pore size on cell proliferation and infiltration in PLLA scaffolds on bone tissue engineering. *J. Biomater. Appl.* 30 (10), 1545–1551.
- Wiradharma, N., Zhang, Y., Venkataraman, S., Hedrick, J.L., Yang, Y.Y., 2009. Self-assembled polymer nanostructures for delivery of anticancer therapeutics. *Nano Today* 4 (4), 302–317.
- Xie, C., Li, X., Luo, X., Yang, Y., Cui, W., Zou, J., et al., 2010. Release modulation and cytotoxicity of hydroxycamptothecin-loaded electrospun fibers with 2-hydroxypropyl- $\beta$ -cyclodextrin inoculations. *Int. J. Pharm.* 391 (1-2), 55–64.
- Xie, J., Wang, C.-H., 2006. Electrospun micro- and nanofibers for sustained delivery of paclitaxel to treat C6 glioma in vitro. *Pharm. Res.* 23 (8), 1817.
- Xu, X., Chen, X., Xu, X., Lu, T., Wang, X., Yang, L., et al., 2006. BCNU-loaded PEG-PLLA ultrafine fibers and their in vitro antitumor activity against Glioma C6 cells. *J. Controlled Release* 114 (3), 307–316.
- Xu, X., Chen, X., Ma, P., Wang, X., Jing, X., 2008. The release behavior of doxorubicin hydrochloride from medicated fibers prepared by emulsion-electrospinning. *Eur. J. Pharm. Biopharm.* 70 (1), 165–170.
- Xu, X., Chen, X., Wang, Z., Jing, X., 2009. Ultrafine PEG-PLA fibers loaded with both paclitaxel and doxorubicin hydrochloride and their in vitro cytotoxicity. *Eur. J. Pharm. Biopharm.* 72 (1), 18–25.
- Xu, W., Zhou, F., Ouyang, C., Ye, W., Yao, M., Xu, B., 2010a. Mechanical properties of small-diameter polyurethane vascular grafts reinforced by weft-knitted tubular fabric. *J. Biomed. Mater. Res. Part A* 92 (1), 1–8.
- Xu, W., Zhou, F., Ouyang, C., Ye, W., Yao, M., Xu, B., 2010b. Mechanical properties of small-diameter polyurethane vascular grafts reinforced by weft-knitted tubular fabric. *J. Biomed. Mater. Res. Part A* 92A (1), 1–8.
- Xu, H., Cai, S., Xu, L., Yang, Y., 2014. Water-stable three-dimensional ultrafine fibrous scaffolds from keratin for cartilage tissue engineering. *Langmuir* 30 (28), 8461–8470.
- Yan, L., Si, S., Chen, Y., Yuan, T., Fan, H., Yao, Y., et al., 2011. Electrospun in-situ hybrid polyurethane/nano-TiO<sub>2</sub> as wound dressings. *Fibers Polym.* 12 (2), 207–213.
- Yang, G., Lin, H., Rothrauff, B.B., Yu, S., Tuan, R.S., 2016. Multilayered polycaprolactone/gelatin fiber-hydrogel composite for tendon tissue engineering. *Acta Biomater.* 35, 68–76.
- Yousif, B.F., Shalwan, A., Chin, C.W., Ming, K.C., 2012. Flexural properties of treated and untreated kenaf/epoxy composites. *Mater. Des.* 40, 378–385.
- Yu, Y., Kong, L., Li, L., Li, N., Yan, P., 2015. Antitumor activity of doxorubicin-loaded carbon nanotubes incorporated poly(lactic-co-glycolic acid) electrospun composite nanofibers. *Nanoscale Res. Lett.* 10 (1), 343.
- Yu, K., Zhu, T., Wu, Y., Zhou, X., Yang, X., Wang, J., et al., 2016. Incorporation of amoxicillin-loaded organic montmorillonite into poly(ester-urethane) urea nanofibers as a functional tissue engineering scaffold. *Colloids Surf. B Biointerfaces* 151, 314–323.
- Yuan, H., de Bruijn, J.D., Zhang, X., van Blitterswijk, C.A., de Groot, K., 2001. Bone induction by porous glass ceramic made from Bioglass®(45S5). *J. Biomed. Mater. Res.* 58 (3), 270–276.
- Zahedi, P., Rezaeian, I., Ranaei-Siadat, S.-O., Jafari, S.-H., Supaphol, P., 2010. A review on wound dressings with an emphasis on electrospun nanofibrous polymeric bandages. *Polym. Adv. Technol.* 21 (2), 77–95.



- Zahedi, P., Rezaeian, I., Jafari, S.H., 2013. In vitro and in vivo evaluations of phenytoin sodium-loaded electrospun PVA, PCL, and their hybrid nanofibrous mats for use as active wound dressings. *J. Mater. Sci.* 48 (8), 3147–3159.
- Zakhem, E., Raghavan, S., Gilmont, R.R., Bitar, K.N., 2012. Chitosan-based scaffolds for the support of smooth muscle constructs in intestinal tissue engineering. *Biomaterials* 33 (19), 4810–4817.
- Zarkoob, S., Eby, R.K., Reneker, D.H., Hudson, S.D., Ertley, D., Adams, W.W., 2004. Structure and morphology of electrospun silk nanofibers. *Polymer* 45 (11), 3973–3977.
- Zeugolis, D.I., Paul, R.G., Attenburrow, G., 2010. The influence of a natural cross-linking agent (*Myrica rubra*) on the properties of extruded collagen fibres for tissue engineering applications. *Mater. Sci. Eng.: C* 30 (1), 190–195.
- Zhang, H., Darvell, B.W., 2010. Synthesis and characterization of hydroxyapatite whiskers by hydrothermal homogeneous precipitation using acetamide. *Acta Biomater.* 6 (8), 3216–3222.
- Zhang, H., Darvell, B.W., 2012. Mechanical properties of hydroxyapatite whisker-reinforced bis-GMA-based resin composites. *Dental Mater.* 28 (8), 824–830. 2018/06/22.
- Zheng, F., Wang, S., Shen, M., Zhu, M., Shi, X., 2013. Antitumor efficacy of doxorubicin-loaded electrospun nano-hydroxyapatite-poly(lactic-co-glycolic acid) composite nanofibers. *Polym. Chem.* 4 (4), 933–941.
- Zhu, J., Marchant, R.E., 2011. Design properties of hydrogel tissue-engineering scaffolds. *Expert Rev. Med. Devices* 8 (5), 607–626.
- Zhu, Y., Ong, W.F., 2009. Epithelium regeneration on collagen (IV) grafted polycaprolactone for esophageal tissue engineering. *Mater. Sci. Eng.: C* 29 (3), 1046–1050.
- Zhu, Y., Leong, M.F., Ong, W.F., Chan-Park, M.B., Chian, K.S., 2007. Esophageal epithelium regeneration on fibronectin grafted poly(L-lactide-co-caprolactone)(PLLC) nanofiber scaffold. *Biomaterials* 28 (5), 861–868.
- Zhu, C., Ma, X., Xian, L., Zhou, Y., Fan, D., 2014. Characterization of a co-electrospun scaffold of HLC/CS/PLA for vascular tissue engineering. *Bio-Med. Mater. Eng.* 24 (6), 1999–2005.

# FIBER-REINFORCED NANOCOMPOSITES: FUNDAMENTALS AND APPLICATIONS

Edited by  
Baoguo Han  
Sumit Sharma  
Tuan Anh Nguyen  
Li Longbiao  
K. Subrahmanya Bhat



Micro & Nano Technologies Series

# Fiber nanobiocompositions for cranioplasty and other orthopedic applications

*Pulak Barua<sup>1,2</sup>, Arnab Mahato<sup>1</sup>, Pradyot Datta<sup>1</sup>,  
Rituparna Sen<sup>2</sup>, Samit Kumar Nandi<sup>3</sup> and Biswanath Kundu<sup>1</sup>*

<sup>1</sup>Bioceramics and Coating Division, CSIR-Central Glass and Ceramic Research Institute, Kolkata, India <sup>2</sup>Government College of Engineering and Ceramic Technology, Kolkata, India

<sup>3</sup>Department of Veterinary Surgery and Radiology, West Bengal University of Animal and Fishery Science, Kolkata, India

## 23.1 Introduction

Orthopedic challenges are on ever increasing trend in our human society, be it replacement of bone and bone joints or repair and regeneration of bone and associated tissues. Moreover as the average life expectancy is getting increased, more medical attention is required toward alleviation of bone-related problems of people, especially the older group. Quick rehabilitation after a surgery/therapy and extension in life with quality are the need of the hour. With growth in population, coupled with rapid industrialization and urbanization, numerous lifestyle-related orthopedic problems are getting surfaced irrespective of age groups, in addition to age- and trauma-related problems [1]. Thanks to the development of newer surgical procedures, bone prostheses or implants, and modern rehabilitation techniques/aids, the crisis could be offset largely so far.

Initially strength comparable to bone and its inertness toward the host environment were the main considerations for development of alternate materials to be used as implants [2–4]. Accordingly there was great thrust toward the development of synthetic materials for tissue regeneration and growth. During 1970s ceramic materials started evolving as a futuristic material having potential of diversified applications. At the same time, limitations of implant materials in use (steel, cobalt, methyl methacrylate) were

getting surfaced [5]. One major limitation of these materials was lack of integration of the implants with the surrounding tissues leading to poor bonding. But ceramic materials showed good compatibility to host environment and good integration ability in laboratory trials. L.L. Hench is credited with pioneering work on the development of new ceramic material in 1970s for biomedical application. He synthesized a bioactive glass trade named 45S5, with broad matrix of  $\text{Na}_2\text{O}-\text{CaO}-\text{SiO}_2-\text{P}_2\text{O}_5$  [3,4]. The new glass was found to have no adverse response from host tissues. It exhibited capability to form new tissues when reacted with body fluid. The new tissues mimicked original tissues or the host tissues. His benchmark work encompassed different composition of bioglass and other biomaterials, their in vitro and in vivo evaluation, and giving a direction to future development of synthetic implant materials (which can be termed as first generation of biomaterials) [6]. It has been reported that as many as 50 prostheses made out of 40 different biomaterials were implanted for conducting clinical evaluation in 1980 [4].

However, all new developments have their own lifespan. With advancement of biotechnology and molecular biology, understanding about cell construction, cell mechanics, cell growth, human tissue generation and growth, and so on also has advanced. A series of further developments followed in different time lines till date that can be labeled as second- and third-generation biomaterials [6]. Newer procedures and implants continually emerged to overcome earlier limitations and/or for qualitative improvement in human life.

With better understanding of material science, a new direction started emerging in the biomaterials development [7]. More and more nanomaterials are being used for achieving bio integration features more efficiently and with the potential of improved end result. It may be recalled that many of these materials were in use in earlier developments too. However, knowledge about the potential of nano-sized materials as compared to micro-sized materials has been realized much later. Hence with the aim of harnessing the potential of nanotechnology new techniques are getting developed. Combinations of different fibers and nanomaterials possess many properties that make them ideal materials to be used in the development of composites for application in orthopedics. Thus a new genre of fiber nanobiocompositions are emerging as implant material and getting tried.

This review aims at exploring present status of orthopedic implant materials for different applications with particular reference to biomaterials and trend in development of fiber nanobiocompositions.

---

## 23.2 Orthopedic application areas

---

Human body comprises of different types of hard and soft tissues, for example, bones, bone joints, cartilage, tendon, muscle. Our skeletal system is made of 208 bones. It helps us to stand erect on ground, perform movements, and take workloads. As different activities are required to be performed by human beings, various orthopedic problems arise. Naturally their solutions are also different. Many of these applications have become specialized areas, for example, cranioplasty, arthroplasty, cochlear applications, cartilage applications, bone tissue engineering. Series of developments have taken place in different phases in these areas. The major areas are discussed in the following sections.

### 23.2.1 Cranioplasty applications

Top most part of the skeletal system is the skull or cranium. The cranial cavity is made of eight cranial bones, frontal, two temporal, two parietal, occipital, sphenoid, and ethmoid bones. Cranial cavity houses the brain and protects it from external abuses.

Cranioplasty is the term given to the surgical procedure performed for rebuilding damaged part of the skull. The damage can occur due to some accident leading to injury of skull and the brain. In some cases, part of skull flap may be removed during surgery following cerebral attack and other complications of brain which leads to raised intracranial pressure and swelling of brain. This neurosurgical procedure is known as decompressive craniectomy [8]. Cranioplasty is also performed as a reconstruction measure after taking out the affected area of cranium for removal of a tumor or infected cranial bone. Cranioplasty procedure helps in many ways. Reconstruction of skull flap protects the brain from further injury and largely restores normal appearance. It eliminates depression and helps the patient to move in social circle freely. Other benefits like improvement with respect to abnormalities in recording electrical activity of brain during EEG monitoring, improvement in blood flow irregularities in brain, and other nerve system-related irregularities [9–11].

History of craniofacial reconstruction dates back to 7000 BCE [9,10]. Some documents cite reconstruction of skull defects of people of ancient civilizations belonging to affluent classes with gold plates during 2000 BCE as evidenced from a Peruvian skull [10,12]. Van Meekeren performed first bone graft from dog to human in 1668 [12,13]. It was in late 19th century when first scientific experimentation of cranioplasty started with bone grafts. Since then autologous and autogenous bone grafts has been increasingly used [14]. Autologous bone grafts carries the risk of infection. Availability of autogenous bone grafts is limited [15]. These limitations of biologic bone grafts led to the development of synthetic alloplastic materials to tackle a large number of skull injuries during world wars [10,15]. During 1930s cranial flaps made with tantalum and vitallium (alloy of cobalt, chromium, and molybdenum) were experimentally used [7,9,14]. Methylmethacrylate (MMA)-based acrylic skull flaps were first used in 1941 [15,16]. They had the advantages of being lightweight, easy moldability to the required contour during surgery itself. But their drawbacks were brittleness and toxic response owing to the presence of monomers [10,16]. Titanium was first used in 1961 for cranioplasty application due to its inertness, lightweight, high mechanical strength, and easy formability. Titanium meshes were particularly useful in those cases where immediate closure of the removed portion of skull was required [17].

In the meantime, understanding on graft–human body interaction with respect to biocompatibility, osteointegration, osteoconduction, etc., when in contact with human tissue and body fluid were much developed. Researches were directed to develop synthetic materials having these biofeatures, known as bioactive materials or biomaterials. One such biomaterial is acrylic composition based on polymethylmethacrylate (PMMA) [9,12,18–20]. PMMA was found to be nontoxic due to the absence of monomers, strong and impact resistance. It can be formed to near net shape of application area of skull during operation itself. Another polymeric compound recently developed is polyether ether ketone (PEEK) [21–23]. It is radiolucent, chemically inert, strong, and elastic. Not only that it is comfortable, but it neither creates artifacts on imaging nor generates heat while in

use. Ceramic compositions based on  $\text{Al}_2\text{O}_3$ , hydroxyapatite (HAp), and calcium sulfate have been developed as biomaterials [24]. Ceramic materials are highly biocompatible, bioactive, and have good mechanical strength. However, they are known to possess poor impact strength and therefore brittle in nature. Bioglasses are another category of bioactive ceramic material and their inclusion as nano- and micro-sized particles in synthetic cranial flaps has been found to induce osteoinduction, osteoconduction, and osteointegration property. Titanium metal still has a good share as material for cranioplasty due to its good biocompatibility, mechanical strength, and radiolucency. The biofeatures have been enhanced by application of bioactive ceramic (HAp) coatings on the surface. Another area of current work is inclusion of controlled drug delivery feature in these synthetic materials. [Table 23.1](#) summarizes important milestones and features of implant materials used in cranioplasty procedure.

### 23.2.2 Load-bearing orthopedic applications

Major functions of human musculo-skeletal system can be defined as providing support to the body, help in movements, and securely housing organs. There are many joints in the skeletal system which take care of the load put upon it by body itself or external loads apart from movement of body. Joints like hip, knee, shoulder are subjected to tremendous stress and strain while body performs different activities. In the process, they wear and tear faster than other parts leading to impaired life functions.

#### 23.2.2.1 Arthroplasty

Arthroplasty is a surgical procedure to restore the function of a joint by replacement of the ailed joint. The term “arthroplasty” originated from Greek word “arthron” (meaning articulate, joint, limb) and “plassein” (meaning to form, forge, feign, mold, make an image of). To alleviate problem in the joint an artificial joint (also called a prosthesis) can be implanted. The joint also be repaired by resurfacing of the bones in contact. Various types of arthritis may affect the joints. Replacement of joints nowadays is a common surgical procedure, majority of which is performed for hip and knee.

It is estimated that every year about 400,000 numbers of total hip joint replacement and 700,000 numbers total knee joint replacements are carried out in United States [26]. National Joint Registry, United Kingdom (NJR) reported data for the year 2017 in its 15th annual report on arthroplasty procedures for England, Wales, Northern Ireland, and the Isle of Man as given in [Table 23.2](#).

##### 23.2.2.1.1 Hip joint

Hip joint is located in a pivotal position in human body. Medically it is referred to as the acetabulo-femoral joint, which is similar to a ball and socket joint. The thigh bone femur has a ball-shaped head on its end that fits into a socket (the acetabulum) formed in the pelvis. Around the hip joint there are large ligaments, tendons, and muscles that hold the bones (the ball and the socket) in place and protect it from dislocating. The hip joints play very important roles in retaining balance, supporting weight of our body while in standing as well as in moving and in maintaining the pelvic inclination angle. But there

**TABLE 23.1** Important milestones and features of implant materials in cranioplasty [9,14,15,18,19,25].

<b>Material</b>	<b>First use year (by)</b>	<b>Favorable feature</b>	<b>Unfavorable feature</b>
<b>Bone graft</b>			
Xenograft (discontinued)	1668 (Meekeren)	Easy availability	Infection, bone resorption, contouring
Autologous	1880 (Macewen)	Acceptance by host tissue	Infection, bone resorption, contouring
Autogenous	1889 (Syedel)	Acceptance by host tissue	Infection, bone resorption, donor site morbidity, contouring, availability
Allogenuous	1917 (Sicard and Dambrin)	Easy availability (cadaver)	Infection, bone resorption
<b>Metal</b>			
Aluminum	1893 (Booth and Curtis)	Malleable, economic, fairly strong	Toxic, disintegration, epileptogenic
Gold	1895 (Gerster)	Inert, malleable	High cost, low strength
Silver	1903 (Sebileau)	Light, malleable, economic	Low strength, toxic, discoloring scalp
Platinum	1929 (Cornioly)	Strong, inert, malleable, biocompatible,	High cost
Vitallium (Co–Cr–Mo)	1941 (Geib)	Strong, noncorrosive	Not malleable
Tantalum	1943 (Fulcher)	Inert, strong, noncorrosive, malleable, contouring, nonabsorbable	Costly, image artifact, sensitive to ambient temperature, heavy
Titanium	1961 (Simpson)	Strong, nontoxic, contouring, noncorrosive, low infection, radiolucent	Costly, image artifacts, no osteointegration
<b>Polymeric compounds</b>			
Celluloid	1890/1891 (Fraenkel/ Von Hinterstoisser)	Easy available, economical, flexible	Toxic, postoperative fluid collection
MMA/PMMA	1940 (Zandler)	Strong, intraoperative contouring, heat resistant, inert, economical, radiolucent	Toxic, infection, brittle, decomposition
PEEK (PAEK)	1998 (–)	Biocompatible, heat resistant, contouring, strong, radiolucent, adjustable elasticity, durable	Moderate cost, 3D planning and imaging for contouring, no osteointegration
<b>Ceramics</b>			
Hydroxyapatite	1989 (Yamashima)	Biocompatible, nontoxic, osteoconduction, osteointegration, contouring	Low tensile strength, brittle, chance of infection, slow osteointegration
Alumina	1986 (Kobayashi)	Hard, inert, biocompatible, osteointegration	Expensive, poor impact resistance, preformed

MMA, Methylmethacrylate; PAEK, polyaryletherketones; PEEK, polyether ether ketone; PMMA, polymethylmethacrylate.

TABLE 23.2 Arthroplasty procedures in England, Wales, Northern Ireland, and the Isle of Man [27].

Arthroplasty	2016 Nos.	2017 Nos.	% over 2016	Average male age in 2017 (years)	Average female age in 2017 (years)
Hip	101,651	105,306	+ 3.6	67.3	69.5
Knee	108,713	112,836	+ 3.8	69.2	69.4
Shoulder	6967	7525	+ 8.0	69.3	74.1

are a number of causes, including nervous, osteoarthritis, infectious, trauma-related, and genetic, that may lead to pain in the hip. Hip fractures are being paid more attention due to higher morbidity and mortality.

**Total hip arthroplasty** Patients with complains of hip arthritis have been found to achieve improvement in their quality of life after performing total hip arthroplasty [28]. It also brings about quite substantial benefit with respect to cost per Quality Adjusted Life Year [29,30]. But many factors influence the final outcome of a total hip arthroplasty (THA) resulting in varying degree of satisfaction among the patients. A number of analytical studies have been carried out with clinical follow up data to find out success level of hip surgery and findings were very much favorable [31].

In a hip replacement procedure, an artificially made hip joint (also named a hip implant) is placed in the body after removal of the damaged part. Indication of joint ailment is pain in the hip and surrounding area mostly caused by osteoarthritis or inflammatory arthritis. Initial treatment starts with management of pain by painkiller medicines, physiotherapy exercises, or minor surgeries. As the problem aggravates with time, hip arthroplasty is recommended. A hip replacement, often known as a hip implant (and sometimes simply as a “device”), is an artificial implant that replaces a damaged hip joint. Joint replacements are mostly resorted to when pain cannot be managed by other methods like painkillers, physiotherapy, or other surgeries. The most common cause of pain is osteoarthritis or inflammatory arthritis.

There are few issues which surgeons have to handle very carefully while performing hip replacement surgery. One challenging task is to keep the leg length same as to original. Extreme care is needed when top part of the femur is removed and the synthetic part is positioned there. Another task is maintaining the original femoral offset. This can get changed if the angle between the neck and shaft part of the prosthesis is different than patient’s original anatomical angle. Also proper alignment needs to be maintained while pushing the shaft of the prosthesis into the central cavity of cut end of femur. Leg length difference and femoral angle difference may lead to a series of problem during postoperative period, for example, instability during movement, lower back pain, abnormal posture, numbness, all of which causes dissatisfaction in the patient’s mind [32–36].

Hip resurfacing is also a surgical procedure that has been recommended as a prospective solution in people younger than 60 years in terms of benefit-to-risk ratio [37]. On the contrary, NJR analyzed a large number of clinical data and observed that hip resurfacing performance was inferior when compared with normal hip replacement procedure in most patients. They also found hip resurfacing is not recommended now for older patient



group, female patients, or younger men as the rates of failure are high. The resurfacing cases accounted for nearly 10% of total number of hip arthroplasty in 2003 but reduced to less than 1% in 2017 [27]. As per fifth annual report 2018 of American Joint Replacement Registry (AJRR), hip resurfacing has come down to 0.4% in 2017 from 2.9% in 2012 [38].

**Material options** The main parts of a hip implant are femoral stem, femoral head, and acetabular cup. Due to repeated attrition between the femoral head and acetabular cup, wearing of these two contacting surfaces leads to the start of arthritic pain. During surgery, the femur is separated from acetabular cup. Top part of the femur with ball is cut and removed at appropriate place. The implant with stem and ball head is fixed. Required repair/replacement of the cup is done. Finally the head of the femur is securely placed in the cup. The four types of fixation procedure for different components are in vogue depending on whether bone cement is used or not in case of primary THA [39]. They are as follows:

- 1 Cemented: Both the femoral stem and synthetic acetabular cup is fixed with cement.
- 2 Uncemented: Both these components are fixed without using cement.
- 3 Hybrid: Here the stem is cemented but the cup is uncemented.
- 4 Reverse hybrid: Here the stem is uncemented but the cup is cemented.

The 15th annual report of NJR reveals that the cemented method was most popular (60%) in 2003, reduced to ~32% in 2010, and in 2017 it was 29%. Uncemented fixation was about 17% in 2003, rose to 45% in 2010, and then declined to 38%. Their share was taken away by hybrid method, which was about 12% in 2003, slightly increased to 15% in 2010, and then gradually increased to 32% in 2017. The share of reverse hybrid is nearly 1% in 2017, mostly done in Sweden and Norway [27].

The parts involved in hip arthroplasty along with different materials used are described as follows.

**Femoral stem:** It is a replica of top part of femur bone. The lower end of the stem is pushed inside the central cavity and secured tightly in place. Some bone cement may be used during this fixation. Recently cementless fixation procedure has become very popular. Obviously the stability and success of the implantation depends heavily on proper alignment and how tightly the stem has been secured. It is also desired that bone cell grow on the implant surface. Synthetic coating is sometimes applied to promote this bone growth.

**Femoral head:** One synthetically made ball is fitted on the top of the artificial stem in place of human anatomic ball head of femur bone. This synthetic ball head can be made of metal or ceramic material and is securely placed into the hip socket. Materials used are cobalt chromium alloy, stainless steel, oxidized zirconium, zirconia ceramic, or alumina ceramic. The ball diameter varies from 22 to 32 mm normally, but in recent years larger diameter balls of 36 and 40 mm are being used for better results.

**Acetabular component:** The femoral head is fitted into the existing acetabular socket of the hip bone after proper surface preparation of the socket bone surface and fixing of an artificial cup on it. This artificial cup is the acetabular component of the prosthesis. Two practices are generally followed. In one practice special wear-resistant plastic cup is used and it is fixed on the anatomical cup with special bone cement. In the second practice

called cementless fixing, a metallic shell is first tightly fitted into the existing cup after thorough preparation of the eroded bone surface [40]. This shell is sometimes secured with special screws. Back of the liner may be made bioactive using special coating. A plastic or ceramic is then fixed onto the metal shell. Acetabular liners are ultra-high molecular weight polyethylene or alumina ceramic. Commonly used material for metal shell is Ti–6Al–4V alloy [41].

*Bearing surface materials* Bearing surface is the contact surface of acetabular cup and the head of the femur that rubs against each other during movement. The following materials have been reported.

**Metal-on-plastic:** In the initial hip replacement procedure, femoral head of the prosthesis was made of metal and the acetabular component was of plastic. Tribological properties of the bearing surface influences the amount of debris released due to repeated rubbing of bearing surfaces. Reduction in such debris generation can help to keep any play between the head and the socket under control. This in turn make hip replacements last longer. Efforts in this area have led to development of highly cross-linked ultra-high molecular weight polyethylene-based cups having very good wear resistance.

**Ceramic-on-plastic:** Ceramic materials have excellent tribological properties as compared to metals. They are highly wear resistant, have high hardness and excellent surface smoothness. Head made with ceramic materials when used with plastic cup was found to generate very less debris. This improved combination is in use for nearly a decade with so far best results in clinical studies.

**Metal-on-metal/Ceramic-on-ceramic:** Artificial hip implants are subject to wear when they are in use for many years. Hence efforts are on to prevent the loosening of artificial hip implants due to wear. Alternative bearing surfaces like metal-on-metal (MoM) and ceramic-on-ceramic (CoC) have been used. Here the head and cup are made of the same material.

MoM hip replacements became popular in the mid-2000, but the NJR identified very poor results for this type of implant. Their use has now largely been abandoned and in less than 0.1% of operations this bearing type is used.

CoC bearings had been in widespread use for nearly two decades [42–44]. In last few years its use has waned as ceramic-on-plastic bearings became more popular.

*Hip resurfacing* In hip resurfacing procedure, instead of removing the femoral head, it is reshaped and covered with a metal cap. One conventional cementless acetabular cup is used in the hip socket. It may be noted that both components are made of metal.

NJR in its 15th annual report has indicated the usage pattern of different bearing surfaces over the years and is summarized in [Table 23.3](#).

#### 23.2.2.1.2 Knee joint

Knee joint is the most affected joints in our human body going by the trend as shown in [Table 23.2](#). Knee joint is where lower end of femur (thigh bone) and upper end of tibia (shin bone) meets and it is covered with a knee cup called patella. The contact surfaces of these bones are covered with articular cartilage which facilitates free movement and protects bone surfaces. Knee joint is subjected to tremendous wear and tear in our lifetime due to various activities like carrying load, walking, running, playing, and exercising. The

TABLE 23.3 Yearwise usage (approx.) pattern of different bearing surfaces in primary THA (in %) [27].

Type of surface	2003	2010	2017
<b>Uncemented</b>			
MoP	36	36	43
CoP	29	12	37
CoC	21	40	19
MoM	8	7	–
CoM	–	2.5	–
Other/uncertain	6	2.5	1
<b>Hybrid</b>			
MoP	68	68	52
CoP	12	12	41
CoC	10	18	6
MoM	5	1	–
CoM	–	–	–
Other/uncertain	5	1	1

CoC, Ceramic-on-ceramic; CoM, ceramic-on-metal; CoP, ceramic-on-plastic; MoM, metal-on-metal; MoP, metal-on-plastic.

knee joint problems may arise due to degradation of the bearing surfaces, degeneration of associated tissues, cartilage, and tendons. All these will manifest as different forms of arthritis, like osteoarthritis [45], rheumatoid arthritis, or arthritis generated from psoriasis.

These days there are an increasing number of knee replacements for young patients who lead active lifestyles or take part in high-demanding sports, for example, athletics and football. These activities place more pressure and wear on the knee joint.

Knee replacement surgery is decided based on the extent of wearing of different parts of a knee joint. Anatomically knee joint has three compartments called medial, lateral, and patella-femoral. Initial treatment with medicine and physiotherapeutic exercises can defer the surgery. Once the extent of arthritic pain becomes unmanageable, knee replacement is considered. Knee replacement may also be required in case of traumatic injuries. In case of severe damage in any one compartment (mostly in medial), partial or unicompartamental knee replacement is done. When damage is in two or more compartments, total knee arthroplasty is performed. The unicompartamental knee replacement had shown large decline in the first half of 1990s mostly due to success of total knee replacement. In recent times, it has received renewed interest due to improved, less invasive surgical procedures, and higher durability.

While deciding total knee replacements, condition of anterior cruciate ligament (ACLi) and posterior cruciate ligament (PCLi) is taken into consideration. These ligaments join femur with tibia. They control forward and backward motion of our knee. The ACLi

provides rotational stability to the knee. It does not allow tibia to slide out in front of femur, while the PCLi prevents tibia from going backward too far. ACLi are normally found severely degenerated in acute arthritic conditions and are removed during a TKA. The PCLi is generally found to be in better condition and may be retained. Based on these criteria TKA can be classified as:

- 1 Nonconstrained knee replacements: In this type of surgery the PCLi is retained. The prosthesis is so designed that the femoral and the tibial components are free to move independently. Stability is provided by patient's own ligament and muscles.
- 2 Semiconstrained knee replacements: In this type of surgery, the PCLi is found unusable and are removed. A special design of prosthesis is used in which the femoral component has a cross member which is passing through a semicircular hinge made on the tibial component. The hinge supplements some stability in the absence of PCLi, still allows the femoral member to articulate freely.
- 3 Constrained knee replacements: These types of prostheses are used in special cases of severely damaged knee in aged persons and mostly during revision surgery. The anatomical ligaments are generally not in a position to provide any support to the prosthesis; hence the components are hinged to gain own support.

The total knee arthroplasty with nonconstrained design is the most common type of knee replacements followed by semiconstrained type. The success rate has been reported to be more than 95%.

In knee prosthesis, femoral end and tibia end are made of metals, commonly alloys of cobalt–chromium and titanium. The bearing portion of the joint (tibial insert) is made of a high-grade, wear-resistant plastic. Bearing combination of metal–plastic is used in knee replacement implants worldwide. As per the fifth annual report 2018 of AJRR, polyethylene tibial inserts are categorized as conventional polyethylene (ultra high molecular weight polyethylene: UHMWPE), cross-linked polyethylene, or vitamin E-impregnated/antioxidant polyethylene. For primary knee arthroplasty procedures performed from 2012 to 2017, usage rates of conventional polyethylene continued to decline, balanced by a steady increase in the use of antioxidant polyethylene over the same time frame from 2.5% in 2012 to over 25% by 2017 [38]. One recent clinical trial with improved design knee prosthesis with alumina ceramic femoral head containing 7% yttria reported very good outcome [46]. In an in vitro study, wear characteristics of insert was compared using alumina ceramic femoral head-UHMWPE insert and Co–Cr alloy femoral head-UHMWPE insert. Wear rate of insert in alumina ceramic femoral head-UHMWPE insert combination was found to be 36% lower [47]. In another instance, Ezzet et al. conducted laboratory studies to compare wear rate of oxidized zirconium femoral component and Co–Cr–Mo alloy femoral head against conventional PE tibial insert and observed 55% less wear with oxidized zirconium femoral component [48].

### 23.2.2.1.3 Shoulder joint

Charles S. Neer II designed the first shoulder replacement system to deal with painful arthritic shoulders [49]. The shoulder replacement has increased, developed, and surged with leaps and bounds all over our planet (53,000 shoulder replacements are done annually in United States only). Shoulder joint is medically termed as gleno-humeral joint. In

human anatomy it is located in the junction of three members, upper arm (humerus), shoulder blade (scapula), and collar bone (clavicle). Shoulder joint is also a ball and socket joint. But here, the rounded cup in the scapula called glenoid is smaller and shallow. The round head of humerus, in contrast to hip joint, does not fit inside the cup, instead just rests on it. This construction allows the humeral head to move multiaxially against the glenoid cup and it is the most mobile joint in our body. The bearing surfaces are covered with thin, very smooth layer of cartilage which allows easy movement of the head within the cup. The circular outer edge of the glenoid is surrounded by labrum, a strong and highly elastic cartilage. It secures the ball head of humerus against the glenoid. The head is further stabilized in place by rotator cuff muscles and tendons extending from the scapula and covering the joint. But due to various reasons like gradual erosion, injury, impact, earlier surgery, cartilage gets degenerated. This degeneration manifests as arthritis.

In total shoulder replacement arthroplasty, mostly metal-in-plastic method is followed. The two parts of the prosthesis are metallic stem with ball head for humerus and polyethylene cup for the glenoid. The stem is tightly pressed into the humerus bone after removing the head. A synthetic high density highly cross-linked polyethylene cup is fixed over the existing glenoid cup. The metal ball of the prosthesis is then position into the synthetic cup.

### 23.2.3 Nonload-bearing skeletal bone applications

The remaining bones, other than joint forming bones, create an interconnected structure and give a shape to our body. Different conditions may lead to fracture or breakage in bone. Anatomically bone construction is such that it can take a large amount of tensile or compressive stress. However, a fracture may occur if the bone is subjected to a dynamic stress like impact of high magnitude. In case of certain medical conditions like osteoporosis, osteogenesis imperfecta (a disease causing brittleness of bone), or some bone-related cancers, the bone may fracture.

The bone fractures are categorized depending on the nature of the breakage. The bone may break into two or more fragments in such a way that fragment ends shifts relative of each other at the breakage point and moves away from normal alignment. This type of fracture is termed “displaced fracture.” In some cases, the breakage of bone takes place, but broken parts do not shift and remain in normal alignment. This type of fracture is termed “nondisplaced fracture.” When the nature of bone fracture is such that the bone does not pierce skin and does not create open wound, it is called “closed fracture.” In worse situations, after breakage, the bone punctures the skin and gets exposed creating an external wound. This form of fracture is named “open fracture.” Open fracture carries the risk of deep bone infections.

For healing the fractured bones, the broken pieces are first brought to normal alignment by manipulation with use of external force or by surgery. This is followed by “immobilization” stage. To heal, the bone pieces must be kept in aligned position for a long duration, typically 2–8 weeks depending on the type of bone, criticality of fracture, impaired blood circulation, or some infection. The conventional plaster casting or plastic braces may be used to keep the bone fragments aligned. In current procedures, metal plates and screws

are used directly on bones for improved and more stable alignment using less invasive surgery. In some cases, special structures called external fixators made out of metal or carbon fiber are fitted outside the body after bone alignment. Steel pins on these structures pierce through the skin and into the bone, thus holding the pieces together in aligned condition.

Osteosynthesis is the medical term used for surgical method of rigid fixation of fracture. Professor Robert Danis, MD of Brussels Faculty of Medicine, wrote his book titled "Théorie et Pratique de L'ostéosynthèse" in 1949 [50]. In this book, he highlighted his pioneering work on stabilizing the fractured pieces of bone using metal plate after they have been aligned by compressive forces. This type of rigid fixation helped in early bone consolidation and improved joining of fragments. The modern osteosynthesis procedures can be considered to have originated from the pioneering work of Dr. Danis who contributed significantly toward development of scientific methods for fixation of internal bone fracture.

#### 23.2.4 Cartilage

Cartilage has composite structure comprising chondrocyte cells dispersed in the form of tiny lacunae within a gelatinous matrix [51,52]. The cartilage is enclosed by a dense fibrous layer called perichondrium. This layer is lined with cells that can secrete hyaline matrix. The cartilage grows by formation of additional matrix and inclusion of new cells formed from the inner chondrogenic lining of the perichondrium. Articulating surfaces of the bones in a joint are covered with a cartilage layer. This layer has many important functions like reducing friction, providing cushion, and help in free painless movement of the joint. The unique viscoelastic property of cartilage originates from its biphasic construction. Approximately 80% by weight of the cartilage is constituted by water and remaining 20% with solid substances. Inorganic ions like sodium, potassium, calcium, and chloride is found in the water phase. The cartilage tissues have limitations like absence of vascular network. So nutrients and oxygen cannot reach the chondrocyte cells and no metabolic activity takes place. Thus regeneration or complete repair of cartilage by natural process does not take place in case of cartilage defects. The repair/regeneration of cartilage defects posed great challenge to the fraternity of doctors and surgeons throughout the globe. Present practice repair of cartilage defects involve surgical procedures like "microfracture" and "mosaicplasty" [53].

In "microfracture" surgery, micro-sized fissures are created on subchondral bone underneath the defective cartilage. Blood and bone marrow seeps through these microfissures and gradually releases cartilage building cells. Dr. Richard Steadman of the Steadman-Hawkins Clinic in Vail, Colorado developed this surgical procedure in the late 1980s and early 1990s.

In "mosaicplasty" surgery, arrays of small cylindrical plugs of bone and cartilage (known as "osteochondral autologous grafts") taken from other donor site are transplanted in the cartilage defect site [54,55]. This procedure came into clinical use in 1992 and found to be effective in management of small and medium size cartilage defects.

Tissue engineering is another promising procedure in which synthetic biomaterial scaffolds are surgically implanted for regeneration and repair of cartilage [53]. In the earlier clinical trials using tissue engineering, the outcome was poor due to poor cell nucleation, growth, and proliferation within the rigid scaffold. Studies have also been carried out using hydrogels, scaffold-free approaches, and cell therapy for regeneration/repair of large cartilage defects.

### **23.2.4.1 Materials for cartilage repair**

#### **23.2.4.1.1 Polymeric compounds**

A number of polymeric compounds have been developed having biocompatibility and biodegradability. These polymeric compounds can be processed with relative ease. Their mechanical properties are also comparable to human cartilage making them suitable for repair of cartilage. Young's modulus of anatomical cartilage is in the order of 0.2–0.3 GPa. Both natural and synthetic polymers have been used in cartilage defects.

##### **23.2.4.1.1.1 Natural polymers**

Common natural polymers include polysaccharides, glycosaminoglycans, and proteins (fibrin, collagen, gelatine). Shortcomings like low stiffness and poor biomechanical properties restrict uses of natural polymers.

##### **23.2.4.1.1.2 Synthetic polymers**

On the other hand synthetically made polymeric materials have the features like controlled biodegradation and tailored mechanical strength. Controlled biodegradation of the polymer helps in providing time and space for new tissue generation without losing structural integrity. The composition of the polymer may be suitably selected to get desired mechanical properties like Young's modulus. Synthetic polymers include poly-lactic acid (PLA), poly-glycolic acid (PGA), poly-lactic-co-glycolic acid (PLGA-D, L isomer), polydioxanone, and poly-ethylene glycol (PEG) [56,57].

##### **23.2.4.1.2 Bioceramics**

Bioactive ceramic materials have excellent features like osteoconductivity and bioresorbability, thus are prospective candidates as a component in the construct for repair of cartilage lesions. Since cartilage consists of 80% water with inorganic ions in it, suitable bioceramics capable of controlled release of such ions have been developed. To mimic anatomical features of human cartilage, composites of polymer/bioceramics have been researched and developed having comparable modulus of elasticity and impact strength. They have been successfully used in clinical trials for repair/regeneration of cartilage tissues. A large number of researches have been directed to incorporate tissue regenerating bioactive ions apart from normal ions like calcium, potassium, sodium, and chlorides in ceramic materials. As a result, numbers of bioceramic products doped with lithium, strontium, manganese, zinc, silicon, etc., have been developed for repair of osteochondral defects. Manganese-doped tricalcium phosphate (TCP) scaffolds have been found to successfully regenerate cartilage and subchondral bone. HAp is another potential bioceramic material included as a component in synthetic bone grafts for repair of

osteocondral defect. But its standalone use is limited due to very slow resorption rate. A combination has been developed using calcium sulfate, a faster resorbing ceramic material, along with HAp. Calcium sulfate will provide space for new cell growth after its resorption. HAp being osteoconductive will help proliferation of cells into and on the bone graft.

### 23.2.5 Cochlear application

Our ear is divided into three compartments. The outer ear receives the sound, transmitted through the ossicles of the middle ear to the inner ear where it is converted to nervous signal in the cochlea. The ossicles are three tiny bones, namely malleus, incus, and stapes, arranged in this order from tympanic membrane (eardrum) to cochlea. The cochlea is a portion of the inner ear that looks like a snail shell (cochlea is Greek for snail). The walls of the hollow cochlea are made of bone, with a thin delicate lining of epithelial tissue.

Loss in hearing ability is a common sensory problem in human being. Hearing ability reduces as we age. About one-third of population aging between 65 to 75 years suffers from some loss in hearing ability in United States. This figure is more in population more than 75 years. Occupational hazard of exposure to excessive noise for long period also causes hearing loss. Initial corrective remedy is use of hearing aids. When the situation is worse and the hair cells inside cochlea ear are not able to convert sound waves into electrical signal and transmit to hearing nerve any longer, a cochlear implant (CI) or “neurobionic prosthesis” surgery is recommended [58]. Cochlear devices are also implanted in children born with deafness. Backed by years of research; these devices have achieved a high level of reliability. 99% of internally placed devices have been reported to be still working even after 10 years of implantation.

The part of a CI device that is surgically placed inside the inner ear consists of an array of miniaturized electrodes housed in a tiny tightly sealed casing and the connecting wires between electrodes and external sound receiving part. The materials that come into contact with tissues of the ear must not generate any toxic response and prevent connective tissue formation on the electrodes so that their auditory nerve stimulation efficiency is not reduced. Also any chance of bacteria and infection causing pathogen spreading via electrode array into cochlea must be eliminated.

#### 23.2.5.1 *Materials for cochlear application*

The success and longevity of the CIs largely depends on the biocompatibility of the materials of construction of different parts, especially, the surfaces which are in intimate contact with ear tissues and body fluid. Materials used in a CI are described as follows.

##### **Silicone:**

Silicone elastomer composed of silicone, dimethylsiloxane polymer, reinforcing silica, and platinum catalyst is commonly used for electrodes. Silicone is known to possess very good biocompatibility property.

##### **Polyimides:**

Polyimides are group of chemically stable polymers used for flexible electrodes. The clinical studies report them as potential materials for electrodes.



**Platinum:**

Platinum metal is known to have no toxic response and is also highly corrosion resistant. High cost prohibits its use as bulk material. Platinum–iridium (90:10) alloy is used as electrode contact and connecting wire. The wires are covered with protective coating of silicone or Teflon (poly-tetrafluoroethylene).

**Titanium:**

Titanium is a much lighter relative to platinum yet a strong metal. Density of platinum and titanium is 21.45 and 4.5 g/cm<sup>3</sup>, respectively. It is highly inert and corrosion resistant. These features make titanium an ideal choice for use as a material for casing of the electrodes. Being metal, a perfect sealing of the joint of two halves of the casing can be achieved.

**Ceramics:**

Ceramics exhibit excellent biocompatibility even in long-term contact with tissue and body fluid. Al<sub>2</sub>O<sub>3</sub>-based composite ceramics are used as casing material and as sealant of the opening in casing through which wires pass. Another advantage of using ceramic casing is that it does not hinder signal transmission significantly. So receiver wires can be housed inside the casing. However, ceramic materials are brittle in nature and possess poor impact resistance. Also there remains uncertainty about sealing tightness and fluid leakage into ceramic casings as reported in some studies.

**23.2.5.2 Advancement in biomaterials for cochlear implant**

Research for development of biomaterials for CI is largely directed toward reactivating the hearing neurons, establishing close contact between electrodes and neurons via neuritis (extensions from neuron cells) or preventing any bacteria or pathogens from causing infections. Other objectives include prohibiting growth of connective tissues or bone tissues on the implants. While integration with surrounding tissues may help in stability of the implant, unlike other orthopedic applications, it can possibly create problem during revision surgery. Also formation of connective tissues on implant inside cochlea might reduce signal transmission efficiency. Surface modification and coating are two main approaches taken for imparting bioactivity.

**23.2.5.2.1 Physical functionalization**

Surface modifications of existing materials by different nanostructuring methods like laser ablation, lithography, two-photon polymerization, laser-induced melting dynamics, and molding have been studied. These nanostructures have been found to induce hydrophobic behavior on the surface. This benefits the implants in two ways. It inhibits formation of connective tissues on the surface and improves interaction between auditory nerve and electrodes as well.

*Coatings* Different bioactive coatings like collagen, carbon nanotubes, and hydrogels have been studied. Collagen can be helpful in survival of spiral ganglion neurons. Carbon nanotubes enhance electrical conductivity of electrodes and prohibit tissue adhesion. Hydrogel coatings being structurally similar to extracellular matrix can be used to

promote integration of nerve cells with electrode surface and also delivery of cells which promote neural regeneration of nerve cells.

### 23.2.6 Wound healing applications

Skin is the largest organ in the human body [59]. A wound is an unforced cut or damage of skin caused by some external physical reasons, heat, or internal pathological reasons [60]. Healing of a wound is a natural yet a complex and dynamic activity of human body. The healing process replaces the damaged cells of skin and underlying tissues with newly formed cells and tissues. Time taken for healing of wound may vary from days to months depending on the extent of wound and the factor causing the wound. A patient needs to be careful about reoccurrence of injury or prevent infection. These precautions may keep a person immobilized or keep away from his activities. So a systemic enhancement of healing process is highly essential.

Right after a wound takes place, the four-stage healing process is initiated by body as a biological response. In the first hemostasis stage, the blood coming out of the wound starts to form clot and prevents further bleeding. In the second inflammatory stage the injured blood vessels releases a secretion consisting of protein, salt, and water that carries repair and healing cells to the wound location. The dead cells along with bacteria and other infection creating organisms are removed during this stage. In the third proliferation stage network of fibrous tissues are formed and reepithelialization starts. Fibroblasts deposit type III collagen in disordered form. New blood vessels start forming along with the start of peripheral nerve repair. The fourth and last stage is called maturation or remodeling stage. In this stage type III collagen is replaced by aligned and cross-linked type I collagen along the tension line. Skin tissues are regenerated and skin attains normal tensile strength.

The required features of wound dressing materials are excellent therapeutic quality, self-healing property, adhesiveness, antibacterial activity, angiogenesis capability, and suitable mechanical strength [61]. Still it remains a challenge to develop a clinical material to meet all the features of an ideal regenerative wound matrix. Available options for wound care range from graft materials (autografts, allografts, and xenografts) to engineered materials, either of biological or synthetic origin [61]. With rapid development in tissue engineering concepts, a shift toward synthetic materials for wound dressing is visible. Wound dressings can be prepared in different forms, for example, films, foams, hydrogel, or hydrocolloids [60]. Polymer films absorb wound secretions, thus providing a wet environment for wounds, which favors quick healing. Polyurethane (PU) has ability to provide good barrier and permeability to oxygen, hence is used in many semipermeable dressings. Cross-linked hydrophilic polymers, for example, poly-vinyl pyrrolidone, poly-acrylamide, and polyethylene oxide have been used to prepare hydrogel [61]. Hydrogels do not get dissolved in water and possess typical characteristics of swelling in contact with water. They are used in the form of elastic tapes or amorphous gel for the purpose of wound dressing. Hydrocolloids are hydrophilic polymers of natural or synthetic origin. Hydrocolloids possess property of encapsulation of materials within it and utilized in wound healing applications. Hydrocolloids can be so designed as to encapsulate drug

substances for controlled release in wounds. The amount of drug release is controlled by controlling the particle size of drug and permeability of gel membrane. Common hydrocolloid gels are Aragose, Alginate, Carrageenan, Pectin, and Gelatin.

Current researches focus on inorganic/organic nanocomposites based on a host of polymeric network in which functional inorganic nanoparticles have been incorporated. Polymeric networks that have been used are chitosan, collagen, poly vinyl alcohol (PVA), poly(sulfobetaine methacrylate), poly-carboxybetaine, PLGA, alginate, and poly(sulfobetaine methacrylate)/poly-(sodium acrylate). The nanoparticles incorporated for evaluating antimicrobial activity were silver (Ag) [62], gold (Au), copper (Cu) or copper oxide (CuO), titanium oxide (TiO<sub>2</sub>), zinc oxide (Zn), graphene or graphene oxide. Dissolution products of bioactive glasses containing functional metal ions (e.g., Cu, Li, Co, Mg, Zn, Sr, Rb, and Ag) have been reported to promote angiogenesis [63]. Angiogenesis takes place when endothelial cells are stimulated by angiogenesis promoting factors, for example, hypoxia-inducible factor-1 $\alpha$  (HIF-1 $\alpha$ , a dimeric protein) [64]. He et al. in their work demonstrated that products released after dissolution of bioglass nanospheres doped with rubidium could help in regeneration of blood vessels by inducing HIF-1 $\alpha$  driven angiogenesis-promoting molecules through stimulation of human umbilical vein endothelial cells [65]. Qu Jin et al. reported designing of self-healing injectable micelle/hydrogel composites with multifunctions as wound dressing for joint skin damage [61]. Liang reported development of a composite hydrogel Gelatine-Dopamine/Chitosan/ polydopamine- carbon nanotubes (GT-DA/CS/PDA-CNT) using GT grafted DA, CS, and PDA-coated, further added with doxycycline antibiotic. This antibacterial, antioxidative, adhesive, and conductive hydrogel has been found as a prospective multifunctional material for wound healing [66].

### 23.2.7 Osteomyelitis applications

Osteomyelitis is an acute infection in the bone and can be life-threatening if not treated timely [67]. Nelaton came up with the term osteomyelitis in 1844 though infected used to be referred by various names before that [68]. *Staphylococcus aureus* is the bacteria which causes bone infection. Osteomyelitis is mostly associated with orthopedic devices like prosthesis or a fracture fixation device [67]. Other reasons can be spreading of infection from one location of body into the bone through blood stream. Bone may get exposed to external environment and catch infection in case of an open fracture or during a surgery. With ever increasing incidences of implantation of orthopedic devices as mentioned earlier and also traumatic bone fractures, incidences of osteomyelitis also tends to proportionately increase. It is reported that osteomyelitis can occur in about 2%–5% of surgeries performed for orthopedic device fixation.

The two main aspects of therapy are surgical containment of the infection like debridement and prolonged administration of antibiotics [69]. Before the introduction of penicillin in the 1940s, osteomyelitis was mainly managed by surgical consisting of extensive debridement, saucerization, and wound packing [70].

In case of implant-related osteomyelitis, major constraint related to conventional administration of antibiotics is formation of biofilm and low vascularity in the affected area.

These prohibit antibiotics to reach infection sites, thus bacteria-killing ability of these drugs are compromised. This necessitates use of some local drug delivery systems.

PMMA bone cements had been traditional bone packing biomaterial and was first considered for local drug delivery [71]. Calculated doses of antibiotic was mixed with PMMA-based cement and used. However, PMMA cements being nonbiodegradable, it becomes site for colonization of bacteria once concentration of antibiotics is minimized [67]. These led to further research for degradable biomaterials for local drug delivery. The different degradable biomaterials-carrying antibiotics studied are polymer-based materials like collagen fleeces [69], ceramic and/or composites based on calcium sulfates, calcium phosphates (CPs) and HAp s, and bioactive glasses [72]. Bioactive glass (S53P4) has been found to act in two ways. It raises the local pH by release of ions on dissolution and increase osmotic pressure in the area surrounding the glass particles. These create an adverse environment for bacteria adhesion and proliferation [73]. Antibiotic-carrying collagen fleeces are reported to have eradication rates of 63%–100%. Ceramic and/or composites, also called bone graft substitutes, showed 80%–100% eradication rates. As for bioactive glasses (S53P4) the eradication rate was 82%–100%. Ryan et al. developed a collagen scaffold incorporating Cu-doped bioglass and reported it as a single step osteomyelitis treatment [74].

### 23.2.8 Bone tissue engineering

Bone tissue transplantation is considered to be second most after the skin [75]. Any orthopedic procedure to deliver successful result, it is imperative that the associated and surrounding tissues should also be in functional state. However, it is also known that any joint or bone injury is associated with damage to the bone and surrounding tissues. Thus need for regeneration or reconstruction of these tissues was felt for a long time and lots of research efforts have been diverted in this area. As a logical consequence, a relatively new stream of biomedical field named “Tissue Engineering” has emerged. In 1993 Dr. Robert Langer from Massachusetts Institute of Technology (MIT) and Dr. Joseph Vacanti from Boston Children Hospitals described tissue engineering as a field that utilizes the knowledge of engineering and life science and this convergence of knowledge resulted in development of bioactive substitutes which can regenerate or improve the functions of a tissue or an organ [76]. In 1997 Prof. Larry Hench, renowned material scientist, and Prof. Julia Polak, renowned pathologist, collaborated and created the Tissue Engineering and Regenerative Medicine Center at Imperial college, London and initiated pioneering work in these areas [77]. As it was natural, the available knowledge of different materials used in orthopedic applications were first utilized and refined. New materials were then developed for customized application.

The primary approaches for bone tissue engineering are development of a 3D scaffold based on ceramic/polymer/composite materials which are biocompatible, osteoconductive, biodegradable, and have osteointegration capability [78,79]. They should have porous structure for cell adhesion and proliferation and the same time have sufficient mechanical strength [80,81]. They should be loaded with other factors like stem cell, protein, and growth factors to promote cell nucleation and growth [78]. Current researches consider incorporation of suitable drug delivery systems in the scaffold as an additional feature.

A host of biomaterials having potential for bone tissue engineering have been studied. Materials like bioglass [75], HAp, and other CP groups and their combinations have been successfully tried. Biodegradable copolymers like PLGA–PCL (poly caprolactone), PLGA–PLLA (poly L-lactic acid), PCL–PLA also have shown promising results [78,82]. Asefnejad et al. prepared a biodegradable PU scaffold using polycaprolactone (PCL) and hexamethylene di-isocyanate and reported its suitability for tissue engineering [83]. Ceramic–polymer composites have been considered as third-generation biomaterials like HAp/bioglass with collagen/chitosan/gelatin/PLGA/PLA/PLLA have also been reported [79,80,84–87]. Liu and Webster studied dispersion of nanoparticles of HAp and titania in PLGA and reported increase in tensile strength and compressive modulus as compared to only PLGA [88]. Another prospective group of material is hydrogel. Hydrogels synthesized from collagen, gelatin, PEG, PVA have been reported [89]. Self-assembling peptides have emerged as novel material for bone tissue engineering in recent times [4]. In summary, a lot of work has been done in the past two decades in search of ideal material for bone tissue engineering. However, some more time will be required to formalize a set of standard materials for job.

## 23.3 Biomaterials for orthopedic applications

A large number of biomaterials have been developed in the past ~80 years for orthopedic applications since 1941 when MMA-based synthetic bone graft was fabricated. Following sections highlight major biomaterials developed functionwise in these years.

### 23.3.1 Implants/ prostheses

Following features are expected from an ideal implant/prosthesis material for orthopedics application:

- biocompatibility,
- chemical inertness,
- high mechanical strength,
- high corrosion resistance,
- high fatigue resistance,
- low young's modulus,
- high resistance to wear, and
- low cost.

The existing biomaterials for implants can be categorized as:

- metals,
- polymers,
- ceramics, and
- composites.

### **23.3.1.1 Metals**

Metallic substances have been extensively employed in orthopedic prosthesis construction because of their excellent mechanical properties and biological inertness [90]. Common metals that are in use are given as follows.

#### **23.3.1.1.1 Titanium and its alloys such as Ti–6Al–4V**

These are predominant metals used for cranial grafts in the form of a mesh owing to excellent biocompatibility and osteointegration characteristics.

#### **23.3.1.1.2 Cobalt–chromium alloy**

These metal alloys have high mechanical strength, high corrosion resistance, and good tribological property. They have been widely used as hip, knee, and shoulder prostheses stem.

#### **23.3.1.1.3 Stainless steel**

Stainless steels are highly corrosion resistant and have high mechanical strength. They find application as temporary implants like internal fixation devices for bone fracture setting. Commonly SS316L grade of stainless steel has been employed for such functions. However, it has inferior fatigue strength as well.

### **23.3.1.2 Polymers**

Polymers find wide range of use in orthopedic applications. Ease of fabrication and possibility of physical and chemical modification for various functionalities make them smart biomaterials. Physical modifications like fiber reinforcement can enhance their strength manifold [1]. Surface nanostructuring as in the case of cochlea electrodes can improve electrode–auditory nerve contacts. Inclusion of active substances like metallic nanoparticles can generate therapeutic capability in them.

#### **23.3.1.2.1 Polyethylene**

Ultra-high molecular weight polyethylene is an organic polymer known to possess high mechanical strength and high biocompatibility. It is extensively used for synthetic cup part of the knee, shoulder, and hip prostheses.

#### **23.3.1.2.2 Polyaryletherketones**

Polyaryletherketones (PAEKs) are a family of organic polymers. Molecular structure of PAEK has alternate ketone and ether groups. They are characterized by high temperature stability and high mechanical strength. These polymers can be continuously used up to 250°C and can be used up to 350°C under short-term loads. They find growing applications as biomaterials in making of cranial flap, joint prosthesis part, spinal implants, etc., after it was established through in vivo trials that these materials are biocompatible in 1980s. This family of polymers came into limelight after successful development of isoelastic stem for hip prosthesis and bone fracture fixation plates [89]. Some the members of PAEK family are given below:

- PEK (polyetherketone),
- PEEK (polyether ether ketone),

- PEKK (polyetherketoneketone),
- PEEKK (polyetheretherketoneketone), and
- PEKEKK (polyetherketoneetherketoneketone).

#### 23.3.1.2.3 Polyurethanes

In last 20 years or so, PUs have emerged as a potential substitute for ultra high molecular weight (UHMW) polyethylene for use in cup part of prosthesis. These materials possess high mechanical strength, lower Young's modulus than UHMWPE, and biocompatible. Segmented polycarbonate urethanes, an advanced PU is also biocompatible, possess enhanced oxidative stability as compared to polyether urethanes. They are also known to have high strength, high impact toughness, and high ductility. These features make them good choice for acetabular cup component.

#### 23.3.1.2.4 Silicone

Silicone polymers are considered as one of the exciting discoveries that took place in recent years. Silicones are known to be biocompatible and biostable polymeric compounds. Silicones are most commonly used as small joint prosthesis finger joints of foot and hand. Two designs of prostheses are prevalent, namely Swanson design and Niebauer design. Both design based on silicone are highly successful. Silicone is also used as electrode and cover material for the connecting wires of CIs.

#### 23.3.1.3 Ceramics

Ceramics have assumed an important role as orthopedic implants. The ceramic materials possess very high strength under compressive force, but they are weak under tensile and shear force. Ceramics have a high Young's modulus. Therefore their selective use may produce extraordinary results. Other ceramic materials like HAp, CP, calcium sulfate have been used as coating of metallic implants for enhancing their bioactivity.

##### 23.3.1.3.1 Oxide

Alumina ( $\text{Al}_2\text{O}_3$ ) and zirconia ( $\text{ZrO}_2$ ) are the two ceramic materials that were used initially for making of implants for their bioinert property. Alumina was first introduced as prosthesis for hip joint by Boutin in April 1970 [91]. Young's modulus of 99% alumina ceramics is in the range of 330–380 GPa compared to that of bone which is 17–21 GPa. This wide difference in Young's modulus value is responsible for higher wear of anatomical bone or bone getting fractured. This can result in cases like ceramic acetabular sockets getting loose prematurely. CoC combinations (e.g., alumina head and alumina socket) exhibited satisfactory results with respect to tribological property and wear in laboratory trials. However, in clinical trials, wear beyond tolerable limit was observed after few years. Failure due to inherent brittleness of ceramic materials prohibited its use as socket. So use of ceramic was restricted to femoral head.

Zirconia is known to be a highly bioinert ceramic oxide. A special treatment of phase transformation from tetragonal to stable monoclinic polymorph called "toughening" imparts excellent mechanical properties to zirconia like high mechanical strength, high fracture toughness, and high wear resistance [92]. Yttria-stabilized toughened zirconia was used successfully for making of hip joint prosthesis and implanted in 1990s. However, it has a shortcoming like low temperature degradation in long-term use which led to premature failure incidences.

TABLE 23.4 Mechanical properties of common oxide ceramics.

Property	Al <sub>2</sub> O <sub>3</sub>	Yttria-stabilized ZrO <sub>2</sub>	Zirconia-toughened Al <sub>2</sub> O <sub>3</sub>
Young's modulus (GPa)	330–380	200–210	360–380
Compressive strength (MPa)	2500–3500	2200–2500	–
Tensile strength, ultimate (MPa)	240	950	259
Flexural strength (MPa)	350	270–550	430
Fracture toughness (MPa m <sup>1/2</sup> )	6	9.5	4–5
Hardness, VH	2000	1300	1440
Poisson's ratio	0.21–0.23	0.3	0.23
Shear modulus (GPa)	140	–	141

As a logical consequence a series of compositions were developed having high hardness, good fracture toughness, and high flexural strength by combining alumina and toughened stabilized zirconia. This led to fabrication of prosthesis components with zirconia-toughened alumina [93] containing yttria-stabilized zirconia up to 25% by weight and alumina-toughened zirconia (ATZ) containing 80 wt.% tetragonal zirconia and up to 20 wt.% alumina. Mechanical properties of some oxide ceramics are given in Table 23.4.

### 23.3.1.3.2 Hydroxyapatite

Bone is a hard tissue and a natural composite material, which contains the mineral HAp [Ca<sub>10</sub>(PO<sub>4</sub>)<sub>6</sub>(OH)<sub>2</sub>] which belongs to CP group of materials. It constitutes about 69% of matter and is present as nano-sized crystals. It contains about 39.68 wt.% calcium, 18.45 wt.% phosphorous with a Ca:P molar ratio of 1.67. HAp has been synthetically produced for large-scale application in orthopedics and dental area.

HAp has excellent osteoconduction, osteointegration, and bioresorbability properties, making it an ideal biomaterial for bone growth. But its poor strength limits its application as standalone implant material of moderate to large size. It has versatile applications as a biomaterial in the form of cement, coating, scaffolds, and nanoparticles in composites.

## 23.3.2 Coatings

Coatings are used to incorporate additional functionality in regular implants like osteointegration, barrier to metal ion release from implants [81] and antimicrobial function. Surface modification/functionalization are done before application of coating in many instances [94].

### 23.3.2.1 Biological coatings

Transforming growth factor protein (TGF-β1, TGF-β2) and bone morphogenetic protein (BMP-2) are two proteins known to promote osteoinductivity [95,96]. These growth factors have been incorporated on metallic implants as biological coatings for improving osteoinduction [97].



### 23.3.2.2 Calcium phosphate coating

CP compound like HAp has been used for coating of metallic implants especially the titanium alloy. Incorporation into HAp of inorganic ions like Sr and Si as trace elements that stimulate bone cell growth have also shown encouraging results.

### 23.3.2.3 Bioactive glass coating

Prof. Larry Hench's novel invention of a bioactive glass substance primarily consisting of  $\text{SiO}_2$ ,  $\text{CaO}$ ,  $\text{P}_2\text{O}_5$  in later part of 1960s and beginning of 1970s was tested to treat bone fracture successfully and was found to integrate with bone. The bioglass composition was trade named as 45S5 and is a pioneering work in the field of bioceramics.

Since then, bioactive glasses or bioglasses have seen phenomenal growth in terms of research. Application areas have enlarged to hard and soft tissue engineering, coatings, scaffolds, etc. Primarily based on  $\text{CaO-SiO}_2\text{-Na}_2\text{O-P}_2\text{O}_5$  system, these glasses release  $\text{Ca}^{2+}$  and  $\text{HPO}_4^{2-}/\text{PO}_4^{3-}$  ions in contact with body fluid which precipitate back as HAp on target site in bone tissue application.

### 23.3.2.4 Organic–inorganic hybrids coating

Hion et al. reported bioactive organic–inorganic hybrid  $\text{CaO-SiO}_2$ –poly(dimethylsiloxane) system as suitable for metal implant coatings [98].

## 23.3.3 Cement materials

### 23.3.3.1 Calcium phosphates

Tadros et al. reported various CPs such as HAp formulations that have been tried for rebuilding of bone tissues [15]. Cranioplasty is an area where cement formulations based on CPs have been found to be highly useful [99,100]. Jinku Kim et al. studied CP-based cement formulations containing biodegradable PLGA fibers (3% w/w) as reinforcement and compared with fiber-free formulations [101]. Bulk material without fiber tends to fragment and debris may cause inflammation. The fiber-reinforced material was found to maintain physical integrity. The bone regeneration was found to be similar.

### 23.3.3.2 PMMA

PMMA cement was first used by Charnley for fixing the prosthesis in total hip arthroplasty in 1958 [102,103]. But certain disadvantages like generation of heat during cure and low biocompatibility at the cement–bone interface were observed [103,104]. Not only that, cements fracture at the cement–prosthesis interface or pores in the cement were also reported. Moreover there were many reported instances of aseptic loosening of an implanted prosthesis as there was no osteointegration and the cement was surrounded by a fibrous tissue capsule after long-term implantation. Some literatures reported that addition of bioactive ceramics like HAp, glass–ceramics A-W, and titanium dioxide are beneficial in terms of providing bioactivity to the PMMA-based bone cement [105,106].

TABLE 23.5 Mechanical properties of common biomaterials.

Material	Young's modulus (GPa)	Fracture toughness (MPa m <sup>1/2</sup> )	Tensile strength (MPa)	Compressive strength (MPa)
Cortical bone	17–21	4	150	170
Bioglass	42	500	35	2
Stainless steel 316L	200	55–95	465–950	1000
Ti–6Al–4V	116	–	897–1034	–
Co–Cr–Mo (ASTM F75)	210–253	–	448–841	–
Bioglass	35	2	42	500
UHMWPE	0.5–1.3	–	20–30	–
PEEK	3–4	–	80–93	–
PMMA	3–5	–	48–76	–
C-fiber-reinforced PEEK	20	–	170	–

PEEK, Polyether ether ketone; PMMA, polymethylmethacrylate.

### 23.3.4 Collagen–HAp

Both Collagen and HAP have the capability of bone regeneration. Collagen–HAP composite scaffolds were experimented to reap the benefit of both the substances and enhance bone regeneration. The composite derive all the bio features from its constituents like biocompatibility, osteoinductivity, osteoconductivity, and bioabsorbability [107,108]. Mechanical properties of some common biomaterials are given in Table 23.5.

## 23.4 Fiber-nanobiocomposites

### 23.4.1 Concept of fiber-reinforced composites

Composite implies an engineered material prepared with two or more different discrete substances intimately mixed to form a uniform matrix which is homogenous in macro scale but may be heterogeneous in micro scale [109]. Composites are prepared to utilize the complementary physical and chemical properties of individual substances. However, certain applications like automotive, aerospace, marine, or sport goods demand many fold strength from a single component or a composite material. This requirement was fulfilled by reinforcing the matrix of the composite with different fibers or whiskers dispersed in the matrix. Conceptually a fiber-reinforced composite has three phases: (1) matrix which is the bulk and continuous phase, (2) reinforcement phase which is a fiber or a whisker, and (3) interface which is the area between the first two phases. Primary objective of fiber reinforcement is to engineer a material having high strength in conjunction with higher Young's modulus. The basic principle is to transfer the applied load to the fibers which possess extraordinary tensile and shear strength [109].

## 23.4.2 Fiber-reinforced biocomposites for orthopedic applications

Composite biomaterials with fiber reinforcement have grown rapidly as an exciting group of materials in last two decades or so. They have been used for a number of orthopedic applications, namely, hip joint prosthesis, cranioplasty, bone fixation plates, bone cements, and tissue grafts.

### 23.4.2.1 Hip joint prosthesis

Metals used for making femoral stem part are commonly SS 316L, Co–Cr alloys, and Ti alloys. All of them have high stiffness value as compared to cortical bone. Cortical bone has stiffness of 15 GPa and tensile strength of 90 MPa as compared to titanium which has stiffness of 110 GPa and tensile strength of 800 MPa. These wide difference of strengths results in faster wear of bone leading to loosening of prosthesis [109]. To address this problem, carbon fiber-reinforced PEEK or polysulfone [110], liquid crystal polymer, and polyetherimide composites were developed. The concern regarding biocompatibility due to generation of carbon debris from carbon fiber during wearing of these composites has been resolved by polishing and coating with HAp or carbon–titanium alloy [111].

### 23.4.2.2 Cranial implants

Fiber-reinforced biocomposites has great potential as cranial implants. Vallittu et al. reported construction of a glass fiber-reinforced polymeric implant with incorporation of bioglass particles on the surface and inside the composite for increased osteoconductivity and osteoinductivity [112]. Keeping in view that cranial defects require long time to close with new bone generation, integrity of implant should not be lost. Hence biodegradable polymer matrices are not preferred. Continuous unidirectional S-glass fibers have been used for reinforcing.

### 23.4.2.3 Fracture fixation plate

For bone fracture fixation, commonly stainless steel plates are used. A second surgery is often performed to remove the steel plates after complete healing of fracture. Brown et al. developed polyacrylonitril fiber-reinforced PEEK composites and found it to be ideal option for this application [113]. A biodegradable and resorbable plate material is desirable so that new bone tissue develops while the plate degrades and second surgery is not needed. Examples of such fiber-reinforced biocomposites are laminated continuous carbon fiber-reinforced PLA, CP glass fiber-reinforced PLA.

### 23.4.2.4 Bone cements

Bone cements with PMMA matrix reinforced with small quantity of carbon or Kevlar fiber has been found to reduce creep and increase fatigue strength.

### 23.4.2.5 Hydrogel

Hydrogel is a novel material being mainly utilized for tissue engineering. Fiber reinforcement improves mechanical strength of hydrogels, which otherwise have very poor strength. As an example, cross-linked poly(2-hydroxyethyl methacrylate) hydrogel

scaffolds for soft tissue engineering of skin were reinforced with spandex and gauze fibers, thereby increasing tensile strength and break point of the hydrogel dramatically [109].

## 23.5 Fiber nanocomposites and fabrication methods

### 23.5.1 Fiber nanocomposites

In ISO/TS 80004, *nanomaterial* is defined as the “material with any external dimension in the nanoscale or having internal structure or surface structure in the nanoscale,” with *nanoscale* defined as the “length range approximately from 1 nm to 100 nm”. This includes both *nanoobjects*, which are discrete pieces of material, and *nanostuctured materials*, which have internal or surface structure on the nanoscale; a nanomaterial may be a member of both these categories. One nanometer ( $10^{-9}$  m) is nearly four times the size of a water molecule (0.275 nm).

Nano-sized materials exhibit extraordinary properties than bulk materials due to high surface area to volume ratio. All earlier developmental works for orthopedic implants centered on bulk and micron size materials with variations in chemistry, macro structure, and bulk properties. Only recently it was realized that the tissue originates from nanostructured substances like extra cellular matrix (ECM) with formation of nano-sized tissue components. For example, bone tissue component collagen molecule has diameter of about 1.6 nm and length of about 300 nm. Other component HAp is in the form of crystallites having size of  $2\text{ nm} \times 20\text{ nm} \times 40\text{ nm}$ . So, use of biomaterials having nano-sized structures can mimic basic nanostructures and cell generation/adhesion/proliferation proceeds rapidly due to very high surface area acting as multiple sites, available on the synthetic nanostructures. This translates into higher deposition of new tissues, quick healing, and longer life of implants without need of revision surgery. If we consider current longevity of a hip or knee prosthesis which are made with micro and bulk materials, it is about 10–15 years. One of the reasons being micro- and macromaterials of these implants could not inflict appropriate cellular stimulation to produce adequate bone tissues for survival for a longer duration [114].

In orthopedic applications, nanotechnology is employed by incorporation of nanoparticles of interest into the nanostructures, that is, nanofibrous scaffolds to increase its osteoconduction, osteointegration, and antimicrobial capability. This may be in the form of coating, surface modification, or impregnation of scaffolds.

Ngiam et al. reported development of nano-HAp-incorporated PLGA/PLGA-collagen blend nanofiber-based scaffold by electrospinning method [115]. Kim et al. reported development of an electrospun gelatin/HAp nanofibrous scaffold resembling human bone matrix and found higher cell adhesion and proliferation when compared with only gelatin scaffold [116]. Study by Li et al. on incorporation of nanoscale reinforcement of graphene and grapheme oxide in HAp showed that the composites thus developed can be used for hard tissue repair/regeneration. The hydrothermal synthesis followed by hot isostatic pressing technique was adopted for making reduced graphene oxide/HAp (rGO/HAp) composites [117]. Zhang et al. combined electrospinning with in situ coprecipitation synthesis and produced nanocomposite fibers of HAp/chitosan after addition of ultra high

molecular weight polyethylene oxide (UHMWPEO). HAp nanoparticles were incorporated in the scaffold thus prepared [118]. Prabhakaran et al. in their study prepared three different nanofibrous scaffolds by electrospinning: PLLA, PLLA/HAp and PLLA/collagen/HAp. The PLLA/collagen/HAp scaffold showed best cell adhesion and growth and mineral deposition also increased [119]. Fujihara et al. developed PCL nanofiber-based membranes and incorporated calcium carbonate nanoparticles into it. PCL/CaCO<sub>3</sub> membranes showed higher cell adherence as compared with only PCL nanofibrous membranes [120]. Erisken et al. used a hybrid twin-screw extrusion/electrospinning process and produced nonwoven mats of PCL with incorporation of  $\beta$ -TCP nanoparticles with staggered distribution of porosity and composition mimicking native tissue structure [121].

### 23.5.2 Fabrication methods of fiber nanobiocomposites

Main methods utilized for making of nanofibrous scaffolds are template synthesis, phase separation, self-assembly, drawing, wet spinning, and electrospinning [122,123]. They are described as follows.

#### 23.5.2.1 *Template synthesis*

Basic principle of this method is extruding a polymer solution through a membrane (known as template) having multiple nano-sized orifices on it using pressure and the fine strands coming out of the membrane is passed through a solidification solution which transform them into nanofibers. The membrane/template can be made out of different materials like polymer, metal, or carbon. While the diameters of the formed fibers correspond to the diameters of the orifice, the length of the fibers is only few microns, thus limiting use of this method.

#### 23.5.2.2 *Phase separation*

The phase separation method is a relatively easy procedure to produce nano-sized fibrous scaffolds for biomedical application and utilizes the principle of thermodynamics. In this method, concerned polymer is dissolved in an appropriate solvent by stirring for a long time at certain gelation temperature. The polymer solution is then subjected to phase separation creating a thermodynamically unstable condition for the solution. The most popular process is thermally induced phase separation (TIPS). In this process, the temperature of the solution is reduced depending on the freezing point of the solvent. This quenching separates the solution into a polymer- and a solvent-rich domain. The polymer-rich phase is subjected to freeze drying (sublimation) to further remove the solvent. What is left behind is a nanofibrous scaffold with fine pores. Parameters like polymer type, its concentration, freezing temperature, and pore creating agents can influence morphology of the scaffold. It is a low-cost simple small-scale method. But its use is limited to only few polymers that are responsive to gelation and phase separation. The fiber diameter ranges from 50 to 500 nm with lengths of about 10  $\mu$ m. Polymer systems like PLGA, PLLA, PEG/PLLA, HAp/chitosan-gelatin, HAp/poly(hydroxybutyrate-co-hydroxyvalerate), PLA-dextran blend have been used by different researches to prepare nanofibrous scaffolds by phase separation method given as follows.

### **23.5.2.3 Self-assembly**

In this method, the atoms and molecules arrange themselves through weak and noncovalent forces. The self-assembly process involves various driving forces such as hydrophobic interactions, electrostatic forces, hydrogen bonding, and van der Waals forces and is influenced by external conditions such as ionic strength and pH. The fibers produced are less than 100 nm in diameter with length of few microns. This method has many limitations like complexity, time consuming, and low productivity.

### **23.5.2.4 Drawing**

Drawing is a low-cost method to produce single fiber. In this method, a polymer solution is first prepared. Sharp tip of a miniature pipette like head is dipped in the solution to contact a droplet with the help of a manipulator and this droplet is rapidly drawn as a liquid fiber. This single fiber is then solidified by fast evaporation of the solvent due to high surface area of the fiber. The steps are repeated to produce required number of nanofibers. Hence it is a discontinuous process. The limitation of this method is it can only use solutions of viscoelastic material, which can withstand the stress formed on fiber while drawing. The diameter of fiber produced may vary from about 100 nm to a few hundred nanometers.

### **23.5.2.5 Wet spinning**

In wet spinning process, polymers are first dissolved in a suitable solvent. The solution is placed in the spinneret which is kept submerged in a chemical bath that causes the fiber to precipitate, and then solidify as it emerges. The fiber can be continuously drawn out from bath by some rotating spindle placed outside the bath. The process gets its name from this “wet” bath.

### **23.5.2.6 Electrospinning**

This method is the most accepted method for producing nanofibers for biomedical application. In this method, continuous fiber can be drawn from a polymer solution through a syringe like setup by application of high electrostatic force. The major components of this equipment are a capillary tube with a needle head of small diameter, a syringe pump to push the solution through the needle, a high voltage supply, and a collector. One of the electrodes is connected to the needle and the other electrode is connected to the collector. The droplet of polymer solution is subjected to a high electrostatic field, enough to overcome the surface tension force. In this condition the charged jet of solution is ejected from the needle tip in the form of continuous fine diameter fiber and drawn toward the collector. The collector can be stationary or rotating.

Other emerging methods are CO<sub>2</sub> laser supersonic drawing, freeze drying, solution blow spinning, plasma-induced synthesis, centrifugal jet spinning, and electrohydrodynamic direct writing.

## 23.6 Conclusions and future direction

An elaborate review has been done on different orthopedic applications including cranioplasty and different materials, including biomaterials, used historically. The review shows that lots of research work has been done to develop an ideal biocompatible material mimicking the host tissue, for example, bone or cartilage and some degree of success has been achieved. Different metals, polymers, ceramics, or hybrids have been evolved for this purpose. However, no material could, so far, match all the properties of the hard and soft tissues in question. Implants/prostheses having dissimilar components have differences with respect to physical and chemical properties. These differences bring thermo-mechanical stress within the assembly and cause ultimate failure of the prosthesis as a whole or by component. Also issue of biointegration with host tissues or surrounding tissues could not be fully resolved. Efforts therefore were focused on molecular level, so as to prepare biocomposites having nano-sized constituents which can trigger signals to host tissue or body fluid to replicate similar tissue cells on or around the implant when placed in the human body. Ultimate objective should be conversion of the composite wholly into similar tissue (bone or cartilage) and become a part of the host tissue completing the reconstruction or repair. Tissue engineering thus appears to be a promising field of research.

In this endeavor, fiber-reinforced biocomposites may become a logical solution for composite biomaterial making. Fiber reinforcement using surface-treated glass fibers, functionalized carbon nanotubes, etc., can provide strength to the order of bone and address brittle fracture issue. Thickness can be varied from few microns (membranes) to few millimeters (bone grafts). These composites may also be tailored to facilitate bonding to metal (femoral stem of hip prosthesis). Thus these fiber nanobiocomposites can be customized for a host of applications, like cranioplasty, joint prosthesis, bone damage repair, cartilage regeneration/repair, skin grafting, wound healing as well as treatment of postjoint replacement infections.

### Acknowledgments

The authors would like to express their sincere thanks and gratitude to the Director, CSIR-CGCRI, Kolkata; Honorable Vice-Chancellor, WBUAFS, Kolkata; and Principal, GCECT, Kolkata for their permission and help at various stages to draft the manuscript both intellectually and technically.

### References

- [1] M. Navarro, A. Michiardi, O. Castano, J.A. Planell, *Biomaterials in orthopaedics*, *J. R. Soc. Interface* 5 (2008) 1137–1158.
- [2] L.L. Hench, *Biomaterials*, *Science* 208 (1980) 826–831.
- [3] W. Bonfield, *Composites for bone replacement*, *J. Biomed. Eng.* 10 (1988) 522–526.
- [4] L.L. Hench, I. Thompson, *Twenty-first century challenges for biomaterials*, *J. R. Soc. Interface* 7 (2010) S379–S391.
- [5] K.E. Tanner, *Bioactive ceramic-reinforced composites for bone augmentation*, *J. R. Soc. Interface* 7 (2010) S541–S557.
- [6] L.L. Hench, *Bioceramics: from concept to clinic*, *J. Am. Ceram. Soc.* 74 (1991) 1487–1510.

- [7] B.D. Ratner, A.S. Hoffman, F.J. Schoen, J.E. Lemons, *Biomaterials Science: An Introduction to Materials in Medicine*, Elsevier, 2004.
- [8] Y.J. Cho, S.H. Kang, Review of cranioplasty after decompressive craniectomy, *Korean J. Neurotrauma* 13 (2017) 9–14.
- [9] S. Aydin, B. Kucukyuruk, B. Abuzayed, S. Aydin, G.Z. Sanus, Cranioplasty: review of materials and techniques, *J. Neurosci. Rural. Pract.* 2 (2011) 162–167.
- [10] A.M. Shah, H. Jung, S. Skirboll, Materials used in cranioplasty: a history and analysis, *Neurosurg. Focus.* 36 (2014) E19.
- [11] U. Spetzger, V. Vougioukas, J. Schipper, Materials and techniques for osseous skull reconstruction, *Minim. Invasive Ther. Allied Technol.* 19 (2010) 110–121.
- [12] L. Chiarini, S. Figurelli, G. Pollastri, E. Torcia, F. Ferrari, M. Albanese, et al., Cranioplasty using acrylic material: a new technical procedure, *J. Cranio-Maxillofacial Surg.* 32 (2004) 5–9.
- [13] D. Donati, C. Zolezzi, P. Tomba, A. Viganò, Bone grafting: historical and conceptual review, starting with an old manuscript by Vittorio Putti, *Acta Orthop.* 78 (2007) 19–25.
- [14] S. Abhay, S.J. Haines, Repairing holes in the head: a history of cranioplasty, *Neurosurgery* 40 (1997) 588–603.
- [15] M. Tadros, P.D. Costantino, Advances in cranioplasty: a simplified algorithm to guide cranial reconstruction of acquired defects, *Facial Plastic Surg.* 24 (2008) 135–145.
- [16] K.S. Blum, S.J. Schneider, A.D. Rosenthal, Methyl methacrylate cranioplasty in children: long-term results, *Pediatric Neurosurg.* 26 (1997) 33–35.
- [17] Q. Yu, L. Chen, Z. Qiu, Y. Zhang, T. Song, F. Cui, Skull repair materials applied in cranioplasty: history and progress, *Transl. Neurosci. Clin.* 3 (2017) 48–57.
- [18] P. Fiaschi, M. Pavanello, A. Imperato, V. Dallolio, A. Accogli, V. Capra, et al., Surgical results of cranioplasty with a polymethylmethacrylate customized cranial implant in pediatric patients: a single-center experience, *J. Neurosurg. Pediatr.* 17 (2016) 705–710.
- [19] J.A. Morales-Gomez, E. Garcia-Estrada, J.E. Leos-Bortoni, M. Delgado-Brito, L.E. Flores-Huerta, A. Adriana, et al., Cranioplasty with a low-cost customized polymethylmethacrylate implant using a desktop 3D printer, *J. Neurosurg.* 130 (2018) 1721–1727.
- [20] R.D. Wallace, C. Salt, P. Konofaos, Comparison of autogenous and alloplastic cranioplasty materials following impact testing, *J. Craniofacial Surg.* 26 (2015) 1551–1557.
- [21] M.M. Hanasono, N. Goel, F. DeMonte, Calvarial reconstruction with polyetheretherketone implants, *Ann. Plastic Surg.* 62 (2009) 653–655.
- [22] B. Lethaus, Y. Safi, M. ter Laak-Poort, A. Kloss-Brandstatter, F. Banki, C. Robbenmenke, et al., Cranioplasty with customized titanium and PEEK implants in a mechanical stress model, *J. Neurotrauma* 29 (2012) 1077–1083.
- [23] P. Scolozzi, A. Martinez, B. Jaques, Complex orbito-fronto-temporal reconstruction using computer-designed PEEK implant, *J. Craniofacial Surg.* 18 (2007) 224–228.
- [24] S. Kobayashi, H. Hara, H. Okudera, T. Takemae, K. Sugita, Usefulness of ceramic implants in neurosurgery, *Neurosurgery* 21 (1987) 751–755.
- [25] A. Badhey, S. Kadakia, M. Mourad, J. Inman, Y. Ducic, *Calvarial Reconstruction*, Seminars in Plastic Surgery, Thieme Medical Publishers, 2017, pp. 222–226.
- [26] S. Scutti, More men, younger Americans having joint replacement surgery, *CNN Health*. <<https://edition.cnn.com/2018/03/2006/health/hip-knee-replacement-surgeries-earlier-study/index.html>>, 2018.
- [27] HQIP, National Joint Registry 15th Annual Report 2018. <<https://www.hqip.org.uk/resource/national-joint-registry-15th-annual-report-2018/#.XarILJzblU>>, 2018.
- [28] A.F. Kamath, N.P. Sheth, H.H. Hosalkar, O.M. Babatunde, G.-C. Lee, C.L. Nelson, Modern total hip arthroplasty in patients younger than 21 years, *J. Arthroplast.* 27 (2012) 402–408.
- [29] M. Pennington, R. Grieve, J.S. Sekhon, P. Gregg, N. Black, J.H. van der Meulen, Cemented, cementless, and hybrid prostheses for total hip replacement: cost effectiveness analysis, *BMJ* 346 (2013) f1026.
- [30] G.H. Smith, S. Johnson, J.A. Ballantyne, E. Dunstan, I.J. Brenkel, Predictors of excellent early outcome after total hip arthroplasty, *J. Orthop. Surg. Res.* 7 (2012) 13.
- [31] A. Judge, N.K. Arden, A. Kiran, A. Price, M.K. Javaid, D. Beard, et al., Interpretation of patient-reported outcomes for hip and knee replacement surgery: identification of thresholds associated with satisfaction with surgery, *J. Bone Jt. Surg. Br.* 94 (2012) 412–418.



- [32] B. Al-Amiry, G. Pantelakis, S. Mahmood, B. Kadum, T.B. Brismar, A.S. Sayed-Noor, Does body mass index affect restoration of femoral offset, leg length and cup positioning after total hip arthroplasty? A prospective cohort study, *BMC Musculoskelet. Disord.* 20 (2019) 422.
- [33] M.M. Innmann, M.W. Maier, M.R. Streit, G. Grammatopoulos, T. Bruckner, T. Gotterbarm, et al., Additive influence of hip offset and leg length reconstruction on postoperative improvement in clinical outcome after total hip arthroplasty, *J. Arthroplast.* 33 (2018) 156–161.
- [34] S.S. Mahmood, S.S. Mukka, S. Crnalic, P. Wretenberg, A.S. Sayed-Noor, Association between changes in global femoral offset after total hip arthroplasty and function, quality of life, and abductor muscle strength: a prospective cohort study of 222 patients, *Acta Orthop.* 87 (2016) 36–41.
- [35] G. Meermans, J.V. Doorn, J.J. Kats, Restoration of the centre of rotation in primary total hip arthroplasty: the influence of acetabular floor depth and reaming technique, *Bone Jt. J.* 98 (2016) 1597–1603.
- [36] M.R. Whitehouse, N.S. Stefanovich-Lawbuary, L.R. Brunton, A.W. Blom, The impact of leg length discrepancy on patient satisfaction and functional outcome following total hip arthroplasty, *J. Arthroplast.* 28 (2013) 1408–1414.
- [37] M.A. Mont, T.P. Schmalzried, Modern metal-on-metal hip resurfacing: important observations from the first ten years, *J. Bone Jt. Surg. Am.* 90 (2008) 3–11.
- [38] K. Bozic, Fifth AJRR Annual Report on Hip and Knee Arthroplasty Data. <[http://ajrr.net/images/annual\\_reports/AAOS-AJRR-2018-Annual-Report-final.pdf?hsCtaTracking=c2794b2145-2018b2050-2405a-af2015c-2666a0841a2730%2017C6996bb2053-2015b2074-2014d2065-bb2051-b2024f2037c2055c2019d](http://ajrr.net/images/annual_reports/AAOS-AJRR-2018-Annual-Report-final.pdf?hsCtaTracking=c2794b2145-2018b2050-2405a-af2015c-2666a0841a2730%2017C6996bb2053-2015b2074-2014d2065-bb2051-b2024f2037c2055c2019d)> , 2018.
- [39] HQIP, National Joint Registry 14th Annual Report 2018. <<https://www.hqip.org.uk/resource/national-joint-registry-14th-annual-report-2017/#.XarMnplzblU>> , 2017.
- [40] R. D'Ambrosi, L. Marciandi, P.V. Frediani, R.M. Facchini, Uncemented total hip arthroplasty in patients younger than 20 years, *J. Orthop. Sci.* 21 (2016) 500–506.
- [41] R.B. Bourne, E. DeSantis, W.M. Goldstein, G.L. Maistrelli, J.W. McCutchen, C.H. Rorabeck et al., Smith & Nephew Synergy Cementless Stem. <[https://www.smith-nephew.com/global/surgicaltechniques/recon/synergy\\_cementless\\_45610101\\_us.pdf](https://www.smith-nephew.com/global/surgicaltechniques/recon/synergy_cementless_45610101_us.pdf)> .
- [42] P.R. Finkbone, E.P. Severson, M.E. Cabanela, R.T. Trousdale, Ceramic-on-ceramic total hip arthroplasty in patients younger than 20 years, *J. Arthroplast.* 27 (2012) 213–219.
- [43] Y.-K. Lee, Y.-C. Ha, J.J. Yoo, K.-H. Koo, K.S. Yoon, H.J. Kim, Alumina-on-alumina total hip arthroplasty: a concise follow-up, at a minimum of ten years, of a previous report, *J. Bone Jt. Surg. Am.* 92 (2010) 1715–1719.
- [44] R.P. Shah, J.A. Sclaro, R. Componovo, J.P. Garino, G.-C. Lee, Ceramic-on-ceramic total hip arthroplasty in patients younger than 55 years, *J. Orthop. Surg.* 22 (2014) 338–341.
- [45] J.T. Evans, R.W. Walker, J.P. Evans, A.W. Blom, A. Sayers, M.R. Whitehouse, How long does a knee replacement last? A systematic review and meta-analysis of case series and national registry reports with more than 15 years of follow-up, *Lancet* 393 (2019) 655–663.
- [46] S. Nakamura, H. Ito, K. Nakamura, S. Kuriyama, M. Furu, S. Matsuda, Long-term durability of ceramic tri-condylar knee implants: a minimum 15-year follow-up, *J. Arthroplast.* 32 (2017) 1874–1879.
- [47] H. Oonishi, M. Ueno, S.C. Kim, H. Oonishi, M. Iwamoto, M. Kyomoto, Ceramic versus cobalt-chrome femoral components; wear of polyethylene insert in total knee prosthesis, *J. Arthroplast.* 24 (2009) 374–382.
- [48] K.A. Ezzet, J.C. Hermida, N. Steklov, D.D. Darryl, Wear of polyethylene against oxidized zirconium femoral components: effect of aggressive kinematic conditions and malalignment in total knee arthroplasty, *J. Arthroplast.* 27 (2012) 116–121.
- [49] F.A. Cordasco, L.E. Wessel, M.D. Hendel, J.B. Ticker, Dr. Charles Neer's last surgical case: a historical perspective, *J. Shoulder Elb. Surg.* 25 (2016) e358–e364.
- [50] A.R. Lesic, S. Zagorac, V. Bumbasirevic, M.Z. Bumbasirevic, The development of internal fixation-historical overview, *Acta Chirurgica Iugoslavica* 59 (2012) 9–13.
- [51] J.W. Alford, B.J. Cole, Cartilage restoration, part 1: basic science, historical perspective, patient evaluation, and treatment options, *Am. J. Sports Med.* 33 (2005) 295–306.
- [52] A.J. Sophia Fox, A. Bedi, S.A. Rodeo, The basic science of articular cartilage: structure, composition, and function, *Sports Health* 1 (2009) 461–468.
- [53] L. Fuentes-Mera, A. Camacho, E. Engel, V. Pérez-Silos, J. Lara-Arias, I. Marino-Martínez, et al., Therapeutic potential of articular cartilage regeneration using tissue engineering based on multiphase designs, In: D.D. Nikolopoulos,

- G.K. Safos, K. Dimitrios (Eds.), *Cartilage Tissue Engineering and Regeneration Techniques*. <<https://doi.org/10.5772/intechopen.846972019>> .
- [54] A. Ozturk, M.R. Ozdemir, Y. Ozkan, Osteochondral autografting (mosaicplasty) in grade IV cartilage defects in the knee joint: 2-to 7-year results, *Int. Orthop.* 30 (2006) 200–204.
- [55] H. Robert, Chondral repair of the knee joint using mosaicplasty, *Orthop. Traumatol.: Surg. Res.* 97 (2011) 418–429.
- [56] E.B. Hunziker, Articular cartilage repair: basic science and clinical progress. A review of the current status and prospects, *Osteoarthr. Cartil.* 10 (2002) 432–463.
- [57] L. Li, F. Yu, L. Zheng, R. Wang, W. Yan, Z. Wang, et al., Natural hydrogels for cartilage regeneration: modification, preparation and application, *J. Orthop. Transl.* 17 (2018) 26–41.
- [58] T. Stöver, T. Lenarz, Biomaterials in cochlear implants, *GMS Curr. Top. Otorhinolaryngol. - Head Neck Surg.* 8 (2009). Doc 10.
- [59] X. Wang, J. Chang, C. Wu, Bioactive inorganic/organic nanocomposites for wound healing, *Appl. Mater. Today* 11 (2018) 308–319.
- [60] M. Mir, M.N. Ali, A. Barakullah, A. Gulzar, M. Arshad, S. Fatima, et al., Synthetic polymeric biomaterials for wound healing: a review, *Prog. Biomater.* 7 (2018) 1–21.
- [61] J. Qu, X. Zhao, Y. Liang, T. Zhang, P.X. Ma, B. Guo, Antibacterial adhesive injectable hydrogels with rapid self-healing, extensibility and compressibility as wound dressing for joints skin wound healing, *Biomaterials* 183 (2018) 185–199.
- [62] X. Bai, S. Sandukas, M. Appleford, J.L. Ong, A. Rabiei, Antibacterial effect and cytotoxicity of Ag-doped functionally graded hydroxyapatite coatings, *J. Biomed. Mater. Res. Part B: Appl. Biomater.* 100 (2012) 553–561.
- [63] S. Kargozar, F. Baino, S. Hamzehlou, R.G. Hill, M. Mozafari, Bioactive glasses: sprouting angiogenesis in tissue engineering, *Trends Biotechnol.* 36 (2018) 430–444.
- [64] Y. Zhou, S. Han, L. Xiao, P. Han, S. Wang, J. He, et al., Accelerated host angiogenesis and immune responses by ion release from mesoporous bioactive glass, *J. Mater. Chem. B* 6 (2018) 3274–3284.
- [65] X. He, Y. Ding, S. Duan, S. Luo, J. Song, C. Peng, et al., Wound dressings based on rubidium-doped bioactive glass nanospheres promote diabetic wound healing, *J. Biomed. Nanotechnol.* 15 (2019) 2059–2071.
- [66] Y. Liang, X. Zhao, T. Hu, Y. Han, B. Guo, Mussel-inspired, antibacterial, conductive, antioxidant, injectable composite hydrogel wound dressing to promote the regeneration of infected skin, *J. Colloid Interface Sci.* 556 (2019) 514–528.
- [67] J.A. Inzana, E.M. Schwarz, S.L. Kates, H.A. Awad, Biomaterials approaches to treating implant-associated osteomyelitis, *Biomaterials* 81 (2016) 58–71.
- [68] S.K. Schmitt, Osteomyelitis, *Infect. Dis. Clin.* 31 (2017) 325–338.
- [69] J.D. Caplin, A.J. Garcia, Implantable antimicrobial biomaterials for local drug delivery in bone infection models, *Acta Biomater.* 93 (2019) 2–11.
- [70] I.I. Momodu, V. Savaliya, Osteomyelitis, StatPearls Publishing, Treasure Island, FL, 2019.
- [71] T.A. van Vugt, J.A.P. Geurts, J.J. Arts, N.C. Lindfors, Biomaterials in treatment of orthopaedic infections, *Management of Periprosthetic Joint Infections*, Woodhead Publishing Series in Biomaterials, Amsterdam, 2017, pp. 41–68.
- [72] C.L. Romano, N. Logoluso, E. Meani, D. Romano, E. De Vecchi, C. Vassena, et al., A comparative study of the use of bioactive glass S53P4 and antibiotic-loaded calcium-based bone substitutes in the treatment of chronic osteomyelitis: a retrospective comparative study, *Bone Jt. J.* 96 (2014) 845–850.
- [73] J. Geurts, T. van Vugt, E. Thijssen, J.J. Arts, Cost-effectiveness study of one-stage treatment of chronic osteomyelitis with bioactive glass S53P4, *Materials* 12 (2019) 3209.
- [74] E.J. Ryan, A.J. Ryan, A. Gonzalez-Vazquez, A. Philippart, F.E. Ciraldo, C. Hobbs, et al., Collagen scaffolds functionalised with copper-eluting bioactive glass reduce infection and enhance osteogenesis and angiogenesis both in vitro and in vivo, *Biomaterials* 197 (2019) 405–416.
- [75] R. Mishra, B. Basu, A. Kumar, Physical and cytocompatibility properties of bioactive glass-polyvinyl alcohol-sodium alginate biocomposite foams prepared via sol-gel processing for trabecular bone regeneration, *J. Mater. Sci.: Mater. Med.* 20 (2009) 2493–2500.
- [76] L.N. Melek, Tissue engineering in oral and maxillofacial reconstruction, *Tanta Dental J.* 12 (2015) 211–223.
- [77] E. Gentleman, J.M. Polak, Historic and current strategies in bone tissue engineering: do we have a hope in Hench? *J. Mater. Sci.: Mater. Med.* 17 (2006) 1029–1035.

- [78] C.M. Agrawal, R.B. Ray, Biodegradable polymeric scaffolds for musculoskeletal tissue engineering, *J. Biomed. Mater. Res.* 55 (2001) 141–150.
- [79] A.R. Boccaccini, J.A. Roelher, L.L. Hench, V. Maquet, R. Jerome, A composites approach to tissue engineering, In: 26th Annual Conference on Composites, Advanced Ceramics, Materials, and Structures: B: Ceramic Engineering and Science Proceedings, Wiley Online Library, 2002, pp. 805–816.
- [80] A. Abdal-hay, K.A. Khalil, A.S. Hamdy, F.F. Al-Jassir, Fabrication of highly porous biodegradable biomimetic nanocomposite as advanced bone tissue scaffold, *Arab. J. Chem.* 10 (2017) 240–252.
- [81] M. Vallet-Regi, Revisiting ceramics for medical applications, *Dalton Trans.* (2006) 5211–5220.
- [82] D.W. Hutmacher, Scaffolds in tissue engineering bone and cartilage, *Biomaterials* 21 (2000) 2529–2543.
- [83] A. Asefnejad, M.T. Khorasani, A. Behnamghader, B. Farsadzadeh, S. Bonakdar, Manufacturing of biodegradable polyurethane scaffolds based on polycaprolactone using a phase separation method: physical properties and in vitro assay, *Int. J. Nanomed.* 6 (2011) 2375–2384.
- [84] P. Chen, L. Liu, J. Pan, J. Mei, C. Li, Y. Zheng, Biomimetic composite scaffold of hydroxyapatite/gelatin-chitosan core-shell nanofibers for bone tissue engineering, *Mater. Sci. Eng. C* 97 (2019) 325–335.
- [85] J. Liuyun, X. Chengdong, J. Lixin, X. Lijuan, Effect of HA with different grain size range on the crystallization behaviors and mechanical property of HA/PLGA composite, *Thermochim. Acta* 565 (2013) 52–57.
- [86] N. Tamai, A. Myoui, M. Hirao, T. Kaito, T. Ochi, J. Tanaka, et al., A new biotechnology for articular cartilage repair: subchondral implantation of a composite of interconnected porous hydroxyapatite, synthetic polymer (PLA-PEG), and bone morphogenetic protein-2 (rhBMP-2), *Osteoarthr. Cartil.* 13 (2005) 405–417.
- [87] J. Zhou, C. Xu, G. Wu, X. Cao, L. Zhang, Z. Zhai, et al., In vitro generation of osteochondral differentiation of human marrow mesenchymal stem cells in novel collagen-hydroxyapatite layered scaffolds, *Acta Biomater.* 7 (2011) 3999–4006.
- [88] H. Liu, T.J. Webster, Mechanical properties of dispersed ceramic nanoparticles in polymer composites for orthopedic applications, *Int. J. Nanomed.* 5 (2010) 299–313.
- [89] A.R. Amini, C.T. Laurencin, S.P. Nukavarapu, Bone tissue engineering: recent advances and challenges, *Crit. Rev. Biomed. Eng.* 40 (2012) 363–408.
- [90] M.B. Nasab, M.R. Hassan, B.B. Sahari, Metallic biomaterials of knee and hip-a review, *Trends Biomater. Artif. Organs* 24 (2010) 69–82.
- [91] P. Boutin, P. Christel, J.M. Dorlot, A. Meunier, A. De Roquancourt, D. Blanquaert, et al., The use of dense alumina-alumina ceramic combination in total hip replacement, *J. Biomed. Mater. Res.* 22 (1988) 1203–1232.
- [92] B. Basu, Toughening of yttria-stabilised tetragonal zirconia ceramics, *Int. Mater. Rev.* 50 (2005) 239–256.
- [93] S. Abbas, S. Maleksaedi, E. Kolos, A. Ruys, Processing and properties of zirconia-toughened alumina prepared by gelcasting, *Materials* 8 (2015) 4344–4362.
- [94] A.A. Campbell, G.E. Fryxell, J.C. Linehan, G.L. Graff, Surface-induced mineralization: a new method for producing calcium phosphate coatings, *J. Biomed. Mater. Res.* 32 (1996) 111–118.
- [95] R. Reyes, A. Delgado, E. Sanchez, A. Fernandez, A. Hernandez, C. Evora, Repair of an osteochondral defect by sustained delivery of BMP-2 or TGF $\beta$ 1 from a bilayered alginate-PLGA scaffold, *J. Tissue Eng. Regenerat. Med.* 8 (2014) 521–533.
- [96] R. Reyes, A. Delgado, R. Solis, E. Sanchez, A. Hernandez, J. San Roman, et al., Cartilage repair by local delivery of TGF- $\beta$ 1 or BMP-2 from a novel, segmented polyurethane/poly(lactic-co-glycolic) bilayered scaffold, *J. Biomed. Mater. Res. Part. A* 102 (2013) 1110–1120.
- [97] R. Cancedda, B. Dozin, P. Giannoni, R. Quarto, Tissue engineering and cell therapy of cartilage and bone, *Matrix Biol.* 22 (2003) 81–91.
- [98] N. Hion, M. Manzano, A.J. Salinas, M. Vallet-Regi, Bioactive CaO-SiO $_2$ -PDMS coatings on Ti6Al4V substrates, *Chem. Mater.* 17 (2005) 1591–1596.
- [99] M.S. Gilardino, D.S. Cabling, S.P. Bartlett, Long-term follow-up experience with carbonated calcium phosphate cement (Norian) for cranioplasty in children and adults, *Plastic Reconstruct. Surg.* 123 (2009) 983–994.
- [100] F. Pourdanesh, N. Latifi, F. Latifi, Complications after craniofacial reconstruction with calcium phosphate cements: a case report and review of the literature, *J. Korean Assoc. Oral. Maxillofac. Surg.* 44 (2018) 207–211.
- [101] J. Kim, S. McBride, B. Tellis, P. Alvarez-Urena, Y.-H. Song, D.D. Dean, et al., Rapid-prototyped PLGA/b-TCP/hydroxyapatite nanocomposite scaffolds in a rabbit femoral defect model, *Biofabrication* 4 (2012) 025003.

- [102] M. Arora, E.K.S. Chan, S. Gupta, A.D. Diwan, Polymethylmethacrylate bone cements and additives: a review of the literature, *World J. Orthop.* 4 (2013) 67–74.
- [103] R. Vaishya, M. Chauhan, A. Vaish, Bone cement, *J. Clin. Orthop. Trauma.* 4 (2013) 157–163.
- [104] F. Pahlevanzadeh, H.R. Bakhsheshi-Rad, E. Hamzah, In-vitro biocompatibility, bioactivity, and mechanical strength of PMMA-PCL polymer containing fluorapatite and graphene oxide bone cements, *J. Mech. Behav. Biomed. Mater.* 82 (2018) 257–267.
- [105] P. Harini, K. Mohamed, T.V. Padmanabhan, Effect of Titanium dioxide nanoparticles on the flexural strength of polymethylmethacrylate: an in vitro study, *Indian J. Dental Res.* 25 (2014) 459–463.
- [106] S. Shinzato, M. Kobayashi, W.F. Mousa, M. Kamimura, M. Neo, Y. Kitamura, et al., Bioactive polymethyl methacrylate-based bone cement: comparison of glass beads, apatite-and wollastonite-containing glass-ceramic, and hydroxyapatite fillers on mechanical and biological properties, *J. Biomed. Mater. Res.* 51 (2000) 258–272.
- [107] L. Chen, Z. Wu, Y. Zhou, L. Li, Y. Wang, Z. Wang, et al., Biomimetic porous collagen/hydroxyapatite scaffold for bone tissue engineering, *J. Appl. Polym. Sci.* 134 (2017) 45271.
- [108] A. Sionkowska, J. Kozłowska, Characterization of collagen/hydroxyapatite composite sponges as a potential bone substitute, *Int. J. Biol. Macromol.* 47 (2010) 483–487.
- [109] A. Iftekhar, *Biomedical Composites, Standard Handbook of Biomedical Engineering and Design*, McGraw-Hill, 2004, pp. 12.11–12.17.
- [110] L.M. Wenz, K. Merritt, S.A. Brown, A. Moet, A.D. Steffee, In vitro biocompatibility of polyetheretherketone and polysulfone composites, *J. Biomed. Mater. Res.* 24 (1990) 207–215.
- [111] L. Bacakova, V. Stary, O. Kofronova, V. Lisa, Polishing and coating carbon fiber-reinforced carbon composites with a carbon-titanium layer enhances adhesion and growth of osteoblast-like MG63 cells and vascular smooth muscle cells in vitro, *J. Biomed. Mater. Res.* 54 (2001) 567–578.
- [112] P.K. Vallittu, Bioactive glass-containing cranial implants: an overview, *J. Mater. Sci.* 52 (2017) 8772–8784.
- [113] S.A. Brown, R.S. Hastings, J.J. Mason, A. Moet, Characterization of short-fibre reinforced thermoplastics for fracture fixation devices, *Biomaterials* 11 (1990) 541–547.
- [114] G. Balasundaram, T.J. Webster, A perspective on nanophase materials for orthopedic implant applications, *J. Mater. Chem.* 16 (2006) 3737–3745.
- [115] M. Ngiam, S. Liao, A.J. Patil, Z. Cheng, C.K. Chan, S. Ramakrishna, The fabrication of nano-hydroxyapatite on PLGA and PLGA/collagen nanofibrous composite scaffolds and their effects in osteoblastic behavior for bone tissue engineering, *Bone* 45 (2009) 4–16.
- [116] H.W. Kim, J.H. Song, H.E. Kim, Nanofiber generation of gelatin-hydroxyapatite biomimetics for guided tissue regeneration, *Adv. Funct. Mater.* 15 (2005) 1988–1994.
- [117] M. Li, P. Xiong, F. Yan, S. Li, C. Ren, Z. Yin, et al., An overview of graphene-based hydroxyapatite composites for orthopedic applications, *Bioact. Mater.* 3 (2018) 1–18.
- [118] Y. Zhang, J.R. Venugopal, A. El-Turki, S. Ramakrishna, B. Su, C.T. Lim, Electrospun biomimetic nanocomposite nanofibers of hydroxyapatite/chitosan for bone tissue engineering, *Biomaterials* 29 (2008) 4314–4322.
- [119] M.P. Prabhakaran, J. Venugopal, S. Ramakrishna, Electrospun nanostructured scaffolds for bone tissue engineering, *Acta Biomater.* 5 (2009) 2884–2893.
- [120] K. Fujihara, M. Kotaki, S. Ramakrishna, Guided bone regeneration membrane made of polycaprolactone/calcium carbonate composite nano-fibers, *Biomaterials* 26 (2005) 4139–4147.
- [121] C. Eriskin, D.M. Kalyon, H. Wang, A hybrid twin screw extrusion/electrospinning method to process nanoparticle-incorporated electrospun nanofibres, *Nanotechnology* 19 (2008) 165302.
- [122] H. Chen, R.K. Truckenmüller, C. van Blitterswijk, L. Moroni, Fabrication of nanofibrous scaffolds for tissue engineering applications, in: A.K. Gaharwar, S. Sant, M.J. Hancock, A.A. Hacking (Eds.), *Nanomaterials in Tissue Engineering: Fabrication and Applications*, Woodhead Publishing, 2013, pp. 158–182.
- [123] T. Lu, Y. Li, T. Chen, Techniques for fabrication and construction of three-dimensional scaffolds for tissue engineering, *Int. J. Nanomed.* 8 (2013) 337–350.



Original Research

# Role of calcium phosphate and bioactive glass coating on in vivo bone healing of new Mg–Zn–Ca implant

Arnab Mahato<sup>1</sup> · Munmun De<sup>2</sup> · Promita Bhattacharjee<sup>3</sup> · Vinod Kumar<sup>2</sup> · Prasenjit Mukherjee<sup>4</sup> · Gajendra Singh<sup>5</sup> · Biswanath Kundu<sup>1</sup> · Vamsi K. Balla<sup>1</sup> · Samit Kumar Nandi<sup>2</sup>

Received: 9 June 2020 / Accepted: 15 March 2021 / Published online: 7 May 2021  
© The Author(s) 2021

## Abstract

Present investigation focuses on development and detailed characterization of a new Mg alloy sample (BM) with and without coating of hydroxyapatite (BMH) and bioactive glass (BMG) by air plasma spray method. After detailed mechano-physico-chemical characterization of powders and coated samples, electrochemical corrosion and SBF immersion tests were carried out. Detailed in vitro characterizations for cell viability were undertaken using MG-63 cell line followed by in vivo tests in rabbit model for studying bone healing up to 60 days. Starting current density increases from BM to BMH to BMG indicating highest resistance towards corrosion in case of BMG samples, however BMH also showed highest  $i_{\text{corr}}$  value suggesting slowest rate of corrosion than BM and BMG samples. Dissolution of calcium ion in case of BMH and BMG control formation of apatite phases on surface.  $\text{Ca}^{2+}$  ions of coatings and from SBF solution underwent reduction reaction simultaneously with conversion of Mg to  $\text{MgCl}_2$  releasing  $\text{OH}^-$  in the solution, which increases pH. Viability and propagation of human osteoblast-like cells was verified using confocal microscopy observations and from expression of bone specific genes. Alkaline phosphatase assay and ARS staining indicate cell proliferation and production of neo-osseous tissue matrix. In vivo, based on histology of heart, kidney and liver, and immune response of IL-2, IL-6 and  $\text{TNF}\alpha$ , all the materials show no adverse effects in body system. The bone creation was observed to be more for BMH. Although both BMH and BMG show rays of possibilities in early new bone formation and tough bone–implant bonding at interface as compared to bare Mg alloy, however, BMG showed better well-sprayed coating covering on substrate and resistance against corrosion prior implanting in vivo. Also, better apatite formation on this sample makes it more favourable implant.

These authors contributed equally: Arnab Mahato, Munmun De

✉ Gajendra Singh  
singhgajender@rediffmail.com  
✉ Biswanath Kundu  
biswa\_kundu@rediffmail.com  
✉ Samit Kumar Nandi  
samitnandi1967@gmail.com

<sup>1</sup> Bioceramics and Coating Division, CSIR-Central Glass and Ceramic Research Institute, Kolkata, India

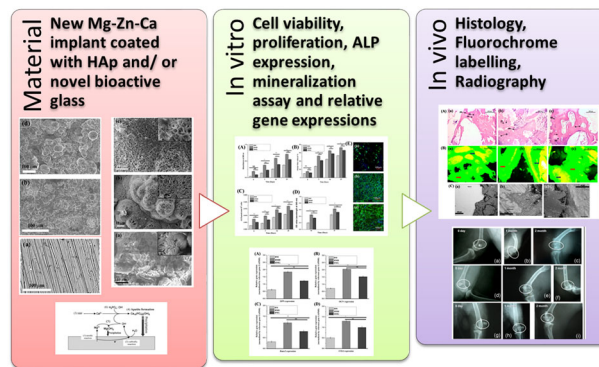
<sup>2</sup> Department of Veterinary Surgery and Radiology, West Bengal University of Animal and Fishery Sciences, Kolkata, India

<sup>3</sup> Materials Science Centre, Indian Institute of Technology, Kharagpur, India

<sup>4</sup> Veterinary Clinical Complex, West Bengal University of Animal and Fishery Sciences, Mohanpur, Nadia, India

<sup>5</sup> Muve Hospital, Surat 395007 Gujarat, India

## Graphical Abstract



## 1 Introduction

Magnesium alloys gathered special interest in recent years in context of structural lightweight applications in temporary implants because of their ability to be gradually dissolved, absorbed, consumed or excreted through urine [1, 2]. High load bearing capacity and fracture toughness compared to existing biodegradable polymers made them more suitable as orthopaedic implant. Biodegradability of these alloy implants implies that they need not be removed through second surgery, thus minimizing trauma and medical expenses [3]. Recent investigations have used Mg alloy based wound closures for gastrointestinal procedure [4] and polymer coated Mg alloy based scaffold for sustained drug release [5]. However, the major obstacle against widespread application is their high corrosion rate [6, 7], which might be attributed to the presence of different impurity elements acting as active cathodic site when in solution. Presence of elements such as Fe, Ni, Cu and Co above their tolerance limit may significantly increase Mg corrosion [8]. Whereas presence of elements such as Ca, Zn, Si and Al up to a certain quantity can improve the mechanical properties as well as corrosion resistance [9, 10]. Depending up on the requirements of biomedical applications, magnesium alloys has been modified through various methods such as surface modification via anodization [11], electrodeposition [12], chemical conversion coatings [13] or organic coatings [14] or alloying. In case of biodegradable implant application, alloying seems to be preferable method as ion release will maintain a continuity. Among the Mg alloy systems, Mg–Ca and Mg–Zn have shown a balance of properties, mechanical and corrosion resistance, suitable for biomedical applications [15]. Calcium helps to improve bone healing process, whereas Zn is known to increase the mechanical strength of the alloy [16]. Inspired by the result, Kirkland et al. prepared and examined a series of ternary Mg–Zn–Ca alloys by varying the ratio of Zn to Ca and came to the conclusion that the corrosion is correlated with alloy microstructure, which can be varied

through changing the ratio [17]. Recent studies on Mg–Zn–Ca alloying system show high mechanical properties, simultaneous high strength and high ductility (yield stress,  $R_{p0.2} > 250$  MPa, ultimate tensile strength  $R_m > 300$  MPa and fracture strain,  $A_f > 20\%$ ) within a composition window of 5–6 wt.% Zn and 0.2–0.4 wt.% Ca [18, 19]. Studies by Mao et al. showed that with increasing Zn content, microstructure is more refined and mechanical properties are improved [20]. Depending on the results, most researchers have assumed that ternary alloys based on Mg–Zn–Ca system are safe for in vivo use. In vivo evaluation of Mg–Zn–Ca system demonstrated no sign of inflammation 4 weeks after first implantation when used in 3-month-old C57BL/6 mice [21]. Another study using  $Mg_{60}Zn_{35}Ca_5$  in pig also supported the utility of Mg–Zn–Ca system in the field of implant application [22]. Park et al. modified the last composition ( $Mg_{62}Zn_{35}Ca_3$ ) to use calcium as a grain refinement agent, whereas Zn to increase mechanical strength. Results confirmed better biocompatibility and improved corrosion resistance as the samples were absorbed completely after 4 weeks from implantation without any inflammatory phase [23]. Thus, adequate amount of Ca and Zn can be added to pure Mg to improve biocompatibility and mechanical property without showing toxicity [24]. According to the available data, it is yet to formulise the effect of Zn, Ca or Zn/Ca ratio in ternary alloy systems. However, to ensure long-term stability, alloying never proved to be enough due to degradation caused by electrochemical corrosion by formation of cathodic sites in microstructure. In order to elongate the stability, degradation must be slowed, in other words corrosion resistance must be increased. Thus, several procedures have been used to retain mechanical properties for longer period, among them surface coating predominates due to its simplicity yet effectiveness towards the requirement. Various physical, chemical, mechanical and biological deposition methods have been adopted for depositing bioactive glass (BG) and bio-ceramic on various substrates [25]. It was suggested that surface coating of Mg-based implant has advantages of gradual

degradation over a period of time along with superior corrosion consistency enabling strength decay [26]. And in this regard, advantages of plasma spray technique include its ease of preparation, coating on unique surface with good adhesion, conformal and pin-hole free films, less leachability, sterile upon preparation and in case of magnesium alloy, less chance of corrosion by atmospheric moisture.

Further, surface modification of Mg alloys can be classified into metallic, ceramic and polymeric according to the chemical characteristics and atomic structure of the coating materials, reviewed by Yin et al. [27]. Choice of coating material has become a topic of interest in many research groups. Different materials such as ceramics and glass (hydroxyapatite (HAp), calcium phosphates, 45S5 bioglass, etc. [28–31]), polymer (PGA, PLA, PEO-PCL, PEA-PLLA, PLG, etc. [32]) and composite (HAp-PCL, F-HAp [33]) have been used according to the implant requirements. CaP coatings done by ion-beam-assisted deposition or electrochemical and chemical treatment reduce the rate of corrosion, but crystal structure, chemical composition, coating morphology and degradation rates differ. Sometimes less cell viability on the longer run was also reported [34]. However, according to the substrate material, component design, cost and end applications, coating thickness requirement and process temperature, plasma spray coating was chosen as one of the coating procedures. And further, keeping the variables in mind BG and HAp were chosen as coating material in the present investigation. BGs when implanted react to physiological fluids and form a strong chemical bond with bone. It forms a hydroxyl carbonate apatite layer on the surface and delay further corrosion. Use of HAp as coating material in hybrid structures and metals has gained attention due to interaction of HAp with tissue [35].

Thus, in the present study, we have developed and used a new ternary system (Mg–Zn–Ca) of Mg alloy based substrates, which was further coated using air plasma spray system with HAp and for the first time with BG S53P4 as well as coating material. Aim of this study is to understand the compositional effect of substrate on coating in long-term use and finally suitability as implant material for bone defect healing in animal models for 60 days.

## 2 Materials and methods

### 2.1 Fabrication of samples

#### 2.1.1 Sample preparation

In the present investigation, we have used a new Mg alloy with alloying elements of ~22.5% Zn and 0.5% Ca by wt. was used as substrate material (henceforth, the samples will be referred as BM). Alloying elements were quantified by X-ray fluorescence spectroscopy (XRF) prior. Further,

phases of alloys were analysed by X-ray diffraction (XRD) (PANalytical, the Netherlands) and Fourier-transformed infra-red spectroscopy (FTIR) (Spectrum 100, PerkinElmer, USA) and scanning electron microscopy-energy dispersive analysis of X-ray (SEM-EDAX) (Phenom proX, Phenom-World B.V., the Netherlands) was used for microstructural and approximate qualitative elemental determination. Samples were cut into rectangular strip/plate with size  $100 \times 10 \times 3$  mm ( $L \times b \times t$ ) using abrasive cutting machine. Surface of the specimens was roughened by 99.9% high pure alumina grit (16 mesh) using a pressure blast (MEC Shot Blasting Equipments Pvt. Ltd., India). Roughness of bare surface was kept around 6–10  $\mu$ m (average). Finally, acetone was used to clean all the samples ultrasonically and dried at room temperature for further use.

BG S53P4 was synthesized by conventional melt-quench method using SiO<sub>2</sub> (Loba Chemie, Mumbai, India, Min. assay 99.7%), CaCO<sub>3</sub> (Min. assay 98.5%), Na<sub>2</sub>CO<sub>3</sub> (Min. assay 99.9%) and (NH<sub>4</sub>)<sub>2</sub>HPO<sub>4</sub> (Min. assay 99%) (Merck, Mumbai, India) as raw materials. Calculated batch were mixed thoroughly and melted at 1360 °C followed by quenching in double distilled water. Frits were collected and extensively milled at 250 rpm using a planetary ball mill (PM100, Retsch, Germany) followed by further grinding and sieving to obtain granules ranging between 70 and 150  $\mu$ m. The powder chemical composition was checked by wavelength dispersive XRF spectrometry. The final powder was also tested to ensure particle size distribution (Microtrac S3500, USA).

On the other hand, HAp was prepared by conventional wet chemical method using A.R. grade calcium hydroxide [Ca(OH)<sub>2</sub>, Central Drug House, India] and ortho-phosphoric acid (H<sub>3</sub>PO<sub>4</sub>, Merck, India) as raw materials. Stoichiometry of reagent materials was maintained in a way (1.67) that pure phase can be obtained. After completion of drop-wise mixing of H<sub>3</sub>PO<sub>4</sub>, solution was kept for 24 h for precipitation. Precipitate was then washed and filtered followed by drying at 80 °C for 24 h. After drying, this was ground and sieved to get homogeneously sized powders. Powder was fired at 800 °C to obtain phase pure HAp. Finally, the same was graded sieved to obtain granules ranging between 70 and 150  $\mu$ m. Sintered (at 1250 °C) free flowing granules were used for subsequent plasma spray coating purpose. Further details have been reported elsewhere [36].

Strips/plates of BM were used for HAp and BG coating by using air plasma spray system (Sulzer Metco, USA) (henceforth, BG and HAp coated BM samples shall be referred as BMG and BMH, respectively). Six-axis manipulator (ABB Engineering, China) was used to obtain uniformity of the coating on substrate. Plasma cathode, a conical tip, was made of thoriated tungsten, while copper was used to make anode/nozzle of the torch with a conical

**Table 1** Spray condition used for plasma spray coating of HAp and bioactive glass on Mg alloy

Coating parameters	HAp coating (BMH)	S53P4 coating (BMG)
Arc current	500 A	350 A
Current	458 A	357 A
Voltage	62.2 V	58.2 V
Argon	55 NLPM	55 NLPM
Hydrogen	3 NLPM	2 NLPM
Flow rate	21 g/min	28 g/min
Water conductivity	39.9 $\mu$ s	39.9 $\mu$ s
Gun distance	6 inch	6 inch
Average time	40 s	35 s

shape that finished in a cylindrical duct 6 mm in internal diameter. Torch generation was carried out using argon (primary plasma gas) and hydrogen (secondary plasma gas). Spray conditions used are detailed in Table 1.

### 2.1.2 Feedstock powder and coating characterization

Phase analyses of the powders were carried out by powder XRD with Cu K $\alpha$  ( $\lambda = 1.54178 \text{ \AA}$ ) radiation [40 kV/30 mA with  $2\theta$  between  $20^\circ$  and  $60^\circ$ , step size of  $0.05^\circ$ ] and further verified by FTIR [KBr pellet method; mid-IR range of  $4000\text{--}400 \text{ cm}^{-1}$ , resolution  $4 \text{ cm}^{-1}$ ] spectroscopy with He-Ne laser IR source.

Similarly, phase analyses of the coatings before and after immersion in stimulated body fluid (SBF) were carried out by XRD and FTIR for molecular structural information. Field-emission scanning electron microscope (FESEM) (Zeiss Supra, 35VP, Germany) equipped with energy-disperse spectrometer attachment were utilized to evaluate both top surface and cross-section morphologies and quantitative elemental allocations of the samples before and after immersion. Prior the study, carbon sputter coating was given ( $\sim 30 \text{ nm}$ ) to make the surface conductive. Coating delamination strength was assessed by scratch tester (Scratch Adhesion Tester, Ducom, USA) having diamond indenter Rockwell C, with tip radius  $200 \mu\text{m}$  with increasing load from 1 to 35 N.

### 2.1.3 Electrochemical corrosion test

Electrochemical corrosion of coated and uncoated samples was carried out in SBF solution with an electrochemical workstation (Bio-Logic Science Instruments SAS, France). Setup contains three-electrode cell (kept at  $37 \pm 0.5^\circ\text{C}$ ) with reference electrode as Saturated calomel electrode (SCE), counter electrode as platinum mesh and sample with  $0.64 \text{ cm}^2$  surface area exposed to the solution as working electrode. Prior the experiment, samples were ground using 1200 grit

emery paper, followed by polishing with  $1 \mu\text{m}$  alumina powder and washing with ethanol (99%). The potentiodynamic polarisation data were collected from  $-0.25 \text{ V}$  (with reference to SCE) to  $1.6 \text{ V}$  with a scanning rate  $10 \text{ mV/s}$ .

### 2.1.4 SBF immersion test

SBF solution was prepared following Kokubo et al. [37], maintained at  $37.4 \pm 0.2^\circ\text{C}$  and pH  $\sim 7.4$  by tris [(hydroxymethyl)aminomethane] buffer during preparation. Surface area of samples to volume of SBF added was maintained at  $1 \text{ cm}^2/15 \text{ mL}$  during the study in closed test tube for 7 and 14 days without replenishing SBF solution in between. Change in weight of sample, pH and supernatant ion concentrations ( $\text{Mg}^{2+}$ ,  $\text{Ca}^{2+}$ ,  $\text{PO}_4^{3-}$ ) was noted with time. After 7 and 14 days, low angle XRD and FTIR were used for assessment of coating composition while FESEM was taken on top surface to verify the microstructure. Quantitative phase analysis of the XRD data was done by using RIR method in X'pert pro HighScore Plus software.

## 2.2 In vitro biocompatibility assessments

### 2.2.1 Cell culture procedure

Cell culture medium containing DMEM, 10% foetal calf serum and 1% penicillin/streptomycin with human osteoblasts-like cells (MG-63) was used and kept in a humidified atmosphere of 5%  $\text{CO}_2$  at  $37^\circ\text{C}$ . 90% confluence cells were counted following the procedure of trypsinization, centrifugation and finally suspended back in media. Sterilization of the samples was carried out using 70% ethanol and UV light for 30 min followed by washing with sterile PBS (pH 7.4) and treated with DMEM medium for 4 h to generate a conducive atmosphere for better sustaining of cells. Implants were partially dried for 2 h to make certain for superior cell penetration. The next step includes drop-by-drop addition of  $20 \mu\text{L}$  of the cell suspension in medium, containing  $10^5$  cells in each sample. The cell loaded samples were kept in a humidified environment, at  $37^\circ\text{C}$ , 5%  $\text{CO}_2$  to facilitate better cell adhesion in the early hour. The cell seeded matrices were kept in medium for 21 days with alternate day replacement of medium.

### 2.2.2 Cell viability assay

MTT assay was carried out to examine the viability of cells at several time points. The procedure involved the incubation of samples in  $5 \text{ mg/mL}$  MTT [3-(4,5-dimethylthiazol-2-yl)-2,5-diphenyl tetrazolium bromide] stock solution (1:10 dilution) using PBS (pH 7.4). After 4 h of incubation, formazan crystals were dissolved in DMSO and the optical



density was measured in spectrophotometer (Bio-Rad, iMark) as per the manufacturer's guidelines.

### 2.2.3 Cell proliferation by alamar blue (AB) assay

Cell proliferation on matrices was measured using AB dye-reduction assay over 21 days using dye-to-media ratio of 1:10. A microplate reader (Thermo Scientific Multiskan Spectrum, Japan) was used to estimate the dye reduction of the incubated samples at 570 and 600 nm (for 4 h in dark condition) using following equation:

% AB reduction =  $[(\epsilon_{ox}\lambda_2)(A\lambda_1) - (\epsilon_{ox}\lambda_1)(A\lambda_2)] / [(\epsilon_{red}\lambda_1)(A'\lambda_2) - (\epsilon_{red}\lambda_2)(A'\lambda_1)] \times 100 \dots (1)$  where  $\epsilon\lambda_1$  (570 nm) and  $\epsilon\lambda_2$  (600 nm) represent the molar extinction coefficient of AB;  $\epsilon_{ox}$  and  $\epsilon_{red}$  in oxidised and reduced form, respectively; absorbance of test wells were  $A\lambda_1$  and  $A\lambda_2$  and  $A'\lambda_1$  and  $A'\lambda_2$  correspond to the absorbance of negative control wells. All given pairs were evaluated at 570 and 600 nm.

### 2.2.4 Alkaline phosphatase (ALP) assay

MG-63 cells (NCCS, Pune, India), seeded with samples, were cultured for a definite time point to quantify the produced alkaline phosphatase spectrophotometrically. Briefly, the cell laden constructs were rinsed with PBS (pH 7.4), homogenised with 1 mL tris buffer (1 M, pH 8.0) and finally sonicated for 4 min in chilled condition. Next, 1 mL of 16 mM p-nitrophenyl phosphate (Sigma) solution was added to 20  $\mu$ L of the supernatant and incubated for 5 min, at 30 °C. The p-nitrophenol produced in presence of ALP was measured by observing the absorbance at 405 nm depicting absorbance, calculated at 405 nm as p-nitrophenol formed and normalized by incubation duration and cell count:  $\mu$ mole/min/ $10^5$  cells.

### 2.2.5 Cellular morphology

Orientation, distribution and morphology of cells were monitored by Laser confocal microscopy (Olympus FV 1000, Olympus, Japan). In brief, samples were fixed with 4% paraformaldehyde for 1 h followed by 5 min cellular

permeabilization using 0.1% Triton X-100 in bovine serum albumin (BSA). Post blocking of samples with 1% BSA for 1 h, actin filaments were stained using Alexa Fluor® 488 and the nuclei with Hoechst 33342. Later, these were imaged by confocal laser microscopy and analyzed with Olympus FV 1000 Advanced software version 4.1 (Olympus, Japan).

### 2.2.6 Gene expression by real-time RT-PCR

RNA extraction was performed on 21 days cultured MG-63 cells on different samples by using Trizol solution (Invitrogen, USA). In brief, cell seed samples were transferred to small vials containing 1.5 mL of Trizol solution and incubated for 15 min. After that, centrifugation was done at 12000 rpm for 10 min/4 °C and the clear supernatant was collected in a fresh tube followed by addition of chloroform, incubated for 5 min at RT. The sample was then mixed for 15 s and again incubated for 5 min at RT. Again the samples were centrifuged at 12000 rpm for 15 min at 4 °C and the top most aqueous layer was transferred to an RNeasy Plus Mini-Spin Column (Qiagen, Germany). According to the manufacturer's protocol, the RNA was washed and eluted repeatedly. Then, RNA samples were reverse-transcribed into cDNA using High capacity cDNA reverse transcription kit (Applied Biosystems, USA) in line with the manufacturer's guidelines.

Using SYBR Green (Applied Biosystems, USA), gene expression was performed by real-time PCR conditions in an ABI Prism® 7000 Sequence Detection System (Applied Biosystems, USA). SYBR Green Supermix, 5  $\mu$ L cDNA templates and 5 pmol/mL of each primer (forward and reverse) were used for real time analysis in a final solution of 50  $\mu$ L volume and plates were loaded using a RT loading platform. Cycling conditions involved an initial denaturation step of 8 min and 45 s at 95 °C followed by 45 cycles of 30 s at 95 °C, 30 s at 58 °C and 30 s at 72 °C. Data were collected at 72 °C in each cycle. CT (threshold cycle) values were calculated using the Relative Quantification software (Applied Biosystems).

Highly purified gene-specific primers for osteopontin (OPN), collagen I, osteocalcin (OCN), Runx2 and house-keeping gene GAPDH (Table 2) were selected bearing in

**Table 2** RT-PCR primer sequences (forward and reverse) used in the current gene expression study

Genes	Forward primer	Reverse primer
Runx2	5'-GCTTCTCCAACCCACGAATG-3'	5'-GAACTGATAGGACGCTGACGA-3'
OCN	5'-AAAGCCCAGCGACTCT-3'	5'-CTAAACGGTGGTGCCATAGAT-3'
Osteonectin	5'-ACAAGCTCCACCTGGACTACA-3'	5'-TCTTCTTCACACGCAGTTT-3'
OPN	5'-GACGGCCGAGGTGATAGCTT-3'	5'-CATGGCTGGTCTTCCCGTTGC-3'
ALP	5'-TCAGAAGCTCAACACCAACG -3'	5'-TTGTACGTCTTGGAGAGGGC -3'
BSP	5'-CAGGGAGGCAGTGACTCTTC-3'	5'-AGTGTGGAAAGTGTGGCGTT-3'
COL I	5'-TCCTGCCGATGTGCGTATC-3'	5'-CAAGTTCGGTGTGACTCGTG-3'
GAPDH	5'-AGGTCGGTGTGAACGGATTG-3'	5'-TGTAGACCATGTAGTTGAGGTCA-3'

mind the literature and synthesized commercially (MWG-Biotech AG Ltd, India). The Ct value of the housekeeping GAPDH gene was used to normalise relative expression levels for each target gene using an identical procedure ( $2^{-\Delta\Delta C_t}$  formula, Perkin Elmer User Bulletin s # 2). Each sample was experimented in triplicate.

### 2.2.7 Mineralization assay by alizarin red S (ARS) staining

The mineralization study was assessed by using the ARS staining dye. In brief, prior to washing thrice with PBS, MG-63 cells loaded constructs were fixed in ice cold 70% ethanol for 1 h. Next, constructs were again washed with distilled water and stained with ARS (40 mM) for 20 min at RT. At the end, the stained constructs were viewed under optical microscope after rigorous washing with distilled water. The principle of the study is to observe the mineralization which occurs due to binding of ARS with calcium salts. This can be qualified by imaging (mentioned above) and quantified by reading the absorbance at 540 nm in microplate reader prior to desorbing the stain by using 10% cetylpyridinium chloride for 1 h.

### 2.3 In vivo biocompatibility studies

Nine mature New Zealand white rabbit (1.5–1.8 kg body weight) were utilized in the present in vivo pre-clinical experiment. The rabbits were maintained in separate cages of temperature and humidity controlled room including provision of standard diet and water. The animals were assigned into three random groups consisting of three animals each. In group I (three animals) bare Mg alloy scaffolds (BM) were implanted bilaterally in distal part of femur bone, whereas BMH and BMG implants were placed in other two groups (groups II and III, respectively). Protocol of Institutional Animal Ethical Committee, West Bengal University of Animal and Fishery Sciences (WBUAFS), India, (Approval No. Pharma/188 (viii) dated 31.07.2015) was strictly followed.

### 2.4 Surgical procedure

Before surgery, distal femur of both hind legs were shaved, cleaned and aseptically prepared. Anaesthesia was achieved with a combination of xylazine hydrochloride (Injection Xylazine, Indian Immunologicals, Ahmadabad, India) at 6 mg/kg body weight and ketamine hydrochloride (Ketalar, Parke-Davis, Hyderabad, India) @33 mg/kg body weight intramuscularly. Skin incision was made in the distal lateral part of the femoral bone in all groups. The femur bone was approached by surgically exposing the skin, subcutaneous tissue, the muscle and finally periosteum. A circular bone defect was created by micromotor dental drilling to press fit

the implants. During this procedure, constant sterile cold water was irrigated at the defect site to prevent thermal necrosis of bone. Respective implants were then press fitted and incised muscles, fascia and skin were apposed with standard suturing techniques.

#### 2.4.1 Postoperative clinical examinations

During the post-operative period, animals were checked for any lameness, swelling of the operated site, oedema and the cardinal signs of local inflammatory reaction up to 2 months.

#### 2.4.2 Radiological examinations

Chronological radiographs of the operated limb were performed at day 0 and afterwards on 1 and 2 months postoperatively (300 mA, M.E. X-Ray Machine, India) to ascertain the proper position of implant within the bony defect.

#### 2.4.3 Histological study

Implanted bone area was collected for histology to assess the status of cell–material interaction. Accordingly, implanted bone tissue samples were collected for all the groups on 2 months postoperatively. Bone sections were initially fixed in 10% formalin for 7 days and afterwards decalcified using Goodling and Stewart's fluid (15 mL formic acid, 5 mL formalin and 80 mL distilled water). The resultant decalcified bone samples were fixed in paraformaldehyde, 4  $\mu$ m tissue sections was prepared from paraffin embedded block and finally stained with haematoxylin and eosin. The stained tissue sections were finally examined under Leica microscope (Leica Microsystems, Weltzar, Germany) for histological examination.

#### 2.4.4 Scanning electron microscopy study

Two month post-implanted bone samples were also checked for interfacial study of new osseous tissue formation using SEM. After carefully removing the soft tissue from the bone, samples were fixed in 2% electron microscope grade glutaraldehyde phosphate solution for 48 h, washed thrice for 30 min with PBS (pH 7.4) and distilled water and finally drying the samples in a series of graded alcohol solutions. Gold sputter coated bone samples were imaged using an FESEM (LEO, UK) for microstructural analysis of newly formed osseous tissue at the interface of bone and material.

#### 2.4.5 Fluorochrome labelling study

Oxytetracycline as fluorochrome marker (Terramycin; Pfizer India, India) @25 mg/kg body weight was injected

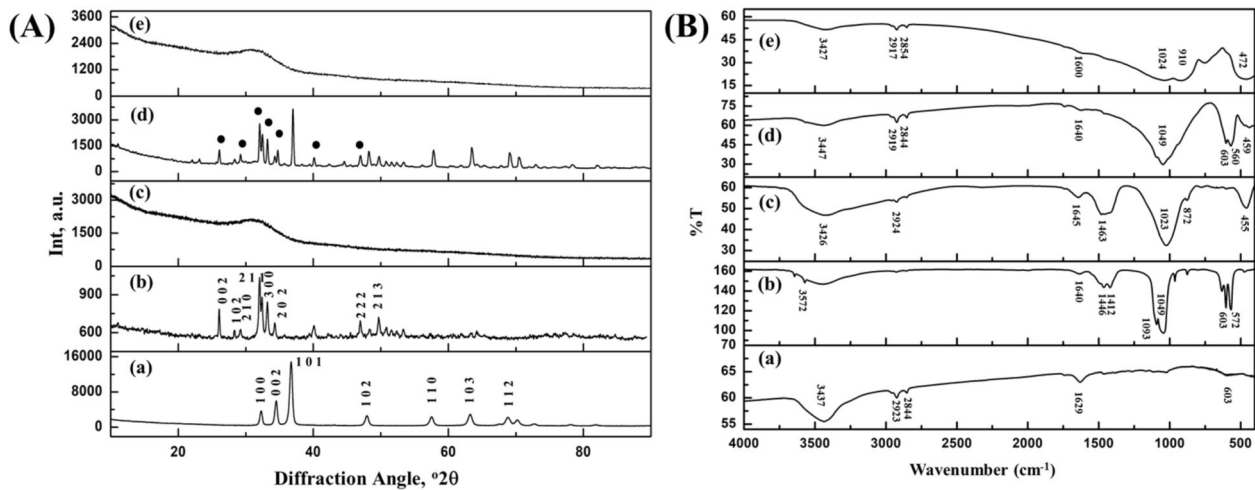


**Fig. 1** A XRD pattern and B FTIR spectra of (a) BM, (b) HAp granules fired at 1250 °C, (c) bioactive glass, (d) BMH (•HAp phase) and (e) BMG

25 days prior to euthanasia of the animals at 2 months, i.e. on the days 35, 36 and 43, 44 (2-6-2) postoperatively. Retrieved implanted bone samples were ground to 20  $\mu\text{m}$  thickness and finally placed under ultraviolet incidental light with a Leica DM 2000 fluorescence microscope. The golden yellow fluorescence (new bone formation) pixels was measured and consequently converted to percentage of new osseous tissue formation.

#### 2.4.6 Toxicological study

Toxicological study of BM, BMH and BMG implanted bone was carried out by histology of three major organs (heart, liver and kidney). To carry out, H&E stained histological sections of heart, liver and kidney from sacrificed animals were prepared to observe any presence of significant cellular changes.

#### 2.4.7 Immunocompatibility study

Amount of host-implant immune compatibility was determined by measuring the concentration of IL2, IL6 and TNF- $\alpha$  cytokine response of the animals post in vivo implantation with biomaterials (i.e. BM, BMH and BMG implants). Blood serum was collected at 1, 2, 4 and 8 weeks post surgery and concentrations of IL2, IL6 and TNF- $\alpha$  were estimated using ELISA kits for rabbit (Invitrogen, USA).

#### 2.5 Statistical analysis

Statistical analysis of the in vivo immune response data was carried out using one-way analysis of variance (ANOVA) with a Tukey's post hoc by ORIGIN software. Absolute mean values and standard deviations were calculated. Data were taken from three samples ( $n = 3$ ).

## 3 Results

### 3.1 Material characterization

#### 3.1.1 Substrate characterization

XRD, FTIR and SEM-EDX of bare substrate (BM) are shown in Figs. 1A-a, B-a and 2A-a, c, e, respectively. SEM exhibited typical ground surface caused by mechanical grinding having EDX and XRF (not shown) confirming alloying materials Mg, Zn and Ca with impurities (such as  $\text{SiO}_2$ ,  $\text{Al}_2\text{O}_3$ , SrO, etc.). XRD indicated crystalline phase-pure magnesium, matched with JCPDS PDF #00-035-0821, while FTIR supported the presence  $\text{H}_2\text{O}$  and Mg-O as a result of environmental corrosion.

#### 3.1.2 Powder characterization

XRD of graded/sieved (80–120  $\mu\text{m}$ ) HAp and BG powders confirmed crystalline HAp phase (Fig. 1A-b) and amorphous glassy phase (Fig. 1A-c) from characteristic peaks [ $2\theta$  values 31.7°, 32.2° and 32.9° corresponding to (211), (112) and (300) planes and matched with JCPDS PDF# 00-009-0432] and amorphous hump, respectively. FTIR spectra (Fig. 1B-b) showed peaks related to vibrational and stretching of phosphate groups (603, 962 and 1093  $\text{cm}^{-1}$ ) and apatite -OH group (3572  $\text{cm}^{-1}$ ) supporting phase purity of HAp along with peaks corresponding to carbonate group (1640  $\text{cm}^{-1}$ ) as well. FTIR of BG sample (Fig. 1B-c) showed peaks at 1023  $\text{cm}^{-1}$  (stretching) and 455  $\text{cm}^{-1}$  (bending) corresponding to Si-O-Si vibrations and that at 872  $\text{cm}^{-1}$  corresponds to O-Si-O stretching. A broad absorption peak at 3426  $\text{cm}^{-1}$  corresponds to intermolecular hydrogen bonded OH, whereas presence of molecular water is also evident by sharp peak at 1645 and 2924  $\text{cm}^{-1}$  and impurities such as ionic nitrates at 1463  $\text{cm}^{-1}$ .

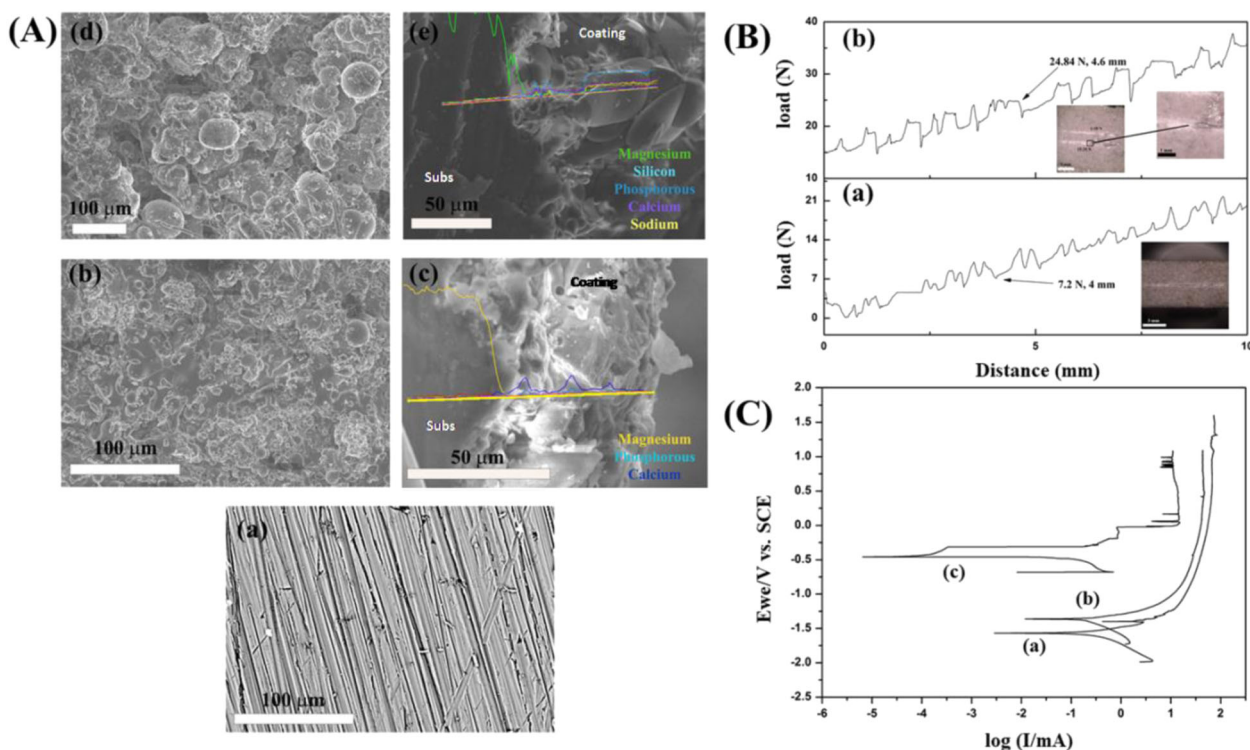


**Fig. 2** **A** Top surface FESEM [(a), (b) and (d) for BM, BMH and BMG, respectively] and interface FESEM-EDAX [(c) and (e) for BMH and BMG]. **B** Scratch profile of (a) BMH and (b) BMG [inset:

optical microscope image of surface]. **C** Tafel plot recorded during corrosion testing in contact with SBF for (a) BM, (b) BMH and (c) BMG samples

Final composition of BG used for plasma spray coating was (approximately by wt.): 53%  $\text{SiO}_2$ , 23%  $\text{Na}_2\text{O}$ , 20%  $\text{CaO}$  and 4%  $\text{P}_2\text{O}_5$ .

### 3.1.3 Coating characterization

Figure 1A-d, e shows the XRD of coated surface of BMH and BMG samples, respectively. BMH samples showed phase mixture of HAp and Mg (73% and 27%, respectively, calculated from Rietveld analysis). Percentage of crystallinity (calculated by Landi et al.'s method [38]) and average crystallite size (calculated by Scherrer's method [38]) of HAp phase is found to be about 74% and 19 nm, respectively. Physically, coating coverage was found to be better in case of BMG compared to other samples with no formation of crystalline/other amorphous phase. Amorphicity of S53P4 was increased after plasma spray process which is reflected by lower intensity of XRD pattern.

Figure 1B-d, e shows FTIR spectra of BMH and BMG, respectively. Wider peaks in comparison with spectra of the HAp powder were found in case of BMH samples. Decrease in the crystallinity of BMH (as seen in XRD) has also been reflected in FTIR. No characteristic peaks were found due to carbonate bond as that of base HAp powder. Broadening of peaks at 560, 603 and 1049  $\text{cm}^{-1}$  and decrease in intensity at 3752 and 632  $\text{cm}^{-1}$  can be observed in case of BMH samples.

Peak broadening (at 472, 1024 and 1600  $\text{cm}^{-1}$ ) can be seen in case of BMG sample also after plasma spray coating.

Figures 2A-b, c and A-d, e show FESEM microstructures of top and interface of plasma sprayed BMH and BMG, respectively. At interface, layer-wise fish scale-like morphology of melted and deformed splat can be seen near vicinity of substrate and at top globular shaped splat along with some porosity ( $\sim 1\text{--}10\ \mu\text{m}$ ) were seen around outside/periphery of BMH samples together with some unmelted particles. Dimensions of pores for BMG were slightly higher (15–30  $\mu\text{m}$ ) with layer-wise globular shaped unmelted/unreacted particles. The thickness of the coating was found to be 50–60  $\mu\text{m}$  for BMH and 90–100  $\mu\text{m}$  for BMG samples. There was sharp decrease in Mg concentration which can be seen from EDAX line scan across interface (cf. Fig. 2A-c, e).

Load-displacement plot obtained after scratch test on BMH and BMG are shown in Figs. 2B-a and B-b, respectively; corresponding optical microscope images of the scratch are also provided. From these results, the delamination load was found to be 7.2 N at 3.8 mm for BMH, whereas in case of BMG, it was 24.84 N at 4.8 mm.

**3.1.3.1 Electrochemical properties** Potentiodynamic polarization curves for BM, BMH and BMG samples are shown in Fig. 2C-a–c, respectively. Corresponding data of corrosion potential ( $E_{\text{corr}}$ ) and corrosion current density ( $i_{\text{corr}}$ ) were

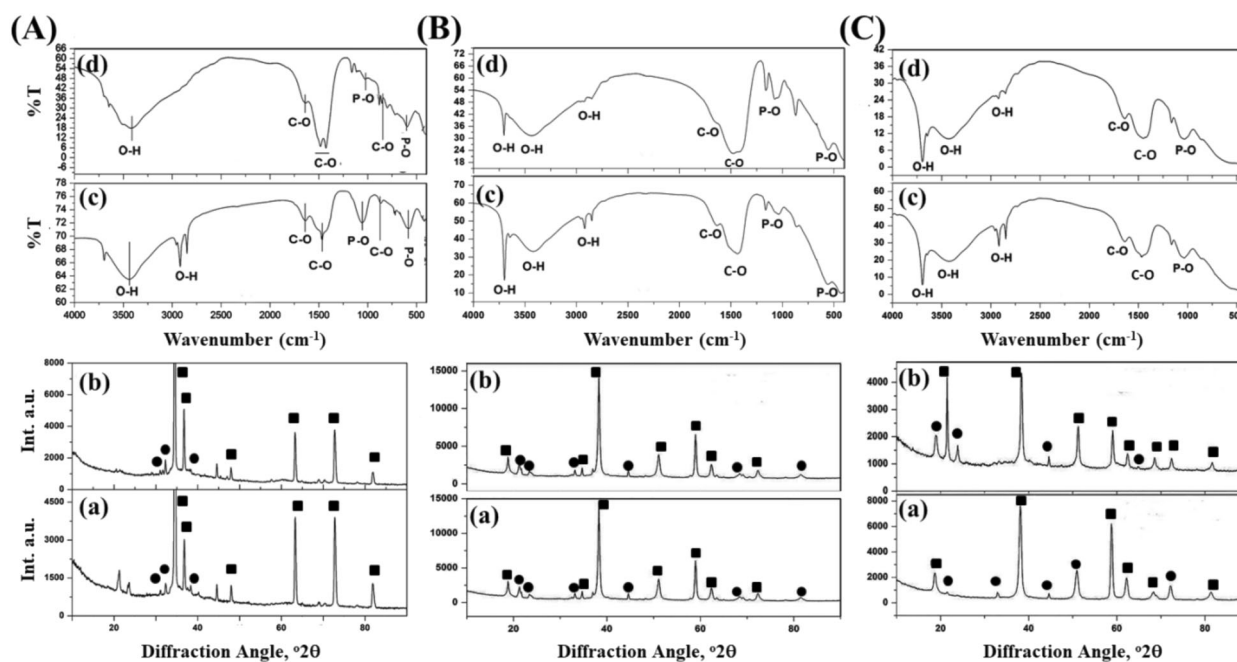


**Fig. 3** XRD pattern and FTIR spectra of the samples after 7 and 14 days of SBF test. **A** BM. **B** BMH. **C** BMG. (a) and (b) are XRDs and (c) and (d) are FTIRs after 7 and 14 days, respectively, [● HAp phase and ■ Mg phase]

evaluated from the curves. For BM, BMH and BMG,  $E_{\text{corr}}$  (mV) values were  $-1540$ ,  $-1420$  and  $-296$ , respectively, with corresponding  $I_{\text{corr}}$  ( $\mu\text{A}$ ) values as 250, 297 and 68, respectively. Decrease in  $E_{\text{corr}}$  of BMH and BMG clearly indicate that both coatings have relatively better resistance to corrosion initiation than BM. However, the corrosion rate appears to be lowest for BMG due to their lowest  $I_{\text{corr}}$ .

**3.1.3.2 SBF immersion test** Figure 3A-a, b, B-a, b and C-a, b shows the XRD pattern after 7 and 14 days of SBF immersion test of BM, BMH and BMG samples, respectively. After 7 days of immersion, the XRD of BM showed 11% HAp (JCPDS PDF #00-19-0272) along with 89% Mg (JCPDS PDF #00-035-0821). Mg phase was found to increase up to 92.7% after day 14 confirming corrosion on the surface. XRD of BM samples also showed decrease in HAp phase crystallinity (11–7.3%) as well as average crystallite size (83–33 nm) after day 14. Both BMH and BMG samples showed formation of HAp (JCPDS PDF #01-086-1201) and calcium phosphate hydroxide (JCPDS PDF #01-083-1887) along with  $\text{Mg}(\text{OH})_2$  (JCPDS PDF #01-076-0667 and #00-044-1482, respectively). Percentage of phases in case of BMH samples was calculated using X'pert pro software and was found to be 7.5% HAp (with average crystallite size 11 nm) and 92.5% magnesium hydroxide. XRD taken after 14 days showed decrease in percentage (7.5–4.5%) of HAp phase (with average crystallite size 4.7 nm). However, in case of BMG samples, Ca–P phase was found to increase from day 7 (31.3%) to day 14 (67.3%) along with average crystallite size of HAp (9.3–11 nm).

FTIR spectra of BM, BMH and BMG samples after days 7 and 14 of SBF immersion study, as shown in Fig. 3A-c, d, B-c, d and C-c, d, supported XRD findings. BM samples showed peaks related to carbonated apatite at 563, 872, 1054, 1468 and 3435  $\text{cm}^{-1}$ . Based on FTIR result, after SBF study of BM samples, the layer obtained contains phosphates and carbonates. A sharp P–O bending mode doublet at 592  $\text{cm}^{-1}$  is suggestive of HAp [39]. However, decrease in C–O and P–O peak intensity supports the decrease in crystallinity as stated in XRD. BMH and BMG samples, on the other hand, showed fingerprints of apatite phase (563, 872, 1042, 1166, 1424, 1640, 2924 and 3700  $\text{cm}^{-1}$  in case of BMH samples and 872, 1042, 1468, 1640, 2924 and 3696  $\text{cm}^{-1}$  in case of BMG samples) along with indication of Mg–O bonding at 450–500  $\text{cm}^{-1}$  wavenumber. A detailed band interpretation is given in Table 3. BMG samples showed more apatite formation than BMH samples after SBF immersion study.

After SBF immersion for 14 days, top surface of bare and coated Mg alloy substrates were found to have different morphologies due to interaction with SBF. BM samples showed (Fig. 4A-a) flower-like apatite deposition, primarily composed of needle shaped crystals covering the entire surface. BMH samples (Fig. 4A-b) exhibited globular apatite microstructure composed of fine interconnected flakes with pores (0.1–1.5  $\mu\text{m}$ ). There was layer-wise apatite formation and when observed at higher magnification the precipitates revealed flake-like crystals with small pores in case of BMG (0.5–1.5  $\mu\text{m}$ ) (Fig. 4A-c and inset) and morphology was found to be denser and closely packed than others.

**Table 3** FTIR peak analysis after SBF immersion study

	BM (cm <sup>-1</sup> )		BMH (cm <sup>-1</sup> )		BMG (cm <sup>-1</sup> )	
	Day 7	Day 14	Day 7	Day 14	Day 7	Day 14
Mg–O	424	420	424	424	424	424
P–O			563	563		
P–O	585	592				
C–O/HPO <sub>4</sub> <sup>3-</sup>	872	879	872	872		872
P–O			1042		1042	1042
P–O	1054			1054		
P–O		1166	1166	1166	1166	1166
C–O		1424	1424	1424		
C–O	1468	1476			1468	1468
H–O–H	1640	1640	1640	1640	1640	1640
Absorbed H <sub>2</sub> O	2851		2851	2851	2851	2851
Absorbed H <sub>2</sub> O	2924		2924	2924	2924	2924
H–O–H	3435	3426	3427	3427	3427	3427
O–H	3700	3694	3700	3700	3700	3696

pH of supernatant solution collected from BM, BMH and BMG samples increased with time (Fig. 4B) in varying rates. Though, after initial 7 days, the increase in pH was higher for BMH samples, however, BMG samples was found to be higher after day 14. Qualitatively, the change in weight of the samples (Fig. 4C) was found to be directly proportional to the formation of apatite on these surfaces. Negligible weight change of BM samples indicate its inability towards apatite formation, whereas the weight gain of BMH (average increase after 7 day was ~3.4% and after 14 day it was ~12.9%) and BMG (average increase in weight after 7 day was ~8.7%, after 14 days this was ~27.2%) demonstrate their apatite precipitation ability. Changes in ion concentration of supernatant with immersion time are another way of correlating bioactivity (w.r.t. apatite formation) as well as corrosion (Fig. 4D-a-c). BM showed increase of Mg ion concentration with time, whereas the solution of BMH samples showed initial

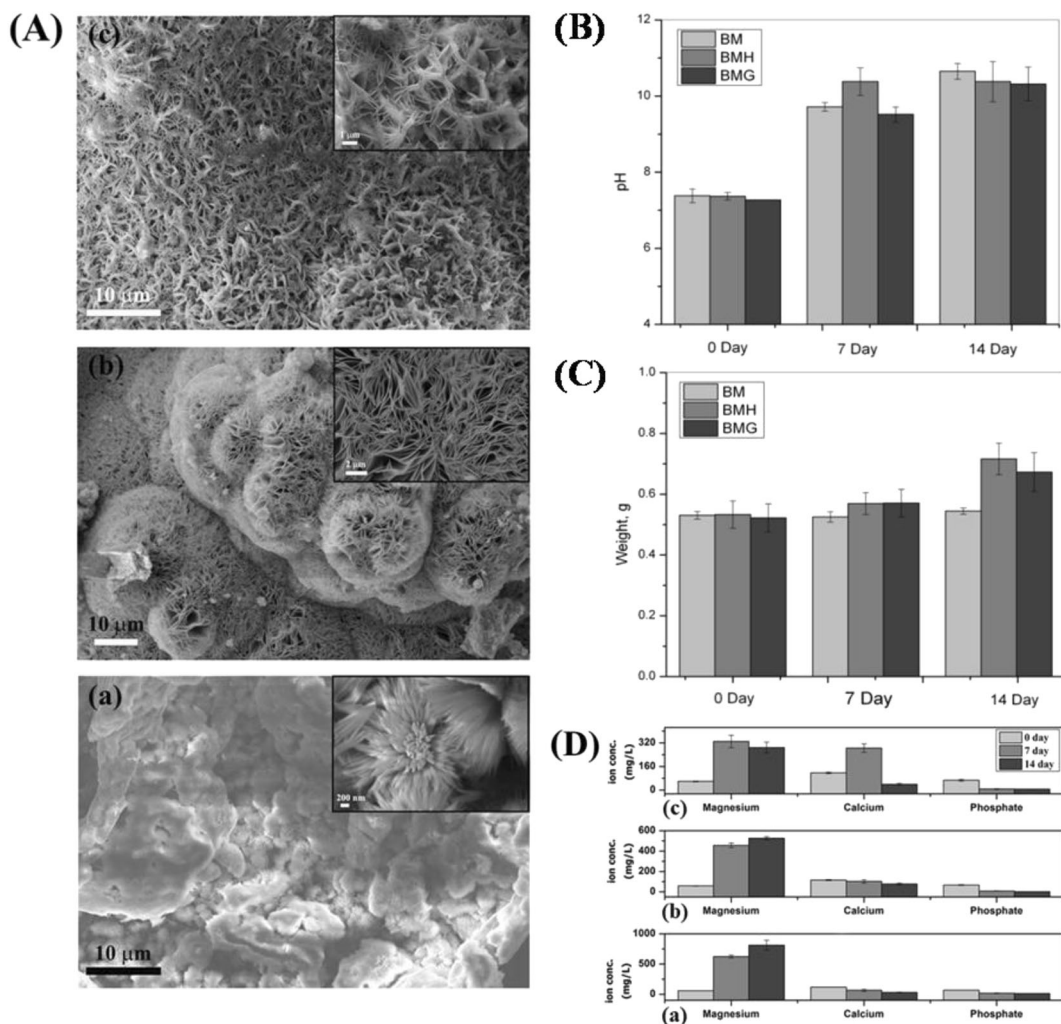


**Fig. 4** A FESEM microstructures after 14 days of SBF study; change of B pH, C weight and D magnesium, calcium and phosphate ion concentration of supernatant of different samples at days 0, 7 and 14. (a) BM, (b) BMH and (c) BMG

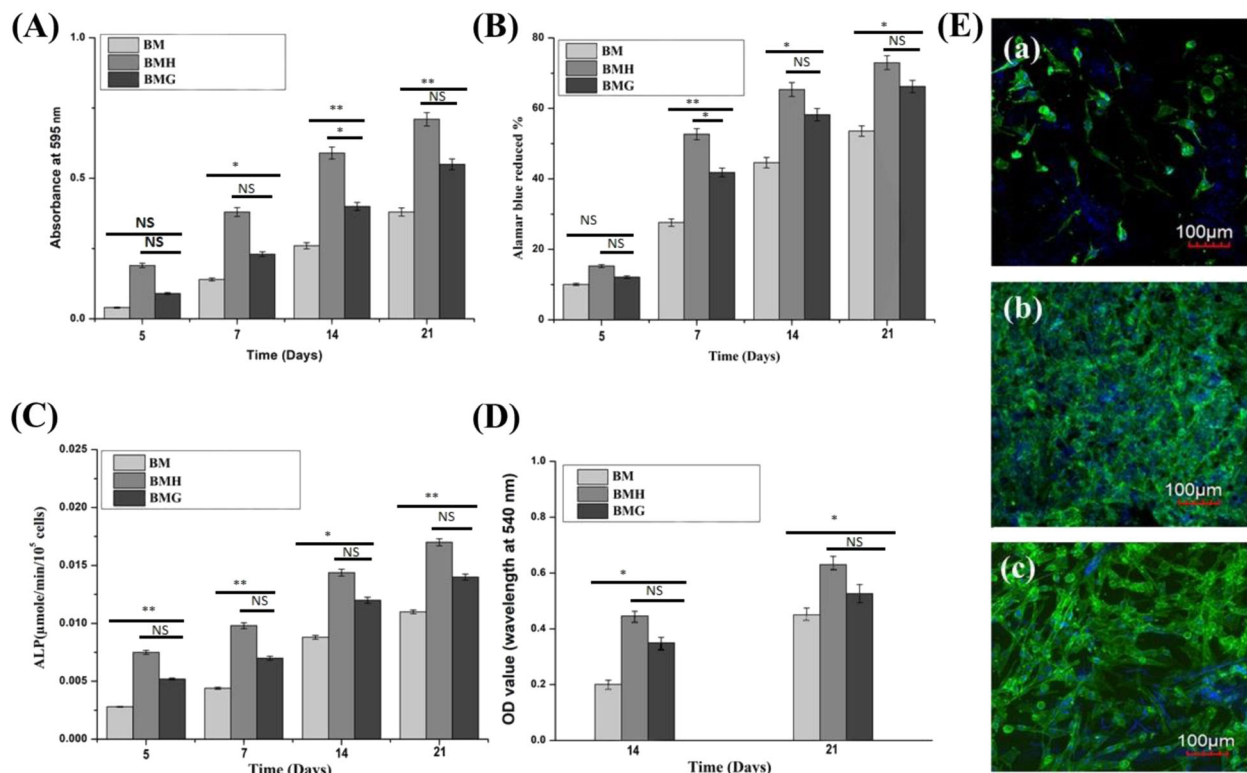


**Fig. 5** MG-63 **A** Cell viability, **B** proliferation, **C** ALP expression and **D** mineralization assay of different samples. **E** Cell morphology (by confocal laser microscopy) of (a) BM, (b) BMH and (c) BMG samples

increase of Mg ions up to day 7 but the rate was decreased at day 14. In case of BMG samples, however, Mg ion was found to be decreased after day 7–14. Calcium ion concentration was decreased in case of BM and BMH after days 7 and 14, but the same increased in BMG after day 7 and eventually decreased at day 14. Supernatant corresponding to BMH and BMG showed lower concentration of phosphates which support higher bioactivity (w.r.t. apatite formation) of the samples.

### 3.2 In vitro biocompatibility assessments

MTT and AB assays were conducted to assess the cytotoxicity of samples. Both results showed that these implants are non-toxic and provide favourable surfaces for cellular proliferation. MG-63 cell viability, cell proliferation and ALP expression on BM, BMH and BMG samples were measured on days 5, 7, 14 and 21 days. Maximum cell viability ( $**p < 0.01$ ,  $***p < 0.001$ ), proliferation ( $*p < 0.05$ ,  $***p < 0.001$ ) and ALP expression ( $**p < 0.01$ ,  $***p < 0.001$ ) were recorded for BMH after 21 days of cell culture as shown in Fig. 5A–C, respectively. Calcium ( $\text{Ca}^{2+}$ ) deposition, on the other hand, measured on day 14 and 21 days (Fig. 5D) showed maximum for BMH again after 21 days of cell culture ( $**p < 0.01$ ,  $***p < 0.001$ ).

#### 3.2.1 Cell morphology

Laser confocal helped to examine cell morphology and spreading of cells on samples. Cell morphology on BM, BMH and BMG are presented in Fig. 5E-a–c. Maximum number of cells are present in BMH as compared to other coated samples. Actin covers total surface of this sample and formed neo matrix which penetrated to sample as well. Actin filaments were stained with Alexa Fluor® 488 (green), nuclei with Hoechst 33342 (blue) and finally examined under confocal at 20 $\times$ .

Cell growth upon different layers of 3D constructs was observed by Z-scanning during confocal microscopy and finally image was taken by merging the different layers. The image depicted abundance and homogeneously dispersed actin filaments on BMH and BMG samples compared to BM. BMH samples showed presence of abundant cells followed by BMG. However, actin sharing was meagre and secluded for BM to just around the cell nuclei.

mRNA expression of representative bone-associated genes, such as OPN, collagen I, OCN and Runx2, help to investigate osteogenic efficacy of different implants. Figure 6 shows the comparison of the gene expression of cells on various samples after 21 days of culture. BMH and BMG samples exhibited relatively higher levels of genes compared to BM samples.

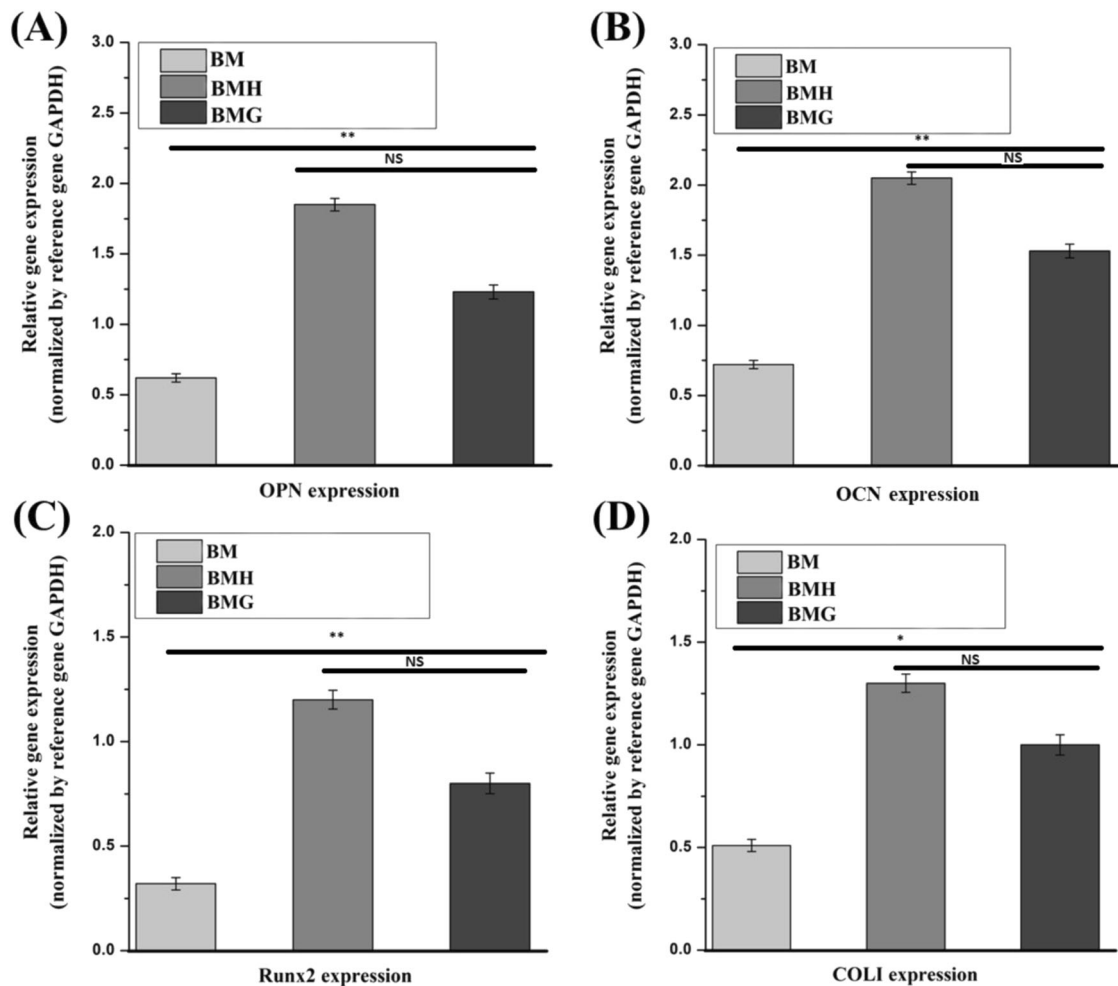


**Fig. 6** Relative gene expressions (normalized by reference gene GAPDH) w.r.t. **A** OPN, **B** OCN, **C** Runx2 and **D** COL1 expression of different samples

However, after the study, substantial difference in gene expression between BMH and BMG was not observed.

### 3.3 In vivo studies

#### 3.3.1 Bone histology

Figure 7A-a-c shows histological picture of implanted bone at 2 months. As shown in Fig. 7A-a, BM implanted bone section depicted a well-developed bony matrix with sufficient number of Haversian canal, bony lacunae and few osteoclasts. Medullary portion was less avascular and occupied by few osteoclasts, osteocytes and scanty amount of mucin. Accumulation of osteocyte was prominent in cortical area. Angiogenesis towards medullary region was lesser in amount (Fig. 7A-a). Bony section of BMH implant depicted bony lamellae characterized by well-developed Haversian system, canaliculi and resorption of bone in pericortical areas. Medullary region was occupied by RBC, scanty amount of mucin, few osteoblasts and

numerous osteocytes. Bony lacunae in some places were invaded by few osteoclast cells. Angiogenesis was prominent in medullary portion although fibrovascularisation was sufficient in cortical mass (Fig. 7A-b). Figure 7A-c shows histological images of BMG implanted bone section. Section depicted presence of abundant osteocytes, osteoclasts and osteoblast. Fibrovascularisation was prominent in cortical area and perimedullary area. Medullary cavity had adipose tissue, few RBC, moderate amount of mucin and osteoblast cell. Angiogenesis was fewer in cortical area than in medullary area (Fig. 7A-c).

#### 3.3.2 Fluorochrome labelling study

Golden yellow florescence in the section depicted new osseous tissue formation, whereas dark sea green colour designates host bone. The BM implant samples at 2 months showed new bone formation mainly at centre part and partially in edges, as pointed out by the presence of golden yellow fluorescence (Fig. 7B). New bone formation was



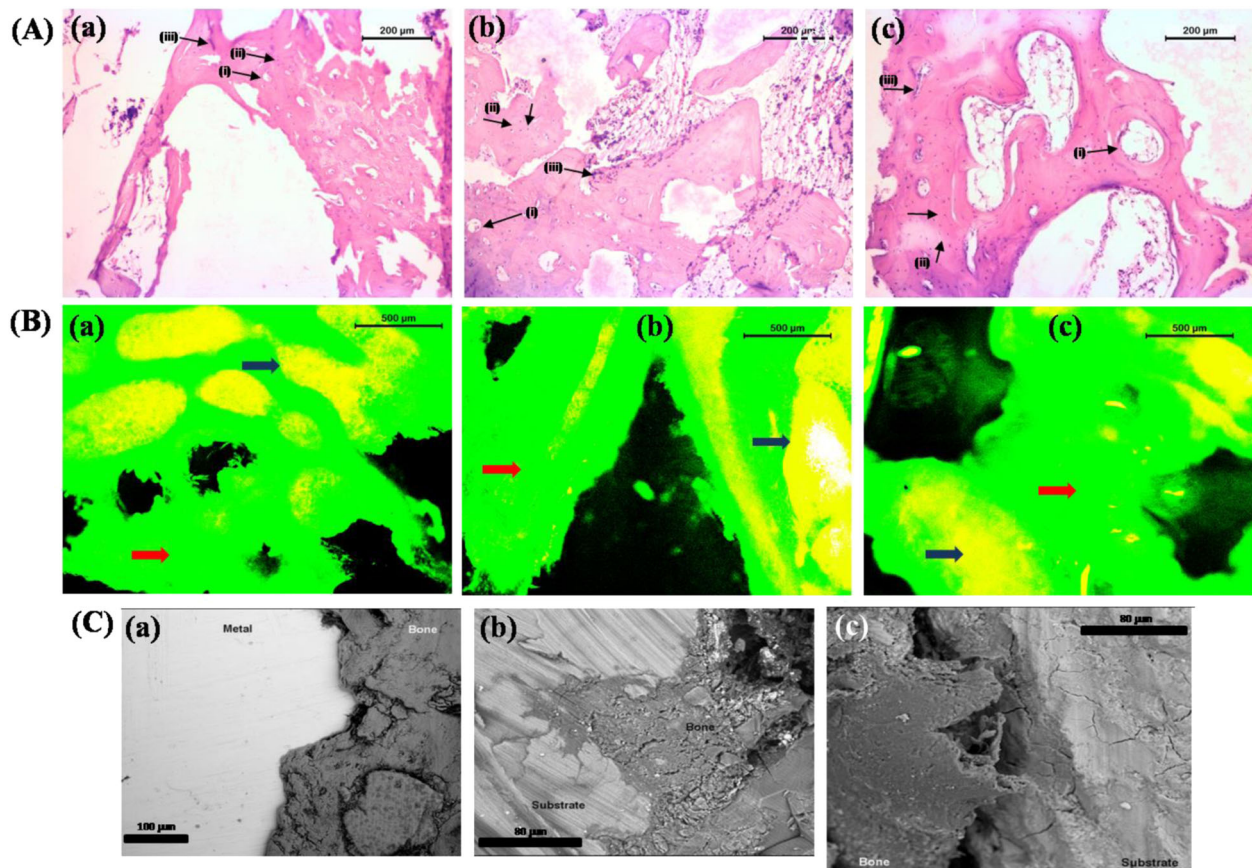


**Fig. 7** **A** Histology [(i) haversian canal, (ii) osteoblasts, (iii) osteoclasts]. **B** Fluorochrome labelling [blue arrow—new bone formation; red arrow—old bone]. **C** SEM images of implanted bone samples after 2 months [(a) for BM, (b) for BMH and (c) for BMG]

nearly 23% in defect area. BMH implant group depicted ample new osseous tissues (~37%) in contrast to other two groups. Although golden yellow fluorescence was mostly limited to peripheral side, a wide deep area of new bone formation was observed. Along this deep zone of golden fluorescence, a narrow band of fluorescence throughout the length was also observed nearly to central part of section indicating bone formation both in central as well as in peripheral zone. In BMG implant group, new bone formation was nearly 29%, mostly in periphery. The new osseous tissue was measured using ImageJ software. The golden colour pixels were calculated and changed to percentage using scale bars from three images each.

### 3.3.3 SEM of bone–implant interface

Scanning electron microscopy of bone–implant interface of BM, BMH and BMG samples are given in (Fig. 7C). It was found that BMH showed best bone apposition in due course of time with little or no interfacial gap, while BMG had also shown similar trend, but due to its conversion of apatite-like layer, metal surface was found to be covered by apatite-like layer with an apposition of bony soft tissue at interface. On

the other hand, BM was found to be replaced with associated interfacial bone with time. Matured bony tissues were noticed in case of BMH with time.

### 3.3.4 Radiology

Figure 8A shows sequential radiology of different implants in distal metaphysis of femur bone in rabbit model. In BM implant, day '0' (day of implantation) radiographs showed a radiodense circular material placed in metaphysis of the distal femur. After 1 month, the material radiodensity was reduced in comparison to earlier time point. A negligible impression of implant was found after 2 months indicating maximum degradation of material vis-à-vis moderate osseous growth in the defect site. Radiodensity of material and bone is comparable (Fig. 8A-a-c). In BMH implant, '0' day radiograph showed radio-opaque material in the distal femoral bone defect. By the end of 1 month, implant was visible in the defect region with comparable radiodensity of host bone although there was a distinct radiolucent gap between bone and implant. At 2 months, implant was visible with similar radiodensity of host bone but there was reduction in diameter of implant indicating degradation was

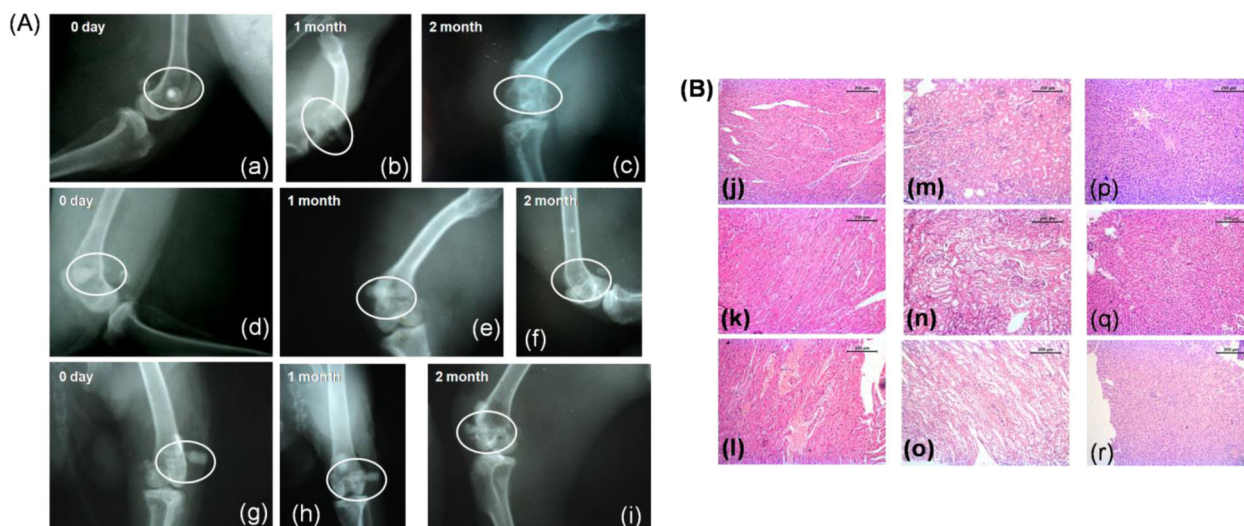


**Fig. 8** **A** Radiographs of BM (a–c), BMH (d–f) and BMG (g–i) implanted bone immediately after implantation (day ‘0’), 1 month and 2 months post surgery. **B** Histological images of heart (j–l), kidney (m–o) and liver (p–r) of BM, BMH and BMG implanted at 2 months post surgery

under process. Radiolucent gap between implant and bone was reduced indicating new osseous tissue formation from the host bone (Fig. 8A–d–f). In BMG implant, ‘0’ day radiograph showed presence of radiopaque implant in created defect of distal metaphysis of femur bone extending up to opposite cortex of bone. At 1 month, implant was visible with comparable radiodensity of host bone. Implant within the bone was under process of degradation as observed by reducing diameter of implant. Radiolucent gap in between implant and bone is negligible. The implant at 2 months showed moderate degradation as observed with loss of round shape of diameter within bony cavity. Radiodensity of implant is approaching to bone density and new bony tissue ingrowths over the defect area (Fig. 8A–g–i).

### 3.3.5 Toxicity study of vital organs

**3.3.5.1 Heart** Figure 8B–a–c shows histological section at 2 months of implantation. Architectural detail of BM implanted heart myofibril retained its vitality with all processes including nuclear prominence, intact cytoplasm and fibrovascular network. Vascularisation of total structure was quite normal. Cellular details and infiltrating cells were within normal limit (Fig. 8B–a). In BMH implant group, section depicted almost normal structure of myocardial tissue characterized by well nuclear detail, cytoplasmic organelles and regularly arranged fibres. Mononuclear cells were predominant in some places without involving oedema or other exudation (Fig. 8B–b). In BMG implant group, section depicted a normal architectural pattern of cardiac tissue without any presence of infiltrating cells (Fig. 8B–c).

**3.3.5.2 Kidney** In case of BM implant, kidney section depicted normal glomerular tufts, tubular architecture and

well-maintained collecting ducts. Peri-glomerular spaces showed normal architectural detail with mild infiltrating cells. Few tubular lining epitheliums showed degeneration to some degree but within normal limit (Fig. 8B–d). Renal architecture of BMH implant was quite normal with glomerular tufts formation and different intact renal tubules. Oozing of RBCs in inter-tubular spaces was seen focally and some tubular epithelium showed necrosis and infiltration with mononuclear cells (Fig. 8B–e). In BMG implant, section showed normal architecture of kidney with glomerular tufts formation and different intact renal tubules (Fig. 8B–f).

**3.3.5.3 Liver** Section of BM implanted liver depicted normal limits of hepatocytes. Some portion of total portal triads showed few infiltration and RBC extravasations. Few hepatocytes showed focal changes with mild necrosis (Fig. 8B–g). In BMH, section depicted normal hepatic architectural detail characterized by well-formed hepatocytes, portal triads and well-made globules. Infiltration of mononuclear cells and von Kupffer cells were within normal limit (Fig. 8B–h). In BMG implant group, hepatic parenchyma showed presence of RBC, mononuclear cell, well-formed central veins and few von Kupffer cells (Fig. 8B–i).

### 3.3.6 In vivo immune response

Figure 9A–C shows the expression of TNF- $\alpha$ , IL-2 and IL-6 at 1, 2, 4 and 8 weeks. The expression of IL-2 at 1, 2, 4 and 8 weeks showed that at the 1st week, the inflammatory response due to the materials increased maximally followed by a gradual fall at the 2nd, 3rd, 4th and finally at the end of 8th week where the immunoreactivity of the implanted animals returned to its baseline as compared to control (normal healthy) animals.  $**p < 0.01$  and  $*p < 0.05$ ,  $n = 3$

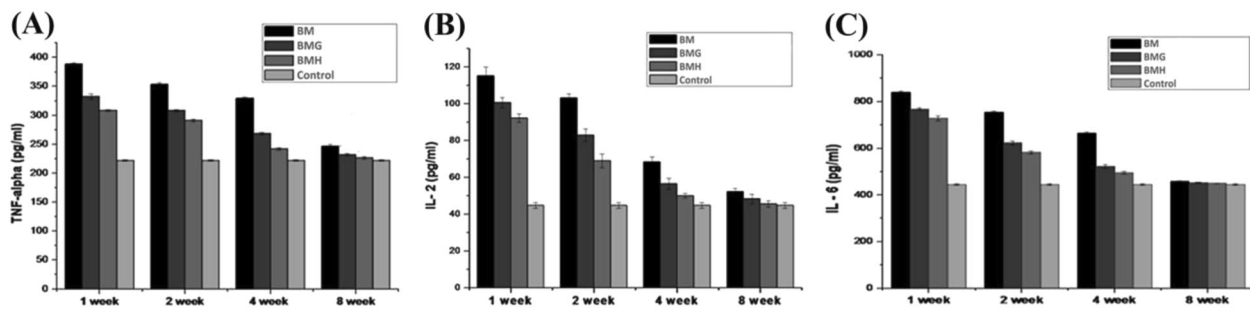


**Fig. 9** Expressions of **A** TNF- $\alpha$ , **B** IL-2 and **C** IL-6 at 1, 2, 4 and 8 weeks for different samples with the reference of control (normal healthy animals)

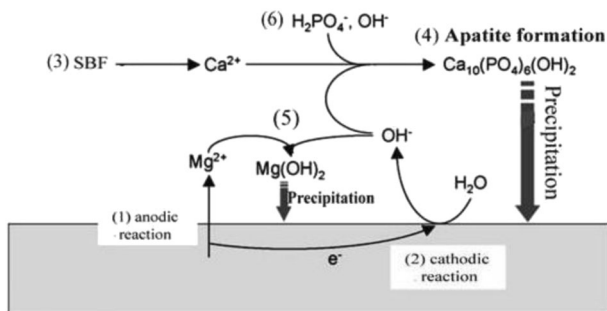


**Fig. 10** Proposed mechanism of corrosion and apatite formation when immersed in SBF

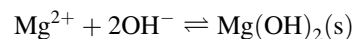
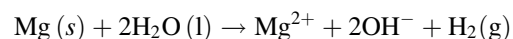
at each time point (one way ANOVA). The expression of IL-6 at 1, 2, 4 and 8 weeks showed that at the 1st week, the inflammatory response due to the materials increased maximally followed by a gradual fall at the 2nd, 3rd, 4th and finally at the end of 8th week where the immunoreactivity of the implanted animals returned to its baseline as compared to control (normal healthy) animals.  $***p < 0.001$ ,  $**p < 0.01$  and  $*p < 0.05$ ,  $n = 3$  at each time point (one way ANOVA). The expression of TNF- $\alpha$  cytokine response at 1, 2, 4 and 8 weeks showed that at the 1st week, the inflammatory response due to the materials increased maximally followed by a gradual fall at the 2nd, 3rd, 4th and finally at the end of 8th week where the immunoreactivity of the implanted animals returned to its baseline as compared to control (normal healthy) animals.  $**p < 0.01$  and  $***p < 0.001$ ,  $n = 3$  at each time point (one way ANOVA).

## 4 Discussion

Magnesium ion has different role in numerous biological functions, for instance, in bone. Bivalent magnesium ions help formation of biological apatite as well as have stimulatory effect on growth of marrow cells [40]. It was also reported that adding up of magnesium in nutrients helps in bone metabolism, whereas deficiency leads to lowered bone

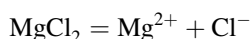
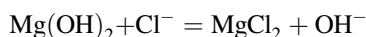
escalation and amplified bone resorption [41]. Now, in case of Mg alloy implants, depending on its composition, faster degradation is observed within bony environment especially in cancellous part of bone than cortical part [3]. Due to rapid degradation of bare Mg-based implants, attempts have also been made to trigger the mechanical integrity irrespective of the implantation site.

Mg alloy mimics comparable elastic modulus and mechanical strength as cortical bone leading to bone regeneration [42]. In physiological environment, Mg alloy decays in contact with water (body fluid) as shown below. Degradation of Mg alloy in body fluids produces  $Mg^{2+}$  cations which are efficiently excreted by kidneys and eliminate them naturally through urine

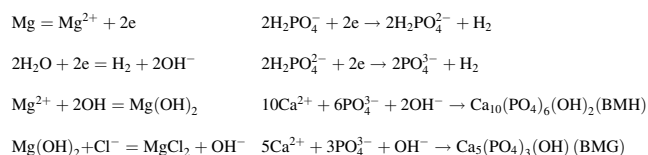


Rapid degradation of Mg and its alloys is a serious concern for degradable implant application. Therefore, several surface modification approaches have been attempted by different groups [43]. Surface modification not only ensures better mechanical integrity by providing resistance against corrosion in biological fluids but also improves bioactivity of these alloys depending on type of coating material. For temporary fracture fixation devices, this combined advantage was found to be suitable, because this could alleviate necessity of second surgery for removal of implant thereby reducing hospital cost and surgical complications too [44]. Among various surface modification techniques, plasma spraying technique helps in chemical control, bio-corrosion resistance as well as reduced substrate fatigue resistance. Further, plasma spraying process enhances surface properties and biocompatibility keeping excellent bulk properties unchanged. In particular, the technique has many advantages in biomedical applications, for example, with regard to film chemistry, better coating adhesion, conformal and pin-hole free films and enhanced infiltration [45]. In the present investigation, plasma spraying was chosen in order to get a firm adhesion/layer-wise formation of

coating with porosity which would act as nucleation site for apatite formation and help different cell functions, ultimately increasing the biocompatibility of the sample. For the first time, plasma spray method using BG material has been employed for a new Mg alloy composition. In plasma spray process using HAp, powders experience high flame temperature, which causes evaporation of water (trapped within pores or part of the HAp lattice structure), resulting decrease in crystallinity (Fig. 1A-d) and low adhesion strength (Fig. 2B-a) [46]. Amorphous S53P4 powders showed firm apposition with the substrate surface after plasma spray coating [which reflected in better adhesions strength (Fig. 2B-b)] without any trace of magnesium phase in XRD (Fig. 1A-e). Microstructure of BMH showed melted and deformed splat near to its substrate, whereas globular shaped splat at the periphery of coating surface (Fig. 2A-c), which can be attributed to better surface cooling on outer surface as compared to inner layers; more cooling led them to more thermodynamically stable shape. Due to its amorphous nature, BAG forms less irregular and globular shaped splat on the surface (Fig. 2A-d). Pores having size ranging 1–10  $\mu\text{m}$  were seen in case of BMH samples, whereas BMG showed interconnected pores ranging 15–30  $\mu\text{m}$ . Interface study confirmed presence of pores up to layers adjacent to BMH substrate which explains lower delamination strength as well as availability of Mg phase in XRD as an effect of Mg ion migration from substrate, on the other hand amorphous BMG showed absence of pores even up to layers adjacent to substrate confirming firm layer-wise formation of coating on surface of substrate. Better homogeneity and superior coverage of BG coating (for BMG) ensured increase in resistance towards corrosion when immersed in SBF solution showing a very high  $E_{\text{corr}}$  value (−296.246 mV vs. SCE) compared to BM (−1540.824 mV vs. SCE) and BMH (−1420.479 mV vs. SCE) samples. Lower resistance of BMH was due to surface pores, which act as pitting corrosion sites [47]. Corrosion current densities ( $i_{\text{corr}}$ ) of coated and uncoated samples indicated that BMG samples exhibited lowest thermodynamic tendency to participate in anodic reaction thus effectively improving resistance followed by BMH and BM samples [48]. However, after initial corrosion, BMH samples tends to form inactive layer of  $\text{Mg}(\text{OH})_2$ , which reduced surface reactivity towards corrosion as stand-alone coating [32]. When immersed in ionic solutions which consist of chloride ( $\text{Cl}^-$ ) ion (SBF), this passive layer converts from  $\text{Mg}(\text{OH})_2$  to soluble  $\text{MgCl}_2$  with time, weakening the surface as well as releasing  $\text{OH}^-$  ions in solution increasing the pH (Fig. 4B).  $\text{MgCl}_2$  dissolves easily in SBF and releases  $\text{Cl}^-$  to continue the chain of corrosion on surface



SBF immersion study, which also involves corrosion, is a very complicated phenomenon where ion exchange occurs simultaneously for apatite formation as well as corrosion. When immersed in SBF, leaching of ions from substrate to solution occurs initially followed by apatite precipitation. Dissolution of calcium ion in case of BMH and BMG control formation of apatite phases on surface.  $\text{Ca}^{2+}$  ions of the coatings and ions from SBF solution underwent reduction reaction simultaneously with conversion of Mg to  $\text{MgCl}_2$  releasing  $\text{OH}^-$  in the solution, which increases the pH as well. Essentially, the reaction stages are outlined by the following equations



Hence, more corrosion leads to higher pH as well as higher  $\text{Mg}^{2+}$  concentration after day 7 in case of BMH samples where porosities in the coating most probably let SBF penetrate to Mg interface which gradually decreases with increasing apatite precipitation up to day 14 with increasing final weight as well. On the other hand, slow increase in pH from day 0 to 7 until day 14 illustrated slower corrosion rate of BMG samples. Therefore, formation and crystallization of apatite layer retards aggressive corrosion during initial days. High calcium concentration of SBF related to BMG samples after day 7 supports leaching of BG which gradually react with phosphates to form apatite layer on surface of sample increasing final weight in this case too. Phase difference of apatite formed might be explained by presence of different ions in solution at different concentrations in accordance with leaching of ions from sample [49]. However, difference in average crystallite size of apatites formed in case of BM, BMH and BMG samples can be explained by the fact that more nucleation site decreases the average crystallite size. As HAp and BAG coatings are porous, they provide much more nucleation site than the uncoated substrate, hence lower average crystallite size, which can be seen from XRD data too. Decrease in average crystallite in case of BM and BMH samples from day 7 to 14 confirms presence of pores on surface created from corrosion. On the other hand, increase in average crystallite size for BMG samples proves better apatite formation on the surface than others. Apatite formation and corrosion is schematically represented in Fig. 10, where  $\text{Ca}^{2+}$  originated from SBF and surface of sample react with  $\text{H}_2\text{PO}_4^-$  to form insoluble apatite. During the process,  $\text{OH}^-$  forms and reacts with leached  $\text{Mg}^{2+}$  to form  $\text{Mg}(\text{OH})_2$ , which also precipitates on surface increasing resistance of

the coating. Depending upon  $\text{Ca}^{2+}$  concentration in SBF solution, different phases of Ca–P form.  $\text{Ca}^{2+}$  concentration difference between supernatant of BMH and BMG after day 7 clearly gave an idea why two different apatite phases formed in BMH and BMG samples.

Cell–materials interactions require initial attachment of cells which can influence ensuing cellular and tissue responses [50]. It is reported that the adhesion and viability of cells depend on culture setting and material surface features. However, rapid degradation of Mg and its alloys leads to concomitant increase in the pH, which can be detrimental to cell adhesion and survival. This can be seen from the in vitro results of BM with least corrosion resistance. Due to absence of coating, pH rapidly increases, whereas for coated Mg alloy samples, degradation of BG is more as compared to HAp resulting less attachment, viability and proliferation of cells in the order of the  $\text{BM} > \text{BMG} > \text{BMH}$  at different time intervals of 5, 7, 14 and 21 days post incubation. Further, coated Mg alloys provide conducive atmosphere for cell connection and expansion. Any protective coatings prevent the entry of water and electrolyte [51], leading to slower corrosion of Mg alloy substrate vis-à-vis diminishing the diffusion rate of  $\text{OH}^-$  from Mg surface to the medium. As a result, the rise of pH of solution neighbouring the Mg sample, which in turn helps to surface attachment of numerous cells and subsequent proliferation.

Underlying principle of protective effect is that, being a reactive metal, bare Mg will act in response with water, precipitation of  $\text{Mg}(\text{OH})_2$  on the surface of Mg and consequent release of  $\text{H}_2$  gas. It is assumed that the accrued Mg  $(\text{OH})_2$  layer on Mg prevents dissolution by avoiding mass diffusion between Mg and the solution [52]. Resultant Mg  $(\text{OH})_2$  is changed to more soluble  $\text{MgCl}_2$  by  $\text{Cl}^-$  [53], which releases  $\text{Mg}^{2+}$  into the solution.  $\text{Mg}^{2+}$  release depends upon severity of Mg corrosion. Accordingly, in the present study, the release of  $\text{Mg}^{2+}$  in cell culture is used to judge protective effect of HAp and BG coating on Mg substrate. It has been observed that there was low release of  $\text{Mg}^{2+}$  from HAp and BG coating compared to BM throughout the incubation period, leading to less corrosion in coated samples. On the other hand, adhesion strength also plays a vital role as corrosion resistance [54].

ALP activity and ARS assay are important tools to calculate mineralization upon implants. Cells resemble an orderly, sheet-like structure when there are considerable levels of mineralization. During the entire period of culture, prerequisite nature of samples includes rising ALP activity, intensity of Alizarin Red staining and stressed actin arrangement of cells upon samples. In the present study, HAp and BG coated samples shows favourable results in comparison to bare Mg alloy. Likewise, images of BMH show unsystematic deposition of actin-stress fibres together with dense cell colony and to some extent on BMG too. In general, in vitro analysis

illustrates considerable perfection of sample properties of HAp and BG coated samples with respect to biocompatibility, cell viability and proliferation and osteoconductivity. Side by side, BMH implant is a notably better choice than BMG implant. In vivo biocompatibility can only be assessed by observing nature and magnitude of inflammation of neighbouring soft tissue reaction in presence of any foreign material. In the present study, although lesser vascularization, fibrous tissue and presence of mononuclear cells in the histological figures are observed, neither significant inflammatory reaction nor formation of gas cavities around the implantation site of bone is pronounced. This advocates that the implants are well accepted in vivo indicating a promising biodegradable implant material.

Radiographic evaluation of implants is a non-invasive technique to assess the position of implant during the healing process. In the in vivo test, radiologically a significantly higher degradation of BM was observed as compared to BMH and BMG implant. There was moderate osseous growth in defect site in BM, whereas more bone formation was observed in coated implants. Enhanced bone formation might be owing to release of Mg ions, because high Mg concentration is essential for bone cell activation [55]. Similar experiment with Mg–Ca pins in bone defect model shows better activity of osteoblasts and osteocytes around the implant [56]. Moreover, it could be expected that enhanced local pH surrounding the implanted area due to gradual corrosion of Mg alloy provides a favourable environment for mineralization. In both coated groups, implants within bone were under the process of gradual degradation as observed by reducing diameter of implant and new bony tissue ingrowths over defect area. This might be due to gradual degradation of Mg alloy from the coated implants. Moreover, during the entire healing process, no gas bubbles are observed owing to gradual release of Mg ions from coated implants during degradation [55, 56]. In the present study, radiological findings can be corroborated with the fluorochrome labelling results. Tetracycline, a bone specific marker, was used for quantifying the amount of new bone formation in the defect area. Tetracycline is deposited in any fracture site during the active mineralization process. BM implant at 2 months showed bone formation mainly at the middle and partially in peripheries, as marked by the presence of golden yellow fluorescence. In BMH and BMG implant group, the intensity of golden yellow fluorescence was more prominent at periphery with wide deep area of new bone formation. The findings of fluorochrome labelling can also be compared with histological results. No noticeable inflammatory effects are observed surrounding the implants indicating biocompatible nature of the implants. In bare Mg alloy, histological section depicted a bony matrix with abundance Haversian canal, bony lacunae and few osteoclasts along with lesser angiogenesis towards medullary region. In BMH, implant showed bony lamellae characterized by well-

developed Haversian system, canaliculi and resorption of bone in pericortical areas signifying presence and delineation of osteogenic cells. In BMG, implant group depicted a large number of osteocytes, osteoclasts and osteoblast proliferation. New bone formation around the bare Mg implants at 2 months might be due to stimulating effect [55, 57]. At 2 months, HAp and BG coated samples depicted more presence of osteoid surface. The explanation for this improved osseous tissue regeneration rates adjacent to these coated implants are due to osteo-proliferative effect of calcium phosphate and BG coating of Mg implants. As the corrosion of the coated implants happens relatively slowly, the corrosion products can be safely eliminated from the body system either through absorption by the adjacent tissues or local blood circulation which corroborated the findings of reduced bone growth caused by magnesium deficiency [58].

SEM examination during the post-surgical period demonstrates better amalgamation of material with the host bone while validating infiltration of osteogenic cells and ultimately resulting into evidence of mineralized matrix. There was no visible interfacial gap between the bone and implant in BMH group. This might be due to invasion of osteoblasts towards the implant structure. For the BMG implant, interfacial gap is more pronounced which might be due to slow invasion of osteoblasts.

Histology of heart, kidney and liver was carried out to assess whether any changes happen in cellular level or not. The results established that no apparent pathological lesions were seen after 2 months of experimentation, indicating safe degradation of implants in vivo and will not create any detrimental effects.

Immune reactivity of the animals implanted with the materials (BM, BMH and BMG) post surgery and normal/control animals (without any implant) was verified by quantifying the amount of IL-2, IL-6 and TNF- $\alpha$  cytokine secretion. Study of host-implant inflammatory response was monitored for initial 2 months post surgery and the results showed that at first 2 weeks, amount of IL-2, IL-6 and TNF- $\alpha$  cytokine secretion was increased preferably because of initial host-foreign body reactions but at the end of 8 weeks, it was comparatively decreased to its baseline quite similar to control group. Comparing with the positive control group, three types of materials showed a varied reactivity, starting from highest response against BM implant followed by BMG and BMH implant. In the first 2 weeks, concentrations of IL-2, IL-6 and TNF- $\alpha$  were found to be drastically higher than the control animals, likewise, from 4 weeks up to the end of the experiment (i.e. 8 weeks), secretions of cytokines (IL-2, IL-6 and TNF- $\alpha$ ) were reasonably decreased down to its normal range. Thus, at the end of 2 months, unlike BM, neither BMG nor BMH implant materials showed any kind of marked immune reactions post surgery, in comparison to the control group.

## 5 Conclusions

Present investigation focuses on development and detailed characterization of a new Mg–Zn–Ca alloy (BM) with and without HAp (BMH) and BG (BMG) coating deposited using air plasma spraying. Electrochemical experiments demonstrated relatively better corrosion resistance of BMH and BMG compared to BM. Among the samples, BMG exhibited lowest  $I_{\text{corr}}$  and  $E_{\text{corr}}$  suggesting its superior in vitro corrosion resistance than BMH. In addition to improved corrosion resistance, coatings clearly enhanced the apatite precipitation ability on present Mg alloy samples. Detailed in vitro cell–materials interaction experiments demonstrated that both BMH and BMG samples induces osteogenesis. In vivo trials on mature New Zealand white rabbits revealed no measurable adverse effects on heart, kidney and liver and immune response suggesting their application potential. BMG implants resulted in accelerated new bone formation, which corroborates our in vitro observations. Overall, our results show that plasma spraying of HAp and BG on this new Mg alloys can be effectively used to control rapid degradation under in vivo conditions.

**Acknowledgements** The authors would like to express their sincere thanks and also gratefully acknowledge the supports of Director, CSIR-CGCRI, and Vice Chancellor, WBUAFS, during the execution of this work; CSIR (both BIOCERAM and MLP0203) for funding and all the personnel who rendered their heartfelt association during each and every characterisation mentioned in the manuscript.

## Compliance with ethical standards

**Conflict of interest** The authors declare no competing interests.

**Publisher's note** Springer Nature remains neutral with regard to jurisdictional claims in published maps and institutional affiliations.

**Open Access** This article is licensed under a Creative Commons Attribution 4.0 International License, which permits use, sharing, adaptation, distribution and reproduction in any medium or format, as long as you give appropriate credit to the original author(s) and the source, provide a link to the Creative Commons license, and indicate if changes were made. The images or other third party material in this article are included in the article's Creative Commons license, unless indicated otherwise in a credit line to the material. If material is not included in the article's Creative Commons license and your intended use is not permitted by statutory regulation or exceeds the permitted use, you will need to obtain permission directly from the copyright holder. To view a copy of this license, visit <http://creativecommons.org/licenses/by/4.0/>.

## References

- Rosemann P, Schmidt J, Heyn A. Short and long term degradation behaviour of Mg-1Ca magnesium alloys and protective coatings based on plasma-chemical oxidation and biodegradable polymer coating in synthetic body fluid. *Mater Corros.* 2013;64:714.

2. Chang L, Tian L, Liu W, Duan X. Formation of dicalcium phosphate dihydrate on magnesium alloy by micro-arc oxidation coupled with hydrothermal treatment. *Corros Sci*. 2013;72:118.
3. Erdmann N, Angrisani N, Reifenrath J, Lucas A, Thorey F, Bormann D, et al. Biomechanical testing and degradation analysis of MgCa<sub>0.8</sub> alloy screws: a comparative in vivo study in rabbits. *Acta Biomater*. 2011;7:1421.
4. Hänzi AC, Metlar A, Schinhammer M, Aguib H, Lüth TC, Löffler JF, et al. Biodegradable wound-closing devices for gastrointestinal interventions: degradation performance of the magnesium tip. *Mater Sci Eng: C*. 2011;31:1098.
5. Edwardá Moulton S, Davidál Misides M, Leonardá Shepherd R, Georgeá Wallace G. Galvanic coupling conducting polymers to biodegradable Mg initiates autonomously powered drug release. *J Mater Chem*. 2008;18:3608.
6. Song GL, Atrens A. Corrosion mechanisms of magnesium alloys. *Adv Eng Mater*. 1999;1:11.
7. Polmear IJ. Light alloys: metallurgy of the light metals. 2nd ed. London, England: Edward Arnold; 1989.
8. Liu M, Uggowitzer PJ, Nagasekhar AV, Schmutz P, Easton M, Song G-L, et al. Calculated phase diagrams and the corrosion of die-cast Mg-Al alloys. *Corros Sci*. 2009;51:602.
9. Sun Y, Zhang B, Wang Y, Geng L, Jiao X. Preparation and characterization of a new biomedical Mg-Zn-Ca alloy. *Mater Des*. 2012;34:58.
10. Datta MK, Chou D-T, Hong D, Saha P, Chung SJ, Lee B, et al. Structure and thermal stability of biodegradable Mg-Zn-Ca based amorphous alloys synthesized by mechanical alloying. *Mater Sci Eng: B*. 2011;176:1637.
11. Xue D, Yun Y, Schulz MJ, Shanov V. Corrosion protection of biodegradable magnesium implants using anodization. *Mater Sci Eng: C*. 2011;31:215.
12. Wang HX, Guan SK, Wang X, Ren CX, Wang LG. In vitro degradation and mechanical integrity of Mg-Zn-Ca alloy coated with Ca-deficient hydroxyapatite by the pulse electrodeposition process. *Acta Biomater*. 2010;6:1743.
13. Chen XB, Birbilis N, Abbott TB. A simple route towards a hydroxyapatite-Mg(OH)<sub>2</sub> conversion coating for magnesium. *Corros Sci*. 2011;53:2263.
14. Sebaa MA, Dhillon S, Liu H. Electrochemical deposition and evaluation of electrically conductive polymer coating on biodegradable magnesium implants for neural applications. *J Mater Sci Mater Med*. 2013;24:307.
15. Li N, Zheng Y. Novel magnesium alloys developed for biomedical application: A review. *J Mater Sci Technol*. 2013;29:489.
16. Avedesian MM, Baker H. ASM specialty handbook: magnesium and magnesium alloys. Materials Park, Ohio,US: ASM International; 1999.
17. Kirkland NT, Birbilis N, Walker J, Woodfield T, Dias GJ, Staiger MP. In vitro dissolution of magnesium-calcium binary alloys: clarifying the unique role of calcium additions in bioresorbable magnesium implant alloys. *J Biomed Mater Res Part B: Appl Biomater*. 2010;95:91.
18. Hanzi AC, Sologubenko AS, Gunde P, Schinhammer M, Uggowitzer PJ. Design considerations for achieving simultaneously high-strength and highly ductile magnesium alloys. *Philos Mag Lett*. 2012;92:417.
19. Gunde P, Hanzi AC, Sologubenko AS, Uggowitzer PJ. High-strength magnesium alloys for degradable implant applications. *Mater Sci Eng: A*. 2011;528:1047.
20. Mao L, Wang Y, Wan Y, He F, Huang Y. Effects of Zn on microstructure and mechanical properties of biomedical Mg-Ca-Zn alloys. *Heat Treat Met*. 2009;34:19.
21. Xie X, Wang X, Wang Y, Zhang G, He Y, Zheng Y, et al. Ca-Mg-Zn metallic glass as degradable biomaterials developed for potential orthopaedic applications. *Bone*. 2010;47:S425. <https://doi.org/10.1016/j.bone.2010.09.249>.
22. Zberg B, Uggowitzer PJ, Löffler JF. MgZnCa glasses without clinically observable hydrogen evolution for biodegradable implants. *Nat Mater*. 2009;8:887.
23. Park RS, Kim YK, Lee SJ, Jang YS, Park IIS, Yun YH, et al. Corrosion behavior and cytotoxicity of Mg-35Zn-3Ca alloy for surface modified biodegradable implant material. *J Biomed Mater Res Part B: Appl Biomater*. 2012;100:911.
24. Pan Y, He S, Wang D, Huang D, Zheng T, Wang S, et al. In vitro degradation and electrochemical corrosion evaluations of microarc oxidized pure Mg, Mg-Ca and Mg-Ca-Zn alloys for biomedical applications. *Mater Sci Eng: C*. 2015;47:85.
25. Baino F, Verne E. Glass-based coatings on biomedical implants: a state-of-the-art review. *Biomed Glasses*. 2017;3:1.
26. Zheng Y, Gu X, Witte F. Biodegradable metals. *Mater Sci Eng: R Rep*. 2014;77:1.
27. Yin Z-Z, Qi W-C, Zeng R-C, Chen X-B, Gu C-D, Guan S-K, et al. Advances in coatings on biodegradable magnesium alloys. *J Magnes Alloy*. 2020;8:42.
28. Rojaee R, Fathi M, Raeissi K. Controlling the degradation rate of AZ91 magnesium alloy via sol-gel derived nanostructured hydroxyapatite coating. *Mater Sci Eng: C*. 2013;33:3817.
29. Noorakma ACW, Zuhailawati H, Aishvarya V, Dhindaw BK. Hydroxyapatite-coated magnesium-based biodegradable alloy: Cold spray deposition and simulated body fluid studies. *J Mater Eng Perform*. 2013;22:2997.
30. Kannan MB, Wallipa O. Potentiostatic pulse-deposition of calcium phosphate on magnesium alloy for temporary implant applications—an in vitro corrosion study. *Mater Sci Eng: C*. 2013;33:675.
31. Yang Y, Zheng K, Liang R, Mainka A, Taccardi N, Roether JA, et al. Cu-releasing bioactive glass/polycaprolactone coating on Mg with antibacterial and anticorrosive properties for bone tissue engineering. *Biomed Mater*. 2017;13:015001.
32. Ostrowski N, Lee B, Enick N, Carlson B, Kunjukunju S, Roy A, et al. Corrosion protection and improved cytocompatibility of biodegradable polymeric layer-by-layer coatings on AZ31 magnesium alloys. *Acta Biomater*. 2013;9:8704.
33. Kaabi Falahieh Asl S, Nemeth S, Tan MJ. Novel biodegradable calcium phosphate/polymer composite coating with adjustable mechanical properties formed by hydrothermal process for corrosion protection of magnesium substrate. *J Biomed Mater Res Part B: Appl Biomater*. 2016;104:1643.
34. Keim S, Brunner JG, Fabry B, Virtanen S. Control of magnesium corrosion and biocompatibility with biomimetic coatings. *J Biomed Mater Res Part B: Appl Biomater*. 2011;96:84.
35. Zhao Y-B, Shi L-Q, Cui L-Y, Zhang C-L, Li S-Q, Zeng R-C, et al. Corrosion resistance of silane-modified hydroxyapatite films on degradable magnesium alloys. *Acta Metall Sin*. 2018;31:180.
36. Kundu B, Soundrapandian C, Nandi SK, Mukherjee P, Dandapat N, Roy S, et al. Development of new localized drug delivery system based on ceftriaxone-sulbactam composite drug impregnated porous hydroxyapatite: a systematic approach for in vitro and in vivo animal trial. *Pharm Res*. 2010;27:1659.
37. Kokubo T. Formation of biologically active bone-like apatite on metals and polymers by a biomimetic process. *Thermochim Acta*. 1996;280:479.
38. Landi E, Tampieri A, Celotti G, Sprio S. Densification behaviour and mechanisms of synthetic hydroxyapatites. *J Eur Ceram Soc*. 2000;20:2377.
39. Canham LT, Reeves CL, Loni A, Houlton MR, Newey JP, Simons AJ, et al. Calcium phosphate nucleation on porous silicon: factors influencing kinetics in acellular simulated body fluids. *Thin Solid Films*. 1997;297:304.

40. Li L, Gao J, Wang Y. Evaluation of cyto-toxicity and corrosion behavior of alkali-heat-treated magnesium in simulated body fluid. *Surf Coat Technol.* 2004;185:92.
41. Rude RK, Gruber HE, Norton HJ, Wei LY, Frausto A, Kilburn J. Dietary magnesium reduction to 25% of nutrient requirement disrupts bone and mineral metabolism in the rat. *Bone.* 2005;37:211.
42. Brar HS, Platt MO, Sarntinoranont M, Martin PI, Manuel MV. Magnesium as a biodegradable and bioabsorbable material for medical implants. *JOM.* 2009;61:31.
43. Zhang F, Cai S, Xu G, Shen S, Li Y, Zhang M, et al. Corrosion behavior of mesoporous bioglass-ceramic coated magnesium alloy under applied forces. *J Mech Behav Biomed Mater.* 2016;56:146.
44. Liu H. Biodegradation and mechanical performance of magnesium-based implants. In: 9th World Biomaterials Congress, Chengdu, China. NY, USA: Curran Associates, Inc.; 2012. p. 357.
45. Yang J, Cui F-Z, Lee IS, Wang X. Plasma surface modification of magnesium alloy for biomedical application. *Surf Coat Technol.* 2010;205:S182.
46. Liao C-J, Lin F-H, Chen K-S, Sun J-S. Thermal decomposition and reconstitution of hydroxyapatite in air atmosphere. *Biomaterials.* 1999;20:1807.
47. Song G, Atrens A, Dargusch M. Influence of microstructure on the corrosion of diecast AZ91D. *Corros Sci.* 1998;41:249.
48. Zeng R-C, Cui L-Y, Jiang K, Liu R, Zhao B-D, Zheng Y-F. In vitro corrosion and cytocompatibility of a microarc oxidation coating and poly (l-lactic acid) composite coating on Mg-1Li-1Ca alloy for orthopedic implants. *ACS Appl Mater Interfaces.* 2016;8:10014.
49. Ducheyne P, Qiu Q. Bioactive ceramics: the effect of surface reactivity on bone formation and bone cell function. *Biomaterials.* 1999;20:2287.
50. Kumari TV, Vasudev U, Kumar A, Menon B. Cell surface interactions in the study of biocompatibility. *Trends Biomater Artif Organs.* 2001;15:37.
51. Gray J, Luan B. Protective coatings on magnesium and its alloys—a critical review. *J Alloy Compd.* 2002;336:88.
52. Yamamoto A, Hiromoto S. Effect of inorganic salts, amino acids and proteins on the degradation of pure magnesium in vitro. *Mater Sci Eng: C.* 2009;29:1559.
53. Altun H, Sen S. Studies on the influence of chloride ion concentration and pH on the corrosion and electrochemical behaviour of AZ63 magnesium alloy. *Mater Des.* 2004; 25:637.
54. Ahn S, Lee J, Kim J, Han J. Localized corrosion mechanisms of the multilayered coatings related to growth defects. *Surf Coat Technol.* 2004;177:638.
55. Witte F, Kaese V, Haferkamp H, Switzer E, Meyer-Lindenberg A, Wirth C, et al. In vivo corrosion of four magnesium alloys and the associated bone response. *Biomaterials.* 2005;26:3557.
56. Li Z, Gu X, Lou S, Zheng Y. The development of binary Mg–Ca alloys for use as biodegradable materials within bone. *Biomaterials.* 2008;29:1329.
57. Yang J, Cui F, Lee I, Zhang Y, Yin Q, Xia H, et al. In vivo biocompatibility and degradation behavior of Mg alloy coated by calcium phosphate in a rabbit model. *J Biomater Appl.* 2012;27:153.
58. Rude R, Gruber H, Wei L, Frausto A, Mills B. Magnesium deficiency: effect on bone and mineral metabolism in the mouse. *Calcif Tissue Int.* 2003;72:32.



# SCIENTIFIC REPORTS



OPEN

## Influence of single and binary doping of strontium and lithium on *in vivo* biological properties of bioactive glass scaffolds

Pintu Kumar Khan<sup>1,\*</sup>, Arnab Mahato<sup>2,\*</sup>, Biswanath Kundu<sup>2</sup>, Samit K. Nandi<sup>1</sup>, Prasenjit Mukherjee<sup>1</sup>, Someswar Datta<sup>2</sup>, Soumya Sarkar<sup>3</sup>, Jayanta Mukherjee<sup>4</sup>, Shalini Nath<sup>5</sup>, Vamsi K. Balla<sup>2</sup> & Chitra Mandal<sup>5</sup>

Effects of strontium and lithium ion doping on the biological properties of bioactive glass (BAG) porous scaffolds have been checked *in vitro* and *in vivo*. BAG scaffolds were prepared by conventional glass melting route and subsequently, scaffolds were produced by evaporation of fugitive pore formers. After thorough physico-chemical and *in vitro* cell characterization, scaffolds were used for pre-clinical study. Soft and hard tissue formation in a rabbit femoral defect model after 2 and 4 months, were assessed using different tools. Histological observations showed excellent osseous tissue formation in Sr and Li + Sr scaffolds and moderate bone regeneration in Li scaffolds. Fluorochrome labeling studies showed wide regions of new bone formation in Sr and Li + Sr doped samples as compared to Li doped samples. SEM revealed abundant collagenous network and minimal or no interfacial gap between bone and implant in Sr and Li + Sr doped samples compared to Li doped samples. Micro CT of Li + Sr samples showed highest degree of peripheral cancellous tissue formation on periphery and cortical tissues inside implanted samples and vascularity among four compositions. Our findings suggest that addition of Sr and/or Li alters physico-chemical properties of BAG and promotes early stage *in vivo* osseointegration and bone remodeling that may offer new insight in bone tissue engineering.

The management of bone defects still remains a challenge for orthopedic surgeons. It has been reported that occurrence of impaired fracture healing of bone defects is nearly 5–10%<sup>1</sup>. In United States alone, 1.3 million people undergo bone graft surgeries each year for skeletal defects resulting from either accidents or disease<sup>2</sup>. Bone grafting, either from autografts or allografts is a well-known surgical procedure although has associated drawbacks of additional surgery, limited availability, potential risks of disease transmission, immunogenic response and long-term complications<sup>3</sup>. To overcome these limitations, the development as well as the availability of new orthobiologic materials to aid in the management of bony defects is rising.

On the other hand, tissue engineering mainly with engineered grafts is now-a-days a major thrust area toward repair and replacement of these diseased and damaged bone tissues. To achieve this goal, bioactive glasses and calcium phosphate have been investigated as bone repair scaffolds but having some limitations<sup>4,5</sup>. Mechanical and osteoinductive properties of scaffold materials can be improved via metallic ions substitution<sup>6</sup>. Among various ion substitutions, strontium (Sr<sup>2+</sup>), zinc (Zn<sup>2+</sup>), magnesium (Mg<sup>2+</sup>) and silicon (Si<sup>4+</sup>) have been widely studied<sup>7–13</sup>. Sr was the only one that was correlated with an increase in bone compression strength<sup>14</sup>. Stimulatory effect of Sr on osteoblasts and inhibitory effect on osteoclasts have been established<sup>15–18</sup>. Further, strontium ranelate has been proven to reduce the incidence of fractures in osteoporotic elderly patients<sup>19</sup>. Similarly, lithium (Li<sup>+</sup>) plays

<sup>1</sup>Department of Veterinary Surgery and Radiology, West Bengal University of Animal and Fishery Sciences, Kolkata, India. <sup>2</sup>Bioceramics and Coating Division, CSIR-Central Glass and Ceramic Research Institute, Kolkata, India. <sup>3</sup>Non-Oxide Ceramics and Composites Division, CSIR-Central Glass and Ceramic Research Institute, Kolkata, India. <sup>4</sup>Institute of Animal Health and Veterinary Biologicals, Animal Resources Development Department, Kolkata, India. <sup>5</sup>Cancer Biology and Inflammatory Disorder Division, CSIR-Indian Institute of Chemical Biology, Kolkata, India. \*These authors contributed equally to this work. Correspondence and requests for materials should be addressed to B.K. (email: biswa\_kundu@rediffmail.com) or S.K.N. (email: samitnandi1967@gmail.com)

Constituent	Mean wt. %			
	BAG	L-BAG	S-BAG	LS-BAG
SiO <sub>2</sub>	55.50	55.77	53.92	55.02
B <sub>2</sub> O <sub>3</sub>	1.38	1.76	2.33	1.00
CaO	23.60	23.95	23.00	23.36
Na <sub>2</sub> O	10.80	10.01	11.00	9.94
P <sub>2</sub> O <sub>5</sub>	5.74	5.85	5.59	5.59
TiO <sub>2</sub>	1.64	1.71	2.00	1.88
Li <sub>2</sub> O	—	0.22	—	0.30
SrO <sub>2</sub>	—	—	1.12	1.00

**Table 1. Chemical composition of the as-prepared powders by ICP-AES.**

a vital role in osteoblast proliferation and differentiation through stimulation of the Wnt signaling pathway<sup>20,21</sup>. An earlier study demonstrated increased *in vitro* proliferative activity only at low Li<sup>+</sup> concentration (0.25 wt. %)<sup>22</sup>.

Bioactive glasses with interconnected porosity with large surface areas are also favorable for bone integration. These materials with such structures have also been found to support angiogenesis<sup>23,24</sup>, osteoproduction by stimulating proliferation and differentiation of osteoprogenitor cells through direct genetic control<sup>25</sup>. Glass-ceramics and bioactive glasses with Sr<sup>2+</sup> doping have been attempted recently<sup>26,27</sup>. Strontium-doped bioactive glasses have also been developed<sup>28</sup>.

Single and binary doping of Sr<sup>2+</sup> and Li<sup>+</sup> on *in vivo* bone regeneration of bioactive glasses scaffolds has not been reported yet. In the present study we have made an attempt to assess the beneficial effects of Sr<sup>2+</sup> and Li<sup>+</sup> doping on *in vivo* bone formation of an interconnected bioactive glass porous scaffold developed in the laboratory through rabbit bone defect model. Detailed phase, composition and microstructure analysis were performed prior using tools like X-ray diffraction (XRD), Fourier transformed infrared spectroscopy (FTIR), differential thermal analysis-thermo-gravimetric analysis (DTA-TGA), quantitative EDAX analysis and scanning electron microscopy (SEM) respectively. The scaffolds were also assessed for its bioactivity in contact with simulated body fluid (SBF) and *in vitro* cyto-toxicity by MTT assay using NIH3T3. The *in vivo* bone regeneration was analyzed using chronological radiography, fluorochrome labeling, SEM, histology and micro-computed tomography ( $\mu$ -CT).

## Materials and Methods

**Bioactive glass scaffold preparation.** Bioactive glass (with or without doping of Li or Sr) was prepared through conventional glass melting procedure using appropriate amounts of reagents like silica (SiO<sub>2</sub>), calcium carbonate (CaCO<sub>3</sub>), dry soda ash (Na<sub>2</sub>CO<sub>3</sub>), decahydrated borax (Na<sub>2</sub>B<sub>4</sub>O<sub>7</sub>·10H<sub>2</sub>O), TiO<sub>2</sub>, di-ammonium hydrogen ortho-phosphate, lithium and strontium carbonate (all inorganic chemicals including the ones referred later in the manuscript were analytical grade from M/s S.D. Fine-Chem Limited, India until specified separately). Briefly, reagents were first mixed homogeneously, melted at 1450 °C in a Pt-crucible, homogeneity was maintained while melting and finally quenched in water to obtain the cullet. Dried cullets were further milled in a high energy ball mill for 3 h in aqueous medium. The final composition of the as-prepared glass powders (obtained by ICP-AES chemical analysis) is given in Table 1. 0.25% Li<sub>2</sub>O and 1% SrO (by weight) doping was used strategically for the base glass composition and nomenclatures like BAG, L-BAG, S-BAG and LS-BAG were given for bioactive glass without doping, Li-, Sr- and binary Li + Sr substitution respectively and used throughout the manuscript.

To fabricate porous scaffolds, milled as-prepared respective glass powders were first mixed with an equal quantity of porogen (scintillation grade naphthalene). The resultant mix was compacted at 150 MPa in a cold-isostatic press (EPSI, Belgium); cut into 8 mm diameter specimens using a low speed diamond saw (Isomet, Buehler, USA). Subsequently, naphthalene was driven off very slowly (from r.t. to 80 °C) with pre-determined rate of schedule, followed by heat treatment at 675 °C except for LS-BAG (650 °C) on a Pt-plate for 6 min. These temperatures were selected after careful assessment of glass-transition temperatures (T<sub>g</sub>) mentioned later. The samples were finally stored in a vacuum desiccator until further use.

**Bioactive glass powders and scaffold characterization.** Both as-prepared and heat treated powders were analyzed for phase by XRD at a diffraction angle of 10–80°2 $\theta$  [X'Pert Pro, Phillips Analytical, Netherlands; Cu K $\alpha$  radiation; scan speed 2° min<sup>-1</sup>. FTIR transmittance spectra was recorded at mid-IR range (4000–400 cm<sup>-1</sup>) [Spectrum 100, PerkinElmer, USA; resolution: 2 cm<sup>-1</sup>; by KBr pellet method] to confirm the functional groups present. On the other hand, DTA-TGA was conducted to determine the thermal profiles of the glass powders [STA 449C, Netzsch, Germany; rate of heating upto 1000 °C: 10 °C/min. with initial sample mass of 5 ± 0.5 mg]. Heat treatment temperatures of BAG, L-BAG, S-BAG and LS-BAG were selected by assessing the T<sub>g</sub> by the same DTA-TGA analysis.

Further, porous scaffolds were first physically characterized for open or apparent porosity (A.P.) and bulk density (B.D.) by water displacement method (Archimedes' principle), then by a table-top SEM (Phenom pro-X, Netherlands) for detailed microstructural characterization and assessment of pore size, shape and morphology with Au/Pd sputter coating on the samples prior. B.D. was calculated by [D/(W-S)] and A.P. by [(W-D)/(W-S)] x 100%, where D, W and S are dry, soaked and suspended weight of the samples respectively while calculating by

the methods mentioned. Variations of pore sizes were calculated by processing several SEM images thus obtained and using free software available (Perfect Screen Ruler v. 2.0) subsequently.

**SBF bioactivity study.** Primary bioactivity study of the bare scaffolds was carried out in contact with SBF, before *in vitro* cell cytotoxicity and *in vivo* pre-clinical study just to check calcium and phosphate ion deposition ability of the samples. Supernatants were analyzed for  $\text{Ca}^{2+}$ ,  $\text{HCO}_3^-$ , and  $\text{HPO}_4^-$  ions. SBF was prepared as per Kokubo *et al.*<sup>29</sup>. All the samples were selected with surface area of sample and volume of SBF taken with ratio of  $2 \text{ mm}^2/\text{mL}$  (e.g.,  $40 \text{ mm}^2/20 \text{ mL}$ ) and soaked for 7 and 14 days. Samples were kept statically at a temperature  $37.4^\circ\text{C}$  with pH 7.4 inside an incubator. After 7 and 14 days, ion concentrations were plotted and analyzed. One of respective samples (from BAG, L-BAG, S-BAG and LS-BAG) was seen for microstructure by FESEM (using Sigma, Carl Zeiss, Germany) after day 14. The samples were dried and carbon sputter coated prior observation.

***In vitro* cell cytotoxicity.** Chemicals used: Iscove's modified Dulbecco's medium (IMDM), phosphate-buffered saline (PBS), formaldehyde, 3-(4,5 dimethyl thiazol-2yl)-2,5 diphenyltetrazolium bromide (MTT), osmium tetroxide, paraformaldehyde, dimethyl sulfoxide (DMSO) were from Sigma Aldrich, St. Louis USA; fetal bovine serum (FBS) and penicillin/streptomycin, trypsin-ethylenediaminetetra acetic acid (EDTA), L-glutamine were from Invitrogen, CA, USA.

Fibroblast (NIH3T3) cell line (NCCS, Pune, India) was cultured in IMDM supplemented with 10% FBS and 1% penicillin-streptomycin (Complete Medium) in a humidified atmosphere of 5%  $\text{CO}_2$  at  $37^\circ\text{C}$ . BAG, S-BAG, L-BAG, LS-BAG scaffolds were autoclaved and then rinsed with 70% alcohol for sterilization. NIH3T3 ( $2 \times 10^3$ ) cells were seeded on scaffolds which were previously placed in a 24 well plate. Cells were allowed to attach on the surface of scaffolds for 2 h. Subsequently another 1.0 mL of complete medium was added in each well and cultured on for 3 and 7 days. Culture medium was changed in every 2 days.

To test cytotoxicity of BAG, S-BAG, L-BAG, LS-BAG scaffolds on cells, MTT assay was carried out after 3 and 7 days of culture. Cell without scaffold was used as control. MTT solution was prepared by dissolving MTT (5.0 mg) in DMSO (1.0 mL). MTT (100  $\mu\text{L}$ ) solution was diluted with IMDM (900  $\mu\text{L}$ ). After removing the previous medium diluted MTT solution was added in each well and incubated for 3 h. Purple coloured formazan crystal which are formed by the oxidation of tetrazolium salt by mitochondrial succinate dehydrogenase enzyme was dissolved in DMSO (500  $\mu\text{L}$ ). The resulting solution (200  $\mu\text{L}$ ) was placed into a 96 well plate and the optical density at 550 nm was measured using plate reader (Thermo Scientific). Each experiment was carried out in triplicate and the results were presented as means  $\pm$  SD.

**Cell morphology by SEM.** NIH3T3 ( $2 \times 10^3$ ) cells were seeded on scaffolds and cultured for 7 days. Scaffolds containing cells were washed with PBS (0.1 M) and fixed with paraformaldehyde (2%) overnight at  $4^\circ\text{C}$ . Subsequently, it was fixed with 2% osmium tetroxide ( $\text{OsO}_4$ ) for 2 h at  $25^\circ\text{C}$ . The fixed samples were then dehydrated in an ethanol series 30%, 50%, 70%, 90% and 100% each for three times, followed by gold sputter coating for SEM observation of cell morphology.

***In vivo* study of rabbit femoral bone defect model.** The animal experiments were performed following an ethical committee approved protocol in accordance with Institutional Animal Ethical Committee (IAEC), West Bengal University of Animal and Fishery Sciences (WBUAFS), West Bengal, India (Permit No. Pharma/IAEC/34 dated 30 June 2014). Sixteen adult New Zealand White rabbits (1.5–2 kg) were randomized into four groups (n = 4): control group I (pure BAG) and the test animals, group II (S-BAG), group III (L-BAG) and group IV (LS-BAG) with bilateral implantation. All surgeries were performed under general intramuscular anesthesia using xylazine hydrochloride (6 mg/kg) (Xylaxin, Indian Immunologicals, India) and ketamine hydrochloride (33 mg/kg) (Ketalar, Parke-Davis, India). Scaffolds were press fitted within the created defects in the distal metaphyseal region of femur and wounds were sutured in three layers (Fig. 1). Subsequently, animals were administered with cefotaxime sodium (Mapra India, India) at 20 mg/kg body weight intramuscularly for 5 days twice daily at 12 h interval and meloxicam at 0.2 mL (Intas Pharmaceuticals, India) once daily. Animals were finally sacrificed after 2 and 4 months of implantation.

**Characterization of *in vivo* samples.** Bone healing in the defect was monitored using chronological radiographs taken immediately after implantation and once in a month up to 4 months. Radiographs were scored independently by double blinded investigators per methods described by Zhukauskas *et al.*<sup>30</sup> (Table 2). For histological analysis, the bone specimens from the healed bone defect were collected, washed thoroughly with normal saline and was immediately fixed in 10% formalin for 7 days. Subsequently, the bone tissues were decalcified using Goodling and Stewart's fluid containing 15 mL formic acid, 5 mL formalin and 80 mL distilled water, followed by fixation with 4% paraformaldehyde. Finally, the samples were embedded in paraffin wax and 4  $\mu\text{m}$  sections were cut from the mount and stained with haematoxyline and eosin finally. Additional scoring system was developed from the histological slide using several *in vivo* biological activities (cellular response) and the response score was marked with '0' for absence, '1' for mild, '2' for moderate, '3' for marked and '4' for severe activity.

For another set of samples, fluorochrome, i.e. oxytetracycline dehydrate (Pfizer India, India) was intramuscularly injected 3 weeks before sacrifice at two time points, i.e., 2 and 4 months (administered at 25 mg/kg body weight). Undecalcified ground sections (20  $\mu\text{m}$ ) were prepared from implanted segments of bone using different grades of sand paper and observed under UV light with Leica DM 2000 bright light phase contrast and fluorescence microscope including Leica Qwain software. Golden yellow fluorescing area was observed to identify newly formed bone and was also measured in  $\mu\text{m}^2$  and converted to percentage of bone formation. The extracted samples were also observed using SEM for bone-implant interfacial characteristics. Samples were first fixed in



**Figure 1.** Surgical placement of the porous scaffolds (with or without doped BAG).

Animal response	Score description
1	Bone just extending into the defect
2	Bone substantially bridging the cortical defect
3	Bone fully bridging the cortex without significant callus
4	Bone fully bridging the cortex with distinct overlying callus

**Table 2.** Radiological scoring system (adopted as per Zhukauskas *et al.*<sup>30</sup>).

5% glutaraldehyde in PBS buffer for 48 hours followed by gradual ethanol series drying. Dried samples were gold coated before imaging using the same desktop SEM, described earlier.

Micro-computed tomography ( $\mu$ -CT) images of extracted bone samples with inserted scaffolds (BAG, L-BAG, S-BAG and LS-BAG) were taken using XT-H 225 (Nikon Metrology, Belgium) with maximum 110 kV rotating target X-ray source (75  $\mu$ A test current), spot size 3  $\mu$ m, resolution:  $\sim$ 12  $\mu$ m and 5-axis manipulator. Images thus obtained were qualitatively assessed for bone in-growth into the scaffolds.

**Statistical analysis.** Radiological and histological images for all groups of animals were analyzed as means  $\pm$  standard deviations and data has been analyzed by SPSS software package (Version 16, SPSS Inc., Chicago, USA) employing two-way ANOVA considering group and month as factors.

## Results and Discussions

**Bioactive glass powder characterization.** Fig. 2a–d shows the DTA thermogram of as-prepared powder samples (melted at 1450  $^{\circ}$ C) without and with Li/Sr doping. Glass transition temperatures ( $T_g$ ) was found to be around 750  $^{\circ}$ C for BAG and 790, 780 and 770  $^{\circ}$ C respectively for L-BAG, S-BAG and LS-BAG with crystallization temperature 862 and 865  $^{\circ}$ C for BAG and L-BAG respectively. With the addition of dopants,  $T_g$  increases

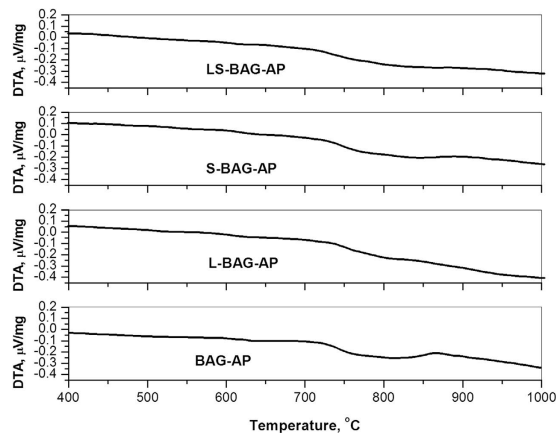


**Figure 2.** DTA profile of as-prepared samples for (a) BAG, (b) L-BAG, (c) S-BAG and (d) LS-BAG.

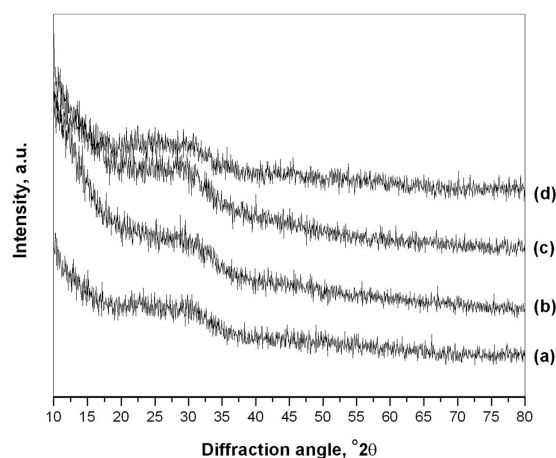


**Figure 3.** XRD patterns of (a) BAG, (b) L-BAG, (c) S-BAG and (d) LS-BAG samples heat treated at their respective temperatures.

from the base composition (BAG) with associated enthalpy increase as well. No adsorbed or structural water loss noticed throughout the temperature regime. Heat treatment temperature of the porous green specimens fabricated later with this powders were selected based on the repeated trials on the porous green specimens with suitable strength, unaffected porous network inside and no incipience of glassy or crystalline phase.

XRD pattern (Fig. 3) of respective heat treated specimens for each composition confirms amorphous nature with broad diffraction at  $2\theta$  ranging between  $20\text{--}35^\circ$  indicative of disorder in the structure and glassy nature of powders. Addition of dopants had no appreciable influence on the glassy structure of base material except slight changes in amorphicity and no appearance of any crystalline peak.

FTIR spectra (Fig. 4) of same powders show presence of hydroxyl ( $\text{-OH}$ ) group around  $3445\text{ cm}^{-1}$ , along with Si-O-Si stretching frequency around  $465\text{ cm}^{-1}$  and Si-O-Si bending frequency around  $1020\text{ cm}^{-1}$  for all samples<sup>31</sup>. Other band assignments included Si-OH symmetric stretch at  $780\text{--}980\text{ cm}^{-1}$  and vibrational mode of asymmetric stretch of Si-O-Si between  $1100\text{--}1000\text{ cm}^{-1}$ . The band assignments are summarized and are given in Table 3.

**Bioactive glass scaffolds characterization.** Fig. 5a–d shows the SEM microstructure of the porous scaffolds for all compositions. Highly amorphous microstructures were obtained with presence of granular appearance throughout of the samples taken at different magnifications. A range of micro- to macro-pores were observed without any grains or crystals.

Due to the amorphous nature, green powders were fused at the boundary with presence of micro-pores between the fused powders. Mean pore sizes of S-BAG and L-BAG samples calculated by image processing was about  $20\text{ }\mu\text{m}$ , while this was  $47\text{ }\mu\text{m}$  and  $8\text{ }\mu\text{m}$  for S-BAG and LS-BAG respectively. All the samples except LS-BAG showed presence of both micro- ( $10\text{--}50\text{ }\mu\text{m}$ ) and macro-pores ( $>50\text{ }\mu\text{m}$ ). For LS-BAG, it was more of coarsening than sintering of particles. For L-BAG, pore size was found to be in the range of  $20\text{--}230\text{ }\mu\text{m}$  with  $1\text{--}2\text{ }\mu\text{m}$  small pores throughout the microstructure. S-BAG on the other hand had pore size in the range of  $30\text{--}260\text{ }\mu\text{m}$  with bi-modal distribution of pores in the range from  $1\text{--}2\text{ }\mu\text{m}$  and  $10\text{--}20\text{ }\mu\text{m}$ . Pore size range for LS-BAG was mainly in the range of  $10\text{--}50\text{ }\mu\text{m}$  with presence of  $1\text{--}2\text{ }\mu\text{m}$  of micro-pores. Amorphous content was found to be more in case of L-BAG and LS-BAG compared to S-BAG and BAG. Most probably Li had played a solute-drag effect

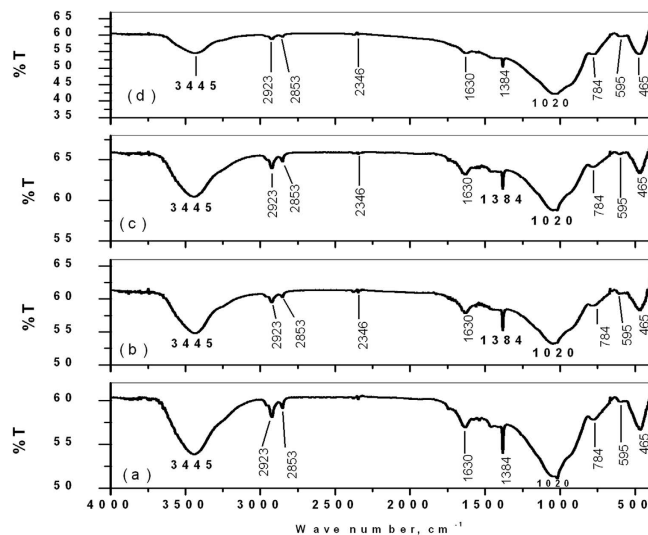


**Figure 4.** FTIR spectra of (a) BAG, (b) L-BAG, (c) S-BAG and (d) LS-BAG samples heat treated at their respective temperatures.

Wave number (cm <sup>-1</sup> )	Band assignment	Wave number (cm <sup>-1</sup> )	Band assignment
465	$\delta$ (Si-O-Si) bending	1630	$\delta$ (OH)
595	P-O of PO <sub>3</sub> <sup>2-</sup> group	2853	-OH (water)
784	$\nu$ (Si-O-Si) tetrahedral	2923	$\nu$ (CH)
1020	$\nu$ (Si-O-Si) asymmetric	3445	$\nu$ (OH)

**Table 3.** Band assignments for the peaks obtained for all samples (cf. Fig. 4).

for coarsening of the base glass particles. That means Li actually facilitated the coarsening so that green powder particles move against each other due to appearance of sharp melt at the interface. The effect was more evident in case of LS-BAG. Strontium on the other hand, did not have such effect as mentioned. As a consequence porous scaffolds made of BAG and S-BAG showed similar percentage of apparent porosity when heat treated as that of naphthalene added while preparing the green compacts. But L-BAG and LS-BAG had much higher percentage of open porosity. As a result bulk densities of the samples were found to be higher in case of BAG and S-BAG than L-BAG and LS-BAG. The data (average values) are presented in Table 4.

**Simulated body fluid (SBF) study.** Fig. 6 shows a composite image showing variations of pH, concentrations of calcium, bi-carbonate and bi-phosphate in the supernatant with time, in contact with SBF. pH of the supernatant of all samples showed slight decreasing tendency with time and upto day 14, which corroborates our earlier findings on similar base glass<sup>32</sup>. For all the samples, Ca ion concentration of the supernatant was increased from 7 to 14 days except S-BAG, which showed increment of Ca ions at day 7 and continuous maintenance upto day 14. For BAG, L-BAG and LS-BAG this increase of Ca was due to dissolution from sample surface. HPO<sub>4</sub><sup>2-</sup> ion conc. on the other hand was decreased from pure SBF, most probably due to phosphate deposition on the surface. Carbonate in the supernatant, showed a decrement at day 7 and subsequent increment at day 14 which was possibly due to more carbonate deposition on the surface at day 7, more dissolution upto day 14 and eventually becoming saturated with the sample. The concentration of the supernatant analysis upto day 14 revealed bioactivity of the samples in terms of more and more -OH and PO<sub>4</sub><sup>3-</sup> ion deposition on the sample surface, which is a potential nucleation site for Ca after day 14 to form hydroxyapatite or carbonated apatite on its surface; but, S-BAG showed better bioactivity as the same deposition was prominent within day 14. The results obtained were compared with the MTT assay study shown later

Fig. 7 show the SEM microstructure of the porous scaffold surface after day 14 of SBF study. This shows formation of apatite like crystals on the surface of S-BAG (Fig. 7c) which was not very clear in case of other samples surfaces. L-BAG and LS-BAG showed amorphous nature of their respective surfaces (Fig. 7b,d), as kinetics of dynamic dissolution and deposition process of Ca<sup>2+</sup>, HCO<sub>3</sub><sup>-</sup> and HPO<sub>4</sub><sup>2-</sup> ions were still in continuation while for BAG (Fig. 7a), deposition of apatite like crystals have started.

**In vitro cell cyto-toxicity study.** From the calculated OD values (550 nm), percent cell (NIH3T3) proliferation was plotted against the days observed and is given in Fig. 8.

It was found that the initial proliferation of cells after day 3 was better than control due to initial attachment of cells. After 7 days, however, this was found to be better in case of L-BAG than the others. Cell growth rate was found to be reduced for all samples than control. All sample surface was considered as non-toxic and

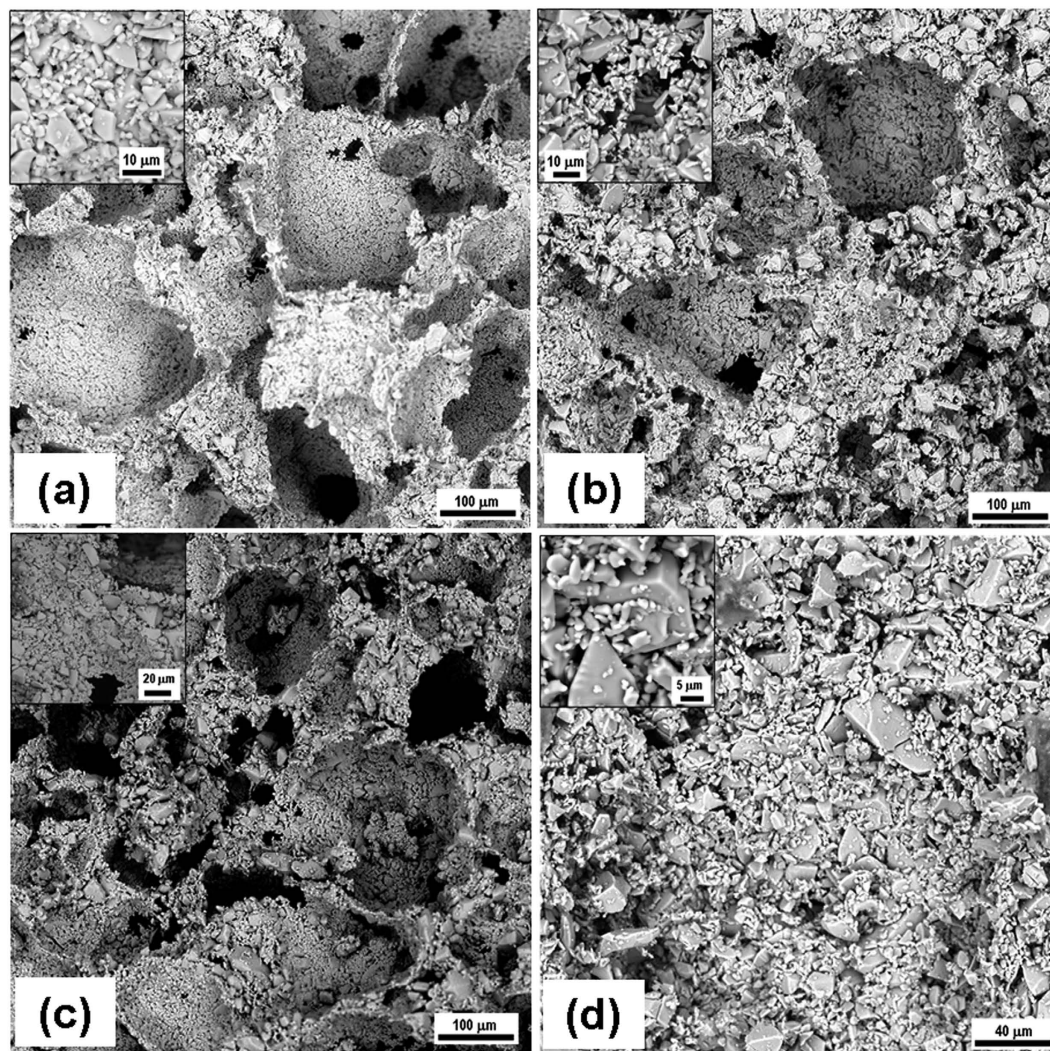


**Figure 5.** SEM microstructure of the porous scaffolds for all compositions (inset: higher magnified site).

Sample	A.P., %	B.D., g/c.c.
BAG	54.4 ± 1.63	1.16 ± 0.02
L-BAG	61.3 ± 1.84	0.97 ± 0.02
S-BAG	56.5 ± 1.7	1.09 ± 0.02
LS-BAG	64.5 ± 1.94	0.84 ± 0.02

**Table 4.** A.P. and B.D. data of the porous scaffolds.

biocompatible. Cell morphology by SEM after day 7 was also revealed similar trend (Fig. 9) as L-BAG showed better NIH3T3 proliferation than other surfaces. Well-grown filopodia (microspikes) or cytoplasmic projections were seen and found to be more pronounced in this case. Filopodia contain actin filaments cross-linked into bundles by actin-binding proteins. Micropores present on the top of surface play pivotal role for better anchorage of the filopodia.

NIH3T3 mouse embryo fibroblast cell lines are regularly used for MTT assay to assess cyto-toxicity with respect to biomaterials' effects on cell growth metabolism<sup>33</sup>. These cells have branched cytoplasm surrounding an elliptical nucleus and can be recognized by abundant rough endoplasmic reticulum and also synthesizes extracellular matrix (ECM) and collagen. NIH3T3 has also capability to detect substrate rigidity beyond the cell border<sup>34</sup>. From the results of Figs 8 and 9, it can be stated that there was substantial effect of Li alone to promote fibroblasts which was found to be least in case of BAG. S-BAG on the other hand, was not contributing extensively towards ECM formation and the gross effect of Li and Sr on cell proliferation was found to be least in case of LS-BAG (Fig. 8). S-BAG however showed better bioactivity in terms of apatite like crystal formation which will expected to contribute towards bone cell colonization *in vivo*. In this case, fibroblast cell extensions consolidated the pore

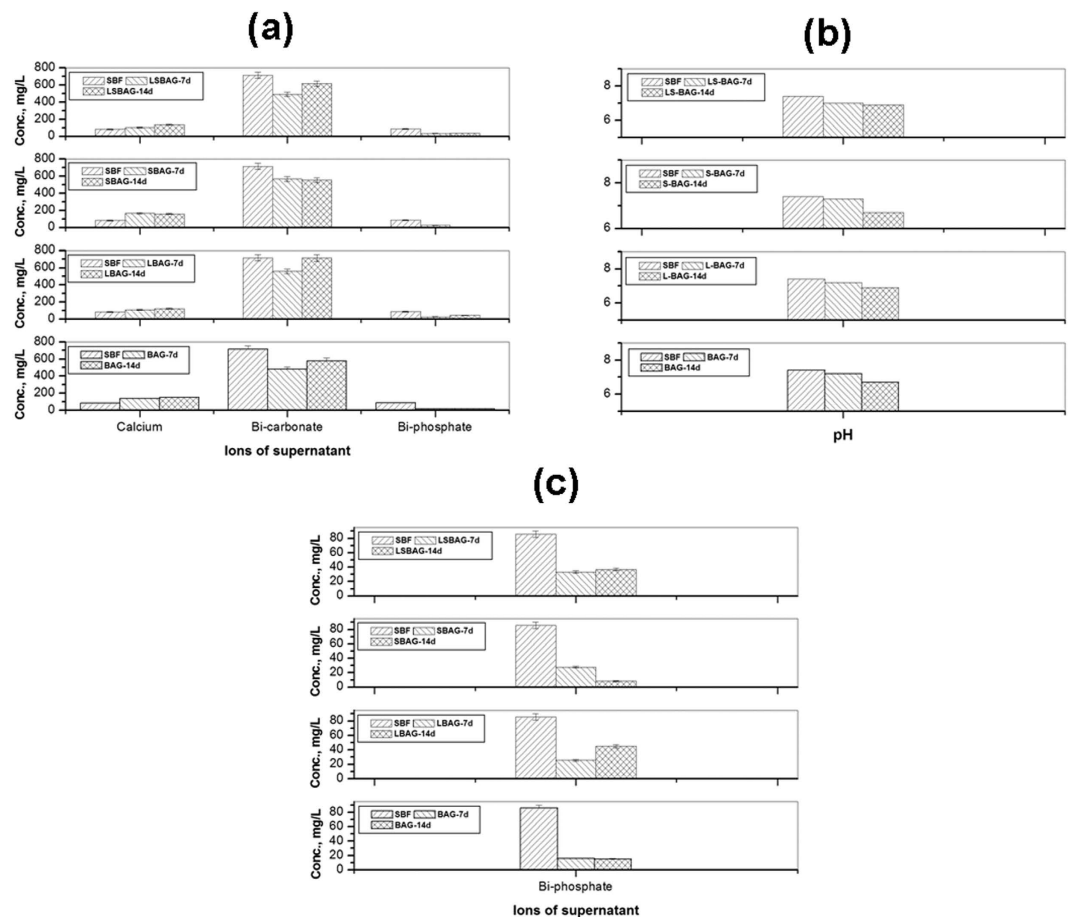


**Figure 6.** Variations of (a) concentration of supernatant ( $\text{Ca}^{2+}$ ,  $\text{HCO}_3^-$  and  $\text{HPO}_4^{2-}$ ), (b) pH of SBF after days 7 and 14 in contact with the porous scaffolds (BAG, L-BAG, S-BAG and LS-BAG); (c) is the magnified part of  $\text{HPO}_4^{2-}$  (a).

site; ECM formed *in situ* alongwith  $\text{HCO}_3^-/\text{HPO}_4^{2-}$  deposition in contact with SBF after 7 days (Fig. 6) may help maturation of bone defect site faster *in vivo*. The combined effect of Li and Sr thus expected to be generate both soft and hard tissue *in vivo*. Most plausible reason behind slower rate of growth of NIH3T3 after 3 days may be the presence of other ions (e.g.,  $\text{Ca}^{2+}$ ) which are also consistent with findings reported elsewhere stating that changes of extracellular calcium concentration can affect balance between proliferation and differentiation in fibroblasts. McNeil *et al.* demonstrated that elevation of extracellular calcium stimulates proliferation-associated signaling pathways in rat fibroblasts<sup>35</sup>.

**Bone in-growth evaluation by micro-CT.** Serial slices of X rays were carried out throughout Z-axis of a particular implanted bone section, images thus obtained were clubbed together and are given in Fig. 10a,b for BAG, 11a,b for L-BAG, 12a,b for S-BAG and 13a,b for LS-BAG after 2 and 4 months respectively. Serial images for BAG taken after 2 and 4 months showed that the porous scaffold has started degrading as revealed after 4 months but maintained its structure after 2 months. From the grey scale quantification it can be shown that BAG samples had higher amount of mature bone tissue after 4 months than the 2 months when more soft tissue apposition was evident. Stability of the implant thus impaired after 4 months which is anticipated to be continued and simultaneously converted to hard cortical tissue. Effect of lithium and strontium can be an interesting parameter which can dictate the degree of bone tissue conversion with time.

Serial sectional images of L-BAG after 2 months showed tissue invasion more in the central part of the implant than the periphery with a clear interfacial gap with the surrounding tissue. Grey scale values were found to be in between of cortical and cancellous tissues after 2 months which indicates that the implant was in the process of being resorbed which was continued up to 4 months. But the degree of resorption was higher in case of L-BAG than the BAG alone. L-BAG samples after 4 months showed very similar grey scale values with that of the cortical part of the bone. However, degradation of the samples was lowered for L-BAG than BAG alone.

S-BAG samples had clearly shown its efficacy expressed towards conversion to more of cortical tissue than the cancellous one. Cortical tissue could be seen at the periphery of the inserted samples as seen after 4 months. LS-BAG samples after 2 months showed close resemblance of the cancellous tissue on the periphery and cortical tissue in the inside of the implanted samples. After 4 months, the same phenomenon continued and the implanted



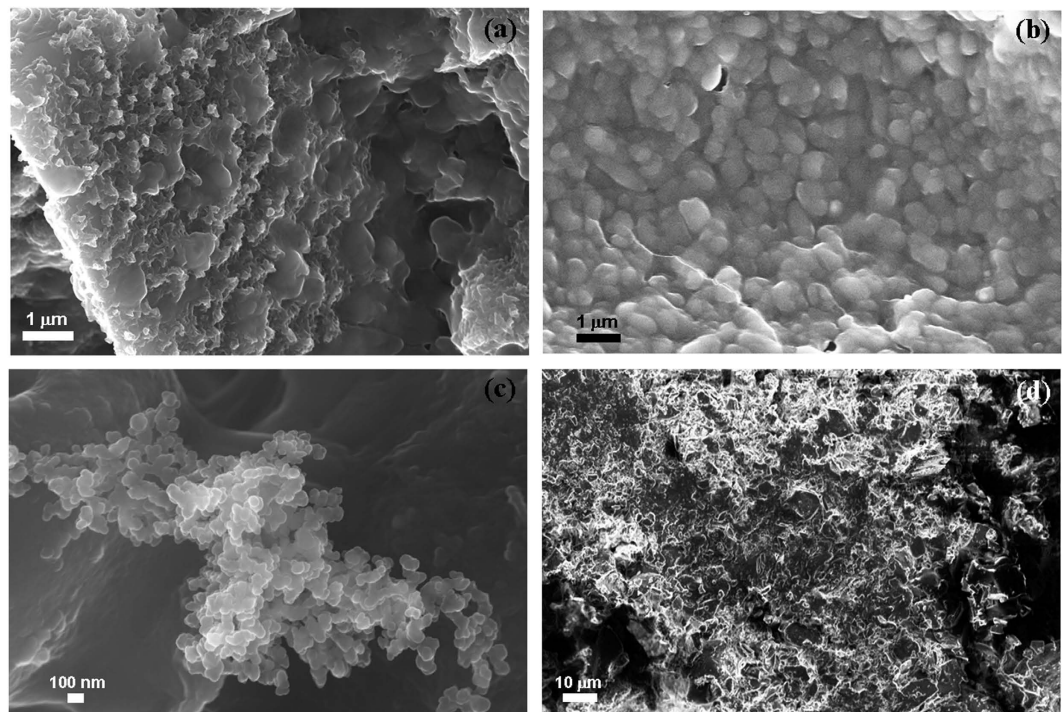


**Figure 7.** SEM microstructure of the porous scaffold surface after day 14 of SBF study; for (a) BAG, (b) L-BAG, (c) S-BAG and (d) LS-BAG.

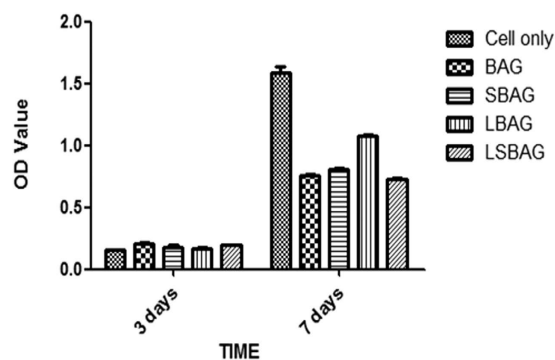


**Figure 8.** MTT assay results; calculated OD values for NIH3T3 expressed on the samples of BAG, L-BAG, S-BAG and LS-BAG after days 3 and 7.

samples were almost 60% converted to the surrounding bone. After 2 months, BAG samples only showed some interfacial gap which was absent for all doped samples.

3D images using micro CT are given in “Supplementary Information” as Fig. 1a,b for BAG, 2a and b for L-BAG, 3a and b for S-BAG and 4a and b for LS-BAG after 2 and 4 months respectively. The extent to which both soft and hard tissue apposed to BAG samples when implanted, cannot be assessed quantitatively from radiography. Tissue and blood vessels could be seen in the 3D representation of the micro CT. Porous nature both in and outside the medullary cavity were noticed in the 3D representation. Different grey scale values in the images represent quality of the bone and its degree of maturity. Implants could be seen from the 3D plots. It was found that mature bone tissue as well as blood vessels engulfed the implant which indicates good vascularisation. Porous nature of the cortical bone was observed in some sections. In a comparison, LS-BAG samples showed highest degree of tissue impregnation and vascularity among the four compositions. Strontium doping synergistically affected bone tissue apposition than glass without any doping. BAG scaffolds without doping actually had lower vascularity potential than the doped ones.

**Radiological examination.** Fig. 14a–d shows radiographs of defect surgery site and their interpretation is presented in Table 5. On the day of surgery, the distal metaphysis of femur showed presence of partial radiodense BAG implant (Fig. 14a) in the defect, which became moth-eaten on 1 month. The implant found to reduce in size

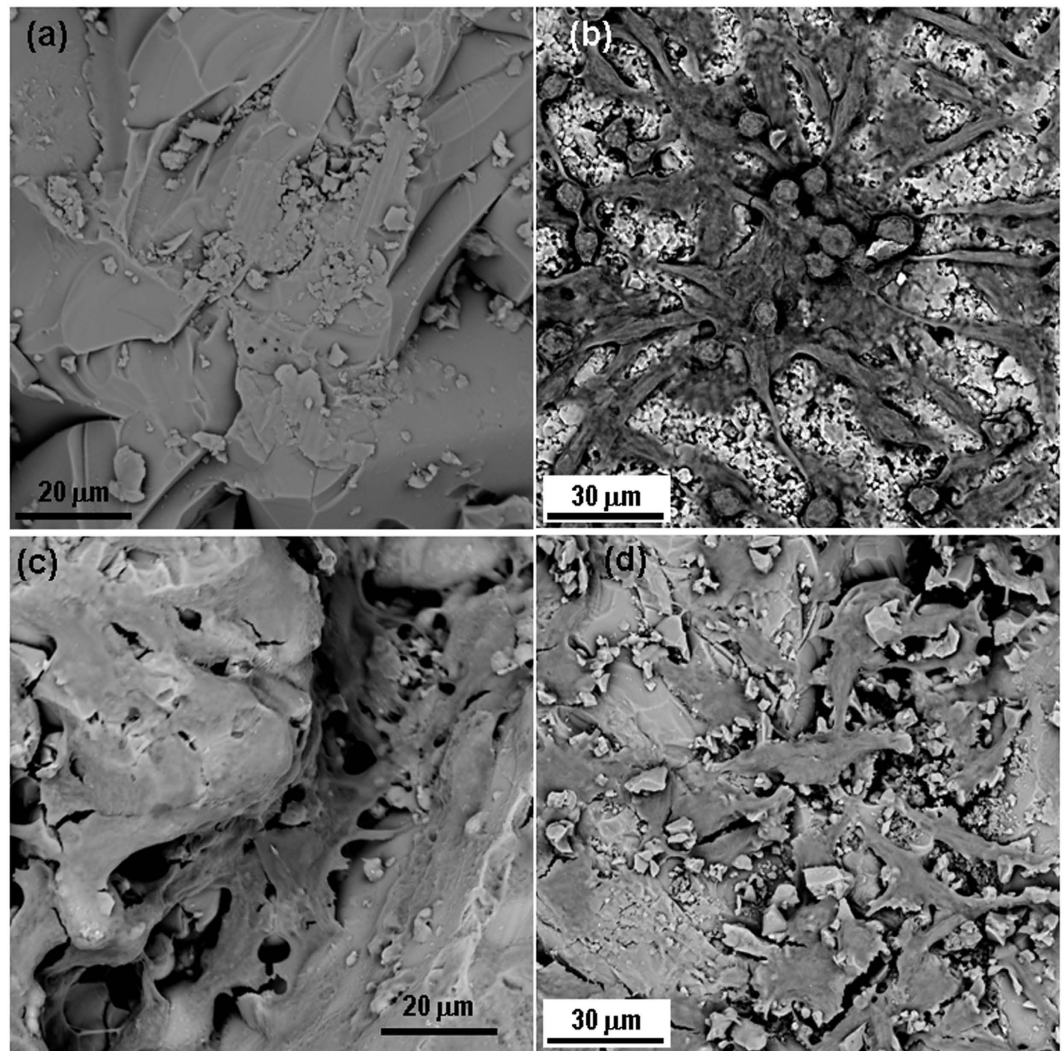


**Figure 9.** SEM cell morphology on the samples of (a) BAG, (b) L-BAG, (c) S-BAG and (d) LS-BAG after 7 days.

gradually with implantation time and almost disappeared at 4 month with irregularly arranged bony tissue. In S-BAG samples (Fig. 14c), the defect radiodensity appeared to be unchanged after 1 month and the defect size shrunk at 2 months. At 3 months, only negligible amount of implant was present in the defect along with newly formed bony tissue and by the end of 4 months both the implant defects could be barely seen from the radiographs. L-BAG samples (Fig. 14b) also showed similar performance as that S-BAG, except that defect healing and new bone formation were enhanced. In LS-BAG samples (Fig. 14d), radiograph showed narrowing of bony defect and shrinkage of implant as early as one month post-operatively. Subsequent radiographs showed no traces of implant and defect. More importantly the radiodensity in defect area was almost identical to that of healthy bone.

**Histological evaluation.** Fig. 15 and Table 6 show the histological section images and evaluation report of bone-implant interface at 2 and 4 months after observing different cellular events. BAG scaffolds (Fig. 15a) showed well formed bony structure containing haversian system, canaliculi and sinusoidal spaces along with deposition of R.B.C., fat cells and scanty numbers of osteoblast in peri-medullary areas after 2 months. Strontium doped scaffolds (S-BAG: Fig. 15b) at 2 month showed prominent osteoblastic activity characterized by sufficient number of haversian canal, canaliculi, lacunae and osteoblastic cells with suitable cytoplasmic ratios. The bony matrix is invaded by highly proliferative branches of vessels containing sufficient amount of R.B.C, bony progenitor cells and focal calcified points. Similarly, L-BAG scaffolds (Fig. 15c) showed well developed bony structure with robust haversian system, osseous canaliculi and bony plates. The LS-BAG samples (Fig. 15d) depicted well formed osseous structure containing haversian canal, lamellae and canaliculi which was invaded by numerous blood vessels along with prominent osteoblastic and osteoclastic activities in the margin of lesion.

Histological evaluations at 4 months for the doped and pure bioactive glasses are also shown in Fig. 15a–d. Compared to 2 months, apparently higher angiogenesis was observed in all doped samples. However, angiogenic proliferation was more in LS-BAG and L-BAG samples compared to other samples. All doped samples showed highly proliferative stage of osteoblast and osteoclast cells (progenitor cells) along with foci of calcification.

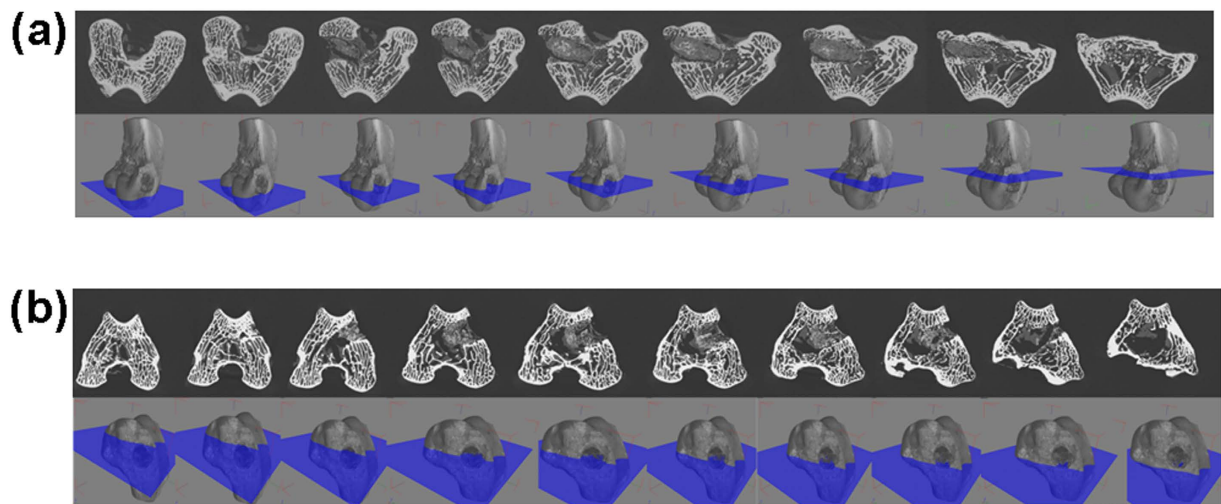


**Figure 10.** Serial slices along the Z-axis in micro-CT. Images are obtained for implanted BAG scaffolds. (a) After 2 months; (b) After 4 months.

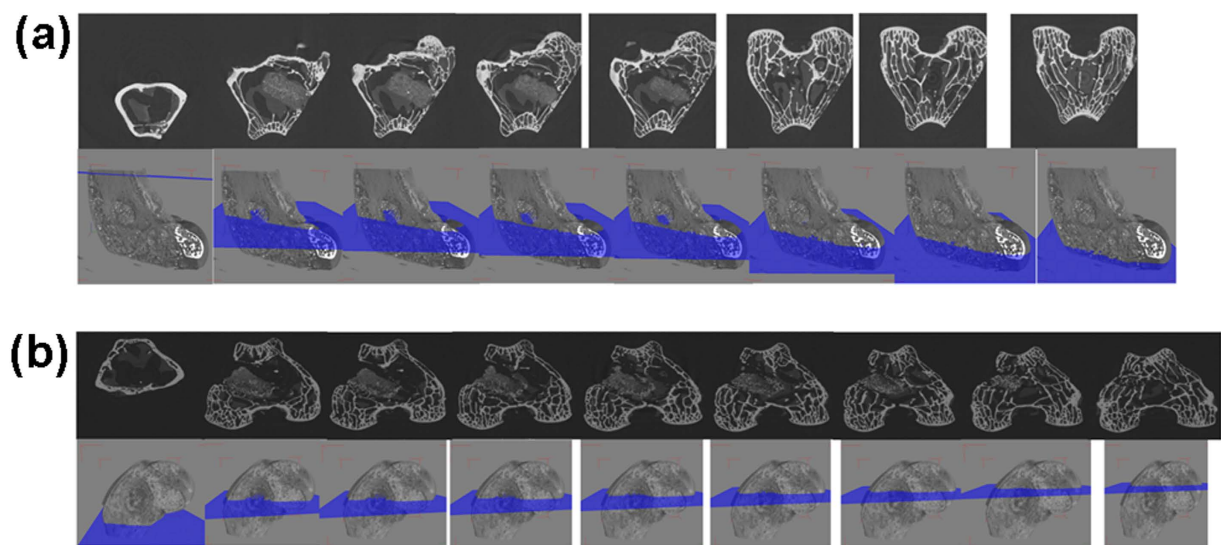


**Figure 11.** Serial slices along the Z-axis in micro-CT. Images are obtained for implanted L-BAG scaffolds. (a) After 2 months; (b) After 4 months.

**Fluorochrome labeling study.** Fig. 16 shows images of samples after oxytetracycline marking, where golden yellow fluorescence represents new bone and dark sea green indicates matured old bone. After 2 months, BAG scaffolds depicted double tone golden yellow fluorescence in a narrow zone in the defect site and the host bone looked dark sea green homogenous color. Relatively, better intensity of new bone formation (golden yellow fluorescence) was observed in S-BAG and LS-BAG at this time point. L-BAG at this time point also showed more new bone formation as compared to pure sample. At 4 months, all the samples depicted more new bone formation as compared to 2 month. However, distinct new bone formation was exhibited in all doped bioactive glass implants. LS-BAG implanted bone showed wide regions of golden yellow fluorescence (new bone formation) indicating rapid bone regeneration. S-BAG bone samples showed scattered and multiple regions new bone formation in defect area demonstrating their effectiveness in bone regeneration. Based on the calculation, percentage of bone formation through fluorochrome labeling images at two time point of 2 and 4 months have been done and is given in Table 7.

**Scanning electron microscopic (SEM) study.** Fig. 17 shows microstructural study of bone implant interface using SEM at two time point of 2 months (Fig. 17a–d) and 4 months (Fig. 17e–h). Effect of lithium and strontium could be established in SEM images and compared with the micro CT images. In all samples, with time, both soft and hard tissue got matured. L-BAG samples had a clear influence on soft tissue interaction with the sample (Fig. 17b,f). Collagenous network was prevalent in case of L-BAG while S-BAG samples (Fig. 17c,g)

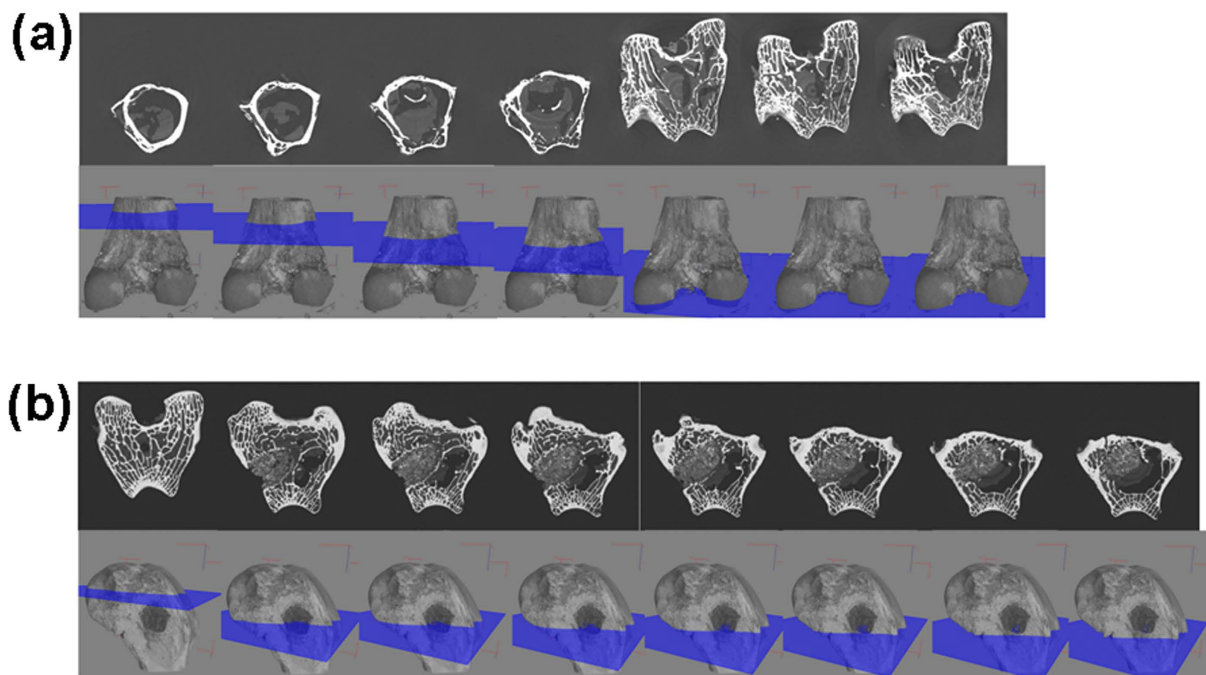


**Figure 12.** Serial slices along the Z-axis in micro-CT. Images are obtained for implanted S-BAG scaffolds. (a) After 2 months; (b) After 4 months.

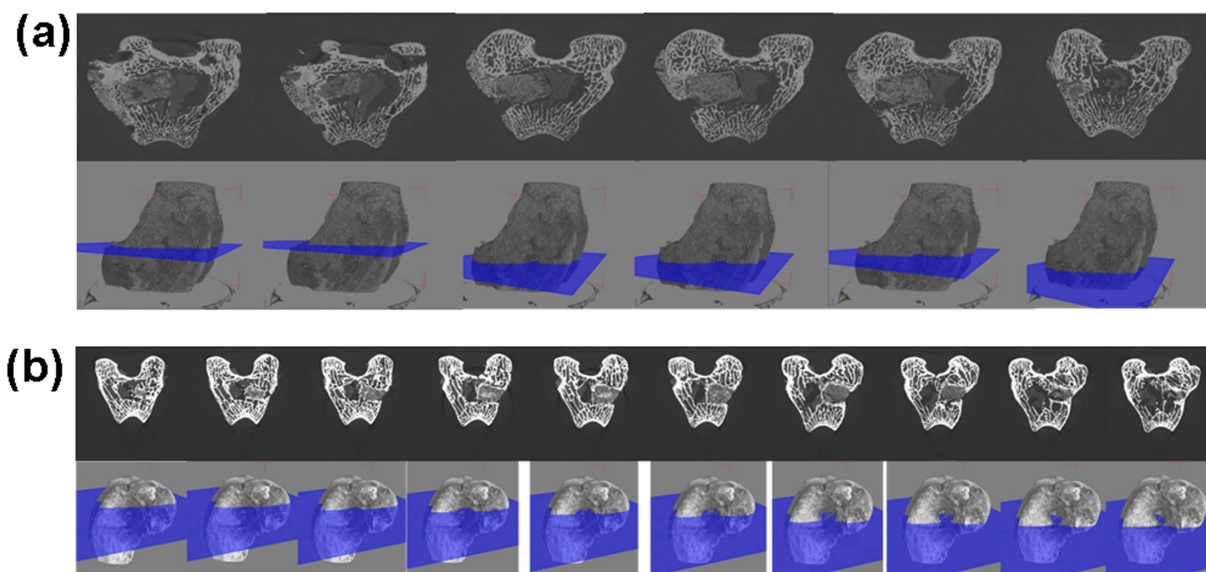


**Figure 13.** Serial slices along the Z-axis in micro-CT. Images are obtained for implanted LS-BAG scaffolds. (a) After 2 months; (b) After 4 months.

showed more of matured osteoblastic tissues apposed to the surface of the sample. LS-BAG on the other hand showed (Fig. 17d,h) both collagenous network and mature bone tissues, which was not only covered the surface but also had invaded the porous network structure of the implant. Interestingly, BAG samples after 4 months showed matured osteoblastic tissues (Fig. 17e), but there was also sporadic presence of RBCs on the surface of samples. Interfacial gap between the implanted samples and the surrounding bone was found more in case of BAG than the other samples. Bony networks could be seen for BAG but no collagenous microstructure. Interfacial gap was absent in case of L-BAG and LS-BAG after 4 months but like the BAG samples, S-BAG also revealed slight interfacial gap after 2 months which however completely absent after 4 months. Granular nature of the porous scaffolds revealed before animal experimentation were absent when implanted. There were no loose or unreacted glass particles after animal study.

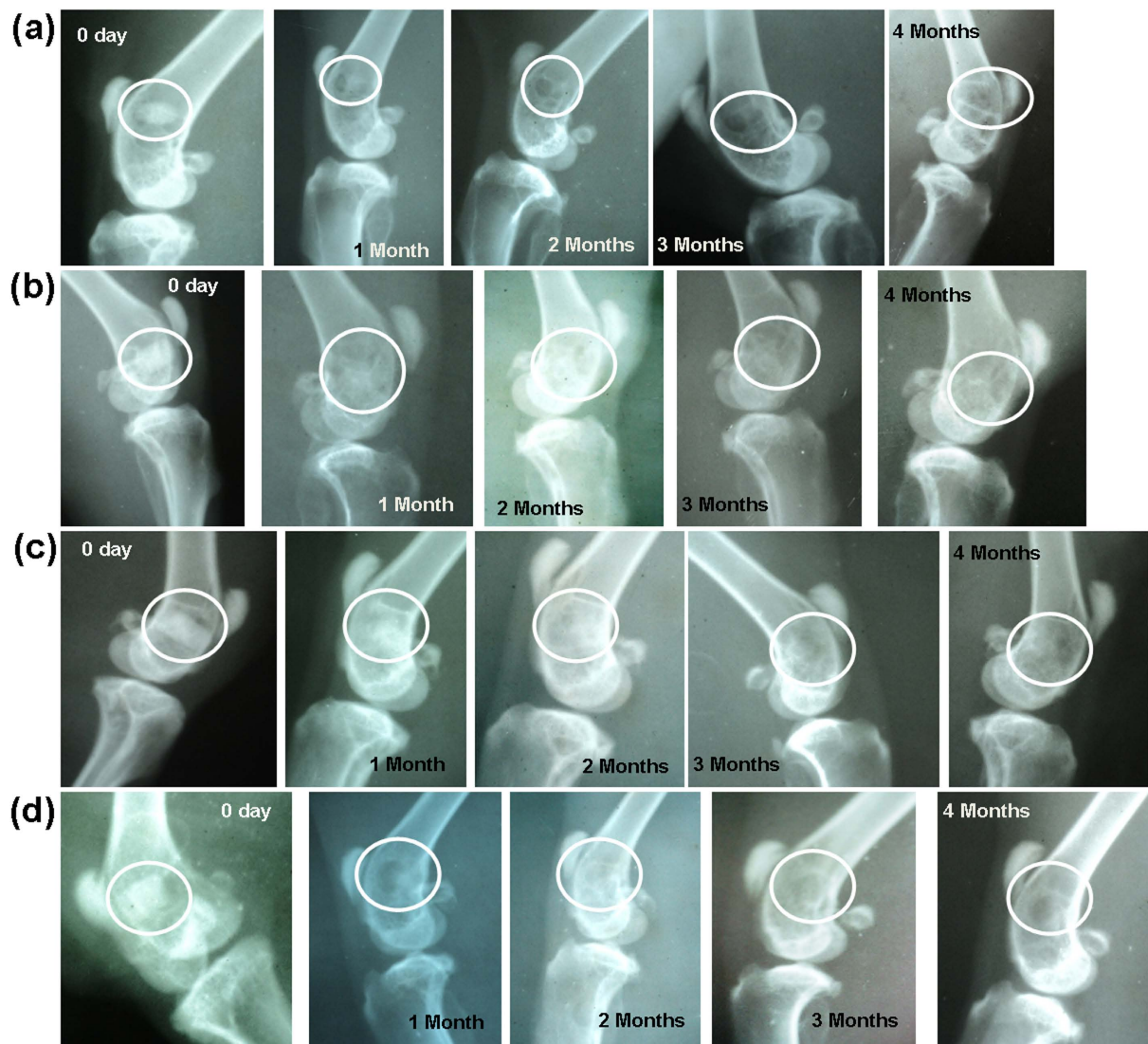


**Figure 14.** Radiographs taken at '0' day, 1, 2, 3 and 4 months post-operatively implanted with (a) BAG, (b) L-BAG, (c) S-BAG and (d) LS-BAG.

Group	1 month	2 month	3 month	4 month	SEM
S-BAG	0.66 <sup>a</sup>	1.00 <sup>a</sup>	1.66 <sup>b</sup>	2.33 <sup>bc</sup>	0.28
LS-BAG	0.66 <sup>a</sup>	0.66 <sup>a</sup>	1.33 <sup>b</sup>	2.33 <sup>c</sup>	0.28
LS-BAG	1.33 <sup>a</sup>	1.66 <sup>ab</sup>	2 <sup>bc</sup>	3 <sup>c</sup>	0.28
BAG	0.33 <sup>a</sup>	0.66 <sup>b</sup>	1 <sup>bc</sup>	1.66 <sup>c</sup>	0.28

**Table 5.** Radiological scoring values of different samples at different time intervals. Values are expressed as Mean  $\pm$  SE. Values with different superscript within a row differs significantly ( $P < 0.001$ ).

Earlier *in vitro* and *in vivo* studies on porous bioactive glass scaffolds demonstrated their potentiality towards bone tissue engineering due to inherent osteoconductive and osteogenic properties<sup>36,37</sup>. Further improvement in biological properties of these scaffolds can be achieved via incorporation of suitable dopants that positively affect osteoblast activities thereby enable early new bone formation<sup>6</sup>. Amalgamation of trace metallic elements into tissue engineering constructs offer low cost, longer shelf life with low regulatory burden and low risk as compared to biologics. Due to these added benefits, delivery of trace metallic element as biological agents is getting considerable attention in tissue engineering and regenerative medicine applications<sup>38–40</sup>. To achieve toward this goal of improving the performance of bioactive glasses, a simpler method was identified to develop lithium and strontium doped glass and to investigate the mechanism of how these next-generation biomaterials can enhance both osteogenesis and angiogenesis for faster patient healing times and high surgical success rates.

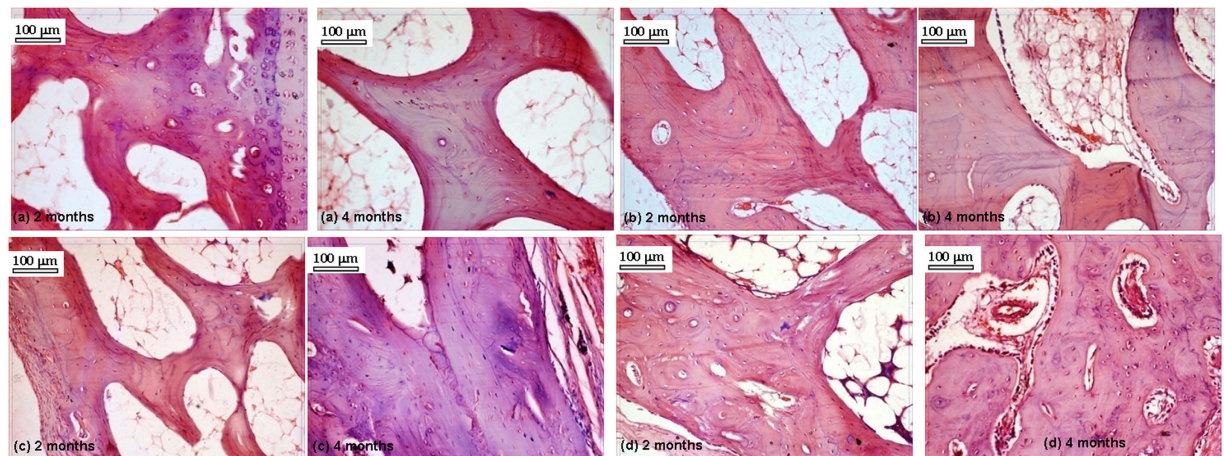


**Figure 15.** Histological sections taken after 2 and 4 months post-operatively implanted with (a) BAG, (b) S-BAG, (c) L-BAG and (d) LS-BAG.

Cellular Response	Time Point (2 month)				Time Point (4month)			
	Group 1	Group 2	Group 3	Group 4	Group 1	Group 2	Group 3	Group 4
Fibro vascular proliferation	1 ± 0.3	1.66 ± 0.3	1.33 ± 0.3	1.66 ± 0.3	1.33 ± 0.3	1.66 ± 0.3	1.33 ± 0.3	1.66 ± 0.3
Mononuclear cell	1 ± 0.23	1 ± 0.23	1 ± 0.23	1.33 ± 0.23	1 ± 0.23	1 ± 0.23	1.33 ± 0.23	1.33 ± 0.23
Osteoclast activity	1 ± 0.23	1.33 ± 0.23	1 ± 0.23	1.33 ± 0.23	1 ± 0.23	1 ± 0.23	1.33 ± 0.23	1.33 ± 0.23
Mucin deposit	1.33 ± 0.16	1 ± 0.16	1 ± 0.16	1.33 ± 0.16	1 ± 0.16	1 ± 0.16	1 ± 0.16	1 ± 0.16
Vascularisation	1 ± 0.26	1.33 ± 0.26	1 ± 0.26	1.66 ± 0.26	1.33 ± 0.26	1.66 ± 0.26	1.33 ± 0.26	2 ± 0.26
Osteoblastic activity	1 ± 0.31	1.66 ± 0.31	1.33 ± 0.31	1 ± 0.31	1.33 ± 0.31	1.66 ± 0.31	1.66 ± 0.31	2.3 ± 0.31

**Table 6.** Histological scoring values of different samples at 2 and 4 months. Values are expressed as Mean ± SE.

$\text{Li}^+$  is new additive ion of interest that brought attention due to its imminent role in osteogenesis. In a very recent study, Miguez-Pacheco *et al.* has shown that substitution of Na by different % of Li in 45S5 bioactive glasses cause decrease in  $T_g$  and  $T_m$  favoring sintering by viscous flow<sup>41</sup> which also consolidates our present finding in case of L-BAG. However, we have also completed cell viability and proliferation studies to further strengthen its potential application. In another study, it has been reported that 75 patients treated with lithium were found to exhibit significantly greater bone mass in several areas compared to 75 normal participants<sup>42</sup>. Similarly, strontium ( $\text{Sr}^{2+}$ ), a non-essential element accounts for 0.035% of the calcium content in our skeleton system and has been shown to boost bone regeneration when incorporated into synthetic bone grafts<sup>43</sup>.

$\text{Li}^+$  doping in bioactive glasses may inhibit GSK3, a negative regulator of the Wnt signaling pathway<sup>44</sup>. Moreover, it activates  $\beta$ -catenin-mediated T cell factor (TCF)-dependent transcription during bone and cartilage fracture healing<sup>45</sup>. Similarly,  $\text{Sr}^{2+}$  enhances osteoclast apoptosis, increases pre-osteoblastic cell proliferation and collagen synthesis and thus decreases bone resorption and preserve bone formation<sup>46,47</sup>. In our study, radiological study revealed gradual replacement of scaffold with new bone after 2 months in all doped samples. Histological study revealed highly proliferative stage of osteoblast and osteoclast cells (progenitor cells) along with angio-proliferation component of bony tissue in doped samples compared to pure samples. This is presumably due to possible role of Sr and Li addition in bioactive glass.  $\text{Sr}^{2+}$  plays a vital role in overall bone turnover through early differentiation of osteoblast that helps in early expression of *cbfa1* gene, indispensable for osteoblast differentiation<sup>48</sup>. Sr can also stimulate the calcium sensing receptor and other equivalent signaling pathways to induce early osteoblast differentiation<sup>46</sup>. The Wnt signaling pathway is one of the most key signal cascades in bone formation and remodeling process<sup>49,50</sup>. A direct link between BMP production and an activated Wnt signaling pathway in osteoblasts has been observed<sup>51,52</sup>. The activation of  $\beta$ -catenin signaling by  $\text{Li}^+$  shows its paramount role for fracture healing<sup>45</sup>. Higher osteoblastic activity and lamellar bone formation are prominent in binary Sr-Li doped bioactive glass which is due to combining effects of both dopants on bone formation processes of resorption and mineral aggregation.

Fluorochrome labeling using tetracycline marker is an indicator for the new bone formation, bone mineralization and remodeling<sup>53</sup>. These stains when incorporated will directly bind to areas undergoing calcification at the bone/osteoid (unmineralized bone) interface. After administration, tetracycline generally follows ionized calcium and deposited to the areas of mineralized tissue<sup>54,55</sup>. The labeled new bone and old bone emit bright golden-yellow and dark-sea green fluorescence respectively when observed under UV light. The method provides practical information in assessing the amount of new bone formation and bone healing<sup>56</sup>. In this study, at 2 months time

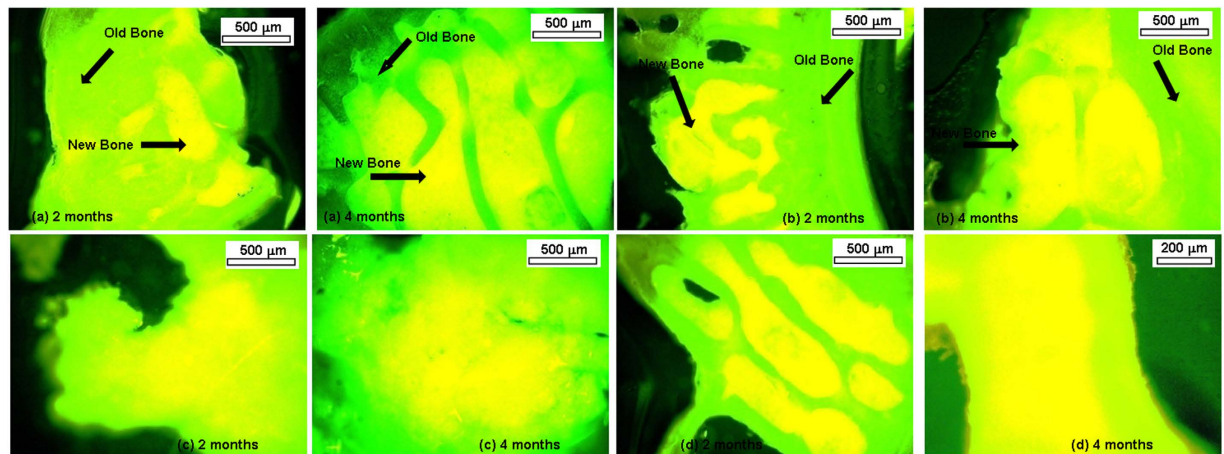


**Figure 16.** Fluorochrome labeling study (after oxytetracycline markings) taken after 2 and 4 months post-operatively implanted with (a) BAG, (b) S-BAG, (c) L-BAG and (d) LS-BAG.

Treatment	2 months	4 months
BAG	32.47 ± 0.439 <sup>bA</sup>	48.29 ± 0.541 <sup>bB</sup>
BAG-Sr	23.663 ± 0.513 <sup>aA</sup>	45.432 ± 0.573 <sup>aB</sup>
BAG-Li	39.459 ± 0.562 <sup>cA</sup>	51.466 ± 0.584 <sup>cB</sup>
BAG-Sr + Li	47.459 ± 0.513 <sup>dA</sup>	54.897 ± 0.588 <sup>dB</sup>

**Table 7.** Percentage of bone formation through fluorochrome labeling images at two time point of 2 and 4 months a, b, c, d means with different superscripts within a column differs significantly among the treatment ( $p < 0.01$ ). A, B mean with different superscript within a row differs significantly between the month of sample within a treatment ( $p < 0.001$ ).

point, the process of new bone formation was moderate in pure bioactive glass and relatively high in all three doped samples. In general, the activity of new bone formation was increased in all samples after 4 months. This may be due to the significant effects of single or binary dopants which may in turn help in cellular proliferation and osteoblastic activity. Previous studies established that Sr can influence cellular activities via the membrane bound calcium sensing receptor, both in osteoblasts and in cells of the osteoclasts lineage<sup>15,57,58</sup>. Moreover, Sr may enhance the ability of MSCs as well as pre-osteoblasts proliferation and differentiation into bone-forming osteoblasts<sup>59</sup>, through Wnt/b-catenin pathway by activating mitogenic signaling<sup>60</sup>. In a similar study using Sr doped HAp-based bioactive glasses implants, the sequential polychrome labeling of bone during *in vivo* osseointegration confirmed homogeneous bone formation around the test implants<sup>61</sup>.

SEM examination revealed both collagenous network and mature bone tissues in L-BAG while S-BAG samples showed more of matured osteoblastic tissues apposed to the surface of the sample. Interfacial gap between the implanted samples and the surrounding bone was found more in pure BAG than the doped other samples. Bony networks could be seen for pure BAG but no collagenous microstructure could be noticed, which is an indirect estimation of poorer bone quality in case of BAG than the other samples. Interestingly, sporadic presence of RBCs on the surface of samples indicating the healing was still continuing. Sr controls key proteolytic enzymes, matrix metalloproteinase-2 (MMP-2) and matrix metalloproteinase-9 (MMP-9) along with osteoprotegerin (OPG) and receptor activator of nuclear factor  $\kappa$ - $\beta$  ligand (RANKL) that is produced by osteoblast cells and are key signaling mechanisms of osteoclast formation and its resorptive activity<sup>62,63</sup>. The combining effect of Sr enhances overall bone turn over by reduced osteoclastic resorption and an enhanced osteoblastic activity.

Micro CT in scaffold research has enabled accurate morphological studies to be carried out, yielding comprehensive data sets<sup>64,65</sup>. It also opened a new paradigm for investigations in tissue engineering<sup>66</sup>. Micro CT thus performed to understand the degree of vascularity as well as the interaction of soft and hard tissue with the material when implanted. In the present study, mature bone tissue as well as blood vessels engulfed the implant which indicates good vascularisation. In a comparison LS-BAG samples showed highest degree of tissue impregnation and vascularity among the four compositions probably due to the synergistic effect of lithium and strontium in particular. After 2 months, serial sectional images of L-BAG indicated that tissue invasion was more pronounced than in the central part of the implant than the periphery with a clear interfacial gap with the surrounding tissue. Grey scale values were found to be in between of cortical and cancellous tissues after 2 months which indicates that the implant was in the process of resorption. But the degree of resorption was higher in case of L-BAG than the BAG alone. S-BAG samples had clearly shown its efficacy expressed towards conversion to more of cortical tissue than the cancellous one. LS-BAG samples after 2 months showed close resemblance of the cancellous tissue on the periphery and cortical tissue in the inside of implanted samples. BAG samples only showed some interfacial

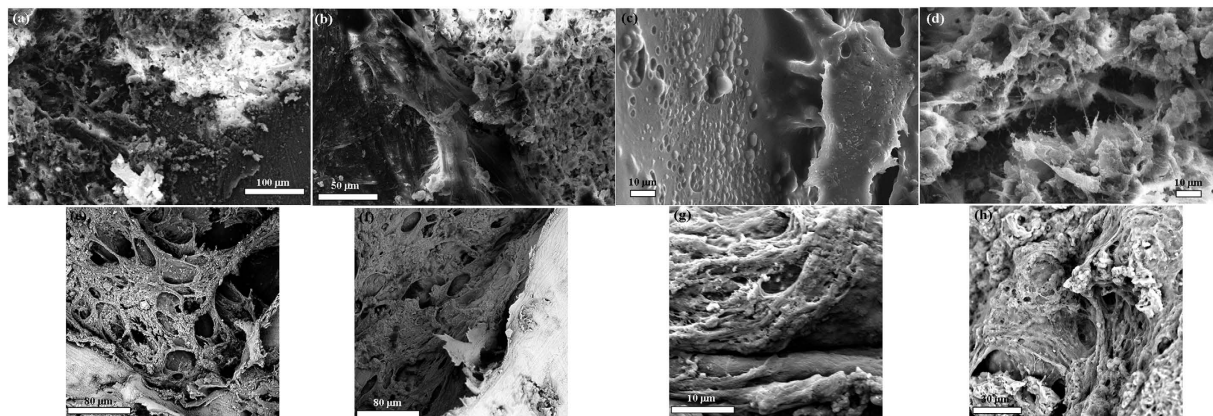


**Figure 17.** SEM images of bone-material (BAG, L-BAG, S-BAG and LS-BAG) interface taken after 2 months (a–d) and 4 months (e–h) post-operatively respectively.

gap which was absent for all doped samples. In a similar study, the bone regeneration ability of different bioactive glass particles has been observed in rabbit model<sup>67,68</sup>.

In summary, this study examines the effects of Sr and Li addition in bioactive glass compositions developed in the lab, the porous scaffolds made thereof for their physico-chemical, *in vitro* and *in vivo* osteogenic properties alone and in combination. All bioactive glass both doped and undoped showed *in vivo* new bone formation during 4 months. Based on the microstructural, histological, radiological, micro CT and fluorochrome labeling results, Sr and/or Li doped bioactive glass showed acceleration of early-stage bone formation at the rabbit model defect site and Sr + Li doped bioactive glass proved to be more effective than other two compositions. Our findings suggest that incorporation of Sr and Li in bioactive glass can effectively enhance early stage *in vivo* osseointegration and bone remodeling properties. The results also suggest that doped bioactive glass might provide a delivery system for bioactive agents to accelerate bone healing and better anchorage of bone implants in orthopedic surgery. However, further detailed studies are needed to elucidate the exact mechanisms of Sr and Li dopants on enhanced bone healing for suitable use in future biomedical applications as a more osteoconductive bone substitute especially on earlier stages after implantation.

## References

1. Drosse, I. *et al.* Tissue engineering for bone defect healing: an update on a multi-component approach. *Injury* **39**, S9–S20 (2008).
2. Langer, R. & Vacanti, J. P. Tissue engineering. *Science* **260**, 920–926 (1993).
3. Marquis, M.-E. *et al.* Bone cells-biomaterials interactions. *Frontiers in bioscience* **14**, 1023–1067 (2009).
4. Nandi, S. K., Kundu, B., Datta, S., De, D. K. & Basu, D. The repair of segmental bone defects with porous bioglass: an experimental study in goat. *Research in Veterinary Science* **86**, 162–173 (2009).
5. Le Nihouannen, D. *et al.* Micro-architecture of calcium phosphate granules and fibrin glue composites for bone tissue engineering. *Biomaterials* **27**, 2716–2722 (2006).
6. Isaac, J. *et al.* Effects of strontium-doped bioactive glass on the differentiation of cultured osteogenic cells. *European Cells and Materials* **21**, 130–143 (2011).
7. Pina, S. & Ferreira, J. M. F. Brushite-forming Mg-, Zn- and Sr-substituted bone cements for clinical applications. *Materials* **3**, 519–535 (2010).
8. Pina, S. *et al.* Biological responses of brushite-forming Zn- and ZnSr-substituted  $\beta$ -tricalcium phosphate bone cements. *European Cells and Materials* **20**, 162–177 (2010).
9. Klammert, U. *et al.* Phase composition, mechanical performance and *in vitro* biocompatibility of hydraulic setting calcium magnesium phosphate cement. *Acta Biomaterialia* **6**, 1529–1535 (2010).
10. Hoppe, A., Guldal, N. S. & Boccaccini, A. R. A review of the biological response to ionic dissolution products from bioactive glasses and glass-ceramics. *Biomaterials* **32**, 2757–2774 (2011).
11. Liu, J., Rawlinson, S. C. F., Hill, R. G. & Fortune, F. Strontium-substituted bioactive glasses *in vitro* osteogenic and antibacterial effects. *Dental Materials* **32**, 412–422 (2016).
12. Martin, R. A. *et al.* An examination of the calcium and strontium site distribution in bioactive glasses through isomorphous neutron diffraction, X-ray diffraction, EXAFS and multinuclear solid state NMR. *Journal of Materials Chemistry* **22**, 22212–22223 (2012).
13. Massera, J. & Hupa, L. Influence of SrO substitution for CaO on the properties of bioactive glass S53P4. *Journal of Materials Science: Materials in Medicine* **25**, 657–668 (2014).
14. Jensen, J. E. B., Stang, H., Kringsholm, B., Pritzl, G. & Sørensen, O. H. Relationship between trace element content and mechanical bone strength. *Bone* **20**, 104 (1997).
15. Bonnelye, E., Chabadel, A., Saltel, F. & Jurdic, P. Dual effect of strontium ranelate: Stimulation of osteoblast differentiation and inhibition of osteoclast formation and resorption *in vitro*. *Bone* **42**, 129–138 (2008).
16. Baron, R. & Tsouderos, Y. *In vitro* effects of S12911-2 on osteoclast function and bone marrow macrophage differentiation. *European Journal of Pharmacology* **450**, 11–17 (2002).
17. Fredholm, Y. C. *et al.* Influence of strontium for calcium substitution in bioactive glasses on degradation, ion release and apatite formation. *Journal of the Royal Society Interface* **9**, 880–889 (2012).
18. Massera, J., Kokkari, A., Narhi, T. & Hupa, L. The influence of SrO and CaO in silicate and phosphate bioactive glasses on human gingival fibroblasts. *Journal of Materials Science: Materials in Medicine* **26**, 1–9 (2015).
19. Reginster, J. Y. *et al.* Effects of long-term strontium ranelate treatment on the risk of nonvertebral and vertebral fractures in postmenopausal osteoporosis: Results of a five-year, randomized, placebo-controlled trial. *Arthritis and Rheumatism* **58**, 1687–1695 (2008).



20. Khorami, M., Hesaraki, S., Behnamghader, A., Nazarian, H. & Shahrabi, S. *In vitro* bioactivity and biocompatibility of lithium substituted 45S5 bioglass. *Materials Science and Engineering: C* **31**, 1584–1592 (2011).
21. Spencer, G. J., Utting, J. C., Etheridge, S. L., Arnett, T. R. & Genever, P. G. Wnt signalling in osteoblasts regulates expression of the receptor activator of NF $\kappa$ B ligand and inhibits osteoclastogenesis *in vitro*. *Journal of Cell Science* **119**, 1283–1296 (2006).
22. Edgington, J. M., Bandyopadhyay, A. & Bose, S. *In vitro* characterization of lithium-doped tricalcium phosphate for bone graft. *Society for Biomaterials Abstract #727* (2011).
23. Keshaw, H., Forbes, A. & Day, R. M. Release of angiogenic growth factors from cells encapsulated in alginate beads with bioactive glass. *Biomaterials* **26**, 4171–4179 (2005).
24. Leach, J. K., Kaigler, D., Wang, Z., Krebsbach, P. H. & Mooney, D. J. Coating of VEGF-releasing scaffolds with bioactive glass for angiogenesis and bone regeneration. *Biomaterials* **27**, 3249–3255 (2006).
25. Xynos, I. D., Edgar, A. J., Buttery, L. D. K., Hench, L. L. & Polak, J. M. Ionic products of bioactive glass dissolution increase proliferation of human osteoblasts and induce insulin-like growth factor II mRNA expression and protein synthesis. *Biochemical and Biophysical Research Communications* **276**, 461–465 (2000).
26. Goel, A., Rajagopal, R. R. & Ferreira, J. M. F. Influence of strontium on structure, sintering and biodegradation behaviour of CaO-MgO-SrO-SiO<sub>2</sub>-P<sub>2</sub>O<sub>5</sub>-CaF<sub>2</sub> glasses. *Acta Biomaterialia* **7**, 4071–4080 (2011).
27. Vestermark, M. T. *et al.* Strontium doping of bone graft extender: Effect on fixation of allografted experimental implants. *Acta Orthopaedica* **82**, 614–621 (2011).
28. Lao, J., Jallot, E. & Nedelec, J.-M. Strontium-delivering glasses with enhanced bioactivity: A new biomaterial for antiosteoporotic applications? *Chemistry of Materials* **20**, 4969–4973 (2008).
29. Kokubo, T., Kushitani, H., Sakka, S., Kitsugi, T. & Yamamuro, T. Solutions able to reproduce *in vivo* surface-structure changes in bioactive glass-ceramic A-W. *Journal of the Biomedical Materials Research* **24**, 721–734 (1990).
30. Zhukauskas, R. *et al.* Histological and radiographic evaluations of demineralized bone matrix and coralline hydroxyapatite in the rabbit tibia. *Journal of Biomaterials Applications* **24**, 639–656 (2010).
31. Baghbani, F., Moztarzadeh, F., Hajibaki, L. & Mozafari, M. Synthesis, characterization and evaluation of bioactivity and antibacterial activity of quinary glass system (SiO<sub>2</sub>-CaO-P<sub>2</sub>O<sub>5</sub>-MgO-ZnO): *In vitro* study. *Bulletin of Materials Science* **36**, 1339–1346 (2013).
32. Soundrapandian, C., Datta, S., Kundu, B., Basu, D. & Sa, B. Porous bioactive glass scaffolds for local drug delivery in osteomyelitis: Development and *in vitro* characterization. *AAPS PharmSciTech* **11**, 1675–1683 (2010).
33. Todaro, G. J. & Green, H. Quantitative studies of the growth of mouse embryo cells in culture and their development into established lines. *The Journal of Cell Biology* **17**, 299–313 (1963).
34. Wong, S., Guo, W.-H. & Wang, Y.-L. Fibroblasts probe substrate rigidity with filopodia extensions before occupying an area. *Proceedings of the National Academy of Sciences* **111**, 17176–17181 (2014).
35. McNeil, S. E., Hobson, S. A., Nipper, V. & Rodland, K. D. Functional calcium-sensing receptors in rat fibroblasts are required for activation of SRC kinase and mitogen-activated protein kinase in response to extracellular calcium. *Journal of Biological Chemistry* **273**, 1114–1120 (1998).
36. Hench, L. L., Splinter, R. J., Allen, W. C. & Greenlee, T. K. Bonding mechanisms at the interface of ceramic prosthetic materials. *Journal of biomedical materials research* **5**, 117–141 (1971).
37. Bosetti, M., Zanardi, L., Hench, L. & Cannas, M. Type I collagen production by osteoblast-like cells cultured in contact with different bioactive glasses. *Journal of Biomedical Materials Research Part A* **64**, 189–195 (2003).
38. Mourino, V., Cattalini, J. P. & Boccaccini, A. R. Metallic ions as therapeutic agents in tissue engineering scaffolds: an overview of their biological applications and strategies for new developments. *Journal of the Royal Society Interface* **9**, 401–419 (2012).
39. Lakhkar, N. J. *et al.* Bone formation controlled by biologically relevant inorganic ions: Role and controlled delivery from phosphate-based glasses. *Advanced Drug Delivery Reviews* **65**, 405–420 (2013).
40. Habibovic, P. & Barralet, J. E. Bioinorganics and biomaterials: Bone repair. *Acta Biomaterialia* **7**, 3013–3026 (2011).
41. Miguez-Pacheco, V. *et al.* Development and characterization of lithium-releasing silicate bioactive glasses and their scaffolds for bone repair. *Journal of Non-Crystalline Solids* **432**, 65–72 (2016).
42. Zamani, A., Omrani, G. R. & Nasab, M. M. Lithium's effect on bone mineral density. *Bone* **44**, 331–334 (2009).
43. Nielsen, S. P. The biological role of strontium. *Bone* **35**, 583–588 (2004).
44. Chalecka-Franaszek, E. & Chuang, D.-M. Lithium activates the serine/threonine kinase Akt-1 and suppresses glutamate-induced inhibition of Akt-1 activity in neurons. *Proceedings of the National Academy of Sciences* **96**, 8745–8750 (1999).
45. Chen, Y. *et al.* Beta-catenin signaling plays a disparate role in different phases of fracture repair: Implications for therapy to improve bone healing. *PLoS Medicine* **4**, e249 (2007).
46. Marie, P. J. Strontium ranelate: a novel mode of action optimizing bone formation and resorption. *Osteoporosis International* **16**, S7–S10 (2005).
47. Roy, M., Bandyopadhyay, A. & Bose, S. Induction plasma sprayed Sr and Mg doped nano hydroxyapatite coatings on Ti for bone implant. *Journal of Biomedical Materials Research Part B: Applied Biomaterials* **99**, 258–265 (2011).
48. Sila-Asna, M., Bunyaratvej, A., Maeda, S., Kitaguchi, H. & Bunyaratvej, N. Osteoblast differentiation and bone formation gene expression in strontium-inducing bone marrow mesenchymal stem cell. *Kobe Journal of Medical Sciences* **53**, 25–35 (2007).
49. Monroe, D. G., McGee-Lawrence, M. E., Oursler, M. J. & Westendorf, J. J. Update on Wnt signaling in bone cell biology and bone disease. *Gene* **492**, 1–18 (2012).
50. Milat, F. & Ng, K. W. Is Wnt signalling the final common pathway leading to bone formation? *Molecular and Cellular Endocrinology* **310**, 52–62 (2009).
51. Lin, G. L. & Hankenson, K. D. Integration of BMP, Wnt and notch signaling pathways in osteoblast differentiation. *Journal of Cellular Biochemistry* **112**, 3491–3501 (2011).
52. Zhang, R. *et al.* Wnt/ $\beta$ -catenin signaling activates bone morphogenetic protein 2 expression in osteoblasts. *Bone* **52**, 145–156 (2013).
53. Kovar, J. L. *et al.* Near-infrared-labeled tetracycline derivative is an effective marker of bone deposition in mice. *Analytical Biochemistry* **416**, 167–173 (2011).
54. Gibson, C. J., Thornton, V. F. & Brown, W. A. B. Incorporation of tetracycline into impeded and unimpeded mandibular incisors of the mouse. *Calcified Tissue Research* **26**, 29–31 (1978).
55. Dahners, L. E. & Bos, G. D. Fluorescent tetracycline labeling as an aid to debridement of necrotic bone in the treatment of chronic osteomyelitis. *Journal of Orthopaedic Trauma* **16**, 345–346 (2002).
56. Nandi, S. K., Ghosh, S. K., Kundu, B., De, D. K. & Basu, D. Evaluation of new porous  $\beta$ -tri-calcium phosphate ceramic as bone substitute in goat model. *Small Ruminant Research* **75**, 144–153 (2008).
57. Chattopadhyay, N., Quinn, S. J., Kifor, O., Ye, C. & Brown, E. M. The calcium-sensing receptor (CaR) is involved in strontium ranelate-induced osteoblast proliferation. *Biochemical Pharmacology* **74**, 438–447 (2007).
58. Hurtel-Lemaire, A. S. *et al.* The calcium-sensing receptor is involved in strontium ranelate-induced osteoclast apoptosis: New Insights into the associated signaling pathways. *Journal of Biological Chemistry* **284**, 575–584 (2009).
59. Barbara, A., Delannoy, P., Denis, B. G. & Marie, P. J. Normal matrix mineralization induced by strontium ranelate in MC3T3-E1 osteogenic cells. *Metabolism* **53**, 532–537 (2004).
60. Caverzasio, J. Strontium ranelate promotes osteoblastic cell replication through at least two different mechanisms. *Bone* **42**, 1131–1136 (2008).

61. Basu, B., Sabareeswaran, A. & Shenoy, S. J. Biocompatibility property of 100% strontium-substituted  $\text{SiO}_2\text{-Al}_2\text{O}_3\text{-P}_2\text{O}_5\text{-CaO-CaF}_2$  glass ceramics over 26 weeks implantation in rabbit model: Histology and micro-Computed Tomography analysis. *Journal of Biomedical Materials Research Part B: Applied Biomaterials* **103**, 1168–1179 (2014).
62. Tat, S. K., Pelletier, J.-P., Mineau, F., Caron, J. & Martel-Pelletier, J. Strontium ranelate inhibits key factors affecting bone remodeling in human osteoarthritic subchondral bone osteoblasts. *Bone* **49**, 559–567 (2011).
63. Boyle, W. J., Simonet, W. S. & Lacey, D. L. Osteoclast differentiation and activation. *Nature* **423**, 337–342 (2003).
64. Mastrogiacomo, M. *et al.* Synchrotron radiation microtomography of bone engineered from bone marrow stromal cells. *Tissue Engineering* **10**, 1767–1774 (2004).
65. Tuan, H. S. & Hutmacher, D. W. Application of micro CT and computation modeling in bone tissue engineering. *Computer-Aided Design* **37**, 1151–1161 (2005).
66. Porter, B. D., Lin, A. S. P., Peister, A., Hutmacher, D. & Guldberg, R. E. Noninvasive image analysis of 3D construct mineralization in a perfusion bioreactor. *Biomaterials* **28**, 2525–2533 (2007).
67. Vogel, M., Voigt, C., Gross, U. M. & Muller-Mai, C. M. *In vivo* comparison of bioactive glass particles in rabbits. *Biomaterials* **22**, 357–362 (2001).
68. Sabareeswaran, A. *et al.* Early osseointegration of a strontium containing glass ceramic in a rabbit model. *Biomaterials* **34**, 9278–9286 (2013).

## Acknowledgements

The authors gratefully acknowledge the funding support of CSIR 12<sup>th</sup> five year plan programme (BIOCERAM) and also supports rendered by the Directors, CSIR-Central Glass and Ceramic Research Institute and CSIR-Indian Institute of Chemical Biology, Kolkata, India and Vice Chancellor, West Bengal University of Animal and Fishery Sciences, Kolkata, India for execution of this work. Personnel related to all material, *in vitro* and *in vivo* characterization are sincerely acknowledged for their kind and generous supports always.

## Author Contributions

B.K. and S.K.N. wrote the main manuscript text; P.K.K. did the animal experimental part; A.M. did the experimental part of material development; P.M. and J.M. performed the surgery part under pre-clinical trial; S.S. performed the micro-CT; S.N. and C.M. contributed *in vitro* cell culture work and post-analysis; S.D. and V.K.B. prepared figures 2–7.

## Additional Information

**Supplementary information** accompanies this paper at <http://www.nature.com/srep>

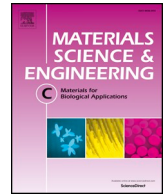
**Competing financial interests:** The authors declare no competing financial interests.

**How to cite this article:** Khan, P. K. *et al.* Influence of single and binary doping of strontium and lithium on *in vivo* biological properties of bioactive glass scaffolds. *Sci. Rep.* **6**, 32964; doi: 10.1038/srep32964 (2016).



This work is licensed under a Creative Commons Attribution 4.0 International License. The images or other third party material in this article are included in the article's Creative Commons license, unless indicated otherwise in the credit line; if the material is not included under the Creative Commons license, users will need to obtain permission from the license holder to reproduce the material. To view a copy of this license, visit <http://creativecommons.org/licenses/by/4.0/>

© The Author(s) 2016



## Development of nano-porous hydroxyapatite coated e-glass for potential bone-tissue engineering application: An *in vitro* approach

Arnab Mahato<sup>a</sup>, Zhang Sandy<sup>b</sup>, Sandip Bysakh<sup>a</sup>, Leena Hupa<sup>b</sup>, Indranee Das<sup>a</sup>, Promita Bhattacharjee<sup>c</sup>, Biswanath Kundu<sup>a,\*</sup>, Goutam De<sup>a</sup>, Samit K. Nandi<sup>d</sup>, Pekka Vallittu<sup>e</sup>, Vamsi K. Balla<sup>a</sup>, Manjima Bhattacharya<sup>a</sup>

<sup>a</sup> CSIR-Central Glass and Ceramic Research Institute (CSIR-CGCR), Kolkata, India

<sup>b</sup> Process Chemistry Centre, ÅboAkademi University, Finland

<sup>c</sup> Materials Science Centre, Indian Institute of Technology Kharagpur, India

<sup>d</sup> Department of Veterinary Surgery and Radiology, West Bengal University of Animal and Fishery Sciences (WBUAFS), Kolkata, India

<sup>e</sup> Institute of Dentistry and Turku Clinical Biomaterials Centre - TCBC, University of Turku, Turku, Finland

### ARTICLE INFO

#### Keywords:

E-glass  
Hydroxyapatite  
Static SBF study  
Quasi-dynamic SBF study  
*In vitro*

### ABSTRACT

To reconstruct the defects caused by craniectomies autologous, bone grafting was usually used, but they failed most commonly due to bone resorption, infections and donor-site morbidity. In the present investigation, an effort has been made for the first time to check the feasibility and advantage of using hydroxyapatite (HAp) coated e-glass as component of bone implants. Sol-gel synthesized coatings were found to be purely hydroxyapatite from XRD with graded and interconnected pores all over the surface observable in TEM. The interconnected porous nature of ceramics are found to increase bioactivity by acting to up-regulate the process of osseointegration through enhanced nutrient transfer and induction of angiogenesis. From TEM studies and nano indentation studies, we have shown that pores were considered to be appropriate for nutrient supply without compromising the strength of sample while in contact with physiological fluid. After SBF immersion test, porous surface was found to be useful for nucleation of apatite crystals, hence increasing the feasibility and bioactivity of sample. However, our quasi-dynamic study showed less crystallization but had significant formation of apatite layer. Overall, the *in vitro* analyses show that HAp coated e-glass leads to significant improvement of implant properties in terms of biocompatibility, cell viability and proliferation, osteoinductivity and osteoconductivity. HAp coating of e-glass can potentially be utilized in fabricating durable and strong bioactive non-metallic implants and tissue engineering scaffolds.

### 1. Introduction

Bone defects may be of congenital origin or, acquired and often require surgical repair with biomaterial implants. Attempts have been made to develop bioactive composite implants to overcome problems, which relate to metal and polymer implants. Metal implants interfere medical imaging and postoperative radiation therapy. In long bones, metal stems of implant cause stress shielding related to bone resorption due to the high elastic modulus of metal [1]. In addition, the released nanoparticles and metal ions are known to cause metallosis and local pseudotumors [2]. Polymer implants of poly(ethylene), poly(methyl methacrylate) and poly(etheretherketone) lack bioactivity and become encapsulated by fibrous tissue, and thus they do not get bonded to bone [3,4]. One of the rapidly increasing clinical indication for the implants

of this kind is decompressive craniectomy [5]. To reconstruct the defects caused by craniectomies autologous, bone grafting was usually used, but they failed most commonly due to bone resorption, infections and donor-site morbidity [6]. Bone graft operations also require prolonged operation time over insertion of alloplastic implants. Several material combinations are available including Mg-alloy [7,8], poly-l-lactic scaffolds [9,10], multimaterial scaffold [11,12] and of course, bioceramics and scaffolds [13]. However, one of the clinically approved novel approach of cranial implant is to utilize biostable e-glass fibers and bioabsorbable bioactive glass as distinguished components in the implant. The durable structure of these biostable glass overcomes the above mentioned shortcomings [14] in these implants.

After the invention of Bioglass® by Prof. L.L. Hench in 1969, it has thoroughly experimented in different fields of biomedical science.

\* Corresponding author.

E-mail addresses: [biswa\\_kundu@rediffmail.com](mailto:biswa_kundu@rediffmail.com), [bkundu@cgcri.res.in](mailto:bkundu@cgcri.res.in) (B. Kundu).

<https://doi.org/10.1016/j.msec.2020.110764>

Received 25 March 2019; Received in revised form 15 February 2020; Accepted 17 February 2020

Available online 19 February 2020

0928-4931/ © 2020 Elsevier B.V. All rights reserved.

Bioactive glasses (BG) have gained extensive interest as alternative alloplastic materials in recent years [15]. The reliability of bioactive glasses is due to their osteoconductive and osteoinductive properties by which they form interfacial bonding with bone *in vivo*, through a series of chemical and biological processes occurring at their surface, leading to the formation of a strong and stable bonding interface by forming hydroxylapatite (HAp) [16–20]. In a nutshell, the processes of HAp formation are ion leaching/exchange, dissolution of the glass network and precipitation and growth of a carbonated apatite (HCA) layer. Currently, bioactive glass (S53P4) is in use as a component of fiber-reinforced composite implants [21,22]. However, a bioactive glass leaches with time in extracellular liquid, it gradually loses mechanical stability and strength due to leaching out of the glass forming ions. This limits their use in load bearing and largely over critical-sized non-load bearing applications of the implants [23,24]. As leaching occurs prior to HAp formation on the surface, high rate of dissolution of glass former ions will decrease the stability of the implant and hamper the progressive bone regeneration. Therefore, slow dissolution of these ions over a long time is essential for retaining the long term stability of the implants [25]. On the other hand, bio-inert e-glass with high corrosion resistance (alumina-calcium-borosilicate glasses with a maximum alkali content of 2 wt%) is sufficiently strong and non-toxic to be used in such requirements. The elastic modulus of e-glass is  $\sim 72.3$  GPa and density 2.58 g/c.c. [26].

In the present investigation, thus, an effort has been made for the first time to combine nano-porous HAp coating on biostable e-glass substrate which obviates leaching of base glass network former/modifier and also minimizes the degradation of mechanical strength with time. The HAp coated e-glass is aimed to be used in the next generation bioactive implants with reduced volume of polymer components. This study describes the process for the HAp coating of e-glass substrate and preliminarily investigates the biological response on the coated material *in vitro*.

## 2. Materials and methods

### 2.1. Materials

Chemically pure and having > 99.5% assay calcium nitrate tetrahydrate [ $\text{Ca}(\text{NO}_3)_2 \cdot 4\text{H}_2\text{O}$ ], sodium chloride [ $\text{NaCl}$ ], sodium hydrogen carbonate [ $\text{NaHCO}_3$ ], magnesium chloride hexahydrate [ $\text{MgCl}_2 \cdot 6\text{H}_2\text{O}$ ], Tris(hydroxymethyl)aminomethane [Tris buffer,  $\text{C}_4\text{H}_{11}\text{NO}_3$ ], calcium chloride dihydrate [ $\text{CaCl}_2 \cdot 2\text{H}_2\text{O}$ ] and sodium sulfatedecahydrate [ $\text{NaSO}_4 \cdot 8\text{H}_2\text{O}$ ] were procured from Merck (Mumbai, India), while phosphorous pentoxide [ $\text{P}_2\text{O}_5$ ], potassium chloride [ $\text{KCl}$ ] and 35.4% hydrochloric acid [ $\text{HCl}$ ] were purchased from S.D. Fine-Chem Ltd. (Mumbai, India). Di-potassium hydrogen phosphate trihydrate [ $\text{K}_2\text{HPO}_4 \cdot 3\text{H}_2\text{O}$ ] was from Sigma-Aldrich (Steinheim, Germany) and ethanol (absolute) was from Merck KGaA (Darmstadt, Germany). Doubly distilled water was used throughout the conducted experiment. Commercially available e-glass (having a composition of 54.3%  $\text{SiO}_2$ –15.2%  $\text{Al}_2\text{O}_3$ –17.2%  $\text{CaO}$ –4.7%  $\text{MgO}$ –8.0%  $\text{B}_2\text{O}_3$ –0.6%  $\text{Na}_2\text{O}$ ) fibers were used to obtain plates after remelting and casting them in a polished steel mould. Plates were used instead of fibers for allowing more precise chemical and biological analysis of the material surface.

### 2.2. Formation of gel

Two clear solutions of  $\text{Ca}(\text{NO}_3)_2 \cdot 4\text{H}_2\text{O}$  (0.1 mol) and  $\text{P}_2\text{O}_5$  (0.003 mol) were made at room temperature separately by stirring them for 30 min., using ethanol (99%, 10 mL) as mutual solvent. Subsequently, they were mixed slowly and stirring was continued for 2 h at room temperature, followed by aging for another 2 h. Increasing viscosity of the gel after first hour was also measured by creep test (Bohlin GEMINI, UK) using cup-and-bob method (shear stress: 0.002 Pa, time: 7200 s).

### 2.3. Fabrication of coated e-glass substrates

Viscous solution, thus obtained (as mentioned in Section 2.2), was tipped on e-glass plate substrates (50  $\mu\text{L}$  on 1 cm  $\times$  1 cm plates with average roughness ( $R_a$ ) of 0.7  $\mu\text{m}$ ) drop-wise followed by drying at room temperature for 18 h. Further, the coated sample was pre-frozen at  $-20$   $^\circ\text{C}$  overnight followed by freeze drying (Eyela FDU.2200, Japan) at 70–80 MPa pressure and  $-83$   $^\circ\text{C}$  for 20 h. The samples were then thermally treated at 850  $^\circ\text{C}$  (heating rate 2  $^\circ\text{C}/\text{min}$ . with 15 min dwelling time). A low speed diamond saw (Buehler, Isomet, USA) was used further for sectioning and characterization.

### 2.4. Characterization of coated e-glass substrates

Surface roughness of the coated and uncoated samples was measured by contact profilometer (Form Talysurf, i120, Taylor Hobson, UK). Phase analysis of the coating was done by X-ray diffraction (XRD) technique in a powder diffractometer using  $\text{CuK}_\alpha$  ( $\lambda = 1.54178$   $\text{\AA}$ ) radiation [PANalytical, The Netherlands]. ‘High Score Plus’ software was used to analyse the XRD data with the help of Inorganic Crystal Structure Database (ICSD, PDF4). To identify the functional groups, Fourier-transformed infrared spectroscopy (FTIR) was performed using PerkinElmer Spectrum 100, USA spectrophotometer with HeNe laser (Class II/2) following the KBr pellet method (2 mg sample: 200 mg KBr). Scratched-off material from surface was used for preparing KBr pellets. To compliment, Raman spectra was performed as well by using STR500 Raman Spectrometer (Technos Instrument, Seki technotron, Japan). The top-surface microstructure and interface of coating cross-section was assessed by field-emission scanning electron microscope (FESEM) (Supra 35VP, Zeiss, Germany). Ca/P molar ratio was measured by taking average from energy dispersive X-ray analysis (EDX) taken at different points of the sample with an accelerating voltage of 15 kV.

Transmission electron microscopy (TEM) (Tecnai G2 30ST, FEI, Netherlands) was performed to obtain the finer details of the microstructure of coating cross-section. Local crystallographic structure was gathered from the selected-area electron-diffraction (SAED) patterns in the TEM. As for the cross-sectional sample preparation for TEM characterization, the coated glass substrates were first cut into pieces of about 2.5 mm  $\times$  10 mm area. Two such cut pieces were glued with coated surfaces face-to-face with ‘Gatan G-1 Epoxy’ (Gatan Inc., USA) and grinded suitably to give a rod like shape of 2.5 mm diameter and 10 mm length. This rod of sandwiched coatings was further glued inside a hollow stainless-steel tube of 3 mm outer diameter using the ‘Gatan G-1 Epoxy’ resin. Cross-sectional slices of about 0.25 mm thickness were cut from the tube filled with the sandwiched coating sample using Buehler low speed diamond saw. Using Gatan Disk Grinder (Gatan Inc., USA) the slices were thinned down to 80  $\mu\text{m}$  and further dimpled at the centre using Gatan dimple grinder (Model 656, Gatan Inc., USA) down to 30  $\mu\text{m}$  at the centre. The dimpled cross-section specimens were finally ion-polished by using Gatan model 691 precision ion polishing system (PIPS, Gatan Inc., USA) with 4 keV Argon ion-beams at 4 $^\circ$  incidence angle on both sides of the cross-sectioned surfaces till perforations to generate electron-transparent thin area of the coating suitable for TEM observation.

### 2.5. Immersion tests in simulated body fluid (SBF)

Static *in vitro* bioactivity (in terms of capability of forming carbonated hydroxyapatite) of coated samples was evaluated in contact with simulated body fluid (SBF) prepared as per Kokubo [27]. Concentrations of the different constituting elements of SBF solution (in mM) taken are as follows:  $\text{Na}^+$  142.0;  $\text{K}^+$  5.0;  $\text{Ca}^{2+}$  2.5;  $\text{Mg}^{2+}$  1.5;  $\text{Cl}^-$  147.8;  $\text{HCO}_3^-$  4.2;  $\text{HPO}_4^{2-}$  1.0;  $\text{SO}_4^{2-}$  0.5. pH was maintained  $\sim 7.4$  by using Tris buffer during preparation. Surface area (SA)/volume (V) ratio of the samples to SBF added was maintained as 1  $\text{cm}^2/15$  mL with constant temperature (37.4  $^\circ\text{C}$ ) during the study (in an incubator in

closed test tubes for 7 and 14 days without refreshing SBF solution in between) [28]. Quasi-dynamic (QD) SBF study was performed by following the same method but by replenishing with fresh SBF solution after every 24 h and up to 14 days. Weight changes of samples and pH change of the dissolution medium (SBF) were recorded up to 14 days.

Samples after static and QD SBF studies after 7 and 14 days were analysed for structure by XRD, FTIR and Raman while surface microstructure evolved were analysed by FESEM and TEM. Samples for microstructural analyses were prepared as described earlier. Top surface of the samples was again assessed for hardness and elastic modulus by nano-indentation method.

Nanoindentation experiments were conducted utilizing a  $5 \times 5$  array on both uncoated and coated e-glass substrates after static and QD SBF studies for 7 and 14 days by load controlled nanoindentation technique with a Berkovich nanoindenter of tip radius 150 nm. A commercial machine (Fischerscope H100-XYp; Fischer, Switzerland) with depth and load sensing resolutions of 1 nm and 0.2  $\mu$ N respectively was used. In the present experiments, the peak load was kept constant at 10mN, while both the loading and the unloading times were kept fixed at 30 s. For all experimental data reported in this work the error bars represent  $\pm 1$  standard deviation of the data.

## 2.6. In vitro biocompatibility study

### 2.6.1. Cell culture procedure

The cell culture medium, for the human osteoblasts like cells (MG-63 cell line) was made of DMEM, 10% foetal calf serum, and 1% penicillin/streptomycin. The cultures were kept till they reached 90% confluence in a humidified environment of 5% CO<sub>2</sub>, at 37 °C. Following confluence, the cells were trypsinized, centrifuged, and suspended back in media for counting. The samples (both bare e-glass and HAp coated e-glass) were sterilized for 30 min. with 70% ethanol and UV light, washed repeatedly with sterile PBS (pH 7.4) followed by treatment with DMEM medium for 4 h to create a better environment for the cells. Just prior to cell seeding, to ensure better penetration of cells, the scaffolds were partially dried for 2 h. Twenty micro-litres of the cell suspension in medium, containing 10<sup>5</sup> cells, were added drop-by-drop on to each sample. Following seeding, to boost cell adhesion in the initial hour, the matrices were maintained in a humidified environment, at 37 °C, 5% CO<sub>2</sub>. The matrices were kept in medium for 14 days, while the medium was replaced every alternate day.

### 2.6.2. Cell viability assay

MTT assay was performed at different points of time over full cell culture duration to investigate the cell viability. The samples were incubated in 5 mg/mL MTT stock solution which was diluted at a ratio of 1:10 using PBS (pH 7.4). Formazan crystal formed post incubation was dissolved in dimethyl sulfoxide and the absorbance of the resulting solutions was measured using the Manufacturer's protocol with spectrophotometer (Bio-Rad, iMark).

### 2.6.3. Cell proliferation by Alamar blue assay

Cell proliferation on samples over 14 days was assessed by Alamar blue dye-reduction. Alamar blue dye was diluted in the culture medium with a 1:10 dye-to-media ratio. Samples were incubated in the dye solution for 4 h in the dark. Dye reduction was determined spectrophotometrically in a microplate reader (Thermo Scientific Multiskan Spectrum, Japan) at 570 and 600 nm. The percentage of dye reduction was calculated from the below-mentioned equation:

$$\%AB \text{ reduction} = \left[ \frac{(\epsilon_{ox\lambda_2})(A\lambda_1) - (\epsilon_{ox\lambda_1})(A\lambda_2)}{(\epsilon_{red\lambda_1})(A'\lambda_2) - (\epsilon_{red\lambda_2})(A'\lambda_1)} \right] \times 100$$

where  $\epsilon\lambda_1$  and  $\epsilon\lambda_2$  were molar extinction coefficient of Alamar blue at 570 and 600 nm respectively,  $\epsilon_{ox}$  in oxidized and  $\epsilon_{red}$  in reduced form;  $A\lambda_1$  and  $A\lambda_2$  were absorbance of the test wells; and  $A'\lambda_1$  and  $A'\lambda_2$  were the absorbance of the negative control wells. All given pairs were values at 570 and 600 nm.

### 2.6.4. Alkaline phosphatase assay (ALP)

Spectrophotometric measurements of the alkaline phosphatase produced by MG-63 cultured on the different samples [29] were carried out. At specific day points, the cell laden constructs were washed with PBS (pH 7.4), homogenized with 1 mL Tris buffer (1 M, pH 8.0), and sonicated for 4 min. on ice. A volume of 20  $\mu$ L of this suspension, was incubated with 1 mL of 16 mM p-nitrophenyl phosphate (Sigma) solution for 5 min., at 30 °C. To measure p-nitrophenol produced in presence of ALP, the absorbance at 405 nm was evaluated and ALP activity was reported as p-nitrophenol produced, normalized by incubation duration and cell count:  $\mu$ mole/min/10<sup>5</sup> cells.

### 2.6.5. Cellular morphology

Laser confocal microscopy was used to examine the cell morphology and the dispersion of the cells on the samples. For confocal laser microscopy, samples after 7 days culture were fixed using 4% paraformaldehyde for 1 h and the cells were then permeabilized over 5 min. by use of 0.1% Triton X-100, prepared in BSA. Samples were then blocked with 1% bovine serum albumin (BSA) for 1 h. The actin filaments were stained using Alexa Fluor<sup>®</sup> 488 and the nuclei with Hoechst 33342. The confocal laser microscopy was performed on Olympus FV 1000 (Olympus, Japan) and post-processing was carried out with Olympus FV 1000 Advanced software version 4.1 (Olympus, Japan).

### 2.6.6. Gene expression by real-time RT-PCR

For total RNA extraction, different samples cultured in MG-63 for 21 days were transferred into 2-mL plastic tubes containing 1.5 mL of Trizol solution (Invitrogen, USA). After brief incubation for 15 min., the treated samples were centrifuged at 12000g for 10 min./4 °C. The supernatant liquid was transferred to a new tube and 200  $\mu$ L of chloroform was added to it. After further incubation for 5 min. at room temperature, the solution was gently mixed for 15 s, followed by incubation for 5 min. at room temperature. The tubes were further centrifuged for 15 min. at 12000g/4 °C. The upper aqueous layer was transferred to an RNeasy Plus mini-spin column (Qiagen, Germany). The RNA was washed and eluted according to the manufacturer's protocol. RNA samples were reverse-transcribed into cDNA using High capacity cDNA reverse transcription kit (Applied Biosystems, USA) according to the manufacturer's protocol.

Real-time PCR conditions were optimized and were performed with SYBR Green (Applied Biosystems, USA) in an ABI Prism<sup>®</sup> 7000 Sequence Detection System (Applied Biosystems, USA). For real-time analysis, SYBR Green supermix, 5 pmol/mL of each forward and reverse primers and 5  $\mu$ L cDNA templates were used in a final reaction volume of 50  $\mu$ L and plates were loaded using a RT loading platform. Cycling conditions included an initial denaturation step of 8 min. and 45 s at 95 °C followed by 45 cycles of 30 s at 95 °C, 30 s at 58 °C, and 30 s at 72 °C. Data collection was enabled at 72 °C in each cycle. CT (threshold cycle) values were calculated using the Relative Quantification software (Applied Biosystems).

Highly purified gene-specific primers for osteopontin (OPN), collagen I, osteocalcin (OCN), Runx2, and housekeeping gene GAPDH were designed based on previous reports [30] and synthesized commercially (MWG-Biotech AG Ltd., India). Relative expression levels for each target gene were normalized by the Ct value of the housekeeping GAPDH gene using an identical procedure ( $2^{-\Delta\Delta Ct}$  formula, Perkin Elmer User Bulletin s  $\approx$  2). Each sample was analysed in triplicate.

### 2.6.7. Mineralization assay by ARS staining

Alizarin Red-S (ARS) staining was used to detect and quantify mineralization. ARS is a dye which binds calcium salts selectively and is widely used for calcium mineral histochemistry. Growth factors loaded samples with MG-63 cells (constructs) were washed three times in PBS and fixed in ice cold 70% ethanol for 1 h. These constructs were washed three times with distilled water and stained with ARS (40 mM) for 20 min. at room temperature. After several washes with distilled water,

these constructs were observed under optical microscope and the stain was desorbed with the use of 10%-cetylpyridinium chloride for 1 h. The dye was collected and absorbance read at 540 nm in microplate reader.

### 2.6.8. Statistics

Mean  $\pm$  standard deviation (SD) data of samples in triplicate ( $n = 3$ ) have been presented. Statistical comparison for different samples was shown using one way analysis of variance (ANOVA). Significant differences were presented as \*\*\*  $p < 0.001$ ; \*\*  $p < 0.01$ ; \*  $p < 0.05$ . Cases where ANOVA gave significant difference, subsequent Tukey's Honest Significant Difference (HSD) method has been adopted.

## 3. Results and discussions

In the present investigation, the main objective was to coat bio-inert E-glass fibers with materials having better corrosion properties than commonly used ceramics. Thus, HAp was selected as a coating material and as a first step, a coating was successfully developed for the first time on e-glass coupons aiming better implant-bone interaction on the substrate with high mechanical strength.

### 3.1. Characterization of the coating

Reaction of  $\text{Ca}(\text{NO}_3)_2 \cdot 4\text{H}_2\text{O}$  with  $\text{P}_2\text{O}_5$  in ethanol results in the formation of a translucent gel, which is a mixture of amorphous HAp, calcium nitrate and  $x\text{CaO} \cdot y[\text{PO}_{m+1}(\text{OH})_n(\text{OEt})_o]$  ( $x$  and  $y$ : arbitrary,  $2m + n + o = 3$ ) [31]. The gel was used for coating only after 2 h from termination of mixing, as its viscosity remains low initially. To get the desired phase, crystallinity and pore size, the coated substrates were sintered at  $850^\circ\text{C}$ . Optical microscope images after sintering showed micro-cracks on top of the coatings due to thermal-expansion co-efficient mismatch between e-glass ( $5.4 \times 10^{-6}/^\circ\text{C}$  at  $25^\circ\text{C}$ ) and HAp ( $14.75 \times 10^{-6}/^\circ\text{C}$  at  $25^\circ\text{C}$  for HAp) [32].

XRD studies (Fig. 1a) of coated substrate confirmed the presence of only hydroxyapatite phase. The major diffraction peaks found at  $31.67^\circ$ ,  $32.83^\circ$ , and  $25.79^\circ$   $2\theta$  matched well with the standard peaks of pure hydroxyapatite crystals as in JCPDS PDF #09-0432 data card. Hence the peaks can be indexed as those of the HAp having hexagonal crystal structure with space group  $\text{P6}_3/\text{m}$  [26]. The average crystallite size calculated from Debye-Scherrer equation was found to be  $26 \pm 3$  nm. The slight expansion of lattice parameters with respect to the standard values has also been observed. The "a/b" axis of the hexagonal crystal expanded from  $9.432 \text{ \AA}$  to  $9.4484 \text{ \AA}$  and "c" axis expanded from  $6.881 \text{ \AA}$  to  $6.907 \text{ \AA}$ . Accordingly, the unit cell volume of the crystal structure was also increased from  $530 \text{ \AA}^3$  (standard hydroxyapatite) to  $534.02 \text{ \AA}^3$  hinting at some effects of thermal stress. The Percentage of crystallinity calculated by using Landi's et al. method [33] was found to be moderately high ( $\sim 89\%$ ) on top surface which is desirable for *in vitro*

or *in vivo* dissolution with time. A small hump at  $30.46^\circ 2\theta$  was due to the presence of  $\beta$ -TCP phase as impurity. As expected, there was no crystalline peak in the bare substrate (Fig. 1a-i), and typical amorphous nature of e-glass was noticed.

The FTIR (Fig. 1b) spectrum of the coating showed four typical vibrational modes of  $\text{PO}_4^{3-}$  ( $\nu_1, \nu_2, \nu_3$  and  $\nu_4$ ) which are found to be present at  $962 \text{ cm}^{-1}$ ,  $472 \text{ cm}^{-1}$ ,  $1047/1089 \text{ cm}^{-1}$  and  $603 \text{ cm}^{-1}$ , respectively. The peak at  $962 \text{ cm}^{-1}$  ( $\nu_1$ ) corresponds to non-degenerate symmetry stretching of P–O bond in the  $\text{PO}_4^{3-}$  group and the peak at  $472 \text{ cm}^{-1}$  ( $\nu_2$ ) is the doubly degenerate phosphate bending mode [34]. The stretching vibration modes of  $\text{PO}_4^{3-}$  group were reflected at  $1047 \text{ cm}^{-1}$  and  $1089 \text{ cm}^{-1}$ . Another peak at  $603 \text{ cm}^{-1}$  states the presence of triply degenerate O–P–O bending ( $\nu_4$ ). The peaks at  $635 \text{ cm}^{-1}$  and  $3572 \text{ cm}^{-1}$  reflect the vibrational and intramolecular-stretching-vibrational mode of hydroxyapatite phase. Especially OH<sup>-</sup> peak at  $3572 \text{ cm}^{-1}$  and  $\text{PO}_4^{3-}$  peak at  $962 \text{ cm}^{-1}$  indicate highly crystalline nature of the coating corroborating the findings of XRD [35]. Raman spectrum (Fig. 1c) acquired from the top coated surface showed characteristic peak of  $\text{PO}_4^{3-}$  ( $\nu_1$ ) at  $961 \text{ cm}^{-1}$  which confirms the HAp phase. There were also two doubly degenerate bending mode ( $\nu_2$ ) at  $429$  and  $445 \text{ cm}^{-1}$  (P–O bond), four triply degenerate asymmetric stretching mode ( $\nu_3$ ) at  $1030, 1046, 1054$  and  $1076 \text{ cm}^{-1}$  (P–O bond), and four triply degenerate bending mode ( $\nu_4$ ) at  $582, 594, 610$  and  $620 \text{ cm}^{-1}$  (O–P–O bond) of phosphate groups present [36]. All bands are characteristically assigned to internal vibrational modes of the phosphate groups.

The FESEM images of the coated top surface after sintering (Fig. 2a) showed mainly rod-like morphology of HAp crystallites with diameters  $200\text{--}300$  nm and lengths between  $1$  and  $1.5 \mu\text{m}$ . Some plate-like morphologies with irregular surface were also observed. HAp crystallites were also found on the crack regions acting as bridge which indicates the coating coverage of the substrate surface. FESEM imaging carried out at interface (Fig. 2b) showed no interfacial gap between substrate and coating and the coating thickness was approximately  $10 \mu\text{m}$ . There was no microstructural feature at the cross-section indicating dense structure.

Further detailed study on the cross-section of microstructure using TEM (Fig. 3a–c) showed interconnectivity of pores with diameters of about  $300\text{--}500$  nm, along with certain agglomeration of crystals. The population density of HAp crystals was found to decrease with a slight increase in crystal size towards periphery of coating layer which is also a reason behind the occurrence of cracks at the surface of coating. With decreasing HAp crystal density, interconnectivity of pores increased along the outer region which were considered to be important, as they acted as path channels for supply of micronutrients and removal of cell excretions required for tissue in-growth in the scaffold [37]. Interface study confirmed firm apposition and close contact of coating with the substrate. Line scan EDX showed (Fig. 3d–e) clear demarcation of phases from substrate to coating, also showing absence of interfacial

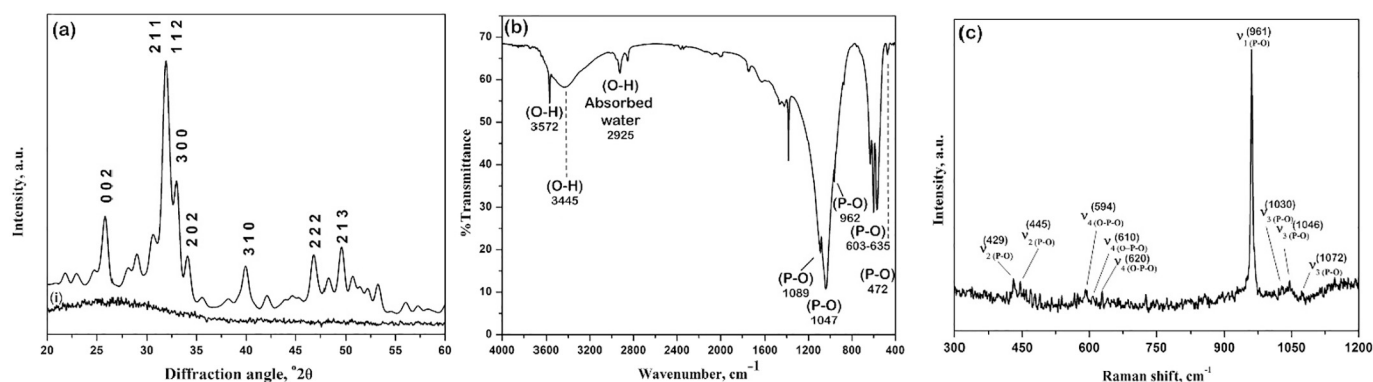


Fig. 1. (a) XRD patterns [along with bare e-glass substrate (i)], (b) FTIR and (c) Raman spectra acquired from the top coated surface.

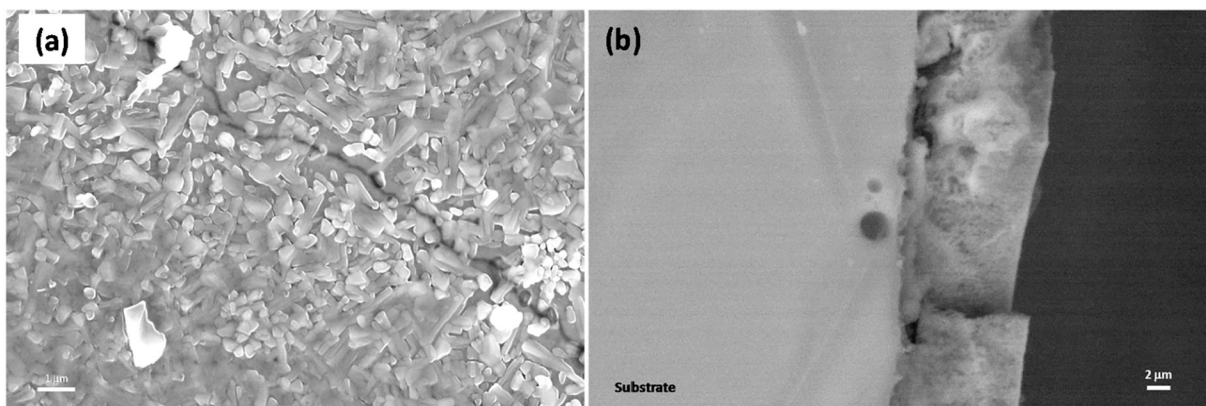


Fig. 2. FESEM microstructure of (a) top coated surface and (b) cross-sectional image showing the interface.

gap. Ca/P ratio was calculated and found to be ~1.67, which also confirms the purity of the hydroxyapatite phase and thus conforms with the XRD and FTIR analyses. The SAED patterns (Fig. 3f) of HAp layer showed clear electron diffraction rings of pure crystalline hydroxyapatite phase, for which  $d = 2.81 \text{ \AA}$  and  $d = 3.44 \text{ \AA}$  correspond to the (211) and the (002) crystallographic planes respectively, of hexagonal hydroxyapatite, which was also found to be in good agreement with the XRD findings.

### 3.2. SBF immersion study (static and quasi-dynamic)

Kinetic SBF study depends on two main factors, dissolution and deposition of ions. These mechanisms in turn depend on the differences of ionic concentration between the sample and the solution in which the former is immersed [38]. Both dissolution and deposition processes

take place simultaneously at different rates. XRD patterns of coated samples after 7 days of static bioactivity study (Fig. 4a-i) indicated the formation of calcium phosphate hydroxide  $[\text{Ca}_{10}(\text{PO}_4)_6(\text{OH})_2]$  (matched with JCPDS PDF #00-054-0022) and calcium carbonate (matched with JCPDS PDF #00-029-0305) with relative percentage of phases being 32.7% and 67.3%, respectively. High percentage of calcium carbonate is due to a higher rate of calcium deposition than its dissolution. The higher deposition of calcium carbonate can be explained by solubility products of calcium carbonate and calcium phosphate hydroxide. This phenomenon is possible only if the solubility product of calcium carbonate is higher than the solubility product of calcium phosphate hydroxide. After 14 days of immersion (Fig. 4a-ii), due to high rate of phosphate deposition, more hydroxyapatite formed (approx. 69.1%) (matched with JCPDS PDF #04-014-8416) with about 30.1% calcium carbonate. Calcium carbonate may accelerate

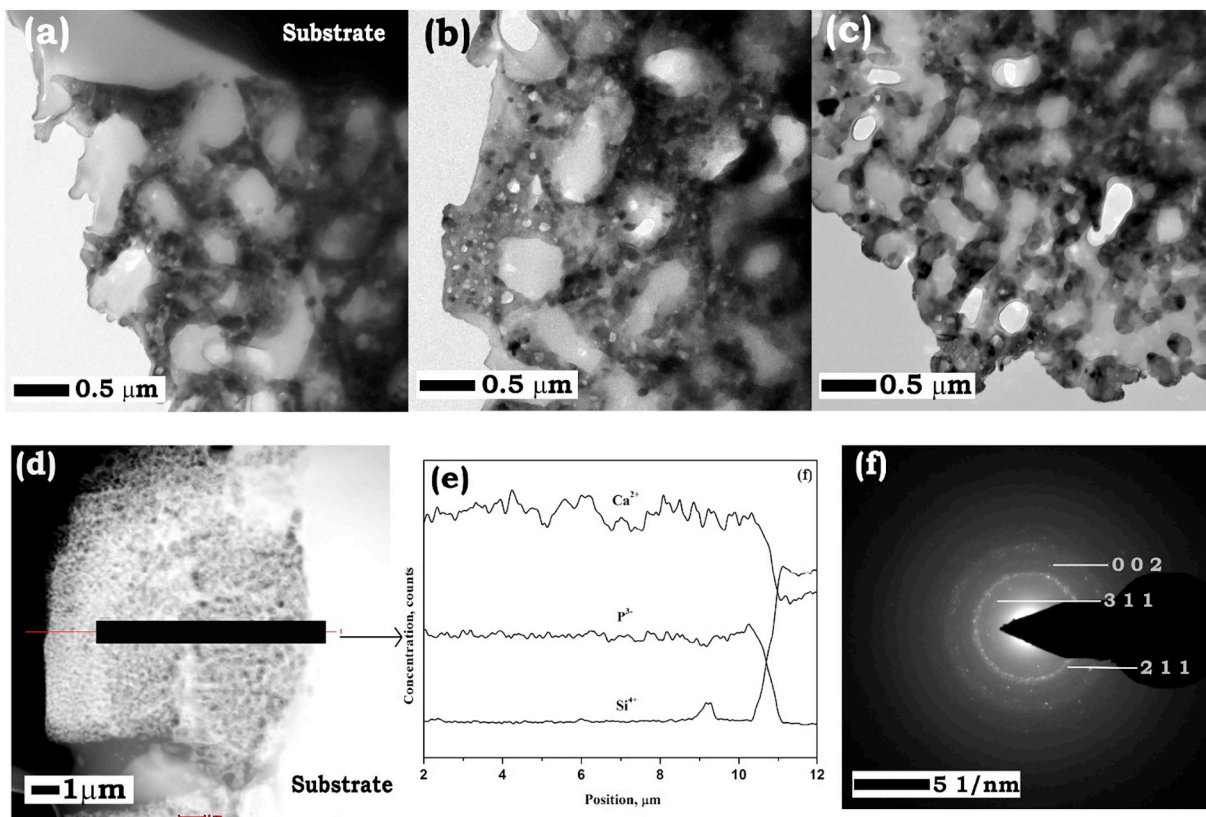


Fig. 3. Cross-sectional TEM images of coated e-glass taken at different regions showing the micro/nano-structural features of the coating's depth and the interface (a-c), EDX line scan (d and e) and SAED pattern (f).

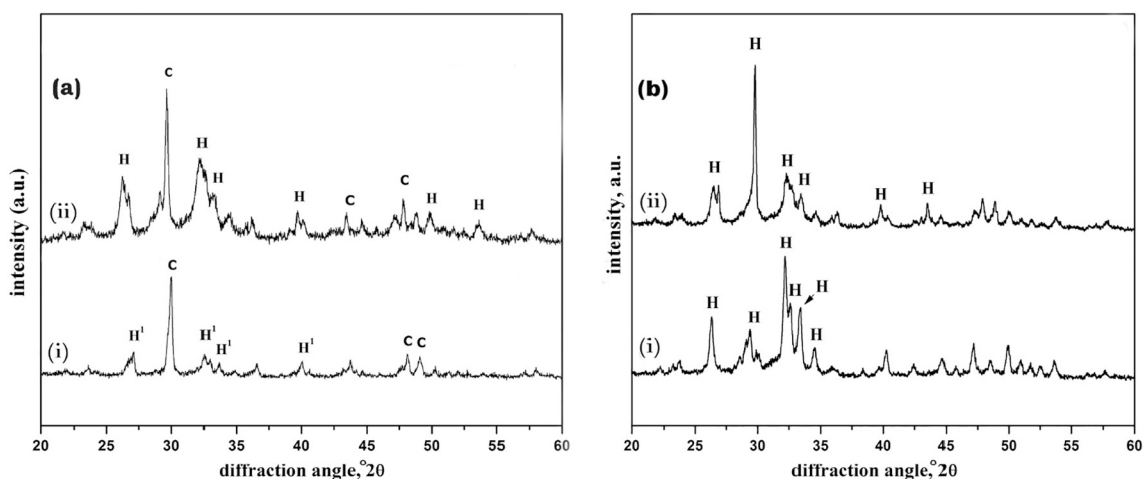


Fig. 4. XRD patterns acquired from the top surface after 7 and 14 days of (a) static and (b) quasi-dynamic SBF study [after (i) 7 and (ii) 14 days] [H = hydroxyapatite, H<sup>1</sup> = calcium phosphate hydroxide and C = calcium carbonate].

interaction between implant and body fluid as blood plasma also contains Ca<sup>2+</sup> and CO<sub>3</sub><sup>2-</sup> ions, hence creating a resemblance between the host and foreign body.

In quasi-dynamic study, deposition or dissolution process cannot be completed when the reacting SBF was replaced with fresh volume of SBF, which increased the difference in the ionic concentrations of the solution and the sample. Therefore, the characteristic peaks of hydroxyapatite (matched with JCPDS PDF #01-086-0740) were seen after 7 days (Fig. 4b-i), however, with time due to the increased difference in the ionic concentrations, the deposition rate increased. After 14 days of quasi-dynamic study (Fig. 4b-ii), the x-ray diffraction peaks of carbonated hydroxyapatite phase (matched with JCPDS PDF #00-019-0272) was seen. This phase might form due to A-type substitution (*i.e.*, carbonate replacing a hydroxyl group) or B-type substitution (*i.e.*, carbonate replacing phosphate group) or both [39].

FTIR spectrum supports the above findings, where the coated e-glass substrates after 7 and 14 days of static SBF study (Fig. 5a-i and ii) showed a decrease in PO<sub>4</sub><sup>3-</sup> peaks at 958 cm<sup>-1</sup> and CO<sub>3</sub><sup>2-</sup> peaks at 873 cm<sup>-1</sup> (related to hydroxyapatite). The presence of carbonate group could be confirmed by the peak at 2347 cm<sup>-1</sup> [35]. In addition, the decrease in peak intensity hints at a reduction in the amount of calcium carbonate phase from day 7 to 14, which corroborates with the XRD findings. The sharp peak of structural -OH group at 3572 cm<sup>-1</sup> could not be found after SBF study, which implies that the A-type substitution

by carbonate group (replacing hydroxyl group) was more prevalent [39]. The peaks representing P-O vibrations at ν<sub>2</sub> bending (~472 cm<sup>-1</sup>), ν<sub>4</sub> bending (~603 cm<sup>-1</sup>), ν<sub>3</sub> (asymmetric stretching around ~1033–1067 cm<sup>-1</sup>) indicated the presence of calcium phosphate hydroxide formation on day 7. A similar trend was noticed on day 14 as well. When subjected to quasi-dynamic SBF study (shown in Fig. 5b-i and ii), a similar reaction behaviour as that of static SBF study (with similar peaks as just mentioned) was observed. The characteristic apatite PO<sub>4</sub><sup>3-</sup> peaks were noticed at 560, 603 and 635 cm<sup>-1</sup>, while the peak at 575 cm<sup>-1</sup> appeared for crystallites of small size [40]. The increasing intensity of CO<sub>3</sub><sup>2-</sup> peak around 1428 cm<sup>-1</sup> after 14 days of the quasi-dynamic SBF study, indicates A-type substitution of carbonate group (*i.e.*, carbonate replacing a hydroxyl group) [39].

Microstructures of top surface of the samples after static SBF study are shown in Fig. 6a and b after 7 and 14 days, respectively. After 7 days (Fig. 6a), dissolution phenomena were dominant so that the needle-like structure of coated sample was missing, with concomitant deposition of calcium carbonate crystals at microcrack regions. As the solubility product of calcium carbonate is higher, it will capture nucleation sites faster than others and the cracks/edges are most favourable sites for crystal growth. Such transformed crystal structures on the top surface signifies prominence of calcium carbonate phase over calcium phosphate hydroxide phase, and was also confirmed from XRD (Fig. 4a-i) and FTIR (Fig. 5a-i). The calculated molar ratio of Ca/P from

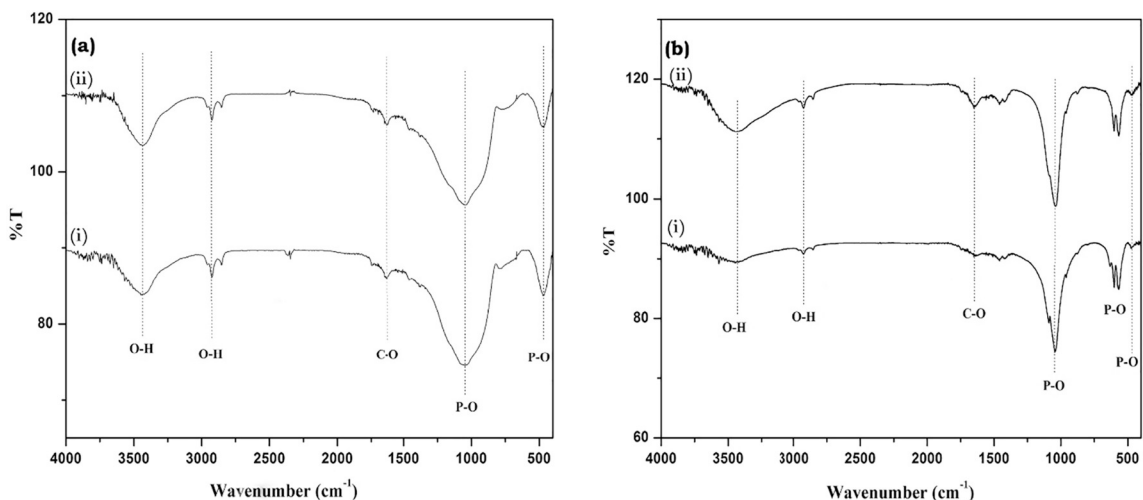


Fig. 5. FTIR spectra of the top surface after 7 and 14 days of (a) static and (b) quasi-dynamic SBF study [after (i) 7 and (ii) 14 days].



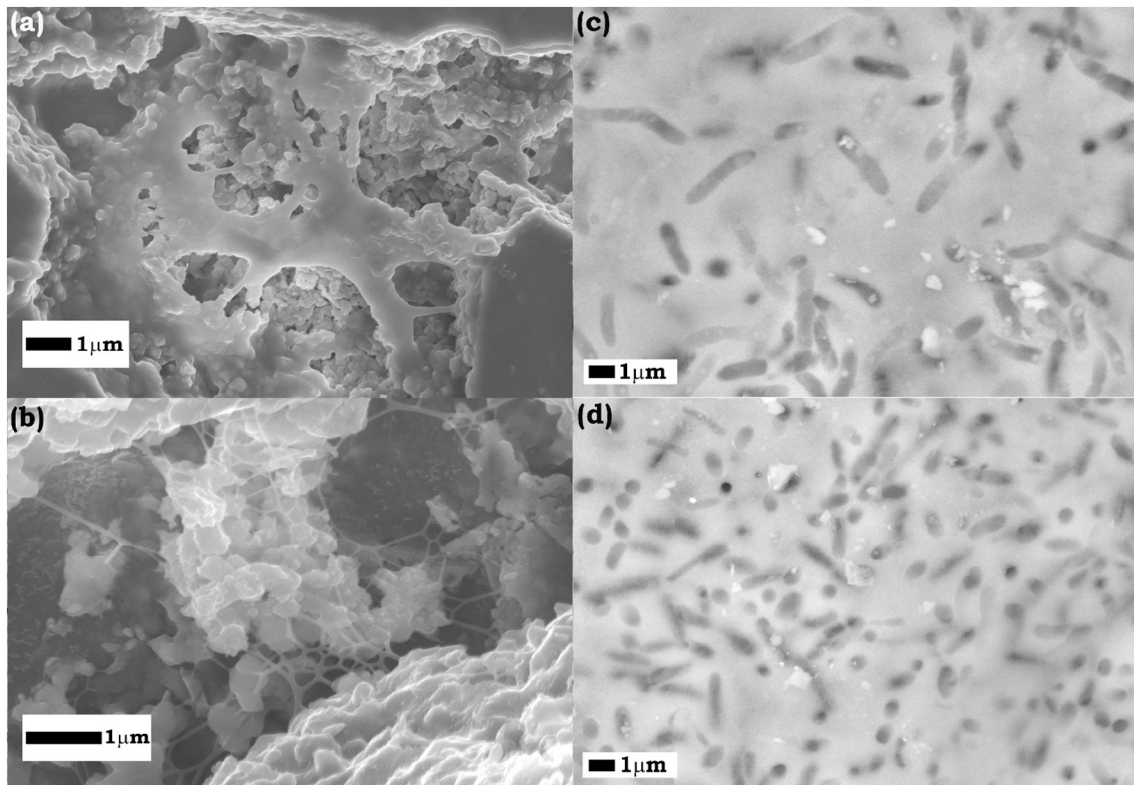


Fig. 6. Microstructure of top surface after static (a – 7 days and b – 14 days) and quasi-dynamic (c – 7 days and d – 14 days) SBF studies.

EDX data of corresponding sample was 1.4, which is the indication of non-stoichiometry [37,41]. After 14 days (Fig. 6b), fresh deposition of HAp crystals could be seen on top surface. The deposits appeared as densely populated with pores of variable dimensions, spread throughout the surface and contained cracks as well. The Ca/P molar ratio after 14 days was found to be 1.67 as calculated from EDX data. In case of quasi-dynamic SBF study, FESEM microstructure depicted a layer of apatite on the top surface of the samples after 7 days (Fig. 6c) and 14 days (Fig. 6d). For day 14, the thickness of the layer increased. Ca/P molar ratio after 7 days was 1.667 which signified the formation of hydroxyapatite phase whereas, after day 14, the ratio became ~1.87, which was the indication of carbonated-hydroxyapatite phase formation, as was also observed in XRD (Fig. 4b-ii).

TEM (Fig. 7a–e) studies revealed the formation of dense calcium phosphate hydroxide nanocrystals after 7 days of static SBF study

(Fig. 7a-inset). Apatite formation on top of the coating was found not to be in a colonised manner; rather it covered the coating surface. The absence of any interfacial gap indicates high biocompatibility and good availability of nucleation sites of the sample. Crystals could also be seen inside surface pores which act as anchor point, and can contribute in favour of increasing the adherence of the apatite layer. In lower magnification (Fig. 7b) imaging, bigger calcium carbonate nanocrystals can be seen, but with less density. EDX (Fig. 7c–d) data supported the existence of the calcium carbonate nanocrystals, by showing different calcium and oxygen ion concentrations at different regions of the coating section. These calcium carbonate nanocrystals are indicated by arrow-heads in the dark-field TEM image (Fig. 7b). The regions with higher concentration of carbon and oxygen represent the calcium carbonate crystal filled region and the rest is covered with calcium phosphate hydroxide. SAED pattern (Fig. 7e-inset) showed clear diffraction

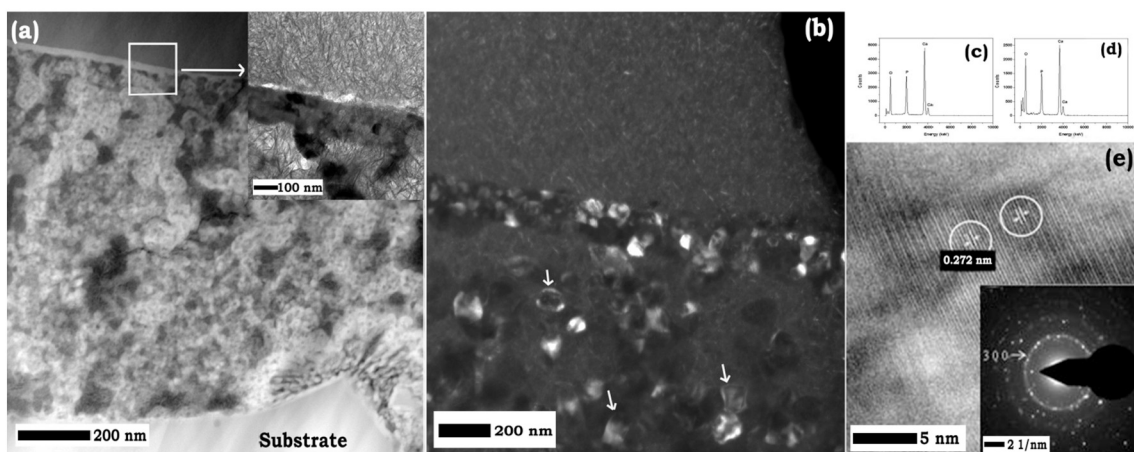


Fig. 7. TEM images of different regions after 7 days of static SBF studies; microstructure (a and the inset, b), EDX (c and d) and HRTEM showing crystalline fringes along with SAED pattern in the inset (e).

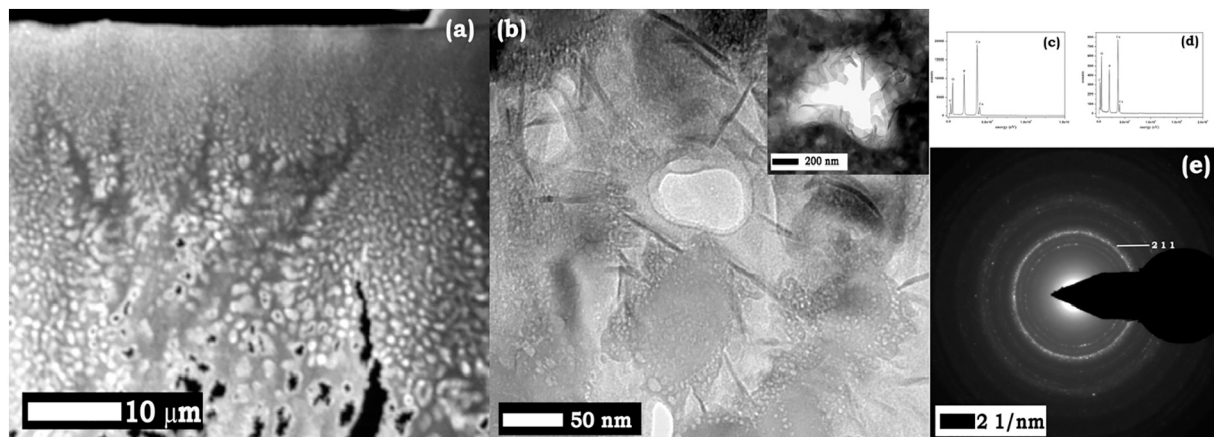


Fig. 8. TEM images of different regions after 14 days of static SBF studies; microstructure (a and b), EDX (c and d) and SAED pattern (e).

rings of crystalline calcium phosphate hydroxide of  $d = 2.72 \text{ \AA}$  corresponding to the (300) crystallographic plane.

After 14 days of static bioactivity study (Fig. 8a–b), extensive apatite deposition almost completely covering the pores of the coating was found on the outer surface. Nucleation of elongated HAP nanocrystals were seen along the periphery of the pores, and this is also the primary stage of crystal growth. Crystal growth is a thermodynamically controlled process, in which the guest crystals use host crystal surface as nucleation sites, or template, for deposition of their own phase [42]. In this case, crystals were found to be more orderly arranged than the 7-day sample which indicates settling and maturation of the crystals with time. EDX (Fig. 8c–d) showed homogeneity in concentrations of Ca and P ions in different regions proving the formation of HAP in higher percentage to be the major phase, which is also in agreement with the XRD analysis. The SAED pattern (Fig. 8e) depicted highly crystalline nature of the coating as strong diffraction rings could be observed clearly. The most prominent diffraction ring corresponds to a “d-spacing” of  $2.794 \text{ \AA}$  representing the (211) crystallographic plane of pure HAP.

In quasi-dynamic SBF study, the TEM images (Fig. 9 a,b and c,d) showed moderate crystallinity near the surface of coating after 7 and 14 days which could be corroborated by the SAED patterns of the respective samples. After 7 days, a crystalline layer composed of hydroxyapatite crystals covered the surface of HAP coated sample. However, initially after day 7, the arrangement of crystals was found to be randomly oriented, indicating the effect of daily replacement of fresh SBF. After 14 days, the population of the crystals were increased which is due to the daily layer by layer deposition of apatite. Also, the crystals were found to be smaller than those of static SBF study as they get less time to complete their crystallization process.

Ca and P ions of the supernatant liquid were analysed by ICP-AES after static and quasi-dynamic SBF study collected at day 7 and 14 and are given in Fig. 10a and b respectively. Static SBF study (Fig. 10a) showed a decrease in concentration of both calcium and phosphate ions after 7 days. This was due to the deposition of ions on the surface of coated samples, leading to the formation of calcium carbonate crystals as well. After 14 days, a slight increase in calcium and phosphate ions helped in decreasing calcium carbonate concentration and changing of phase from calcium phosphate hydroxide to HAP. The supernatant fluid after quasi-dynamic SBF study (Fig. 10b) showed a series of small changes in calcium and phosphate ion concentrations leading to variation in Ca/P molar ratio and ultimately resulting in different CaP phase/s in XRD.

From load-displacement curves, Young's modulus (E) and hardness (H) were calculated based on Oliver and Pharr method [43]. When indenter is pressed against sample, elastic and plastic deformation occurs simultaneously, resulting impression conforming indenter shape.

During unloading, displacement recovered for elastic, eventually providing elastic solution for modeling contact process. H is defined as indentation load divided by projected contact area (measured from contact depth from load-displacement curve). Thus it's the mean pressure which a material can support under load. E, on the other hand, can be calculated from initial unloading contact stiffness or the initial slope of unloading curve. We have calculated the parameters for both coated e-glass substrates (CEG) and after 7 and 14 days immersion under static (7d-s and 14d-s) and quasi-dynamic (7d-Q and 14d-Q) condition and are shown in Table 1. It has been found that both H and E of HAP coating on e-glass substrates were increased after static and QD studies. The effect is more pronounced for static SBF immersion as there is no fresh replenishment each day like QD process. Significant kinetic enhancement of H and E for static samples was due to more ordered crystalline deposition of apatites after 14 days, thus corroborating the findings of TEM. Significant increase of H and E after 7 days of QD study was due to uniform apatite crystal formation on top which became disordered after day 14 owing to daily change of fresh buffer and hence decrement of E and close values of H.

### 3.3. In vitro biocompatibility studies

#### 3.3.1. Cell viability, proliferation assay and alkaline phosphatase assay (ALP)

Cell viability (by MTT), proliferation (by Alamar blue assay) and ALP expression of MG-63 on bare and coated e-glass samples were measured on days 5, 7, 14 and 21. Maximum cell viability was recorded for coated e-glass after 21 days of cell culture (statistically significant  $**p < 0.01$ ,  $***p < 0.001$ ) (Fig. 11a). Leachates obtained after 7 and 14 days showed noticeable difference of cell viability between the control and the sample (Fig. 11a). Maximum cell proliferation in AlamarBlue™ test was recorded for coated e-glass after day 21 (statistically significant,  $*p < 0.05$ ,  $***p < 0.001$ ) (Fig. 11b). Starting from initial days, the HAP coated e-glass sample was found to be way more prone towards cell proliferation than being under control. This can be justified by the fact that the HAP coated surface exhibits a greater availability of potentially colonisable space by the grown osteoblasts, which once attached, can spread at a higher rate than the control. Another crucial factor for the cell to adhere and increase cellular activity is the adsorption of protein on the surfaces, which are abundant in case of HAP coated samples due to its interconnected porous structure [44] MTT and Alamar blue result supported each other's interpretation that both samples do not have any associated cytotoxicity. ALP expression indicates surface activity of the sample towards bone mineralization. ALP occurs at very early stages of osteogenesis and hydrolyses of the organic phosphates releasing phosphorus ions, which are important for the process of extracellular matrix mineralization. High ALP expression of

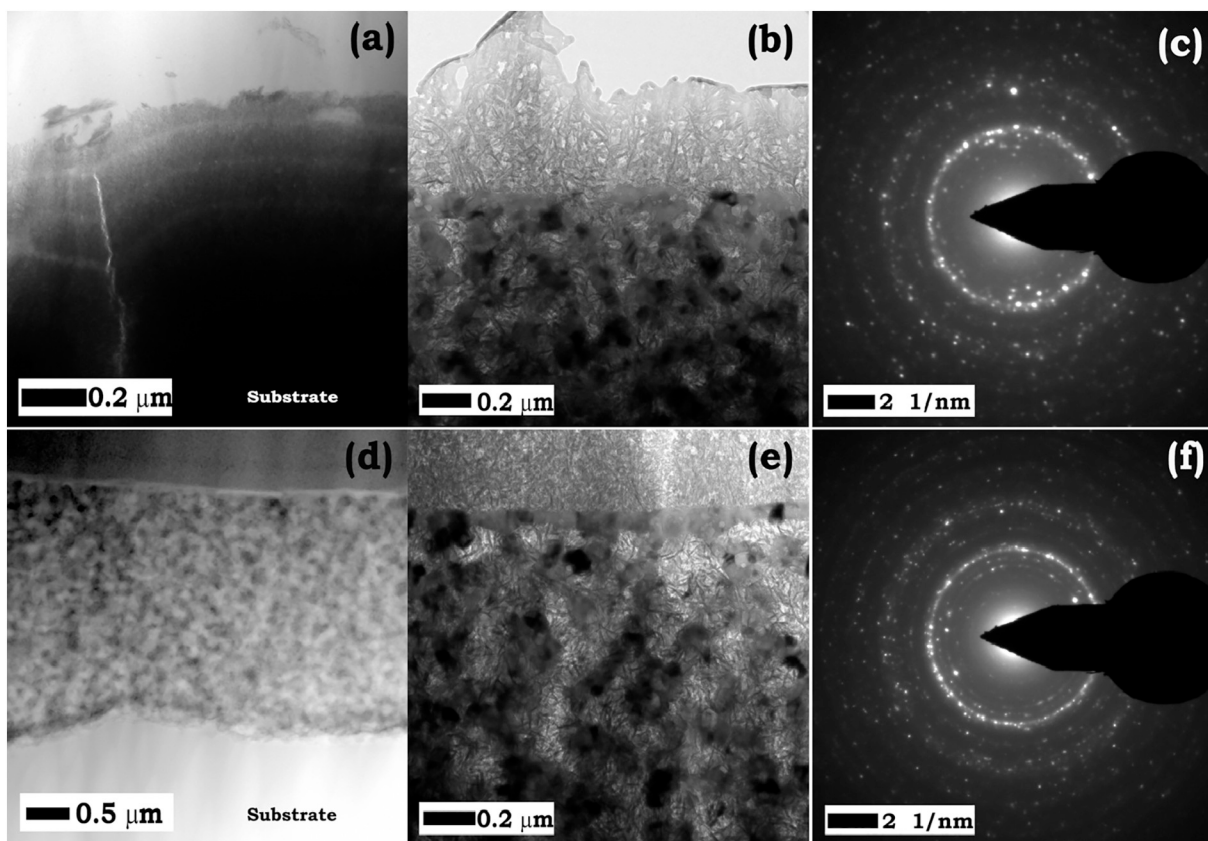


Fig. 9. TEM images of different regions after 7 and 14 days of quasi-dynamic SBF studies; (a, b and c) microstructure and SAED pattern after 7 days and (d, e and f) microstructure and SAED pattern after 14 days.

the coated sample shows higher activity, which is beneficial to the collagen fiber synthesis, formation of calcium nodules, and the maturation of bone mineralization. It also increases with the maturation of osteoblasts [45,46]. Maximum ALP expression was recorded for coated samples after 21 days of cell culture (statistically significant,  $**p < 0.01$ ,  $***p < 0.001$ ) (Fig. 11c) that clearly indicates the non-cytotoxicity as well as the bioactivity of the coated samples.

ARS staining helps to measure the mineral content of the sample which is important for apatite formation on the surface. Calcium ( $Ca^{2+}$ ) deposition was measured on day 14 and 21 (Fig. 11d). Maximum  $Ca^{2+}$  deposition was recorded for coated e-glass substrates after 21 days of cell culture (statistically significant,  $**p < 0.01$ ,  $***p < 0.001$ ).

Table 1

Nano indentation values of H and E of different samples.

Sample	H (GPa)	E (GPa)
CEG	0.05 ± 0.01	2.46 ± 0.7
7d-s	0.16 ± 0.07	11.9 ± 2.2
14d-s	1.57 ± 0.14	32.9 ± 2.4
7d-Q	0.37 ± 0.07	33.1 ± 5.7
14d-Q	0.37 ± 0.07	24.3 ± 5.3

### 3.3.2. Cell morphology within the samples by laser confocal microscopy

Cell morphology on bare and coated e-glass samples are given in Fig. 12a and b respectively. Maximum number of cells was present in

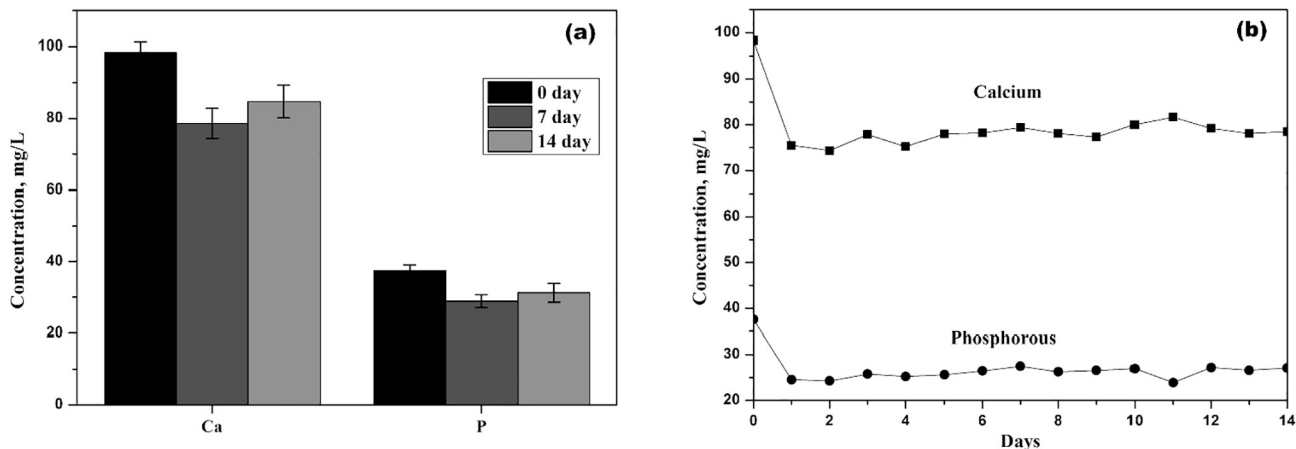


Fig. 10. Concentration of different ions of supernatant in (a) static and (b) quasi-dynamic SBF study at day 7 and 14.

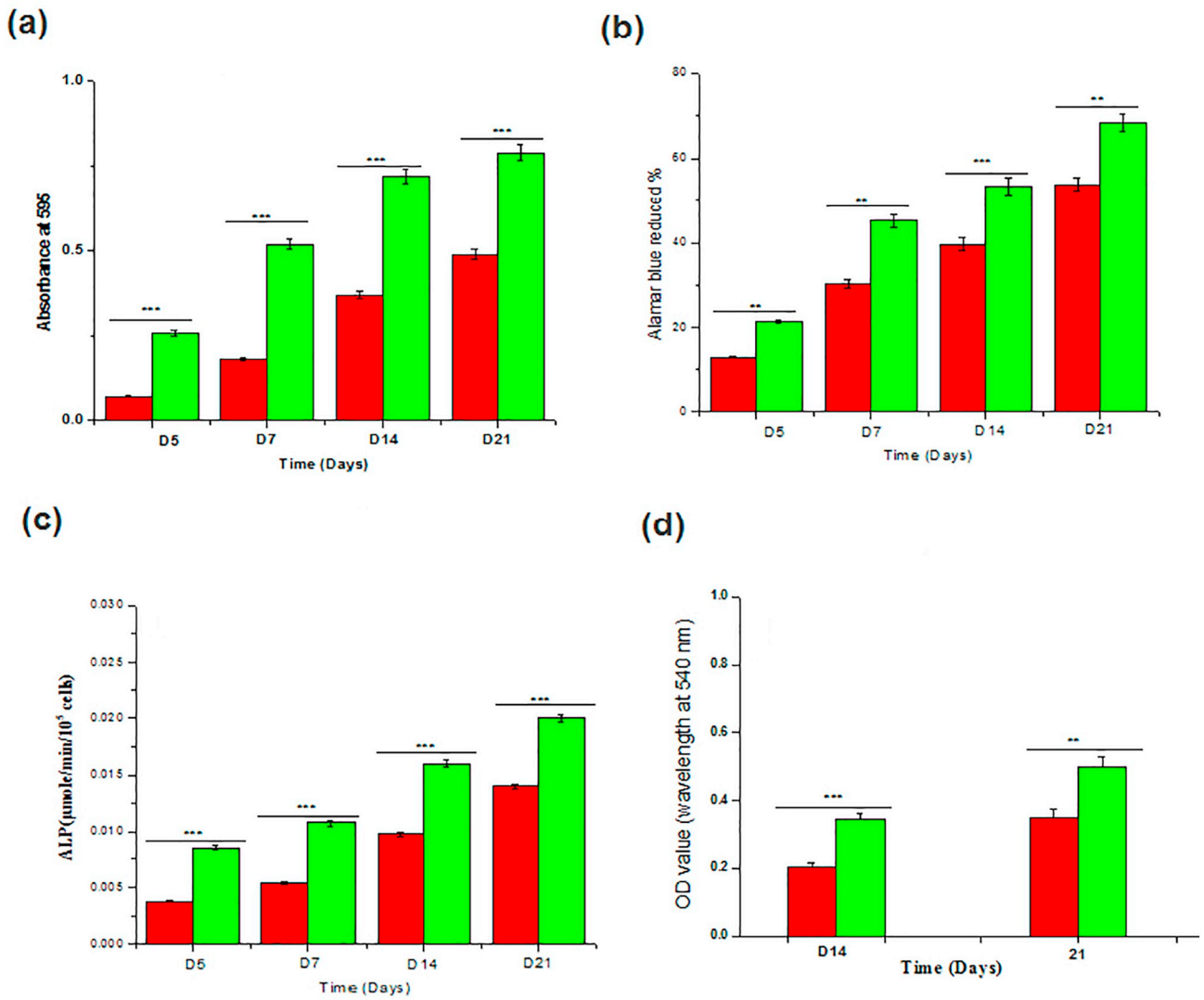


Fig. 11. Response of osteoblast like cells (MG-63) seeded on e-glass substrate and coated surfaces, cultured for 21 days at 37 °C and 5% CO<sub>2</sub> humidified atmosphere; (a) viability (b) proliferation of cells and (c) alkaline phosphatase (ALP) activity, (d) quantification of mineral deposition using ARS staining. \*\*\* p < 0.001, \*\* p < 0.01 and \* p < 0.05, n = 3 at each time point.

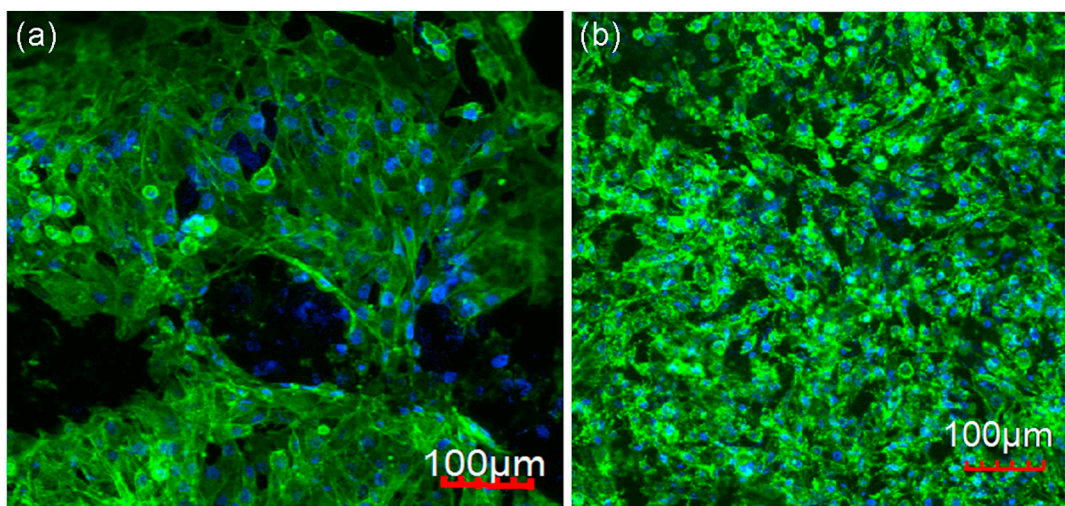


Fig. 12. Cytoskeletal actin organization and distribution of MG-63 cells grown on (a) e-glass substrate and (b) coated surface at day 7.

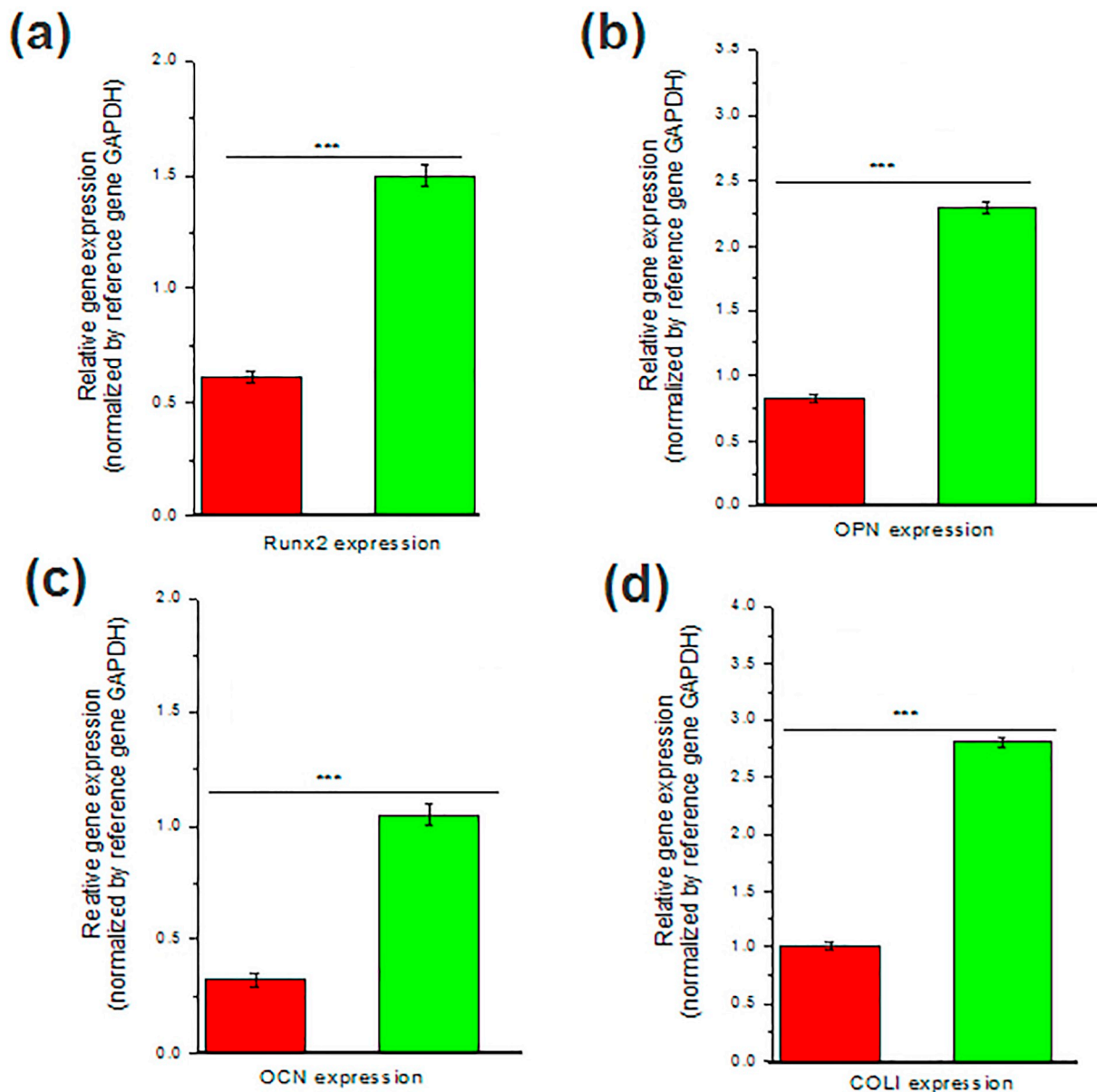


Fig. 13. Levels of mRNA for osteogenic specific genes ((a) Runx2, (b) OPN, (c) OCN and (d) COL1) of MG-63 cultured on e-glass substrate and coated surface for 3 weeks. \*\*\*  $p < 0.001$ , \*\*  $p < 0.01$  and \*  $p < 0.05$ , data are presented as mean  $\pm$  SD,  $n = 3$ .

coated e-glass compared to the bare substrate. For coated samples, actin covers the entire surface, forming neo matrix and penetrated into the sample, due to the porous nature of the coating. Since cell cytoskeleton organization is important for cell attachment and morphology, the actin filaments were stained using Alexa Fluor® 488 (green), nuclei were stained with Hoechst 33342 (blue) and examined under confocal at  $20\times$  [47]. 3D constructs were Z-scanned during confocal microscopy to examine cell growth upon different layers. Scans across multiple layers were then merged into the final image. The images showed extensive and uniform distribution of the actin filaments on coated e-glass. However, for bare e-glass, actin distribution was sparse and isolated to be present just around the cell nuclei.

### 3.3.3. Gene expression by real time RT-PCR

Gene expression involved in bone mineralization and maturation in the osteoblastic cells was analysed when in contact with the materials. Osteogenesis process evolves proteins such as osteopontin (OPN), osteocalcin (OCN), collagen type I (COL-I) and RUNX-2. In the early stages of osteoblastic development and mineralization, OPN is secreted,

and acts by binding with the organic and inorganic phase to promote tissue adhesion. OPN gene expression is also associated with increased cell adhesion [48]. Variations in mRNA expression levels of bone specific (OCN, OPN, RUNX2 and COL1) markers were detected (Fig. 13a–d) in each sample, when the samples ( $n = 3$ ) were averaged and normalized against the housekeeping gene (GAPDH). Coated e-glass showed significantly higher level of gene expression of markers such as OPN and OCN than control (bare e-glass), indicating an advanced differentiation process, osteoblastic maturation and bone mineralization.

*In vitro* biocompatibility evaluation, a basic biological test for biomaterials plays a significant role to assess cell/biomaterial interactions. A prerequisite step in the process of cell-material surface interactions is the attachment of dependent cells, which in turn can influence ensuing cellular and tissue responses [49]. The E-glass is known to be bio-inert, chemically durable, strong with high mechanical strength, and can be used as an implant when composed with other bioactive materials. HAP is classified as osteoconductive, because it supports new bone growth on the implant along bone-implant interface. Hence, e-glass can hold the mechanical integrity of the sample, while HAP provides the

necessary ingredients for bone regeneration.

Since a categorical attribute of osteoblasts is mineralization as osteogenesis matures, ALP activity and ARS mineralization assay are used to quantify such mineralization upon implants [50]. Substantial levels of mineralization lead to cells having an orderly, sheet-like structure. Increasing ALP activity over the culture duration, intensity of Alizarin Red staining, and confocal images that show stressed actin arrangement of cells upon the implants. Encouraging results were found for samples particularly with HAp coated e-glass compared to bare e-glass. Similarly, the images from confocal laser microscopy show random actin-stress fibers along with dense cell colony deposits across the coated implant and to a slightly less extent on the bare implant. Effective adherence of cells onto implants leads to formation of ordered ECM [50] and the presence of ECM is a requirement for successful tissue reconstruction. Nano-scaled structure of HAp conceivably contributes to the favourable cyto-compatibility of the implants. Progression of cell proliferation from Day 7 to Day 14 is a little slow for all the implants [Fig. 11(b)]. This slightly restricted progress may be ascribed to the cells requiring some time to adjust and adapt to the 3D matrix upon being transferred from the 2D cultures [50].

Overall, the *in vitro* analyses show that the HAp coated e-glass leads to significant improvement of implant properties in terms of biocompatibility, cell viability and proliferation, osteoinductivity and osteoconductivity. HAp coating of e-glass can potentially be utilized in fabrication of durable bioactive non-metallic implants and tissue engineering scaffolds.

#### 4. Conclusion

In the present study, the feasibility and advantages of using HAp coated e-glass as component of bone implants were assessed. The synthesized coatings were found to be purely hydroxyapatite from XRD with graded and interconnected pores all over the surface observable in TEM. The interconnected porous nature of ceramics are found to increase bioactivity by acting to up-regulate the process of osseointegration through enhanced nutrient transfer and induction of angiogenesis. From TEM studies, the pores were found to be bigger around periphery whereas tinier adjacent to substrate, which is also considered to be appropriate for nutrient supply without compromising the strength of sample while in contact with physiological fluid. After SBF immersion test, the porous surface was found to be useful for nucleation of the apatite crystals, hence increasing the feasibility and bioactivity of the sample. However, our quasi-dynamic study showed less crystallization but had significant formation of apatite layer. Overall, the *in vitro* analyses show that HAp coated e-glass leads to significant improvement of implant properties in terms of biocompatibility, cell viability and proliferation, osteoinductivity and osteoconductivity. HAp coating of e-glass can potentially be utilized in fabricating durable bioactive non-metallic implants and tissue engineering scaffolds. These results indicate the successful development of a new generation of glass/ceramic bone implant with both bioactivity (improved bone-implant interaction) and strong mechanical strength, and can be applied in loading bearing application areas.

#### 5. Statement of significance

To reconstruct the defects caused by craniectomies autologous, bone grafting was usually used, but they failed most commonly due to bone resorption, infections and donor-site morbidity. In the present investigation, an effort has been made for the first time to develop nanoporous hydroxyapatite (HAp) coating on bio-inert e-glass substrate which obviates leaching of the base glass network former/ modifier and also reduce the lack of mechanical strength with time. Sol-gel synthesis method was adopted for HAp and freeze-drying method to develop a coating on e-glass substrates/ coupons. After thorough characterization samples were evaluated for static and quasi-dynamic SBF immersion up

to 14 days. *In vitro* biocompatibility studies [including cell culture, viability, proliferation by Alamar blue assay, Alkaline Phosphatase assay (ALP), morphology, gene expression by real-time RT-PCR and mineralization assay by ARS staining] was carried out thereafter using MG-63 cell line. Interconnected porous nature of ceramics is found to increase bioactivity by acting to up-regulate the process of osseointegration through enhanced nutrient transfer and induction of angiogenesis. According to the TEM observation, pores were found to be bigger around periphery whereas tinier adjacent to the substrate, which is also considered to be appropriate for nutrient supply without compromising the strength of sample while in contact with the physiological fluid. The SBF immersion test indicated that porous surface was useful for nucleation of apatite crystals (a primary requirement of bone reconstruction *in vivo*), hence increasing the feasibility and bioactivity of the samples. However, the quasi-dynamic study showed less crystallization but a significant formation of apatite layer. Overall, *in vitro* analyses show that HAp coated e-glass leads to significant improvement of implant properties in terms of biocompatibility, cell viability, and proliferation, osteoinductivity, and osteoconductivity.

#### CRediT authorship contribution statement

**Arnab Mahato:** Writing - original draft, Methodology, Validation, Formal analysis, Investigation. **Zhang Sandy:** Validation, Investigation. **Sandip Bysakh:** Formal analysis. **Leena Hupa:** Resources. **Indraneel Das:** Investigation. **Promita Bhattacharjee:** Investigation, Formal analysis. **Biswanath Kundu:** Writing - review & editing, Formal analysis. **Goutam De:** Funding acquisition. **Samit K. Nandi:** Supervision. **Pekka Vallittu:** Supervision. **Vamsi K. Balla:** Supervision. **Manjima Bhattacharya:** Formal analysis.

#### Declaration of competing interest

The authors declare no competing financial interest and/or conflict of interest.

Further, please note that one of the co-authors Goutam De is presently associated with Institute of Nano Science and Technology, Mohali 160062, India and co-author Manjima Bhattacharya is presently associated with Department of Engineering Science and Humanities, Siliguri Institute of Technology, Techno India Group, Hill Cart Road, P.O. Sukna, Siliguri 734009, West Bengal, India.

#### Acknowledgements

The authors thank and gratefully acknowledge Department of Science and Technology (DST), Government of India for funding from Indo-Finland Bilateral Project (Sanction no. INT/FINLAND/P-11). Thanks are also due to all personnel who rendered their heartfelt association during each and every characterisation mentioned in the manuscript. Part of this study also emerged from research by BioCity Turku Biomaterials and Medical Device Research Program ([www.biomaterials.utu.fi](http://www.biomaterials.utu.fi)).

#### References

- [1] J.A. Motherway, P. Verschueren, G. Van der Perre, J. Vander Sloten, M.D. Gilchrist, 6th World Congress of Biomechanics (WCB 2010). August 1–6, 2010, Springer, Singapore, 2010, pp. 776–779.
- [2] D.M. Vasconcelos, S.G. Santos, M. Lamghari, M.A. Barbosa, *Biomaterials* 84 (2016) 262–275.
- [3] C. Reyes, E. Mason, C.A. Solares, *International Archives of Otorhinolaryngology* 18 (2014) 179–186.
- [4] J.A. Goldstein, J.T. Paliga, S.P. Bartlett, *Current Opinion in Otolaryngology and Head and Neck Surgery* 21 (2013) 400–409.
- [5] S. Honeybul, K.M. Ho, C.R. Lind, G.R. Gillett, *J. Neurotrauma* 28 (2011) 2199–2200.
- [6] J.E. Zins, C.-J. Langevin, S. Nasir, *Journal of Craniofacial Surgery* 21 (2010) 1755–1760.
- [7] C. Shuai, B. Wang, Y. Yang, S. Peng, C. Gao, *Compos. Part B* 162 (2019) 611–620.

- [8] C. Shuai, S. Li, S. Peng, P. Feng, Y. Lai, C. Gao, *Materials Chemistry Frontiers* 3 (2019) 544–562.
- [9] C. Shuai, Y. Li, G. Wang, W. Yang, S. Peng, P. Feng, *Int. J. Biol. Macromol.* 126 (2019) 1116–1124.
- [10] C. Shuai, W. Guo, P. Wu, W. Yang, S. Hu, Y. Xia, P. Feng, *Chem. Eng. J.* 347 (2018) 322–333.
- [11] P. Feng, P. Wu, C. Gao, Y. Yang, W. Guo, W. Yang, C. Shuai, *Advanced Science* 5 (2018) 1700817.
- [12] P. Feng, J. He, S. Peng, C. Gao, Z. Zhao, S. Xiong, C. Shuai, *Mater. Sci. Eng. C* 100 (2019) 809–825.
- [13] F. Bairo, G. Novajra, C. Vitale-Brovarone, *Frontiers in Bioengineering and Biotechnology* 3 (2015) 202.
- [14] P.K. Vallittu, *J. Mater. Sci.* 52 (2017) 8772–8784.
- [15] T. Engstrand, L. Kihlström, E. Neovius, A.-C.D. Skogh, T.K. Lundgren, H. Jacobsson, J. Bohlin, J. Åberg, H. Engqvist, *J. Neurosurg.* 120 (2014) 273–277.
- [16] L.L. Hench, J. Wilson, *An Introduction to Bioceramics*, World Scientific, 1993.
- [17] Q. Fu, E. Saiz, M.N. Rahaman, A.P. Tomsia, *Mater. Sci. Eng. C* 31 (2011) 1245–1256.
- [18] A. Elshahat, *Egyptian Journal of Plastic and Reconstructive Surgery* 30 (2006) 113–119.
- [19] S.M.R. Tuusa, M.J. Peltola, T. Tirri, L.V.J. Lassila, P.K. Vallittu, *J. Biomed. Mater. Res. B Appl. Biomater.* 82 (2007) 149–155.
- [20] A.K. Gosain, *Plast. Reconstr. Surg.* 114 (2004) 590–593.
- [21] M.J. Peltola, P.K. Vallittu, V. Vuorinen, A.A.J. Aho, A. Puntala, K.M.J. Aitasalo, *Eur. Arch. Otorhinolaryngol.* 269 (2012) 623–628.
- [22] J.M. Piitulainen, J.P. Posti, K.M.J. Aitasalo, V. Vuorinen, P.K. Vallittu, W. Serlo, *Acta Neurochir.* 157 (2015) 681–687.
- [23] H. Niiranen, T. Pyhälä, P. Rokkanen, M. Kellomäki, P. Törmälä, *J. Biomed. Mater. Res. A* 69 (2004) 699–708.
- [24] L.L. Hench, *J. Am. Ceram. Soc.* 74 (1991) 1487–1510.
- [25] L.L. Hench, *J. Eur. Ceram. Soc.* 29 (2009) 1257–1265.
- [26] P.S. Prevéy, *J. Therm. Spray Technol.* 9 (2000) 369–376.
- [27] T. Kokubo, *Biomaterials* 12 (1991) 155–163.
- [28] T. Kokubo, H. Takadama, *Biomaterials* 27 (2006) 2907–2915.
- [29] P. Bhattacharjee, B. Kundu, D. Naskar, T.K. Maiti, D. Bhattacharya, S.C. Kundu, *Biopolymers* 103 (2015) 271–284.
- [30] P. Bhattacharjee, D. Naskar, T.K. Maiti, D. Bhattacharya, S.C. Kundu, *RSC Adv.* 6 (2016) 26835–26855.
- [31] W. Weng, J.L. Baptista, *J. Mater. Sci. Mater. Med.* 9 (1998) 159–163.
- [32] Y.W. Gu, K.A. Khor, P. Cheang, *Biomaterials* 24 (2003) 1603–1611.
- [33] E. Landi, A. Tampieri, G. Celotti, S. Sprio, *J. Eur. Ceram. Soc.* 20 (2000) 2377–2387.
- [34] R.N. Panda, M.F. Hsieh, R.J. Chung, T.S. Chin, *J. Phys. Chem. Solids* 64 (2003) 193–199.
- [35] L. Berzina-Cimdina, N. Borodajenko, *Research of Calcium Phosphates Using Fourier Transform Infrared Spectroscopy, Infrared Spectroscopy-Materials Science, Engineering and Technology*, InTech, 2012.
- [36] S. Koutsopoulos, *J. Biomed. Mater. Res.* 62 (2002) 600–612.
- [37] G.A. Stanciu, I. Sandulescu, B. Savu, S.G. Stanciu, K.M. Paraskevopoulos, X. Chatzistavrou, E. Kontonasaki, P. Koidis, *Journal of Biomedical & Pharmaceutical Engineering* 1 (2007) 34–39.
- [38] D. Shi, G. Jiang, J. Bauer, *J. Biomed. Mater. Res.* 63 (2002) 71–78.
- [39] M.E. Fleet, X. Liu, P.L. King, *Am. Mineral.* 89 (2004) 1422–1432.
- [40] D.S. Brauer, N. Karpukhina, M.D. O'Donnell, R.V. Law, R.G. Hill, *Acta Biomater.* 6 (2010) 3275–3282.
- [41] H.M. Kim, T. Himeno, M. Kawashita, T. Kokubo, T. Nakamura, *J. R. Soc. Interface* 1 (2004) 17–22.
- [42] F.B. Bagambisa, U. Joos, W. Schilli, *J. Biomed. Mater. Res.* 27 (1993) 1047–1055.
- [43] W.C. Oliver, G.M. Pharr, *J. Mater. Res.* 7 (1992) 1564–1583.
- [44] A.A. El Hadad, E. Peon, F.R. Garcia-Galvan, V. Barranco, J. Parra, A. Jimenez-Morales, J.C. Galvan, *Materials* 10 (2017) 94.
- [45] A.G. Dias, M.A. Lopes, A.T. Trigo Cabral, J.D. Santos, M.H. Fernandes, *J. Biomed. Mater. Res. A* 74 (2005) 347–355.
- [46] H. Liao, A.-S. Andersson, D. Sutherland, S. Petronis, B. Kasemo, P. Thomsen, *Biomaterials* 24 (2003) 649–654.
- [47] R. Ravichandran, J.R. Venugopal, S. Sundarajan, S. Mukherjee, S. Ramakrishna, *Biomaterials* 33 (2012) 846–855.
- [48] R.F. do Prado, F.S. de Oliveira, R.D. Nascimento, L.M.R. de Vasconcelos, Y.R. Carvalho, C.A.A. Cairo, *Mater. Sci. Eng. C* 52 (2015) 194–203.
- [49] T.V. Kumari, U. Vasudev, A. Kumar, B. Menon, *Trends in Biomaterials and Artificial Organs* 15 (2002) 37–41.
- [50] P. Bhattacharjee, D. Naskar, H.-W. Kim, T.K. Maiti, D. Bhattacharya, S.C. Kundu, *Eur. Polym. J.* 71 (2015) 490–509.



# Applications of Different Bioactive Glass and Glass-Ceramic Materials for Osteoconductivity and Osteoinductivity

Arnab Mahato<sup>1</sup>, Biswanath Kundu,<sup>1,\*</sup> Prasenjit Mukherjee<sup>2</sup> and Samit Kumar Nandi<sup>3</sup>

<sup>1</sup>Bioceramics and Coating Division, CSIR-Central Glass and Ceramic Research Institute, Kolkata, India

<sup>2</sup>Department of Teaching Veterinary Clinical Complex, West Bengal University of Animal and Fishery Sciences, Mohanpur, India

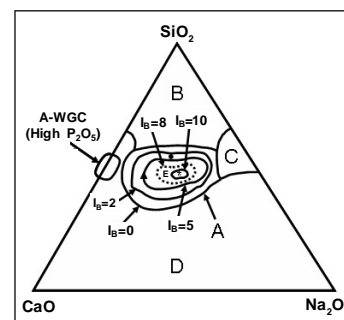
<sup>3</sup>Department of Veterinary Surgery and Radiology, West Bengal University of Animal and Fishery Sciences, Kolkata, India

[MS received December 06, 2016; Revised copy received July 21, 2017; Accepted July 24, 2017]

## ABSTRACT

Throughout the world, research has been carried out in development of new methods and materials involving multidisciplinary approach for effective bone tissue repair and regeneration. Amid various biomaterials, bioactive glass material has drawn considerable attention due to their superior biocompatibility, degradability, ion leaching phenomena and propagation of osteogenic cells. In this concise review, effort has been made to summarize different material combinations available as composition to elaborate their biological properties both *in vitro* and *in vivo*, reaction kinetics in simulated body fluid, effect of different constituents of bioactive glass and glass-ceramic compositions, porosity, etc and finally these materials' applications as bone graft substitutes and various clinical applications have been detailed. In this review an attempt has been made to sum up the recent advancement of different bioactive glass and composite materials for osteoconductivity and osteoinductivity in orthopaedic surgical challenges.

[Keywords: Bioactive glass, Bioglass®, Osteoconductivity, Osteoinductivity, Hydroxycarbonate apatite, 45S5, S53P4, Bone graft]



## Introduction

For effective bone tissue repair and regeneration research has been carried out in designing of new materials involving multidisciplinary approach. Numerous scaffold systems for bone tissue engineering have been introduced with novelty in scaffolds' design, drug and protein growth factors impregnation, mechanical strength and neo bone forming ability, etc. Nonetheless, autograft has still no alternative way for bone tissue repair. Autografts fail to meet in general medical requirement for orthopaedic implants. Alternative sources of allograft and xenograft are detrimental as may cause disease transmission and immune rejection. Accordingly, synthetic material plays a crucial role to meet the vast demand, apart from its limitations of strength, properties of osteoconduction, osteoinduction, osseointegration and biodegradation. To overcome such drawbacks, current research has been paying attention on improvement of newer biomaterials, enhanced alteration of structural and mechanical properties, performance enhancement of biocompatibility,

osteoinductivity and addition of osteogenic cells onto scaffolds to trigger bone renewal.

During bone healing, extracellular matrix (ECM) containing collagen fibre and mineralized calcium phosphate is released from osteoblasts.<sup>1, 2</sup> A biomaterial scaffold having three-dimensional (3D) fibrous structure mimicking the ECM is prerequisite for successful bone regeneration in non load bearing defects.<sup>3-5</sup> Moreover, the scaffolds should not show any inflammatory or immunogenic reaction, be bioactive (ability to bond with bone) and bioresorbable, permit new bone formation, be cost effective, easily sterilizable, have optimal mechanical properties<sup>6-9</sup> and controllable interconnected porosity with pore diameter of no less than 100  $\mu\text{m}$  (allow cells to grow within pores and angiogenesis).<sup>10-12</sup>

In bone tissue engineering, a number of biomaterials are presently being used as bone graft alternatives that include bioceramics, magnesium phosphate, sulfate, carbonate, calcium silicate and collagen. Some other materials, like metal alloys (titanium, cobalt-chrome), ceramics (zirconia, alumina), are also being used for the same purpose, but having the drawbacks of resorbability and impaired osseointegration at the bone-implant

\*Corresponding author; email: biswa\_kundu@rediffmail.com, bkundu@cgcri.res.in



interface. However, synthetic biodegradable polymers, like polycaprolactone (PCL), polyethylene glycol (PEG) and polylactic-co-glycolic acid (PLGA), show positive interaction with cells without any deleterious effects in body system.<sup>13, 14</sup>

Amid various biomaterials, bioactive glass material has drawn considerable attention due to their superior biocompatibility, degradability, ion leaching phenomena, enhancing the adhesion and production of osteogenic cells.<sup>15, 16</sup> Mechanism of ion leaching includes exchange of monovalent cations ( $\text{Na}^+$  or  $\text{K}^+$ , with  $\text{H}_3\text{O}^+$ ) from glass, increase in pH of solution as a consequence which enables osteoblast synthesis subsequently.<sup>17, 18</sup> The macroporous structure with large surface areas of bioactive glass favours bone bonding.

Pores of bioactive glass are also advantageous for resorption and bioactivity<sup>19</sup> with nearly ten times more strength than the contact osteogenesis.<sup>20</sup> High modulus and brittle nature limits its potential widespread application and thus used widely as coating of metal implants which forms calcium-deficient carbonated calcium phosphates with time.

The aim of this review is to summarize the current advancement of different bioactive glass and glass-ceramic materials for osteoconductivity and osteoinductivity in orthopaedic surgical challenges.

### Bioactive Glass Materials

Prof. L. L. Hench discovered (in the year 1969) that various compositions of glasses, when implanted to living tissues, could bond chemically with bone.<sup>21-43</sup> These 'bioactive glasses', since discovery, have mostly been used as bone substitutes for repair of damaged tissues.<sup>31, 44</sup> certain compositions of the same formed bond with soft tissues and bone as well.<sup>40, 41, 45</sup> Kinetic modification of surfaces when implanted *in vivo*,<sup>26, 29</sup> and formation of hydroxycarbonate apatite (HCA) on top leading to bonding at interface with tissues are some of very interesting characteristics of these bioactive glasses. An interface is developed between materials and tissues that oppose considerable mechanical forces. Faster surface reaction leads to faster bonding with living tissues, however, with low mechanical properties.

To make the glass surface with enhanced surface reactivity in contact with physiological fluids, high amounts of CaO and  $\text{Na}_2\text{O}$  are added (with relatively high CaO/ $\text{P}_2\text{O}_5$  ratio).<sup>46</sup> Bioactive glasses with no Na or with novel dopants have also been developed over last few years which include fluorine,<sup>47</sup> magnesium,<sup>48, 49</sup> strontium,<sup>50-52</sup> iron,<sup>53</sup> silver,<sup>54-57</sup> boron,<sup>58-61</sup> potassium<sup>62</sup> or zinc.<sup>63, 64</sup>  $\text{Ag}_2\text{O}$  impregnated bioactive glass compositions reduce microbes due to antimicrobial efficacy of  $\text{Ag}^+$  ions.<sup>56, 65</sup> Texture of the matrix could be tailored by using sol-gel method to obtain controlled  $\text{Ag}^+$  delivery.  $\text{B}_2\text{O}_3$  in CaO- $\text{SiO}_2$  system enhances bioactivity due to presence of more soluble boric compounds, leading to supersaturation of  $\text{Ca}^{2+}$  ions of SBF (simulated body fluid)

and thus Si-OH groups of borosilicate glass helped apatite formations as it acted as nucleation sites.<sup>66</sup> Moreover, zinc addition helps in better cell attachment by maintaining the pH of SBF solution as well as causes osteoblast proliferation. Figure 1 shows  $\text{Na}_2\text{O}$ -CaO- $\text{P}_2\text{O}_5$ - $\text{SiO}_2$  glass composition (constant 6 wt% of  $\text{P}_2\text{O}_5$ ) dependence for hard and soft-tissue bonding. Region A is the bioactive-bone bonding boundary, composition of which forms bond with bone. Region B (e.g. composition of those silica glasses have applications including window, bottle or slides of microscope) behaves almost inert and forms fibrous morphology at implant-tissue interface. Region C compositions are resorbable, which, within a day disappears when implanted. Region D is not practical technically and not tested *in vivo*. Collagen part of soft-tissues usually adheres strongly in case of glass compositions shown in region E (Fig. 1).

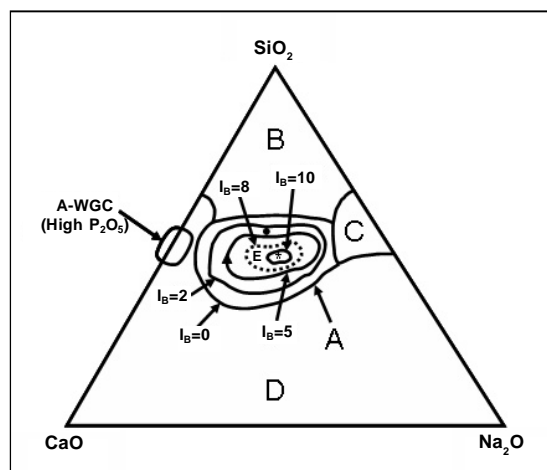


Fig. 1 –  $\text{Na}_2\text{O}$ -CaO- $\text{P}_2\text{O}_5$ - $\text{SiO}_2$  based bioactive glass and glass-ceramics compositions and their influence on hard and soft tissue bonding; Region A has constant 6 wt%  $\text{P}_2\text{O}_5$  composition, soft tissue bonding at region E is inside dashed line with bioactivity index (level of bioactivity of a material related to the time with >50% of interface bonded)  $I_b > 8$  [\*: 45S5 Bioglass®, ▲: Ceravital®, ●: 55S4.3 Bioglass®, (...): soft-tissue bonding;  $I_b = 100/t_{0.5bb}$ , where  $t_{0.5bb}$  is the time with more than 50% of implant surface bonded to surrounding bone<sup>29, 46</sup>]

Melt-quench is still the most popular method to develop bioactive glasses<sup>67-73</sup> followed by sol-gel method.<sup>74, 75</sup> In the sol-gel method, metal-organic and metal-salt precursors are used for sol preparation first, followed by gel formation with time which includes completion of reaction and/or aggregation and finally heat treatment with stepwise drying, removal of organics and crystallization.<sup>76</sup> It is a low temperature phenomenon for development of porous glasses with high specific surface area.<sup>77</sup> Recently, both micron and nano-scale particles have been developed as a part of this application<sup>57, 78, 79</sup> including, combining biodegradable polymers and bioactive glass.<sup>80-85</sup> Bioactive glass-ceramics having both osteoconduction and osteoinduction properties are classified as Class A bioactive materials<sup>44, 71, 86, 87</sup> and only osteoconductivity

as Class B materials. Bioactive glass, if heated above its **crystallization temperature** (610°-630°C), **produces bioactive glass-ceramics**<sup>71, 78, 88, 89</sup> and during the heating process, parent glass shrinks, porosity reduces and mechanical strength increases.<sup>87</sup> However, bioactive glasses are not being used presently as an alternative to load-bearing implants owing to their limited strength and low fracture toughness,<sup>44, 87, 88, 90</sup> and thus, it still remains an orthopaedic challenge.<sup>91, 92</sup>

### Reaction Kinetics

Bioactive glass, when comes in contact with simulated body fluid (SBF) or tris buffer saline (TBS), following simultaneous reactions occur<sup>20, 46, 86, 93-95</sup> (Fig. 2):

- 1) Exchange of H<sup>+</sup> or H<sub>3</sub>O<sup>+</sup> with alkali or **alkaline earths** of glass network with interfacial pH typically more than 7.4.
- 2) Local release of silicic acid [Si(OH)<sub>4</sub>] by actions of hydroxyl ions with -Si-O-Si-O-Si-. For glasses with >60% silica content, dissolution rate decreases with increase of bridging oxygens of such glasses. Subsequently, there is structural rearrangements of Si-OH by polycondensation and silica rich gel.
- 3) Formation and precipitation of amorphous calcium-phosphate rich layer came from **glass and solution and** further crystallization to carbonated hydroxyapatite (HCA).

Hydrated silica actually helps for growth of HCA and it is almost established that above reaction mechanisms are neither dependent on presence of living tissues nor *in vivo* conditions and can occur in contact with water as well. However, subsequent bond with surrounding tissues depends on the following:

- 1) Attachments of biological substance on HCA-SiO<sub>2</sub> layer
- 2) Activity of macrophages or phagocytes
- 3) Stem cell attachment

- 4) Differentiation
- 5) Cell matrix formation and
- 6) Mineralization

To study the silicate glasses, which is considered to be an inorganic silicon 'polymer' cross-linked by oxygen, elucidation of network connectivity or cross-link density is vital.<sup>96</sup> Network connectivity refers average number of additional cross-linking bonds (essentially more than two) other than oxygen, which forms network anchor. This is based on comparative number of network-forming oxides (bridging oxygens) and network-modifiers (non-bridging oxygens).<sup>97</sup> The network connectivity of a glass can dictate various physical properties including its solubility.<sup>98</sup> Silicate network formers with low network connectivity (low molecular mass as well) are potentially bioactive owing to their ease to go into solution and increased solubility.<sup>97</sup> Glass properties have also been determined by substitution of sodium oxide for calcium oxide.<sup>99</sup> The basis of bioactive glass systems should be mole per cent substitutions than weight per cent when considered on a structural level. Weight per cent basis may hide the composition-property relationships of bioactive glass owing to non-calculation of the degree of disruption of the glass network.<sup>99, 100</sup> In order to maintain same numbers of non-bridging oxygen, one mole of NaO should be added if one mole of CaO is removed from a highly disrupted glass network to maintain same network connectivity value. Wallace *et al.*<sup>97</sup> used this concept for designing bioactive glass compositions having controllable physico-chemical and biological properties.

### Fabrication

Different methods of fabrication and post heat-treatment have important role on properties of bioactive glass and glass-ceramics subsequently. Many researchers described different fabrication methods including sugar or salt leaching, microsphere emulsification sintering, foam

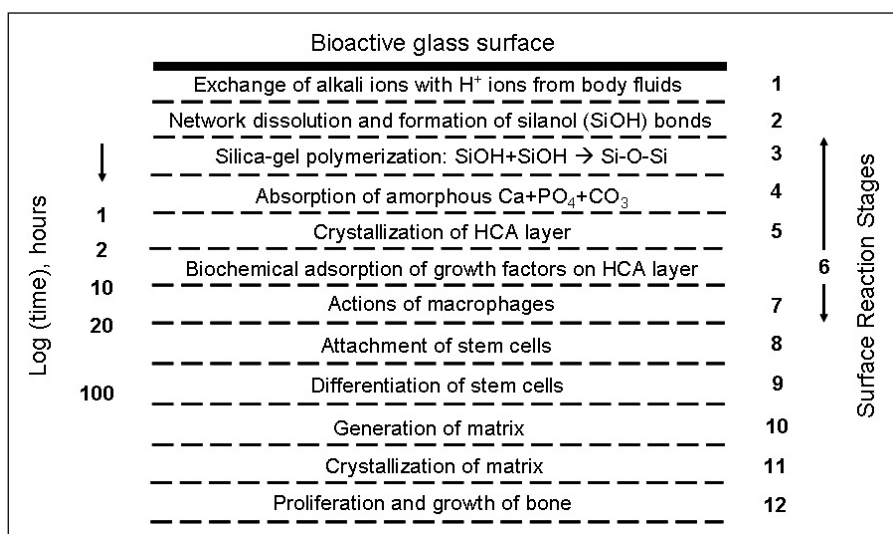


Fig. 2 – Typical reaction kinetics for forming bond between bone and bioactive glass<sup>86, 95</sup>

replication, temperature dependent phase separation, electro-spinning, rapid prototyping, etc after optimizing structure, properties and mechanical integrity of scaffolds,<sup>101, 102</sup> textile and foam coating methods<sup>103–105</sup> and biomimetic approach.<sup>106, 107</sup> Another area of research which is of significance in bone-tissue engineering is mimicking the nanostructure of natural bone by designing and incorporating nano-topographic features on surface.<sup>72, 108–110</sup> Many researchers have also raised the scaffold manufacturing procedure to a height.<sup>68, 70, 85, 105, 111, 112</sup>

Polymeric materials and foaming agents are added to form the pores of bioactive glass and glass-ceramics.<sup>113</sup> Rainer *et al.*<sup>114</sup> used bioactive glass-loaded polyurethane foam (*in situ*) for preparation of scaffolds of bone tissue engineering. This method was found to be very suitable for 3D processing and tailor-made applications in reconstructive surgery. Lin *et al.*<sup>115</sup> reported porous bioactive glass-ceramics up to preclinical trial and used polyethylene glycol (HO(C<sub>2</sub>H<sub>4</sub>O)-nH) with particle sizes ranging between 5 and 500 μm as foaming agent prior to obtaining porous scaffolds. Due to uniform distribution of

porous channels (as seen from microstructures), better bony in-growth and bioresorption of implants could be seen. Similar type of porosity can be generated by addition of organic polymers, e.g. dry/wet woods, crops (from food processing and wood finishing)<sup>116</sup> to completely degrade at temperatures above 600°C and make the scaffold porous. Apatite layers formed when bioactive glasses are used *in vitro / in vivo*, also closely depend on variations of texture properties (pore size, volume, structure) of biomaterials. For example, owing to higher surface area and pore volume, apatite formation and thus bioactive behaviour were greatly enhanced.<sup>117</sup>

In the SiO<sub>2</sub>-Na<sub>2</sub>O-CaO-P<sub>2</sub>O<sub>5</sub> glass system (like ordinary soda-lime-silica glasses), certain percentages with specific proportions of the compositions show bonding to bone<sup>26, 31, 33, 37, 47, 61, 118–127</sup> (Table I).

### Bioactive Glass as Bone Graft Substitute

Bioactive glasses in the form of porous implants, fibers and microspheres and being bioactive (interact with the body) show both osteoconductive and osteoinductive

Table I : Different bioactive glasses

Sl. No.	Name of the bioactive glass	Composition (%)												
		SiO <sub>2</sub>	P <sub>2</sub> O <sub>5</sub>	CaO	Ca(PO <sub>3</sub> ) <sub>2</sub>	CaF <sub>2</sub>	MgO	MgF <sub>2</sub>	Na <sub>2</sub> O	K <sub>2</sub> O	Al <sub>2</sub> O <sub>3</sub>	B <sub>2</sub> O <sub>3</sub>	Ta <sub>2</sub> O <sub>5</sub> /TiO <sub>2</sub>	ZnO
1.	45S5 Bioglass® <sup>31</sup>	45	6	24.5	–	–	–	–	24.5	–	–	–	–	–
2.	45S5.4F Bioglass® <sup>31, 118</sup>	45	6	14.7	–	9.8	–	–	24.5	–	–	–	–	–
3.	45B15S5 Bioglass® <sup>119, 120</sup>	30	6	24.5	–	–	–	–	24.5	–	–	15	–	–
4.	52S4.6 Bioglass® <sup>121</sup>	52	6	21	–	–	–	–	21	–	–	–	–	–
5.	55S4.3 Bioglass® <sup>121</sup>	55	6	19.5	–	–	–	–	19.5	–	–	–	–	–
6.	KGC Ceravital® <sup>26</sup>	46.2	–	20.2	25.5	–	2.9	–	4.8	0.4	–	–	–	–
7.	KGS Ceravital® <sup>26</sup>	46	–	33	16	–	–	–	5	–	–	–	–	–
8.	KGy213 Ceravital® <sup>26</sup>	38	–	31	13.5	–	–	–	4	–	7	–	6.5	–
9.	A/W glass-ceramics <sup>37</sup>	34.2	16.3	44.9	–	0.5	4.6	–	–	–	–	–	–	–
10.	MB glass-ceramics <sup>33</sup>	19-52	4-24	9-3	–	–	5-15	–	3-5	3-5	12-33	–	–	–
11.	S45P7 <sup>122</sup>	45	7	22	–	–	–	–	24	–	–	2	–	–
12.	S53P4 <sup>123</sup>	53	4	20	–	–	–	–	23	–	–	–	–	–
13.	13-93 <sup>124</sup>	53	4	20	–	–	5	–	6	12	–	–	–	–
14.	4-Mar <sup>125</sup>	50.5	1	22.5	–	–	6	–	5	15	–	–	–	–
15.	18-04 <sup>125</sup>	54.5	4	20	–	–	4.5	–	15	–	–	2	–	–
16.	23-04 <sup>125</sup>	56.25	1	20	–	–	4.5	–	5	11.25	–	2	–	–
17.	H2-02 <sup>61</sup>	53	2	22	–	–	4.5	–	6	11	0.5	1	–	–
18.	CEL-2 <sup>47</sup>	45	3	26	–	–	7	–	15	4	–	–	–	–
19.	55S <sup>126</sup>	55	4	41	–	–	–	–	–	–	–	–	–	–
20.	H <sup>127</sup>	46.2	2.6	26.9	–	–	–	–	24.3	–	–	–	–	–
21.	HZ5 <sup>127</sup>	44.4	2.5	25.9	–	–	–	–	23.4	–	–	–	–	3.8
22.	HZ10 <sup>127</sup>	42.5	2.4	4.8	–	–	–	–	22.5	–	–	–	–	7.8
23.	HZ20 <sup>127</sup>	38.8	2.2	22.6	–	–	–	–	20.5	–	–	–	–	15.9

properties.<sup>128</sup> Bioactivity is mostly due to the SiO<sub>2</sub> content; presence of 45-52% SiO<sub>2</sub> lift up the bonding of bioglass with bone.<sup>129</sup> The bioactivity and biocompatibility of bioactive glass increase when it is combined with hydroxyapatite<sup>130</sup> and ultimately leads to increased mechanical strength in comparison with calcium phosphate when used alone. The mechanism behind that is a silicate-rich layer is formed in contact with body fluids leading to strong mechanical graft-bone bonding. That triggers formation of hydroxyapatite layer. As a result new bone formation accompanied by protein absorption occurs, which, in turn, attracts mesenchymal stem cells, macrophages and osteoprogenitor cells. Consequently, osteoblasts are produced by dissemination of osteoprogenitor cells into matrix.<sup>129, 131</sup> Owing to sub-optimal mechanical properties of bioactive glass, other ceramic components are occasionally reinforced with the bioactive glass. Alternate way to increase mechanical strength and biological absorbability of SiO<sub>2</sub>-CaO bioactive glass is incorporation of Na<sub>2</sub>O into bioactive glass by sol-gel process, leading to formation of a hard yet biodegradable crystalline phase when sintered.<sup>132</sup> When calcium concentration (GC5) is increased or P<sub>2</sub>O<sub>5</sub> (GP2) is decreased, mechanical properties of potassium fluorrichterite (KNaCaMg<sub>5</sub>Si<sub>8</sub>O<sub>22</sub>F<sub>2</sub>) glass-ceramics are improved. This can be used in development of medical devices anticipated for bone tissue repair.<sup>133, 134</sup> Foaming with rice husks produces a new porous bioactive glass (45S5) with sufficient mechanical support when sintered at 1050°C for 1 h and can maintain bioactivity and biodegrade at later stages.<sup>135</sup>

Greater filler effects of bioactive glass is observed in comparison with autogenous bone in rat cancellous bone defect models.<sup>136</sup> Bioactive glass in conjunction with allogenic demineralized bone matrix triggered bone formation without any adverse cellular reaction.<sup>137-139</sup> The composite scaffolds comprising bioactive glass-collagen alone and in combination with phosphatidylserine showed greater biocompatibility and osteogenesis effects. The said composites fulfilled the criteria to be used in bone tissue engineering and proved itself to have tremendous possibility in bone regeneration.<sup>140, 141</sup> Incorporation of mesenchymal stem cell with hyaluronic acid enhances healing of the bone defect during scaffold preparation.<sup>142</sup> Bone-bonding response is greatly enhanced by micro-roughening of bioactive glass surface.<sup>143</sup> Being biocompatible it shows no inflammatory response in tissues and resorption of glass fiber scaffolds are observed within 6 months.<sup>144</sup> Porous bioactive glass when used experimentally in goat bone defect model, promoted new bone formation that suggests its potential for orthopaedic reconstructive procedures.<sup>145</sup> Apart from its role in bone tissue engineering, it has also beneficial role to enhance neovascularization during soft tissue engineering of larger size.<sup>146</sup> Neovascularization is extremely essential irrespective of hard and soft tissue healing which can be accomplished by delivery of lower amount of bioactive glass in site.<sup>147</sup>

Silica-based bioactive glasses are usually used for dental restoration and bone implants and it also has the ability to deliver drugs to site in conditions like bone infections, defects, fractures (due to osteoporosis) and tumours. Mesoporous silica micro-/nano-particles have potentiality to be used as vehicle which can release anti-cancer drugs within specific malignant cells.<sup>148, 149</sup> Clinically, GTR (guided tissue regeneration) with collagen membrane (CM) merged with autogenous bone, either as graft or combined with bioactive glass, are compared and concluded that autogenous bone can be mixed with bioactive glass where there is less amount of harvested bone. Jebahi *et al.*<sup>150</sup> evaluated the performance of freeze dried bioactive glass containing 17 wt%-chitosan composite (BG-CH) in bone defects of ovariectomized rat and found incorporation of 17 wt% CH with BG matrix to significantly enhance the bioactivity and osteoinductive property. Moreover, it increased Ca and P ion concentrations in the implanted microenvironment.<sup>150, 151</sup> Strontium ranelate has immense importance in the treatment of osteoporosis, hence, incorporation of bioactive strontium into mesoporous bioactive glass scaffold enhances fracture repair process.<sup>152</sup>

Bioactive glass has inherent properties to be used as scaffold materials; borate or borosilicate composition induces new bone formation and doping with Cu, Zn or Sr enhances healthy bone growth. Bioactive glass has important role to enhance neovascularization and neocartilage formation.<sup>153</sup> Osteoconductive and osteointegration properties of borate bioactive glass were evaluated in rabbit model by synchrotron micro-CT, with precise resolution, and resulted in detailed visualization of biomaterial-bone assimilation and detailed microarchitecture of both glass graft and newly formed trabecular bone. Moreover, teicoplanin-loaded borate glass showed osteoconduction.<sup>154</sup>

Bioactive glass in particulate form enhances bone mineralization but may result in inflammation and particle migration. Thus incorporation of chondroitin sulfate-(CS) based bioadhesive improves amalgamation of the bioactive glass as well as prevents particle migration, promotes bone regeneration and provides mechanical stability by encapsulating bone marrow.<sup>155</sup> Modified (as explained earlier) potassium fluorrichterite (KNaCaMg<sub>5</sub>Si<sub>8</sub>O<sub>22</sub>F<sub>2</sub>) glass-ceramics gave direct bone tissue contact *in vivo* through new bone formation and cell proliferation along implant surface into medullary space. But, inclusion of P<sub>2</sub>O<sub>5</sub> improves osteoconductivity and mechanical stability to a larger extent.<sup>156</sup> 6 mol% P<sub>2</sub>O<sub>5</sub> containing bioactive glasses (SiO<sub>2</sub>-P<sub>2</sub>O<sub>5</sub>-CaO-Na<sub>2</sub>O-CaF<sub>2</sub>) upon heat treatment, are crystallized to mixed sodium calcium fluoride orthophosphates and fluorapatite which have excellent properties of osteoconduction as well as bone regeneration.<sup>157</sup>

Osteoinductive properties of the glass, on the other hand, results due to dissolution products of glass (mainly, soluble silica and calcium ions) which stimulates osteogenic cells leading to bone matrix.<sup>69</sup> *In vitro* human

osteoblastic cells cultured on bioactive glasses, produce collagenous extracellular matrix (ECM), which eventually forms bone nodules without any **supplementation** and absence of phosphate in the composition,<sup>158</sup> whereas other bioceramics need osteogenic supplements like dexamethasone and b-glycerophosphate to be incorporated.<sup>159-161</sup> It also increases intracellular calcium levels<sup>162, 163</sup> and upregulate various gene. Calcium ions and soluble silica from bioactive glass also help to stimulate osteoblastic cell division, growth factors production and ECM proteins.<sup>164</sup>

*In vitro* study shows that MSCs are differentiated into osteoblasts and osteoclasts irrespective of presence or absence of BMP-2 when cultured on bioactive sol-gel coatings with low silica content (40 mol% SiO<sub>2</sub>, 54 mol% CaO, 6 mol% P<sub>2</sub>O<sub>5</sub>),<sup>165</sup> that accelerates osteogenesis and remodelling. Whereas, MSCs differentiate only into osteoblasts when cultured on glass coatings of high silica content (80 mol% SiO<sub>2</sub>, 54 mol% CaO, 6 mol% P<sub>2</sub>O<sub>5</sub>). *In vitro* culture of human adipose stem cells on bioactive glasses show differentiation into osteogenic cells in presence of osteogenic supplements.<sup>166</sup>

Studies with sol-gel derived electrospun composite fibrous membranes (using 45SiO<sub>2</sub>-24.5CaO-24.5Na<sub>2</sub>O<sub>6</sub>-P<sub>2</sub>O<sub>5</sub> and 43SiO<sub>2</sub>-24.5CaO-24.5Na<sub>2</sub>O<sub>6</sub>-P<sub>2</sub>O<sub>5</sub>-2Fe<sub>2</sub>O<sub>3</sub> system pre-mixed with polyvinyl alcohol) revealed that the magnetic particles embedded in the scaffolds have a synergistic effect on osteoinductivity with and without external magnetic field<sup>167</sup> where magnetic particles play a key role in providing osteoinductive properties to the composite scaffolds.<sup>168</sup>

### Clinical Applications

Bioactive glass coated screw was evaluated clinically for Weber type B ankle fractures in 37 patients without screw loosening within 2 years.<sup>169</sup> Other clinical claim of bioactive glass included vertebroplasty,<sup>170, 171</sup> treatment of unstable distal radius fracture,<sup>172</sup> tympanoplastic reconstruction,<sup>173</sup> as filler in benign tumour surgery,<sup>136</sup> facial bones reconstruction,<sup>174</sup> management of periodontal bone defects,<sup>175, 176</sup> obliteration of frontal sinuses,<sup>177-179</sup> repairing of orbital floor fractures,<sup>180, 181</sup> lumbar fusion,<sup>182</sup> reconstruction of maxillary sinus,<sup>183</sup> cement-less acetabular cups (with metal back-up)<sup>184</sup> and restoration of iliac crest defect post bone graft harvesting.<sup>185</sup> The allergenic mesenchymal stem cells can be delivered from a thermoplastic, viscous carrier with a granular bioactive glass scaffold in a clinically convenient form that was proved to be efficient osteogenic substance during early stages of canine alveolar repair.<sup>186</sup>

Bioactive glasses have also been used for spinal fusion, coatings for orthopaedic metal implants, replacement of bone, in dentistry (like periodontology and endodontology), bone tissue engineered scaffolds, composites and regenerative medicine.<sup>164, 187, 188</sup> In clinical dentistry, bioactive glasses (particles, porous or dense scaffolds) have been used extensively.<sup>164</sup>

The composite product of bioactive glass-ceramics A-W (apatite-wollastonite) and bioactive surface-modified Ti-metal is used clinically as bone substitute (e.g. artificial vertebrae and iliac crest) due to its better bone-bonding ability and superior mechanical strength in contrast to human cortical bone.<sup>189</sup> Good osteoinduction, ectopic bone formation occur in muscle when this porous Ti metal (after strong acid treatment and post heat-treatment) was used.<sup>190, 191</sup> Likewise, heat treated porous Ti metal after subsequent exposure to HCl treatment and NaOH treatment also showed remarkable osteoinduction<sup>192</sup> and osteoconduction.<sup>193-195</sup>

### Conclusions

During the past decades, biomedical materials have shown a new vista for effective hard tissue and dental repair as well as in local drug delivery systems. This has enhanced life expectancy as well as meets the social commitments for quality life. A considerable stride towards the exploitation of synthetic biomaterials in bone and dental tissue engineering has been **pain**. Amid various biomaterials, bioactive glass has shown paramount interest in clinical regenerative medicine due to its inducing capacity as active biomineralization *in vivo*. Initially, it has been thought for its efficacy in bone repair and restoration. Of late, it has eventually become a very striking biomaterial of choice in various clinical settings like in dental, maxillofacial and ear implants, soft tissue regeneration, coating of metallic implants, drug delivery system, septic wound dressing, growth factors carriers, bioactive peptides, etc. In coming days, bioactive glass may be utilized in a more befitting way by the scientists/ researchers/ clinicians for well being of human kind.

**Acknowledgements:** The authors gratefully acknowledge the support by the Director, CSIR-Central Glass and Ceramic Research Institute, Kolkata, India and Vice Chancellor, West Bengal University of Animal and Fishery Sciences, Kolkata, India. Financial support from Council of Scientific and Industrial Research [through CSIR 12th five year plan programme (BIOCERAM)] is also acknowledged.

### References

1. S. Marastoni, G. Ligresti, E. Lorenzon, A. Colombatti and M. Mongiat, *Connect. Tissue Res.*, **49**, 203-206 (2008).
2. R. Cancedda, *Curr. Pharm. Design*, **15**, 1334-1348 (2009).
3. K. E. M. Benders, P. R. van Weeren, S. F. Badylak, D. B. F. Saris, W. J. A. Dhert and J. Malda, *Trends Biotechnol.*, **31**, 169-176 (2013).
4. A. O. Brightman, B. P. Rajwa, J. E. Sturgis, M. E. McCallister, J. P. Robinson and S. L. Voytik-Harbin, *Biopolymers*, **54**, 222-234 (2000).
5. G. Xiao, R. Gopalakrishnan, D. Jiang, E. Reith, M. D. Benson and R. T. Franceschi, *J. Bone Mineral Res.*, **17**, 101-110 (2002).
6. E. L. Chaikof, H. Matthew, J. Kohn, A. G. Mikos, G. D. Prestwich and C. M. Yip, *Ann. New York Acad. Sci.*, **961**, 96-105 (2002).
7. T. Goff, N. K. Kanakaris and P. V. Giannoudis, *Injury*, **44**, S86-S94 (2013).

8. J. R. Jones, P. D. Lee and L. L. Hench, *Philos. Trans. Royal Soc. London A: Mathe. Phys. Eng. Sci.*, **364**, 263-281 (2006).
9. B. F. Ricciardi and M. P. Bostrom, *Sem. Arthropl.*, **24**, 119-123 (2013).
10. L. G. Griffith, *Ann. New York Acad. Sci.*, **961**, 83-95 (2002).
11. V. Karageorgiou and D. Kaplan, *Biomaterials*, **26**, 5474-5491 (2005).
12. S. Levenberg and R. Langer, *Curr. Topics Develop. Biol.*, **61**, 113-134 (2004).
13. D. W. Hutmacher, *Biomaterials*, **21**, 2529-2543 (2000).
14. M. Kellomaki, H. Niiranen, K. Puumanen, N. Ashammakhi, T. Waris and P. Tormala, *Biomaterials*, **21**, 2495-2505 (2000).
15. M. Neo, T. Nakamura, C. Ohtsuki, T. Kokubo and T. Yamamuro, *J. Biomed. Mater. Res.*, **27**, 999-1006 (1993).
16. C. Ohtsuki, H. Kushitani, T. Kokubo, S. Kotani and T. Yamamuro, *J. Biomed. Mater. Res.*, **25**, 1363-1370 (1991).
17. K. K. Kaysinger and W. K. Ramp, *J. Cell. Biochem.*, **68**, 83-89 (1998).
18. W. K. Ramp, L. G. Lenz and K. K. Kaysinger, *Bone Miner.*, **24**, 59-73 (1994).
19. P. N. De Aza, Z. B. Luklinska, C. Santos, F. Guitian and S. De Aza, *Biomaterials*, **24**, 1437-1445 (2003).
20. O. H. Andersson, G. Liu, K. Kangasniemi and J. Juhanoja, *J. Mater. Sci.: Mater. Med.*, **3**, 145-150 (1992).
21. K. D. Groot, *Bioceramics of Calcium Phosphate*, CRC Press, Boca Raton, FL, USA (1983).
22. K. D. Groot, in: *Bioceramics: Material Characteristics Versus In Vivo Behaviour*, Vol. 523, Eds. P. Ducheyne and J. Lemons, Annals of New York Academy of Sciences, New York, USA (1988).
23. K. D. Groot, C. P. A. T. Klein, J. G. C. Wolke and J. De Blicke-Hogervorst, pp. 3-15 in: *Handbook of Bioactive Ceramics*, Vol. II, Eds. T. Yamamuro, L. L. Hench and J. Wilson, CRC Press, Boca Raton, FL, USA (1990).
24. K. D. Groot and R. Z. LeGeros, pp. 268-277 in: *Bioceramics: Material Characteristics Versus In Vivo Behaviour*, Vol. 523, Eds. P. Ducheyne and J. Lemons, Annals of New York Academy of Sciences, New York, USA (1988).
25. P. Ducheyne, L. L. Hench, A. Kagan, 2nd, M. Martens, A. Bursens and J. C. Mulier, *J. Biomed. Mater. Res.*, **14**, 225-237 (1980).
26. U. Gross, R. Kinne, H. J. Schmitz and V. Strunz, *CRC Crit. Rev. Biocompat.*, **4**, 155-179 (1988).
27. U. Gross and V. Strunz, *J. Biomed. Mater. Res.*, **19**, 251-271 (1985).
28. L. L. Hench, p. 23 in: *Biomaterials and Clinical Applications*, Eds. A. Pizzoferrato, P. G. Marchetti, A. Ravaglioli and A. J. C. Lee, Elsevier, Amsterdam, The Netherlands (1987).
29. L. L. Hench, p. 54 in: *Bioceramics: Materials Characteristics Versus In Vivo Behaviour*, Vol. 523, Eds. P. Ducheyne and J. Lemons, Annals of New York Academy of Sciences, New York, USA (1988).
30. L. L. Hench and E. C. Ethridge, *Biomaterials: An Interfacial Approach*, Academic Press, New York, USA (1982).
31. L. L. Hench, R. J. Splinter, W. C. Allen and T. K. Greenlee, *J. Biomed. Mater. Res.*, **5**, 117-141 (1971).
32. L. L. Hench and J. Wilson, *Science*, **226**, 630-636 (1984).
33. W. Holand, W. Vogel, K. Naumann and J. Gummel, *J. Biomed. Mater. Res.*, **19**, 303-312 (1985).
34. S. F. Hulbert, J. C. Bokros, L. L. Hench, J. Wilson and G. Heimke, pp. 189-213 in: *High Tech Ceramics*, Ed. P. Vincenzini, Elsevier, Amsterdam, The Netherlands (1987).
35. M. Jarcho, *Clin. Orthop. Relat. Res.*, **157**, 259-278 (1981).
36. T. Kitsugi, T. Yamamuro and T. Kokubo, *J. Bone Joint Surg. Am.*, **71**, 264-272 (1989).
37. T. Kokubo, S. Ito, S. Sakka and T. Yamamuro, *J. Mater. Sci.*, **21**, 536-540 (1986).
38. T. Kokubo, M. Shigematsu, Y. Nagashima, M. Tashiro, T. Nakamura, T. Yamamuro and S. Higashi, *Bull. Instt. Chem. Res. Kyoto Univ.*, **60**, 260-268 (1982).
39. T. Nakamura, T. Yamamuro, S. Higashi, T. Kokubo and S. Itoo, *J. Biomed. Mater. Res.*, **19**, 685-698 (1985).
40. J. Wilson, G. H. Pigott, F. J. Schoen and L. L. Hench, *J. Biomed. Mater. Res.*, **15**, 805-817 (1981).
41. T. Yamamuro, L. L. Hench and J. Wilson, *Bioactive Glasses and Glass-Ceramics*, Vol. I, CRC Press, Boca Raton, FL, USA (1990).
42. T. Yamamuro, J. Shikata, Y. Kakutani, S. Yoshii, T. Kitsugi and K. Ono, p. 107 in: *Bioceramics: Material Characteristics Versus In Vivo Behaviour*, Vol. 523, Eds. P. Ducheyne and J. E. Lemons, Annals of New York Academy of Sciences, New York, USA (1988).
43. S. Yoshii, Y. Kakutani, T. Yamamuro, T. Nakamura, T. Kitsugi, M. Oka, T. Kokubo and M. Takagi, *J. Biomed. Mater. Res.*, **22**, 327-338 (1988).
44. L. L. Hench, *J. Mater. Sci.: Mater. Med.*, **17**, 967-978 (2006).
45. J. Wilson and D. Nolletti, pp. 283-302 in: *Handbook of Bioactive Ceramics, Vol. I: Bioactive Glasses and Glass-Ceramics*, Eds. T. Yamamuro, L. L. Hench and J. Wilson, CRC Press, Boca Raton, FL, USA (1990).
46. L. L. Hench, *J. Am. Ceram. Soc.*, **74**, 1487-1510 (1991).
47. C. Vitale-Brovarone, M. Miola, C. Balagna and E. Vernè, *Chem. Eng. J.*, **137**, 129-136 (2008).
48. C. Vitale-Brovarone, E. Vernè, M. Bosetti, P. Appendino and M. Cannas, *J. Mater. Sci.: Mater. Med.*, **16**, 909-917 (2005).
49. C. Vitale-Brovarone, E. Vernè, L. Robiglio, P. Appendino, F. Bassi, G. Martinasso, G. Muzio and R. Canuto, *Acta Biomater.*, **3**, 199-208 (2007).
50. E. Gentleman, Y. C. Fredholm, G. Jell, N. Lotfibakhshaiesh, M. D. O'Donnell, R. G. Hill and M. M. Stevens, *Biomaterials*, **31**, 3949-3956 (2010).
51. M. D. O'Donnell and R. G. Hill, *Acta Biomater.*, **6**, 2382-2385 (2010).
52. H. B. Pan, X. L. Zhao, X. Zhang, K. B. Zhang, L. C. Li, Z. Y. Li, W. M. Lam, W. W. Lu, D. P. Wang, W. H. Huang, K. L. Lin and J. Chang, *J. Royal Soc. Interf.*, **7**, 1025-1031 (2010).
53. C.-S. Hsi, H.-Z. Cheng, H.-J. Hsu, Y.-S. Chen, and M.-C. Wang, *J. Eur. Ceram. Soc.*, **27**, 3171-3176 (2007).
54. A. Balamurugan, G. Balossier, D. Laurent-Maquin, S. Pina, A. H. S. Rebelo, J. Faure and J. M. F. Ferreira, *Dental Mater.*, **24**, 1343-1351 (2008).
55. M. Bellantone, H. D. Williams and L. L. Hench, *Antimicrob. Agents Chemother.*, **46**, 1940-1945 (2002).
56. J. J. Blaker, S. N. Nazhat and A. R. Boccaccini, *Biomaterials*, **25**, 1319-1329 (2004).

57. J. Delben, O. Pimentel, M. Coelho, P. Candelario, L. Furini, F. b. Alencar dos Santos, F. b. de Vicente and A. Delben, *J. Therm. Anal. Calorim.*, **97**, 433-436 (2009).
58. M. F. Gorriti, J. M. P. López, A. R. Boccaccini, C. Audisio and A. A. Gorustovich, *Adv. Eng. Mater.*, **11**, B67-B70 (2009).
59. X. Liu, W. Huang, H. Fu, A. Yao, D. Wang, H. Pan and W. Lu, *J. Mater. Sci.: Mater. Med.*, **20**, 365-372 (2009).
60. X. Liu, W. Huang, H. Fu, A. Yao, D. Wang, H. Pan, W. Lu, X. Jiang and X. Zhang, *J. Mater. Sci.: Mater. Med.*, **20**, 1237-1243 (2009).
61. E. Munukka, O. Leppäranta, M. Korkeamäki, M. Vaahio, T. Peltola, D. Zhang, L. Hupa, H. Ylänen, J. Salonen, M. Viljanen and E. Eerola, *J. Mater. Sci.: Mater. Med.*, **19**, 27-32 (2008).
62. V. Cannillo and A. Sola, *Ceram. Int.*, **35**, 3389-3393 (2009).
63. V. Aina, G. Malavasi, A. Fiorio Pla, L. Munaron and C. Morterra, *Acta Biomater.*, **5**, 1211-1222 (2009).
64. S. Haimi, G. Gorianc, L. Moimas, B. Lindroos, H. Huhtala, S. Rätty, H. Kuokkanen, G. K. Sándor, C. Schmid, S. Miettinen and R. Suuronen, *Acta Biomater.*, **5**, 3122-3131 (2009).
65. P. Saravanapavan, J. E. Gough, J. R. Jones and L. L. Hench, *Key Eng. Mater.*, **254-256**, 1087-1090 (2003).
66. H. S. Ryu, J. H. Seo, H. Kim, K. S. Hong, H. J. Park, D. J. Kim, J. H. Lee, D. H. Lee, B. S. Chang and C. K. Lee, p. 261 in: *Bioceramics 15*, Eds. B. Ben-Nissan, D. Sher and W. Walsh, Trans Tech Publications, Zurich-Uetikon, Switzerland (2003).
67. X. Chen, Y. Meng, Y. Li and N. Zhao, *Appl. Surf. Sci.*, **255**, 562-564 (2008).
68. V. Guarino, F. Causa and L. Ambrosio, *Expert Rev. Med. Devices*, **4**, 405-418 (2007).
69. L. L. Hench and J. M. Polak, *Science*, **295**, 1014-1017 (2002).
70. D. W. Hutmacher, J. T. Schantz, C. X. F. Lam, K. C. Tan and T. C. Lim, *J. Tissue Eng. Regen. Med.*, **1**, 245-260 (2007).
71. J. R. Jones, pp. 52-71 in: *Tissue Engineering Using Ceramics and Polymers*, Vol. 1, Eds. A. R. Boccaccini and J. E. Gough, Woodhead Publishing Ltd, CRC Press, Cambridge, UK (2007).
72. J. R. Jones, *J. Eur. Ceram. Soc.*, **29**, 1275-1281 (2009).
73. S. K. Misra, S. P. Valappil, I. Roy and A. R. Boccaccini, *Biomacromolecules*, **7**, 2249-2258 (2006).
74. A. Balamurugan, G. Balossier, J. Michel, S. Kannan, H. Benhayoune, A. H. S. Rebelo and J. M. F. Ferreira, *J. Biomed. Mater. Res. Part B: Appl. Biomater.*, **83B**, 546-553 (2007).
75. G. Radha and K. Ashok, *Biomed. Mater.*, **3**, 034005 (2008).
76. T. Olding, M. Sayer and D. Barrow, *Thin Solid Films*, **398-399**, 581-586 (2001).
77. P. Sepulveda, J. R. Jones and L. L. Hench, *J. Biomed. Mater. Res.*, **58**, 734-740 (2001).
78. T. J. Brunner, R. N. Grass and W. J. Stark, *Chem. Comm.*, **13**, 1384-1386 (2006).
79. M. Vollenweider, T. J. Brunner, S. Knecht, R. N. Grass, M. Zehnder, T. Imfeld and W. J. Stark, *Acta Biomater.*, **3**, 936-943 (2007).
80. A. Liu, Z. Hong, X. Zhuang, X. Chen, Y. Cui, Y. Liu and X. Jing, *Acta Biomater.*, **4**, 1005-1015 (2008).
81. H. H. Lu, S. F. El-Amin, K. D. Scott and C. T. Laurencin, *J. Biomed. Mater. Res. Part A*, **64A**, 465-474 (2003).
82. S. K. Misra, T. Ansari, D. Mohn, S. P. Valappil, T. J. Brunner, W. J. Stark, I. Roy, J. C. Knowles, P. D. Sibbons, E. V. Jones, A. R. Boccaccini and V. Salih, *J. Royal Soc. Interf.*, **7**, 453-465 (2010).
83. S. K. Misra, T. I. Ansari, S. P. Valappil, D. Mohn, S. E. Philip, W. J. Stark, I. Roy, J. C. Knowles, V. Salih and A. R. Boccaccini, *Biomaterials*, **31**, 2806-2815 (2010).
84. S. K. Misra, D. Mohn, T. J. Brunner, W. J. Stark, S. E. Philip, I. Roy, V. Salih, J. C. Knowles and A. R. Boccaccini, *Biomaterials*, **29**, 1750-1761 (2008).
85. S. Yang, K.-F. Leong, Z. Du and C.-K. Chua, *Tissue Eng.*, **7**, 679-689 (2001).
86. L. L. Hench, *J. Am. Ceram. Soc.*, **81**, 1705-1728 (1998).
87. I. Thompson and L. Hench, *Proc. Inst. Mech. Eng., Part H: J. Eng. Med.*, **212**, 127-136 (1998).
88. A. R. Boccaccini, pp. 26-36 in: *Biomaterials, Artificial Organs and Tissue Engineering*, 1st edition, Eds. L. L. Hench and J. R. Jones, Woodhead Publishing Ltd, CRC Press, Cambridge, UK (2005).
89. A. R. Boccaccini, Q. Chen, L. Lefebvre, L. Gremillard and J. Chevalier, *Faraday Discuss.*, **136**, 27-44 (2007).
90. I. D. Thompson, pp. 48-58 in: *Biomaterials, Artificial Organs and Tissue Engineering*, 1st edition, Eds. L. L. Hench and J. R. Jones, Woodhead Publishing Ltd, CRC Press, Cambridge, UK (2005).
91. Q. Fu, M. N. Rahaman, B. S. Bal and R. F. Brown, *J. Biomed. Mater. Res. Part A*, **93A**, 1380-1390 (2010).
92. J. M. Kanczler and R. O. Oreffo, *Eur. Cell Mater.*, **15**, 100-114 (2008).
93. L. L. Hench, p. 73 in: *Biomaterials Science: An Introduction to Materials in Medicine*, Eds. B. D. Ratner, A. S. Hoffman, F. J. Schoen and J. E. Lemons, Academic Press, San Diego, USA (1996).
94. L. L. Hench and Ö. H. Andersson, pp. 41-62 in: *An Introduction to Bioceramics*, Vol. 1, Eds. L. L. Hench and J. Wilson, World Scientific Publishing, Singapore (1993).
95. L.-C. Gerhardt and A. R. Boccaccini, *Materials*, **3**, 3867-3910 (2010).
96. N. H. Ray, *Inorganic Polymers*, Academic Press, London, UK (1978).
97. K. E. Wallace, R. G. Hill, J. T. Pembroke, C. J. Brown and P. V. Hatton, *J. Mater. Sci.: Mater. Med.*, **10**, 697-701 (1999).
98. R. Hill, *J. Mater. Sci. Lett.*, **15**, 1122-1125 (1996).
99. M. W. G. Lockyer, D. Holland and R. Dupree, *J. Non-Cryst. Solids*, **188**, 207-219 (1995).
100. Z. Strnad, *Biomaterials*, **13**, 317-321 (1992).
101. S. Yang, K.-F. Leong, Z. Du and C.-K. Chua, *Tissue Eng.*, **8**, 1-11 (2002).
102. H.-S. Yun, S.-E. Kim and Y.-T. Hyeon, *Chem. Comm.*, **21**, 2139-2141 (2007).
103. M. A. De Diego, N. J. Coleman and L. L. Hench, *J. Biomed. Mater. Res.*, **53**, 199-203 (2000).
104. L. Francis, D. Meng, J. C. Knowles, I. Roy and A. R. Boccaccini, *Acta Biomater.*, **6**, 2773-2786 (2010).

105. D. Mohamad Yunos, O. Bretcanu and A. Boccaccini, *J. Mater. Sci.*, **43**, 4433-4442 (2008).
106. A. L. Oliveira, J. F. Mano and R. L. Reis, *Curr. Opin. Solid State Mater. Sci.*, **7**, 309-318 (2003).
107. J. M. Taboas, R. D. Maddox, P. H. Krebsbach and S. J. Hollister, *Biomaterials*, **24**, 181-194 (2003).
108. C. C. Berry, M. J. Dalby, R. O. C. Oreffo, D. McCloy and S. Affrosman, *J. Biomed. Mater. Res. Part A*, **79A**, 431-439 (2006).
109. M. M. Stevens and J. H. George, *Science*, **310**, 1135-1138 (2005).
110. T. J. Webster and E. S. Ahn, *Tissue Engineering II*, Vol. 103, pp. 275-308, Springer, Berlin, Germany (2007).
111. A. R. Boccaccini and J. J. Blaker, *Exp. Rev. Med. Devices*, **2**, 303-317 (2005).
112. K. Rezwani, Q. Z. Chen, J. J. Blaker and A. R. Boccaccini, *Biomaterials*, **27**, 3413-3431 (2006).
113. K. H. Karlsson, H. Ylänen and H. Aro, *Ceram. Int.*, **26**, 897-900 (2000).
114. A. Rainer, S. M. Giannitelli, F. Abbruzzese, E. Traversa, S. Licoccia and M. Trombetta, *Acta Biomater.*, **4**, 362-369 (2008).
115. F.-H. Lin, Y.-Y. Huang, M.-H. Hon and S.-C. Wu, *J. Biomed. Eng.*, **13**, 328-334 (1991).
116. P. Sooksaen, S. Suttiruengwong, K. Oniem, K. Ngamlamiad and J. Atireklapwarodom, *J. Met. Mater. Miner.*, **18**, 85-91 (2008).
117. M. Vallet-Regí, C. V. Ragel and A. J. Salinas, *Eur. J. Inorg. Chem.*, **2003**, 1029-1042 (2003).
118. L. L. Hench, D. B. Spilman and D. Nolletti, pp. 99-104 in: *Biological and Biomechanical Performance of Biomaterials*, Eds. P. Christel, A. Meunier and A. J. C. Lee, Elsevier, Amsterdam, The Netherlands (1986).
119. L. L. Hench and H. A. Paschall, *J. Biomed. Mater. Res.*, **8**, 49-64 (1974).
120. L. L. Hench, H. A. Paschall, W. C. Allen and G. Piotrowski, *Natl. Bur. Stand. Special Publ.*, **415**, 19-35 (1975).
121. L. L. Hench and A. E. Clark, pp. 85-105 in: *Biocompatibility of Orthopaedic Implants*, Vol. 2, Eds. D. F. Williams and G. D. Winter, CRC Press, Boca Raton, FL, USA (1982).
122. Ö. H. Andersson, K. H. Karlsson, K. Kangasniemi and A. Xli-Urpo, *Glastech. Ber.*, **61**, 300-305 (1988).
123. M. Zehnder, E. Söderling, J. Salonen and T. Waltimo, *J. Endodont.*, **30**, 220-224 (2004).
124. Q. Fu, M. N. Rahaman, B. S. Bal, R. F. Brown and D. E. Day, *Acta Biomater.*, **4**, 1854-1864 (2008).
125. J. Zhang, M. Wang, J. M. Cha and A. Mantalaris, *J. Tissue Eng. Regen. Med.*, **3**, 63-71 (2009).
126. C. Loty, J. M. Sautier, M. T. Tan, M. Oboeuf, E. Jallot, H. Boulekbache, D. Greenspan and N. Forest, *J. Bone Miner. Res.*, **16**, 231-239 (2001).
127. L. Linati, G. Lusvardi, G. Malavasi, L. Menabue, M. C. Menziani, P. Mustarelli and U. Segre, *J. Phys. Chem. B*, **109**, 4989-4998 (2005).
128. P. V. Giannoudis, H. Dinopoulos and E. Tsiridis, *Injury*, **36**, S20-S27 (2005).
129. V. V. Valimaki and H. T. Aro, *Scand. J. Surg.*, **95**, 95-102 (2006).
130. K. Cholewa-Kowalska, J. Kokoszka, M. Łączka, Ł. Niedźwiedzki, W. Madej and A. M. Osyczka, *Biomed. Mater.*, **4**, 055007 (2009).
131. L. L. Hench and H. A. Paschall, *J. Biomed. Mater. Res.*, **7**, 25-42 (1973).
132. Q.-Z. Chen, Y. Li, L.-Y. Jin, J. M. W. Quinn and P. A. Komesaroff, *Acta Biomater.*, **6**, 4143-4153 (2010).
133. S. Bandyopadhyay-Ghosh, P. E. P. Faria, A. Johnson, D. N. B. Felipucci, I. M. Reaney, L. A. Salata, I. M. Brook and P. V. Hatton, *J. Biomed. Mater. Res. Part A*, **94**, 760-768 (2010).
134. S. Bhakta, D. K. Pattanayak, H. Takadama, T. Kokubo, C. A. Miller, M. Mirsaneh, I. M. Reaney, I. Brook, R. van Noort and P. V. Hatton, *J. Mater. Sci.: Mater. Med.*, **21**, 2979-2988 (2010).
135. S.-C. Wu, H.-C. Hsu, S.-H. Hsiao and W.-F. Ho, *J. Mater. Sci.: Mater. Med.*, **20**, 1229-1236 (2009).
136. J. T. Heikkila, H. J. Aho, A. Yli-Urpo, R.-P. Happonen and A. J. Aho, *Acta Orthopaed. Scand.*, **66**, 463-467 (1995).
137. O. Erdemli, O. Captug, H. Bilgili, D. Orhan, A. Tezcaner and D. Keskin, *J. Mater. Sci.: Mater. Med.*, **21**, 295-308 (2010).
138. K. J. Pajamaki, O. H. Andersson, T. S. Lindholm, K. H. Karlsson and A. Yli-Urpo, *Ann. Chir. Gynaecol. Suppl.*, **207**, 137-143 (1993).
139. K. J. Pajamaki, O. H. Andersson, T. S. Lindholm, K. H. Karlsson, A. Yli-Urpo and R. P. Happonen, *Ann. Chir. Gynaecol. Suppl.*, **207**, 155-161 (1993).
140. B. Marelli, C. E. Ghezzi, J. E. Barralet, A. R. Boccaccini and S. N. Nazhat, *Biomacromolecules*, **11**, 1470-1479 (2010).
141. C. Xu, P. Su, X. Chen, Y. Meng, W. Yu, A. P. Xiang and Y. Wang, *Biomaterials*, **32**, 1051-1058 (2011).
142. C. Xu, P. Su, Y. Wang, X. Chen, Y. Meng, C. Liu, X. Yu, X. Yang, W. Yu and X. Zhang, *J. Biomed. Mater. Res. Part A*, **95**, 495-503 (2010).
143. A. Itala, J. Koort, H. O. Ylanen, M. Hupa and H. T. Aro, *J. Biomed. Mater. Res. Part A*, **67**, 496-503 (2003).
144. L. Moimas, M. Biasotto, R. Di Lenarda, A. Olivo and C. Schmid, *Acta Biomater.*, **2**, 191-199 (2006).
145. S. K. Nandi, B. Kundu, S. Datta, D. K. De and D. Basu, *Res. Veter. Sci.*, **86**, 162-173 (2009).
146. R. M. Day, A. R. Boccaccini, S. Shurey, J. A. Roether, A. Forbes, L. L. Hench and S. M. Gabe, *Biomaterials*, **25**, 5857-5866 (2004).
147. A. Leu, S. M. Stieger, P. Dayton, K. W. Ferrara and J. K. Leach, *Tissue Eng. Part A*, **15**, 877-885 (2008).
148. D. Arcos and M. Vallet-Regi, *Acta Mater.*, **61**, 890-911 (2013).
149. V. S. Yadav, S. C. Narula, R. K. Sharma, S. Tewari and R. Yadav, *J. Oral Sci.*, **53**, 481-488 (2011).
150. S. Jebahi, H. Oudadesse, X. V. Bui, H. Keskes, T. Rebai, A. El Feki and H. El Feki, *Afr. J. Pharm. Pharmacol.*, **6**, 1276-1287 (2012).



151. S. Jebahi, H. Oudadesse, F. Z. Faouzi, J. Elleuch, T. Rebai, H. Keskes, A. Mostafa, A. El Feki and H. El Feki, *J. Mater. Sci. Eng.*, **2**, 128(1-8) (2013).
152. L. Wei, J. Ke, I. Prasadam, R. J. Miron, S. Lin, Y. Xiao, J. Chang, C. Wu and Y. Zhang, *Osteopor. Int.*, **25**, 2089-2096 (2014).
153. M. N. Rahaman, D. E. Day, B. S. Bal, Q. Fu, S. B. Jung, L. F. Bonewald and A. P. Tomsia, *Acta Biomater.*, **7**, 2355-2373 (2011).
154. Q. Fu, W. Huang, W. Jia, M. N. Rahaman, X. Liu and A. P. Tomsia, *Tissue Eng. Part A*, **17**, 3077-3084 (2011).
155. S. Yang, Q. Guo, L. S. Shores, A. Aly, M. Ramakrishnan, G. H. Kim, Q. Lu, L. Su and J. H. Elisseeff, *J. Biomed. Mater. Res. Part A*, **103**, 235-242 (2015).
156. S. Bhakta, P. E. Faira, L. A. Salata, P. J. de Oliveira Neto, C. A. Miller, R. van Noort, I. M. Reaney, I. M. Brook and P. V. Hatton, *J. Mater. Sci.: Mater. Med.*, **23**, 2521-2529 (2012).
157. D. S. Brauer, M. N. Anjum, M. Mneimne, R. M. Wilson, H. Doweidar and R. G. Hill, *J. Non-Cryst. Solids*, **358**, 1438-1442 (2012).
158. J. R. Jones, O. Tsigkou, E. E. Coates, M. M. Stevens, J. M. Polak and L. L. Hench, *Biomaterials*, **28**, 1653-1663 (2007).
159. J. E. Gough, J. R. Jones and L. L. Hench, *Biomaterials*, **25**, 2039-2046 (2004).
160. E. A. B. Effah Kaufmann, P. Ducheyne and I. M. Shapiro, *Tissue Eng.*, **6**, 19-28 (2000).
161. M. Bosetti and M. Cannas, *Biomaterials*, **26**, 3873-3879 (2005).
162. I. A. Silver, J. Deas and M. Erecinska, *Biomaterials*, **22**, 175-185 (2001).
163. I. D. Xynos, A. J. Edgar, L. D. K. Buttery, L. L. Hench and J. M. Polak, *J. Biomed. Mater. Res. Part A*, **55**, 151-157 (2001).
164. J. R. Jones, *Acta Biomater.*, **9**, 4457-4486 (2013).
165. M. Karpov, M. Laczka, P. S. Leboy and A. M. Osyczka, *J. Biomed. Mater. Res. Part A*, **84**, 718-726 (2008).
166. S. Haimi, L. Moimas, E. Pirhonen, B. Lindroos, H. Huhtala, S. Raty, H. Kuokkanen, G. K. Sandor, S. Miettinen and R. Suuronen, *J. Biomed. Mater. Res. Part A*, **91**, 540-547 (2009).
167. N. Shankhwar, M. Kumar, B. B. Mandal and A. Srinivasan, *Mater. Sci. Eng.: C*, **69**, 1167-1174 (2016).
168. S. N. Ayrapetyan and M. S. Markov, *Bioelectromagnetics Current Concepts: The Mechanisms of the Biological Effect of Extremely High Power Pulses*, Springer Science and Business Media, The Netherlands (2006).
169. G. S. Andreassen, P. R. Hoiness, I. Skraamm, O. Granlund and L. Engebretsen, *Arch. Orthopaed. Trauma Surg.*, **124**, 161-165 (2004).
170. E. T. Middleton, C. J. Rajaraman, D. P. O'Brien, S. M. Doherty and A. D. Taylor, *Brit. J. Neurosurg.*, **22**, 252-256 (2008).
171. J. Palussiere, J. Berge, A. Gangi, A. Cotten, A. Pasco, R. Bertagnoli, H. Jaksche, P. Carpeggiani and H. Deramond, *Eur. Spine J.*, **14**, 982-991 (2005).
172. B. J. Hartigan and M. S. Cohen, *Hand Clinics*, **21**, 449-454 (2005).
173. R. Reck, *The Laryngoscope*, **93**, 196-199 (1983).
174. E. Suominen and J. Kinnunen, *Scand. J. Plastic Reconstr. Surg. Hand Surg.*, **30**, 281-289 (1996).
175. J. A. Leonetti, H. M. Rambo and R. R. Thronson, *Implant Dentistry*, **9**, 177-182 (2000).
176. J. H. Villaca, A. B. Novaes Jr, S. L. S. d. Souza, M. Taba Jr, G. O. Molina and T. L. L. Carvalho, *Brazil. Dental J.*, **16**, 67-74 (2005).
177. M. Peltola, *Acta Oto-Laryngol.*, **120**, 167-169 (2000).
178. M. J. Peltola, J. T. K. Suonpaa, H. Andersson, H. S. Maattanen, K. M. J. Aitasalo, A. Yli-Urpo and P. J. Laippala, *J. Biomed. Mater. Res.*, **53**, 161-166 (2000).
179. J. Suonpaa, J. Sipila, K. Aitasalo, J. Antila and K. Wide, *Acta Oto-Laryngol.*, **117**, 181-183 (1997).
180. K. Aitasalo, I. Kinnunen, J. Palmgren and M. Varpula, *J. Oral Maxillof. Surg.*, **59**, 1390-1395 (2001).
181. I. Kinnunen, K. Aitasalo, M. Pollonen and M. Varpula, *J. Cranio-Maxillof. Surg.*, **28**, 229-234 (2000).
182. K. Ido, Y. Asada, T. Sakamoto, R. Hayashi and S. Kuriyama, *Spinal Cord*, **38**, 315-318 (2000).
183. M. Scala, M. Gipponi, S. Pasetti, E. Dellacha, M. Ligorio, G. Villa, G. Margarino, G. Giannini and P. Strada, *In Vivo*, **21**, 541-547 (2007).
184. H. S. Hedia, T. T. El-Midany, M. A. N. Shabara and N. Fouda, *Biomed. Mater.*, **1**, 127-133 (2006).
185. S. Asano, K. Kaneda, S. Satoh, K. Abumi, T. Hashimoto and M. Fujiya, *Eur. Spine J.*, **3**, 39-44 (1994).
186. D. Mylonas, M. D. Vidal, I. J. De Kok, J. D. Moriarity and L. F. Cooper, *J. Prosthodont.*, **16**, 421-430 (2007).
187. A. R. Boccaccini, M. Erol, W. J. Stark, D. Mohn, Z. Hong and J. F. Mano, *Compos. Sci. Technol.*, **70**, 1764-1776 (2010).
188. C. Vitale-Brovarone, F. Bairo, F. Tallia, C. Gervasio and E. Verne, *J. Mater. Sci.: Mater. Med.*, **23**, 2369-2380 (2012).
189. T. Kokubo and S. Yamaguchi, *Int. J. Appl. Glass Sci.*, **7**, 173-182 (2016).
190. T. Kawai, M. Takemoto, S. Fujibayashi, H. Akiyama, M. Tanaka, S. Yamaguchi, D. K. Pattanayak, K. Doi, T. Matsushita and T. Nakamura, *PLoS One*, **9**, e88366 (2014).
191. T. Kawai, M. Takemoto, S. Fujibayashi, H. Akiyama, S. Yamaguchi, D. K. Pattanayak, K. Doi, T. Matsushita, T. Nakamura and T. Kokubo, *J. Mater. Sci.: Mater. Med.*, **24**, 1707-1715 (2013).
192. M. Takemoto, S. Fujibayashi, M. Neo, J. Suzuki, T. Matsushita, T. Kokubo and T. Nakamura, *Biomaterials*, **27**, 2682-2691 (2006).
193. M. Takemoto, S. Fujibayashi, M. Neo, J. Suzuki, T. Kokubo and T. Nakamura, *Biomaterials*, **26**, 6014-6023 (2005).
194. S. K. Nandi, B. Kundu and S. Datta, pp. 69-116 in: *Biomaterials Applications for Nanomedicine*, Ed. R. Pignatello, InTech, Zurich, Switzerland (2011).
195. N. Bovo, Thesis, Universitat Politècnica de Catalunya (UPC), BarcelonaTech, Barcelona, Spain (2007).

Available online at [www.sciencedirect.com](http://www.sciencedirect.com)
[www.elsevier.com/locate/jmbbm](http://www.elsevier.com/locate/jmbbm)

## Research Paper

# Development and effect of different bioactive silicate glass scaffolds: In vitro evaluation for use as a bone drug delivery system



Chidambaram Soundrapandian<sup>a</sup>, Arnab Mahato<sup>b</sup>, Biswanath Kundu<sup>b,\*</sup>,  
Someswar Datta<sup>b</sup>, Biswanath Sa<sup>c</sup>, Debebrata Basu<sup>b,1</sup>

<sup>a</sup>Department of Pharmaceutics, Himalayan Pharmacy Institute, East Sikkim 737136, India<sup>b</sup>Bioceramics and Coating Division, CSIR-Central Glass and Ceramic Research Institute, Kolkata 700032, India<sup>c</sup>Department of Pharmaceutical Technology, Jadavpur University, Kolkata 700032, India

## ARTICLE INFO

## Article history:

Received 22 May 2014

Received in revised form

2 August 2014

Accepted 10 August 2014

Available online 17 August 2014

## Keywords:

Bioactive glass

Acellular static in vitro bioactivity

MTT

Wound healing assay

Drug delivery system and model

## ABSTRACT

Local drug delivery systems to bone have attracted appreciable attention due to their efficacy to improve drug delivery, healing and regeneration. In this paper, development and characterization of new formulations of bioactive glass into a porous scaffold has been reported for its suitability to act as a drug delivery system in the management of bone infections, in vitro. Two new glass compositions based on  $\text{SiO}_2\text{-Na}_2\text{O-ZnO-CaO-MgO-P}_2\text{O}_5$  system (BGZ and MBG) have been developed which after thorough chemical and phase evaluation, studied for acellular static in vitro bioactivity in SBF. Porous scaffolds made of these glasses have been fabricated and characterized thoroughly for bioactivity study, SEM, XRD, in vitro cytotoxicity, MTT assay and wound healing assay using human osteocarcinoma cells. Finally, gatifloxacin was loaded into the porous scaffold by vacuum infiltration method and in vitro drug release kinetics have been studied with varying parameters including dissolution medium (PBS and SBF) and with/without impregnation chitosan. Suitable model has also been proposed for the kinetics. 63–66% porous and 5–50  $\mu\text{m}$  almost unimodal porous MBG and BGZ bioactive glass scaffolds were capable of releasing drugs successfully for 43 days at concentrations to treat orthopedic infections. In addition, it was also observed that the release of drug followed Peppas–Korsmeyer release pattern based on Fickian diffusion, while 0.5–1% chitosan coating on the scaffolds decreased the burst release and overall release of drug. The results also indicated that MBG based scaffolds were bioactive, biocompatible, noncytotoxic and exhibited excellent wound healing potential while BGZ was mildly cytotoxic with moderate wound healing potential. These results strongly suggest that MBG scaffolds appear to be a suitable bone drug delivery system in orthopedic infections treatment and as bone void fillers, but BGZ should be handled with caution or studied elaborately in detail further to ascertain and confirm the cytotoxic nature and wound healing potential of this glass.

© 2014 Elsevier Ltd. All rights reserved.

\*Corresponding author. Tel.: +91 9831772081; fax: +91 33 24730957.

E-mail address: [biswa\\_kundu@rediffmail.com](mailto:biswa_kundu@rediffmail.com) (B. Kundu).<sup>1</sup>Passed away on 10 May 2012.

## 1. Introduction

From the beginning of this decade, local drug delivery systems to bone have attracted appreciable attention due to their efficacy in improving drug delivery, healing and regeneration (Cartmell, 2009). Considerable effort has been exerted to develop biologically acceptable materials and carrier systems to locally deliver drug in bone (Luo and Prestwich, 2001). Bioceramic materials are a class of biomaterials that can both chemically bond with bone and act as a drug carrier in prolonged-release drug delivery systems (Soundrapandian et al., 2009). Bioactive glasses and related silicate glass-ceramics constitute a much-preferred subgroup of bioceramics due to their high bioactivity and their ability to activate genes in osteoblast cells that stimulate new bone formation (Yunos et al., 2008). Considerable success has also been reported in the fabrication of bioactive glass scaffolds and their application (Gadre and Gouma, 2006).

Irrespective of the success in the development of drugs, devices and surgeries, orthopedic surgeries fail at an embarrassing rate due to infection. The prevention of post-surgical infection remains a major challenge due to difficulties in making conventionally administered antibiotics effectively available at the site. Physiological barriers that limit the supply, pathological conditions that escalate the demand, i.e., the concentration of the drug [10 times the minimum inhibitory concentration (MIC) for antibiotics], and the period of treatment (4–6 weeks) constitute the prime reasons for failure (Soundrapandian et al., 2007). Local drug delivery systems provide higher concentrations of drugs at the required site than those achieved with parenteral application (Kundu et al., 2010b; Nandi et al., 2009a) and are hence considered an area of potential future in orthopedic infection eradication.

The potential use of bioactive glass material as a drug delivery system has not been studied in great detail. Previous studies have mainly focused on biopolymers (Yagmurcu et al., 1999; Zhang et al., 1994a, 1994b), which were found to not be ideal for bone repair (because they do not chemically bond with bone) beyond drug delivery. In some of the studies, mesoporous bioactive glass materials have been studied for use as a drug delivery system (Domingues et al., 2004), but the effect of different cations and anions available in the composition has not been studied in detail. Moreover, their effect on long-term drug elution kinetics, particularly for the treatment of osteomyelitis, has also not been examined. Inorganic–organic composites have also been tested for this purpose, but with limited success (Arcos et al., 2001). In this paper, we present the development and characterization of new formulations of bioactive glass into a porous scaffold and their suitability to act as a drug delivery system in the management of bone infections in vitro.

## 2. Materials and methods

### 2.1. Preparation and characterization of different glass compositions

Two new glass compositions based on a SiO<sub>2</sub>–Na<sub>2</sub>O–ZnO–CaO–MgO–P<sub>2</sub>O<sub>5</sub> system (hereafter referred to as BGZ and MBG) were

prepared from reagent grade quartz (SiO<sub>2</sub>), calcium carbonate (CaCO<sub>3</sub>), light magnesium carbonate (MgCO<sub>3</sub>), dry soda ash (Na<sub>2</sub>CO<sub>3</sub>), di-ammonium hydrogen ortho-phosphate [(NH<sub>4</sub>)<sub>2</sub>HPO<sub>4</sub>] and zinc oxide (ZnO) using a conventional glass melting procedure. All raw materials were of analytical grade and sourced from S.D. Fine-Chem, India. Briefly, the raw materials were melted in air in a platinum crucible at 1400 °C for 30 min., and the molten glass was quenched (Kundu et al., 2011). The glass frits resulting from the quenching operation were powdered in a planetary ball mill, sieved and stored in an airtight container until further use. Table 1 presents the compositions of both glasses (assessed via thorough conventional chemical analysis). A differential thermal analysis (DTA) and a derivative differential thermal analysis (DDTA) were conducted using a DTA (STA 449C, Netzsch, Germany) to determine the thermal profiles of the glass powders. Scans were conducted between 40 and 850 °C heated at a rate of 5 °C/min. Profiles were collected over three repeats with a sample mass of 5±0.5 mg. Fourier transformed infrared (FTIR) transmittance spectra were recorded at wave numbers ranging from 4000 to 400 cm<sup>-1</sup> using a Spectrum 100 instrument (Spectrum 100, PerkinElmer, USA) with a resolution of 2 cm<sup>-1</sup> to confirm the functional groups present. Potassium bromide (KBr) pelleted discs that consisted of approximately 2 mg of sample and 200 mg of KBr were employed. The X ray diffraction (XRD) patterns of powdered glass was recorded at a diffraction angle of 20–60° (2θ) using a X'Pert Pro (Phillips Analytical, Netherlands) X ray diffractometer with Cu K<sub>α1</sub> radiation (λ=1.5406 Å) at a scan speed of 2° min<sup>-1</sup>.

### 2.2. Preparation of porous bioactive glass scaffolds and their characterization

The respective glass powders were first mixed with an equal quantity of porogen (naphthalene). The resultant mix was compacted at 150 MPa in a cold-isostatic press (EPSI, Belgium). Subsequently, specimens of required dimensions (φ 8 mm) were sliced with a low speed saw (Isomet, Buehler, USA). The naphthalene was evaporated from the samples via very slow drying up to 80 °C, followed by sintering at approximately 725 °C on a Pt–Rh plate for 6 min. The samples were finally stored in a vacuum desiccator until further use. The porosity of the blocks was measured using water displacement method (Archimedes' principle), and the pore size distribution was measured using a mercury porosimeter (PM60, Quantachrome, USA) with an applied pressure ranging from 0 to 3000 psi.

**Table 1 – Compositions of the glasses.**

Composition	BGZ (mol%)	MBG (mol%)
SiO <sub>2</sub>	55.9	58
Na <sub>2</sub> O	11.8	12
CaO	16.14	18
P <sub>2</sub> O <sub>5</sub>	2.5	7
ZnO	1.24	2.4
MgO	9.93	2.6
K <sub>2</sub> O	2.5	–

### 2.3. Acellular static in vitro bioactivity test

The acellular static in vitro bioactivities of both glass powders were evaluated in simulated body fluid (SBF) as detailed by Kokubo and Takadama (2006). The ratio of the respective glass powder's weight to the SBF volume was 1.5 mg/mL, and the temperature was maintained at 37 °C in tightly closed polystyrene bottles for 1, 3 and 7 days without refreshing the SBF solution, which was finally analyzed by FTIR. While for glass scaffolds, this was conducted for up to 7 days in the same way. The scaffolds were studied after definite time intervals using a scanning electron microscope (SEM) (Steroscan 430i, Leo, UK) and XRD analysis. The weight changes of the scaffolds together with change in the pH of the dissolution medium (SBF) were also recorded for up to 28 days.

### 2.4. Cytotoxicity test

The cytotoxicity of the glass powders and scaffold samples was tested in vitro. Both direct contact and test on extracts were performed following the standard specifications of ISO10993-5 (2009). The in vitro cytotoxicity tests were performed using sterilized specimens of test samples, negative controls and positive controls. For the direct contact method, all of the specimens, including the negative control (ultra-high-molecular-weight polyethylene) and positive control (poly-vinyl chloride), were tested in triplicate and placed on a sub-confluent monolayer of osteoblast-like human osteosarcoma cells (MG-63) cells in DMEM (Dulbecco's modified eagle medium). After incubating the cells with test samples at 37 ± 2 °C for 24 ± 1 h, the cell culture was examined microscopically for a cellular response around test samples. For the extract method, the extract was prepared by incubating test materials with physiological saline at 37 ± 2 °C for 72 ± 2 h and medium to obtain an extraction ratio of 1.25 cm<sup>2</sup>/mL. The resultant extracts (100%) were diluted further with media to also obtain concentrations of 50% and 25%. Different dilutions of extracts of test samples, negative controls (ultra-high-molecular-weight polyethylene) and positive controls (dilute phenol) were placed in triplicate on a sub-confluent monolayer of human osteosarcoma cells (MG-63) cells. After incubating the cells with extracts of test samples and controls at 37 ± 2 °C for 24 ± 1 h, the cell cultures were microscopically examined for a cellular response.

### 2.5. MTT assay

The MTT assay was developed to measure cell survival and proliferation (Mosmann, 1983). Approximately 1600 cells were seeded into each well of a 96-well plate. In addition, 100 µL of the culture medium alone was added to the bottom row as a negative control. When the cells reached confluence after 24 h, the medium was removed by aspiration, and 100 µL of the experimental medium was added to each well. Only 25% of the leached product was used for this experiment. A control set without any test sample was also prepared. The dimethyl thiazolyl diphenyl tetrazolium (MTT) solution was prepared at a concentration of 5 mg/mL in phosphate buffered saline (PBS) just before use and filtered by passing through a 0.22-µm filter. After 24 h, 48 h and 72 h of treatment, 10 µL of MTT solution was added to each well, and the incubation was continued for

another 3 h. All of the medium was then removed by inverting and tapping the plates, and 100 µL of dimethyl sulfoxide (DMSO) was added to each well. The spectrophotometric absorbance at 540 nm was then measured via an enzyme linked immunosorbent assay (ELISA) reader. Non-cytotoxic, mildly cytotoxic, moderately cytotoxic and severely cytotoxic cellular responses were scored as 0, 1, 2 and 3, respectively.

### 2.6. Wound healing assay

A wound healing assay was also performed with human osteosarcoma cells (MG-63). The cells were grown in complete media. When the cells were 70–80% confluent, they were trypsinized and placed in a 6-well plate in complete media. Next day, a scratch wound was made across each well of the 6-well plate using a pipette tip. In this experiment, 25% of the leached glass was used because we needed to maintain the cells for 72 h to take the image. The image was taken after 0 h, 24 h, 48 h and 72 h under a microscope with 100 × magnification.

### 2.7. Preparation of drug loaded porous glass scaffolds

Porous glass scaffolds were loaded with the drug gatifloxacin via the vacuum infiltration method. Scaffolds of known weight were immersed in a drug solution and subjected to a vacuum of 9.67 t/square inch for 20 min. The vacuum was released after the stated period, and the scaffolds were allowed to dry at ambient conditions. The formulation variables, such as the concentration of the drug solution used for the loading drug, the type of drug and the polymer coating, were varied to study their influence on the in vitro drug release. Table 2 presents the list of formulation codes and the applied variables.

The amount of drug loaded in the scaffold was measured by determining the concentration of drug solution before and after the infiltration process (Zhu and Kaskel, 2009). The concentration of drug solution was determined by suitably diluting an aliquot with the respective medium and analyzing it in an UV-spectrophotometer (Lambda 45, PerkinElmer, USA) at 287 nm for gatifloxacin. The drug concentration was determined from the calibration curves constructed using known concentration of gatifloxacin. The drug loading in scaffolds was determined according to the difference between the initial and final weight of blocks.

### 2.8. In vitro drug release studies

The drug-loaded scaffolds were immersed in 5 mL of PBS (pH 7.4) and maintained at 37 °C. Aliquots were removed at selected intervals from 24 h to 43 days and analyzed by UV spectrophotometry. The study was terminated when the samples failed to release more than 1.2 µg drug/mL/day or at 43 days, whichever was earlier. The set limit value was averaged per day by dividing the measured concentration by the number of days between the sampling. In vitro drug release studies were similarly conducted in SBF (pH 7.4).

To study the kinetics and mechanism of drug release from the scaffolds, the in vitro drug release data of gatifloxacin in different dissolution mediums were fitted to the Higuchi

**Table 2 – List of drug loaded glass formulations with the variables applied.**

Scaffold code	Conc. of drug in loading ( $\mu\text{g/mL}$ )	Conc. of chitosan in coating (% w/v)	Dissolution medium	Scaffold code	Conc. of drug in loading ( $\mu\text{g/mL}$ )	Conc. of chitosan in coating (% w/v)	Dissolution medium
BGZ-3	25	–	PBS	MBG-3	25	–	PBS
BGZ-4	12.5	–	PBS	MBG-4	12.5	–	PBS
BGZ-5	6.25	–	PBS	MBG-5	6.25	–	PBS
BGZ-7	25	0.5	PBS	MBG-7	25	0.5	PBS
BGZ-8	25	1.0	PBS	MBG-8	25	1.0	PBS
BGZ-9	25	–	SBF	MBG-9	25	–	SBF

(Eq. (1)), Hixon–Crowell (Eq. (2)) and Korsmeyer–Peppas (Eq. (3)) models as follows:

$$A_t = k_H t^{0.5} \quad (1)$$

$$(AR_t)^{1/3} = k_{HC} t \quad (2)$$

$$A_t/A_\infty = k_{KP} t^n \quad (3)$$

where  $A_t$  is the amount of drug released at time  $t$ ;  $AR_t$  is the amount of unreleased drug at time  $t$ ;  $A_\infty$  is the amount of drug released at time  $\infty$ ;  $k_H$ ,  $k_{HC}$  and  $k_{KP}$  are the release constants for the Higuchi, Hixon–Crowell and Korsmeyer–Peppas models, respectively (Czarnobaj, 2008; Merchant et al., 2006). In Eq. (3), ‘ $n$ ’ is the exponent indicative of the release mechanism.

### 3. Results and discussions

The addition of antimicrobials to bone substitutes is an intelligent way to protect augmentation procedures from infection. Both the release of antimicrobials and the resorption of bone substitutes occur simultaneously to control the probability of infection and favor bone healing, especially during the early stage of implantation (Van de Belt et al., 2001). Local antimicrobial prophylaxes by loading popular biomaterials, such as hydroxyapatite and bioactive glass, with drugs demonstrated appreciable success (Kundu et al., 2011, 2010b; Nandi et al., 2009a, 2009b). During the last few decades, the interest in fabricating bioactive materials based drug delivery systems has increased. Hydroxyapatite and bioactive glasses are among the most preferred materials for exploitation. Several comparative studies have proved the efficacy of bioactive glass as a better biodegradable ceramic that enhances the proportion of bone formation and bonding in vivo compared to hydroxyapatite (Hong et al., 2009; Leng et al., 2005; Mistry et al., 2010; Nair et al., 2006). Hence, we opted to apply new composites of bioactive glasses as a carrier for drug delivery to control post-surgical orthopedic infections.

The glass composite was formulated from a  $M_2O$ – $RO$ – $ZnO$ – $SiO_2$  glass system, where  $M=Na$  and  $K$  and  $R=Ca$  and  $Mg$ . Silica-based glasses consisting of  $SiO_2 < 60$  mol%, high  $Na_2O$  and  $CaO$  contents, and a high  $CaO/P_2O_5$  ratio are expected to be highly bioactive (Agathopoulos et al., 2006; Bang et al., 2008).  $Mg$  and  $Ca$  ions were employed as network modifiers to increase the degradation of bioactive glass. From a biological point of view, magnesium acts as a glue that binds calcium

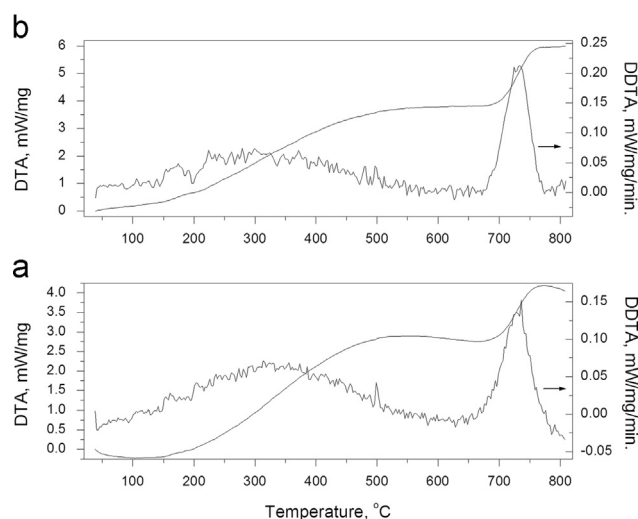


**Fig. 1 – DTA/DDTA thermogram of as-prepared (a) BGZ powder and (b) MBG powder.**

and fluorine to build bone, without which calcium and fluorine will be flushed out of the system (Rodale and Taub, 1971). From a material science point of view, the addition of potassium to bioactive glass reduces the tendency for crystallization, while the presence of potassium appears to increase bone formation (Bushinsky et al., 1997). The presence of zinc oxide in the composite was based on its ability to modify bioactivity, enhance protein synthesis in the bone tissues and promote bone formation (Aina et al., 2009; Ma and Yamaguchi, 2001).

The DTA and DDTA results (Fig. 1) indicated a glass softening temperature of  $< 750$  °C. Comparing the DTA profiles of BGZ and MBG subjected to various heating rates indicated that thermal degradation did not induce adverse changes in the sample. This finding assures that any change in the heating rate during synthesis will not affect the composition of the glass and the scaffold formed. Furthermore, the glass transition temperatures ( $T_g$ ) were calculated from Fig. 1a and b and found to be  $\sim 700$  °C and  $\sim 715$  °C for BGZ and MBG glasses, respectively. This finding demonstrates that the  $T_g$  of BGZ is slightly less due to the addition of alkali metals (Mazurin, 2007). The firing temperature of the green and dried scaffolds was selected based on their respective  $T_g$ . This firing temperature was 725 °C due to the non-vitrification of scaffolds and subsequent pore closure at that temperature.

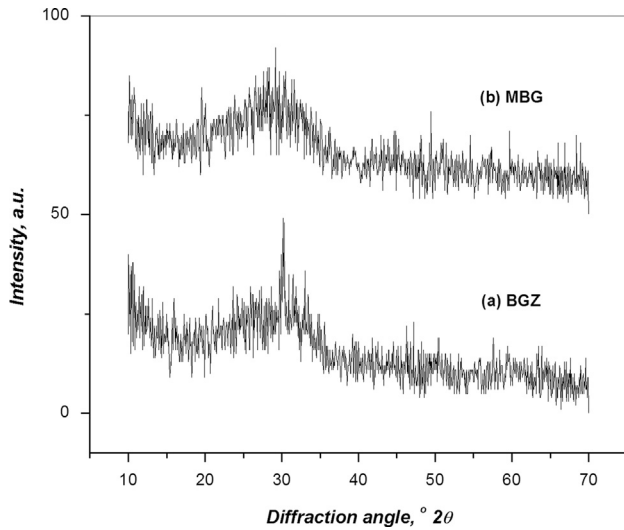


**Fig. 2 – X ray diffraction pattern of (a) BGZ powder and (b) MBG powder.**

The XRD patterns of BGZ (Fig. 2a) and MBG (Fig. 2b) indicated the amorphous nature of the respective powders, which is desirable for in vivo applications. A very small, low-intensity hump is also evident in Fig. 2a, which may be indicative of negligible crystallization when formed (due to presence of  $\text{CaSiO}_3$ , wollastonite). Conversely, the FTIR (Fig. 3a for BGZ and 3b for MBG) showed two broad strong absorption bands at  $\sim 1032 \text{ cm}^{-1}$  and  $467 \text{ cm}^{-1}$ , which can be assigned to Si-O and P-O vibrations, respectively. The broad small band at  $\sim 780 \text{ cm}^{-1}$  may be due to the bending vibrations of Si-O-Si bridges. However, the presence of different groups, such as Zn-O and phosphates, cannot be accurately identified because of the superimposition of different peaks. As the  $\text{SiO}_2$  content decreased and the alkali and alkali-earth oxide contents increased, the maximum transmittance of the Si-O (stretching) band shifted towards higher values until  $1032 \text{ cm}^{-1}$  and the intensity increased from MBG to BGZ. The intensity of the band associated with the Si-O-NBO groups (NBO: non-bridging oxygen) decreased and slightly diffused at  $\sim 952 \text{ cm}^{-1}$ . This finding actually corroborated the findings of Serra et al. (2003).

Fig. 4a and b illustrate the FTIR spectra of BGZ and MBG glass powders before and after soaking in SBF for different time periods (1, 3 and 7 days). Before soaking in SBF, the BGZ sample exhibited the bending and stretching vibrations of Si-O bonds at  $455, 762$  and  $1040 \text{ cm}^{-1}$ . After soaking in SBF, the peaks representing P-O vibrations at  $560, 960$  and  $1220 \text{ cm}^{-1}$  indicated hydroxyapatite formation. The peak at near  $1625 \text{ cm}^{-1}$  was assigned to  $\text{OH}^-$  entrapped in apatites (Conz et al., 2005). However, MBG exhibited vibrations of Si-O-Si bonds at  $467$  and  $\sim 1020 \text{ cm}^{-1}$  before soaking in SBF. After soaking in SBF, a peak at  $1490 \text{ cm}^{-1}$  assigned to C-O vibrational bands and peaks near  $955, 1075$  and  $1205 \text{ cm}^{-1}$  assigned to the P-O bonds could be observed, which indicated the formation of hydroxyapatite with carbonate groups. The peak near  $1636 \text{ cm}^{-1}$  is due to the  $\text{OH}^-$  entrapped within apatites and higher intensities at around  $3500 \text{ cm}^{-1}$  with time also confirming this entrapment after 7 days (Conz et al., 2005). BGZ showed a more open amorphous structure due to

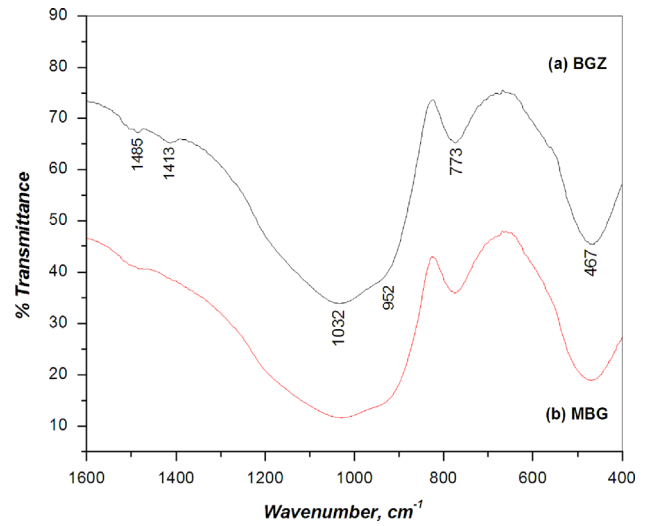


**Fig. 3 – FTIR spectrum of (a) BGZ powder and (b) MBG powder.**

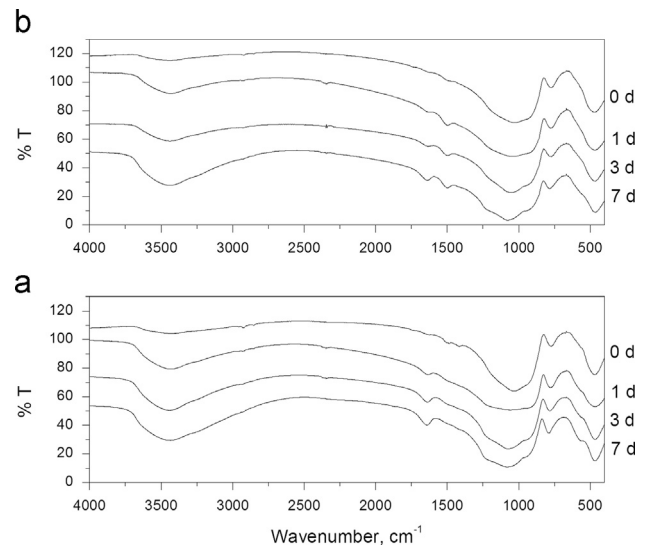


**Fig. 4 – FTIR spectra of (a) BGZ and (b) MBG glass subjected to acellular in vitro bioactivity study at various periods.**

the increased addition of alkali network modifiers prior to the submersion in SBF. Additional cations in the structure reduce the degree of connectivity by replacing bridging oxygen with NBO in silicon-oxygen groups.

Fig. 5a and b present the pore size distribution data of the BGZ and MBG scaffolds, respectively. For BGZ (Fig. 5a), pores were mainly unimodal, and their sizes predominantly ranged from  $5$  to  $50 \mu\text{m}$ , indicating that they were suitable for drug delivery applications (Soundrapandian et al., 2007) because small pores are known to sustain the release better than large pores (Chai et al., 2007). For BGZ scaffolds, the bulk density, open and closed porosity were calculated to be  $\sim 0.8 \text{ g/cm}^3$ ,  $\sim 66\%$  and  $\sim 4\%$ , respectively, while these values were  $\sim 0.9 \text{ g/cm}^3$ ,  $\sim 63\%$  and  $\sim 2\%$ , respectively, for the MBG scaffolds. These values are in a range that generally is agreed upon for rapid osteointegration (Hing, 2005). Over 90% of the total porosity consists of open and interconnected pores. Open and

interconnected pores are considered important, as they are the path channels for the supply of nutrients and removal of cell excretions required for tissue in-growth in porous scaffolds. Furthermore, the sizes of pores predominantly ranged from 10 to 30  $\mu\text{m}$ , indicating that they would facilitate the high adsorption of drug and sustain the release better than bone in-growth (Seeley et al., 2008; Soundrapandian et al., 2007). However, these pores could favor cell function better, as mammalian cells are typically 10–20  $\mu\text{m}$  in size (Yannas, 1992).

Fig. 6A1, A2 and A3 shows the SEM images of BGZ porous scaffold surface subjected to acellular in vitro bioactivity studies for various periods (0D—day '0', 1D—'1' day, 7D—'7' days). The formation of apatites on the surface of bioceramics plays an essential role in the bonding of the biomaterial to

living bone and is considered an indication of in vivo bioactivity (Saint-Jean et al., 2005). Deposits of apatites were visible after one day. However, they were trace deposits and mostly individual scattered structures. The SEM pictures taken after three (not presented here) and seven days exhibited an increase in the deposits with dense clusters of apatites after seven days. This finding indicated that the time of exposure influenced the deposition of apatites.

Bioactivity is the phenomenon of eliciting a biological response at the material–biological site interface resulting in the formation of bonds between them following a series of biophysical and biochemical reactions at the interface. Bioactivity can be tested in vitro via the ability of the material to deposit apatites on its surface. The development of a layer consisting hydroxyapatite (HAp) on the surface of BGZ indicates its ability to bond with bone (Kontonasaki et al., 2002). Unlike polymers, bioactive materials favor apatite deposition, and hence, the weight change of scaffolds could be on negative or positive.

Fig. 6B1, B2 and B3 shows the SEM images of a MBG porous scaffold surface subjected to an acellular in vitro bioactivity study for various periods (0D—day '0', 1D—'1' day, 7D—'7' days). The structure remained intact for the entire study period. However, the surface exhibited significant changes after soaking in SBF for different times. After soaking in SBF for 1 day, the surface was covered with apatites. After 3 days, the number of deposits began to increase due to the increased size of apatites. At the end of 7 days, the deposits appeared as dense structures covering the entire surface. The smooth and blunt edges on the surface before immersion were totally absent, and rough and highly porous microstructural features were observed after 7 days, which indicates both the degradation of glass samples and the deposition of hydroxyapatite. Pores of variable dimensions that were formed during deposition of apatites were also visible.

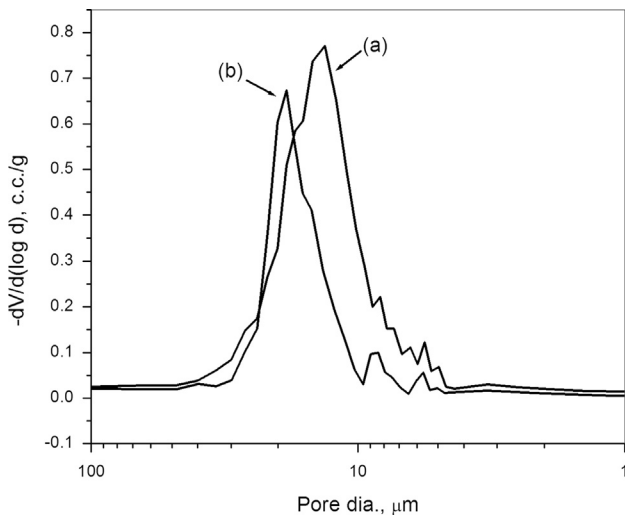


Fig. 5 – Pore size distribution of (a) BGZ and (b) MBG scaffolds.

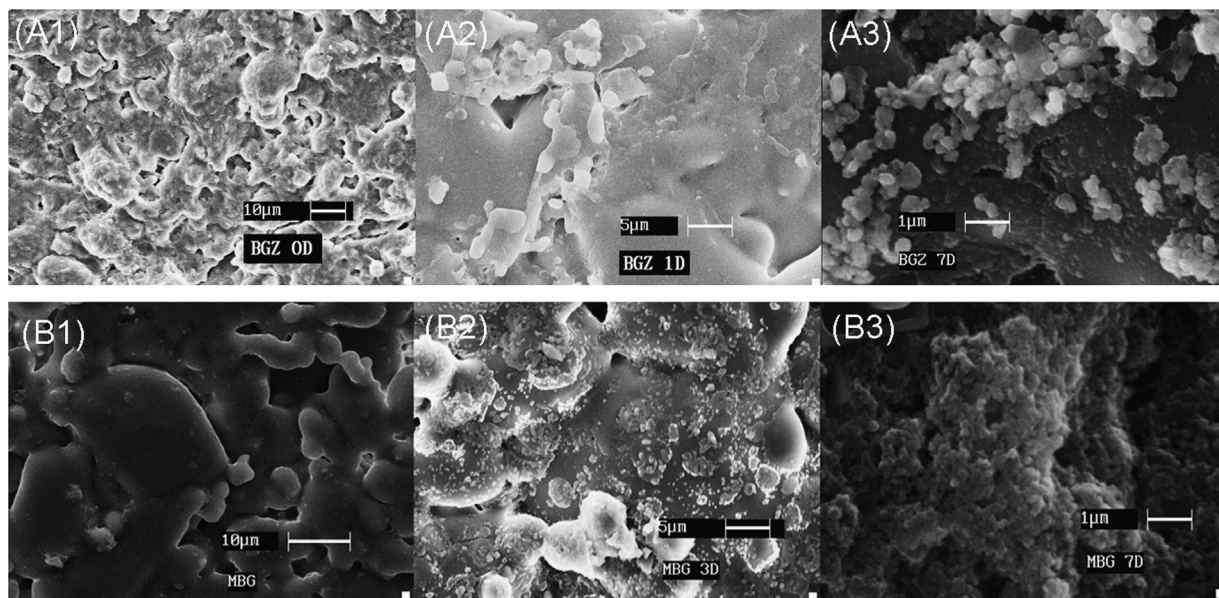


Fig. 6 – SEM images of BGZ (A1), (A2) and (A3) and MBG (B1), (B2) and (B3) scaffold surface subjected to acellular in vitro bioactivity study at various periods (0D—day '0', 1D—'1' day, 7D—'7' days).

The % cumulative weight loss (Fig. 7) and XRD (Fig. 8) reflected the deposition of apatites on the surface of BGZ and MBG after different time intervals. Initial weight losses of up to 10.3% and 0.82% were observed for MBG after 7 days and BGZ after 14 days, respectively. Subsequently, both of the scaffolds continuously gained mass, i.e., 4.2% and only approximately 0.56% for MBG and BGZ, respectively. MBG was found to be more bioactive than BGZ with respect to apatite formations, as revealed after 28 days. The pH of the SBF was found to be almost constant for BGZ at ~8 and very slightly varied around 8 for MBG up to day 28. Conversely, XRD showed peaks for crystalline HAp (JCPDS PDF 09-0432) after day 7 for BGZ (Fig. 8a), which remained amorphous for MBG (Fig. 8b). The result can be correlated with the weight loss at day 7 for MBG scaffolds, where dissolution was the prime phenomenon for non-stoichiometric or amorphous apatite phase deposited on the surface. Conversely, a much smaller weight loss (~0.62%) after day 7 may be indirect evidence of the formation of crystalline HAp on the BGZ surface.

The direct contact and extract method (Fig. 9a) tests indicate BGZ is mildly cytotoxic. The aim of the cytotoxicity tests was to examine whether the presence or degradation/dissolution of BGZ affected the growth of MG63 cells. This cell line was preferred, as it has previously been used in biocompatibility studies and exhibits a number of features similar to those of typical human osteoblasts (Clover and Gowen, 1994; Ferraz et al., 2007). The cellular response as measured by the scale was 1, indicating mildly cytotoxic effects. The negative control showed a non-cytotoxic response, and the positive control yielded a severely cytotoxic response, as expected. The MTT assay for cell viability (Fig. 10a) also showed BGZ to be mildly cytotoxic. The principle of the MTT method is that the tetrazolium ring in MTT is cleaved by the dehydrogenase present in active mitochondria, which results in the formation of an insoluble MTT formazan product (Slater et al., 1963). Therefore, the amount of these crystals serves as an estimate for the number of mitochondria, and hence, the

number of living cells in the samples. BGZ affected the cellular proliferation, and the cellular viability decreased with the time of exposure. A high percentage (72%) was observed

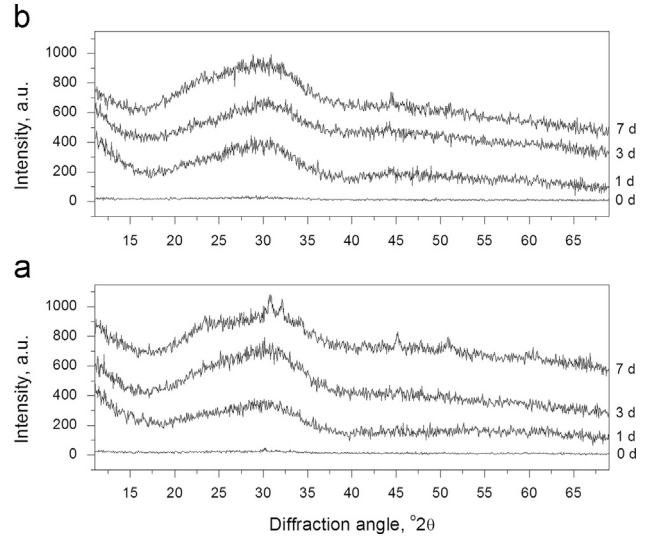


Fig. 8 – XRD of (a) BGZ and (b) MBG glass subjected to acellular in vitro bioactivity study at various periods.

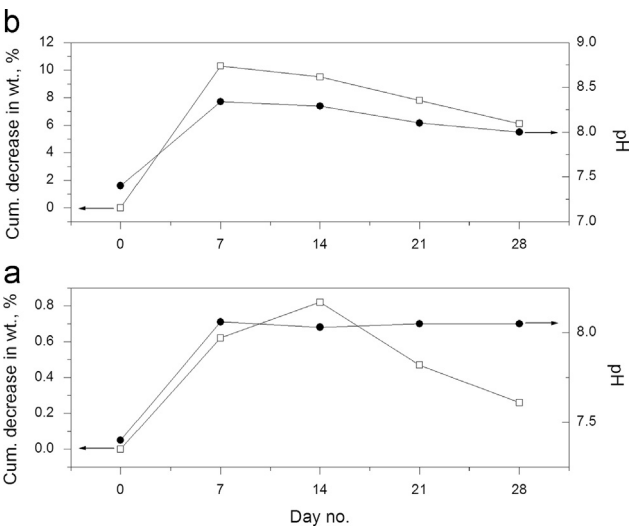


Fig. 7 – Cumulative change in scaffold weight when subjected to acellular in vitro bioactivity study at various periods.

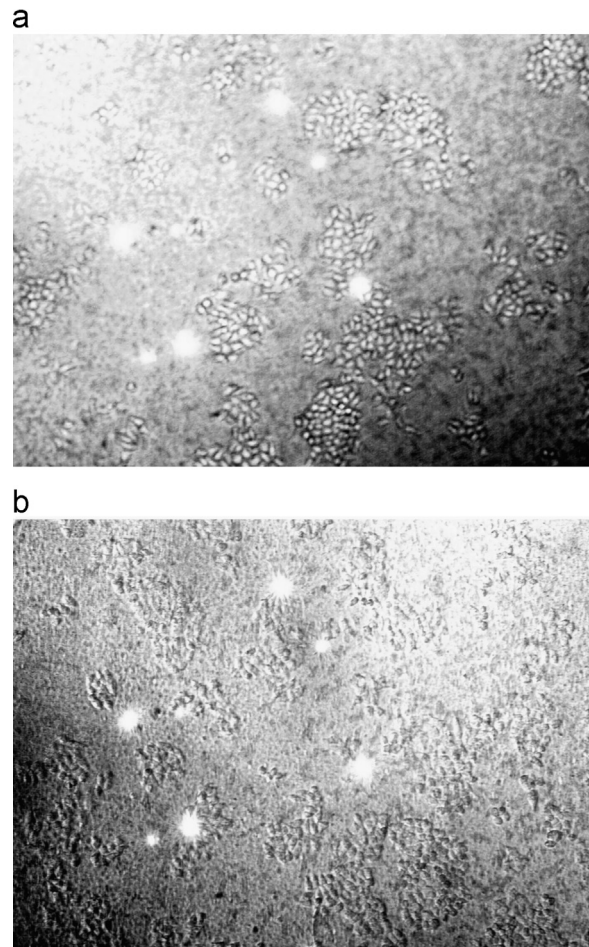


Fig. 9 – Cytotoxicity test (test on extract method). Cell survival plates treated with 25% concentration of (a) BGZ extract and (b) MBG extract.



in only the first 24 h sample, and the cell survival percentage was only 28% at the end of 72 h. This finding implied that this bioactive glass might exhibit cytotoxic effects in vivo. However, the test was carried out with a solution of the sample, and this type of dissolution is very unlikely in vivo. Nevertheless, further studies are needed.

The direct contact and extract method (Fig. 9b) cytotoxicity tests indicated MBG to be non-cytotoxic. The cellular response as measured by the scale was 0, indicating non-cytotoxic behavior. The negative control yielded a non-cytotoxic response, and the positive control yielded a severely cytotoxic response, similar to the results above. The MTT assay for cell viability (Fig. 10b) also demonstrated the non-cytotoxic nature of MBG. MBG did not affect the cell proliferation, and the cellular viability was maintained at levels higher than 87%. A low percentage was also observed only for the first 24 h sample, after which the cell survival percentage began to increase. This finding implied that this bioactive glass is suitable for implantation, without any significant cytotoxic effects. Although crystalline HAp formed after day 7, BGZ scaffold showed mild cyto-toxicity after day 3, most probably due to the faster dissolution of other

pro-osteoblast ions (e.g., Zn, Mg) as well as the lower phosphate concentration in the original scaffold.

The wound healing assay showed moderate healing for BGZ samples. Fig. 11A presents the pictures of streaked plates from 0–72 h. The wound healing assay is a simple assay that can be used to test the effect of BGZ on cell migration. The basic steps involve creating a “wound” in a cell monolayer, capturing the images at the beginning and at regular intervals during cell migration to close the wound and comparing the images to quantify the migration rate of the cells. A decrease in the diameter of the streak could be observed from the first 24 h and 48 h pictures. However, the streak disappeared in the 72 h picture due to the mild cytotoxic nature and considerable cell death, indicating the moderate wound healing potential of BGZ. Conversely, Fig. 11B presents the pictures of the streak plate from 0–72 h, which were similar. A decrease in the diameter of the streak could be observed in the first 24 h and 48 h pictures. The complete disappearance of the streak in the 72 h picture is an excellent indication of the healing potential of MBG for MG63 cells.

### 3.1. Drug delivery system

The drug loading efficiency was calculated to be 2.2 and 2.1% for the BGZ and MBG scaffolds, respectively. For the in vitro drug release, the cut-off limit of the drug was fixed at  $\geq 1.2 \mu\text{g/mL/day}$ , i.e., at least 10 times the minimum inhibitory concentration (MIC) of *Staphylococcus aureus* based on the MIC range for *S. aureus* (ATCC 29213) (NCCLS, 2002) in order to deliver the drug above the biofilm eradication concentration (BEC). Biofilms are one of the major causes for relapse of infection and are generally considered to require more than 10-fold the MIC to kill planktonic cells (Soundrapandian et al., 2007).

Fig. 12 presents the release profiles of gatifloxacin from scaffolds prepared by immersion in drug solutions of varying concentrations. Of the 3 studied formulations, BGZ-5 and MBG-5, which were prepared by immersion in a drug solution of the lowest concentration (6.25 mg/mL), released 99.6% and 99.3% in just 2 days, respectively. Both the BGZ-4 and MBG-4 formulations could not sustain the release for the entire study period and released more than 90% of the drug in 2 days and 98.8% in 15 days, respectively. However, formulations BGZ-3 and

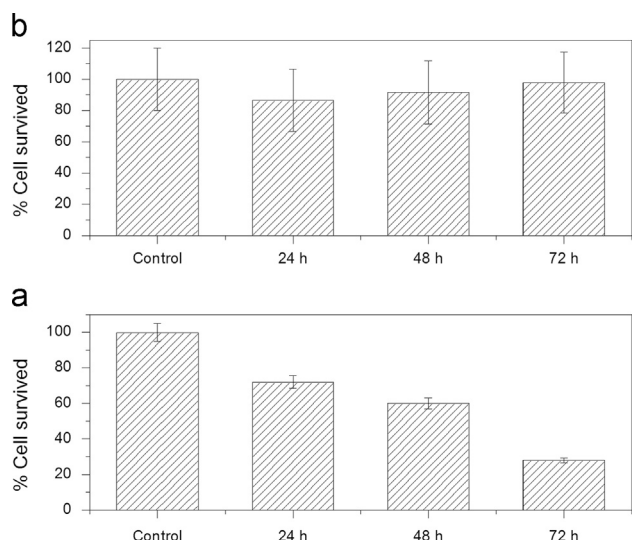


Fig. 10 – Cell survival percentage treated with (a) BGZ and (b) MBG observed at various time intervals.

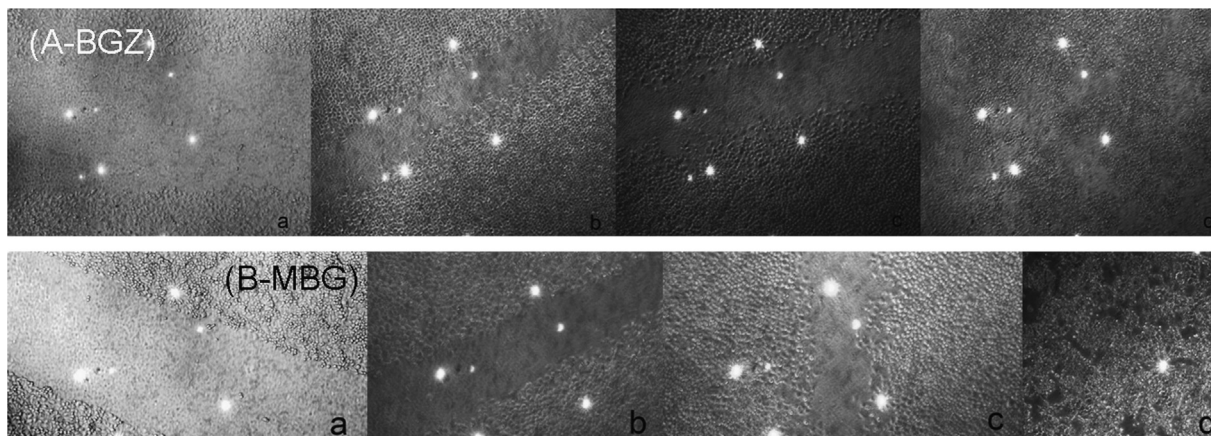
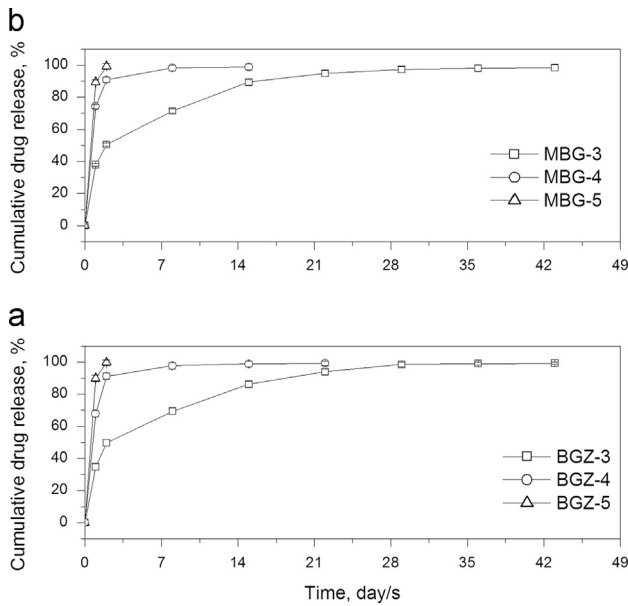


Fig. 11 – Wound healing assay pictures at various time for BGZ (A) and MBG (B).



**Fig. 12 – Effect of concentration of drug in loading solution on drug release for (a) BGZ and (b) MBG scaffolds.**

MBG-3 were found to better sustain the drug release for extended periods. A decrease in the concentration of the drug in the loading solution lowered the drug entrapment in the scaffold (data not presented here). When a scaffold is immersed in a dilute drug solution, fewer drug molecules will enter into the pores, and hence, the pore channels of the scaffolds contain fewer drug molecules. A low drug entrapment will also result in the formation of thinner films at the scaffold-dissolution medium interface according to basic mass transfer phenomena. These conditions probably resulted in the reduced resistance to the diffusion of drug molecules, which favored faster drug release.

Bioceramic scaffolds act more like a reservoir, and drug molecules exist in the scaffolds in four different states (Xia and Chang, 2006). A considerable portion of the drug molecules is attached to the exterior surface of the bioactive glass scaffold, while the majority is trapped in the pore channels where drug molecules exist in three different states. One fraction of the drug molecules exists at the pore channel openings, while the remainder exists in the pore channels where molecules may or may not be bonded to the pore wall surface. The scaffolds were loaded with gatifloxacin by immersing them in drug solution and applying negative pressure. This process attaches drug molecules to the pore channels and the surface. In addition, the drug molecules contain highly electronegative atoms/groups, such as  $F^-$ ,  $N^{3-}$  and  $OH^-$ , which could form hydrogen bonds with the  $Si-OH$  and  $P-OH$  groups in the scaffold or at pore wall surface. Hence, the drug molecules adhered to the surface would clearly be released faster, while those inside the pore channels would be released in a sustained fashion, as the drug must diffuse through the channel (Kundu et al., 2011, 2010b).

Although the BGZ scaffolds could release gatifloxacin for more than 6 weeks above the set limit, a considerable part of the drugs was released in one day. Coating the scaffolds

could significantly reduce this burst release, and coating bioceramic scaffolds with polymer also results in the formation of organic-inorganic composite scaffolds. Chitosan was selected, as it is a natural polymer with excellent biocompatibility, non-toxic, biodegradable and bioresorbable (Noble et al., 1999; Rossi et al., 2008; Ubaidulla et al., 2009). These properties and their various antibacterial, antifungal, hemostatic and wound healing biological activities (Baldrick, 2010; Kong et al., 2008; Park et al., 2008) make it an interesting polymer. The effect of coating of BGZ scaffolds with chitosan on drug release was compared with BGZ-3. Fig. 13 illustrates the release of gatifloxacin from uncoated (BGZ-3) and coated (BGZ-7 and BGZ-8) scaffolds. Although coating the scaffolds could significantly reduce the burst release of the drug and provide for extended release during the study period, the BGZ-8 formulation, which was coated with highest concentration of chitosan (1% w/v), failed to maintain the set limit (1.2  $\mu\text{g}/\text{mL}/\text{day}$ ) in the final week. Conversely, BGZ-7, which was coated with 0.5% chitosan, could reduce the release on the initial day and maintain the drug release concentration above the set limit for the entire study period (Kundu et al., 2010a). Although coatings could be successfully applied to control drug release, the presence of a polymer coat on bioceramics may affect the bioactivity by delaying the release process (Soundrapandian et al., 2009).

Similar observations were made for MBG scaffolds. Here, MBG-8, which was also coated with the highest concentration of chitosan (1% w/v), failed to maintain the set limit in the final week. However, although MBG-8 failed to maintain the set limit, which was fixed based on the higher end of MIC, the formulation was very successful in releasing the drug above 0.3  $\mu\text{g}/\text{mL}/\text{day}$ , a limit based on the lower end of MIC. However, MBG-7 could both reduce the burst release and maintain the drug release concentration above the set limit for the entire study period.

Drug release studies are generally conducted in a dissolution medium of PBS (Soundrapandian et al., 2007, 2009). However, bioceramics may react with SBF and form apatites

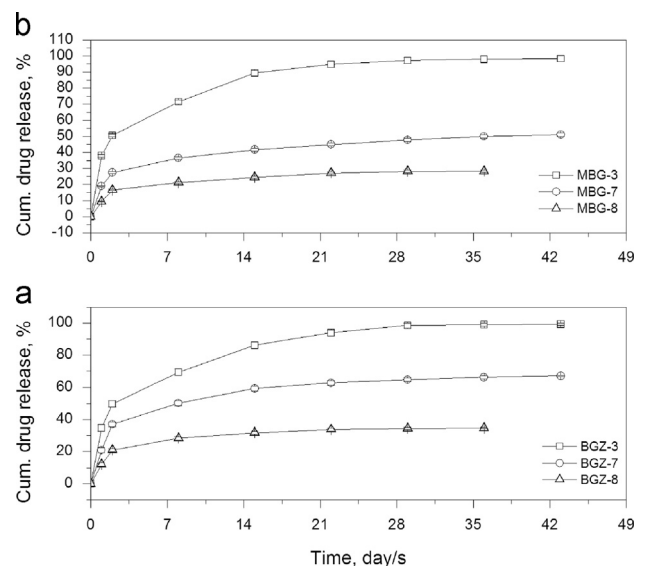


**Fig. 13 – Effect of coating and concentration of polymer solution on drug release for (a) BGZ and (b) MBG scaffolds.**

on the surface, which could alter the drug release (Kundu et al., 2010b). The effect of dissolution media on drug release was studied using BGZ-3, and the results are shown in Fig. 14. The difference in the release profiles became apparent in the first 24 h. The drug release in SBF was lower than that in PBS, and the difference became more prominent over time (Kundu et al., 2010b). While BGZ-3 released approximately 34% (37.9% for MBG-3) of the drug in the first 24 h, BGZ-9 released only approximately 26% (29.5% for MBG-9), both of which were lower than the release (78%) reported earlier for the same drug from nonporous monolithic-polymer controlled systems (El-Kamel and Baddour, 2007). At the end of the study period, the amount of drug released (from BGZ) in SBF was approximately 16% less than that in PBS (while it was 21% less for MBG), although the release of the drug exceeded the set concentration limit. This finding indicates that the same scaffold could successfully deliver drugs for a few weeks more in SBF. The release profiles shows that the sustained release of the drug from the scaffolds in SBF was also influenced by the formation of apatites. The lowest concentrations of drug released per day from MBG-3 and MBG-9 were 2.0 and 7.6  $\mu\text{g}/\text{mL}$ , respectively. The release of drug from MBG scaffolds was lower in SBF than PBS due to the formation of apatites. A similar influence of SBF on drug release was reported earlier from polycaprolactone–tricalcium phosphate composites for growth factors (Rai et al., 2005).

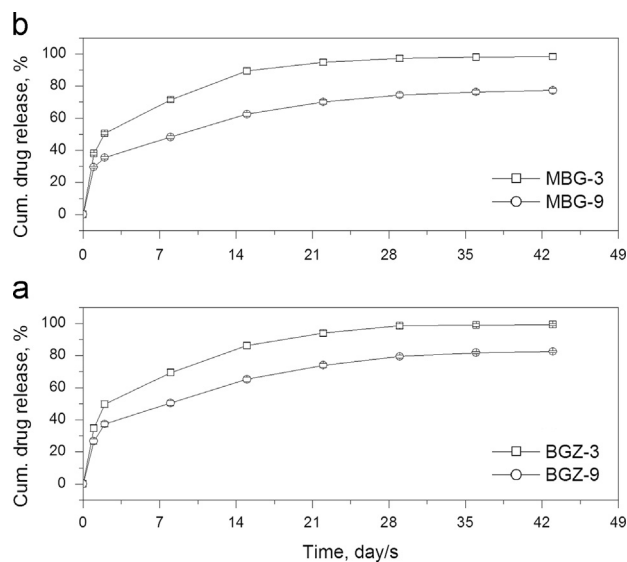


Fig. 14 – Effect of dissolution medium on drug release for (a) BGZ and (b) MBG scaffolds.

Comparing the results of various models studied (Table 3) showed that the in vitro release of the drug from MBG and BGZ scaffolds followed the Korsmeyer–Peppas model more closely, with the values of “n” varying from 0.29–0.23 and 0.29–0.32, respectively, which was indicative of Fickian diffusion. The theoretical analysis and models of drug release employed to describe the release from polymers can also be applied for bioceramics (Melville et al., 2008). The release of drug from both the scaffolds was found to be diffusion-dependent, as previously reported for bioceramic carriers (Melville et al., 2008; Pham et al., 2002). However, previous reports have only applied Higuchi’s and lacked comparisons with other models. The release pattern of the drug from MBG scaffolds fit the Korsmeyer–Peppas model better than Higuchi’s model. The advantage of the Korsmeyer–Peppas model is that it could be applied for spherical or cylindrical shapes, the mechanism of drug transport could be identified and the swelling and dissolution processes could be simultaneously identified in cases that consider diffusion. With “n” values below 0.45 for cylindrically shaped systems, the model indicates the drug to be released via Fickian diffusion. The erosion of the delivery system irrespective of the dissolution medium had a comparatively lesser effect on the drug release, as exhibited by the low  $R^2$  values of the Hixon–Crowell model.

#### 4. Conclusion

The results of this study indicated that 63–66% porous and 5- to 50- $\mu\text{m}$  nearly unimodal bioactive glass scaffolds (MBG and BGZ) formed with a new composition of bioactive glass could successfully release drugs for 43 days at concentrations to treat bone infections. In addition, the release of drugs followed the Peppas–Korsmeyer release pattern based on Fickian diffusion, and increasing the implant size and drug load of the scaffold prolonged the release, while a 0.5–1% chitosan coating on the pore surface of the scaffolds decreased the burst release and the overall release of the drug. The results also indicated that MBG-based scaffolds were bioactive, biocompatible, non-cytotoxic and exhibited excellent wound healing potential, while BGZ was mildly cytotoxic with moderate wound healing potential. These results strongly suggest that MBG scaffolds appear to be a suitable bone drug delivery system for the treatment of orthopedic infections and as bone void fillers, but BGZ should be handled with caution or studied elaborately in detail to further ascertain and confirm the cytotoxic nature and wound healing potential of this glass.

Table 3 – Modeled in vitro release kinetics.

Formulation	Higuchi $R^2$	Hixon–Crowell $R^2$	Korsmeyer–Peppas		Formulation	Higuchi $R^2$	Hixon–Crowell $R^2$	Korsmeyer–Peppas	
			$R^2$	n				$R^2$	n
BGZ-3	0.9226	0.7894	0.972	0.32	MBG-3	0.9024	0.7579	0.9706	0.29
BGZ-9	0.9662	0.9082	0.987	0.29	MBG-9	0.9682	0.9113	0.9911	0.23

## Acknowledgements

The authors wish to express their sincere thanks to the Director CSIR-Central Glass and Ceramic Research Institute, Kolkata, India, Vice Chancellor, Jadavpur University, Kolkata, India and the Principal, Himalayan Pharmacy Institute, East Sikkim, India for their generous and kind support to this work. All the personnel related to the characterization of the materials are sincerely acknowledged. Department of Science and Technology (DST), Government of India is also thankfully acknowledged for their financial support vide INT/FINLAND/P-11 towards this work.

## REFERENCES

- Agathopoulos, S., Tulyaganov, D.U., Ventura, J.M.G., Kannan, S., Saranti, A., Karakassides, M.A., Ferreira, J.M.F., 2006. Structural analysis and devitrification of glasses based on the CaO–MgO–SiO<sub>2</sub> system with B<sub>2</sub>O<sub>3</sub>, Na<sub>2</sub>O, CaF<sub>2</sub> and P<sub>2</sub>O<sub>5</sub> additives. *J. Non-Cryst. Solids* 352, 322–328.
- Aina, V., Malavasi, G., Fiorio Pla, A., Munaron, L., Morterra, C., 2009. Zinc-containing bioactive glasses: surface reactivity and behaviour towards endothelial cells. *Acta Biomater.* 5, 1211–1222.
- Arcos, D., Ragel, C.V., Vallet-Regí, M., 2001. Bioactivity in glass/PMMA composites used as drug delivery system. *Biomaterials* 22, 701–708.
- Baldrick, P., 2010. The safety of chitosan as a pharmaceutical excipient. *Regul. Toxicol. Pharmacol.* 56, 290–299.
- Bang, H.-G., Kim, S.-J., Park, S.-Y., 2008. Biocompatibility and the physical properties of bio-glass ceramics in the Na<sub>2</sub>O–CaO–SiO<sub>2</sub>–P<sub>2</sub>O<sub>5</sub> system with CaF<sub>2</sub> and MgF<sub>2</sub> additives. *J. Ceram. Process. Res.* 9, 588–590.
- Bushinsky, D.A., Riordon, D.R., Chan, J.S., Krieger, N.S., 1997. Decreased potassium stimulates bone resorption. *Am. J. Physiol.* 272, F774–F780.
- Cartmell, S., 2009. Controlled release scaffolds for bone tissue engineering. *J. Pharm. Sci.* 98, 430–441.
- Chai, F., Hornez, J.C., Blanchemain, N., Neut, C., Descamps, M., Hildebrand, H.F., 2007. Antibacterial activation of hydroxyapatite (HA) with controlled porosity by different antibiotics. *Biomol. Eng.* 24, 510–514.
- Clover, J., Gowen, M., 1994. Are Mg-63 and Hos Te85 human osteosarcoma cell-lines representative models of the osteoblastic phenotype? *Bone* 15, 585–591.
- Conz, M.B., Granjeiro, J.M., Soares, G.d.A., 2005. Physicochemical characterization of six commercial hydroxyapatites for medical-dental applications as bone graft. *J. Appl. Oral Sci.* 13, 136–140.
- Czarnobaj, K., 2008. Preparation and characterization of silica xerogels as carriers for drugs. *Drug Delivery* 15, 485–492.
- Domingues, Z.R., Cortés, M.E., Gomes, T.A., Diniz, H.F., Freitas, C. S., Gomes, J.B., Faria, A.M.C., Sinisterra, R.D., 2004. Bioactive glass as a drug delivery system of tetracycline and tetracycline associated with  $\beta$ -cyclodextrin. *Biomaterials* 25, 327–333.
- El-Kamel, A.H., Baddour, M.M., 2007. Gatifloxacin biodegradable implant for treatment of experimental osteomyelitis: in vitro and in vivo evaluation. *Drug Delivery* 14, 349–356.
- Ferraz, M.P., Mateus, A.Y., Sousa, J.C., Monteiro, F.J., 2007. Nanohydroxyapatite microspheres as delivery system for antibiotics: release kinetics, antimicrobial activity, and interaction with osteoblasts. *J. Biomed. Mater. Res.* 81A, 994–1004.
- Gadre, S.Y., Gouma, P.I., 2006. Biodoped ceramics: synthesis, properties, and applications. *J. Am. Ceram. Soc.* 89, 2987–3002.
- Hing, K.A., 2005. Bioceramic bone graft substitutes: influence of porosity and chemistry. *Int. J. Appl. Ceram. Technol.* 2, 184–199.
- Hong, Z., Reis, R.L., Mano, J.F., 2009. Preparation and in vitro characterization of novel bioactive glass ceramic nanoparticles. *J. Biomed. Mater. Res. A* 88, 304–313.
- ISO10993-5, 2009. Biological evaluation of medical devices: Part 5 tests for in vitro cytotoxicity. *Int. Organiz. Stand.*
- Kokubo, T., Takadama, H., 2006. How useful is SBF in predicting in vivo bone bioactivity?. *Biomaterials* 27, 2907–2915.
- Kong, M., Chen, X.G., Liu, C.S., Liu, C.G., Meng, X.H., le, J., Yu, 2008. Antibacterial mechanism of chitosan microspheres in a solid dispersing system against *E. coli*. *Colloids Surf., B* 65, 197–202.
- Kontonasaki, E., Zorba, T., Papadopoulou, L., Pavlidou, E., Chatzistavrou, X., Paraskevopoulos, K., Koidis, P., 2002. Hydroxy-carbonate apatite formation on particulate bioglass in vitro as a function of time. *Cryst. Res. Technol.* 37, 1165–1171.
- Kundu, B., Lemos, A., Soundrapandian, C., Sen, P.S., Datta, S., Ferreira, J.M.F., Basu, D., 2010a. Development of porous HAP and  $\beta$ -TCP scaffolds by starch consolidation with foaming method and drug-chitosan bilayered scaffold based drug delivery system. *J. Mater. Sci.—Mater. Med.* 21, 2955–2969.
- Kundu, B., Nandi, S.K., Dasgupta, S., Datta, S., Mukherjee, P., Roy, S., Singh, A.K., Mandal, T.K., Das, P., Bhattacharya, R.N., Basu, D., 2011. Macro-to-micro porous special bioactive glass and ceftriaxone-sulbactam composite drug delivery system for treatment of chronic osteomyelitis: an investigation through in vitro and in vivo animal trial. *J. Mater. Sci.—Mater. Med.* 22, 705–720.
- Kundu, B., Soundrapandian, C., Nandi, S.K., Mukherjee, P., Dandapat, N., Roy, S., Datta, B.K., Mandal, T.K., Basu, D., Bhattacharya, R.N., 2010b. Development of new localized drug delivery system based on ceftriaxone-sulbactam composite drug impregnated porous hydroxyapatite: a systematic approach for in vitro and in vivo animal trial. *Pharm. Res.* 27, 1659–1676.
- Leng, Y., Xin, R., Chen, J., 2005. A comparative study of bioceramics in vitro and in vivo. *Key Eng. Mater.* 284–286, 11–14.
- Luo, Y., Prestwich, G.D., 2001. Novel biomaterials for drug delivery. *Exp. Opin. Ther. Patents* 11, 1395–1410.
- Ma, Z.J., Yamaguchi, M., 2001. Role of endogenous zinc in the enhancement of bone protein synthesis associated with bone growth of newborn rats. *J. Bone Miner. Metab.* 19, 38–44.
- Mazurin, O., 2007. Problems of compatibility of the values of glass transition temperatures published in the world literature. *Glass Phys. Chem.* 33, 22–36.
- Melville, A., Rodríguez-Lorenzo, L., Forsythe, J., 2008. Effects of calcination temperature on the drug delivery behaviour of Ibuprofen from hydroxyapatite powders. *J. Mater. Sci.—Mater. Med.* 19, 1187–1195.
- Merchant, H.A., Shoaib, H.M., Tazeen, J., Yousuf, R.I., 2006. Once-daily tablet formulation and in vitro release evaluation of cefpodoxime using hydroxypropyl methylcellulose: a technical note. *AAPS PharmSciTech* 7, Article, 78.
- Mistry, S., Kundu, D., Datta, S., Basu, D., 2010. Effect of alloplastic graft materials in treatment of periapical defects. *Clin. Dent.* 4, 53–59.
- Mosmann, T., 1983. Rapid colorimetric assay for cellular growth and survival: application to proliferation and cytotoxicity assays. *J. Immunol. Methods* 65, 55–63.
- Nair, M.B., Varma, H.K., Kumary, T.V., Babu, S.B., John, A., 2006. Cell interaction studies with novel bioglass coated hydroxyapatite porous blocks. *Trends Biomater. Artif. Organs* 19, 108–114.
- Nandi, S.K., Kundu, B., Ghosh, S.K., Mandal, T.K., Datta, S., De, D.K., Basu, D., 2009a. Cefuroxime-impregnated calcium phosphates

- as an implantable delivery system in experimental osteomyelitis. *Ceram. Int.* 35, 1367–1376.
- Nandi, S.K., Kundu, B., Mukherjee, P., Mandal, T.K., Datta, S., De, D.K., Basu, D., 2009b. In vitro and in vivo release of cefuroxime axetil from bioactive glass as an implantable delivery system in experimental osteomyelitis. *Ceram. Int.* 35, 3207–3216.
- Noble, L., Gray, A.I., Sadiq, L., Uchegbu, I.F., 1999. A non-covalently cross-linked chitosan based hydrogel. *Int. J. Pharm.* 192, 173–182.
- Park, Y., Kim, M.H., Park, S.C., Cheong, H., Jang, M.K., Nah, J.W., Hahm, K.S., 2008. Investigation of the antifungal activity and mechanism of action of LMWS-chitosan. *J. Microbiol. Biotechnol.* 18, 1729–1734.
- Pham, H.H., Luo, P., Genin, F., Dash, A.K., 2002. Synthesis and characterization of hydroxyapatite-ciprofloxacin delivery systems by precipitation and spray drying technique. *AAPS PharmSciTech* 3, E1.
- Rai, B., Teoh, S.H., Ho, K.H., 2005. An in vitro evaluation of PCL-TCP composites as delivery systems for platelet-rich plasma. *J. Control Release* 107, 330–342.
- Rodale, J.I., Taub, H.J., 1971. *Magnesium, The Nutrient that Could Change Your Life*. Pyramid Publications, New York.
- Rossi, S., Marciello, M., Sandri, G., Bonferoni, M.C., Ferrari, F., Caramella, C., 2008. Chitosan ascorbate: a chitosan salt with improved penetration enhancement properties. *Pharm. Dev. Technol.* 13, 513–521.
- Saint-Jean, S.J., Camire, C.L., Nevsten, P., Hansen, S., Ginebra, M.P., 2005. Study of the reactivity and in vitro bioactivity of Sr-substituted alpha-TCP cements. *J. Mater. Sci.—Mater. Med.* 16, 993–1001.
- Seeley, Z., Bandyopadhyay, A., Bose, S., 2008. Tricalcium phosphate based resorbable ceramics: influence of NaF and CaO addition. *Mater. Sci. Eng., C* 28, 11–17.
- Serra, J., Gonzalez, P., Liste, S., Serra, C., Chiussi, S., Leon, B., Perez-Amor, M., Ylanen, H.O., Hupa, M., 2003. FTIR and XPS studies of bioactive silica based glasses. *J. Non-Cryst. Solids* 332, 20–27.
- Slater, T., Sawyer, B., Strauli, U., 1963. Studies on succinate-tetrazolium reductase systems. III. Points of coupling of four different tetrazolium salts. *Biochim. Biophys. Acta* 77, 383–393.
- Soundrapandian, C., Datta, S., Sa, B., 2007. Drug-eluting implants for osteomyelitis. *Crit. Rev. Ther. Drug Carrier Syst.* 24, 493–545.
- Soundrapandian, C., Sa, B., Datta, S., 2009. Organic-inorganic composites for bone drug delivery. *AAPS PharmSciTech* 10, 1158–1171.
- Ubaidulla, U., Khar, R.K., Ahmad, F.J., Tripathi, P., 2009. Optimization of chitosan succinate and chitosan phthalate microspheres for oral delivery of insulin using response surface methodology. *Pharm. Dev. Technol.* 14, 96–105.
- Van de Belt, H., Neut, D., Schenk, W., van Horn, J.R., van Der Mei, H.C., Busscher, H.J., 2001. *Staphylococcus aureus* biofilm formation on different gentamicin-loaded polymethylmethacrylate bone cements. *Biomaterials* 22, 1607–1611.
- Xia, W., Chang, J., 2006. Well-ordered mesoporous bioactive glasses (MBG): a promising bioactive drug delivery system. *J. Control Release* 110, 522–530.
- Yagmur, M.F., Korkusuz, F., Guersel, I., Korkusuz, P., A˘rs, A., Hasirci, V., 1999. Sulbactam-cefoperazone polyhydroxybutyrate-co-hydroxyvalerate (PHBV) local antibiotic delivery system: In vivo effectiveness and biocompatibility in the treatment of implant-related experimental osteomyelitis. *J. Biomed. Mater. Res.* 46, 494–503.
- Yannas, I.V., 1992. Tissue regeneration by use of collagen-glycosaminoglycan copolymers. *Clin. Mater.* 9, 179–187.
- Yunos, D.M., Bretcanu, O., Boccaccini, A., 2008. Polymer-bioceramic composites for tissue engineering scaffolds. *J. Mater. Sci.—Mater. Med.* 43, 4433–4442.
- Zhang, X., Wyss, U.P., Pichora, D., Goosen, M.F., 1994a. Biodegradable controlled antibiotic release devices for osteomyelitis: optimization of release properties. *J. Pharm. Pharmacol.* 46, 718–724.
- Zhang, X., Wyss, U.P., Pichora, D., Goosen, M.F.A., 1994b. A mechanistic study of antibiotic release from biodegradable poly(D, L-lactide) cylinders. *J. Controlled Release* 31, 129–144.
- Zhu, Y., Kaskel, S., 2009. Comparison of the in vitro bioactivity and drug release property of mesoporous bioactive glasses (MBGs) and bioactive glasses (BGs) scaffolds. *Microporous Mesoporous Mater.* 118, 176–182.